University of Southampton

Faculty of Engineering and Physical Sciences
Institute of Sound and Vibration

MONTANA: a high-level noise prediction framework for Future Novel Aircraft

by

Daniel Constantinos Amargianitakis
BEng
ORCiD: 0000-0003-1381-2668

A thesis for the degree of
Doctor of Philosophy

February 17, 2024

University of Southampton

Abstract

Faculty of Engineering and Physical Sciences
Institute of Sound and Vibration

Doctor of Philosophy

MONTANA: a high-level noise prediction framework for Future Novel Aircraft

by Daniel Constantinos Amargianitakis

The motivation behind the research presented in this thesis is to establish noise considerations and assessment in the design process of air vehicles, as early as the preliminary design stage. This will allow noise emissions to have a driving role in the design choices. To enable such contributions, adequate models must be developed to deal with the significant data constraints, rapid iterative design procedures and turn around times, of the early design stages.

This thesis describes the development of MONTANA (**Mo**dular **N**ovel **T**ransport **A**ircraft **N**oise **A**ssessor) a high level noise framework for the assessment of novel aircraft, from their technologies, to operational considerations. MONTANA focuses the concept of a lumped source model that represents any given air vehicle, in terms of the individual noise source mechanisms. The lumped source model is then used in a multitude of ways to estimate cetification point levels, Noise-Power-Distance curves and airport community noise levels.

On the noise source level, focus is given on the development and validation of scaling laws for propeller/rotor tonal noise, for the prediction of changes in noise as a function of variation in design and operation. The procedure is then implemented within a total aircraft noise source to estimate Noise-Power-Distance curves for novel aircraft designs.

The second problem deals with the airport/community aspect of aircraft noise. The ISVR code RANE (Rapid Aviation Noise Evaluator) is updated to include, amongst others, the definition of three-dimensional aircraft directivity in the generation of noise surfaces, and consequently noise exposure footprints and contours. Modifications to the flight path generation model were included, to allow for novel VTOL (Vertical Takeoff and Landing) operations to be easily modelled and studied. Conical quadric surfaces were introduced as means of modelling quasi-static power setting variation. Finally, a source rotation model was implemented for a preliminary study into the transition phase of VTOL capable fixed wing aircraft.

Through a multi-level benchmarking process, in addition to two presented use-cases for assessment of regional hydrogen aircraft and fully-electric Advanced Air Mobility vehicles, MONTANA demonstrated the potential and usefulness in contributing towards identifying important trade-offs, quantifying the impact of design parameters and driving effective planning and decision-making.

Contents

List of Figures **xi**

List of Tables **xxiii**

Declaration of Authorship **xxv**

Acknowledgements **xxvii**

Symbols and Abbreviations **xxxiii**

1 Introduction **1**
1.1 Current state-of-the-art gaps and problems . . . 4
1.2 The MONTANA model . . . 5
1.3 Research Aims . . . 8
1.4 List of Original Contributions . . . 8
1.5 List of Publications . . . 9
1.6 Thesis Structure . . . 10

2 Aircraft and Airport Noise **13**
2.1 Whole Aircraft noise modelling . . . 13
2.1.1 Aircraft noise definitions . . . 13
2.1.2 Noise Levels . . . 14
2.1.3 Lumped source model: far-field acoustics . . . 14
2.1.4 Aircraft Noise metrics . . . 21
2.1.4.1 Noise certification metrics overview . . . 21
2.1.4.2 Available MONTANA output metrics . . . 22
2.1.4.3 Subjective and Non-subjective Metric Definitions . . . 23
2.1.5 Noise Certification and regulations . . . 28
2.2 Aircraft Noise Sources . . . 29
2.2.1 Conventional fixed wing noise sources and models . . . 30
2.2.1.1 Airframe . . . 31
2.2.1.2 Engine/Propulsion . . . 32
2.2.2 Conventional helicopter rotor noise sources . . . 34
2.2.3 Conventional noise source models . . . 35
2.2.4 Novel aircraft sources . . . 35
2.3 Propeller noise . . . 38
2.4 Noise propagation . . . 43
2.5 Aircraft operations . . . 44

2.5.1 Noise mitigation through operations . . . 45
2.6 Noise-Power-Distance curves . . . 46
2.7 Existing Prediction Tools . . . 50
2.7.1 Aircraft noise source models . . . 50
2.7.2 Airport noise frameworks and models . . . 51
2.8 Low noise design process and uncertainty quantification . . . 54
2.8.1 Design Considerations . . . 55
2.8.2 Uncertainty quantification . . . 55
2.9 Validation and Verification of tools . . . 55
2.10 Summary . . . 56

3 Novel aircraft and technologies 57
3.1 The advent of Electric aircraft . . . 57
3.1.1 Benefits and drawbacks of electric aircraft . . . 59
3.2 Hydrogen aircraft: potential future of civil aviation . . . 62
3.3 Innovative technologies . . . 63
3.3.1 Correlation to noise . . . 68
3.4 Summary . . . 69

4 Methodology I: Noise source model 71
4.1 Choice of baseline scenario/aircraft . . . 72
4.2 Lumped source model . . . 73
4.2.1 Differential Method: Working with changes in noise, ΔPWL . . . 74
4.2.2 Linear approximations to noise estimation models . . . 75
4.3 Propeller tonal noise variation . . . 79
4.3.1 Asymptotic approximation of frequency domain propeller tonal noise model . . . 80
4.3.2 Blade integral approximation . . . 90
4.4 Overall sound power . . . 95
4.5 Variation of propeller tonal noise . . . 98
4.6 Individual source directivities and spectral properties . . . 100
4.7 Generation of computational NPD curves . . . 101
4.8 Summary . . . 103

5 Methodology II: Airport noise model 105
5.1 Original RANE capabilities . . . 107
5.2 RANE v2 model overview . . . 110
5.3 Airport model . . . 111
5.3.1 Flight path discretisation . . . 111
5.3.2 Coordinate systems . . . 113
5.3.3 Flight path . . . 113
5.4 Analytical Principles of the noise surface . . . 116
5.4.1 Flyover procedure overview . . . 117
5.4.2 Case 1: Isotropic/omnidirectional sources . . . 120
5.4.3 Case 2: Directive Source in Polar angle, θ . . . 121
5.4.4 Case 3: Totally anisotropic sources . . . 122
5.4.5 Constructing the final footprint/contour . . . 124

5.5 Modelling Source directivity function using Spherical Harmonics 128
5.6 Power setting variation over time 133
5.7 Contour area 138
5.8 Contour Extremities 138
5.9 Finite Segment Correction 140
5.9.1 Derivation of finite segment correction for three-dimensional directivity patterns 142
5.9.2 Comparison between finite and infinite segments 146
5.10 Airport scenarios and aircraft fleet modelling 150
5.11 Summary 151

6 Methodology III: Rotating Source 153
6.1 Rotating source 153
6.1.1 Stationary (Hovering) aircraft 156
6.1.2 Flyover operation 159
6.1.3 Vertical takeoff/landing operation 161
6.1.4 Aircraft as a lumped noise source & directivity 162
6.1.5 Numerical Simulation 164
6.1.5.1 Discretisation 164
6.1.5.2 Noise surfaces from discretised observer locations 165
6.1.6 Implementation 166
6.1.6.1 Hover 166
6.1.6.2 Flyover 166
6.1.6.3 Vertical takeoff 172
6.2 Summary 188

7 Verification 191
7.1 Source Model verification 191
7.1.1 Absolute levels and harmonic shape 192
7.1.2 Comparison to Hanson frequency domain model 201
7.1.3 Propeller noise scaling parameters 207
7.1.4 Comparison between estimated and published NPD curves 209
7.1.5 Discussion: Sources of errors in outdoor aircraft noise prediction . 215
7.2 Airport noise model verification 223
7.2.1 Grid-point method 224
7.2.2 Comparison with AEDT 229
7.2.3 Discussion 240
7.3 Error analysis 245
7.3.1 Comparison between analytic and numerical integration of Directivity Functions 245
7.3.2 Linear approximation error analysis 245
7.4 Summary 249

8 Case Studies I: Next generation regional aircraft 251
8.1 Overview 251
8.2 Baseline regional aircraft 251
8.3 Concepts 253
8.4 Concept Performance 258

8.5 Noise source considerations . . . 259
8.5.1 Directivity and Installation effects . . . 262
8.5.2 Noise prediction risks . . . 263
8.6 Noise predictions . . . 264
8.6.1 NPD curves . . . 264
8.6.2 Discussion . . . 270
8.6.3 Certification points compared to baseline . . . 274
8.6.4 Single operation footprints . . . 277
8.7 Discussion & Final Remark . . . 280
8.8 Summary . . . 281

9 Case Studies II: Electric VTOL rotorcraft 283
9.1 Overview . . . 283
9.2 Mission Planning . . . 284
9.2.1 London VTOL network . . . 284
9.2.2 Vertical flight profiles . . . 287
9.3 Architecture and design space discussion . . . 289
9.3.1 Baseline Aircraft . . . 290
9.3.2 Design . . . 291
9.3.2.1 Subsystem considerations . . . 292
9.3.3 Performance . . . 293
9.4 Noise Predictions . . . 295
9.4.1 NPD curves . . . 296
9.4.2 Noise exposure contour maps . . . 298
9.4.3 Effect of noise source Directivity . . . 301
9.5 Summary . . . 305

10 Conclusions and Future studies 307
10.1 Recommendations for future research . . . 311

Appendix A PHOENICS: Preliminary sizing tool 313
Appendix A.1 Outline . . . 313
Appendix A.2 Background: Aircraft performance . . . 314
Appendix A.3 Propulsive efficiency in electric aircraft design . . . 317
Appendix A.4 Momentum Theory . . . 321
Appendix A.5 PHOENICS: Conceptual design tool . . . 322
Appendix A.6 PHOENICS: Performance estimation . . . 324
Appendix A.7 PHOENICS: Range estimation . . . 335

Appendix B Technical details and assumptions of the SAE AIR 1845 procedure for developing NPD curves 341

Appendix C Step by step methodology of applying the SAE AIR 1845 computational step 343

Appendix D Implementation of full Hanson frequency domain model for discrete propeller noise 345
Appendix D.1 Methodology Overview . . . 346

Appendix D.2 Propeller Performance 346
Appendix D.3 Hanson method for propeller harmonic noise 350
Appendix D.4 Validation 352

Appendix E Finite segment correction integrals. 357

Appendix F Individual noise source directivity data. 359

Bibliography 363

List of Figures

1.1 Detailed flow diagram of the MONTANA framework. 7

2.1 Diagram of point source radiating noise in three-dimensional acoustic field. Adapted from Blake [14]. 16
2.2 Diagram representing a single aircraft noise event and the associated noise metrics. 25
2.3 (A) Illustration of departure and approach noise contours and contour area as a function of the limits presented in the noise Chapters of Annex 16. (B) Example noise exposure, $L_{eq,T}$, contour for London Heathrow Airport for the year 2015. 28
2.4 Large aircraft certification reference points [34]. 29
2.5 Depiction of most relevant noise sources on-board of conventional turboprop and turbofan aircraft. 30
2.6 Evolution of engine noise strength from Low BPR all the way to modern Ultra-high BPR engines. 31
2.7 Comparison of component noise source levels during approach and takeoff for conventional turbofan. 33
2.8 Cross-sections of a HBP turbofan and a turboprop engine, identifying the individual noise source mechanisms present. 34
2.9 Example of SPL spectra for electric motor at 5,370 RPM. (Top) Motor only. (Bottom) Two-bladed propeller and motor. 37
2.10 Propeller Aerodynamic Noise breakdown. Adapted from [76]. 39
2.11 Geometry of rotating source and acoustic field. The rotating source position $\mathbf{y_i}$ vector is parametrically defined through the radial coordinate r_0 [60]. 39
2.12 Example harmonic content of propeller noise sources as predicted by implementation of the Hanson frequency domain model. 41
2.13 (A) Directivity index [dB ref $\theta = \pi/2$] of dipole (solid line) relative to a monopole (dashed line). (B) Dipole directivity (non-dimensional) factor version of A. (C) Directivity factors for loading and thickness noise as predicted by Hanson Equation 2.29. 42
2.14 Variation of broadband noise with Mach number and spanwise location on rotor blade. 43
2.15 Geometrical model of takeoff operation for airport noise predictions. . . . 44
2.16 Noise abatement takeoff climb procedures NADP 1 and 2, as suggested by the ICAO Doc 8168 [95]. 46
2.17 Illustration of actual experimental NPD flight operations. 47
2.18 Three type of flight Profiles for heliport operations. 49

2.19 Illustration of segmentation of a continuous flightpath. The green path represents the realistic continuous trajectory, while the red linear segments the discrete path. 52

3.1 Pipistrel Velis Electro, the world's first EASA Type-Certified electric aircraft. 59
3.2 Airbus ZEROe concept aircraft, from left to right: 1. Turbofan, 2. Turboprop, 3. Blended-wing body. 62
3.3 Various scaling laws for electric motors based on state-of-the-art automotive and industrial and high temperature superconductor motors. 65
3.4 Battery specific energy and density trends. 65
3.5 DEP concept renderings, from left to right: 1. NASA X-57 Maxwell, 2. Airbus EcoPulse™, 3. ISVR DEP Cessna 172 (model designed and rendered by author for illustration purposes). 67
3.6 The effect of the propeller wake velocities on the lift distribution of a blown relative to an unblown wing. Modified from [158]. 68

4.1 Flow diagram of the MONTANA noise source modelling framework. . . . 72
4.2 Bessel functions of the first kind as a function of blade passing frequency. The vertical dotted lines depict the position where the arguments of the Bessel function equals the order. Blade number, $B = 2$. 82
4.3 The large argument approximation for Bessel function order of 2 is compared to the actual Bessel function value, Blade number, $B = 2$. 82
4.4 The decaying term of the large argument approximation for Bessel function (blue) compared to the actual Bessel function value. The decaying term approximates the peaks of the Bessel function better as the argument goes to infinity. Blade number, $B = 2$. 83
4.5 The small argument approximation for Bessel function order of 2 and 4 is compared to the actual Bessel function value, Blade number, $B = 2$. . . . 83
4.6 Bessel function J_{mB}, its small argument asymptotic approximation and their derivatives for increasing tip Mach number. Depicted are three modes m of a two bladed propeller ($B = 2$) and a flight Mach number of 0.23. . 85
4.7 Thickness noise 85
4.8 Examples of chordwise loading distributions 87
4.9 The natural limits imposed on constant $\alpha_1, \alpha_2, \alpha_3$ for normal operating conditions. 88
4.10 The source term and Sectional Mach number varying as function of radial position for the first harmonic. Properties: Blade number $B = 2$, Flight Mach number $M_x = 0.3$ and Tip Mach number $M_t = 0.8$ 89
4.11 Integrand magnitude versus of the position along the propeller. The area under the graph represents the value of the integral. For low tip Mach numbers, as expected as the harmonic number increases the area decreases. 91
4.12 Geometrical setup during steady, level flyover operation between the moving aircraft and the stationary observer. 102

5.1 Flow diagram overview of RANE workflow. 106
5.2 Illustration of interpolation between two known power settings P_i and P_{i+1}, and two known distances d_i and d_{i+1} when working with tabulated NPD data. 108

5.3 Diagram visualising the concentric nature of noise surfaces of different SEL values. For a constant PWL output along the segment, the outermost surfaces represent low levels, while surfaces closer to the flight path have higher values. . . . 109
5.4 Detailed flow diagram of the proposed airport noise model. . . . 110
5.5 Three-dimensional flightpath segmentation. . . . 112
5.6 Two views of the three main coordinate systems used in RANE. Airport system (X, Y, Z), flight path/segment system $\mathbf{U} = (u, v, w)$ and orthogonal projection of $\mathbf{U}$, (x, y, z). . . . 114
5.7 Definition of the flightpath Cartesian coordinate system for each segment k, with respect to the orthogonal projection system (x, y, z) 114
5.8 Polar and azimuthal angles defining observer location. . . . 117
5.9 Two views of the flight path/segment system $\mathbf{U} = (u, v, w)$ and the flyover procedure. . . . 118
5.10 Diagrams illustrating the difference between noise surfaces resulting from iso-tropic and aniso-tropic noise sources. . . . 125
5.11 Illustrations of noise surfaces surrounding the flight path. . . . 127
5.12 Generic conical noise surface defined by lengths a and b. . . . 134
5.13 Conical noise surface coordinate shift. . . . 135
5.14 Flight path generated with three segments. . . . 136
5.15 Noise exposure contour for takeoff operation including thrust cut-back. Comparison between original RANE and version 2. . . . 136
5.16 Demonstration of power transition segment and its effect on the ground contour. . . . 137
5.17 Modelling of connecting regions through the use of Bezier curves. . . . 139
5.18 Two different cases of using Bezier curves to approximate segment connections compared to the grid-method (See following Section). . . . 140
5.19 Finite segment correction geometry diagram. . . . 143
5.20 Comparison of finite and infinite segment length on the noise radius. A spherical harmonic expansion with coefficients $A_\ell^m = [1\ 0\ 0\ 0]$ is used. Subplots indicate a range different values of the segment length to noise radius ratio. . . . 146
5.21 Comparison of finite and infinite segment length on the noise radius. A spherical harmonic expansion with coefficients $A_\ell^m = [1\ 0\ 0\ 1]$ is used. Subplots indicate a range different values of the segment length to noise radius ratio. . . . 147
5.22 Comparison of finite and infinite segment length on the noise radius. A spherical harmonic expansion with coefficients $A_\ell^m = [1\ 0.5\ 0\ 0]$ is used. Subplots indicate a range different values of the segment length to noise radius ratio. . . . 148
5.23 Comparison of finite and infinite segment length on the noise radius. A spherical harmonic expansion with coefficients $A_\ell^m = [1\ 1\ 1\ 1]$ is used. Subplots indicate a range different values of the segment length to noise radius ratio. . . . 149

6.1 Source and aircraft coordinate systems. . . . 154

6.2 Rotorcraft hovering at altitude h over an observer location (left) and a lumped acoustic source representation of the rotorcraft performing the same operation (right). Note, the acoustic source is rotating about its horizontal axis, representing the initiation of a transition to horizontal flight by the rotation of the rotor plane from parallel to perpendicular to the ground. 157
6.3 Diagram of simplified vertical takeoff operation. 162
6.4 Simple dipole source performing a two segment vertical takeoff operation. Purple rings indicate observer positions at equal distances from the two segments. Three observer locations are positioned on the ground, one directly under the horizontal flight path (green), one at $\varphi = 45^o$ w.r.t the vertical segment, and one at $\varphi = 90^o$. 162
6.5 Observer rings. 164
6.6 Observer locations relative to source position (left). Time histories of directivity function values as source rotates. (right). First column shows Y_1^0 rotating about y-axis, while second column Y_3^0 rotating about $\hat{\omega} = [0.57, 0.57, 0.57]$ axis. 167
6.7 Cumulative value of spherical harmonic at the observer locations for 6 different scenarios. The resulting noise surface is also shown for each case. 168
6.8 Noise exposure footprints for various source conditions. 169
6.9 Illustation of the flyover operation as performed by an ideal rotation dipole, indicated are the vertical planes on which rings of observer points are located. 170
6.10 Cartesian plots: Time history of spherical harmonic value directed at each observer. Polar plots: Cumulative value of the spherical harmonic as a result of a level flyover at each observer. Plots (a) to (f) show the variation in the cross-section along the length of the segment during a single flyover operation. 171
6.11 Estimated noise surface cross-sections. Each plot represents a single flyover operation. The different coloured lines indicate different locations along the x-axis. 172
6.12 Flyover noise surfaces. Cross-sections such as the one presented in Figure 6.11 are used to generate the three-dimensional surfaces. 173
6.13 Ground noise exposure footprints. The result of the intersection of the noise exposure surfaces in Figure 6.12 and the airport ground plane. . . . 174
6.14 Source coordinate time history. 175
6.15 Perspective of the source reference frame in three-dimensional space. The vector q and its orthogonal components are also illustrated. 176
6.16 Illustration of the source reference frame translating along the flightpath. The vector q indicates the position of an observer, on one of the rings, in the perspective of the source frame. The orthogonal components of vector q, q_1, q_2, q_3 are also illustrated. 177
6.17 Components of position vector $q = (q_1, q_2, q_3)$ indicating direction to the vertical rings of observers relative to the source. A side view of the flightpath (black) is embeded in the first sub-plot indicating the position of the observer ring (red). The lines representing q_1, q_2, q_3 are coloured depending on the specific observer on the ring, also embeded in the first sub-plot with each observer having its own colour and marker shape. . . . 178

6.18 Components of position vector $q = (q_1, q_2, q_3)$ indicating direction to the horizontal rings of observers relative to the source. A side view of the flightpath (black) is embeded in the first sub-plot indicating the position of the observer ring (red). The lines representing q_1, q_2, q_3 are coloured depending on the specific observer on the ring, also embeded in the first sub-plot with each observer having its own colour and marker shape. . . . 179
6.19 Time history of spherical harmonic,$|Y_1^0|$, value pointing in the direction of each observer location on the rings. A side view of the flightpath (black) is embeded in the first sub-plot indicating the position of the observer ring (red). The lines representing q_1, q_2, q_3 are coloured depending on the specific observer on the ring, also embeded in the first sub-plot with each observer having its own colour and marker shape. 180
6.20 Time history of spherical harmonic,$|Y_1^0|$, value pointing in the direction of each observer location on the rings. A side view of the flightpath (black) is embeded in the first sub-plot indicating the position of the observer ring (red). The lines representing q_1, q_2, q_3 are coloured depending on the specific observer on the ring, also embeded in the first sub-plot with each observer having its own colour and marker shape. 181
6.21 Time history of spherical harmonic,$|Y_3^0|$, value pointing in the direction of each observer location on the rings. A side view of the flightpath (black) is embeded in the first sub-plot indicating the position of the observer ring (red). The lines representing q_1, q_2, q_3 are coloured depending on the specific observer on the ring, also embeded in the first sub-plot with each observer having its own colour and marker shape. 182
6.22 Time history of spherical harmonic,$|Y_3^0|$, value pointing in the direction of each observer location on the rings. A side view of the flightpath (black) is embeded in the first sub-plot indicating the position of the observer ring (red). The lines representing q_1, q_2, q_3 are coloured depending on the specific observer on the ring, also embeded in the first sub-plot with each observer having its own colour and marker shape. 183
6.23 Noise surface cross-sections for vertical takeoff operation. Rotation of angle $\theta = \pi/2$ occurs during horizontal segment. 184
6.24 Cross-section of vertical (first column) and horizontal segments (second column). 185
6.25 Noise exposure surfaces generated for horizontal segment of takeoff operation. Vertical segment is accounted for in the calculation of the cumulative noise level on the observer rings surrounding the flightpath. 186
6.26 Noise exposure surfaces generated for vertical takeoff operation. The red surface represents the observer locations surrounding the vertical segment, while the blue surface the horizontal ones respectively. 187

7.1 Comparison of first 10 harmonics as predicted by four different methods for an average chord length of $c = 0.15$m. OASPL values are indicated in the box on the bottom left of each figure. 195
7.2 Comparison of first 10 harmonics as predicted by four different methods for an average chord length of $c = 0.15$m. A-weighting has been applied to the noise levels. OASPL values are indicated in the box on the bottom left of each figure. 196

7.3 Comparison of first 10 harmonics as predicted by ESDU 76020 model and the proposed fundamental and shape function method based on Hanson, for an average chord length of $c = 0.15$m. OASPL values are indicated in the box on the bottom left of each figure. 197
7.4 Comparison of first 10 harmonics as predicted by ESDU 76020 model and the proposed fundamental and shape function method based on Hanson, for an average chord length of $c = 0.15$m. A-weighting has been applied to the noise levels. OASPL values are indicated in the box on the bottom left of each figure. 198
7.5 Comparison of first 10 harmonics as predicted by four different methods for an average chord length of $c = 0.20$ m. OASPL values are indicated in the box on the bottom left of each figure. 199
7.6 Comparison of first 10 harmonics as predicted by four different methods for an average chord length of $c = 0.20$m. A-weighting has been applied to the noise levels. OASPL values are indicated in the box on the bottom left of each figure. 200
7.7 Parametric study on the accuracy of the small argument Bessel function approximation relative to analytic solution for harmonic loading noise as given by Hanson. Operation parameters are given in annotation within the figures. 202
7.8 Parametric study on the accuracy of the small argument Bessel function approximation relative to analytic solution for harmonic loading noise as given by Hanson. Operation parameters are given in annotation within the figures. 202
7.9 Estimated change in the fundamental tone as a function of axial loading and propeller rotation speed (rpm). The $z = 0$ plane is indicated with grey colour. 204
7.10 Estimated change in OASPL between a baseline case and a modified (novel) scenario for various loading conditions. Comparison is made between original Hanson model and MONTANA in estimating changes, and error (difference) between the two models is given on the right-hand axis. 205
7.11 Estimated change in OASPL between a baseline case and a modified (novel) scenario for various propeller rotation speeds. Comparison is made between original Hanson model and MONTANA in estimating changes, and error (difference) between the two models is given on the right-hand axis. 206
7.12 Estimated change in the harmonics relative to the fundamental tone as a function of axial loading. The $z = 0$ plane is indicated with grey colour. . 206
7.13 Estimated change in the harmonics relative to the fundamental tone as a function of flight Mach number. The $z = 0$ plane is indicated with grey colour. 206
7.14 Estimated change in the harmonics relative to the fundamental tone as a function of propeller rotation speed (rpm). The $z = 0$ plane is indicated with grey colour. 207
7.15 Individual propeller noise sources as function of observer polar location. Sound pressure of fundamental tone (m = 1) indicated for a range of rotation speeds. Scaling laws indicated in top right axis, showing the collapsed results. 208

7.16 Total propeller harmonic noise as function of observer polar location. Sound pressure of fundamental tone (m = 1) indicated for a range of rotation speeds. Scaling laws indicated in top right axis, showing the collapsed results. 209
7.17 Comparison between the predicted (by MONTANA) and published (measured) departure NPD curves for the Cessna 172. 210
7.18 Comparison between the predicted (by MONTANA) and published (measured) departure NPD curves for the BN-2 Islander. 210
7.19 Comparison between the predicted (by MONTANA) and published (measured) departure NPD curves for the DHC-6 Twin Otter. 210
7.20 Comparison between the predicted (by MONTANA) and published (measured) departure NPD curves for the ATR42-600. 211
7.21 Comparison between the predicted (by MONTANA) and published (measured) departure NPD curves for the ATR72-212A. 211
7.22 Comparison between the predicted (by MONTANA) and published (measured) departure NPD curves for the DHC-8 (Dash 8) Q400. 211
7.23 Comparison between the predicted (by MONTANA) and published (measured) departure NPD curves for the Airbus A400M. 212
7.24 Comparison between the predicted (by MONTANA) and published (measured) departure NPD curves for the Schweiser 300C helicopter. 214
7.25 Comparison between the predicted (by MONTANA) and published (measured) departure NPD curves for the Aerospeciale SA 365N Dauphin helicopter. 215
7.26 Comparison between the predicted (by MONTANA) and published (measured) departure NPD curves for the Boeing Vertol 234 helicopter. 216
7.27 NPD departure predictions (continuous lines) for the De Havilland Canada Dash 8-300 using four different baseline aircraft. The predicted NPD curves are compared to published NPD data. 217
7.28 Set-up of grid-point method flight path and receivers. 224
7.29 Discretisation example of flightpath segments for grid-point method. . . . 225
7.30 An example contour map calculated using the grid method. 226
7.31 The 70 dB SEL contour of an isotropic source. Contour area comparison between RANE v2 and the grid-point method. 227
7.32 The 75 dB SEL contour of an isotropic source, conventional Take-off with cutback. Contour area comparison between RANE v2 and the grid-point method. 228
7.33 Isotropic source during vertical take-off. 229
7.34 Vertical flight profile for various fixed wing aircraft. 233
7.35 Comparison between the RANE v2 and AEDT 3c prediction for fixed wing aircraft. 234
7.36 Comparison between the RANE v2 and AEDT 3c prediction for fixed wing aircraft. 235
7.37 Comparison between the RANE v2 and AEDT 3c prediction for fixed wing aircraft. 236
7.38 Comparison between the RANE v2 and AEDT 3c prediction for fixed wing aircraft. 237
7.39 Vertical flight profile for the Eurocopter AS365 Dauphin for departure. . . 239

7.40 Procedure of treating numerical data as inputs to RANE v2. The output spherical harmonic expansion of Figure 7.40b is then used to generate the required noise surfaces. 240
7.41 (Left) SEL Noise-Power-Distance curves for the Boeing Vertol 234 for a constant speed departure. The three curves indicate three lateral locations of observers. The green crosses indicate the intersection of the 55 dB SEL line with the curves. These points are used to generate a polynomial function that describes the variation in the azimuthal direction (Right). . 241
7.42 Comparison between the RANE v2 and AEDT 3c prediction for three different helicopters. 242
7.43 Departure SEL noise exposure contour map for Boeing CH-47 Chinook. Comparison between AEDT and RANE predictions. 243
7.44 Comparison of the analytical and numerical calculation of the integral in Equation 5.47 for four different directivity functions of which the coefficients from left to right are: $A_\ell^m = [1\ 0\ 0\ 0]$, $A_\ell^m = [0\ 0\ 0\ 1]$, $A_\ell^m = [1\ 1\ 0\ 0]$, $A_\ell^m = [1\ 1\ 1\ 1]$. 245
7.45 First order Taylor series (linear) approximation of the Hanson model. The tangent line slopes are calculated using the partial derivative w.r.t each parameter $\Delta\eta_j$. Baseline parameters shown, $D = 1.4m$, $B = 4$, $M_x = 0.4$, RPM = 2000. 248
7.46 Approximation error as a function of change in parameters $\Delta\eta_j$. 249

8.1 Small regional aircraft. 252
8.2 Large regional aircraft. 253
8.3 General arrangement of Concept A1, with gaseous hydrogen supplied fuel cell electric propulsion [215]. 255
8.4 Renderings of Concepts B7 and B8. 256
8.5 Predicted departure NPD curve for Concept A1 (solid line) compared to the baseline Islander departure NPD curves (dashed lines). 265
8.6 Predicted departure NPD curve for Concept B4 (solid line) compared to the baseline Twin Otter departure NPD curves (dashed lines). 266
8.7 Predicted departure NPD curve for Concept B7 (solid line) compared to the baseline Twin Otter departure NPD curves (dashed lines). 266
8.8 Predicted departure NPD curve for Concept B8 (solid line) compared to the baseline Twin Otter departure NPD curves (dashed lines). 266
8.9 Predicted departure NPD curve for Concept G1 (solid line) compared to the baseline Twin Otter departure NPD curves (dashed lines). 267
8.10 Predicted departure NPD curve for Concept D1 (solid line) compared to the baseline ATR72-600 departure NPD curves (dashed lines). 267
8.11 Predicted departure NPD curve for Concept Z1 (solid line) compared to the baseline A320neo departure NPD curves (dashed lines). 267
8.12 Predicted approach NPD curves for Concept A1 (solid line) compared to the baseline Islander approach NPD curves (dashed lines). 268
8.13 Predicted approach NPD curves for Concept B4 (solid line) compared to the baseline Twin Otter approach NPD curves (dashed lines). 268
8.14 Predicted approach NPD curves for Concept B7 (solid line) compared to the baseline Twin Otter approach NPD curves (dashed lines). 269
8.15 Predicted approach NPD curves for Concept B8 (solid line) compared to the baseline Twin Otter approach NPD curves (dashed lines). 269

8.16 Predicted approach NPD curves for Concept G1 (solid line) compared to the baseline Twin Otter approach NPD curves (dashed lines). 269
8.17 Predicted approach NPD curves for Concept D1 (solid line) compared to the baseline ATR72-600 approach NPD curves (dashed lines). 270
8.18 Predicted approach NPD curves for Concept Z1 (solid line) compared to the baseline approach NPD curves (dashed lines). 270
8.19 Difference in concept flyover certification level relative to reference aircraft and margin to corresponding limits. 275
8.20 Difference in concept flyover certification level relative to reference aircraft and margin to Chapter 10 limit. 275
8.21 Summary of certification level for larger regional concepts. Chapter 14 limits for flyover, lateral and approach certification points are indicated for reference as well as the level of the baseline aircraft. 276
8.22 SEL noise footprint comparison for one approach and one departure operation of the baseline B-N Islander and Concept A1. Calculations for baseline aircraft performed with AEDT and RANE. 278
8.23 SEL noise footprint comparison for one approach and one departure operation of the baseline DHC-6 Twin Otter and Concept B8. Calculations for baseline aircraft performed with AEDT and RANE. 278
8.24 SEL noise footprint comparison for one approach and one departure operation of the baseline ATR42-600 and Concept D1. Calculations for baseline aircraft performed with AEDT and RANE. 278
8.25 SEL noise footprint comparison for one approach and one departure operation of the baseline A220-100 and Concept Z1 (Rolls-Royce plc). Calculations for baseline aircraft performed with AEDT and RANE. . . . 279

9.1 Conformed and proposed AAM network operating in the south-west of Germany currently being designed and studied by Lilium and partners. . 284
9.2 The busiest London underground stations of passengers in 2019 and 2020 (in million entries and exits). 285
9.3 Map of Greater London, identifying possible locations for vertiports in a future AAM network. All five major London airports are included. Red dots show these possible locations. 286
9.4 Map of central London, identifying possible locations for vertiports in a future AAM network. Red dots show these possible locations. 287
9.5 London inner city AAM network. 287
9.6 Vertical flight profiles possibilities. Flight altitude is determined by total distance covered. 289
9.7 Three-dimensional illustration of network connections and the trajectories of aircraft operating the inner city connection network. 289
9.8 Baseline aircraft, Bell 429 GlobalRanger. 291
9.9 Forward flight performance of Concept 1 rotorcraft. 294
9.10 Forward flight performance of Concept 2 rotorcraft. 295
9.11 Forward flight performance of Concept 3 rotorcraft. 295
9.12 Departure NPD curves generated with MONTANA for all Concept rotorcraft. 296
9.13 Approach NPD curves generated with MONTANA for all Concept rotorcraft. 297
9.14 Flyover NPD curves generated with MONTANA for all Concept rotorcraft. 297
9.15 Hover NPD curves generated with MONTANA for all Concept rotorcraft. 297

9.16 65dB SEL sound exposure contour comparison between the three Concept air vehicles. . . . 298
9.17 SEL sound exposure contour map for Concept 1. Inner city network. . . . 300
9.18 SEL sound exposure contour map for Concept 2. Inner city network. . . . 300
9.19 SEL sound exposure contour map for Concept 3. Inner city network. . . . 301
9.20 Visual illustration of the Y_2^2 spherical harmonic. The distance of any point on the surface from the origin equals the value of the spherical harmonic at that location defined by (θ, φ). . . . 302
9.21 SEL sound exposure contour maps for Concept 3, using with the directivity function defined as $D(\theta, \varphi) = Y_2^2(\theta, \varphi)$. Inner city network. . . . 302
9.22 Visual illustration of the spherical harmonic expansion given by coefficients of Table 9.3. The distance of any point on the surface from the origin equals the value of the spherical harmonic expansion at that location defined by (θ, φ). Data from [185]. . . . 303
9.23 SEL sound exposure contour maps for Concept 3, using with the directivity function defined as a spherical harmonic expansion using coefficients measured by Krebbs et al. Inner city network. . . . 304
9.24 SEL sound exposure contour maps for Concept 3, using with the directivity function defined as a spherical harmonic expansion using static directivity data for a Boeing Vertol. Inner city network. . . . 304

Appendix A.1 Schedule of the civil aeroplane development process. . . . 314
Appendix A.2 Primary forces acting on fixed wing aircraft (A) and rotorcraft during hover (B) and forward flight (C). . . . 315
Appendix A.3 Typical constraint analysis diagram indicating the possible design space for a fixed wing aircraft. Combination of T/W and W/S that lie in the white region constitute viable design. . . . 316
Appendix A.4 Calculated wing-loading versus thrust-to-weight-ratio diagram. The indicated design point is that of a Cessna 172 Skyhawk. . . . 316
Appendix A.5 Helicopter power required for level flight at a given gross weight and altitude. . . . 317
Appendix A.6 Illustration of a propulsive device moving through stationary air with velocity V_∞ . . . 318
Appendix A.7 Comparison of the hover efficiency of various aircraft designs. . 320
Appendix A.8 Figure generated using Equation A.7. . . . 321
Appendix A.9 Diagram of conceptual design flowchart as performed in this thesis. The methodology is applied to both fixed-wing and rotorcraft vehicles. . . . 323
Appendix A.10 Force balance diagram for aircraft following arbitrary tree-dimensional flightpath. The vertical (left) and horizontal (right) planes are shown. . . . 325
Appendix A.11 Force diagram of fixed-wing aircraft in the takeoff operation. Momentum theory considerations are also shown. . . . 327
Appendix A.12 Force diagram of fixed-wing aircraft in the steady, level cruise operation. Momentum theory considerations are also shown. . . . 329
Appendix A.13 Force diagram of fixed-wing aircraft in the climb operation. Momentum theory considerations are also shown. . . . 330
Appendix A.14 Force diagram of rotorcraft vehicle in a hover operation. Momentum theory considerations are also shown. . . . 332

Appendix A.15 Solution to the inflow equations A.49 and A.50 for a series of forward speeds, using two different numerical solutions. 334
Appendix A.16 Force diagram of rotorcraft vehicle in a forward flight operation. Forward flight accounts for climb and decent operations. Momentum theory considerations are also shown. 335

Appendix D.1 Flowchart showing the general overview of the main processes involved in the implementation of the Hanson method. 346
Appendix D.2 Flowchart of the performance calculation process in order to generate the appropriate inputs for the Hanson method. 350
Appendix D.3 Lift and drag axes in advance direction and including induced flow [60]. Note that the term z is also referred to as r/R 351
Appendix D.4 Velocity diagram including the induced velocity. 351
Appendix D.5 SR-2 propeller design characteristics. 353
Appendix D.6 Validation of performance parameters of the propeller at various operational conditions. Flight Mach number is set to $M_x = 0.1$ and 75% pitch set to 38 deg. Literature data from [260]. 353
Appendix D.7 Radial lift distribution for the same conditions as Figure D.6 and an advance ratio of $J = 1.4$, representing tip relative Mach number of $M_t \approx 0.24$ 354
Appendix D.8 Comparison of the fundamental tone and OASPL polar directivity prediction versus literature data [259]. Conditions replicated, $J = 0.423$, $M_t = 0.67$ and $M_x = 0.09$ 354
Appendix D.9 Comparison of far-field OSPL polar directivity prediction versus literature data [261]. 355

Appendix F.1 Fan inlet noise directivity index [53, 20]. 360
Appendix F.2 Fan discharge noise directivity index [53, 20]. 360
Appendix F.3 Single stream jet noise direcitivity adjustment [262, 263, 20]. . 361
Appendix F.4 Dual stream jet noise directivity adjustment [264, 265, 20]. . . 361

List of Tables

1.1 Noise Goals Expressed as EPNdB below Chapter 14 levels. ICAO Environmental Report 2019. 2

2.1 Summary of component level noise prediction methods. 36

3.1 Megawatt-scale electric Machine developments sponsored by NASA, [149]. 64

5.1 Flightpath segment parameters. 136

6.1 Parameters defining flyover operation. 170
6.2 Parameters defining takeoff operation. 175

7.1 Design and operation characteristics of the Cessna 172 194
7.2 Propeller powered aircraft performance inputs used for verification study. 212
7.3 Continuation of Table 7.2. 212
7.4 Helicopter performance inputs used for verification study. 213
7.5 List of basic performance and design parameters of the Dash 8 Q400 and the baseline aircraft of choice. 215
7.6 Example input parameter table for conventional procedures of an omnidirectional noise source. 227
7.7 Example input parameter table for vertical take-off procedures of an omnidirectional noise source. 228
7.8 Fixed wing aircraft used for benchmarking RANE v2. 231

8.1 Design and performance parameter overview for concepts developed by project NAPKIN. 254
8.2 Power setting range assumptions for the approach operation, and NPD calculation. 259
8.3 Summary of installation effect noise corrections for ducted-fan and propeller propulsion systems. 263
8.4 Potential unaccounted for noise sources. 264
8.5 Predicted noise margins expressed as cumulative EPNdB below reference aircraft noise levels for project NAPKIN concepts. 280
8.6 Predicted noise margins expressed as cumulative EPNdB below Chapter 14 levels for project NAPKIN concepts 280

9.1 Design characteristics of the Concepts. 294
9.2 Performance characteristics of the Concepts. 295
9.3 Spherical harmonic directivity coefficients A_ℓ^m of the 500 Hz one-third Octave band for a fixed-wing turbofan aircraft. Data from [185]. 303

Declaration of Authorship

I declare that this thesis and the work presented in it is my own and has been generated by me as the result of my own original research.

I confirm that:

1. This work was done wholly or mainly while in candidature for a research degree at this University;
2. Where any part of this thesis has previously been submitted for a degree or any other qualification at this University or any other institution, this has been clearly stated;
3. Where I have consulted the published work of others, this is always clearly attributed;
4. Where I have quoted from the work of others, the source is always given. With the exception of such quotations, this thesis is entirely my own work;
5. I have acknowledged all main sources of help;
6. Where the thesis is based on work done by myself jointly with others, I have made clear exactly what was done by others and what I have contributed myself;
7. None of this work has been published before submission

Signed:..... Date:.....

Acknowledgements

First, I would like to thank my supervisor Prof. Rod Self for giving me the opportunity to join a great research group and introducing me to the field of aircraft noise and aeroacoustics. His advice, guidance and honesty allowed me to develop my critical thinking and articulation, skills crucial for my journey in research.

Next, my gratitude goes to my supervisors Dr. Antonio Torija and Dr. Athanasios Synodinos, for the continuous support, feedback and insights on my work, despite their difficult schedules. Their great experience and knowledge of the field, gave meaning and structure to my work.

Last on the list of advisors, but definitely not least, I would like to thank Dr. Anderson Proença. Thanks for the great conversations and advice on academic and personal topics. Hopefully way more to come in the future over a pint.

I extend my appreciation to all the members of the ISVR UTC that shared an office with me. I learned a lot from great the conversations at the coffee breaks and made my time as a PhD student an experience I will cherish forever. Additionaly, I would like to thank my current colleagues in the Rolls-Royce Noise Engineering team, for understanding and supporting me durring the writting of this thesis.

Additionally, I would like to thank project NAPKIN and all the members of the consortium for the feedback on my work, as well as providing various forms of data.

To all my friends and basketball teammates who inspired me in one way or another, thank you! You all contributed, in some form or another. To Eva, thanks for the support, encouragement and patience you showed me over the course of this work and write-up.

Finally, I would like to thank my mother and brother, for the love, support and belief they have always shown me.

To my mother and grandmother

“ *Ὁ βίος βραχύς, ἡ δὲ τέχνη μακρή, ὁ δὲ καιρὸς ὀξύς, ἡ δὲ πεῖρα σφαλερή, ἡ δὲ κρίσις χαλεπή.* ”

Ιπποκράτης,

“ *Life is short, and art long, opportunity fleeting, experimentations perilous, and judgment difficult.* ”

Hippocrates,

Symbols and Abbreviations

Symbols

A	Propeller disk Area
A_T	Total noise contour area due to the total of N
B	number of blades
c_0	ambient speed of sound, (m s^{-1})
C	$= \rho_0 c_0/(4\pi p_{ref}^2)$, constant
C_D	Drag Coefficient
C_L	Lift Coefficient
C_T	$= T/qA$Thrust Coefficient given by momentum theory
$D(\theta, \phi)$	Directivity factor
D	propeller diameter, (m)
E_a	Acoustic energy, Joules
E^*	Batteries specific energy
F_1	spectral shape function
I	Acoustic intensity
J	Advance ratio
J_{mB}	Bessel function of the first kind, of order $= mB$
K	Total number of flight segments
L	Event sound-level (scale undefined)
$L_{A,max}$	Maximum A-weighted level
$L_{E,ajk}$	Single event noise exposure level contribution from each segment k of each flight track j and for each aircraft a within the fleet
L_E	Single event sound exposure level (SEL)
$L_{eq,T}$	Energy-equivalent sound-level integrated over the period T
L_{eq}	Energy Equivalent sound level
L_{f_1}	sound pressure level of fundamental tone, (dB)
L_{max}	Maximum sound-level during an event
L_p	Sound Pressure Level, dB
L_w	Sound Power Level, dB
M	Mach number
M_h	$= \sqrt{M_T^2 + M_x^2}$, helicoidal (advance) Tip Mach number
M_r	$= \sqrt{z^2 M_T^2 + M_x^2}$, blade section Mach number

M_t	$= \Omega R_t / c_0$, tip rotational Mach number
M_x	$= V / c_0$, flight Mach number
M_{eff}	Effective tip Mach number
$\mathbb{P}_{rad}$	Acoustic sound power, Watts
$\mathbb{P}_{ref}$	$= 10^{-12}$ Watts, reference power
P	Power; Power-setting parameter in NPD analysis
P_{mB}	complex Fourier coefficient of p
R	distance between observer and propeller
R_n	Noise Radius
R_t	propeller radius, (m)
R_{ac}	Electric vehicle range
T	Time period; event duration
T_0	Reference time for integrated sound level
W	Weight
$\mathcal{W}$	Weighting coefficients
$\bar{C_L}$,$\bar{C_D}$	average section lift and drag coefficients
$\bar{t_b}$	average maximum thickness to chord ratio
$\mathbf{S}$	Orthogonal matrix
$\mathbf{U}$	$= (u\ v\ w)^T$, Position vector
d_p	Perpendicular distance from an observation point to the flight path (slant distance)
d_λ	Scaled distance
f	Frequency; or Mathematical function
f_L	Loading noise spectral shape function
f_V	Thickness noise spectral shape function
h	Altitude
k	Wavenumber
k_x and k_y	axial and radial wavenumbers
l	Perpendicular distance from an observation point to the ground track
m	Harmonic number
n	Number of sources
n_s	Propeller index, or RPM/60
p	sound pressure, (Pa)
p_{ref}	$= 20\mu Pa$, Reference effective acoustic pressure
p_{rms}	Effective (root-mean-square) pressure
q	Dynamic Pressure
r_{ref}	= 1 m, Directivity sphere reference radius
s	Segment length
t	time
v, V	Airspeed
v_{ref}	Reference airspeed for which NPD data are defined
ini,end	Limits of integration

len	Length of the noise contour

Greek Letters

α	Parameter used for calculation of the finite segment correction ΔF
α_1	Loading noise Bessel function constant
α_2	Thickness noise Bessel function constant
α_3	Thickness noise chordwise wavenumber constant
β	Elevation angle of aircraft relative to ground plane
γ	Inclination angle
$\Gamma(l)$	Lateral attenuation distance factor
δ_f	Flap deflection angle
$\Delta\ x$	Displacement in the x dimension as a consequence of the different inclination angles (γ)
ΔF	finite segment correction
ΔI	Engine-installation effects adjustment
Δt	Time increment
Δv	Duration adjustment
$\Delta x, \Delta y$	Displacement in the x and y directions, respectively
Δ	indicates change in noise level, (dB)
ΔL_{f_1}	Change in noise level of fundamental tone
$\eta_{(...)}$	Noise source parameters
η_p	$= Jk_T/k_P$, Propeller Efficiency
θ	Polar directivity angle
κ	Flight track specifier
$\Lambda(\beta)$	Long range air-to-ground lateral attenuation
Λ_y	(Orthogonal) rotation matrix
$\Lambda(\beta, l)$	Lateral attenuation adjustment
Λ_T	Total lateral adjustment
ρ	radial coordinate
ρ_0	density of the fluid, (kg m^{-3})
ϕ	Depression angle
ψ	Angle of rotation in the horizontal plane
φ	Azimuthal directivity angle
Ψ_D, Ψ_L, Ψ_V	transforms of drag, lift and thickness source terms
ω	Blade-passing rate
Ω	Propeller rotation rate

Coordinate Systems & Vectors

u, v, w	Orthogonal coordinate system with the u axis is aligned with the k^{th} flightpath segment, with position vector $\mathbf{U} = (u\ v\ w)^T$
X, Y, Z	Common orthogonal coordinate system for all k flightpath

	segments, Airport system
x, y, z	Orthogonal coordinate system for each k^{th} flightpath segment with the x axis parallel to the airport system X axis, with position vector $\mathbf{X} = (x\ y\ z)^T$
θ, φ, r	Spherical coordinate system representing lumped source emission angles and distance used for NPD flyover procedures and lateral attenuation definition.
θ, φ, r	Source frame spherical coordinate system, in the context of Chapter 6
Θ, Φ, R	Aircraft frame spherical coordinate system, in the context of Chapter 6
d_p, φ, u	Cylindrical coordinate system for each k^{th} flightpath segment, in the context of Chapter 6

Subscripts

0	Baseline Aircraft
a	Aircraft
i	Individual noise source
j	Flight track; individual parameter influencing noise source i
k	Individual flight track segment
m	Number of aircraft movements
n	Common flight track segments for the whole aircraft fleet

Abbreviations

AAM	Advanced air mobility
ACARE	Advisory Council For Aeronautics Research In Europe
AEDT	Aviation Environmental Design Tool
ANP	Aircraft noise & performance
AR	Aspect Ratio
ATC	Air Traffic Control
BHP	Break horsepower
BPF	Blade Passing Frequency
BPF	Blade passing
CAA	Civil Aviation Authority
CG	Centre of Gravity
CNT	Corrected net thrust
CP	Certification Point
CS	Certification Specifications
DEP	Distributed Electric Propulsion
DP	Distributed Propulsion
EASA	European Aviation Safety Agency
EASA	European Aviation Safety Agency
ECAC	European Civil Aviation Conference

ECAC	European civil aviation conference
EPNL	Effective perceived noise level
ESDU	Engineering Sciences Data Unit
FAA	Federal Aviation Administration
FAR	Federal Aviation Regulations
GA	General aviation
HMA	Heliport Manoeuvre Area
ICAO	International Civil Aviation Organization
IFR	Instrument flight rules
IGE	In ground effect
INM	Integrated Noise Model
ISO	International Standards Organization
L/D	Lift to Drag ratio
MLW	Maximum Landing Weight
MST	Maximum static thrust
MTOM	Maximum Takeoff Mass
MTOW	Maximum Takeoff Weight
NAPKIN	New Aviation, Propulsion, Knowledge and Innovation Network
NPD	Noise-Power-Distance
OASPL	Overall Sound Pressure Level
OEW	Overall Empty Weight
OGE	Out of ground effect
PAX	Passengers
PNL	Perceived Noise Level
PNLT	Tone Corrected Perceived Noise Level
PWL	Sound Power Level
PWL	Sound Power Level
QC	Quota Count
RANE	Rapid Aviation Noise Evaluator
SA	Sustainable Aviation
SAE-AIR	Society of Automotive Engineers - Aerospace Information Report
SARP	Standards and Recommended Practices
SEL	Sound exposure level
SFC	Specific Fuel Consumption
SPL	Sound Pressure Level
STOL	Short Takeoff And Landing
TCDS(N)	Type certificate data sheet (for Noise)
UAM	Urban air mobility
UAV	Unmanned aerial vehicles
UKRI	UK Research and Innovation government agency
VFR	Visual flight rules

VTOL	Vertical Takeoff And Landing
WP	Waypoint
eVTOL	electric Vertical Takeoff & Landing

Chapter 1

Introduction

Aircraft manufacturers and research engineers have reached a point in the acoustical treatment of aircraft components where reductions of tenths of a decibel are considered great accomplishments. These reductions, as important as they are, will not be enough to accommodate the ambitious aircraft noise reduction goals set by several organisations. The idea that aircraft have to be designed from the bottom up with their acoustical impact as one of the main driving design parameters is dominating. Simultaneously, the rapid development of the Advanced Air Mobility (AAM) sector, a market that promises great benefits to the community but also great threats in terms of operation and noise immissions, also requires the design of air vehicles that consider noise as a priority.

In an effort to drive low emission design of air vehicles worldwide, manufactures, aviation agencies and councils are collectively setting new industry standards. Part of this effort, is directed towards noise immissions, and is reflected by the ambitious goals and regulations set by ACARE [1], NASA [2, 3], EASA [4] and ICAO [5, 6]. Table 1.1 summarises the noise goals set by the ICAO for various classifications of aircraft. Technological improvements, fleet renewal and increased operational efficiency have been able to partially counterbalance the impact of recent growth in flight numbers and therefore noise output. However, integration of new categories of aircraft must be done with care to avoid undermining progress in mitigating environmental and noise impacts.

As a clarification, in the context of noise, the terminology *immissions* is adopted throughout this thesis, meaning the total aircraft noise levels as perceived at ground-based observers, whereas *emissions* describe the aircraft noise levels as generated at the source.

The growth in the aviation industry [7], [8] is closely followed by numerous global organisations and research institutions for its environmental impact. Global climate change is driving industries to adopt net-zero carbon emissions strategies by implementing renewable energy alternatives and forcing advancements in fuel use

Table 1.1: Noise Goals Expressed as EPNdB below Chapter 14 levels. ICAO Environmental Report 2019.

Noise goals (Δ dB)				
EIS Date	Business Jet	Regional Jet	Single Aisle	Twin Aisle
2027	10.0	14.5	15.5	19.5
2037	15.0	17.0	24.0	26.5

efficiencies. In the UK aviation world, projects such as the ATI's (Aerospace Technology Institute) FlyZero [9] or the UKRI (UK Research and Innovation) future flight challenge, are striving to develop the strategies, the technologies and the computational tool capabilities to meet the stringent noise and emissions reduction goals set by ACARE, NASA and ICAO. In summer of 2022, the UK Department for Transport (DfT) published the Jet Zero Strategy [10] on how the UK aims to neutralise the impact of aviation on the planet. Jet Zero addressed technologies such as SAF (sustainable aviation fuel) with short term implementation strategies, all the way to hydrogen and electric flight demonstrators and publicly funded research and developments projects to accelerate the transition.

The introduction of future novel aircraft therefore depends on a few key factors:

- Efficient and Quiet Vehicles: Research and development of technologies and configurations that optimise performance and speed and minimise noise and cost.
- Increased design freedom: design aircraft that effectively take advantage of the benefits of fully electric and hybrid electric technologies.

To achieve this, NASA in their "Strategic Implementation Plan" document [2] notes as a significant priority the development of computational, experimental, and analytical tools and methods to allow rapid design, and validation of a broad range of innovative vertical lift air vehicles.

Current design practices often disregard noise considerations early in the conceptual phase. Aircraft costumer requirements and economic viability drive the design, whereas noise may often wrongly be considered as a secondary parameter. This leads to noise being considered late in the design process, and for it to be assessed as a consequence of achieving other design goals. Concepts therefore are not optimised for noise with the same rigour as performance.

The second reason for noise consideration being omitted at the early design stages lies in the nature of aerodynamically generated noise. Noise may be regarded as an unwanted consequence of meeting other design deliverables. Characterising it as a "consequence" entails knowledge of the mechanisms and geometry responsible for the noise are required

before it may be studied. Noise tools, to do so, may be characterised into two main categories, noise source prediction tools and community/airport noise tools.

Current state-of-the-art noise source tools trade complexity and high computational and time requirements in exchange for increased accuracy. Hybrid models combine numerical aerodynamic simulations with analytic, semi-empirical or even further numerical models for the acoustics in order to capture the exact physics leading to noise. Although accurate and insightful, the application of such tools at the conceptual level is practically impossible. Additionally, airport noise tools used throughout industry and academia require large datasets of aircraft noise level variation with operation/performance, as well as detailed flight trajectory data. The total source to ground (observer) calculation procedure requires steps consisting of large computational time and data, both causing restrictions or even being unattainable at the conceptual phase of design.

Introducing noise to the conceptual and preliminary design stages requires the following important considerations:

- Tools able to perform high-level fast calculations match the rate of design iterations.
- Tools that require limited input data for when exact geometry and operation have not yet converged or frozen in the design.
- Tools with the capacity to explore a wide range of design possibilities including the introduction and use of novel / cutting edge technologies. These tools are required to have the capability of capturing the effect of novel acoustic behaviour such as:

  - new sources of noise, or new combinations of sources.

  - the directive nature of the noise radiated by the source and the effect on the ground.

  - the spectral content

  - the effect of novel operations (eg. transition from vertical to horizontal flight of a tilt-wing) on individual sources, on the whole aircraft as a noise source, and on the noise on the ground.

- Tools with the ability to assess community exposure and fleet scale operations around airports, and are not limited to examining the affect of individual source variation as a function of design.
- Tools that consider aircraft operations (conventional and novel) at the high-level and effect on the ground noise.

1.1 Current state-of-the-art gaps and problems

In order to design a tool that meets the above objectives, an assessment of current tools and gaps is necessary. There are a number of problems with the current tools that demand attention. These may be separated as follows:

- Aeroacoustic and aircraft noise assessment tools are often focused on individual noise source mechanisms, and not part of a whole air vehicle framework, to assess the impact in realistic operational scenario. A framework that unifies such individual methods is necessary.
- Adoption of standard tool interfaces and compatibility. Conducting studies from the individual source level, to NPD generation, to noise exposure generation, requires the juggling of inputs and output formats that is time-consuming and requires additional effort beyond the acoustical assumptions and model setup. MONTANA addresses the interfaces between internal components such as the steps between the individual source level, to NPD generation, to noise exposure generation. Considerations for future adoption of an industry standard such as CPACS (Common Parametric Aircraft Configuration Schema) [11] are also required.
- Capability is limited to conventional fixed wing turbofan aircraft, with new techniques and requirements extremely difficult to implement.

From the acoustic capability perspective, current limitations are identified as:

- Noise sources: Flexibility is required in the acoustic modeling of air vehicles, allowing the definition of multiple individual constituent noise sources, that are not limited to conventional tubofans, with the potability of easily extending the types and number of available sources.
- Directivity: current considerations allow for directivity variation only in the polar direction. This assumption becomes limiting when trying to estimate the lateral certification point specified by Chapter 14. It also limits the calculation of noise exposure contours to only directly under the flightpath, with additional corrections required to account for lateral directivity at all other locations on the ground. Lacking azimuthal directivity entails reliance on less than perfect lateral attenuation models that may be very inaccurate for novel aircraft.
- Spectra/frequency content: the adopted standard of the 24 one-third-octave band spectral shapes often proves to be limiting. Further flexibility is required to allow for source methods with higher fidelity data, larger frequency ranges and (ideal) discrete tonal data to be included within the whole aircraft model, and framework.

- Novel operations: current aircraft operations considered are takeoff and landing of conventional fixed-wing aircraft. This is to accommodate the calculation of certification points and noise contours according to Annex 16 and Doc29 specifications. This limits the applicability to VTOL enabled air vehicles such as conventional helicopter and possible future AAM class rotorcraft.

- Transient performance: current practice relies on a segmentation methodology that assumes constant (steady-state) performance and operation along each individual segment. Although this assumption may be reasonable for conventional operations, VTOL operations are characterised time-varying behaviour during landing, takeoff, acceleration, deceleration and transition phases. In addition, conventional takeoff cut-back procedures for noise abatement (see NADP 1 and 2, in Section 2.5) also form a transient manoeuvre that is not accurately modelled by a segment method. Features that would allow the modelling of transient performance in the context of a lumped source model as the one used in MONTANA are:

  - Effect of sound power level variation with time. Sound power emission by each individual source to be dictated by the transient performance of such manoeuvres.

  - Effect of directivity variation with time/power setting. Orientation of the aircraft is neglected, therefore the manoeuvres such pitch control and banking during turn are not accounted for. In addition to orientation, power setting directly affect the directivity of the whole aircraft, as the balance between each individual source directivity changes according to operating conditions.

  - Effect of spectral content variation with time/power setting.

  - Effect of acceleration and deceleration noise exposure on the ground. Acceleration and deceleration are functions of power setting and therefore directly correlated to transient performance. The direct effect on noise exposure levels is manifested through exposure time, however, flight effects, and particularly the management and balance of flight affected individual sources (how they vary with accelerated flight, and whether additional sources are introduced and/or removed) are generally not considered.

1.2 The MONTANA model

This thesis presents MONTANA (Modular Novel Transport Aircraft Noise Assessor), a high-level framework for the analysis and exploration of air vehicle design space in terms of noise output and community noise exposure. MONTANA addresses the current gap in noise prediction tools and is accordingly used as an academic research tool to provide acoustic consultations for projects that aim to design the future zero emission aviation market.

MONTANA builds on the ISVR whole aircraft noise prediction tools and allows the integration of the various components such as Sy.No.PoD [12] and Rapid Aviation Noise Evaluator (RANE) [13]. In addition to the already existing capability, the aim of this thesis is to develop and update the models and frameworks within MONTANA to allow for the evaluation of noise immission of propeller powered air vehicles, fixed wing and rotorcraft with inherent three-dimensional directivity properties.

The MONTANA model consists of the following main components: the individual source models/methods, the lumped source model, the calculation of the Noise-Power-Distance curves, and finally the airport noise modelling or creation of noise exposure contour maps. Each step of the process, in that order, requires a set of inputs and generates a set of outputs, subsequently picked up by the next step of that process. Figure 1.1 shows an analytic flow diagram of the framework, clearly depicting the inputs and outputs of each component.

The individual source models/methods are used to generate sets of deltas which when combined with baseline (known) absolute noise levels in an appropriate source balance, compose the lumped source model reflecting the acoustic emission of the concept air vehicle. The lumped source is then numerically flown to produce the NPD curves. These topics are explored in Chapter 4.

The NPD outputs are then used with additional flightpath (trajectory and aircraft performance) data in the airport noise model RANE. Chapter 5 discusses the RANE modelling techniques in detail. The outputs of RANE are noise footprints and contours for aircraft operating in communities around airports. Noise levels are predicted in a variety of subjective and non-subjective metrics, discussed in Chapter 2.

The contributions of this thesis are clearly illustrated in Figure 1.1 amongst the "established" methods from literature that are also included in the overall process. These are explicitly discussed in Section 1.4.

Noise predictions are done on a source level and combined to form a total (lumped) representation of the aircraft as a noise source. MONTANA is designed to be independent of the specific noise prediction methods/algorithms for the various sources, as well as sound propagation techniques. This allows for future applications of MONTANA to be modified to the specific needs of the prediction problem, whether higher or lower fidelity in prediction is required for example.

The modular aspect of MONTANA forms the most significant requirement for the development procedure. As MONTANA aims to be applied to a wide range of air vehicles, from fixed wings to rotorcraft of various sizes and configurations it will need to provide a flexible means by which its feature-set can be extended. This is necessary to permit the implementation and addition of features as new methods and approaches for

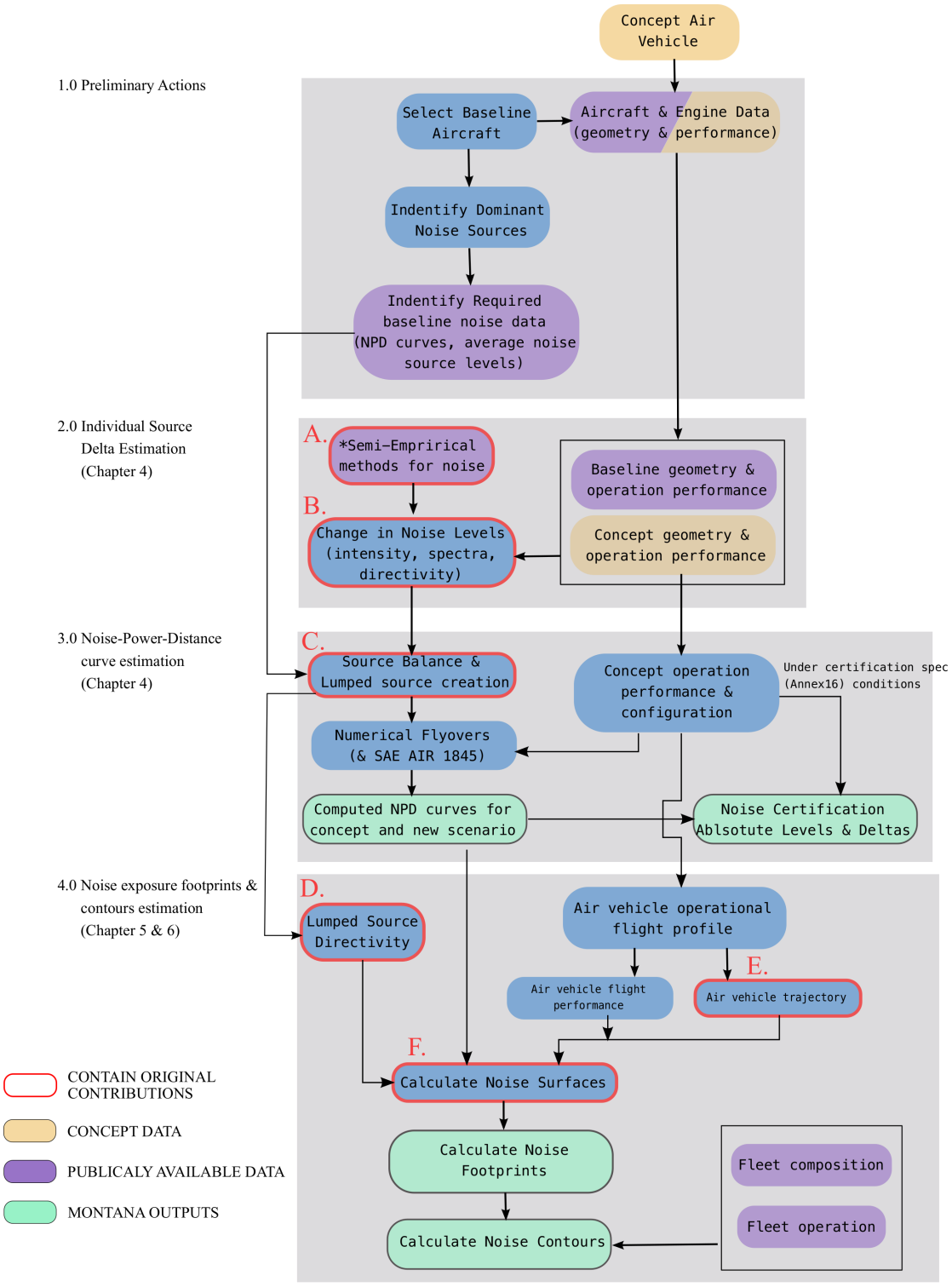

* Individual noise source methods are sourced from literature, however they are modified to allow for the integration with the source delta methodology.

FIGURE 1.1: Detailed flow diagram of the MONTANA framework.

predicting engine, aircraft and installation/interaction noise become available and regulations and requirements change over time.

1.3 Research Aims

Following are some key features addressed through the present research:

- Improve and develop an efficient and fast computing noise modelling framework to aid the design of novel aircraft, able to perform large number of case study calculations in limited time in order to help explore the design space of novel aircraft in terms of noise immissions.
- Extend the modelling capabilities to include a wide variety of air vehicles, from fixed-wing regional, narrow-body and wide-body aircraft, to traditional single rotor helicopters and novel VTOL rotorcraft.
- Introduce a simple and flexible way of modelling noise source three-dimensional directivity.
- Develop simple scaling relations for propeller/rotor noise sources applicable to propeller power fixed-wing aircraft and AAM rotorcraft and implement them into the framework to compute whole aircraft noise levels on the ground.

1.4 List of Original Contributions

With reference to Figure 1.1 the detailed original contributions described in this thesis are as follows:

A. An asymptotic approximation to the Hanson frequency domain model for propeller harmonic noise was developed. The resulting propeller harmonic noise scalling laws were used to connect overall sound power emission of a single propeller system to design and operational parameters.

B. The delta methodology [12] was generalised to account for changes in spectral content (tonal and broadband) and changes in three-dimensional directivity, as well as sound power level (PWL).

C. The delta lumped source model was generalised for the use with any individual noise source prediction method for which the Jacobian of the method may be estimated (or approximated).

D. A model of noise source three-dimensional directivity using a spherical harmonic expansion that allows input in analytical and numerical format.

E. A closed-form analytical model (with full derivations) was developed for the generation of noise exposure contours of novel aircraft around airport and helipads.

The capabilities applicable to novel aircraft are: (a) directive noise sources, (b) independently rotating noise sources, (c) power variation with time and d. novel operations including but not limited to vertical takeoff and landing, hovering and flight condition transition.

F. Case Study: Noise certification point and noise exposure contour assessments was performed on a series of regional hydrogen powered aircraft.

G. Case Study: A simple model of an AAM network operating in London UK was created. Three AAM concepts were conceptually designed and sized, with different propulsion architectures. The impact of the different propulsion systems and overall noise directivity was assessed through the generation of noise exposure contours.

1.5 List of Publications

The research within this thesis has led to the following publications.

Accepted for publication in scientific journals:

- Amargianitakis, D.C., Self, R.H., Proença, A.R., Synodinos, A.R. and Torija, A.J., Towards estimating Noise-Power-Distance curves for propeller powered zero emission hydrogen aircraft. Accepted for publication, Journal of Aircraft 2023.
  - Corresponds to Chapter 4
- Amargianitakis, D.C., Self, R.H., Torija, A.J., Proenca, A. and Synodinos, A.P., Closed-form analytical approach for calculating noise contours of directive aircraft noise sources. Accepted for publication, AIAA Journal 2023.
  - Corresponds to Chapter 5

Presented at conferences:

- Amargianitakis, D.C., Self, R., Proenca, A., Torija Martinez, A. and Synodinos, A., 2022. Generation of noise exposure contours for eVTOL aircraft including transition. In 28th AIAA/CEAS Aeroacoustics 2022 Conference (p. 3088).
  - Corresponds to Chapter 6
- Amargianitakis, D.C., Self, R., Proenca, A., Boyd, C., Westcott, O., Ferraro, M., Erbil, M.A. and Entwistle, R., 2022. Measurement and Modelling of Noise-Power-Distance Curves of a Fixed-Wing UAV. In 28th AIAA/CEAS Aeroacoustics 2022 Conference (p. 3037).

- Amargianitakis, D.C., Self, R.H., Torija, A.J. and Synodinos, A.P., 2019, September. Influence of sound reflection on aircraft directivity and lateral attenuation on the ground. In INTER-NOISE and NOISE-CON Congress and Conference Proceedings (Vol. 259, No. 3, pp. 6740-6751). Institute of Noise Control Engineering.
- Amargianitakis, D.C., Self, R.H., Torija, A.J., Proenca, A. and Synodinos, A.P., 2021. Closed-form analytical approach for calculating noise contours of directive aircraft noise sources. In AIAA AVIATION 2021 FORUM (p. 2175).
- Amargianitakis, D., Self, R.H., Proença, A.R., Synodinos, A.R. and Torija, A.J., 2021, August. Towards predicting noise-power-distance curves for propeller and rotor powered aircraft. In INTER-NOISE and NOISE-CON Congress and Conference Proceedings (Vol. 263, No. 3, pp. 3909-3920). Institute of Noise Control Engineering.

Technical reports/articles:

- Self, R.H., Humphreys, V. and Amargianitakis, D.C., 2022, FlyZero Noise Report. ATI: Aerospace Technology Institute.
- Self, R.H. and Amargianitakis, D.C., 2022, Project NAPKIN Noise: An assessment of the noise impact of zero emission regional hydrogen aircraft and their operation. UK Research and Innovation.

1.6 Thesis Structure

Chapter 2 introduces the concepts of whole aircraft noise modelling and airport noise. Starting from basic acoustic theory definitions an understanding on how it is applied to the field of aircraft noise and more specifically airport and community noise. Industry standard noise metrics and methodologies are explained along with the noise certification procedure and regulations regarding aircraft operations in the vicinity of urban communities. Present dominant turbo-fan and turbo-prop noise sources are discussed, and how these will be affected with a transition to electric flight, along with key noise source features that are relevant to this study. Finally, brief reviews of aviation/airport noise tools and aeroacoustic noise source models are presented.

Chapter 3 provides some background theory on the design considerations of future zero-emission aircraft, with a focus on hydrogen powered and electric aircraft. The engineering reasons for an industry transition into electrically propelled aircraft are presented in addition to the limitations. Significant aircraft design parameters are discussed in context to power requirement, total energy requirements and noise.

Chapter 4 represents the aeroacoustics contribution of this thesis. Linear and asymptotic approximations for propeller noise models are presented with the goal of defining effective scaling laws to serve as inputs to computationally generated NPD curves, and therefore also MONTANA's airport noise module.

Chapter 5 represents the airport noise contribution of this thesis. It explains the closed-form analytical model (MONTANA's airport noise module referred to as RANE v2) developed in order to generate noise exposure contours around airports. Key features such as three-dimensional source directivity, source spectral content etc. are discussed in detail along with the applicability to novel aircraft.

Chapter 6 presents a preliminary model and study on the effect of independent source rotation, aimed at capturing the effects of propulsion system and/or vehicle orientation relative to the ground during takeoff and landing operations.

Chapter 7 presents the bench-marking of the propeller noise approximation method and the additional capabilities added to the airport noise tool. Published NPD curves for existing propeller powered vehicles are compared to the computationally estimated ones in Chapter 5. Noise exposure contours generated in Chapter 4 are compared against an in-house developed grid method and the industry standard tool AEDT for a variety of source characteristics and aircraft operations. Finally, limitations of the proposed models as well as an error analysis are discussed.

Chapters 8 and **9** demonstrate the capabilities of the MONTANA with studies of novel regional hydrogen powered fixed wing aircraft and fully-electric AAM rotorcraft. Noise exposure contours of different design iterations and variants are compared and the effects of dominant parameters are discussed.

Chapter 10 presents the authors conclusions and considers potential future work.

Chapter 2

Aircraft and Airport Noise

In this Chapter the theoretical background of aircraft and airport noise is established. Although extensive, this Chapter serves as an introduction to the Whole Aircraft Noise field and prediction. Definitions of acoustic parameters are given and put in to context relating to aircraft and aircraft specific noise sources. Current definitions of noise metrics, their applications and differences in measuring aircraft noise are described, as well as their role in aircraft noise certification. The relation of aircraft operations/performance to noise is established and connected to the concept of Noise-Power-Distance (NPD) curves. Finally, a summary of the state-of-the-art airport/aircraft noise prediction models is used to identify the gaps in the current model landscape.

2.1 Whole Aircraft noise modelling

2.1.1 Aircraft noise definitions

Aircraft noise can be defined as the noise generated by aircraft (or generally air vehicles), their propulsion systems and other components. More specifically, aircraft noise is predominantly driven by the field of aeroacoustics, as the noise generated is overwhelmingly fluid/air-induced along with the interaction of fluids with solid boundaries of various types.

The basic definitions and relationships presented follow the analysis and notation presented by Blake [14, 15], unless otherwise stated. Fluid mechanics and acoustics texts, to the like of Morse and Ingard [16], Pierce [17], Fahey [18], and Kinsler [19] may also be referred to.

2.1.2 Noise Levels

Noise consists of pressure waves over a wide range of amplitudes and frequencies. For a source radiating acoustic sound power $\mathbb{P}_{rad}$, a corresponding sound power level L_w is defined as,

$$L_w := 10 \log \left[\frac{\mathbb{P}_{rad}}{\mathbb{P}_{ref}} \right], \quad [L_w] = dB \quad \text{(decibel)} \tag{2.1}$$

where

$$\mathbb{P}_{ref} := 10^{-12} \ \text{W} \tag{2.2}$$

The acoustic energy radiated by any source is manifested through the square of the spatial average mean-square sound pressure. Because of the large range of rms-values which are resolved by the human ear, a logarithmic scale is used for the most important acoustic quantities. The sound pressure level L_p or SPL due to an acoustic source at any arbitrary location in space is defined as,

$$L_p := 10 \log \left[\frac{p_{rms}^2}{p_{ref}^2} \right], \quad [L_p] = dB \quad \text{(decibel)} \tag{2.3}$$

where p_{rms} is the root-mean-square of the acoustic pressure signal (wave) at that location and,

$$p_{ref} := 2 \cdot 10^{-5} \ \text{Pa} \tag{2.4}$$

is the international reference pressure, and threshold of hearing. PWL and SPL are measured in units of decibel (dB).

2.1.3 Lumped source model: far-field acoustics

The above definitions concern a single point in space, and the total acoustic field (signal) received at it. Generally, acoustic sources radiate in all of three-dimensional space. In addition, the total acoustic field at any observer location may be attributed to multiple sources of sound.

In airport noise, observers are located at distances which are multiple orders of magnitude larger than the noise generating components of the aircraft. At these observers positions, the specific locations of individual noise sources with respect to the aircraft airframe are less important, and it may be assumed that the far-field acoustic radiation from an acoustic centre of the overall aircraft. This is the definition of a *lumped source* model. However, this simplification comes with caveats, which will become apparent throughout this thesis.

A lumped source is a modelling technique that allows the combination of multiple individual sources, originating in the same space with respect to the far-field, to be described by the total radiated sound power $\mathbb{P}_{rad}$.

Considering for example an aircraft, the total noise emission is made up of the contributions from individual noise sources with a total sound power of $\mathbb{P}_{rad}$. Assuming s is the total number of sources contributing to the observed sound field, the total sound power is then,

$$\mathbb{P}_{rad} = \sum_{i=1}^{s} \mathbb{P}_{i,rad} \tag{2.5}$$

where i indexes through the individual sources. Each individual source has characteristics such as directivity, spectral content, amplitude etc. that contribute to the overall sound power radiated by the source.

Therefore, assuming a far-field problem, where the range is much greater than both the size of the source (region) and the acoustic wavelength, the average power radiated over a spherical surface surrounding the source (see Figure 2.1),

$$\mathbb{P}_{rad} = \iint_{S_0} \frac{p^2_{\text{rms}}(\mathbf{x})}{\rho_0 c_0} r^2 \sin\varphi \, d\varphi \, d\theta \tag{2.6}$$

where S_0 represents a spherical surface surrounding the source region and is always perpendicular to the direction of propagation, $\mathbf{x}$ the spatial position vector and p^2_{rms} represents the mean square, of the instantaneous fluctuating sound pressure.

The average acoustic energy radiated is given by the integrals the instantaneous power flux over a period of time T and boundary area S over which the transmission occurred. The instantaneous power flux (power per unit area) is called acoustic intensity and may be denoted, $\mathbf{I}$. As by definition the acoustic intensity is a function of spacial position and time. Therefore, the average acoustic energy emitted by a source may now be written as,

$$E_a = \int_0^T \iint_S \mathbf{I}(\mathbf{x}, t) \cdot \mathrm{d}\mathbf{S}(\mathbf{x}) \mathrm{d}t \tag{2.7}$$

where $d\mathbf{S}(\mathbf{x})$ is the infinitesimally small surface vector, and $\mathbf{x}$ is the acoustic field position vector, see Figure 2.1.

Through the solution of the one dimensional wave equation [19, 16], i.e. assuming propagation is only along the radius from the source, the intensity of the acoustic field may be calculated through the acoustic pressure. Using the far-field acoustics assumption while also assuming a nearly stationary medium, the instantaneous acoustic intensity is defined as,

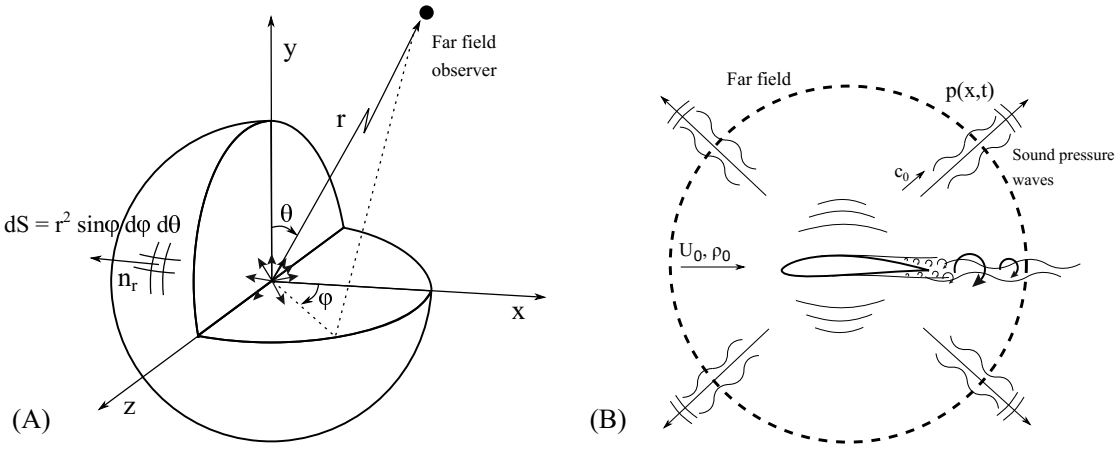

FIGURE 2.1: Diagram of point source radiating noise in three-dimensional acoustic field. Adapted from Blake [14].

$$\mathbf{I}(\mathbf{x}) = p^2_{\text{rms}}(\mathbf{x})\rho_0 c_0 \tag{2.8}$$

where $\rho_0 c_0$ are the ambient air density and speed of sound, respectively; with their product defined in acoustics as the specific acoustic impedance of the fluid. The relation therefore between the overall acoustic sound power radiated and the acoustic pressure field as,

$$\mathbb{P}_{rad} = \iint_{S_0} \frac{p^2_{\text{rms}}(\mathbf{x})}{\rho_0 c_0} d\mathbf{S}_r(\mathbf{x}) \tag{2.9}$$

It is useful to define the notion of a spatial average intensity $\bar{I}$, as it is critical in the later definition of the lumped source directivity. The average intensity of a lumped source is defined as the time and spacial integral over a sphere surrounding the source,

$$\overline{I} = \frac{1}{T}\int_0^T \iint_{S_0} \mathbf{I}(\mathbf{x}, t)\, \mathrm{d}\varphi\, \mathrm{d}\theta\, \mathrm{d}t \tag{2.10}$$

The relation of the overall sound power as a function of the average intensity $\bar{I}$ is therefore trivially,

$$\mathbb{P}_{rad} = 4\pi r^2 \bar{I} \tag{2.11}$$

Three-dimensional directivity

The tendency of a noise source to radiate varying amount of acoustic energy into different directions is what is described as a source's directional behaviour. The

directional properties of individual and lumped noise sources are described using what is known as the directivity factor D. It is defined as,

$$D(\theta, \varphi) = \frac{I(\theta, \varphi)}{\overline{I}} \tag{2.12}$$

The purpose of the directivity factor is to isolate (decouple) the directional properties of the source from the total generated acoustic energy. The terms "directivity sphere" or "directivity hemi-sphere" are often used in literature when the three-dimensional radiation pattern is of interest; as opposed to singular angles in the polar direction for example. It may take various forms, often analytical or numerically (most often the case as experimental data in normalised and stored in tabulated data form, see ANOPP [20] for example). In this thesis, the term directivity function will be used interchangeably with directivity factor, as mainly analytical functions are used to describe the directional properties of sources. A directivity index may also be defined as,

$$DI(\theta, \varphi) = 10 \log D(\theta, \varphi) \tag{2.13}$$

with units of dB.

The definition of the directivity function as the ratio of the sound intensity in a specific direction to the mean intensity ensures the overall acoustic power is normalised. This condition is satisfied if the integration over the entire spherical surface surrounding the source returns the power of the source,

$$\int_{S_0} \frac{\mathbb{P}_{rad} D}{4\pi} \, \mathrm{d}S = \mathbb{P}_{rad}(j) \tag{2.14}$$

where j denotes the power setting. Or in terms of the directivity function, $D(\theta, \varphi)$,

$$\int_S D(\theta, \varphi) \, \mathrm{d}S = 1 \tag{2.15}$$

Assuming a lumped source model for an aircraft, the total directivity D may be given in terms of the directivities of the individual source comprising it. The total directivity is given in the form a weighted energy sum as,

$$D(\theta, \varphi) = \frac{\sum_{s=1}^{n} \mathbb{P}_s D_s(\theta, \varphi)}{\sum_{s=1}^{n} \mathbb{P}_s} \tag{2.16}$$

with s and n being the source index and total number of individual sources respectively, while $\mathbb{P}_s$ and D_s are the sound power radiated and directivity of source s.

The definitions of the emission angles θ and φ and reference frames in this Section follow that of the diagram in Figure 2.1 for consistency with the previous definitions and those used by Blake [14]. However, Chapter 5 introduces a new definition, most commonly adopted in the aircraft noise discipline and Noise-Power-Distance generation.

Frequency content considerations

Many factors influence the behaviour and characteristics of noise waves, with a significant one being frequency content. Noise sources are typically either broadband or tonal in nature. Simple pressure waves may be defined by fluctuations of a single frequency, known as tones. However, real noise sources emit random pressure fluctuations composed of signals of infinitely many frequencies, broadband noise. In order to decompose any random sound pressure signal into its frequency components it is usual practice to use a Fourier transform. The Fourier transform of a randomly fluctuating time dependent acoustic pressure signal is,

$$P_a(\mathbf{x},\omega) = \int_{-\infty}^{+\infty} p_a(\mathbf{x},t)e^{+i\omega t}\,\mathrm{d}t \tag{2.17}$$

and its inverse,

$$p_a(\mathbf{x},t) = \frac{1}{2\pi}\int_{-\infty}^{+\infty} P_a(\mathbf{x},\omega)e^{-i\omega t}\,\mathrm{d}\omega \tag{2.18}$$

where $f = \omega/2\pi$ is the frequency and $i = \sqrt{-1}$. Equation 2.18 clearly states that the time domain (real space) pressure fluctuation in nothing but the summation of all of its frequency components $P_a(\mathbf{x},\omega)$. p_a is the spatially and temporally dependent acoustic pressure signal, while P_a are Fourier series coefficients.

Broadband components are typically associated with random turbulence or mixing that occur over a wide range of frequencies (such as turbulence generated by the airframe components extending into the airflow) while tonal components are associated with periodic steady state movements that excite certain frequencies (such as rotating engine components).

This indicates that energy is spread across the frequency spectrum. Using the definitions of average power radiated from earlier, we may use the Fourier transform to estimate the distribution of power into the frequency components composing the original signal. The average power radiated may be written as,

$$\mathbb{P}_{rad} = \lim_{T\to\infty}\frac{1}{T}\int_{-\infty}^{+\infty}\iint_{S_0}|P_a(\omega)|^2\,\mathrm{d}\mathbf{S}(\mathbf{x})\,\mathrm{d}\omega \tag{2.19}$$

with the integrand of the time integral being defined as the power spectral density, $S_{pp}(\omega)$.

In aircraft noise, the characterisation of sounds and their frequency components is usually done with what is known as the one-third octave band spectrum [21]. The power spectral density is divided into intervals or bands. Each band level is defined as,

$$L_p^i = 20 \log \left[\frac{p_{i,\mathrm{rms}}(f_i^c)}{p_{ref}} \right] \tag{2.20}$$

where the index i, in this case, denotes individual bands; each frequency band is characterised by the centre frequency f_i^c and the bandwidth $\Delta f_i = f_i^u - f_i^l$ (the subscripts denote the upper and lower frequencies). Specifically for the one-third octave band the bandwidth is not constant across all bands but proportional to the centre frequency, $\Delta f_i = (2^{1/6} - 2^{-1/6}) f_i^c$ and $f_i^c = 2^{i/3} f_0^c$, whereby international standard the reference centre frequency is $f_0^c = 1$ kHz.

Lumped noise source definition

Combining the definition of the SPL in Equation 2.3 along with Equations 2.5, 2.8 and 2.11 we can define a single total noise source representative of the aircraft as a whole, a lumped acoustic source. The SPL radiated by a lumped source at a far-field observer location is,

$$\boxed{L_p(\theta, \varphi, r, f) = 10 \log \left[\frac{\mathbb{P}_{rad} D(\theta, \varphi) \bar{S}_{pp}(f)}{r^2} C \right]} \tag{2.21}$$

where $C = \rho_0 c_0 / (4\pi p_{ref}^2)$ is a constant, and r is the distance between the observer and the lumped source. Noise emitted from a source decays with the distance between the source and observer due to spherical spreading. The power spectral density, $\bar{S}_{pp}(f)$, is normalised to the overall power radiated by the source and describes the distribution of acoustic power in to the frequency components generated by the source. Finally, $D(\theta, \varphi)$ describes the directionality characteristics of the source.

Individual noise source addition

Combining individual sources of noise to create a lumped source representation of the aircraft as a whole is not as simple as adding the acoustic energy of the individual components. Considerations need to be made due to the nature of acoustic waves.

The resulting acoustic field at any observer in space due to the combination or addition of acoustic waves, is strongly dependent on the acoustic parameters, i.e frequency content, amplitude, phase and directivity as well as the relative position of the individual sources contributing to the total field. Interaction of the waveforms may lead to constructive and destructive interference, if noise originates from the same source or

different sources but have the same frequency and waveform. In this case, the noise sources are called coherent. Such mechanisms can alter the noise field in the region of source (near-field), but also the final acoustic energy that propagates to the far-field. A simple example of coherent sounds are two identical tones.

All the individual contributions from each of the sources make up a distributed region of sources that define the acoustic field which is propagated outward to a point in free space. Individual contributions support or interfere in the physical summing process based on the instantaneous phase relationships among the various sources. In more complex/realistic physical scenarios the acoustic radiation is calculated as a weighted integral of the source distribution. The integral must consider both the entire propagation process to the far-field and the acoustic phase interactions between the components of the source distribution.

Let $p_a(\mathbf{x}, t)$ be the acoustic pressure due to single noise source, expressed in the complex domain. Then, the acoustic power $\mathbb{P}_{rad}(\mathbf{x})$ at the observer position x is $\mathbb{P}_{rad}(\mathbf{x}) = |p_a(\mathbf{x}, t)|^2 = p_a^*(\mathbf{x}, t)p_a(\mathbf{x}, t)$ where * indicates complex conjugation. Acoustic interference, as a result of coherent noise waves concerns the issue of the acoustic energy when the noise field is due to a sum two (or more) waves. Now assume p_a is the result of two individual waves $p_{a,\mathrm{A}}$ and $p_{a,\mathrm{B}}$ then,

$$p_a(\mathbf{x}, t) = p_{a,\mathrm{A}}(\mathbf{x}, t) + p_{a,\mathrm{B}}(\mathbf{x}, t) \tag{2.22}$$

with the subsequent acoustic power being,

$$\begin{aligned} \mathbb{P}_{rad}(\mathbf{x}) = |p_a(\mathbf{x}, t)|^2 = |p_{a,\mathrm{A}}(\mathbf{x}, t)|^2 + |p_{a,\mathrm{B}}(\mathbf{x}, t)|^2 \\ + (p_{a,\mathrm{A}}^*(\mathbf{x}, t)p_{a,\mathrm{B}}(\mathbf{x}, t) + p_{a,\mathrm{A}}(\mathbf{x}, t)p_{a,\mathrm{B}}^*(\mathbf{x}, t)) \end{aligned} \tag{2.23}$$

The interpretation of the above equation is that, the acoustic power at observer x is the acoustic power at x due to the noise source A plus the acoustic power at x due to the noise source B plus an extra term. This extra term, which is the interference term, can add (constructive) or subtract (destructive) energy at the observer location.

For incoherent sounds, such as broadband noise components, have randomly interacting wave fronts and it can be presumed that $p_{a,\mathrm{A}}^*(x, t)p_{a,\mathrm{B}}(x, t) + p_{a,\mathrm{A}}(x, t)p_{a,\mathrm{B}}^*(x, t) = 0$. Direct incoherent addition of sound pressure levels is expressed as,

$$L_p = 10 \log \sum_{i=1}^{s} 10^{L_{p,i}/10} \tag{2.24}$$

where L_p is the final noise level and $L_{p,i}$ the levels of the individual sources.

Specifically, in the case of MONTANA, individual sources are assumed to be incoherent. The reasoning for this assumption can be summarised as follows:

- Imperfect manufacturing and aeroelastic behaviour of components lead to discrepancies in noise mechanisms that would otherwise be expected to generate the same waveforms under the same operating conditions. A characteristic example are tone generating mechanisms for rotating turbomachinery components such as fans, axial compressors and turbines.
- Regarding turbomachinery components, engine performance and operation generally dictates that generated tones are of different frequencies; between components of the same engine and different ones.
- Atmospheric effects and turbulence [22][23] generally impose random disturbances on signals causing decorrelation effects. This results in incoherent noise signals reaching the observer locations.
- Flight effects (such as Doppler frequency shifts) and propagation distance variation can also contribute to signal decorrelation [24].

2.1.4 Aircraft Noise metrics

In order to limit and slowly reduce the number of people exposed to significant amounts of aircraft noise, aircraft certification agencies, such as the ICAO and FAA, impose noise limits on manufactures in order for them to gain airworthiness certification. These noise limits are given in terms of noise metrics.

Generally, noise metrics fulfil two purposes: quantifying the amount of acoustic energy generated by aircraft that reaches any given observer location, and quantifying the impact of that acoustic energy on humans specifically. For the prior, the term noise emission is used, and considers noise generated at the source (ICAO Balanced Approach to Aircraft Noise Management [25] : Reduction of Noise at Source). The latter, is coined the term noise immission, and takes into account the human response and perception due to aircraft noise.

2.1.4.1 Noise certification metrics overview

The aircraft certification process and specifically the aircraft noise certification process requires the aircraft OEM (original equipment manufacturer) seeking certification for a particular product to provide a suit of experimental (measured) and predicted data as evidence that the noise certification limits that apply to aircraft in questions are not exceeded. Depending on the type of aircraft, the certification rules that apply, and the

authority giving the certification the noise metrics vary. A review on aviation noise metrics by Feng et al. [26], summarises the use, benefits and drawbacks of metrics in use worldwide.

The ICAO Annex 16 [27] define the Standards and Recommended Practices for aircraft noise certification to be used by any regulation authority. Additionally, it covers international specifications relating to aircraft noise measurement and evaluation methods, such as metric evaluation and the static to flight projection process.

Annex 16 classifies aircraft (air vehicles) into Chapters, depending on air vehicle type, propulsion system architecture and MTOW. Different chapters specify the noise level limits, as well as the operating procedures under which the limits must be measured and/or calculated. The metrics used in each Chapter may very. Below are listed the main Chapters of Annex 16 with the aircraft type they apply to and the metric used:

- Chapter 3 & 14 - Subsonic jet aeroplanes and Large propeller aeroplanes: EPNL
- Chapter 6 - Propeller-driven not exceeding 8,618 kg (before 1988): Maximum A-weighted noise level, L_{ASmax}
- Chapter 8 - Helicopters: EPNL
- Chapter 10 - Propeller-driven not exceeding 8,618 kg: Maximum A-weighted noise level, L_{ASmax}
- Chapter 11 - Helicopters not exceeding 3,175 kg: SEL
- Chapter 13 - Tilt-Rotors: EPNL

The calculation process for the Effective Perceived Noise Level (EPNL) from measured data is defined in Appendix 1 (before 1977) & Appendix 2 (after 1977), while the process for maximum A-weighted noise level (LASmax) is in Appendix 6.

Regardless of which chapter of the Annex any air vehicle must comply to, with the respective required metrics, additional noise data is typically made available to the certificating authority for use beyond noise type certification, e.g. land-use planning purposes. Such additional data may be in EPNL, SEL, LASmax and one-third octave SPLs.

2.1.4.2 Available MONTANA output metrics

MONTANA is primarily concerned with quantifying the noise emission and immission changes of novel air vehicles relative to baseline scenario during single flyover events. Noise emission changes concern noise at the source, specifically how the radiation

pattern, spectral content and absolute levels vary as a function of implementing new designs, technology and operating conditions.

The first point of interest for MONTANA is the impartial (based on the acoustic energy received, proportional to p_{rms^2}) quantification of aircraft noise received at the observer locations. The prediction of such levels and metrics, mirrors the experimental data gathering and analysis portion of the noise certification process. As a next step, human perception is accounted for, with the introduction of subjective metrics.

For this reason the primary metrics used throughout this thesis are acoustic energy based, SPL or OASPL as an instantaneous metric, while SEL is extensively used as the predominant event exposure metric. These metrics allow the quantification of how the total acoustic energy generated by an air vehicle is distributed in three-dimensional space and across frequencies, and finally, what proportion of that energy reaches observers on the ground during operation. In addition, SEL is the choice of metric for helicopters not exceeding 3,175 kg, a category of air vehicles closely resembling that of AAM and UAM vehicles; under careful consideration such helicopters and their certification noise levels and NPD curves can be used as baselines for the prediction of AAM noise. Finally, although Chapter 6 and Chapter 10 certify aircraft using L_{ASmax}, the ANP database provide NPD curves for SEL levels, allowing for the comparative studies of noise exposure of such regional aircraft.

However, as the objective of MONTANA is to provide meaningful technical insight to novel air vehicle noise certification and community noise impact, specific human subjective units/metrics are also considered and provided as outputs.

2.1.4.3 Subjective and Non-subjective Metric Definitions

In the case of subjective metrics, humans perception and reaction to noise does not only respond to changes in pressure level. Other variables such as,

- frequency content and more specifically the tonality of the noise,
- amplitude of the noise (sound wave)
- overall time exposed to the noise,
- time pattern (continuity, fluctuation, impulsiveness and intermittency of the noise signal)
- the period over which the noise is observed (nighttime, day time etc.)

impact the final perceived noise by humans. Therefore, to appropriately capture and quantify these effects engineers and psychoacousticians have defined a variety of metrics to measure and describe noise originating from aircraft.

One further classification, of relative importance to the noise surface method presented in this Thesis, as well as to the concept of EPNL, is that of exposure levels, or otherwise integrated. Such levels require a time history of noise levels to be calculated and therefore become relevant within the concept of a "noise event". Following are the definitions and calculation processes of available noise metrics in MONTANA.

Instantaneous sound level metrics

Instantaneous sound level metrics, as captured by the name, consider the noise at one instance in time. These metrics can be classified into: frequency weighted metrics and calculated metrics.

The sensitivity of the human ear is strongly dependent on the frequency of the perceived noise. The so-called *noise weightings* are the simplest way of capturing this sensitivity. Different weightings are applied to frequency band levels to create a bias towards low, high or mid-frequencies (depending on the application) in the Overall Sound Pressure Level (OASPL). The A-weighting is the most widely used and applicable weighting among the 4 internationally agreed weightings (A-, B-, C- and D-weighting), which attempts to alter the values of the measured sound in different frequencies so that the result would better reflect what we actually hear (equal loudness contours ISO 226:2023). Such weightings are based on the concept of equal loudness and derived contours by Fletcher and Munson [28].

The Perceived Noise Level (PNL) is a metric designed to capture the complex signature of aircraft noise more completely than simple weighted sound levels. PNL is a loudness [29] based metric calculated by converting the loudness corrected sound pressure levels in each third-octave band to noy values [30]. The "noy" is the unit of a series of increments resulting from the divided decibel scale. The noy values are then summed in a particular manner to give the final PNL metric. PNL is measured in the units of PNdB.

Tone-corrected Perceived Noise Level (PNLT) applies a correction to the PNL metric to account for tonality of the noise signal. The tone correction factors are dependent on the frequency of the tone and its excess level over the level of the noise present in the adjacent third-octave frequency bands. PNLT is measured in units of TPNdB. PNL and PNLT are referred to as calculated metrics.

Single event metrics

Single event metrics are based on a time history of the instantaneous level generated by a single operation of an aircraft, Figure 2.2. This effectively introduces an event duration, from the time the noise if first perceived to when it is no longer audible.

The Maximum sound level, L_{max} is the instantaneous peak noise level recorded at an observer location in the duration of the noise event. Most commonly the A-weighting is used and is referred to as $L_{A,max}$ with unit of dB(A).

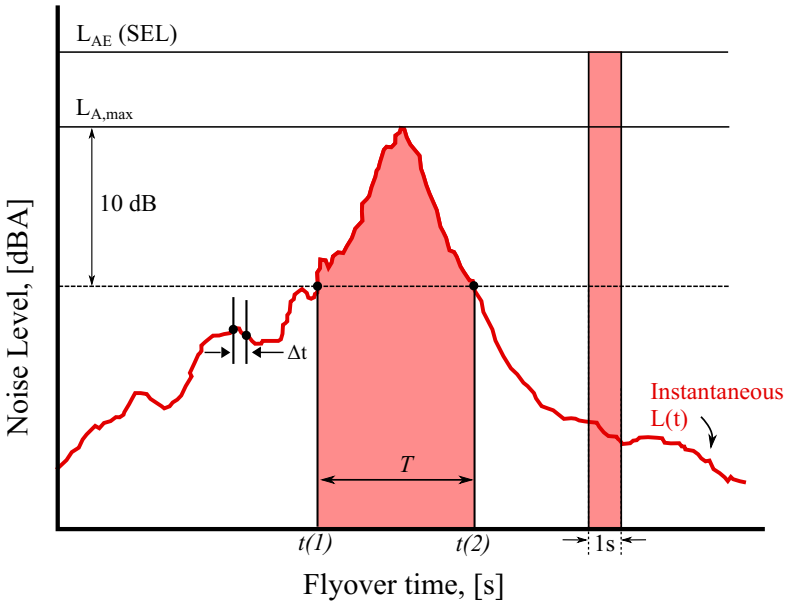

FIGURE 2.2: Diagram representing a single aircraft noise event and the associated noise metrics.

The sound exposure level (SEL or L_E) is the first metric out of a series of average energy level metric. The SEL may be described as the sound level of duration equal to one second (1s) that contains the same total acoustic energy as the whole event (the area of the vertical bar in Figure 2.2 is equal to the red area under the time history; the width of the bar is equal to 1 s). In the context of the SEL the event is defined using the 10-dB down rule, meaning the event time interval, $[t_1,\ t_2]$ is defined during which the level is 10 dB down from the maximum sound pressure level (L_{max}). Mathematically it is calculated as,

$$\text{SEL} = 10\log \int_{t_1}^{t_2} \frac{p^2(t)}{p_{ref}^2}\,\mathrm{d}t \tag{2.25}$$

Un-weighted, A or C-weighted Sound Exposure Level (SELA or SELC) can be calculated. The SEL is measured in units of dB.

The average Sound Level ($L_{eq,T}$) also known as the equivalent continuous noise level, is the sound level of duration equal to the period $T = t_2 - t_1$ of the event (same definition as SEL) that contains the same energy as the total event,

$$L_{eq,T} = 10\log \frac{1}{T}\int_{t_1}^{t_2} \frac{p^2(t)}{p_{ref}^2}\,\mathrm{d}t = 10\log\left[\frac{1}{T}\sum_{i=1}^{n} 10^{L_{p,i}/10}\,\Delta t\right] \tag{2.26}$$

where $L_{p,i}$ are discrete SPLs taken at time intervals Δt. As with the SEL, A-weighted levels may be used instead of SPL, then we may refer to the metric as Average

A-weighted Sound Level, L_{AeqT}. Both L_{eqT} and L_{AeqT} have units of dB and dB(A) respectively.

EPNL

Effective Perceived Noise Level (EPNL) is probably the most commonly used metric in aircraft and airport noise. The ICAO defines the complex calculation process of EPNL in Annex 16 Appendix 2 [27], relevant for air vehicles certified under Chapters 3, 4, 8, 13 and 14. The FAA's FAR Part 36 Appendix A [31] provides the same definition (Section A36.4 Calculation of Effective Perceived Noise Level From Measured Data).

The process of calculating the EPNL levels (ICAO Annex 16 section 4 of Appendix 2) is closely coupled with the noise level measurement process on the ground, and the noise certification test operations/procedures (details are presented in Section 2.1.5).

EPNL is a single number measure of an aircraft noise event taking into account the subjective effects of aircraft noise on humans. The following considerations were made when designing the EPNL metric as an effective way of measuring human response to aircraft noise:

- perceived noisiness, instantaneous perceived noise level, PNL
- subjective response to the presence of spectral irregularities
- tone correction, PNLT
- noise (event) duration, PNLTM, 10 dB down period
- effective perceived noise level, integrated event exposure level

The final expression for the EPNL of an aircraft event, calculated using a discrete series of PNLT(k) is,

$$\text{EPNL} = 10 \log \frac{1}{t_0} \sum_{k_F}^{k_L} 10^{0.1 PNLT(k)} \, \Delta t \tag{2.27}$$

or in many cases simplified for $t_0 = 10$ and $\Delta t = 0.5$ as,

$$\text{EPNL} = 10 \log \sum_{k_F}^{k_L} 10^{0.1 PNLT(k)} - 13 \tag{2.28}$$

where $10 \log 0.5/10 = -13$ is a constant relating to the one-half second values of PNLT(k) to the 10-seconds reference duration t_0. The variables k_F and k_L denote the first and last 10 dB-down points, respectively; whereas k_M would denote the point of PNLTM occurrence. EPNL is measured in units of EPNdB.

Multiple event metrics

Variations on the previously defined metrics allow for consideration of multiple events or multiple aircraft operations over larger periods of time. These metrics account for the overall aircraft movements at an airport during periods of 16-hours or 24-hours for example.

The Day-Night Level,L_{dn} (also referred to as DNL) for example, is an equivalent continuous A-weighted sound pressure level with an addition of 10 dB during the night-time. This metric penalises aircraft that operate during night hours (as effectively being noisier) due to the fact that the majority of the population is asleep.

Noise exposure footprint and contours

Although noise exposure contours are inherently not a metric, they represent a great way of visualising other metrics at observer locations around airports. They are used by airport management teams and other organisations around the world to drive airport plan decision-making and to help inform manufacturers and governing agencies on the scale of the effect aircraft have on the community they operate in. Noise exposure contours and how to efficiently generate them form a great part of the research within this thesis and the main topic of Chapter 4.

A distinction is made between noise exposure footprints and contours. Noise exposure footprints are the result of single event operations. Footprints are visual method of interpreting individual aircraft noise immissions relative to certification limits. For example, the top part of Figure 2.3 (A) illustrates the evolution on footprint area and shape when determined my the limits set by the various noise Chapters of Annex 16.

On the other hand, contours are the result of aircraft fleet operation. These present a realistic measure of the noise exposure experience by communities surrounding airports. Figure 2.3 (B) shows such a contour for London Heathrow Airport in the year 2015. Contours take into account fleet composition, operation models, realistic aircraft flight trajectories and performance and are usually the result of high-fidelity modelling, measurements or a combination of the two.

Note on the use of 1/3$^{\text{rd}}$ octave bands

MONTANA follows the standard practices with respect to the spectrum type used for the calculation of the previously mentioned metrics. The IEC standard (61260-1:2014 [33]) specification for one-third-octave bands is used, for the standard 24 frequency bands from band number 17 to 40 (centre frequencies 50 Hz to 10,000 Hz). This is predominantly driven by the ANP database data format, which provides the baseline spectra for the MONTANA studies presented herein. Equivalent definitions are provided by the ANSI S1.11-2004 standard. A square band-pass filter is used across the whole framework (summation of tonal/discrete spectrum to SPL/Hz band spectrum).

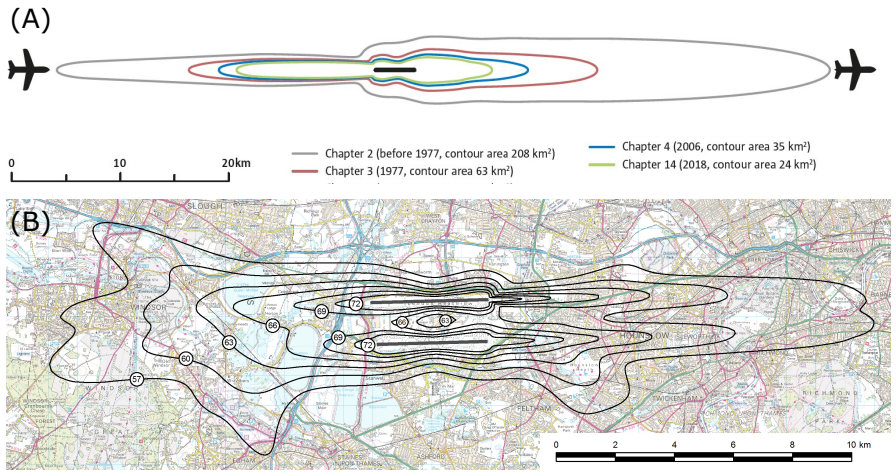

FIGURE 2.3: (A) Illustration of departure and approach noise contours and contour area as a function of the limits presented in the noise Chapters of Annex 16 [27]. (B) Example noise exposure, $L_{eq,T}$, contour for London Heathrow Airport for the year 2015 [32].

2.1.5 Noise Certification and regulations

The noise limits are different for aircraft according to their, a. air vehicle type (fixed wing, helicopter, tilt-rotor etc.), b. age, c. weight (maximum takeoff mass, MTOM and maximum landing mass, MLM) and d. propulsion system type. Depending on the type of aircraft, the limits are measured at specific reference locations in the vicinity of airports, called certification points.

Small aircraft

In the context of this thesis "small aircraft" are defined as: propeller-driven aeroplanes not exceeding 8,618 kg, as per Chapter 10 of the ICAO Annex 16. Aircraft certified under this Chapter must limit $L_{A,max}$ levels at one certification point, the takeoff reference noise measurement point. The takeoff reference is located on the extended centre line of the runway at a distance of 2,500 m from the start of takeoff roll, while the mass of the aircraft must be the MTOM at which certification is requested.

Large transport aircraft Large transport aircraft include subsonic jet aircraft and propeller-driven aircraft over 5,700 kg or 8,618 kg, depending on their age. These aircraft are certified in accordance with Chapters 3, 4 and 14 of the ICAO Annex 16. The certification points in this class of aircraft are three: a. lateral full-power, b. flyover and c. approach. In many cases the lateral and flyover point are referred to together as takeoff certification point, where a cumulative noise level is defined as the sum of the two individual noise levels. The location of three points can be seen in Figure 2.4 relative to the runway. Note the lateral certification point is different for jet-powered aircraft and propeller-driven. The metric used is the EPNL, with specific limits imposed as function of MTOM/MTOW.

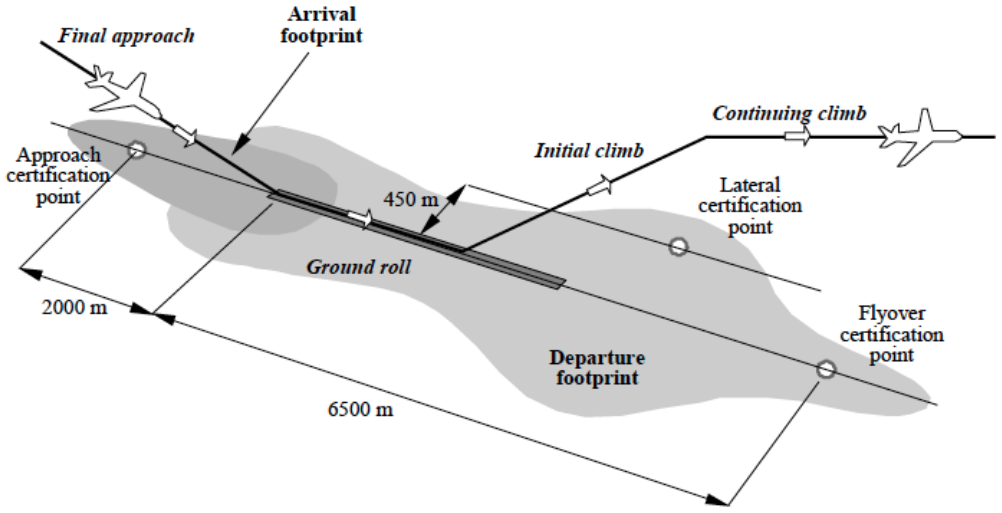

FIGURE 2.4: Large aircraft certification reference points [34].

Helicopters

Helicopters are certified under Chapters 8 and 11 of the ICAO Annex 16 (Chapter 11 applying only to helicopters not exceeding 3,175 kg maximum certificated takeoff mass), while a separate Chapter and procedure is allocated to tilt-rotors (Chapter 13). The reference noise measurement points defer slightly to their fixed wing aircraft counterparts. The takeoff and approach procedures require limits to be met at three locations each. In addition, three more reference points are required in an overflight (term flyover is used within this thesis) operation. The metric used, again is the EPNL.

2.2 Aircraft Noise Sources

Aircraft capitalise on the interaction between the air and the aircraft airframe in order to generate lift and propulsive thrust. This multitude of interactions are different in scale and properties. They are also responsible for the vast variety of noise sources present on air vehicles.

Aircraft aeroacoustics deals with aerodynamic noise generated as a result of the relative motion of solid body components of the aircraft frame or streams of fluid and the surrounding fluid. Aerodynamic noise in acoustic terms may be separated into two main categories: discrete (tonal) noise and broadband noise. Discrete tonal noise signals may be further categorised into pure tones, tones and complex tones [35]. Two further types of aerodynamic noise may be observed from aircraft, that is impulse noise and “bangs” [36, 37, 38, 39, 40, 41] (for example sonic booms) but are not dealt with in this thesis.

Within aircraft aeroacoustics a noise source is typically defined as particular mechanism or process (e.g. vortex interaction, buffeting, reflection) or may be defined as noise originating from some particular component (e.g. propeller, landing gear, fan, jet etc

noise sources). All of these sources may contain discrete and broadband noise components.

2.2.1 Conventional fixed wing noise sources and models

Fixed wing aircraft typically belong to one of two families, airliners and general aviation (GA) aircraft. Without it being a defining rule, the main reason for differentiating these two families of aircraft is the type of propulsion system and size. Modern airliners typically use turbofan or turboprop engines to generate thrust. General aviation vehicles due to their size and power requirement use propellers powered by reciprocating engines. As the majority of the noise generated by an aircraft emanates from the propulsion system, the types of noise sources present on each family of aircraft varies significantly. Following is a brief breakdown of the dominant noise sources present on conventional fixed wing.

The dominant sources present on modern airliners may be seen in Figure 2.5.

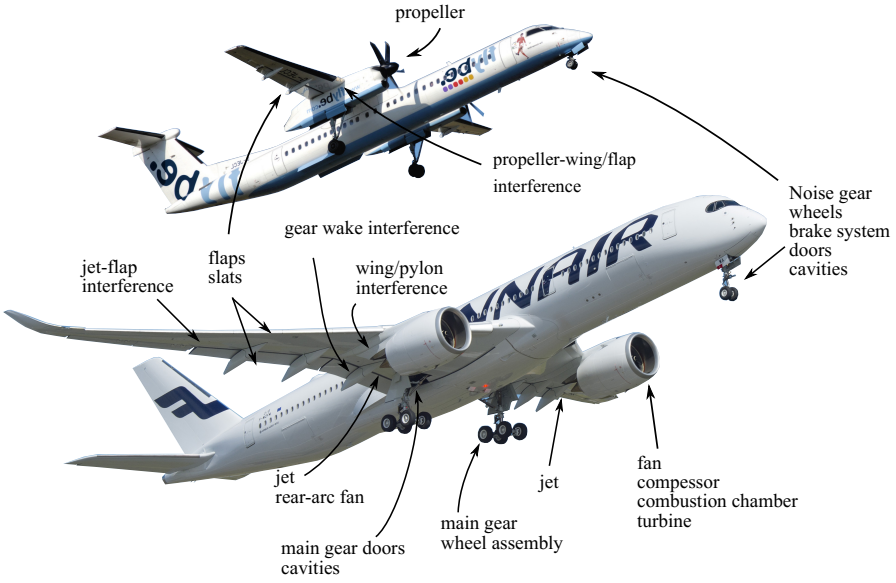

FIGURE 2.5: Depiction of most relevant noise sources on-board of conventional turboprop and turbofan aircraft.

Although for most flight regimes engine noise sources dominate, this is not the case with approach and landing operations. Due to minimal thrust requirement and the addition of high flap and slat settings and extended landing gear, airframe noise significantly contributes the overall aircraft noise as received on the ground. This is also supplemented by the fact that ever-increasing bypass ratios (BPR) reducing the acoustic strength of the engines sources. A generic source breakdown at approach and takeoff condition can be seen in Figure 2.7. The relative dominance of individual noise sources has evolved throughout the years, as engine bypass ratios have been growing (resulting

in fan and jet velocities reductions), current Ultra-High Bypass ratio engines have significantly different noise signatures to earlier turbojets (Figure 2.6).

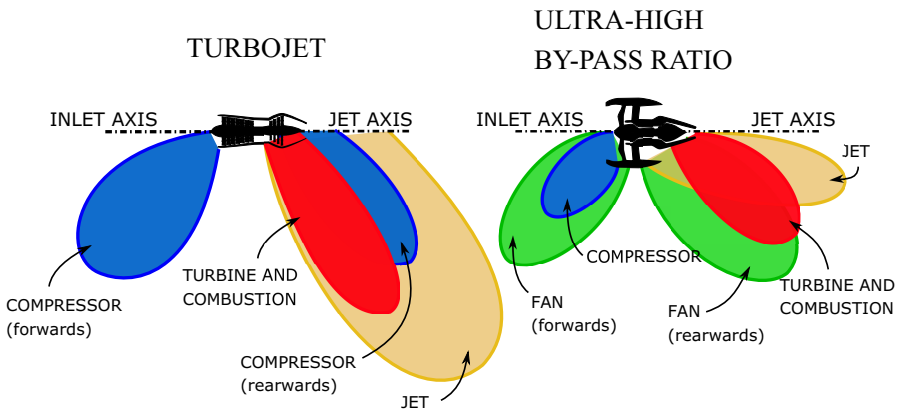

FIGURE 2.6: Evolution of engine noise strength from Low BPR all the way to modern Ultra-high BPR engines.

The variation of PWL of the various source components, results in large changes in the frequency content and directivity of the aircraft as a whole; with previously masked components, now contributing significantly to the noise at particular angles. An obvious example is that of the rearward fan component, which was previously less dominant and covered by the jet source.

2.2.1.1 Airframe

Airframe noise is the global term used for the noise generated by components of the aircraft airframe as it moves through the air. The interaction of the airflow with the aircraft (wing, fuselage, landing gear etc.) causes the formation of turbulent structures within the flow. The size and properties of these structures is strongly dependent on the component geometry and the flow driving mechanisms (pressure gradients, friction). The frequency content of the noise is correlated to the size of the turbulent structures and is regarded as broadband.

Specific noise-generating mechanisms (Figure 2.5), include flap and wing trailing edges, flap side edges, undercarriage gear sources, cavity mechanisms, and sources associated with the fuselage and wing turbulent boundary layers. Additional noise is associated with high-lift devices and configurations, as well as their involvement in interaction sources between the airframe and the propulsion system, such jet-flap interaction.

The general signature of airframe noise is a complex combination of broadband and tonal noise. Trailing-edge, flap side-edge and undercarriage noise, all contribute to the broadband component of airframe noise. Unsteady separated flow (vortex shedding) and wake interactions between due to airframe geometry of varying sizes, gives rise to broadband sound over a wide frequency range. A great number of discrete frequencies

are seen, typically in the low frequency range, between 50 Hz and 500 Hz, due to resonance mechanisms, often cavity related [36].

Large variation in intensity and spectral shape is observed across airframe architectures and designs. Correlations from full-scale aircraft data often scale the OASPL with the fifth and/or sixth power of the aircraft velocity and with directional dependence of a single compact dipole (with vertical axis); however the formulas are simply convenient approximate fits to data in which a number of mechanisms are probably comparably important, and are not blanket theorems to be applied to all cases.

As a typical example, the airframe noise of the standard Boeing 747-100 and 747-200 is substantially different from that of the 747SP, the latter having a much simpler single-flap system instead of the triple-flap system fitted to the standard 747 [36]. Additionally, experimental data of a Boeing 747 [42] showed a total "clean to dirty" PNL increase of 10 to 12 dB.

Airframe noise becomes significatly more important at the approach condition for conventioanl fixed-wing, for the following reasons. First, the low power requiement of the approach operation means the source balance tips in to the favour of airframe noise, as the propulsion system will be operating in relatively favourable low noise operating conditions. Second, the required "dirty" configuration of the airframe (extended high-lift devices and landing gear) at approach, will contribute to the increase in intesity of airframe noise. Finally, the combination of the final approach glide-scope of 3 degrees, and low airspeed, means that the aircraft is significantly closer to the ground for longer; increasing the noise exposure on communities beneath the approach flightpath.

Airframe model

In the context of whole aircraft noise prediction, MONTANA requires the contribution of airframe noise components for completeness of lumped source model. MONTANA uses the implementation of the Fink [43, 44] model by Synodinos [12] to generate noise level deltas as a function of variation in aircraft airspeed and flap deflection. At the time of its development, the Fink model provided a combination of a wide range of full-scale and model data representative of the dominant theoretical ideas widely accepted as correct. Since, other comprehensive models have been developed, based on additional experimental and computational data as well as analytical developments; such a model is the once presented by Guo [45, 46].

2.2.1.2 Engine/Propulsion

The main two propulsion system architectures of interest are turbofan and turboprops. An illustration of the dominant sources present on such engines is presented in Figure 2.8.

In current generation turbofans fan and jet noise sources dominate the spectrum and field shape. In the case of turboprops the propeller tonal self noise (steady and unsteady) typical dominates. Smaller contributions from other internal components are audible at different phases of flight [21, 36].

Engine jet noise is regarded as the turbulence mixing noise produced by the high temperature and velocity exhaust jet. Noise is generated my the mixing of the core exhaust jet, the bypass jet with the free-stream flow (shear layers). The well known eighth power law relates the intensity of the jet noise source to the eight power of the exhaust velocity ($I_{jet} \approx U_j^8$). This result was first introduced by Lighthill [47]as the Lighthill's acoustic analogy, in which the unsteady fluid flow is replaced by a volume distribution of equivalent acoustic sources throughout the entire flow field. He essentially proved that any approximations in attempting to solve for the fluctuating acoustic density (starting from the exact flow equations, conservation of mass, momentum and energy) would result in huge errors due to the fact that the energy radiated in terms of noise is almost a negligible fraction compared to kinetic energy of the jet.

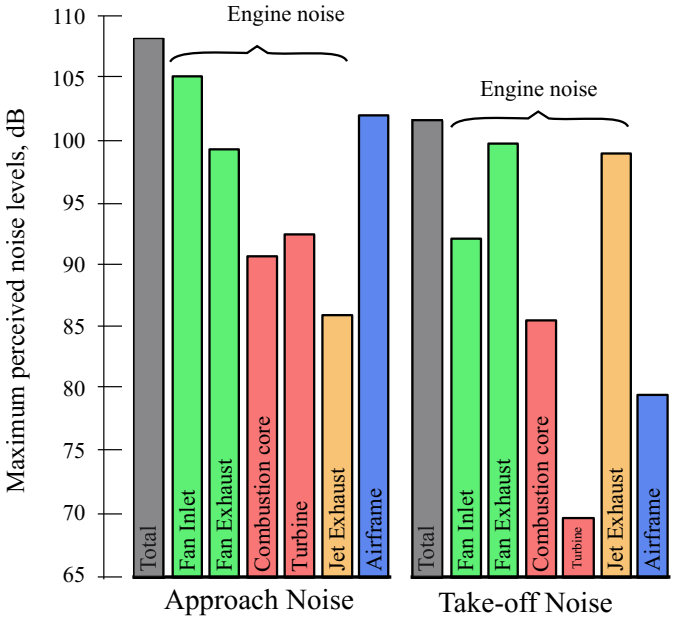

FIGURE 2.7: Component noise source levels during flyover for conventional turbofan. Adapted from [36].

Turbo-machinery captures all the components within a typical turbofan engine. This includes the fan, compressor, turbine and associated stators. Turbo-machinery is characterised by distinct tonal content due to the rotating blades of the fan, compressor and turbine. Broadband noise is also present, but becomes more significant at lower tip speeds. Finally, acoustic coupling to and propagation within the fan duct causes further interference and acoustic modes to develop.

Combustion and core

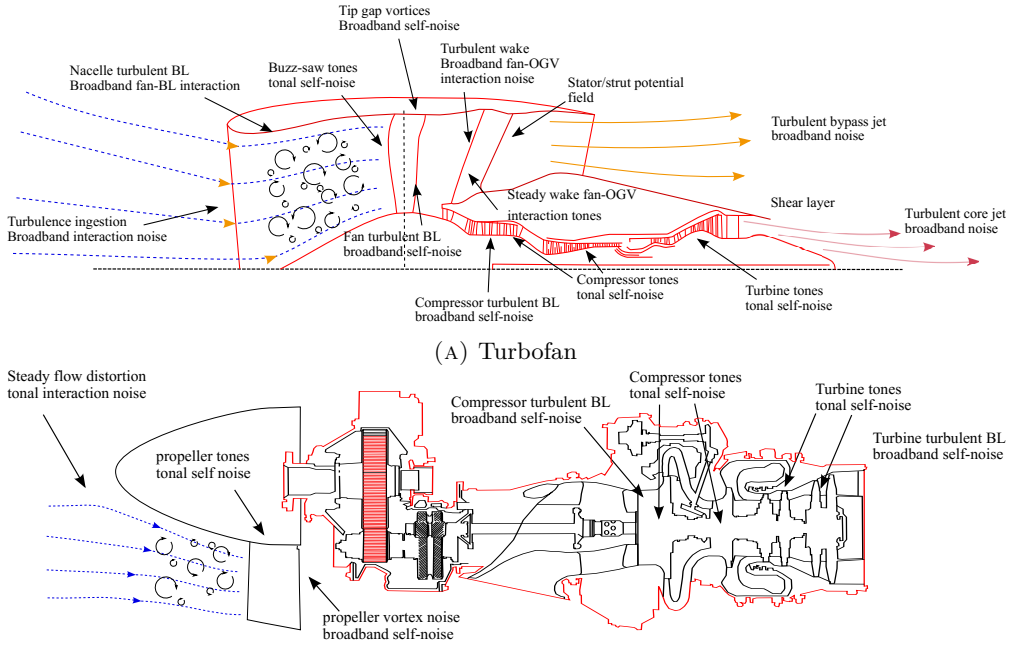

FIGURE 2.8: Cross-sections of a HBP turbofan and a turboprop engine, identifying the individual noise source mechanisms present.

Combustion noise mechanism relate to both gas turbine engines and reciprocating engines. In gas turbines noise is associated with the unsteady processes of volumetric expansion and contraction in the combustion chamber[48].

Exhaust noise often prevails in piston engine noise. Broadband in nature, unabated exhaust noise is most intense at low frequencies. Although there is also significant discrete noise related to the frequency of cylinder firings, modern exhausts, mufflers, and resonators are quite good at reducing the radiated acoustic energy.

2.2.2 Conventional helicopter rotor noise sources

Rotor noise is aeroacoustically characterised as a very similar noise generator as propeller noise. Composed of two very distinct components, discrete tonal and broadband noise, the aeromechanical noise generating mechanisms can be broken down into the deterministic sources of thickness, loading, blade-vortex interactions and high-speed impulsive noise. These sources are generally responsible for the dense tonal content of rotor noise, while the non-deterministic effects of turbulence ingestion, blade-wake interactions and blade self-noise make up the broadband component of the noise.

The similarities in noise generating mechanisms between rotors and propellers allow the analysis and review of the noise sources to be done simultaneously. This is done in Section 2.3. However, although present in both systems, high-speed impulsive noise and

blade-vortex interaction noise do tend to dominate the rotor noise spectrum, while taking a back seat in the propeller case. A brief breakdown of these two sources follows.

Impulsive noise is due to the advancing blade (in forward flight) reaching transonic and supersonic tip Mach numbers. It is characterised by loud, sharp, periodic sounds caused by a dramatic increase in amplitude and increases in in-plane (rotor plane) acoustic energy radiation. It is a form of thickness noise that dominates the waveform when present, and distinguishes rotorcraft noise from other types of noise.

Blade-vortex interaction (BVI) noise as described by the name is cause when rotors interact with previously shed tip vortices by the preceding rotors. As blade rotation and tip-vortices are periodic phenomena, BVI noise is also periodic occurring at deterministic locations around the rotor circumference. It is described by many as the main source of annoyance for rotorcraft due to the high number of harmonics contained within. The BVI source is due to propeller loading effects, and therefore is contained within the dipole term of the Ffowcs Williams-Hawkings (FW-H) equations [49] or the simplified Farassat Formulation 1A [50], [51].

2.2.3 Conventional noise source models

A summary on components level prediction models is given in Table 2.1. Prediction models used in the definition of lumped sources in this thesis are also indicated. Except propeller steady harmonic noise, all other models base their implementation into the MONTANA framework on the work by Synodinos [12, 52].

Additional method and tool summaries are available in these references [70, 35, 71, 72].

2.2.4 Novel aircraft sources

Electric motor noise

In the absence of a gas turbine or reciprocating engine propulsion system, the noise sources associated with rotating turbo-machinery and combustion also vanish. In the case of fully electric prototype aircraft, especially in the sub-regional (UAM) market (see Chapter 3), a combination of electric motors and propellers are often the propulsion system of choice.

Current prediction methods for electric motor noise largely depend on semi-empirical methods using data from large industrial electric motors and/or small unmanned air-vehicle (drone) motors, and then applying scaling laws and vibration analysis.

The sound produced in electric motors is predominantly caused by time-varying electromagnetic forces, producing vibrations. These vibrations are what drive the

TABLE 2.1: Summary of component level noise prediction methods.

Individual source prediction methods	
Noise Source	Prediction methods
Engine-order tones (buzzsaw)	NASA TMX-71763* [53], Benzakein & Morgan [54]
Subsonic fan	NASA TMX-71763* [53]
Compressor	NASA TMX-71763* [53]
Turbine	NASA TMX-73566 [55]
Combustion	SAE ARP 876C [56]
Jet (single-flow, round nozzle)	SAE ARP 876C [56]
Jet (coaxial flows)	MDOE[57], JeNo[58]
Propellers	SAE AIR 1407 [59], NASA TMX-83199 [20], Hanson [60],Farassatt [61]
Helicopters	NASA TMX-80200[62], PSU-WOPWOP [51, 63, 61]
Airframe	Fink, FAA Report RD-27-29* [64], Boeing airframe [65, 45, 66, 46]
Flight effects	Bryce [67], Cocking [68],NASA TMX-79155952* [69]
Methods marked with an asterisk are used within this thesis.	

acoustic field. Research by NASA [73],[74],[75] consider the noise produced by the motor negligible compared to the fan and jet noise, in a DEP setup. This however may not be the case in the propulsion systems developed for urban air mobility systems, as motor noise scaling is not yet well-defined.

Motor noise consists of the following features[1]:

- Tones are the most important noise source
- Presence of broadband noise source
- Motor noise peaks in a direction normal to the motor rotor axis.
- Loading the motor increases acoustic emission for some conditions and configurations
- Strong motor tones can be amplified by the propeller loading by 5 to 15 dB and can exceed the propeller noise levels (see Figure 2.9).

These empirical correlations extrapolated to larger motors predict the sound power levels to be lower than the fan noise for a commercial subsonic aircraft: a. 8 to 20 dB for 1 MW motor powering a regional jet-size aircraft. b. -17 to 29 dB for 13.8 MW motor powering a 737-size aircraft. Motor tone predictions for high power density motors show

[1](Based on experimental results using small brushless DC motors[73])

that the noise can be significantly higher or lower than the empirical correlations and exceeds the stated uncertainty[74].

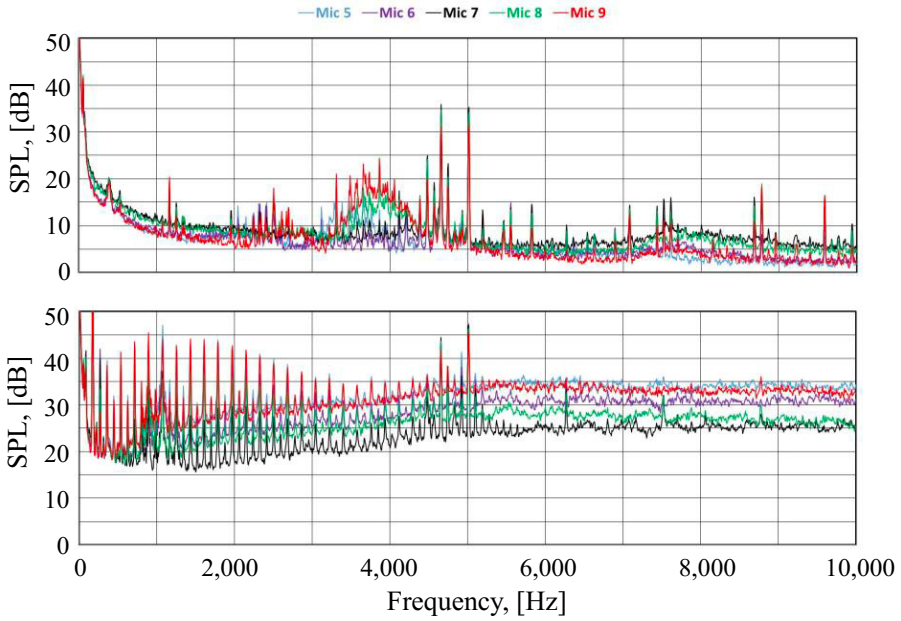

FIGURE 2.9: SPL spectra for electric motor at 5,370 RPM. (Top) Motor only. (Bottom) Two-bladed propeller and motor. Figures reproduced from [74, 75].

Even with the lower sound power levels predicted for the motor, it is possible that a portion of a flyover during approach will include motor noise depending on the motor installation. Motors mounted within the engine core will likely have enough insertion loss due to the installation (20 dB) that the motor noise will be insignificant [74],[75].

There is still a clear need to undertake noise measurements of the full scale commercial electric planes once they are available to fully understand their noise characteristics and any different source noise directivity considerations that may need to be used for noise modelling. As of this stage in the study they are omitted, but are to be included in terms additional source modelling (if available) or as a delta correction.

Hydrogen combustion

Similar to conventional kerosine, hydrogen combustion noise is driven by the unsteady processes of volumetric expansion and contraction, however flame attachment due to high reactivity of H_2 has a significant effect on how low-swirl injectors responce to self-excited flame oscillations. This leads to significantly higher acoustic driving due to the compact shape of the flame and its flame folding dynamics. Mitigation of flame attachment and/or deferring the formation of the outer shear layer is needed to avoid such noise generation dynamic mechanisms.

Other

Additional noise sources due to the architectural and design of novel aircraft include interaction of individual propulsor aerodynamic and acoustic fields, interaction of airframe components with the propulsors and fuselage scoop/intake, engine valves. Flow over open cavities or cut-outs in the surfaces of aircraft often produces intense pressure oscillations in the cavity which radiates discrete noise. Such sources are grossly dependent on the configuration selected for any particular design and are therefore hard to generalise.

2.3 Propeller noise

As the topic of propeller noise is of particular interest to this thesis, a quick summary of the noise generating mechanisms and techniques of assessments is given. An overview of the Hanson frequency domain model for the prediction propeller steady harmonic noise is also provided, as it forms the basis of the analysis carried out in Chapter 4 and the derivation of the scaling laws.

Noise generated by propellers has been generally separated into two categories: the *periodic* and the *broadband* components [76] [36]. Rotational or periodic noise is defined as sound identified at discrete frequencies occurring at harmonics of the blade passing frequency (function of number of blades). Vortex or broadband noise is a product of the unsteady pressure field associated with vortices generated by the blade aerofoil trailing edge and tips along with turbulence effects associated noise sources. Rotational noise is sub-categorised into, 1. thrust and torque noise and 2. thickness noise, with the first dominating at rotational speeds within the domain of incompressible assumptions. Nevertheless, in literature on the reduction of overall propeller noise, at high flight speeds thickness noise may exceed that of thrust and torque, with vortex noise also having an important contribution[77].

A single-rotating open rotor generates rotor-alone tones which are produced by thickness, loading and quadrupole sources. Such tones occur at integer multiples of the rotor's blade passing frequency (BPF). Thickness noise is produced by the periodic volume displacement of air by the rotating blades. Its amplitude is dependent on the geometry of the blades. This source is equivalent to a surface distribution of monopole sources. Steady loading noise is produced by the steady surface stresses acting on the surface of the blades. Whereas thickness noise is generally important at high velocities, the loading noise component is dominant at low and moderate speeds [36], [78] and [79].

Discrete noise (Hanson frequency domain model)

The Hanson model is a far-field frequency domain model for a single rotating propeller using a helicoidal surface representation of the blades. Hanson's formulation was chosen in this study as it accounts for the linear thickness and loading sources and the

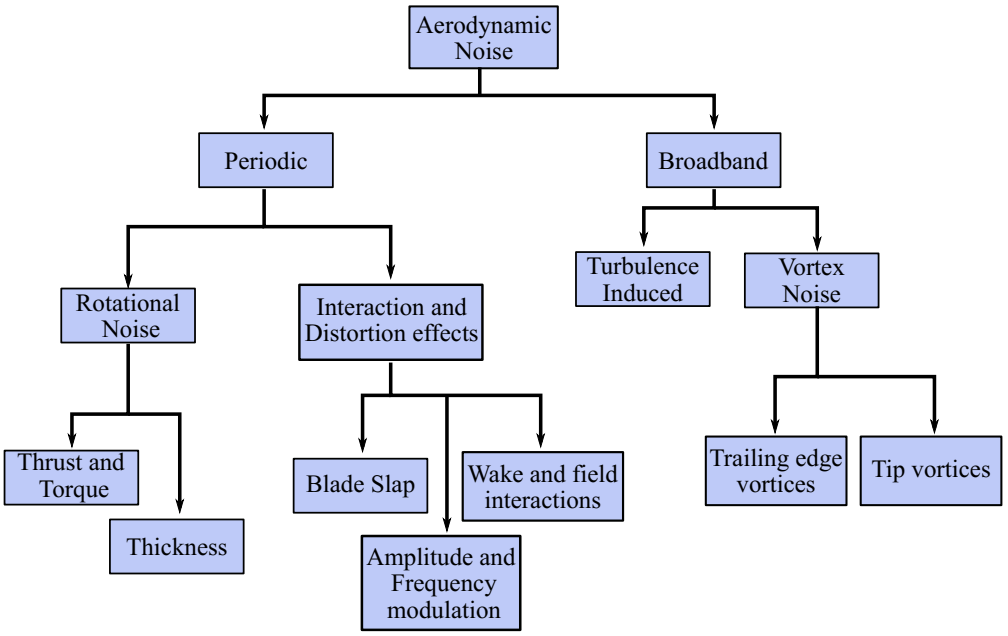

FIGURE 2.10: Propeller Aerodynamic Noise breakdown. Adapted from [76].

nonlinear quadrupole sources (although omitted due to the operation regime) including forward flight effects, and to this day represents a unifying theory of propeller harmonic noise. Hanson published an extension to the method to account for unsteady-loading which will also be omitted for the analysis presented within this thesis.

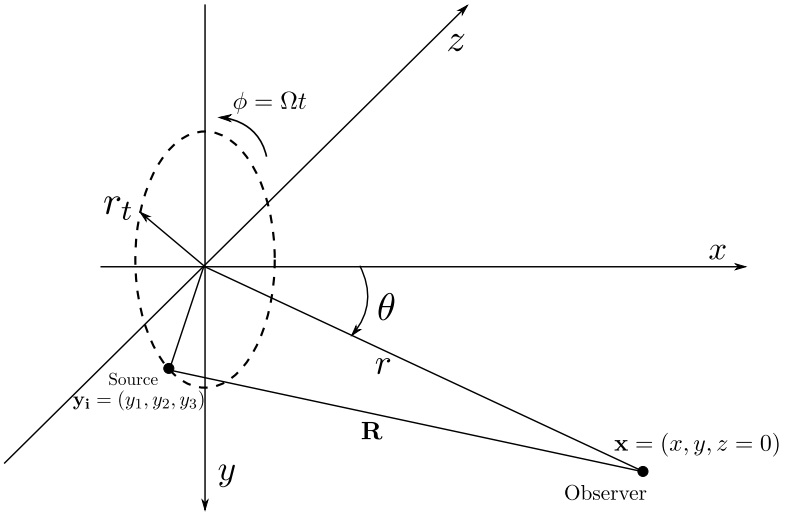

FIGURE 2.11: Geometry of rotating source and acoustic field. The rotating source position $\mathbf{y_i}$ vector is parametrically defined through the radial coordinate r_0 [60].

Hanson's derivation starts at the Goldstein [80] version of the acoustic analogy. Using approximations from thin wing aerodynamic theory, the propeller blade is modelled as an average surface between the blade upper and lower surfaces.

As a result, the source strengths are derived from the geometry of the real blades, but their point of application is the average helicoidal surface. To study the effects of blade

design and operation parameters Hanson recast his solution into a form that explicitly displays these variables. This form is duplicated here for the ease of the reader and is the starting point of the asymptotic analysis and scaling model in Chapter 4.

Let the propeller of interest be of diameter D (and radius r_t) and number of blades B. The chord-to-diameter ratio is given by B_D, while the maximum thickness-to-chord ratio by t_b. The propeller is assumed to be in flight with a representative axial Mach number of M_x. The propeller is rotating at an angular rate of Ω, giving the propeller tip Mach number as M_t. Due to the forward and rotational motion, each blade section sees a relative Mach number of $M_r = \sqrt{M_x^2 + z^2 M_t^2}$, where $z = r_0/r_t$ is the normalised radial coordinate. The loading characteristics are defined in terms of the aerodynamic coefficients C_L and C_D, returning the dimensional force per unit spanwise length (Newton/meter) when multiplied by $1/2\rho_0 c_0^2 M_r^2$. The location of the observer is given by the polar angle θ in the plane perpendicular to the propeller plane, while the distance between the centre of the propeller hub and the observer is given by r. A detailed illustration of the reference frame can be seen in Figure 2.11. The noise harmonics are given in terms of their Fourier transform coefficients P_{Vm}, P_{Dm} and P_{Lm} for the thickness, drag and lift sources respectively,

$$\begin{Bmatrix} P_{Vm} \\ P_{Dm} \\ P_{Lm} \end{Bmatrix} = -\frac{\rho_0 c_0^2 B \sin\theta}{8\pi\Big(y/D\Big)\Big(1 - M_x \cos\theta\Big)} \exp\left[imB\left(\frac{\Omega r}{c_0} - \frac{\pi}{2}\right)\right] \times \int_0^1 M_r^2 \exp\left(i\phi_s\right) J_{mB}\left(\frac{mBzM_t \sin\theta}{1 - M_x \cos\theta}\right) \begin{Bmatrix} k_x^2 t_b \Psi_V(k_x) \\ ik_x (C_D/2) \Psi_D(k_x) \\ ik_y (C_L/2) \Psi_L(k_x) \end{Bmatrix} \mathrm{d}z \tag{2.29}$$

where c_0 and ρ_0 are the ambient speed of sound and air density, ϕ_s represents a phase lag due to blade sweep (neglected further on in this study as simple blade geometry is assumed). The mode number is m, giving the harmonics as multiples of the BPF, $\Omega B/2\pi = \mathrm{RPM} \times B/60$. The non-dimensional wave numbers k_x and k_y are defined by,

$$k_x = \frac{2mBB_D M_t}{M_r(1 - M_x \cos\theta)} \tag{2.30}$$

$$k_y = \frac{2mBB_D}{zM_r}\left(\frac{M_x - M_r^2 \cos\theta}{1 - M_x \cos\theta}\right) \tag{2.31}$$

In this form, Ψ_V,Ψ_D and Ψ_L represent the Fourier transforms of the three sources, axial loading (lift/thrust), tangential loading (drag/torque) and displacement (thickness). The

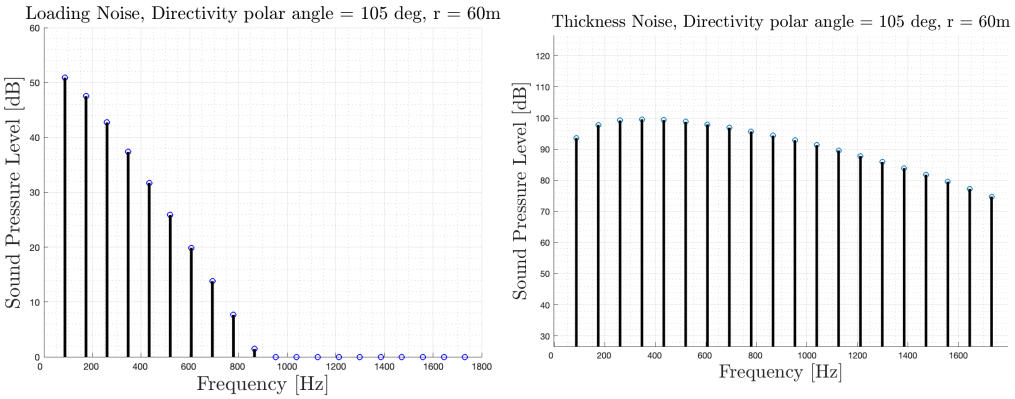

(A) Loading noise.

(B) Thickness noise.

FIGURE 2.12: Example harmonic content of propeller noise sources as predicted by implementation of the Hanson frequency domain model.

thickness and loading source distributions of the blade are also given by Fourier transforms,

$$\begin{Bmatrix} \Psi_V(k_x) \\ \Psi_D(k_x) \\ \Psi_L(k_x) \end{Bmatrix} = \int_{-\frac{1}{2}}^{\frac{1}{2}} \begin{Bmatrix} H(x) \\ f_D(x) \\ f_L(x) \end{Bmatrix} \exp\left(ik_x x\right) \mathrm{d}x \tag{2.32}$$

where $f_L(x)$ and $f_D(x)$ are chordwise lift and drag distribution functions and $H(x)$ the chordwise thickness distribution of the blade.

Finally, the contributions of the individual sources may be summed $P_{mB} = P_{Lm} + P_{Dm} + P_{Vm}$ to get the Fourier transform coefficient of the pressure at the m^{th} harmonic of the blade passing frequency. The far-field time domain fluctuating acoustic pressure may be given by,

$$p(t) = 2\mathrm{Re}\left[\sum_{m=1}^{\infty} P_{mB} \exp\left(-imB\Omega\right)\right] \tag{2.33}$$

Figure 2.12 shows an example prediction of the discrete tones due to general aviation sized propeller.

The directivity of the three sources is also given by Equation 2.29. Each harmonic radiates noise uniquely, while the total acoustic filed directivity may also be calculated. Figure 2.13 gives example of generic monopole and dipole directivity as reference to the Hanson directivities predicted by Equation 2.29.

Broadband noise

Propeller broadband noise is a form of loading noise that originates from several stochastic sources of unsteady loading [63]. The stochastic or random nature of

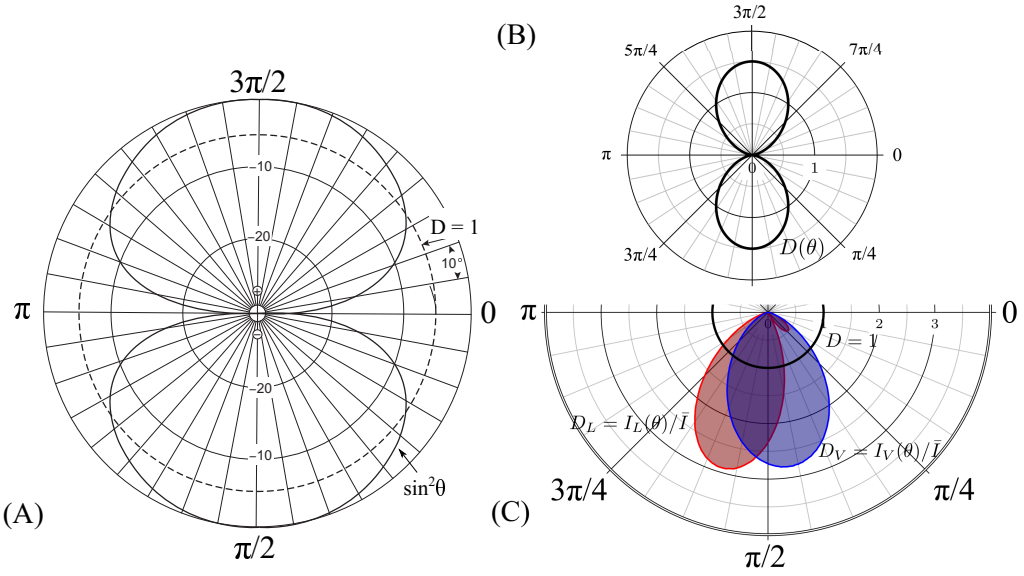

FIGURE 2.13: (A) Directivity index [dB ref $\theta = \pi/2$] of dipole (solid line) relative to a monopole (dashed line). (B) Dipole directivity (non-dimensional) factor version of A. (C) Directivity factors for loading and thickness noise as predicted by Hanson Equation 2.29.

broadband noise makes prediction by first-principles methods difficult. For this reason semi-empirical noise models are usually used when assessing the contribution of broadband noise.

Pegg [62] published a comprehensive review on propeller broadband noise prediction capabilities based upon methods by Lowson [81, 82, 83], Hubbard [84] and King [85]. The methods focus on three sources: 1. boundary layer noise, 2. inflow turbulence noise and 3. vortex noise. Example of the relative contributions from the four (vortex noise is separated into tip vortex and general vortex noise) broadband noise sources can be seen in Figure 2.14.

Another, more extensive method for estimating broadband noise was proposed by Brooks, Pope and Marcolini [86] in 1989. The model analyses five self-noise mechanisms due to boundary-layer phenomena:

- boundary-layer turbulence passing over the trailing edge
- separated-boundary layer and stalled-aerofoil flow
- vortex shedding from laminar-boundary-layer instabilities
- vortex shedding from blunt trailing edges
- turbulent vortex flow that exists near the tips of lifting blades.

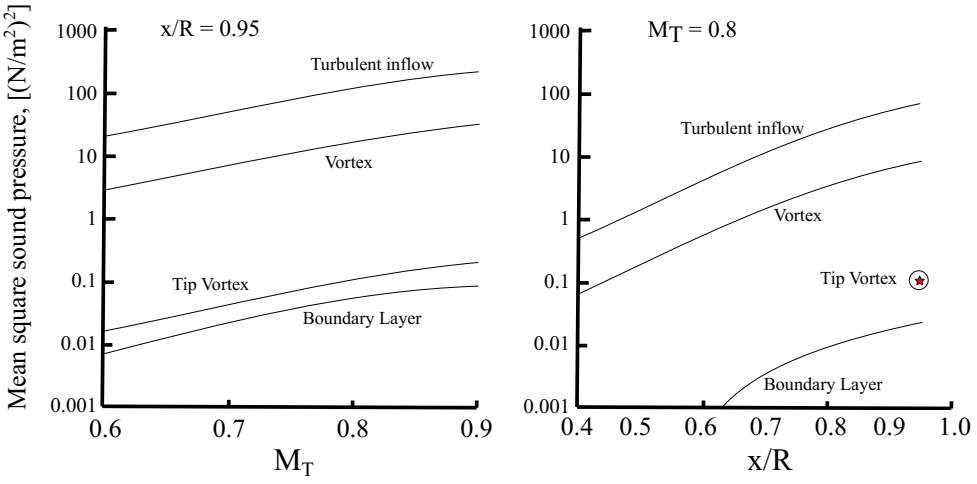

FIGURE 2.14: Variation of broadband noise with Mach number and spanwise location on rotor blade. Figure reproduced from data from [62].

2.4 Noise propagation

Propagation involves additional factors that will influence the magnitude of noise received at observers. These include atmospheric attenuation, diffraction and reflection as well as spherical spreading. Atmospheric absorption refers to the decrease in noise intensity due to the dissipation of acoustic energy to viscous effects and molecular interactions and is a function of meteorological factors such as temperature, pressure and humidity. Generally higher frequency noise sources dissipate energy and thus are more attenuated in the atmosphere than lower frequencies [87]. Noise attenuation through the atmosphere at a given frequency increases with decreased humidity [87] as dry air is denser and absorbs more acoustical energy than moist air. Temperature impact on attenuation depends on frequency and humidity [87]. Commonly used models for predicting and accounting for atmospheric attenuation are the SAE ARP 866A [88] and SAE AIR-1845 [89] methodologies (used in this thesis), as well as the updated SAE-ARP-5534 [90] or Rickley et al. [91]. The ISO 9613-1/ANSI S 1. 26-1995 [92] is also a widely accepted method for the prediction of such effects.

Ground effects, terrain, and any additional sound insulation at the observers are also factors. Whether the surface at the observers is acoustically “hard” or “soft” will impact the noise signature at the ground. Acoustically hard surfaces will generally result in stronger reflection of sound waves and depending on the geometry of the sound wave source and observer location can result in constructive or destructive interference of sound waves [93]. Acoustically soft surfaces such as grassy terrain will result in a stronger absorption of sound wave energy. ESDU in the UK has developed a series of models for the prediction of ground effects and reflection including, ESDU 89036 and ESDU 94036 [94].

2.5 Aircraft operations

So far what has been discussed is noise generation at the source and reception at the observer location. Reduction of said noise is not limited to reducing the noise generated at the source; meaning the aircraft. Such reductions comprise one out of four proposed ways of limiting noise at airports and the surrounding communities by the ICAO's Balanced Approach to Aircraft Noise Management [5, 6],

- Reduction of noise at the source,
- land-use planning and management,
- noise abatement operational procedures, and
- operating restrictions.

As discussed in the aircraft metrics Section 2.1.4 the time period exposed to noise is of great importance, hence the need for average acoustic energy metrics. What determines the time exposure is the speed of the aircraft and the geometry of the aircraft trajectory relative to a specific observer. The use of noise preferential runways and routes may alleviate noise exposure levels for certain observers, by increasing the distance to the flightpath. This idea of optimising flight trajectories around airports for noise is what is labeled *noise abatement operational procedures*. The relation of observer location and flightpath geometry may be visualised in Figure 2.15, where the example of a turn over/past an observer drastically increases noise exposure.

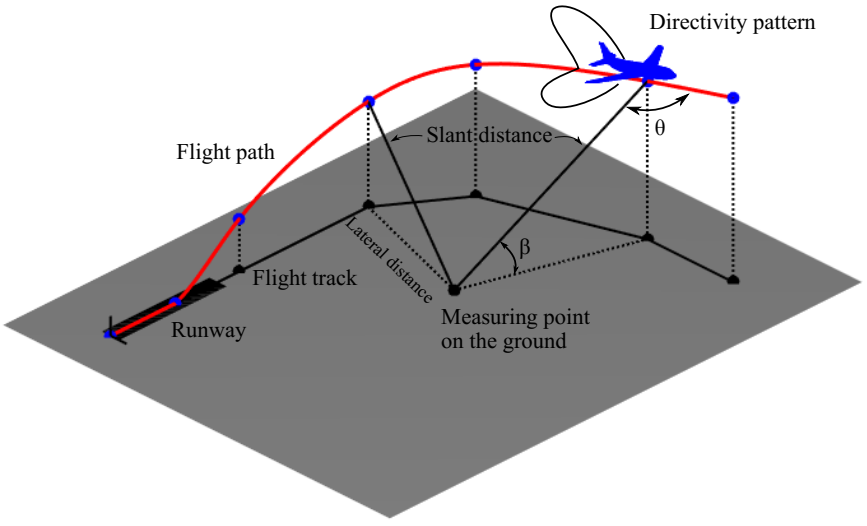

FIGURE 2.15: Geometrical model of takeoff operation for airport noise predictions.

2.5.1 Noise mitigation through operations

Aircraft operations introduce a trade-off of operational parameters. An aircraft performing a takeoff operation could do so in a low power setting, velocity and climb angle. This would result in reduced noise source strength, due to low lower power requirements during a shallow and slow climb. However, this results in the aircraft remaining close to the ground for a longer time period. The other option would be to climb away from the ground as steeply and fast as possible, at the cost of high thrust requirement and therefore noise generation. This trad-off is at the centre of the concept of noise mitigation through operations.

Section 7 of ICAO Doc 8168 Part 1 proposed three types of noise abatement procedures to be used when appropriate and safety is not compromised. These include:

- use of noise preferential runways,
- use of noise preferential routes
- use of noise abatement takeoff or approach procedures.

The final point correlates directly to the trade-off described. For takeoff Doc 8168 provides guidance on how to perform two types of Noise Abatement Departure Procedures (NADP 1 and 2). A description of the procedures may be seen in Figure 2.16. Critical point along the trajectory are dictated by V_2 the takeoff safety speed and V_{ZF} the zero flap speed. The NADP procedures take advantage of reduced power/reduced drag techniques (or a combination of both), to alter the acceleration segment according to the requirements (provide noise reduction to areas in proximity to the runway, or to more distance areas of the community).

Similar techniques may be employed for approach operations, such as a continuous descent approach. Details and guidance on such operations may be found in Doc 8168 [95] and Doc 9931 [96].

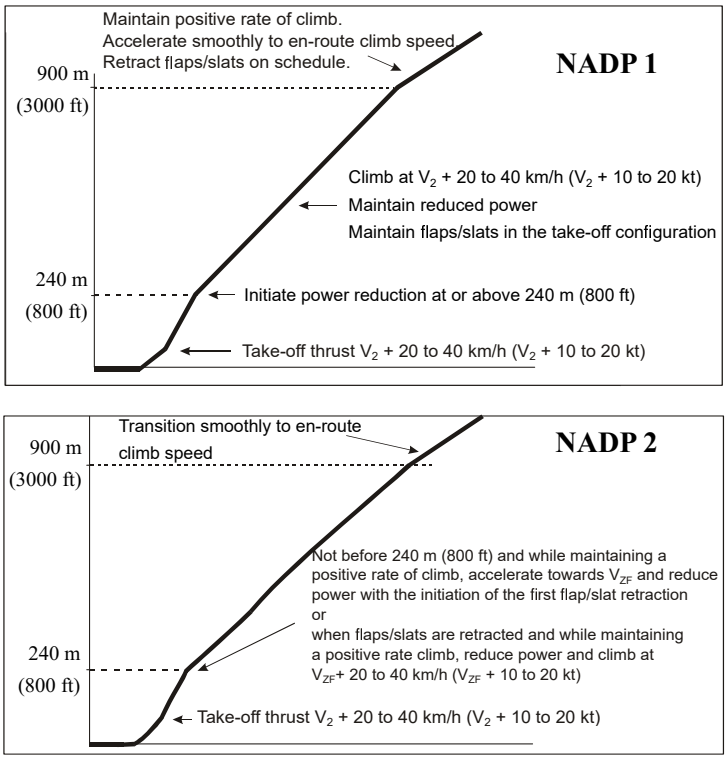

FIGURE 2.16: Noise abatement takeoff climb procedures NADP 1 and 2, as suggested by the ICAO Doc 8168 [95].

2.6 Noise-Power-Distance curves

The topics within this Section are important to this thesis and are therefore considered in detail.

All airport noise models consider the following three main parameters when calculating noise on the ground. The implementation, however, of these within each model varies allowing for the wide range in fidelity.

- The subject noise source (as discussed may be a lumped noise source consisting of many individual sources), defined by a radiating sound power and sound directivity.
- The aircraft trajectory. The aircraft trajectory depends on many parameters, the type of operation (e.g. departure, approach), the type and size along with the operating weight aircraft, naming a few. The trajectory defines the geometry between the aircraft (source) and the observer locations on the ground.
- The aircraft power setting. As mentioned this determines both the trajectory and the energy that is radiated in terms of acoustic waves.

It is of common practice to use Noise-Power-Distance (NPD) curves in the airport noise as it presents a simple yet efficient way of relating the sound power radiated (both

instantaneous and time averaged) by the source at different aircraft power settings to different propagation distances and configurations (i.e types of operations), in a tabulated database. The NPD process standardises the collection of full scale aircraft noise data for certification requirements and operational noise modeling.

Noise measurements tests are not only performed for certification purposes at the approach, sideline and flyover conditions. Additional tests are performed to gather noise data in various operational conditions, for example, different aircraft weights or airframe configurations (i.e. flap settings and landing gear). In order to gather the data necessary to calculate the noise levels in all flight scenarios, four or five flights with more than 100 test points are often conducted for the certification of a new aircraft type [97].

The resulting noise datasets are what are defined as Noise-Power-Distance curves. NDP curves are generated for all (large civil) aircraft during certification or in many cases additional individual flyover noise measurement campaigns. Flightpath/trajectory and weather data is also retrieved from such campaigns to enable normalisation of the noise levels to reference distances and conditions. Aircraft operational noise can then be modelled by combining and interpolating different curves to approximate real trajectories.

The collection of NPD data is done separately for the approach and takeoff conditions. For approach certification, the standard approach slope of 3 degrees must be used to calculate the noise level in all flight conditions. Numerous measurements are made using various thrusts and, consequently, various slopes that are aimed at the measurement spot. At approach speed, the aircraft is stabilised in level flight on the runway axis. Once the required approach path is intercepted, the pilot starts descending on the needed slope with modifications to the thrust. For each decent slope the objective is to fly over the 120-meter reference noise measurement point. Throughout the whole decent until just after the measurement window, the thrust, slope, and speed are maintained. Figure 2.17 illustrates this procedure for approach and takeoff NPD curves.

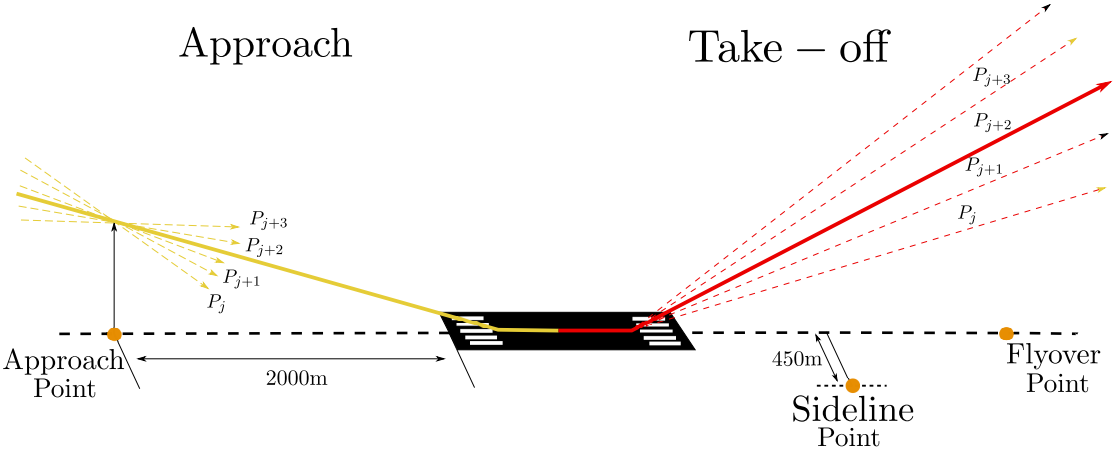

FIGURE 2.17: Illustration of actual experimental NPD flight operations.

For instance, the approach speed must be maintained with a precision of 3% while the lateral tolerance is around 20 m [27]. Measurements with the gear up or down at the minimum idle thrust are also taken.

Given that there are two certifications points, determining the noise levels during takeoff is more difficult. Additionally, in accordance with operational guidelines, the thrust reduction to "climb thrust" may be carried out before passing the flyover reference noise measurement point. To enable consistency, repeatability and reproducibility the operations are simplified to constant thrust climb manoeuvres past the flyover point. The climbs are comprised of a range of engine thrusts, from takeoff thrust to climb thrust. This method enables the noise level to be calculated at both measurement locations under all operational circumstances. This results in the flyover condition being a purely computational noise level, calculated by "knitting" together contributions from multiple constant thrust climbs.

Takeoff operations and their certification tests are not performed from a stand still at the start-of-roll. An equivalent procedure, beginning with a low-level flypast to join the computed takeoff trajectory, is permitted by the certification authorities in order to save money and time and avoid numerous landings and takeoffs. To cover all operational scenarios, these tests are done with various takeoff weights and takeoff configurations.

The international aircraft noise and performance (ANP) database [98] is the main source of NPD data for this thesis. It has been built in collaboration of aircraft manufacturers and certification authorities while it is maintained and constantly updated by EUROCONTROL.

Helicopters

Noise-Power-Distance curves for helicopters and rotorcraft with VTOL capabilities differ largely to the equivalent of fixed wing aircraft. As helicopters have been around for more than half a century, a methodology for creating the different types of curves has been already developed. As UAM aircraft operational procedures are expected to closely replicate those of helicopters the methodology is presented as a mean of understanding noise immissions from vertical and hover flight enabled vehicles. The original methodology (presented here) was developed by the FAA [99] and used for the development of NPD curves serving as input data for Airport Noise software INM. Changes to the final method applied to UAM vehicles may be required.

Helicopter operational procedures are developed from three distinctly different flight profiles (Figure 2.18) for originating or terminating from appropriately sized heliports (or heliport manoeuvre area, HMA correctly termed). All potential terminal manoeuvres and flight phases are applicable to VRF and IFR (Visual and Instrument flight rules respectively) operations and can contain combinations of flight phases, from any of the baseline profiles.

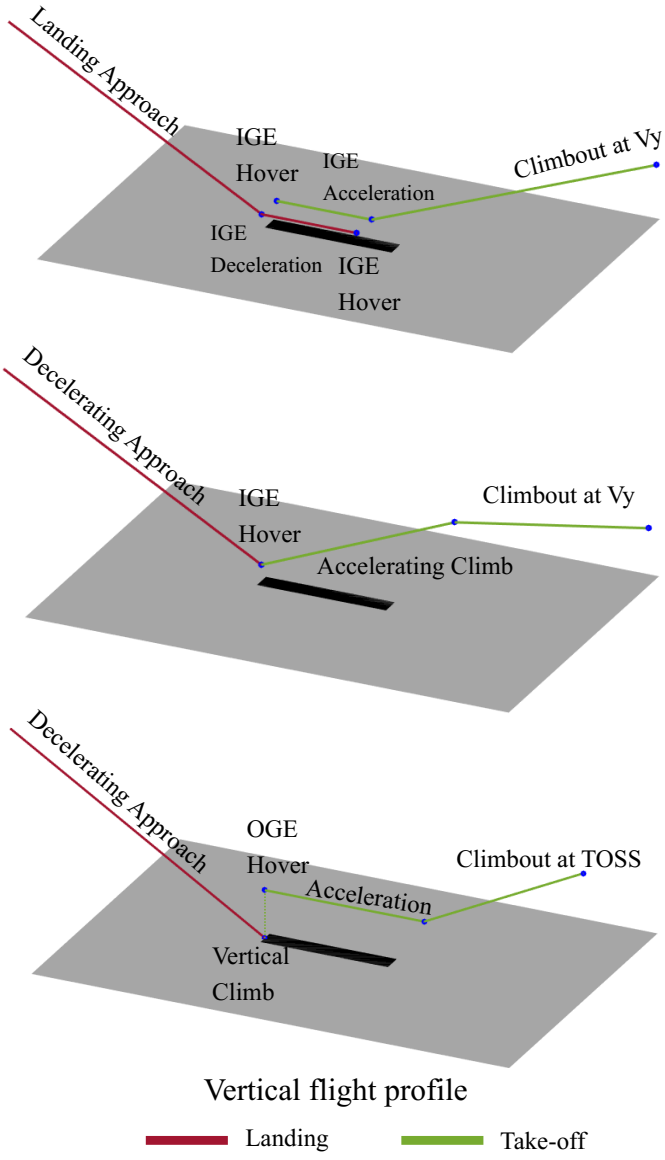

FIGURE 2.18: Three type of flight Profiles for heliport operations.

The HMA size is determined by the distance required to accelerate to a given climb airspeed at takeoff, for a specific departure profile. During approach operations, VFR approach angles of 6 to 9 deg are common for commercial operations with passengers, and rarely become as steep as 12 degrees. In terms of noise, significant deviations in noise levels occur if blade-slap approach regimes are entered.

Noise curve development process is split into two main procedures a. Air-to-ground data extrapolation and b. Ground-to-ground (low angle) propagation. In Air-to-ground noise levels are adjusted in approximately the same manner as in fixed wing aircraft. The one-third-octave sound pressure level spectrum for each selected event is the starting point for any given extrapolation. Each band sound pressure level in the spectrum is then “decayed” to longer slant distances using adjustments for spherical spreading and atmospheric attenuation.

Ground-to-ground propagation follow the techniques in Doc29 [34] and [100] for lateral attenuation and ground attenuation. Alternative methodologies are provided for cases when a spectrum is unavailable [99].

As seen in Figure 2.18, the three flight profiles can be broken down into segments with drastically different operational mechanics and parameters (which account for different noise generating mechanisms and sources). In order to realistically recreate a specific departure/approach profile four types of curves are used: a. takeoff noise curves, b. approach noise curves, c. level flyover noise curves and d. hover noise curves.

2.7 Existing Prediction Tools

Tools for predicting aircraft noise are generally classified into two groups "best practice" and "scientific" [72]. Best practice tools are typically fully empirical methods based on the data collected through full scale or rig experimental measurements and are best applied to existing technologies and aircraft. Deviations from the conditions of the measured data are commonly corrected through factors, which themselves are based on additional datasets, approximations and often mathematical models. Such tools are described as semi-empirical, and try to combine the cost-effective computational requirements of empirical methods with the benefit of introducing physics based modelling, to increase the application field beyond that of the underlying data. Semi-empirical tools lie between "best practice" and "scientific" tools.

Scientific or theoretical tools are genarally overlap with physics-based models and are governed by the computational intensity, detailed and often propriatery input requiments. Scientific tools are often considered high-fidelity methods. Examples of scientific tools are Computational Fluid Dynamics (CFD) and Computational Aeroacoustics (CAA) tools or other finite element-based tools for propagation and analytical mathematical models. Quasi-static flight simulation tools, as well as three-dimensional ray-tracing model also fall under this category.

Airport noise prediction tools, as well as individual noise source prediction methods can fall under both classes, as will be discussed, with specific references to several tools.

2.7.1 Aircraft noise source models

ANOPP 2

The NASA Aircraft Noise Prediction Program 2 (ANOPP 2) is a varying fidelity noise model allowing for users to choose between low computational cost modelling for design space exploration and design optimisation, or detailed high-fidelity simulating models for the advancement of noise mechanism and phenomena understanding. Conventional and

unconventional designs may be assessed through the use of aircraft noise component prediction, distributed sources, propulsion system installation effects and propagation to the far-field. The method is based on nested Ffowcs Williams and Hawkings surfaces [101] allowing for the range in fidelity.

DLR tools

The DLR (German Aerospace Centre) has developed a suit of tools over the past decades able to assess aircraft noise from a component level all the way to airport fleet scenarios. TAU [102] and PIANO [103] assess noise emission on a component level, while PANAM [104] conducts noise immission studies of entire aircraft operating at different flight configurations. Component level predictions are based on numerical and semi-empirical models developed from experimental investigations. PANAM is responsible for combining individual noise sources and generating overall noise radiation patterns for entire aircraft. Modular flight trajectories are used to calculate noise on the ground.

EMPA tools

FLULA 2 and sonAIR are aircraft noise models designed by Empa (Swiss Federal Laboratories for Materials Science and Technology). sonAIR is the new generation tool being designed and aimed at replacing the currently used model FLULA2. Both models are based on a point source (lumped source) with a specific directivity pattern. The source is flown along a discretised flightpath, while SPL levels are recorded at receiver locations on the ground. Flight radar data of real flights may be used to increase accuracy and detail of the studies. sonAIR allows for shielding (buildings, topography, ground reflections and foliage attenuation) effects to also be accounted for.

PSU-WOPWOP

PSU-WOPWOP [105, **?**] is an aeroacoustic prediction model for helicopter main-rotors. It uses Farassat's Formulation 1A [106, 107] of the Ffowcs Williams-Hawkings equation to calculate acoustic pressure. With amendments made by Goldman [63] the model is capable of including broadband noise sources as well as the discrete-frequency noise sources. The package also outputs effective perceived noise level (EPNL), as expected for calculating the certification levels.

2.7.2 Airport noise frameworks and models

In the realm of airport noise prediction, following the international guidance on aircraft noise modelling [34, 108], tools usually take one of two routes: 1. Segmentation or integrated approach or 2. simulation methods. Simulation models represent the most straightforward way of calculating airport noise. Noise receptors are modelled as grid on the ground (terrain may be accounted for), the aircraft then flies along a very finely discretised version of an otherwise continuous flightpath. For every time step the aircraft

moves from one point to another, and aircraft performance variables vary depending on the actual performance at that location in space and time. A sound level (any desirable metric) history is therefore created at each location on the observer grid. Although this method closely replicates reality and has the potential to produce greatly accurate predictions it has very high computational demands and requires detailed information about the performance, noise source properties of aircraft.

Segmentation or integrated approach represents best practice for airport noise modelling. It is adopted by the main airport noise tools and is recommended by the Doc29 Report on Standard Method of Computing Noise Contours around Civil Airports. It is based on dividing the flightpath into a series of linear segments along which the aircraft maintains principle parameters constant (e.g. velocity, noise power). An example takeoff flightpath is illustrated in Figure 2.19. The noise contribution for each segment is estimated by calculating what fraction of the infinite segment noise corresponds to that particular segment. The infinite segment noise data corresponds to NPD flyover data, for which comprehensive databases already exist and have been collected for years.

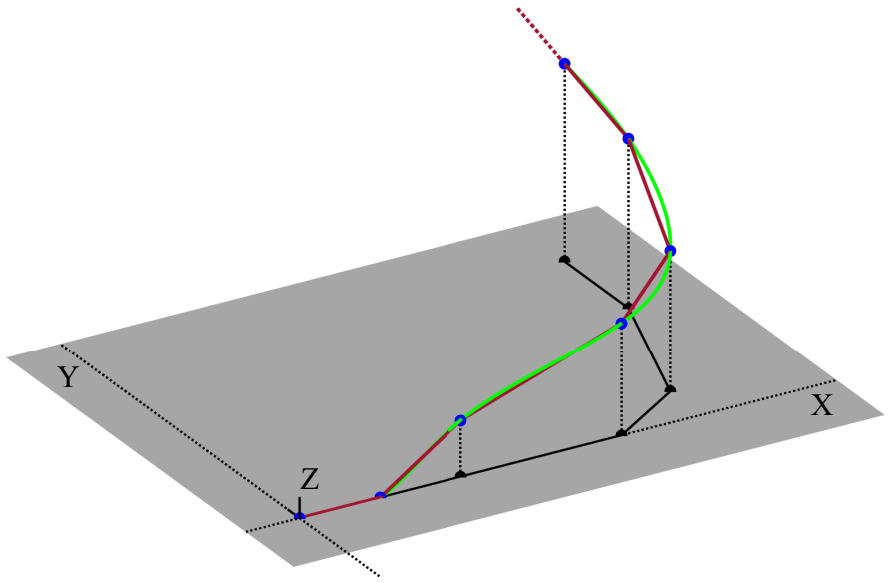

FIGURE 2.19: Illustration of segmentation of a continuous flightpath. The green path represents the realistic continuous trajectory, while the red linear segments the discrete path.

NASA FRAMEWORK

Led by the contributions of Rizzi et al. [109], NASA is leveraging their suite of aircraft noise and performance tools to develop the next generation airport noise framework. Combining the whole aircraft noise prediction capability of ANOPP2, with models for the evaluation of air-vehicle aerodynamics and dynamics (e.g. CAMRAD II [110]) three-dimensional noise spheres are created for vehicles as a function of time throughout an event [111, 112]. Then using simulated flights, NPD curves for conventional fixed-wing and rotorcraft style operations (modes)/maneuvers are generated [112]. Slight

modifications to the FAA's AEDT allow for the use of these NPD curves in combination with flight trajectory and fleet definitions to calculate the noise exposure in communities in the vicinity of any flight operation, conventional or novel [113, 114]. Finally, the noise received at the observer location is processed through using a series of psychoacoustic models and metrics to measure the impact aircraft noise has on humans [115].

IMPACT

Integrated aircraft noise and emissions modelling platform (IMPACT) is a model developed by Eurocontrol. It includes aircraft performance and trajectory modules allowing for trade-off studies between fuel economy and noise/emissions to be conducted. It is based on the ICAO Doc 9911 [108] and ECAC Doc. 29 [34] recommendations, while inputs are taken from Eurocontrol's various databases. Aircraft performance is calculated using the most recent BADA 4 [116, 117, 118] model and the outputs are noise contours, surface and population counts, estimates of fuel burn and emissions. IMPACT also includes calculation for helicopter and rotorcraft based on their BADA Family H [119] performance model and extensive noise database.

AEDT

The FAA's Aviation Environmental Design Tool (AEDT) is a comprehensive airport noise tool used by governing agencies and airport management bodies worldwide to conduct highly detailed studies, at the cost of computational time and efficiency. It uses NPD curves and the integrated model methodology as suggested by the ICAO Doc29 recommendations. AEDT allows for studies from single flights to airport scenarios at the regional, national, and global levels. Noise immissions are outputted in a range of metrics, varying from instantaneous to averaged levels.

Recent updates to AEDT (e.g. version 3c) introduced a variety of new features for aircraft performance and noise modelling. The ability to enter user defined flight profiles through ANP or BADA 4 procedural profiles allow for further flexibility when dealing with VTOL and STOL (Short takeoff and landing) vehicles, while improved drag models allow for a negative thrust value displayed for some approach segments when more drag than thrust is being generated.

RANE

RANE [13] is a simplified airport noise prediction model developed in the ISVR, University of Southampton. It uses the concept of noise surfaces and noise radii to produce noise exposure contours for conventional and novel aircraft. An extensive look into the modelling techniques employed by RANE can be found in Chapter 4. This thesis extends the capabilities of RANE for use with highly directive noise sources and vertical takeoff and landing (VTOL) capable vehicles.

ANCON2

ANCON, is a European National model, which follows the methodology detailed in [65]. ANCON is the mathematical model used to produce the annual Leq(16-hour) aircraft noise exposure contours published by the Department of Environment, Transport and the Regions (DETR) and previously by the Department of Transport (DoT). It is also used to produce noise exposure forecasts for use in airport planning studies and similar aircraft noise models are used in many other countries.

STAPES

STAPES is a joint EC/EASA/EUROCONTROL project to develop a model capable of calculating the total number of people exposed to certain noise load levels at major airports in Europe, for use in EU and ICAO noise policy work. Core noise model is based on specifications from ECAC Doc 29 and ICAO Document 9911. The STAPES noise model has been validated against UK ANCON2 model, but the software is a complete new development.

SONDEO and ARMONEA

The software developed by Anotec consists of a pre- and post-processor for the existing noise model software, already developed by Anotec under private funding. The contour module (NCM) calculates noise contours of L_{den} and L_{night} according to [120]. The noise and performance databases used are those provided by INM, since these are one of the few globally accepted datasets publicly available. The population module (PM) is capable of overlaying the noise contours from NCM on population maps, so as to determine the number of people affected by noise.

ARMONEA is based on the SOPRANO platform, a complex aircraft noise source prediction program, developed in EU projects and at present the main common tool for aircraft noise predictions in Europe. Its flexibility allows for its adaptation to a variety of applications, and it is envisaged that the power of SOPRANO will greatly contribute to the success of ARMONEA.

2.8 Low noise design process and uncertainty quantification

Designing aircraft for low noise emission and immission, deals with introducing low noise technologies to the design and operation of air vehicles. Doing so has major implications on target aeroplane noise levels, major design considerations in achieving these levels, operational considerations and their effect on noise, and the sequencing and timing of the design and development process.

When designing new aircraft concepts, or modifications to an existing design, airframe and propulsion system manufacturers set target noise immission levels, in order to

comply with the certification authority limits, but also airport limits, targeting specific operability and reduced associated fees, making the final design more appealing to airline customers. This process of target setting requires a combination of aircraft noise prediction capability, as well as noise measurements and analysis techniques in order to demonstrate compliance to the certification authorities, but also provide guarantees to the prospective customers of the aircraft being developed.

2.8.1 Design Considerations

From a community immission point of view, the design parameters that will impact the final level the most are considered on the aircraft (air vehicle) architecture level, i.e. number of propulsors/engines, positions of propulsors, type of propulsors, thrust-to-weight ratio, lift-to-drag ratio (airframe design). Such considerations are closely tied with the propulsors/engine architecture itself, i.e. propeller diameter, propeller rotation speed, bypass ratio, propulsors size and mass, propulsors thrust-to-weight ratio.

These considerations, will at a high-level define operating conditions, and the types of aeroacoustics noise sources present on any given design. Trade-offs between total takeoff thrust, climb performance and noise levels at the sideline and flyover certification points are examples of typical application of noise prediction frameworks.

2.8.2 Uncertainty quantification

During the low-maturity state of conceptual and preliminary design, many configurations and design points are predicted. As the design matures, the predictions are refined, using frozen design parameters, as well as performance, aerodynamic, and noise test data. To ensure consistent prediction methodology, and to reflect the maturity and uncertainty of any given noise level prediction, the standard process includes, an uncertainty analysis, or a calculation of the degree of uncertainty relative to the nominal estimates or the probability that the actual levels will differ from the estimates by a specific amount when the compliance demonstrations are carried out.

All aircraft noise provisions, standards as well as the process of compliance demonstration is outlined in the appropriate certification documentation by the ICAO [27, 121], and the FAA [122].

2.9 Validation and Verification of tools

Aircraft noise prediction validation is a complex multilayered process, intervening at every step of the modelling and prediction sequence. This process has often been

criticised as lacking a scientific basis and rigour. This is attributed to the difficulty of building reliable datasets, from an engine sub-system level, to the aircraft system in-flight performing standard noise operations, all the way to measuring noise levels on the ground.

As one of the industry standards, Doc 29 presents some quality control and validation suggestions across all layers of the aircraft prediction process. The process identifies key criteria aimed at reliability, consistency, accuracy and others, all of which are to be considered in the context of the tool being developed, the intended application of the tool, the specific studies under-taken, as well as data being used, and data source authentication. As a summary, the practical recommendations are: problem definition, establishing performance criteria, assess alternative modelling approaches, state assumptions and limitations, identify data sources, compare with measurements where applicable, undertake sensitivity analysis [123, 34]. Filiponne [72] presents a flow diagram and discussion of possible interpretations of the Doc29 validation suggestions.

This thesis dedicates Chapter 7 to the verification of MONTANA, at various stages of the prediction.

2.10 Summary

This Chapter presented the theoretical background of sound/noise modelling as used in the field of aircraft noise and aeroacoustics. Aircraft noise modelling was broken down into its constituent parts presenting theory, standard practice, legislative implications as well as human impact and how it is measured. Finally, the academic and industry landscape of aircraft noise prediction was set, pointing to the gaps that the MONTANA framework intends to fill.

Chapter 3

Novel aircraft and technologies

Attempting to fill gaps in aircraft noise prediction, on top of considering new modelling techniques, implies targeting novel case studies and model applications previously unprioritised, bypassed or overlooked.

This Chapter provides a contextual and theoretical background of electric powered aircraft as they comprise the main target application of MONTANA. Fully or hybrid electric aircraft are gaining much ground in the research and development world of aircraft, and are anticipated to form a great fraction of the total aircraft fleets worldwide in the years to come. The theory and background of specific design decisions is introduced in regard to aircraft design and propulsion principles can help explain the consequences on noise generation.

3.1 The advent of Electric aircraft

The aviation world is slowly reaching a turning point. Environmental concerns are driving industry and academic research and development teams to investigate and steadily transition from fossil fuel sources to hybrid and fully electric powered aircraft. Advances in battery technology have already been proven to be effective in the automotive industry [124].

In the aviation world electric and hybrid-electric energy and power systems pose significantly different advantages and disadvantages compared to those of the automotive industry. Critical technologies for electric aircraft include electric motors and battery/energy storage devices. Available electric motor and power-management systems are adequate, while the scalable properties and increased efficiency compared to combustion engines, along with the decoupled nature between the power sources and propulsive devices (motors plus propeller/fans etc.) allow for many different revolutionary designs. In addition to fully electric architecture, hydrogen is being

considered as an alternative to kerosene fuel. The high energy density of hydrogen allows for implementation in larger applications such as regional, single aisle and wide-body fixed wing aircraft, while the propulsion system architecture allows for the choice between direct combustion of the hydrogen or a hybrid solution with the use of fuel-cells and electric propulsors. The caveat however, lies in the fact that storage and distribution of hydrogen becomes significantly more challenging due to its low density.

The technology and implementation of fully electrical or hybrid systems in aircraft is of particular interest for this thesis. As in the automotive and marine industries, the adoption of such systems is inevitable as they offer increases in total efficiency, significant reduction in emissions and increased reliability and safety. Noise emissions are also on the list of positive outcomes, however, the aviation industry presents many more viability questions and challenges with regard to electrification.

Aircraft weight and the weight penalties induced by the current state-of-the-art technologies for power storage (i.e. batteries) and power delivery systems are limiting factors for the full adoption of fully-electric architectures. This is especially true for large passenger aircraft, where long range and high fuel economy are the driving design parameters. Concepts for such vehicles, typically employ hybrid solutions where, for example, turbofan/turbojet engines are used in conjunction with on-board batteries to power electric fans [125, 126, 127, 128, 129].

These limitations although considerable, are less of a factor for small/lighter aircraft, which do not require the multitude of non-propulsive systems (such as the highly sophisticated mechanical, hydraulic and pneumatic systems). This allowed researches and manufactures to start creating retrofitted versions of existing aircraft, such as the electric Cessna 172 and Pipistrel's Taurus Electro or WATTsUP electric trainer [130], to gain an insight on the possibility of fully-electric flight. Pipistrel met production certification in the summer of 2020, for their Velis Electro (Figure 3.1), being the first ever type certified electric powered aeroplane.

Incumbent aerospace manufactures are taking the leading role, with many new promising "start-ups" also greatly contributing. The electrification programs in general may categorised into four types: 1. General Aviation (GA) or recreational aircraft, 2. Urban Air Mobility (UAM), 3. Regional/Business aircraft and last but not least 4. Large commercial aircraft. This thesis focuses on types 1 and 2 with occasional application to types 3 category aircraft. The prevalence of specific combinations of power and thrust production and delivery systems amongst prototypes allows the presented methodologies to be applicable to a wide rage of vehicles. The most obvious design decision being that of the propeller/rotor.

FIGURE 3.1: Pipistrel Velis Electro, the world's first EASA Type-Certified electric aircraft. Photo by [131].

3.1.1 Benefits and drawbacks of electric aircraft

The priorities of propulsion system architecture selection are driven by emissions, fuel consumption and noise. The adoption of fully electric systems contributes beneficially to all three of those components. However, the assessment and quantification of the benefits comes at a cost, as the multi-disciplinary nature of aircraft design, does not allow for trivial conclusions to be drawn. The implementation of electric machines is not as simple as extrapolating the positive effects of individual components to the overall system. Following, is an outline of the benefits and drawbacks current electric aircraft design has to deal with. For greater details and comprehensive analysis the reader is encouraged to read further [132, 133, 134, 135].

Benefits

Most of the benefits of fully-electric (also hybrid) aircraft stem from the nature of electric machines, or in particular, electric motors (EM). In contrast to traditional turbofan engines, EM's may be scaled to appropriate sizes depending on the application, without losses in performance and efficiency. This property opens up new degrees of freedom for designers, allowing for large number of propulsors to be distributed all across the airframe of the vehicle.

Distributed propulsion (DP, or distributed electric propulsion, DEP), as it is commonly termed, may be exploited in numerous ways to improve vehicle aerodynamics, vehicle control, and importantly acoustics. DEP is also enabled by the fact that the energy sources (batteries in this case) are mechanically decoupled from the thrust generating devices or power consumers, such as the EM's. Along with the scaling properties of EMs, this decoupling allows for more flexible way of integrating the propulsion system to the airframe.

Performance-wise, traditionally in turbofan engines, the fan, compressor and turbine form a mechanical chain coupling together torque and speed. This limits any potential efficiency gain of individual components, possible through speed control. The elimination of direct shaft or gearbox drive allows for individual components to be optimised and operated independently to increase performance during different manoeuvres or flight conditions.

As the energy source is no longer integrated within the propulsor, it allows for different energy sources to be considered. For fully-electric aircraft the obvious choice is the use of batteries, however many proposed concepts employ different configurations of turbojet/tubofan along with generators to produce the required electric power to drive the propulsors.

The increase in number of propulsors directly benefits the aerodynamic performance and propulsive efficiency due to the increased effective bypass ratio (BPR). Additional improvements to the aerodynamic performance may be realised through the use of wing flow circulation control. Lift augmentation or drag reduction is achieved by distributing propulsor units above, below, or embedded in the traditional wing configurations. This may result in either higher aspect ratio wings, that are smaller, more efficient in cruise conditions and structurally easier to develop, or for a given aircraft weight, reduce the wing loading allowing for shorter takeoff distances or more aggressive climb, both being important to noise exposure on the ground. Control surface and overall engine sizing may also benefit from lift augmentation designs. The size and positioning possibilities of propulsors may also help improve other inefficiencies, such as wingtip vortex losses. Propulsors placed at the wingtip reverse the motion of the tip vortex cancelling some swirl, resulting in a more efficient wing design.

According to IATA [136], the increase in number of propulsors will not lead higher maintenance costs, due to less maintenance required by individual EM being less complex and having fewer moving parts. However, in the case of engine failure DEP architectures must follow the regulations and certification requirements of all multi-engine aircraft. This requires the aircraft able to perform a takeoff operation at a minimum safe climb gradient after the loss of an engine (one-engine-inoperative (OEI) takeoff condition). This condition typically results in weight, drag, and cost penalties, due to the engines and control surfaces having to be oversized to account for the extra performance and trim margin required in the case of OEI. DEP architectures are by design redundant. Previously mentioned features, such as control of individual propulsors and lift augmentation along with the additional design freedom allows DEP aircraft to eliminate these penalties, as the N3-X concept studies have proven [137, 138].

Due to the absence of internal combustion, as opposed to their air-breathing counterparts, the operation of an EM does not directly depend on the air density and therefore altitude. This allows for further downsizing of the propulsion system. Finally,

electric motors do not produce emissions while operating, which makes them a critical technology for reaching the aircraft environmental goals for 2050.

Drawbacks

The main obstacle in the development path of electric (mostly fully-electric) aircraft is energy storage and the weight penalties associated with mechanisms for storing and supplying electric power. The additional weight of the storage system itself is only compounded by transmission systems and follow-on structural growth. Specifically, an electric propulsion architecture could be comprised of generators, rectifiers, distribution wiring, fault protection, inverters, motors, and the thermal control for those components.

The main disadvantage is the low battery energy density, e_b of actual batteries technologies, which makes it not viable for most aircraft. A simple analysis by Traub et al. [139] on a modified Breguet Range equation for fully electric aircraft shows how the direct penalty on takeoff gross weight due to energy storage is inversely proportional to e_b and linear with range. This is especially noticeable for long range requirements. Additionally, batteries do not lose mass during flight compared to jet fuel, inducing an extra power requirement (for the same mission) therefore leading to again an oversized power supply [132].

Current batteries have a specific energy on the cell level of up to 200 Wh/kg. For comparison, the specific energy of aviation fuel is approximately 12,000 Wh/kg, two orders of magnitude larger. Projected values such as 650 and 750 Wh/kg are 15 and 30 years respectively away from large scale consumer production [133]; however it is estimated that regional hybrid-electric aircraft could operate at around a 50 % hybridization factor [139, 140] by using batteries with a specific energy of around 500 Wh/kg, predicted to be available in the next 5 years.

The very limited energy density of batteries is an established issue for electrifying flight. Yet, it is not the only limiting parameter. Specific power (in kW/kg) also limits the performance capability and hence implementation of battery powered systems. High power requirements for operations such as takeoff and climb (especially for VTOL and eVTOL aircraft where thrust-to-weight ratios > 1 are required) would require drastically over-sized power supplies due to low power output per kilogram of weight of current battery technology. The high power requirements and inability to perform gliding manoeuvres of VTOL aircraft at takeoff requires excessive redundancy for risk and failure management which is yet to be appropriately defined by the certification bodies, for these types of novel technologies.

All these weight penalties ultimately lead to adjustments of the propulsion system to meat the increase in power demand, required to overcome higher rated maximum takeoff weight and meet other performance requirements (climb rate, maximum speed etc.). This adjustment in turn requires higher power output and larger capacities out of the

energy supply system leading in to this vicious cycle. This cycle effectively prohibits long-range, manned, all-electric flights at today's technology levels.

3.2 Hydrogen aircraft: potential future of civil aviation

A particularly interesting sub-category of electric air-vehicles is that of hydrogen powered aircraft. Hydrogen propulsion systems powered aircraft are either equipped with hydrogen-powered fuel cells or with hydrogen-based jet engines, or a hybrid of hydrogen turbines and fuel cells. Direct combustion of hydrogen and hydrogen-powered fuel cells emit zero CO2 emissions, and according to Clean Sky 2 and Fuel Cells & Hydrogen 2 Joint Undertaking [141] (a technology initiative under the EU's new funding programme for research and innovation, Horizon 2020) demonstrate a 30-50 % reduction in impacts from contrail and cirrus formation, compared to kerosene aircraft. The study estimates that hydrogen combustion could reduce climate impact in flight by 50-75%, and with fuel-cell technology by 75-90%.

The biggest flaw to hydrogen-powered flight is the extra weight required for fuel storage, be it in gaseous or liquid form. The requirement of maintaining the hydrogen in a reasonable volume means building tanks capable of keeping the fuel well below its 20 K boiling point, and at pressures of 250-350 bar for the gaseous form.

Airbus has produced three concepts for hydrogen-fuelled airliners with capacities of up to 200 passengers and ranges of 2000 nautical miles (3700 km) or more. Each is proposed to be powered by a hybrid system of combustion turbines and fuel-cell-driven motors. In a turboelectric configuration, a hydrogen-fuelled gas turbine drives an electric generator, and the fan is driven by an electric motor (Figures 3.2).

FIGURE 3.2: Airbus ZEROe concept aircraft, from left to right: 1. Turbofan, 2. Turboprop, 3. Blended-wing body.

Compared to hydrocarbons, liquid hydrogen has a much lower energy per unit volume (noting the limiting factor for batteries powered systems is energy per unit mass, while hydrogen systems suffer from low energy per unit volume).

The most important components in a hydrogen aircraft and infrastructure are:

- Hydrogen tanks: Hydrogen can be stored as pressurized gas or in liquid form. Compared to kerosene, LH2 tanks are still about four times as big. Since LH2 needs to remain cold and heat transfer must be minimized to avoid vaporization of hydrogen, spherical or cylindrical tanks are required to keep losses low.
- LH2 fuel system: The distribution, vaporization, and feeding of LH2 to the fuel cells or turbines. Low temperatures must be handled by pipes, valves, and compressors; boil-off needs to be kept low; and leakage and embrittlement of material avoided.
- Fuel cells: A fuel-cell powered aircraft converts hydrogen into electricity that then drives an electric motor and a fan or propeller. Proton-exchange membrane (PEM) fuel cells are suggested for aviation use as they represent the most advanced technology, with others being investigated for such applications [142].
- Hydrogen direct-burning turbines: In H2 combustion aeroplanes LH2 is directly burned in a turbine, much like kerosene, to create thrust. Modern gas turbines could burn hydrogen with relatively few modifications.
- Fuel supply chain: The infrastructure to produce, liquify, and dispense the hydrogen is one drastically different to that of fossil fuels. Large electrolysis or natural gas reformation centres would be required, while gaseous pipeline delivery or on-site production appear at the only viable solutions for large aviation hubs.
- Airport refuelling: Due to the higher volume of the hydrogen fuel refuelling would still be much slower requiring increased number of fuel trucks or additional fuel hoses. Nevertheless, preliminary estimates forecast the required turnaround times to be possible [143].

3.3 Innovative technologies

In order for all novel aircraft to meet future certification requirements, key technologies must be further developed while others require break-through innovations; This will allow novel regional fixed wing vehicles to enter service by 2035; larger single-aisle zero-emission aircraft by 2050 [144] and the UAM market to initiate operations by 2030 [145, 146].

Electric Motors

In electric propulsion systems, the electric motor converts the stored electrical energy in fuel cells/batteries to mechanical energy; more specifically rotational mechanical energy used to drive a propeller, rotor or fan. Electric motor technology has been accelerated in recent years due to the promising adoption of fully electric vehicles in the automotive industry. Analysis of the different types of electric motors, including direct current,

induction, synchronous motors, found that permanent magnet synchronous motors have better overall performance [147]. However, direct correlation to aeronautical applications is not as straightforward as it may appear. Hybrid-electric, turbo-electric and all-electric aircraft will all require light, efficient and high power density motors to fit in with the weight and size constraints of an aircraft. Modern turbo-shaft engines have a specific power of approximately 7.7 kW/kg, whilst current state-of-the-art automotive electric motors only manage approximately half that at 3.5 kW/kg [148]. Table 3.1 presents current research conducted by NASA sponsorships into electric machine development for large passenger aircraft, noting that specific power goals are almost double those observed in current air breathing technology.

TABLE 3.1: Megawatt-scale electric Machine developments sponsored by NASA, [149].

Electric motor research			
	University of Illinois	Ohio State University	NASA Glenn Research Centre
Cont. power rating, [MW]	1	2.7	1.4
Specific Power goal, [kW/kg]	16	13	16
Eff. goal, %	> 96	> 96	> 98
Motor type	Permanent magnet	Induction	Wound field
Speed, [RPM]	18,000	2,500	6,800
Nominal dimensions	Cyl. 0.45 m by 0.12 m	Ring 1.0 m by 0.12 m	Cyl. 0.40 m by 0.12 m

Finally, state-of-the-art electric motor scaling models have been developed using a variety of automotive and industrial motors [150]. Additions to the scaling models were made by Sinsay et al. [73] whilst also comparing high temperature superconductor motors. The results may be seen in Figure 3.3.

Batteries

A recent survey by Venkatasubramanian et al. [151] into the requirements of battery-powered aircraft and the available chemistries that will enable the transition to battery powered flight, concluded that a specific energy of 600 Wh per kilogram would be achievable with the next decade, however limiting the application to UAM vehicles and small regional aircraft. Large regional or single isle commuter aircraft would

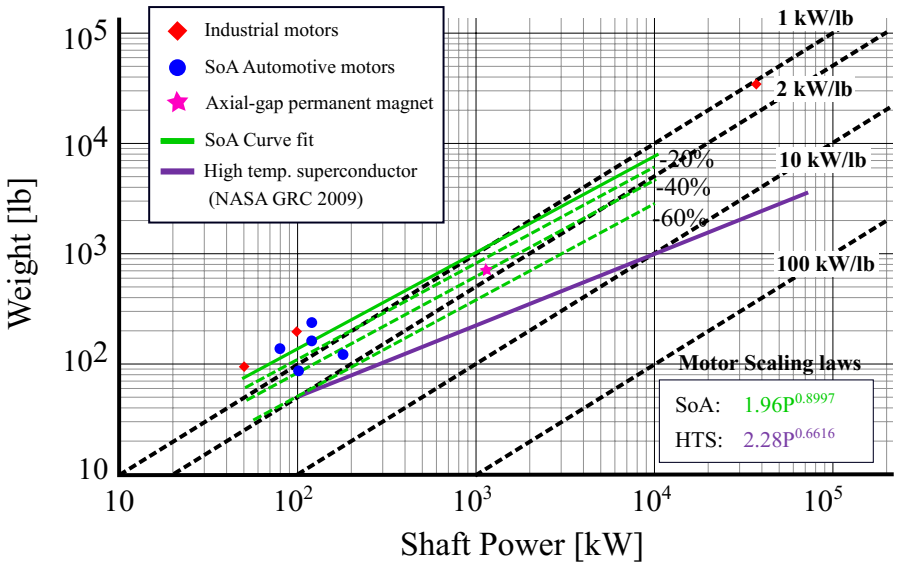

FIGURE 3.3: Various scaling laws for electric motors based on state-of-the-art automotive and industrial and high temperature superconductor motors. Based on work from [150].

effectively require pack-level specific energy in the range of 1,200 - 2,000 Whkg^{-1}, unattainable by current chemistries. Figure 3.4 indicates various battery technologies in a Cartesian map of specific energy versus energy density, with the most promising Li-polymer show potential for achieving 0.650 kWhkg^{-1}and beyond, before the end of the decade.

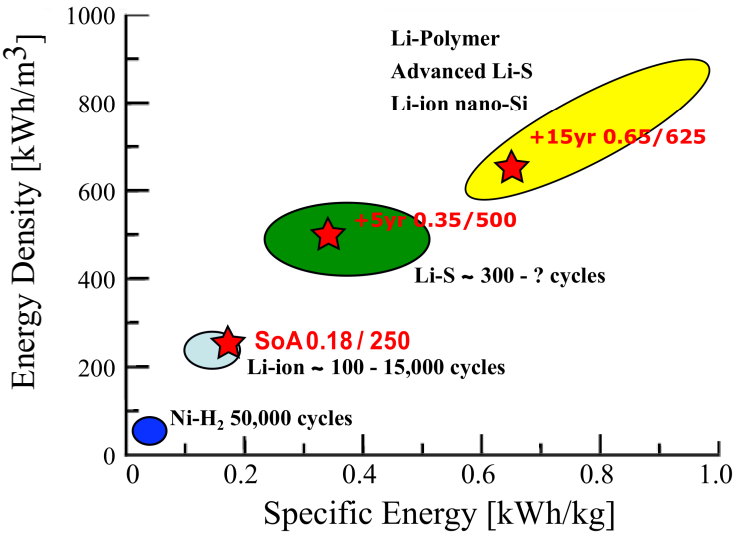

FIGURE 3.4: Battery specific energy and density trends. Adapted from [150].

The very low capabilities in terms of energy storage of batteries, is partially offset by the high efficiency of electric drive architectures, as compared to the low thermal efficiency of conventional turboshaft driven rotor systems. As a result, power delivery and thermal

management of power systems become additional concerns, previously of significantly smaller scale.

Distributed Electric Propulsion (DEP)

The idea of distributing propulsion units across the entire airframe has been around since the early decades of aviation. The implementation of distributed propulsion (DP) would result in a largely oversized propulsion system and great weight penalty. Although exceptions do exist in military aircraft, the most common multi-engine (other than two) configurations use four wing mounted turbofans/turboprops, with notable mentions in the civil aviation category being the Boeing 747 and the Airbus A380. DEP systems replace the traditional reciprocating or turbojet/turbofan engines with electric motors, taking advantage of their scaling properties and ease of maintenance. Examples of industry and academic designed concepts/prototypes are shown in Figure 3.5, illustrating the distribution of propulsors along the wing span. Characteristics of DEP propulsion systems are presented bellow:

- High effective BPR may be achieved. In the context of fully electric the BPR definition no longer holds (as no turbine core flow exists), therefore an more appropriate description would be: increased mass flow rate allowed by increase in effective disk area.
- Variable disk loading may be achieved by toggling the operation of individual propulsors to optimally match propulsive characteristics to the operating flight conditions.
- DEP configurations demonstrate an increased level of fault tolerance which is provided under failures of individual propulsor or electric power source units, as compared to traditional propulsion schemes (this was demonstrated by Synodinos [12]).
- The flexibility of propulsor placement enables an additional degree of control in terms of influence on the aircraft forces and moments.
- Lift augmentation may be implemented by placing a distribution of tractor style propellers/fans along the span of the wing. This results in a smaller wing optimised for cruise,
- The large number of rotors and electric motor propulsion will allow the rotors to operate at low tip speeds, which can greatly diminish noise relative to an aircraft with fewer large rotors (Case study Chapter 8).
- The distribution of propulsor units along the trailing edge of the wing or towards the tail-end of the fuselage allows for Boundary Layer Ingestion (BLI) concepts. By re-energising the boundary layer, BLI concepts promise drag reductions in cruise resulting in fuel economy.

FIGURE 3.5: DEP concept renderings, from left to right: 1. NASA X-57 Maxwell, 2. Airbus EcoPulse™, 3. ISVR DEP Cessna 172 (model designed and rendered by author for illustration purposes).

High-Lift propellers

The integration of the propulsion system and the airframe has potential of providing increases in aerodynamic/propulsion efficiency [152]. Multiple studies on airframe-propulsion integration, including DP architectures demonstrate the benefits of such systems, with the results enhancing the overall vehicle mission performance [153],[154],[155]. Distributed high-lift propellers take advantage of the propeller-wing interactions to effectively act as a high-lift device during low speed operation. A thorough review of the topic is provided by Veldhuis [156] and Patterson [157].

The flow induced by the propeller may be decomposed into two components, the axial and tangential components. The axial velocity (in the same direction as the propeller axis) component is responsible for thrust generation and commonly is the largest of the two. Due to potential flow principles, the pressure differential across the propeller causes the flow to begin to accelerating in the axial direction upstream of the disk. This acceleration continues as the flow moves downstream of the disk. The tangential component of velocity, often referred to as swirl, is generally regarded as an inefficiency, as it is not useful for producing thrust.

Swirl is caused by a combination of the finite length of the blade causing tip vortices, trailing edge vortices and flow separation from the blades. High-Lift propellers take advantage of the swirl, by placing the wing in proximity to the propellers causing a beneficial alteration to the lift distribution along the wing. The lift distribution changes as function of the effective angle of attack each wing section is exposed to. The swirl induced by the propeller tends to increase the angle of attack of wing sections aft of the upward moving half of the propeller plane and decrease the angle of attack of those wing sections downstream of the downward moving side.

For an effectively designed propeller blown wing, the net increase in lift across the entire span should be positive, i.e. as in Figure 3.6, the sections of the wing in the wake of the upward moving side of the propeller disk see and increase in lift due to both the swirl and axial velocity increases in the slipstream (green region), whereas the sections of the wing in the wake of the downward moving side see a reduction in lift due to the swirl (red region), but it is not decreased as much as the opposite side is increased due to the axial velocity increase in the flow there.

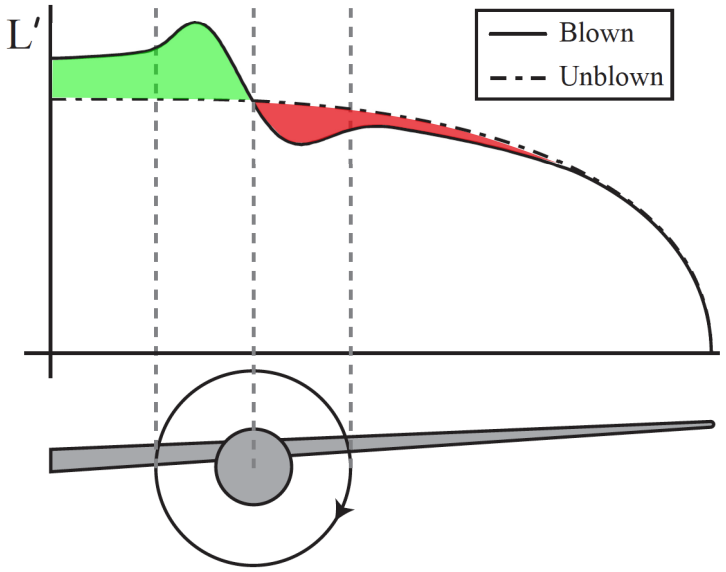

FIGURE 3.6: The effect of the propeller wake velocities on the lift distribution of a blown relative to an unblown wing. Modified from [158].

The SCEPTOR aircraft (NASA X-57 Maxwell) [159] manages a maximum lift coefficient ($C_{L,max}$) of 4.4 at 55 knots, compared to the baseline aircraft (Tecnam P2006T) of 1.8, which is representative for this class of aircraft [160].

3.3.1 Correlation to noise

A general theme exists in the current estimations of what the noise signatures of electrically powered aircraft will be; this is a shift in the total source balance from few dominant sources to a larger number of slightly less dominant sources. Previously, few source mechanisms dominated the noise signature of aircraft, as is the case for fan and jet noise on conventional turbofan engines, while propeller self noise on turboprops. This will remain the case for concept designs that do not deviate drastically from conventional architectures. New architectures, allow the treatment of those dominant sources on a conceptual design level, meaning that previously "covered" sources of noise now take the forefront of the noise signature. Such sources are predominantly expected to be interaction based, due to the air vehicle configurations possible.

The noise signatures associated with DEP aircraft were shown to have drastically different character to other air vehicles in the size class [161, 162]. Although isolated, single and counter-rotating propeller set-ups have been studied for decades, the interaction noise sources and interference of multiple distributed, side-by-side rotors/propellers is yet to be fully understood. Depending on operation, amplitude and phase modulations may generate vast fluctuations in the radiated sound.

From the discussion in section 2.3 of Chapter 2, it is evident that the propeller tip Mach number has the most effect in increasing subsonic propeller tonal noise. The tip Mach number depends on simply the propeller rotational speed (RPM) and the diameter. Given the distribution of multiple propellers (or rotors) on the airframe, as discussed above, the individual diameter of the propellers will decrease, as will the resulting tip Mach number for a given RPM setting. However, increases in propeller rotational speeds may be required to counterbalance the scaling of thrust generation with diameters. Constant speed (variable-pitch) propellers could also be implemented to supplement the thrust requirements. Thrust generation may also be augmented by an increase in the number of blades per propeller as well as size of the individual blades (increase of chord-to-diameter ratio and thickness); keeping in mind the correlation of thickness noise to blade geometry.

As with contra-rotating and open rotors, acoustic and aerodynamic interference may occur between the two blade rows causing a number of further interaction tones (other than blade passing frequency, BPF, harmonics) to be generated. This generally corresponds to increase in noise levels relative to single rotors [163],[164]. Advanced numerical and experimental studies, such as references [165],[166] [167],[168],[169] are currently exploring the adverse and favourable effects of such configurations in terms of aerodynamics and acoustics.

The increase of rotational speed of the smaller diameter propellers, at the same time causes a shift of the frequency output of the noise towards the higher end of the spectrum. This is due to a higher fundamental tone and therefore higher harmonics. In addition, experimental measurements of small unmanned aerial vehicles (drones) suggest that the frequency spectra of such vehicles contain large amounts of broadband noise especially at the higher frequencies, with broadband noise sources dominating particular operations [170, 171]. An increase in broadband noise is also noticed as the number of propellers increase. These effects may lead to novel DEP vehicles being vastly more annoying despite meeting noise certification requirements [172, 173, 174, 175].

3.4 Summary

The introduction of electric propulsion systems has the potential to drastically modify noise immissions of air vehicles in years to come. Adequately understanding the trade-offs and having the right tools to explore the design space at all stages of design is recognised as a critical component of the transition to a zero emission, low noise aviation industry.

At this point, the necessary context to aircraft noise and the proposed application space of MONTANA has been presented, allowing for the proposed noise prediction framework methodology to be introduced. This is done in the following three Chapters.

Chapter 4

Methodology I: Noise source model

The first component of MONTANA is the definition of the lumped source model and the delta methodology. These are addressed in this Chapter, along with the process of generating NPD curves once the lumped representation of the air vehicle as a noise source has been achieved.

There are two fundamental components of the modelling techniques that when combined provide the simple yet functional propeller noise prediction capability of MONTANA. The first, is the backbone of the framework's architecture: the lumped source model of a study aircraft is defined as the sum of known levels of a baseline aircraft and the changes in levels of individual noise sources of the study aircraft relative to the baseline. This approach leverages a linear approximation approach to estimate changes in the overall radiates noise as a function of multiple individual sources and their influencing parameters. The second aspect is the approach of the calculation of deltas (ΔL) for the specific propeller steady tonal noise source.

These deltas are then combined, with other calculated deltas for other individual sources (using for example the methods described by Synodinos [12]), in the lumped source framework to provide an acoustic model for the whole aircraft.

Figure 4.1 shows a flow diagram of the framework and identifying the two key components previously mentioned. Specifically, the prediction starts from a baseline aircraft, whose acoustic performance in known and well understood. The baseline aircraft may be seen as the predecessor of the novel aircraft concept whose noise immissions are being predicted. This means, that although new technologies are implemented and operational changes will occur, the final new aircraft still resembles the baseline. This assumption, carries on to the mathematical assumption of linear approximation used in order to combine the individual noise source changes and apply

them to the baseline aircraft. The extent to which the linear approximation holds is dependent on the individual model used to produce the scaling for any particular noise source. Any prediction model may be used for any of the present sources (or any other additional delta e.g. liners), however producing the appropriate dimensional scaling laws may be easier for some models over others. As this thesis focuses on regional/sub-regional and UAM vehicles the propeller and its acoustic properties are prioritised. An asymptotic analysis of the Hanson frequency domain model is presented, with the results being inputted to the linear lumped source model. The lumped source model is then used to produce NPD curves for the previously mentioned aircraft types.

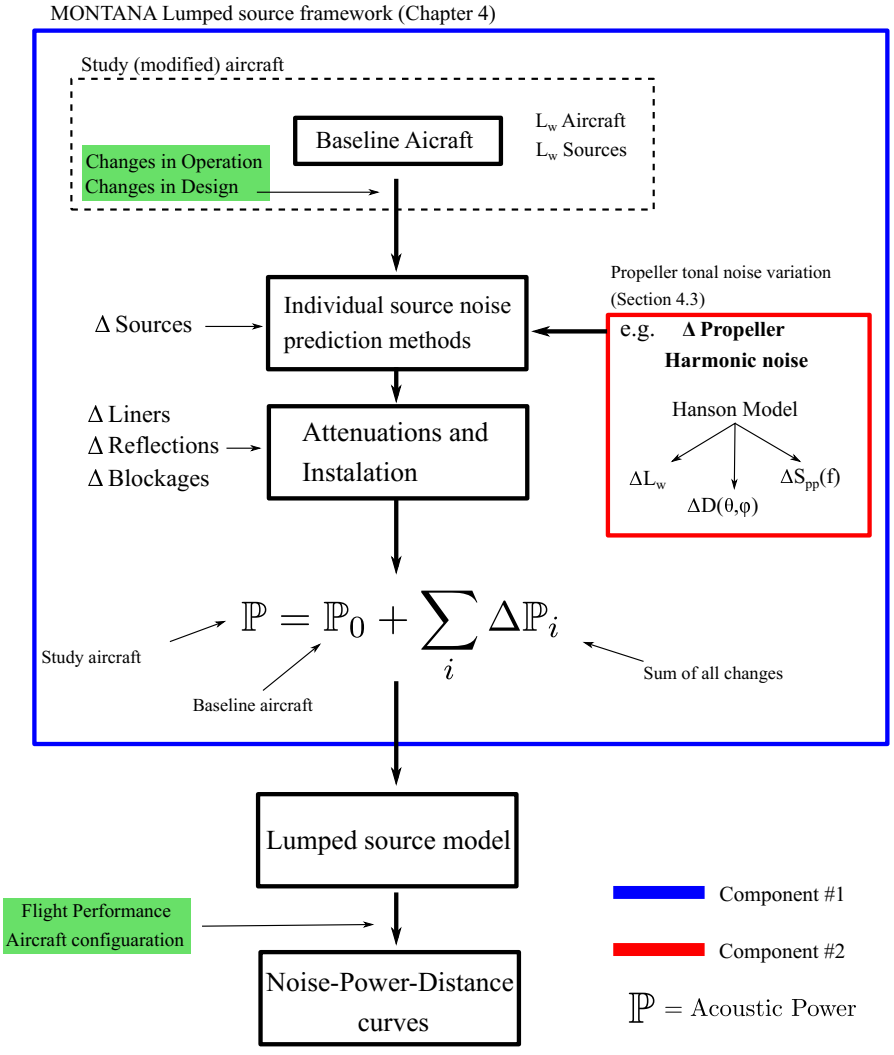

FIGURE 4.1: Flow diagram of the MONTANA noise source modelling framework.

4.1 Choice of baseline scenario/aircraft

The first major step in applying the MONTANA framework is determining the baseline scenario or baseline aircraft to base the prediction of the concept off of. As will be

discussed in detail in the development of the lumped source model and the validation, the choice of the baseline air vehicle has a large effect on the accuracy of the final predicted levels.

The factors considered when choosing the baseline air vehicles relative to the concept are primarily the operation type, the propulsion system and airframe architecture, the constituent noise sources contributing to the overall noise emission, and finally, data availability. Although MONTANA is designed to forgo the requirement of high fidelity inputs, it still requires data such as NPD curves for the baseline aircraft, average noise levels of individual noise sources, as well as geometry and performance data at the conditions of the measured noise levels.

The choice of baseline air vehicle goes in hand with the principles of aircraft design, where assumptions of baseline characteristics (aerodynamic performance, geometry) of a concept are based on historical trends and preceding similar designs of aircraft, before slowly iterating towards the concepts' new requirements. In most cases exact predecessors for any particular model of aircraft (A320 to A320neo family) form the best informed baseline choices.

From the noise prediction point of view, the architecture of the air vehicle should generally allow for the same aeroacoustic mechanisms to develop during operation.

4.2 Lumped source model

Considering a baseline aircraft produces $L_{w,0}$ levels of noise, it consists of noise sources emitting overall sound power $\mathbb{P}_0$. As a result of operational or technological changes, the acoustic noise sources on the aircraft may change in number, magnitude and other acoustic properties, e.g. spectral content. The sound power may therefore be written in terms of the baseline aircraft and changes in power of the individual sources. Therefore, denoting s the total number of noise sources after the modifications and i an individual noise source that changed by acoustic power $\Delta\mathbb{P}_s$ we may write,

$$\mathbb{P} = \mathbb{P}_0 + \sum_{i=1}^{s} \Delta\mathbb{P}_i \tag{4.1}$$

noting that for noise sources that previously did not exist, $\Delta\mathbb{P}_i = \mathbb{P}_i$ and for sources that were removed, $\Delta\mathbb{P}_i = -\mathbb{P}_i$. Therefore, in order to calculate the acoustic emission of the novel aircraft design, knowledge on the acoustic output of the baseline aircraft is required, along with the individual changes of the acoustic sources.

Converting to a total sound power level, the PWL of the new concept may be written as,

$$
\begin{aligned}
L_w &= 10\log\left(\frac{\mathbb{P}_0}{\mathbb{P}_{ref}} + \frac{\sum \Delta\mathbb{P}_i}{\mathbb{P}_{ref}}\right) \\
&= 10\log\left[\frac{\mathbb{P}_0}{\mathbb{P}_{ref}}\left(1 + \frac{(\sum \Delta\mathbb{P}_i)/\mathbb{P}_{ref}}{\mathbb{P}_0/\mathbb{P}_{ref}}\right)\right] \\
&= L_{w,0} + 10\log\left[1 + \frac{\sum_{i=1}^{s} \Delta\mathbb{P}_i}{\mathbb{P}_0}\right]
\end{aligned}
\tag{4.2}
$$

where $L_{w,0}$ is the known sound level (measured) of a baseline scenario and i is indexing through a total number s of acoustic sources. So the sum over $\Delta\mathbb{P}_i$ describes the correction to noise levels of individual sources when making changes to the parameter that defines the baseline level, $L_{w,0}$. The change in PWL due to changes in the sound power of individual sources, of the modified aircraft, is given by,

$$
\Delta\text{PWL} = 10\log\left[1 + \frac{\sum_{i=1}^{s} \Delta\mathbb{P}_i}{\mathbb{P}_0}\right] \tag{4.3}
$$

Equation 4.3 provides a high-level relationship of how changes in sound power radiated by the individual noise source mechanisms affect the overall noise emission of the aircraft.

4.2.1 Differential Method: Working with changes in noise, ΔPWL

Individual sources depend on parameters that decide the characteristics of the source such as directivity, spectral content etc. For each individual source i out of a total number of sources s, assume a predictive method M exists such that the output is determined by a scalar-valued function $f : \mathbb{R}^n \to \mathbb{R}$. The output in this case may take the form of the RMS pressure, as this is a direct indicator of source intensity.

$$
p^2_{rms,i} = f_i(\boldsymbol{\eta}) = f_i(\eta_1, \eta_2, ..., \eta_n) \tag{4.4}
$$

$\boldsymbol{\eta}$ denotes an input vector with a number of components n that affect source i.

The SPL emitted by a baseline known configuration is then expressed as the sum over the individual sources,

$$L_{p,0} = 10 \log \left[\frac{\sum_{i=1}^{s} p_{rms,i}^2(\boldsymbol{\eta}_0)}{p_{ref}^2} \right] \tag{4.5}$$

The summation of $p_{rms,i}^2$ in such a manner assumes an incoherent nature of the sources. This is discussed in detail in Chapter 2, as by references [21, 176, 72].

4.2.2 Linear approximations to noise estimation models

First, we establish the general mathematical background in differential analysis that can then be applied to functions and models for the estimation of noise levels and changes in them. Once changes in levels (Δ L) relative to the baseline case may be estimated, they may be combined with the baseline levels to give absolute level prediction of the study aircraft. The theory presented is based on the work by Berkill & Berkill [177, 178] and adapted for the need of acoustic lumped source definition and analysis.

Total derivative as a linear map

Resuming to the idea that function f of Equation 4.4 appropriately describes the relation of the influencing parameters and the output p_{rms}, the derivative provides a measure of how sensitive the output is to changes of input values. Conceptually, the definition of the total derivative expresses the idea that df_a is the best linear approximation to f at the point a. This can be made precise by quantifying the error in the linear approximation determined by df_a. To do so, write

$$f(a+h) = f(a) + df_a(h) + \varepsilon(h), \tag{4.6}$$

where $\varepsilon(h)$equals the error in the approximation. To say that the derivative of f at a is df_a is equivalent to the statement

$$\varepsilon(h) = o(\|h\|), \tag{4.7}$$

The total derivative df_a is the unique linear transformation for which the error term is this small, and this is the sense in which it is the best linear approximation to f. By definition, a function $f : U \to \mathbb{R}^m$ is said to be (totally) differentiable at a point $a \in U$ if there exists a linear transformation $df_a : \mathbb{R}^n \to \mathbb{R}^m$ such that,

$$\lim_{x \to a} \frac{\|f(x) - f(a) - df_a(x-a)\|}{\|x-a\|} = 0. \tag{4.8}$$

if all the partial derivatives of f at a exist and are continuous in a neighbourhood of a, then f is differentiable at a. When this happens, then in addition, the total derivative of

f is the linear transformation corresponding to the Jacobian matrix of partial derivatives at that point.

Taylor series of multivariable functions

The linear approximation is obtained by the use of Taylor's theorem for the case $n = 1$ on a twice continuously differentiable function f of one real variable,

$$f(x) \approx f(a) + f'(a)(x - a) \tag{4.9}$$

This is a good approximation when x is close enough to a; since a curve, when closely observed, will begin to resemble a straight line. Therefore, the expression on the right-hand side is just the equation for the tangent line to the graph of f at $(a, f(a))$. For this reason, this process is also called the tangent line approximation. In the case of a scalar-valued function of a single variable the slope of the tangent line is determined by the derivative $f'(a)$ at a. In the general case of $f : \mathbb{R}^n \to \mathbb{R}^m$, the derivative of the function f is replaced by the Jacobian matrix which can be thought of as describing the amount of "stretching", "rotating" or "transforming" that the function imposes locally near that point.

This can be seen by starting at the Taylor series of scalar-valued function of multiple variables ($f : R^n \to R$),

$$\begin{aligned} f(x_1, \ldots, x_d) &= \sum_{n_1=0}^{\infty} \cdots \sum_{n_d=0}^{\infty} \frac{(x_1 - a_1)^{n_1} \cdots (x_d - a_d)^{n_d}}{n_1! \cdots n_d!} \left(\frac{\partial^{n_1 + \cdots + n_d} f}{\partial x_1^{n_1} \cdots \partial x_d^{n_d}} \right) (a_1, \ldots, a_d) \\ &= f(a_1, \ldots, a_d) + \sum_{j=1}^{d} \frac{\partial f(a_1, \ldots, a_d)}{\partial x_j} (x_j - a_j) \\ &\quad + \frac{1}{2!} \sum_{j=1}^{d} \sum_{k=1}^{d} \frac{\partial^2 f(a_1, \ldots, a_d)}{\partial x_j \partial x_k} (x_j - a_j)(x_k - a_k) \\ &\quad + \frac{1}{3!} \sum_{j=1}^{d} \sum_{k=1}^{d} \sum_{l=1}^{d} \frac{\partial^3 f(a_1, \ldots, a_d)}{\partial x_j \partial x_k \partial x_l} (x_j - a_j)(x_k - a_k)(x_l - a_l) + \cdots \end{aligned} \tag{4.10}$$

Taking the first order term only results in the linear approximation of the function around the point $[a_1, \ldots, a_d]$. The "slope" in this case is given by the total derivative. The total derivative of f at a may be written in terms of its Jacobian matrix, which is a row matrix:

$$Df_a = \begin{bmatrix} \frac{\partial f}{\partial x_1}(a) & \cdots & \frac{\partial f}{\partial x_n}(a) \end{bmatrix}. \tag{4.11}$$

Meaning that the linear approximation given by the truncated Taylor series of a multivariable function may be expressed as,

$$f(\boldsymbol{x}) = f(\boldsymbol{a}) + \sum_{|\alpha| \leq k} \frac{Df_a}{\alpha!}(\boldsymbol{x} - \boldsymbol{a})^{\alpha} \tag{4.12}$$

This linear approximation property of the total derivative implies that if a vector of small changes Δx with respect to point a,

$$\Delta x = \begin{bmatrix} \Delta x_1 & \cdots & \Delta x_n \end{bmatrix}^{\mathsf{T}} \tag{4.13}$$

the T denotes a transpose matrix, so that this vector is a column vector, then

$$f(a + \Delta x) - f(a) \approx Df_a \cdot \Delta x = \sum_{i=1}^{n} \frac{\partial f}{\partial x_i}(a) \cdot \Delta x_i. \tag{4.14}$$

Heuristically, this suggests that if $dx_1, \ldots, dx_n$ are small increments in the coordinate directions, then

$$df_a \approx \sum_{i=1}^{n} \frac{\partial f}{\partial x_i}(a) \cdot dx_i. \tag{4.15}$$

The Jacobian matrix represents the differential of f at every point where f is differentiable. In the even more general case where $f : \mathbb{R}^n \to \mathbb{R}^m$ is a vector-valued function of a vector variable, the Jacobian take the form of a matrix,

$$\mathbf{J} = \begin{bmatrix} \dfrac{\partial \mathbf{f}}{\partial x_1} & \cdots & \dfrac{\partial \mathbf{f}}{\partial x_n} \end{bmatrix} = \begin{bmatrix} \nabla^{\mathrm{T}} f_1 \\ \vdots \\ \nabla^{\mathrm{T}} f_m \end{bmatrix} = \begin{bmatrix} \dfrac{\partial f_1}{\partial x_1} & \cdots & \dfrac{\partial f_1}{\partial x_n} \\ \vdots & \ddots & \vdots \\ \dfrac{\partial f_m}{\partial x_1} & \cdots & \dfrac{\partial f_m}{\partial x_n} \end{bmatrix} \tag{4.16}$$

Application to Lumped source model

Assuming a vector of changes to the parameters equivalent to the changes in Equation 4.13,

$$\Delta \eta = \begin{bmatrix} \Delta \eta_1 & \cdots & \Delta \eta_n \end{bmatrix}^{\mathsf{T}} \tag{4.17}$$

acoustic radiation due to source i after changes of $\Delta\eta$ may be approximated using,

$$f(\boldsymbol{\eta}_0 + \Delta\boldsymbol{\eta}) \approx f(\boldsymbol{\eta}_0) + \sum_{j=1}^{n} \frac{\partial f}{\partial \eta_j}(\boldsymbol{\eta}_0) \cdot \Delta \eta_j \tag{4.18}$$

where $\boldsymbol{\eta}_0 = [\eta_{0,1}, \cdots . \Delta\eta_{0,n}]$ denotes the input vector of parameters that correspond to the baseline level $L_{w,0}$.

Applying the changes to the baseline configuration in order to incorporate new technologies or operational procedures is reflected in the SPL in the following manner (for convenience $p^2_{rms,i}$ is replaced by f_i representing the function for that particular source):

$$\begin{aligned} L_p &= 10\log\left(\frac{\sum_{i=1}^{s} p^2_{rms,i}(\boldsymbol{\eta}_0+\Delta\boldsymbol{\eta})}{p^2_{ref}}\right) \\ &= 10\log\left(\frac{\sum_{i=1}^{s}\left[f_i(\boldsymbol{\eta}_0)+\sum_{j=1}^{n}\frac{\partial f_i}{\partial \eta_j}(\boldsymbol{\eta}_0)\cdot\Delta\eta_j\right]}{p^2_{ref}}\right) \\ &= 10\log\left[\frac{\sum_{i=1}^{s} f_i(\boldsymbol{\eta}_0)}{p^2_{ref}}\left(1+\frac{\sum_{i=1}^{s}\sum_{j=1}^{n}\frac{\partial f_i}{\partial \eta_j}(\boldsymbol{\eta}_0)\cdot\Delta\eta_j}{\sum_{i=1}^{s} f_i(\boldsymbol{\eta}_0)}\right)\right] \\ &= 10\log\left[\frac{\sum_{i=1}^{s} f_i(\boldsymbol{\eta}_0)}{p^2_{ref}}\right]+10\log\left(1+\frac{\sum_{i=1}^{s}\sum_{j=1}^{n}\frac{\partial f_i}{\partial \eta_j}(\boldsymbol{\eta}_0)\cdot\Delta\eta_j}{\sum_{i=1}^{s} f_i(\boldsymbol{\eta}_0)}\right) \\ &= L_{p,0}+\Delta L \end{aligned} \tag{4.19}$$

where it is evident that:

$$\Delta L = 10\log\left(1+\frac{1}{\sum_{i=1}^{s} f_i(\boldsymbol{\eta}_0)}\left(\sum_{i=1}^{s}\sum_{j=1}^{n}\frac{\partial f_i}{\partial \eta_j}(\boldsymbol{\eta}_0)\cdot\Delta\eta_j\right)\right) \tag{4.20}$$

The double sum in expression 4.20 makes it easy to see that a generalisation to the total emitted noise by the aircraft may be made. Assuming the total noise output of the entire vehicle may be represented by a single function vector-valued $\boldsymbol{f}:\mathbb{R}^n\rightarrow\mathbb{R}^s$ where $\boldsymbol{f}=[f_1,\ \cdots,\ f_s]$. As previously s is the number of individual sources accounted for and n the number of parameters each source s is dependent upon. The change in noise with respect to the baseline aircraft using a linear approximation may be given by,

$$\boxed{\Delta L = 10\log\left(1+\frac{\boldsymbol{J}_f(\boldsymbol{\eta}_0)\cdot\Delta\eta_j}{\sum_{i=1}^{s} f_i(\boldsymbol{\eta}_0)}\right)} \tag{4.21}$$

where $\boldsymbol{J}_f$ is the Jacobian of the vector-valued function f given by Equation 4.16.

The truncation of the Taylor series has an associated error. Given any differentiable (noise) function, we can expand it as a first degree polynomial (or higher if more terms are used) at a given point. If the associated truncation error is reasonably small enough, the polynomial expansion through Taylor's series becomes a good approximation to the function. The remainder term R_k can be estimated by,

$$R_k = f(x_1, \ldots, x_d) - T_k(x_1, \ldots, x_d) \tag{4.22}$$

where k in this case denotes the order of the polynomial ($k = 1$ in the case of MONTANA) and effectively the truncation point, and T_k denotes the Taylor series approximation of f.

The above proves to be a good test when the derivatives may be estimated (numerically or analytically), however practically, this approach will when dealing with known non-linear relationships between root-mean-square pressure and any parameter, non-linear regimes (for example transonic/supersonic) or fundamentally non-linear noise sources.

4.3 Propeller tonal noise variation

As the main application of MONTANA is propeller powered air vehicles, the lumped noise source model must be coupled with methods for generating deltas for propeller noise sources. This Section therefore focuses on the development of a simplified scaling model able to predict changes in propeller harmonic noise levels between two propellers with different geometry and operation characteristics.

The relations developed herein, are a result of applying an asymptotic study on the Hanson frequency domain model. Changes in the independent variables are directly correlated to the change in the dependent one, that being the noise in terms of an RMS pressure of sound power. The predicted changes are then used in expression 4.21 along with other individual source changes to assess the whole aircraft.

The methodology includes an elegant way of including the tonal spectral content of propeller noise when calculating the change in noise (ΔPWL) between configurations. This is achieved through the use of a spectral shape function. A spectral shape function and propeller source directivity function are also derived from the asymptotic approximation of the Hanson frequency domain model. Other appropriate functions may be used to define the spectral content shape and directivity according to the application.

4.3.1 Asymptotic approximation of frequency domain propeller tonal noise model

The use of analytical formulas for the derivation of scaling laws is advantageous as direct insight to the influence of design geometry and operating conditions have on the fundamental and its harmonics, may be accomplished without full scale experimental procedures. Literature suggests that for propeller harmonic noise single global scaling law exists and rather analytical time or frequency domain models may be used (with the disadvantage of a slight increase in computational time and power as well as input requirement) to get much more accurate estimation of the sound power (total acoustic energy) emission [179].

For the ease of the reader, Hanson's prediction from Equation 2.29 is repeated below. In this instance the terms have been segregated into groups and named for the convenience of the following analysis.

$$\begin{Bmatrix} P_{Vm} \\ P_{Dm} \\ P_{Lm} \end{Bmatrix} = \underbrace{-\frac{\rho_0 c_0^2}{8\pi}}_{\text{Constants}} \underbrace{\frac{1}{y}}_{\substack{\text{Spherical} \\ \text{spreading}}} \underbrace{\frac{\sin\theta}{\left(1 - M_x \cos\theta\right)}}_{\substack{\text{Directivity,} \\ \text{Doppler term}}} \underbrace{DB}_{\substack{\text{Design} \\ \text{parameters}}}$$
$$\times \int_0^1 M_r^2 \exp\left(i\phi_s\right) \underbrace{J_{mB}\left(\frac{mBzM_t \sin\theta}{1 - M_x \cos\theta}\right)}_{\text{Bessel term}} \underbrace{\begin{Bmatrix} k_x^2 t_b \Psi_V(k_x) \\ ik_x (C_D/2) \Psi_D(k_x) \\ ik_y (C_L/2) \Psi_L(k_x) \end{Bmatrix}}_{\text{Source terms}} dz \tag{4.23}$$
$$\times \underbrace{\exp\left[imB\left(\frac{\Omega r}{c_0} - \frac{\pi}{2}\right)\right]}_{\text{Phase term}}$$

Blade radial integral

This integral over the radius of the blade determines the contribution of each blade section toward each harmonic. It takes into account the variation of the geometry along the propeller (chord, thickness, sweep etc.) along with the variation of performance i.e. loading (axial and tangential). This term includes contributions of three major parameters that dictate the final behaviour of the integral. These parameters are the section relative Mach number M_r (i.e. the Mach number the aerofoil profiles sees at different positions along the propeller radius), the Bessel function and the source term. There is also an extra term that deals with the effect of sweep of the propeller blades, but this will be omitted at this stage of the study as we assume zero sweep. Each of these terms will be dealt with individually.

Bessel function approximation

The Bessel function appears in all harmonic noise terms P_{Vm}, P_{Dm} and P_{Lm}. In the original Hanson derivation, the Bessel function appears as Jacobi-Anger expansion [180] of exponentials of trigonometric functions. Taking the far field approximation in cylindrical coordinates, the form of the spatial derivative is such that the radial variation is solved by Bessel functions.

The resulting Bessel function contributes to the spectral shape of the radiated noise and the overall level and is sometimes referred to a "radiation-factor". This is due to the presence of the mode number m in the argument and in the order of the Bessel function. The argument $mBzM_t \sin\theta/(1 - M_x \cos\theta)$ takes maximum values within the plane off rotation, that is $\theta = 90^o$, and is equal to $mBzM_t$.

The Bessel function present is of the first kind. The order is given by mB, where m in the mode number and B is the blade number. It is evident therefore that each harmonic uses a different order Bessel function. To simplify the analysis, the argument of the Bessel function is rewritten to contain α_1, such that,

$$J_{mB}\left(\frac{mBzM_t \sin\theta}{1 - M_x \cos\theta}\right) = J_{mB}\Big(mBz\alpha_1\Big) \tag{4.24}$$

where

$$\alpha_1 = M_t \sin\theta/(1 - M_x \cos\theta) \tag{4.25}$$

The exact behaviour of α_1 can be seen in Figures 4.9. For reasonable values of the parameters for a general aviation vehicle, α_1 takes values around or less than 1. Typically, in literature Bessel function are described as "damped oscillations", as can be seen in Figure 4.2 for a given order the amplitude of the oscillatory behaviour decays as the argument $z \to +\infty$. This leads to the decaying nature of the higher harmonics as the argument of the Bessel function is a function of the mode number m, or $J_{mB}(f(m))$.

In order to approximate the behaviour of the Bessel functions as the harmonic number increases, we are going to look at the asymptotic expansions for large and small arguments. As α_1 is almost always ≤ 1 the arguments of the Bessel functions are $\approx mB$. The vertical black lines in Figure 4.2, indicate the point where the argument $z = mB$. Therefore, for each order m, the value of the Bessel function occurs before the first peak.

The large argument expansion, Eq 4.26 of Bessel functions assumes $arg \to \infty$. This is not strictly true for our case, but the decaying term in this approximation gives us a good approximation.

$$J_{mB}\Big(mB\alpha_1\Big) \sim \sqrt{\frac{2}{\pi mB\alpha_1}} \cos\Big(mB\alpha_1 - 0.5\pi mB - 0.25\pi\Big) \tag{4.26}$$

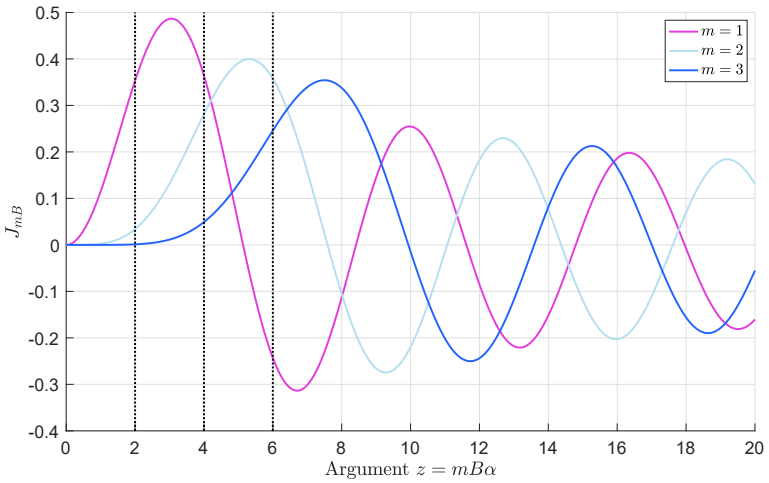

FIGURE 4.2: Bessel functions of the first kind as a function of blade passing frequency. The vertical dotted lines depict the position where the arguments of the Bessel function equals the order. Blade number, $B = 2$.

The full large argument expansion can be seen in Figure 4.3 while the decaying term of it in Figure 4.4.

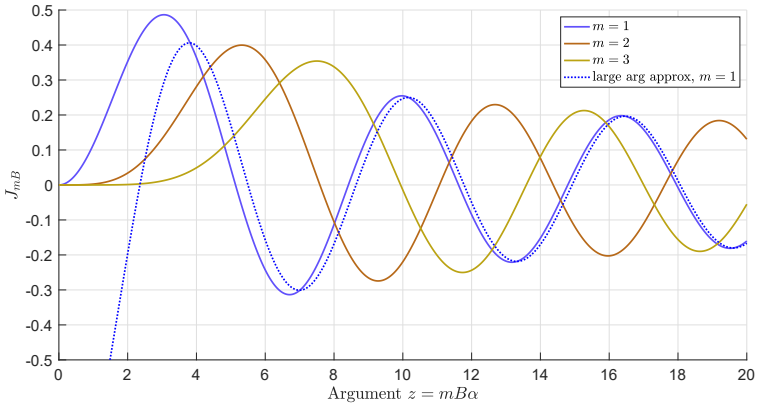

FIGURE 4.3: The large argument approximation for Bessel function order of 2 is compared to the actual Bessel function value, Blade number, $B = 2$.

The small argument expansion, Eq 4.27 of Bessel functions assumes $z = mB\alpha_1 \to 0$. This approximation more accurately represents the behaviour of α_1, and can be seen in Figure 4.5. For tip Mach numbers applicable to general aviation vehicles the argument $mBzM_t$ remains approximately equal (or slightly smaller) to the order mB of the Bessel functions where its value peaks. This behaviour may be approximated using the small argument asymptotic formula. The asymptotic approximation of the Bessel function in Equation 4.23 may be given by,

$$J_{mB}\Big(mB\alpha_1\Big) \sim \frac{1}{(mB)!}\left(\frac{mB\alpha_1}{2}\right)^{mB} \tag{4.27}$$

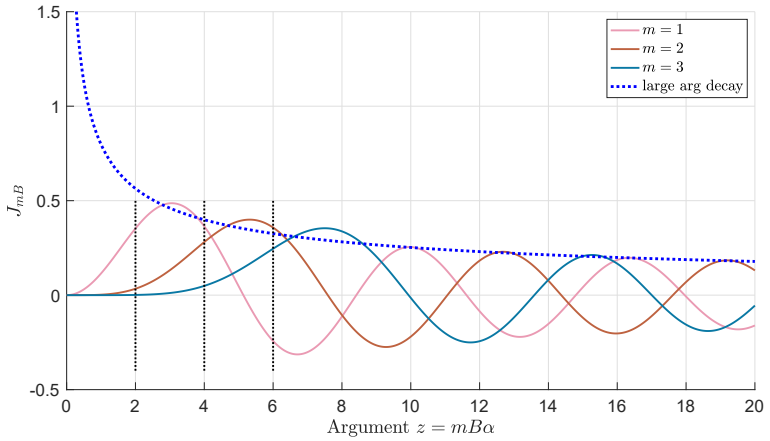

FIGURE 4.4: The decaying term of the large argument approximation for Bessel function (blue) compared to the actual Bessel function value. The decaying term approximates the peaks of the Bessel function better as the argument goes to infinity. Blade number, $B = 2$.

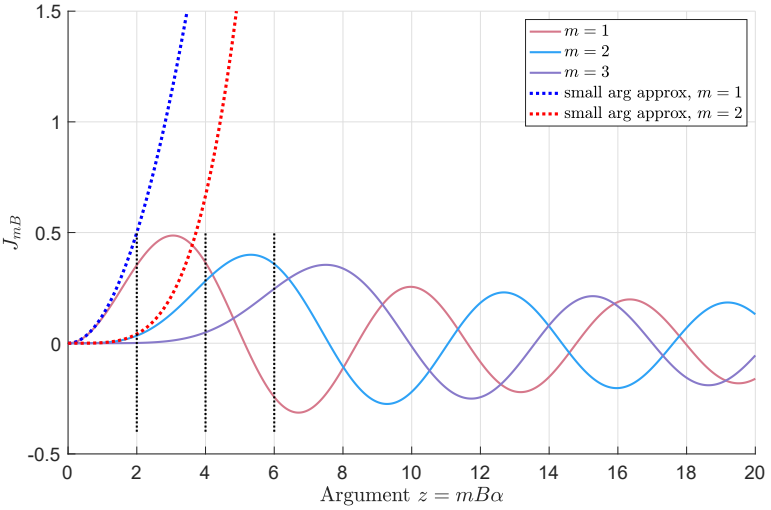

FIGURE 4.5: The small argument approximation for Bessel function order of 2 and 4 is compared to the actual Bessel function value, Blade number, $B = 2$.

In general, Bessel functions $J_n(x)$ decay rapidly for values of argument less than the order of the functions, i.e., for $|x| < |n|$. If we consider sound radiated at $\theta = 90$ deg from the blade tip ($z_0 = 1$), the low-efficiency criterion is $|mBM_T| < |mB|$ or

$$M_s \equiv M_T < 1 \tag{4.28}$$

where in this case $n = mB$ is the order and $x = \arg J$ represent the argument.

Considering the final goal of determining changes in noise, the behaviour of the Bessel function approximation derivative is important. Thus, we concentrate on,

$$J'_{mB} = J'_{mB}(\arg J) \tag{4.29}$$

$$J'_{mB} \sim \left(\frac{1}{(mB)!} \left(\frac{\arg J}{2} \right)^{mB} \right)' \tag{4.30}$$

where the Bessel function argument is as defined in Equation 4.24.

The derivatives of a Bessel functions with respect to their argument are also Bessel functions. For example, as given by the recurrence relations [180],

$$\frac{\partial J_{mB}(z)}{\partial z} = \frac{1}{2}\left[J_{mB-1}(z) - J_{mB+1}(z)\right] = \frac{mB}{z} J_{mB} - J_{mB+1}(z) \tag{4.31}$$

However, if using a small argument approximation to estimate changes, it's derivative determines the scale of these changes and the equivalent error relative to the actual values. Simply carrying out the differentiation in Equation 4.30 we get,

$$\frac{\partial}{\partial z} \left(\frac{1}{mB!} \left(\frac{z}{2} \right)^{mB} \right) = \frac{mB}{2(mB)!} \left(\frac{z}{2} \right)^{mB-1} \tag{4.32}$$

which as expected is a polynomial of degree $mB - 1$ with respect to $\arg J$. The behaviour of Equation 4.32 relative to that of the actual derivative may be seen in Figure 4.6.

As expected the derivatives also conform to the small argument asymptotic behaviour, as $\arg J \to 0$. This results in consistent over estimation occurring as $\arg J \to \sqrt{mB+1}$ [181], as the small argument approximation holds for $0 < \arg J \ll \sqrt{mB+1}$.

Source term

The source terms (the terms in braces of the integral in Equation 4.23) may be broken down into two components: a spectrum shape component and a spectrum level component. The $\mathbf{\Psi}$ terms represent the effect of chordwise noncompactness, that is, interference at the observer location of signals emitted from various source locations along the chord, contributing to the spectrum shape definition. Chordwise blade geometry and loading is what determines these characteristics, therefore we assume a simple parabolic thickness distribution and uniform lift and drag distribution. The wavenumber k_x, can be considered the noncompactness parameter.

At this stage the blade geometry has been approximated in number of different ways, specifically outlining the simplifying assumptions we have:

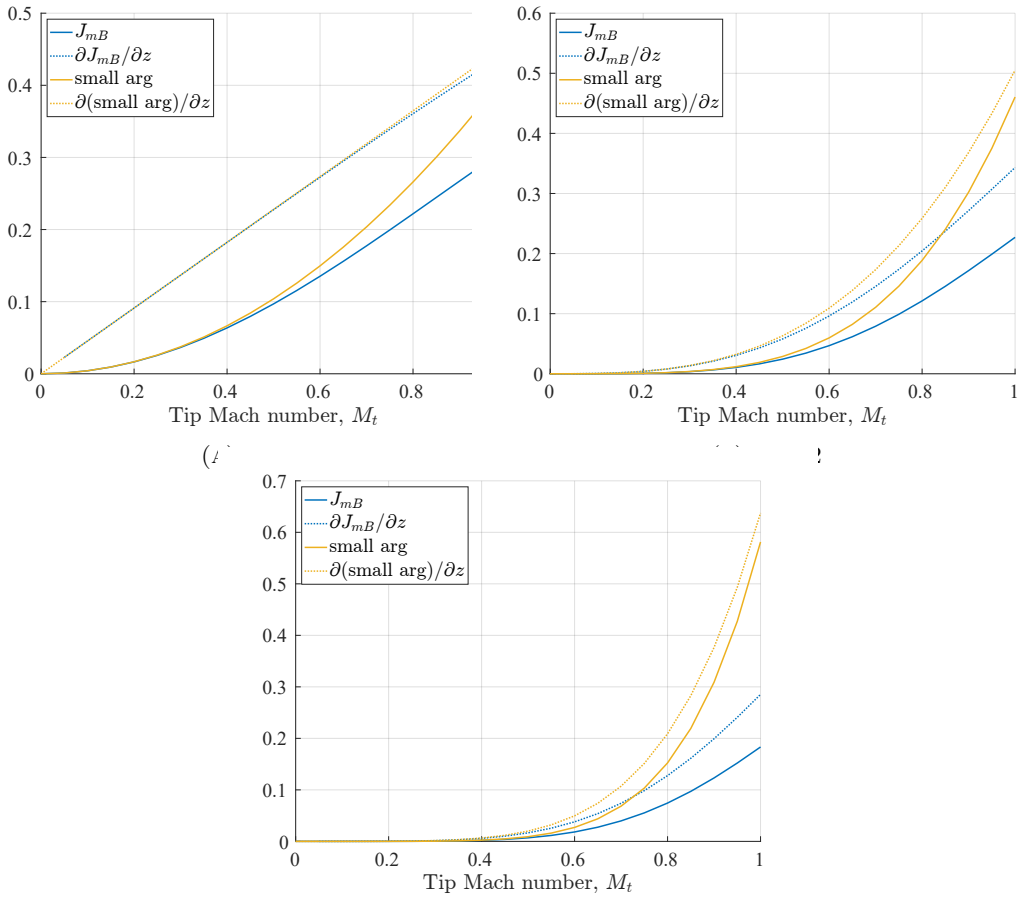

(c) $m = 3$

FIGURE 4.6: Bessel function J_{mB}, its small argument asymptotic approximation and their derivatives for increasing tip Mach number. Depicted are three modes m of a two bladed propeller ($B = 2$) and a flight Mach number of 0.23.

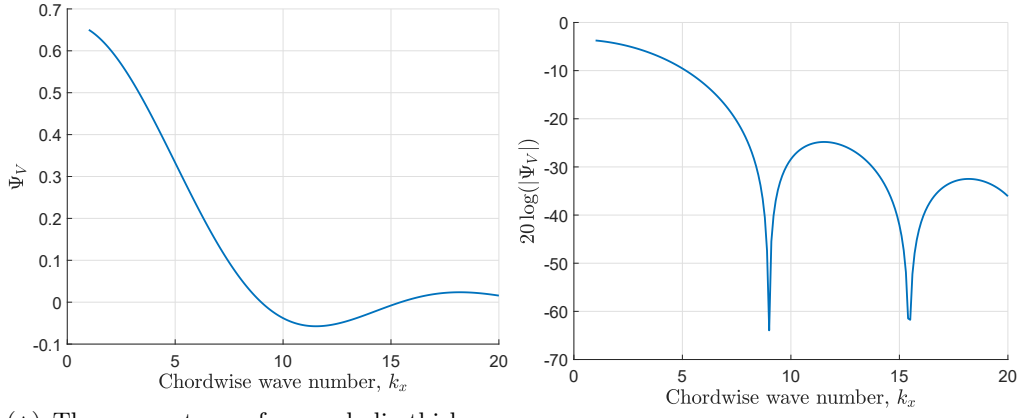

(a) The source term of a parabolic thickness distribution along the airfoil chord as a function of chordwise wave number, k_x

(b) Reduction of thickness noise from blade element due to chordwise noncompactness.

FIGURE 4.7: Thickness noise

- Parabolic chordwise thickness distribution.
- Uniform chordwise loading distribution.
- No sweep.
- Uniform chordwise thickness distribution, average thickness.
- Uniform radial loading distribution, average lift and drag coefficients.

Nevertheless, these assumptions are required, as detailed data of the blade and its loading characteristics are not known. Simple analytical expressions [36] are convenient to use, in this case, for the chordwise thickness and loading distributions, $H(x)$, $f_D(x)$ and $f_L(x)$ respectively.

$$H(x) = 1 - (2x)^2 \tag{4.33}$$

$$f_L(x) = 1 \tag{4.34}$$

$$f_D(x) = 1 \tag{4.35}$$

The distributions are then inserted to equation 4.23 in the form of their Fourier transforms calculated by Equation 2.32.

Specifically, the chordwise thickness becomes,

$$\Psi_V = \begin{cases} 2/3 & k_x = 0 \\ \frac{8}{k_x^2}\left[\frac{2}{k_x}\sin\left(\frac{k_x}{2}\right) - \cos\left(\frac{k_x}{2}\right)\right] & k_x \neq 0 \end{cases} \tag{4.36}$$

and the loading distributions coefficients,

$$\Psi_L = \begin{cases} 1 & k_x = 0 \\ \frac{2}{k_x^2}\sin\left(\frac{k_x}{2}\right) & k_x \neq 0 \end{cases} \tag{4.37}$$

Using a simple parabolic thickness distribution the variation of Ψ_V with k_x can be seen in Figure 4.7. For reasonable variation to the thickness distribution function $H(x)$ the variation in Ψ_V is very small (especially for general aviation parameters)[36]. The uniform chordwise loading distribution may be substituted with a "peaky" distribution (see Figure 4.8) in the case where additional accuracy is required, and input is available. However, as suggested by [36], the presented transforms should be accurate enough for most work at low harmonic order, and preliminary predictions.

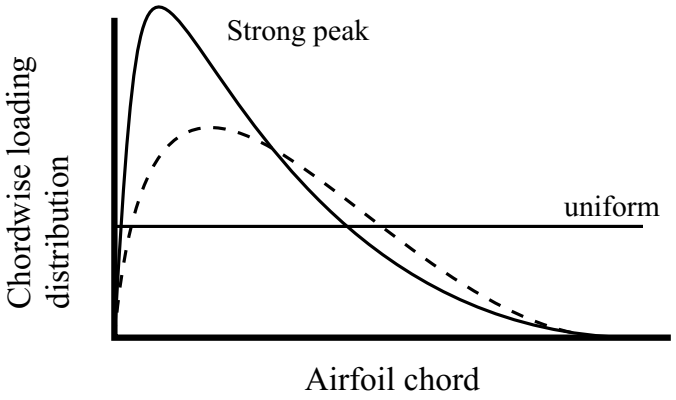

FIGURE 4.8: Examples of chordwise loading distributions

As the chordwise wavenumber, k_x is a function of the sectional Mach number it is useful to see how the source function varies along the propeller radius. That can be seen in Figure 4.10. It is also useful to write k_x and k_y as follows:

$$k_x = \frac{mB\alpha_2}{M_r(z)} \tag{4.38}$$

and

$$k_y = \frac{2mBM_2\alpha_3}{zM_r(z)} \tag{4.39}$$

where

$$\alpha_2 = \frac{M_t}{1 - M_x \cos\theta} \tag{4.40}$$

and

$$\alpha_3 = \frac{M_x - M_r^2 \cos\theta}{1 - M_x \cos\theta} \tag{4.41}$$

The thickness, drag, and lift noise components are directly proportional to the thickness ratio t_b, drag coefficient C_D, and lift coefficient C_L, respectively. The source term $k_x^2 \Psi_V t_b$ is an intricate term as it depends on both harmonic number and the position along the propeller. This is because the chordwise distribution of thickness is needed to compute Ψ_V.

Combining the non-compactness effect relation along with the proportionality we may estimate the source term transforms by,

$$\Psi_V(k_x) \approx \frac{1}{k_x^2} = \left[\frac{M_r(1 - M_x \sin\theta)}{2mBB_DM_t}\right]^2 \tag{4.42}$$

$$\Psi_D(k_x) = \Psi_L(k_x) \approx \frac{1}{k_x} = \left[\frac{M_r(1 - M_x \sin\theta)}{2mBB_DM_t}\right] \tag{4.43}$$

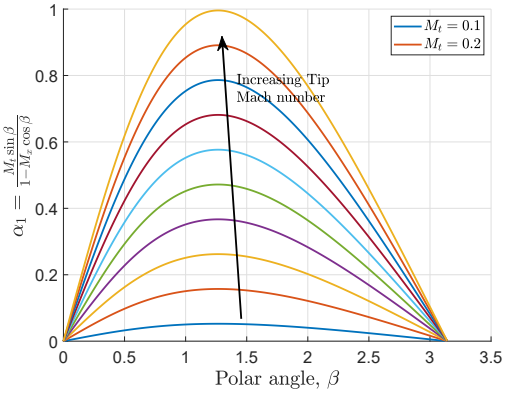

(A) Bessel function argument constant α_1 for different Tip Mach numbers

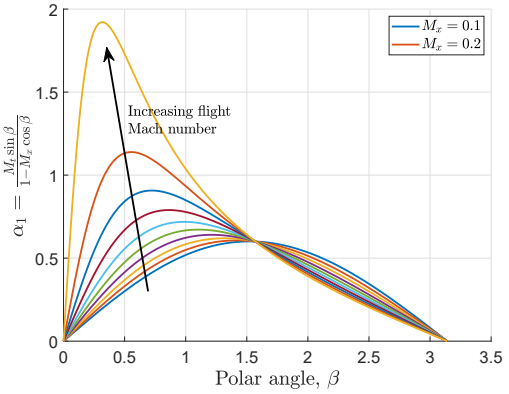

(B) Bessel function argument constant α_1 for different flight Mach numbers

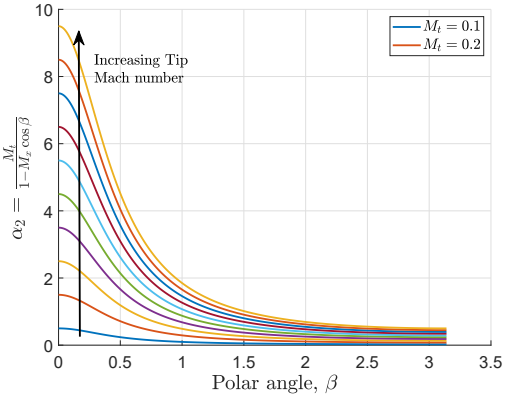

(C) Wavenumber function constant α_2 for different Tip Mach numbers

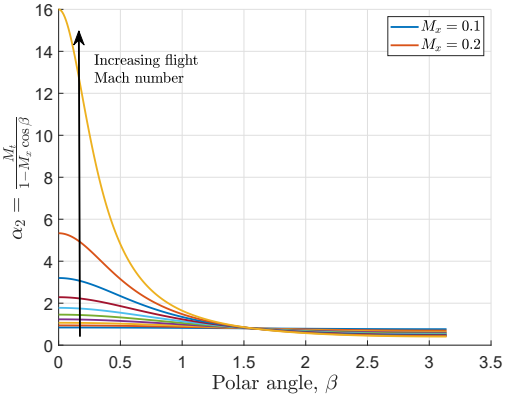

(D) Wavenumber function constant α_2 for different flight Mach numbers

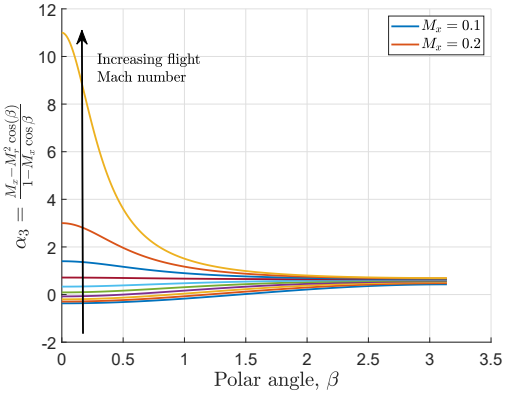

(E) Wavenumber function constant α_3 for different flight Mach numbers, for $M_t = 0.2$

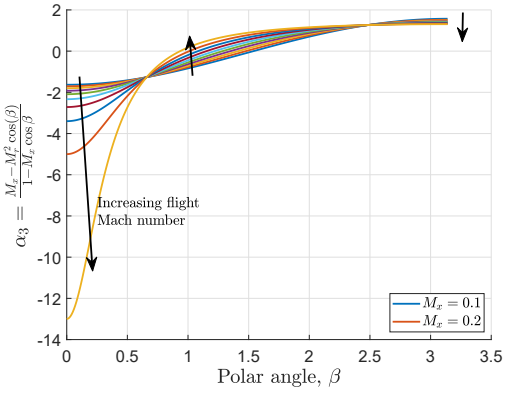

(F) Wavenumber function constant α_3 for different flight Mach numbers, for $M_t = 0.8$

FIGURE 4.9: The natural limits imposed on constant $\alpha_1, \alpha_2, \alpha_3$ for normal operating conditions.

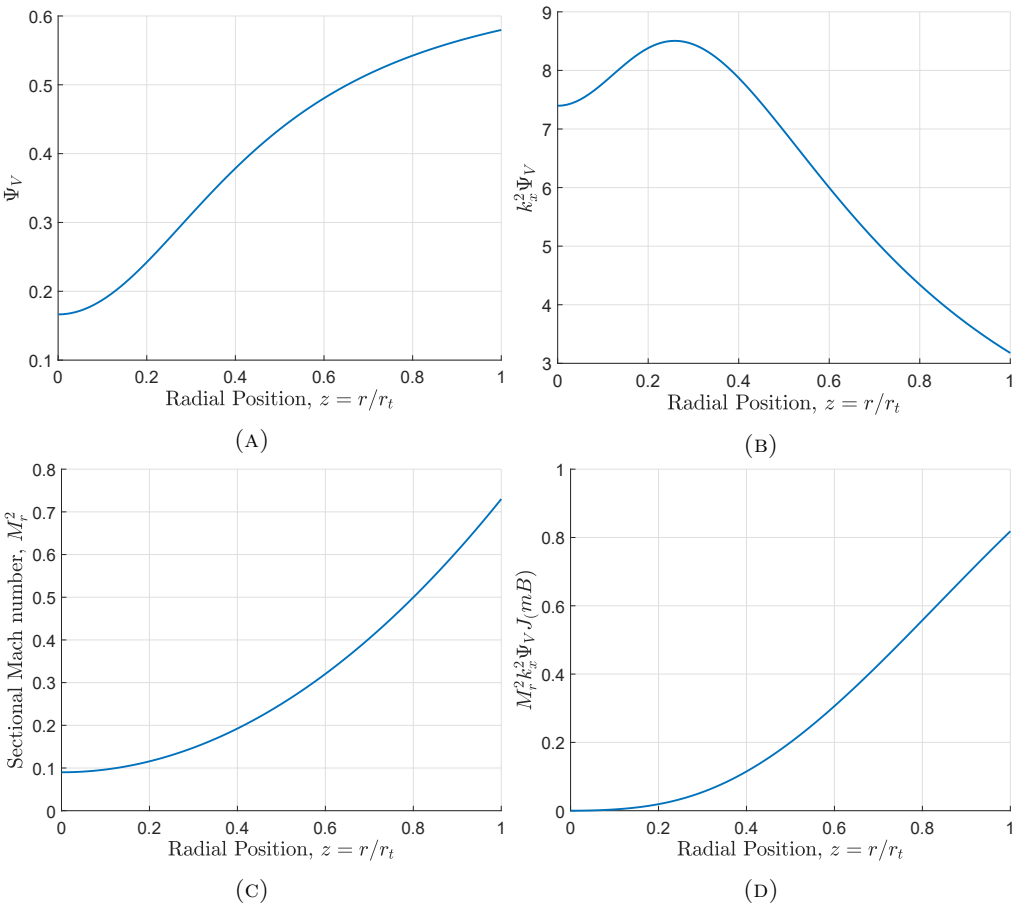

FIGURE 4.10: The source term and Sectional Mach number varying as function of radial position for the first harmonic. Properties: Blade number $B = 2$, Flight Mach number $M_x = 0.3$ and Tip Mach number $M_t = 0.8$

Therefore, the individual source contributions may be estimated as simple functions of the blade thickness, t_b and blade loading, C_L and C_D,

$$k_x^2 t_b \Psi_V(k_x) \approx t_b \tag{4.44}$$

$$k_x (C_D/2) \Psi_D(k_x) \approx C_D/2 \tag{4.45}$$

$$k_y (C_L/2) \Psi_L(k_x) \approx \frac{C_L k_y}{2k_x} \approx \frac{(M_x - M_h^2 \cos\theta)}{2M_t} C_L \tag{4.46}$$

Section relative Mach number

The section relative Mach number is defined as,

$$M_r^2 = M_x^2 + z^2 M_t^2 \tag{4.47}$$

where M_x and M_t are the flight and tip Mach numbers respectively. Figure 4.10 shows how the sectional Mach number varies along the propeller radius. For a flight mach number of zero, the sectional mach number will tend towards the tip mach number as the position approaches the tip radius. Therefore, the outer portions of the propeller close to the tip will have larger sectional mach number and will therefore contribute significantly more to the total integral value.

The dominating term within the integral in the radial direction is the square of the section relative Mach number, M_r^2. The section relative Mach number takes maximum at the tip of the propeller, and is equal to the helical Mach number M_h. We may estimate the value of the integral by assuming it is directly proportional to $\int \propto M_h^2$, and for a static case proportional to $\int \propto M_t^2$, as can be seen,

$$M_r^2 \approx M_h^2 = M_x^2 + M_t^2 \tag{4.48}$$

This assumption implies that the thickness and loading sources are applied on the propeller tip section. To correct the thickness and loading parameters to account for the entire blade we assume the thickness ratio at the blade tip takes the average value over the blade, $t_b(z=1) = \bar{t_b}$, and the loading coefficient follow accordingly, $C_D(z=1) = \bar{C_D}$ and $C_L(z=1) = \bar{C_L}$ (Note: the loading parameters C_D and C_L may instead be defined in terms of thrust and torque, dT/dz and dQ/dz respectively, with the integral over the radius giving the thrust and torque acting on the blade).

4.3.2 Blade integral approximation

The entire integral of Equation 4.23 accounts for the geometry of the blade, and the loading conditions on the blade. The thickness noise source is directly proportional to the volume of the blades which is equal to volume of air that it displaces; the integral over the radius combined with the definition of other geometric parameters such as the chord-to-diameter ratio, the thickness-to-chord ratio etc. is what defines the thickness source strength. In the derivation of the Hanson method, the monopole source is within the blade volume integrals (or specifically the helicoidal volume created by the motion of the blade), however, due to the thin plate assumption, the volume of the blade is assumed to be negligible, and therefore the thickness noise source is represented by the sum of source strengths calculated as functions of the previously mentioned parameters. The geometry of the blade determines the blade loading, and therefore also the dipole (lift and drag) noise sources. The same thin-wing assumption, has a knock on effect to the loading sources, and are therefore also represented by the sum of the dipole distributions on the upper and lower surfaces of the blade. The integral has taken a one dimensional form, meaning the only independent variable is now the radial position along the blade z.

In this case the area below the function decreases as the harmonic number increases (Figure 4.11), representing the decaying behaviour characteristic to a low tip Mach number. The value of the integral as a function of mode number does not always decay as m increases.

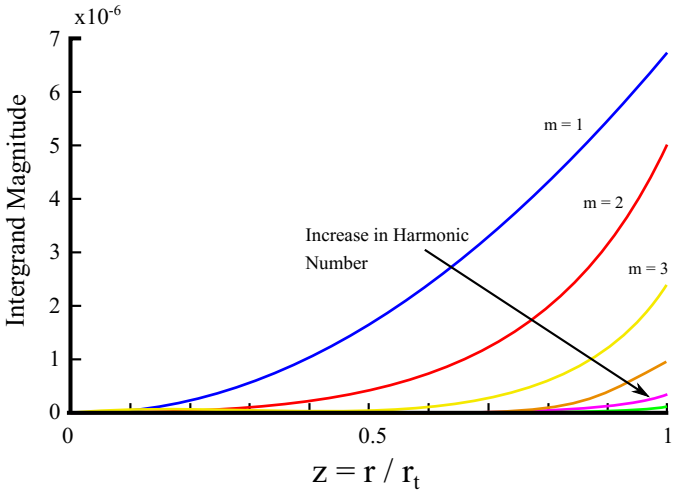

FIGURE 4.11: Integrand magnitude versus of the position along the propeller. The area under the graph represents the value of the integral. For low tip Mach numbers, as expected as the harmonic number increases the area decreases.

Each of the three sources are treated separately as individual integrals, and following the evaluation, the Fourier coefficients P_{mV}, P_{mL} and P_{mD} are added together to provide the total noise field due to the propeller harmonic sources.

Thickness noise source integral evaluation

The integral giving P_{Vm} may therefore be written and simplified as following,

$$\int_0^1 M_r^2 \frac{t_b}{(mB)!} \left(\frac{mBzM_t \sin\theta}{2\left(1 - M_x \cos\theta\right)} \right)^{mB} \mathrm{d}z \tag{4.49}$$

$$= \frac{t_b}{(mB)!} \left(\frac{mBM_t \sin\theta}{2\left(1 - M_x \cos\theta\right)} \right)^{mB} \int_0^1 \left(M_x^2 + z^2 M_t^2 \right) z^{mB} \mathrm{d}z \tag{4.50}$$

Ignoring the constant terms outside the integral for the time being, and applying the zero flight Mach number condition, the integral may be written as the sum of two simpler integrals,

$$\int_0^1 \left(z^{mB} M_x^2 + z^{mB+2} M_t^2 \right) \mathrm{d}z \tag{4.51}$$

$$1^{\text{st}} : \int_0^1 M_t^2 z^{mB+2}\,\mathrm{d}z = \frac{M_t^2}{mB+3} \tag{4.52}$$

$$2^{nd} : \int_0^1 z^{mB} M_x^2\,\mathrm{d}z = \frac{M_x^2}{mB+1} \tag{4.53}$$

Final integral for thickness noise in hover:

$$\int_0^1 \cdots \mathrm{d}z = \frac{t_b}{(mB)!}\left(\frac{mBM_t\sin\theta}{2\left(1-M_x\cos\theta\right)}\right)^{mB}\left[\frac{M_t^2}{mB+3}+\frac{M_x^2}{mB+1}\right] \tag{4.54}$$

Loading noise source integral evaluation: Lift/axial component

Following similar integration techniques, the integral may be evaluated to the loading components of the noise. For lift,

$$\int_0^1 M_r^2 J_{mB}\left(\frac{mBzM_t\sin\theta}{1-M_x\cos\theta}\right)\frac{mBB_D}{zM_r}\left(\frac{M_x-M_r^2\cos\theta}{1-M_x\cos\theta}\right)\frac{C_L}{k_x}\mathrm{d}z \tag{4.55}$$

$$= \frac{1}{(mB)!}C_L\left(\frac{mBM_t\sin\theta}{2\left(1-M_x\cos\theta\right)}\right)^{mB}\frac{1}{M_t}\int_0^1 M_r^2 z^{mB-1}\left(M_x-M_r^2\cos\theta\right)\mathrm{d}z \tag{4.56}$$

$$\text{const}\int_0^1 \left(M_x^2+z^2M_t^2\right)z^{mB-1}\left(M_x-\left(M_x^2+z^2M_t^2\right)\cos\theta\right)\mathrm{d}z \tag{4.57}$$

Simplifying into the sum of 6 integrals,

$$1^{\text{st}} : \int_0^1 M_x^3 z^{mB-1}\,\mathrm{d}z = \frac{M_x^3}{mB} \tag{4.58}$$

$$2^{\text{nd}} : -\int_0^1 \cos\theta M_x^4 z^{mB-1}\,\mathrm{d}z = -\frac{\cos\theta M_x^4}{mB} \tag{4.59}$$

$$3^{\text{rd}} : -\int_0^1 \cos\theta M_x^2 M_t^2 z^{mB+1}\,\mathrm{d}z = -\frac{\cos\theta M_x^2 M_t^2}{mB+2} \tag{4.60}$$

$$4^{\text{th}} : \int_0^1 M_t^2 M_x z^{mB+1}\,\mathrm{d}z = \frac{M_t^2 M_x}{mB+2} \tag{4.61}$$

$$5^{\text{th}} : -\int_0^1 \cos\theta M_t^2 M_x^2 z^{mB+1}\,\mathrm{d}z = -\frac{\cos\theta M_t^2 M_x^2}{mB+2} \tag{4.62}$$

$$6^{\text{th}} : -\int_0^1 \cos\theta M_t^4 z^{mB+3}\,\mathrm{d}z = -\frac{\cos\theta M_t^4}{mB+4} \tag{4.63}$$

Therefore the final value of the lift integral is,

$$\begin{aligned}\frac{1}{(mB)!}C_L\left(\frac{mBM_t\sin\theta}{2\left(1-M_x\cos\theta\right)}\right)^{mB}\frac{1}{M_t}\\ \times\left[\frac{M_x^3}{mB}-\frac{\cos\theta M_x^4}{mB}-\frac{\cos\theta M_x^2 M_t^2}{mB+2}+\frac{M_t^2 M_x}{mB+2}-\frac{\cos\theta M_t^2 M_x^2}{mB+2}-\frac{\cos\theta M_t^4}{mB+4}\right]\end{aligned} \tag{4.64}$$

Loading noise source integral evaluation: Drag/tangential component

$$\int_0^1 M_r^2 J_{mB}\left(\frac{mBzM_t\sin\theta}{1-M_x\cos\theta}\right)C_D\mathrm{d}z \tag{4.65}$$

$$\begin{aligned}&\text{const}\int_0^1 z^{mB}\left(M_x^2+z^2M_t^2\right)\mathrm{d}z\\ =&\text{const}\ M_t^2\int_0^1 z^{mB+2}\sin\left(\frac{k_x}{2}\right)\mathrm{d}z\\ =&\frac{C_D}{(mB)!}\left(\frac{mBM_t\sin\theta}{2\left(1-M_x\cos\theta\right)}\right)^{mB}\left[\left(\frac{M_t^2}{mB+3}+\frac{M_x^2}{mB+1}\right)\right]\end{aligned} \tag{4.66}$$

Combining of the above mentioned procedures and adding the contributions of the individual sources together we may estimate $P_{mB} = P_{Vm} + P_{Dm} + P_{Lm}$ as,

$$
\begin{aligned}
P_{mB} = -\frac{\rho_0 c_0^2}{8\pi}\frac{1}{y}\sin\theta DB\frac{1}{(mB)!}\left(\frac{mBM_t\sin\theta}{2}\right)^{mB} \\
\text{Thickness}\left\{ \times\left(t_b\left[\frac{M_t^2}{mB+3}+\frac{M_x^2}{mB+1}\right]\right.\right. \\
\text{Lift}\left\{ +C_L\frac{1}{M_t}\left[\frac{M_x^3}{mB}-\frac{\cos\theta M_x^4}{mB}-\frac{\cos\theta M_x^2 M_t^2}{mB+2}\right.\right.\right. \\
\left.\left.\left. +\frac{M_t^2 M_x}{mB+2}-\frac{\cos\theta M_t^2 M_x^2}{mB+2}-\frac{\cos\theta M_t^4}{mB+4}\right]\right. \\
\text{Drag}\left\{ +C_D\left[\frac{M_t^2}{mB+3}+\frac{M_x^2}{mB+1}\right]\right)
\end{aligned}
\tag{4.67}
$$

A greater simplification

Common practice in the literature is to evalutate the integral over the blade at the point of maximum lift, $L(z = r/R)$ along the radius of the blade. Propellers are typically designed for this property to occur beetween $0.7R$ and $0.85R$ [14, 76]. The blade is modelled as if the blade characteristics and performance along the radius equals that of the maximum lift location.

The greater simplification effectively assumes constant section relative Mach number, M_r, across the span of the propeller blade. Additionaly, the Bessel function, is no longer span location dependant, therefore the radiation efficieny of the entire blade becomes that of the maximum lift coeffient. The impact of making this assuption is the removal of scaling factors/coeficients in Equation 4.67 that are functions of mB, the order of the harmonics. Neglecting the coefficents would result in the over prediction of the absolute values of the harmonics, with the error incressing as the harmonic number increases. However, when estimating changes (deltas) in the harmonic levels, the impact of the coeffiencts per harmonic deminishes, for example, in the case of thickness noise, $P_{Vm} \propto 1/(m+1)$, therefore for a scenario where the change in noise level for a thickness harmonic of m is of interest $\Delta L = 10\log_{10}\left[p_{V,m}^2/p_{V,m,0}^2\right]$, the impact of the coefficient is negated.

In the case of MONTANA, following the methodology of representing the integral by a single blade section, the blade tip is chosen as the representive location. This is the same assumption used to approxiamte the source terms in Section 4.3.1. As we are interested in the sound power output as a function of design and operational parameter

we must first estimate the intensity which is proportional to p_{rms}^2, therefore we have,

$$p_{m,rms}^2 = \langle P_{mB} P_{mB}^* \rangle \approx \underbrace{\left(\frac{\rho_0 c_0^2}{8\pi}\right)^2}_{\text{constants}} \underbrace{\left(\frac{1}{y}\right)^2}_{\text{Spherical Spreading}} \underbrace{D^2 M_h^4 \left[\bar{t_b} + \frac{\bar{C_D}}{2} + \frac{\bar{C_L}(M_x - M_h^2 \cos\theta)}{2M_t}\right]^2}_{\text{Design/operation parameters}}$$

$$\times \underbrace{\left(\frac{\sin\theta}{(1 - M_x \cos\theta)}\right)^{4mB+2}}_{\text{Directivity}} \underbrace{\left(\frac{1}{(mB)!}\right)^2 \left(\frac{mBM_t}{2}\right)^{2mB}}_{\text{Spectral Shape}} \tag{4.68}$$

The asymptotic approximation allows for some simple observations to be made regarding the influence of the tip Mach number. Assuming as previously, $M_t < 1$ the M_t^{2mB} term in Equation 4.68 shows that at a given rotation rate propellers with larger blade number generate less sound and furthermore the contribution of the higher harmonics rapidly decreases with increasing harmonic order m while the tip rotation speed remains subsonic. This allows for a modelling technique used by Heidmann for the estimation of fan discrete-tone and combination-tone noise [53], to be applied. The procedure involves predicting the spectrum level and spectrum shape. The spectrum level is defined at each design/operation point by the fundamental tone, while the levels of remaining spectral frequencies are estimated by referencing the blade passing frequency and the spectral shape function. However, unlike Heidmann the spectrum shape is not constant, rather a function of the blade number and tip mach number.

The $\sin\theta$ present within the Bessel function argument, and therefore in the approximation relation, causes highly documented dipole behaviour of the propeller. The radiated noise diminishes towards the propeller axis as approached from both front and rear directions. Additionally, the Doppler factor $(1 - M_x \cos\theta)$ causes a shift of that directivity pattern into the forward hemisphere with respect to the propeller plane.

4.4 Overall sound power

The overall sound power output of the system may therefore be evaluated through the average intensity emitted over angles θ and φ, which may be evaluated in the far field through the root-mean-square,

$$\mathbb{P}_{rad} = \frac{1}{\rho_0 c_0} \int_0^{2\pi} \int_0^{\pi} |p_{rms}|^2 R^2 \sin\theta \, d\theta d\varphi \tag{4.69}$$

The calculation of $\mathbb{P}_{rad}$ depends on the integration over the spherical surface surrounding the source. The integral over φ takes a trivial answer as rotational symmetry exists around the propeller axis. When considering the evaluation of the integral over the polar angle θ over in the interval $\theta \in (0, \pi)$ the solution is no longer trivial. The problem may again be divided into two cases, a. a static (or hovering) propeller, meaning $M_x = 0$ and b. the case where mean flow is non-zero, $M_x \neq 0$ and assuming subsonic flight speeds ($M_x < 1$).

The overall sound power is given as a sum over all modes m, therefore Equation 4.69 may be written as,

$$\mathbb{P}_{rad} = \frac{1}{\rho_0 c_0} \int_0^{2\pi} \int_0^{\pi} \left[2 \sum_{m=0}^{\infty} p_{m,rms}^2 \right] R^2 \sin\theta \, d\theta d\varphi \tag{4.70}$$

The sound power radited by each mode may evaluated by calcualtaing the surface integral for each individual mode m.

$$\mathbb{P}_{rad} = \frac{2\pi R^2}{\rho_0 c_0} \sum_{m=0}^{\infty} \left[\int_0^{\pi} p_{m,rms}^2 \sin\theta \, d\theta \right] \tag{4.71}$$

Regarding the integration over θ, the polar angle in Equation 4.71, the square of the Fourier pressure coefficients may be written as,

$$p_{m,rms}^2 = b_0 \frac{\sin^{2mB+2}\theta}{1 - M_x \cos\theta} \left(b_1 + b_2 \cos\theta + b_3 \right)^2 \tag{4.72}$$

where the constants b_0,b_1, b_2, b_3 and b_4 with respect to θ are,

$$b_0 = \left(-\frac{\rho_0 c_0^2}{8\pi} \frac{1}{y} DB \frac{1}{(mB)!} \left(\frac{mBM_t}{2} \right)^{mB} \right)^2 \tag{4.73}$$

$$b_1 = t_b \left[\frac{M_t^2}{mB+3} + \frac{M_x^2}{mB+1} \right] \tag{4.74}$$

$$\begin{aligned} b_2 = & C_L \frac{1}{M_t} \left[\frac{M_x^3}{mB} - \frac{\cos\theta M_x^4}{mB} - \frac{\cos\theta M_x^2 M_t^2}{mB+2} \right. \\ & \left. + \frac{M_t^2 M_x}{mB+2} - \frac{\cos\theta M_t^2 M_x^2}{mB+2} - \frac{\cos\theta M_t^4}{mB+4} \right] \end{aligned} \tag{4.75}$$

$$b_3 = C_D \left[\frac{M_t^2}{mB+3} + \frac{M_x^2}{mB+1} \right] \tag{4.76}$$

The integral in Equation 4.71 then becomes,

$$\int_0^{\pi} b_0 \frac{\sin^{2mB+2}\theta}{1 - M_x \cos\theta} \left(b_1 + b_2 \cos\theta + b_3\right)^2 \, d\theta \tag{4.77}$$

The evaluation of the integral could be considered for two cases: i. a hover case, where $M_x = 0$ and ii. a climb/forward flight case, where $M_x \neq 0$. In the absence of a freestream velocity, the calculation of the integral significantly simplifies as the helicoidal surface reduces to a disk and therefore the section relative Mach number only depend on the tip Mach number.

Zero flight Mach number, $M_x = 0$

Assuming a zero flight Mach number, M_x, the integral simplifies further, while the lift term also reduces significantly. Following some algebraic manipulation, the value of the above integral may be written as the sum of the following three integrals,

$$b_0 b_{1,3}^2 \int_0^{\pi} \sin^{2mB+3}\theta \, d\theta \tag{4.78}$$

$$2 b_0 b_{1,3} b_2 \int_0^{\pi} \sin^{2mB+3}\theta \cos\theta \, d\theta = 0 \tag{4.79}$$

$$b_0 b_2^2 \int_0^{\pi} \sin^{2mB+3}\theta \cos^2\theta \, d\theta \tag{4.80}$$

where $b_{1,3} = b_1 + b_3$. The first integral may be evaluated using a simple recursion relationship,

$$I_n = \int_0^{\pi} \sin^n \theta \, d\theta = \frac{n-1}{n} I_{n-2}, \quad \text{with } I_0 = \pi \quad \text{and } I_1 = 2 \tag{4.81}$$

The second integral is equal to zero always as $\cos\theta$ is anti-symmetric in the interval $[0,\ \pi]$. Finally, the third integral may be estimated using recursion and by setting $\nu = 2$ in the following general formula,

$$\int_0^{\pi/2} \sin^{\nu} x \cos^n x dx = \begin{cases} \frac{[(\nu-1)(\nu-3)\cdots 1][(n-1)(n-3)\cdots 1]}{(\nu+n)(\nu+n-2)\cdots 2}\,(\pi) & \nu, n \text{ even} \\ \frac{[(\nu-1)(\nu-3)\cdots (2 \text{ or } 1)][(n-1)(n-3)\cdots (2 \text{ or } 1)]}{(\nu+n)(\nu+n-2)\cdots (2 \text{ or } 1)} & \text{otherwise} \end{cases} \tag{4.82}$$

4.5 Variation of propeller tonal noise

Combining the methodology presented in Section 4.2 and the result for the overall sound power radiated by the propeller harmonic noise model, the SPL for any study aircraft using a propeller may be estimated using the known noise levels from a baseline scenario and the changes in noise (ΔSPL or ΔPWL) as calculated by the approximation model in Section 4.4.

The individual harmonic levels may be related to the fundamental tone by some spectra shape function, allowing for the SPL to be written as,

$$L_{p,0} = 10\log_{10}\left(\sum_{f}^{\infty} 10^{\left[L_{f_1,0}+F_1\left(\frac{f}{f_{1,0}}\right)\right]/10}\right) \tag{4.83}$$

with $f = mB\Omega$ and $f_1 = B\Omega$ represent the frequency of mode m and the fundamental tone respectively, while $L_{f_1,0}$ is the SPL of the baseline fundamental. F_1 denotes the spectra shape function.

When modifications in terms of operational and/or design parameters are made, changes to the fundamental tone, ΔL_{f_1} and the shape of the harmonics ΔF_1 are observed, leaving the new SPL as,

$$L_p = 10\log_{10}\left(\sum_{f}^{\infty} 10^{\left[L_{f_1,0}+F_1\left(\frac{f}{f_{1,0}}\right)+\Delta L_{f_1}+\Delta F_1\left(\frac{f}{f_1}\right)\right]/10}\right) \tag{4.84}$$

where,

$$L_{f_1} = L_{f_1,0} + \Delta L_{f_1} \tag{4.85}$$

represents the new level of the fundamental tone, and

$$L_m(f) = L_{f_1} + \Delta F_1(f/f_1) \tag{4.86}$$

represents the new sound level of the harmonics (narrowband spectrum).

Returning to Equation 4.68, we may consider a case where modifications to a baseline aircraft are made. The change in level of the fundamental frequency observed may be estimated by setting $m = 1$ in both cases. The resulting acoustic sound pressure is then denoted p_{f_1} and $p_{f_1,0}$ for the modified and baseline cases, respectively. The change in fundamental tone level between the two cases is then,

$$\Delta L_{f_1} = 10\log_{10}\left(\frac{p_{f_1}^2}{p_{f_1,0}^2}\right) \tag{4.87}$$

or

$$\begin{aligned}\Delta L_{f_1} = {} & 20\log_{10}\left(\frac{y}{y_0}\right) + 20\log_{10}\left(\frac{BD}{B_0D_0}\right) + 40\log_{10}\left(\frac{M_h}{M_{h_0}}\right) \\ & + 20\log_{10}\left(\frac{t_b + C_D/2 + C_L(M_x - M_h^2\cos\theta)/(2M_t)}{t_{b,0} + C_{D,0}/2 + C_{L,0}(M_{x,0} - M_{h,0}^2\cos\theta_0)/(2M_{t,0})}\right) \\ & + 20\log_{10}\left(\frac{B_0!}{B!}\right) + 20\log_{10}\left(\frac{(BM_t)^B}{B_0M_{t,0})^{B_0}}\right) \\ & + 20\log_{10}\left(\frac{[\sin\theta/(1 - M_x\cos\theta)]^{2B+1}}{[\sin\theta_0/(1 - M_{x,0}\cos\theta_0)]^{2B_0+1}}\right)\end{aligned} \tag{4.88}$$

where the subscript 0 denotes the values corresponding to the condition before the modifications were applied (baseline).

Separating all terms including the mode number m in Equation 4.68 we may define a function S. This function determines the shape of the harmonics.

$$S(m) = \left(\frac{\sin\theta}{1 - M_x\cos\theta}\right)^{4mB+2}\left(\frac{1}{(mB)!}\right)^2\left(\frac{mBM_t}{2}\right)^{2mB} \tag{4.89}$$

Normalising this expression by its value for $m = 1$,

$$\frac{f}{f_1}(m) = \frac{S(m)}{S(1)} = \left(\frac{\sin\theta}{1 - M_x\cos\theta}\right)^{4B(m-1)}\left(\frac{B!}{(mB)!}\right)^2\left(\frac{BM_t}{2}\right)^{2B(m-1)} m^{2mB} \tag{4.90}$$

noting that $\frac{f}{f_1}(1) = 1$ by definition. Finally, the change in level of the harmonics ($m > 1$) between a baseline case and a modified counterpart may be given by,

$$\Delta F_1\left(\frac{f}{f_1}\right) = 20m\log_{10}\left(\frac{m^B}{m^{B_0}}\right) + 20\log_{10}\left(\frac{B!(mB_0)!}{B_0!(mB)!}\right)$$
$$+ 20\log_{10}\left(\frac{(BM_t)^{B(m-1)}}{(B_0M_{t,0})^{B_0(m-1)}}\right) \tag{4.91}$$
$$+ 40\log_{10}\left(\frac{[\sin\theta/(1-M_x\cos\theta)]^{B(m-1)}}{[\sin\theta_0/(1-M_{x,0}\cos\theta_0)]^{B_0(m-1)}}\right)$$

4.6 Individual source directivities and spectral properties

The result in Section 4.5 refers to a single individual source, that is in this case propeller steady harmonic noise. However, the definition of a lumped source requires the combination of multiple individual noise sources to represent the entire aircraft as a single point noise source. The directivity and spectral content of the lumped source are therefore a function of the characteristics' baseline scenario and changes $\Delta D(\theta,\varphi)$, $\Delta S_{pp}(f)$ of all the individual sources accounted for.

Specifically, for the directivity characteristics this means,

$$DI(\theta,\varphi) = DI_0(\theta,\varphi) + \sum_{i=1}^{s}\Delta DI_i(\theta,\varphi) \tag{4.92}$$

where DI refers to the directivity index in dB. While for the spectral content,

$$S_{pp}(f) = S_{0,pp}(f) + \sum_{i=1}^{s}\Delta S_{i,pp}(f) \tag{4.93}$$

where all S in this case are in a log scale and therefore in dB.

In the context of using normalised functions to describe the directivity distribution functions, the total lumped source directivity may be written as weighted sum of the individual directivity functions as presented in Equation 2.15.

In the same way, the total lumped source spectral context may be defined as,

$$\bar{S}_{pp}(f) = \frac{\sum_{i=1}^{s}\mathbb{P}_s\bar{S}_{i,pp}(f)}{\sum_{s=1}^{n}\mathbb{P}_s} \tag{4.94}$$

where the $\bar{}$ denotes the normalised power spectral density.

An interesting point to make is that from the perspective of the lumped source, the directivity and spectral content are treated as two independent properties of the source. Generally, directivity is frequency dependent, and therefore each direction may be seen to have a frequency distribution associated to it. Depending on what method/ model is used to predict the changes in noise levels, this relationship may be captured, however is lost once combined using the current implementation of the lumped source method. This discussion is continued in Chapter 5, where the implementation and use of spherical harmonics may be leveraged in future updates to MONTANA to capture this effect.

4.7 Generation of computational NPD curves

The contents of this section aims to extend the framework presented by Synodinos et al. [12], for the generation of NPD curves from the derived change in overall PWL (ΔPWL) and spectral shape of the propeller harmonic sources.

The procedure involves the standard, steady-level flyover of the aircraft, directly over a stationary observer, as depicted in Fig. 4.12. In addition, the NPD curves of the baseline scenario used to compute the ΔPWL are required. The baseline NPD data is back-propagated to the source PWL where the estimated ΔPWL for the novel scenario is added. The changes to the $1/3^{rd}$ octave band spectra are also accounted for at this lumped source stage. Once the adjusted spectra have been acquired, spherical spreading, A-weightings and atmospheric attenuation are accounted for, and thus OASPL NPD levels at all 10 standard slant distances are generated.

The aircraft performs the flyover at a reference airspeed and reference atmospheric conditions at a number of power settings $\mathbb{P}_{rad}(j)$ (i.e. thrust settings). The polar emission angle θ is defined as in Figure 4.12. Ten standard slant distances are used. Each curve signifies a specific power setting usually defined by the aircraft corrected net thrust (CNT) or a in terms of a percentage (%) of maximum static thrust (usually for propeller powered aircraft). The slant distance d_p is the parameter used to describe the geometry between the aircraft flightpath and the observer. It is defined as the shortest distance between the specified observer and any point on the flightpath. In the case of directly overhead flyover, the slant distance is equal to the altitude of the flyover. For each power setting $\mathbb{P}_{rad}(j)$ a discrete time history of SPL is calculated through a simulated flyover.

The standard SAE AIR1845 [89] computational step is then used to acquire noise exposure NPD curves in SEL or EPNL metrics. For in-depth description the reader is encouraged to follow the procedure described in [12] and [34] along with the SAE AIR1845 [89, 100]. Sound propagation and atmospheric attenuation is also handled as suggested by Doc29 using SAE-ARP 866A [88].

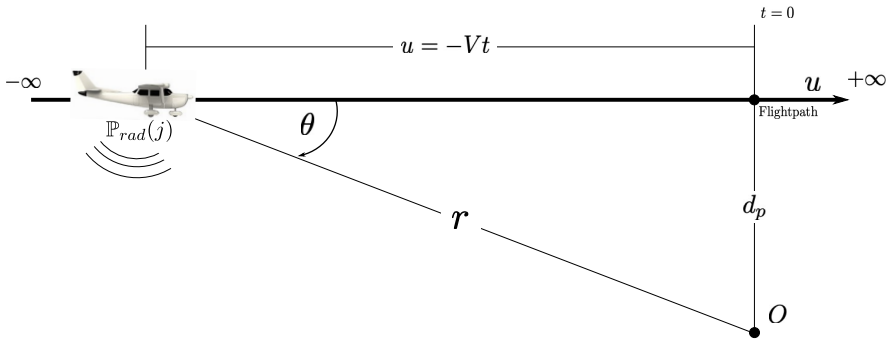

FIGURE 4.12: Geometrical setup during steady, level flyover operation between the moving aircraft and the stationary observer.

The procedure is outlined in the form of bullet points where differences between propeller aircraft and conventional turbofan aircraft are specified.

- A baseline scenario is chosen (Section 4.1) with experimentally measured $L_{\mathrm{A,max}}$ NPD level at distance d, polar angle θ and operating condition. The NPD level is coupled with a normalised $1/3^{\mathrm{rd}}$ spectrum shape at the chosen operating condition.

- The measured $L_{\mathrm{A,max}}$ is back propagated to the source. This means dimensionalising the spectrum shape for the given $L_{\mathrm{A,max}}$, the removal of the A-weighting, the removal of the atmospheric attenuation correction and the correction for spherical spreading. This process is presented in detail by Synodinos et al. [12, 52].

- A lumped noise sources is appropriately defined to represent the aircraft of interest. This "total" noise source is made up of the dominant individual noise sources that contribute to the overall noise emission of the aircraft.

- The change in SPL ($\Delta L_p(d, j)$) is calculated using the changes in individual noise sources levels. The changes in individual sources are calculated using appropriate noise prediction methods. In the case of propeller harmonic noise source, the change in noise is calculated with the procedure described in the previous section.

- $\Delta L_p(d, j)$ is added to the baseline NPD level to yield the aircraft L_p corresponding to the new scenario at the same power setting, and slant distance. In the case of the propeller sources, the new SPL is calculated using Eq. (4.84) taking into account the change in fundamental frequency level, and spectra shape.

- Changes ΔL_p reflecting changes in power settings of the modified scenario are calculated using the same procedure only using the L_p corresponding to the new scenario as a baseline level.

- The levels at the remaining engine power settings at the same distance d are obtained by adding the noise level variation ΔL_p resulting from changing the engine power to the first level $L_p(d, j)$ of the modified scenario.
- The SAE AIR1845 computational step is then used to propagate the levels at distance d, the remaining NPD distances. This step accounts for atmospheric attenuation corrections.
- Finally, A-weighting is reapplied and the $1/3^{\text{rd}}$ spectra logarithmically summed to get the total $L_{\text{A,max}}$ of the modified scenario.

At this point $L_{\text{A,max}}$ NPD curves have been derived. The next few steps summarise the procedure for the development of the L_{AE} NPD curves.

- Using the estimates of the total sound power emitted (at power setting j) of the modified scenario and the directivity characteristics of the aircraft, computational flyover is performed at an altitude equal to distance d, and the L_{AE} is calculated at an observer point directly under the flightpath by integration.
- Using the L_{AE} and the previously derived $L_{\text{A,max}}$ NPD curve (at power setting j) the L_{AE} is calculated at the remaining NPD slant distances.
- This procedure is carried out for every power setting of interest.

4.8 Summary

At this point, a lumped source model of the air vehicle has been created, using the constituent individual source methods and their scaling relations. Particular emphasis has given to the propeller self noise sources, thickness and loading, by deriving asymptotic scaling relations from the frequency domain helicoidal surface model by Hanson.

These relations are fundamentally based on operating condition and geometry of the given propellers (or rotors) and their blades. Thickness source strength is modelled as function of the average blade section thickness. Loading noise strength are modelled as functions of the average blade section lift and drag of the coefficients, themselves calculated using a lifting-line model. Source non-compacteness effects are modelled using chordwise distribution of the thickness and the loading characteristics, using a parabolic curve to describe the chordwise thickness variation, while uniform (constant) variation was assumed for the lift and drag.

Radiation characteristics are defined by the general far-field result for any helically convected source (as defined in [60]) for given forward and rotational speeds. The final

directional properties for each blade passing mode are shaped by the differences in wavenumber description of individual the propeller sources.

The final representation of the air vehicle as a lumped noise source has been used to perform numerically simulated steady and level flyovers, calculating event noise level time histories on the ground observers and converted into NPD curves of desired metrics, through standard process.

These NPD curves are going to serve as the main noise data input of the airport noise tools presented in the next Chapters.

Chapter 5

Methodology II: Airport noise model

This chapter covers the airport noise and flight procedure modelling component of this thesis. As suggested by the name, the topic involves estimating noise exposure levels around airports and specifically the simplified airport noise tool RANE (Rapid Aviation Noise Evaluator), which uses NPD curves as a main input of noise data. The original RANE tool was developed by A.J. Torija et al. [13] with the intent of providing high-level calculations of aviation noise around airports in the context multidisciplinary strategic environmental assessment. The model is based on the noise exposure footprint model of Stewart and Carson [182] of NASA, for isotropic conventional fixed wing aircraft and their operations. Zaporozhets et al. [183] have also implemented the concept of the noise radius in a tool for environmental assessment around airports. The single event footprint capabilities were expanded upon by Torija to enable the model to calculated exposure contour of entire fleets assuming an average trajectory for the whole fleet.

The extension to RANE include the following features:

1. Implementation of total three-dimensional aircraft directivity.
2. Modification of flight path discretisation method, to include novel VTOL operations and manoeuvres.
3. Ability to use traditional three-point lateral (left,right and centre) NPD curves to account for lateral directivity effects. (Complements point number 1. of this list).
4. Much improved modelling of the complex region between flight path segments.
5. Preliminary model for accounting for power variation throughout segments.

6. Preliminary modelling of noise surfaces and contours for rotating three-dimensional sources.

The most impactful contribution in RANE v2 is that of the three-dimensional directivity. The method implemented within this chapter allows the user to specify the aircraft directivity to the level of detail equivalent to that of the available data or to specify simplified analytical approximations of the directivity based on knowledge of the aircraft and the individual noise sources it is comprised of. The implementation of aircraft directivity along with the treatment of the connecting regions between the discretised segments, allows for increased accuracy in predicting the noise exposure area as well as the locations of the radiated noise.

Figure 5.1 shows a flow diagram of the calculation process used by RANE v2. The main three inputs for a footprint calculation are: a. Noise-Power-Distance curves of the aircraft to be assessed at all relevant power settings and operational modes, b. aircraft total directivity, (in an ideal situation where data is abundant the directivity would be specified at all power settings), this may be in the form of discretised numerical data or simple analytical expressions and c. simplified aircraft trajectory data (this data may be broken into two parts, flight path geometry and aircraft performance along the flight path).

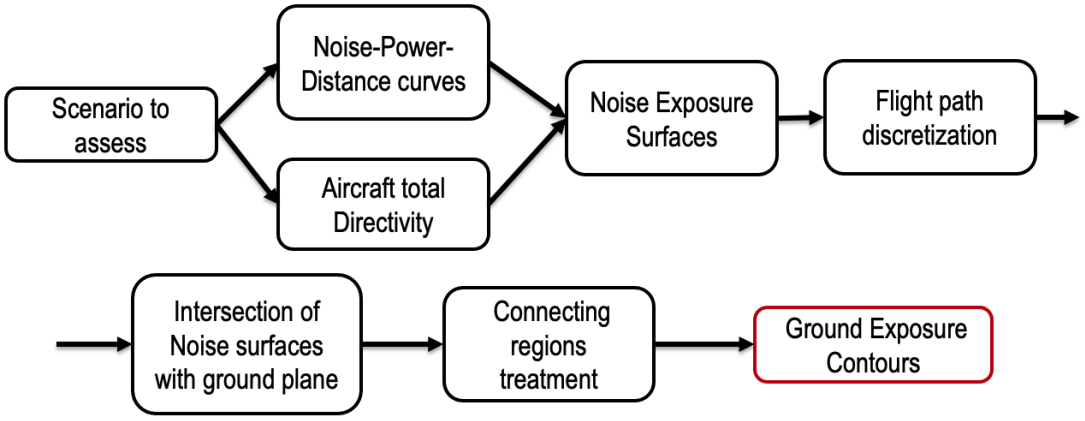

FIGURE 5.1: Flow diagram overview of RANE workflow.

These inputs are used to generate a series of noise exposure surfaces along the flight path. The intersection of the noise surfaces with the two-dimensional airport plane result in the two-dimensional iso-lines. Depending on the number of operations/events over which the assessment is taking place, the iso-lines either represent the noise exposure footprints or noise exposure contours. Finally, corrections to the footprints/contours is performed at the connecting regions to adjust for the noise of multiple segments interacting at specific observer locations.

5.1 Original RANE capabilities

Detailed information of original RANE may be found in the paper by Torija et al. [13] with additional mathematical explanation in the NASA report [182].

RANE is a simplified airport noise model. The methodology does not use the ECAC doc 29 [34] grid-point method, however it is similar to it by being an "integrated" model (or a segmentation model). Integrated models use discrete segments to represent the aircraft flight path. The contributions to the overall noise at the observer locations of each of these segments are essentially "pre-integrated". The pre-integrated noise data is in the form of NPD curves. The infinite path NPD assume steady straight flight conditions at a reference speed in specified reference atmospheric conditions. The received sound event levels, both maximum and time integrated, directly beneath the aircraft as a function of distance and specified flight configuration. The noise contribution from one finite segment results from the correction of the infinite NPD noise data according to the *energy fraction* (see section 5.9).

In RANE the corrected noise contribution of one segment is used to define what is known as the Noise Radius. Due to the assumption that the aircraft is represented as an isotropic noise source, the noise radius R is only a function of the aircraft power-setting / flight-configuration and the noise level value of interest. Therefore, for a given power setting P_n and flight configuration (e.g. takeoff flap setting, approach flap setting) using the appropriate NPD curves, the slant distance at which the noise level of interest $L(d)$ occurs may be calculated. Including correction Δv_n for flight speeds different to reference speed, the noise radius R_n for each segment n may be given by [34, 13],

$$L(P) = L(P_i) + \frac{L(P_{i+1}) - L(P_i)}{P_{i+1} - P_i} (P - P_i) \tag{5.1}$$

$$L(d) = L(d_i) + \frac{L(d_{i+1}) - L(d_i)}{\log_{10}(d_{i+1}) - \log_{10}(d_i)} (\log_{10}(d) - \log_{10}(d_i)) \tag{5.2}$$

Using Equations 5.1 and 5.2, a given sound-level $L(P, d)$ can be calculated for any combination of power-setting P and distance d. The interpolation process is illustrated in Figure 5.2.

Inverting the problem, any slant distance (or in the context of RANE noise radius R_n) may be calculated given a noise level of interest. Given the NPD tabulated power settings P_i and P_{i+1} for which sound-levels are provided at some set of distances, the intermediate power setting noise levels are denoted $L(P_n)$. $L(d)$ as mentioned is the sound-level for which the noise footprint/contour is to be calculated, $L(P_n, d_i)$ is the first sound-level greater than $L(d)$ as tabulated in NPD database (for power-setting P_n), while $L(P_n, d_{i+1})$ is the first sound-level smaller than $L(d)$ (for power-setting P_n).

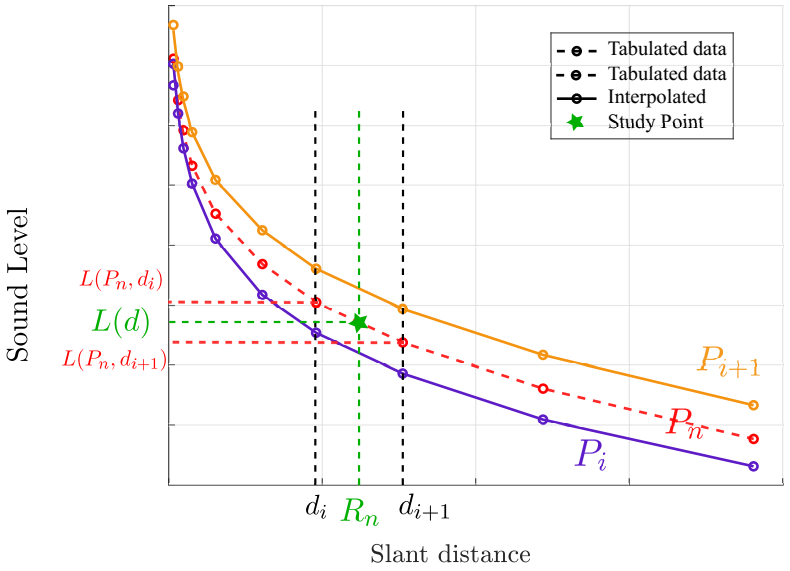

FIGURE 5.2: Illustration of interpolation between two known power settings P_i and P_{i+1}, and two known distances d_i and d_{i+1} when working with tabulated NPD data.

Distances d_i and d_{i+1} are the tabulated distances for which sound-levels are provided, used to calculate the intermediate distance d, corresponding to $L(P_n, d_i)$ and $L(P_n, d_{i+1})$ respectively. Therefore, combining Equations 5.1 and 5.2 and solving for the noise radius,

$$R_n = 10 \exp\left\{\left[\left(\left[(L(P_n, d_i) + \Delta v_n) - L(d)\right] \times \frac{\log_{10} d_{i+1} - \log_{10} d_i}{(L(P_n, d_{i+1}) + \Delta v_n) - (L(P_n, d_i) + \Delta v_n)}\right) + \log_{10} d_i\right]\right\} \tag{5.3}$$

Finally the duration adjustment Δv_n is given by,

$$\Delta v_n = 10 \log_{10}\left[\frac{v_{ref}}{v_n}\right] \tag{5.4}$$

and is expressed in dB. Where v_{ref} is the reference velocity of the NPD data used, and v_n the actual velocity of the aircraft while flying along segment n. Figure 5.3 indicates the relation of the noise radius and the noise level of interest.

Once the noise radius for each of the segments has been calculated, it is used in conjunction with the other three flight parameters (inclination angle, rotation angle, segment length) that define the flight path segment, to generate the series of cylindrical noise surfaces surrounding the entire flight path. For a single flight path, the coordinates of the boundaries and areas of a noise footprint/contour are defined by the intersection of such cylindrical surfaces with the ground surface. The final noise footprint/contour on

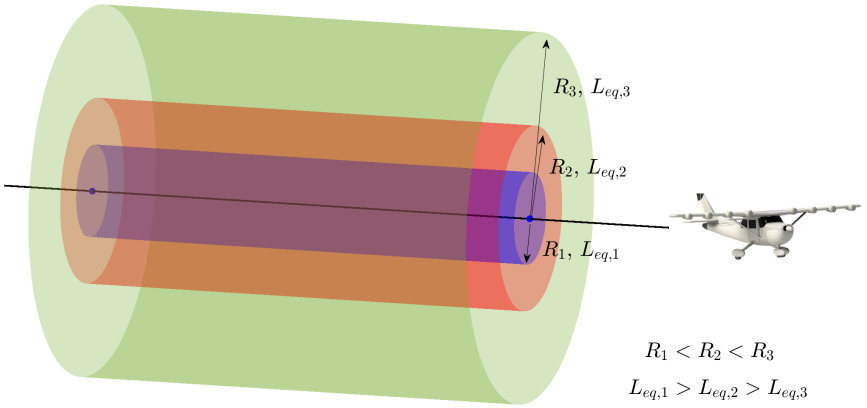

FIGURE 5.3: Diagram visualising the concentric nature of noise surfaces of different SEL values. For a constant PWL output along the segment, the outermost surfaces represent low levels, while surfaces closer to the flight path have higher values.

the ground is composed by the contribution of each individual segment (as illustrated later in Figure 5.16).

5.2 RANE v2 model overview

RANE, as an airport noise tool, can be broken down into the following distinctive parts:

- The definition of the operation and the flight path geometry.
- The definition of the aircraft as a noise source.
- The definition and calculation of the noise iso-surfaces.
- Calculation of the complete 2D noise contour.
- The definition of the desired outputs and post-processing (error correction and prediction accuracy improvement).

The typical calculation procedure is detailed within the flowchart in Figure 5.4.

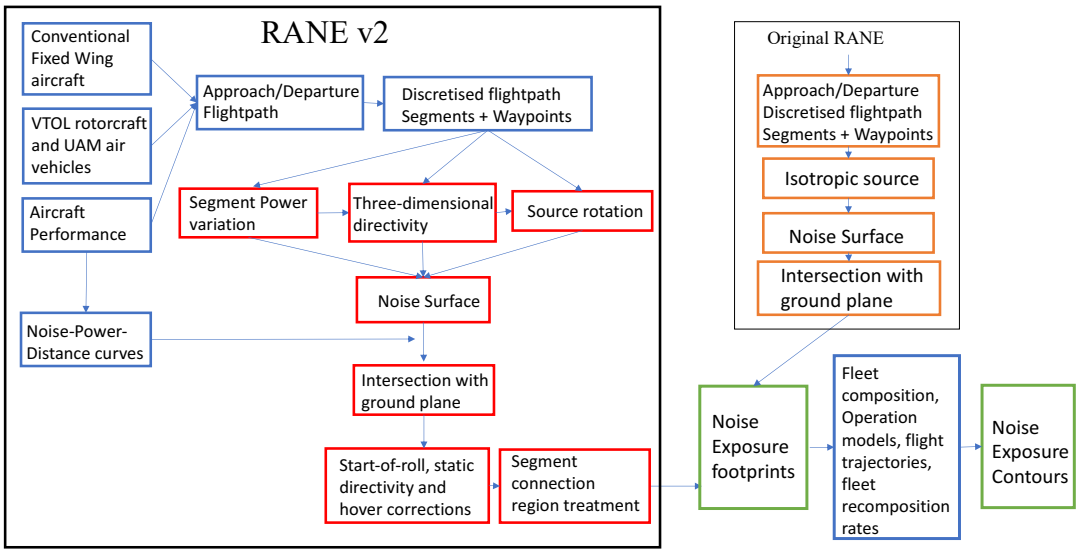

FIGURE 5.4: Detailed flow diagram of the proposed airport noise model.

A calculation is initiated with the choice of aircraft (type of air vehicle) for which the calculation/study is to be performed. The nature of the vehicle (eg. fixed wing, VTOL, tilt-wing etc.) along with its performance capabilities limit the possible operations that particular vehicle can perform. However, all vehicles perform what we will define as *airport operations* (or total operations). Airport operations are essentially of two types, departures and approaches. In practice other operations may exist, such as low passes, aborted takeoffs, go-arounds etc. but represent such a small proportion of the total aircraft operations at any given airports they are neglected. The term total operations, leads on to the fact that these operations are the product of many smaller/simpler operations (or manoeuvre) chained in succession.

Once the desired aircraft and total operation have been chosen, the aircraft performance and operational state explicitly define the trajectory and the aeroacoustic properties (essentially definition of the noise source) of the aircraft. The operation state (or mode) is determined by the vehicle configuration during a specific manoeuvre and is a function of vehicle weight. Performance describes the combination of propulsion system and total aircraft ability to generate the required thrust and lift in order to perform an operation. Performance determines the capabilities of the given aircraft at a given weight, further defining the trajectory and noise immissions.

Each aircraft has a series of NPD curves associated with it. For conventional aircraft, as discussed, these may be found in databases such as the ANP one. While for novel aircraft, methods such as [12] and the content of Chapter 4 of this thesis, allows for the generation of the required NPD data. In RANE v2, NPD curves are the link between noise emission, aircraft performance and aircraft trajectory. However, the crux of the methodology exists in an intermediate step, allowing the pre-integrated levels to be propagated to the ground from each part of the flight path simultaneously. This is possible due to the implementation of *noise surfaces* or in the simplified isotropic noise source case the *noise radius*.

Noise surfaces are essentially the result of the integration over time of the aircraft performing a particular operation (details in Section 5.4). To define a noise surface (or a series of noise surfaces) the only additional information other than the NPD curves is the three-dimensional directivity of the aircraft at each operating state.

For the particular scenario, the type of aircraft and total operation has defined the possible flight paths and associated NPD curves. Depending on the operating state the flight path is discretised into flight path segments. The segments are chosen such that performance parameters remain constant throughout each segment. This means, each segment is allocated a specific NPD curve and a three-dimensional directivity that depends on operating state and performance. Using the segment specific NPD curve and directivity, a noise surface may be defined for each of the segments.

Finally, the noise footprint may be evaluated using every noise surface surrounding the totality of the flight path. The metric of the footprint depends on the metrics of the input NPD curves.

5.3 Airport model

5.3.1 Flight path discretisation

The discretisation or segmentation procedure in RANE (and consequently in RANE v2) is performed in such a way that specific NPD data may be adapted to each discrete

segment according to aircraft flight conditions. Each segment, therefore, of the discretised flight path represents a finite section of an infinitely long path for which a corresponding NPD curve exists (or may be interpolated from the tabulated NPD data). The continuous flight path (trajectory) is therefore modelled as the aggregate of finite sections, each belonging to an infinite path, replicating the geometry of the motion of the aircraft in space, Figure 5.5. Segmentation may therefore be regarded as a trade-off of accuracy and efficiency. Closely replicating a continuous curved flight path (with variations in aircraft performance/operating parameters along it) requires a large amount of segments, which in the case of RANE increases the number of noise surfaces to be calculated.

Also, the use of NPD data biases the use of fewer long segments to represent the real trajectory. NPD data is the result of constant power, flight speed and aircraft configuration throughout flyover events. The SPL time history at an observer of such flyover event mimics that of a mathematically infinite flightpath, meaning the aircraft should start performing the constant power and flight speed operation before it is audible (the definition of audible in many cases is the 10 dB down window) to the observer, maintain past the closest point of approach, until it is again inaudible. Therefore, NPD data may be assumed to be mathematically equivalent to an infinite length flightpath flyover.

When modelling the flightpath however, longer segments are closer in the limit to the infinite path they are taken from and therefore the error appearing from the aircraft flying only along the finite segment instead of the infinite path the NPD curves are based on is smaller. The discussion of what is regarded as a finite segment and the correction applied may be found in Section 5.9 of this Chapter.

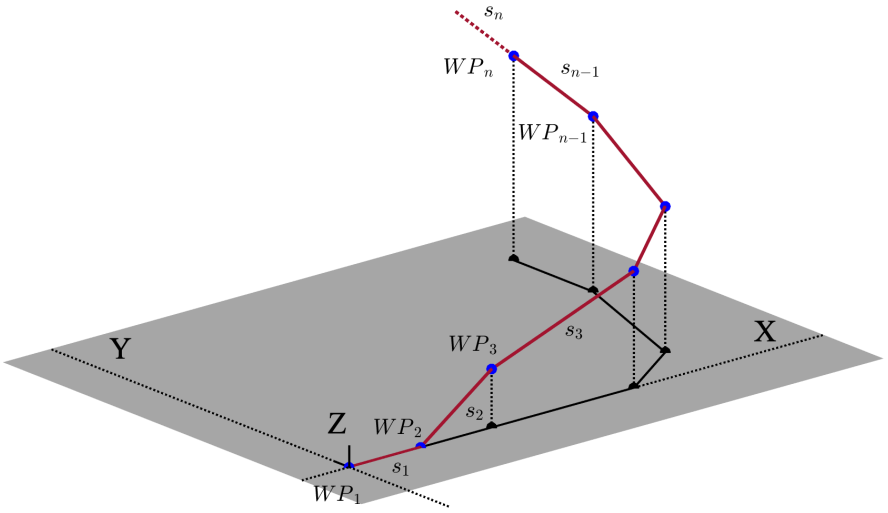

FIGURE 5.5: Three-dimensional flightpath segmentation.

5.3.2 Coordinate systems

The entire flight path and the final noise exposure footprints/contours are defined in the global (inertial) airport reference frame (X, Y, Z). This is a right-handed Cartesian frame, with the $X - Y$ defining the ground plane, on which ground observers are located, and Z defined perpendicular to that plane providing the height (altitude) spacial dimension. This coordinate system can be seen in Figures 5.5 and 5.6.

In order to calculate the noise along each segment k, we define two local (for each segment) Cartesian coordinate systems. First, the flight path orthogonal coordinate system (u, v, w) is defined. The u unit vector is aligned with the k_{th} flightpath segment (see Figure 5.6 and 5.7). The origin of the (u, v, w) coordinate system is positioned at way-point WP_k, providing reference within the global airport coordinate system (X, Y, Z). Let us also define an orthogonal coordinate system (x, y, z), in which for each k flightpath segment x is the projection of the u axis on the ground horizontal plane, and the y axis is coincident with the v axis (rotation around the y axis).

The transformation between the two position vectors $\mathbf{U} = (u\ v\ w)^T$ and $\mathbf{x} = (x\ y\ z)^T$ is,

$$\mathbf{x} = \Lambda_y \mathbf{U} \tag{5.5}$$

where Λ_y is an orthogonal matrix given by,

$$\Lambda_y = \begin{bmatrix} \cos\gamma_k & 0 & -\sin\gamma_k \\ 0 & 1 & 0 \\ \sin\gamma_k & 0 & \cos\gamma_k \end{bmatrix} \tag{5.6}$$

5.3.3 Flight path

Flight path segments are the three-dimensional representation of the aircraft trajectory as it performs an approach or departure operation. The segments must accurately capture the geometry of the trajectory, while also the variation of engine power and speed along it. Each segment has to be defined by the geometrical coordinates of its end points and the associated speed and engine power parameters of the aircraft (on which sound emission depends). The location of the end points define the geometry of the flight path, while the speed, engine power parameters and configuration determine the appropriate NPD for each segment, and therefore acoustics. The end points of the segments are called way-points and carry the information about the following segment. Way-point 1 located at the origin of our (X, Y, Z) airport coordinate system, and represents the start/end of a total airport operation. The overall flight path is divided into $k = 1, ..., K$, with K representing the total number of segments. The set of

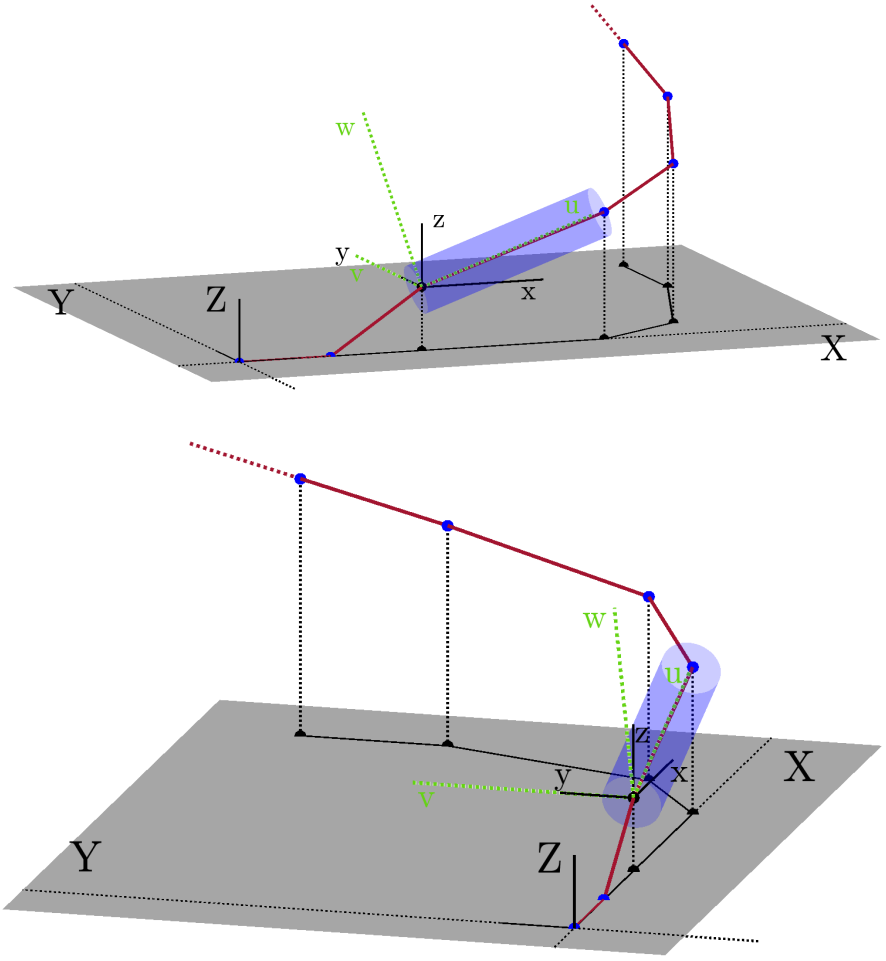

FIGURE 5.6: Two views of the three main coordinate systems used in RANE. Airport system (X, Y, Z), flight path/segment system $\mathbf{U} = (u, v, w)$ and orthogonal projection of $\mathbf{U}$, (x, y, z).

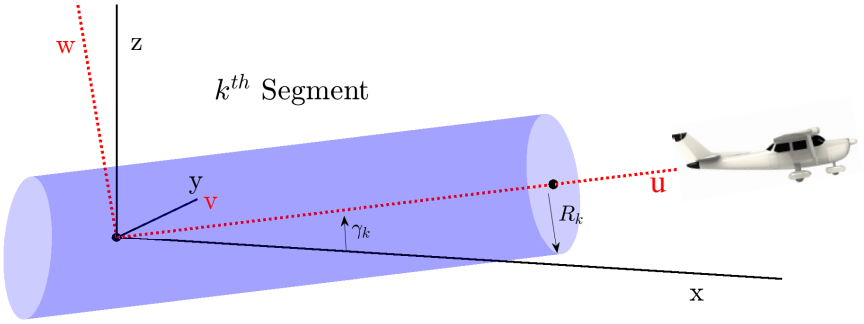

FIGURE 5.7: Definition of the flightpath Cartesian coordinate system for each segment k, with respect to the orthogonal projection system (x, y, z)

way-points therefore ranges from 1 to $(K + 1)$ with WP_k with the general k^{th} segment laying between way-points WP_k and WP_{k+1}.

Each segment is characterised by the following:

1. an angle ψ describing the rotation of each segment in the airport plane. Measured positive counterclockwise from the airport X axis to the segment.
2. an inclination angle γ measured positive above the horizontal $X-Y$ plane.
3. a segment length s.
4. noise radius R, a distance from the aircraft corresponding to the desired Sound Exposure Level (SEL) noise contour and specified power setting.
5. a directivity function $D(\theta, \varphi)$ describing the sources directional radiation properties along that segment.

The position of the k^{th} segment depends essentially on the location of the way-point WP_k and the values of γ_k and ψ_k it carries. The coordinates of WP_k are therefore given relative to all the proceeding way-points and segments. If (X_k, Y_k, Z_k) are the coordinates of the k_{th} way-point in the (X, Y, Z) airport coordinate system, they may be estimated by,

$$\begin{bmatrix} X_k \\ Y_k \\ Z_k \end{bmatrix} = \sum_{k=1}^{K-1} R_k \lambda_k \tag{5.7}$$

where $\lambda_k = [s_k,\, 0,\, 0]^T$ is the k^{th} segment location vector before it is rotated into the correct position according to the angles ψ_k and γ_k. R_k is the three-dimensional rotation matrix given by,

$$R_k = R_Z(\psi_k) R_Y(\gamma_k) R_X(\alpha) = \begin{bmatrix} \cos\psi_k & -\sin\psi_k & 0 \\ \sin\psi_k & \cos\psi_k & 0 \\ 0 & 0 & 1 \end{bmatrix} \begin{bmatrix} \cos\gamma_k & 0 & -\sin\gamma_k \\ 0 & 1 & 0 \\ \sin\gamma_k & 0 & \cos\gamma_k \end{bmatrix} \begin{bmatrix} 1 & 0 & 0 \\ 0 & \cos\alpha & -\sin\alpha \\ 0 & \sin\alpha & \cos\alpha \end{bmatrix} \tag{5.8}$$

The rotations of the segments are performed with respect to the airport coordinate unit vectors as denoted in the individual rotation matrices R_Z, R_Y and R_X (R_X is essentially an identity matrix, $\alpha = 0$, as rotations of a segment about the X-axis do not influence its location in space). The sum in Equation 5.7 represents the translation of each way-point, and therefore segment, according to all previous way-points. The angles ψ_k and γ_k are the Euler angles of the rotation matrix with a yaw, pitch, roll convention adopted.

Each way-point location will act as an origin when generating the noise surfaces corresponding to each segment. Then all noise surfaces will be referenced back into the airport coordinate system (X, Y, Z).

In the case where a highly detailed study is required, while at the same time abundance of data regarding real trajectory geometry is available, 3D curve discretization techniques may be used to approximate the continuous, finite-length 3-D curve with a piece-wise linear one. Such methods may be found in [184] and equivalent literature. However, additional considerations may be required to correct the segmentation according to performance data, at each location on the flight path.

5.4 Analytical Principles of the noise surface

The fundamental principle of the noise surface method assumes the flightpath for any given operation may be broken down into a small number of large linear segments along which flight performance parameters (aircraft and propulsion system) remain constant. This has the knock-on effect on the noise levels for the majority of all observer locations on the ground to be dominated by the noise generated by a single large segment. The large linear segments are mathematically treated as being infinitely long, with the noise exposure at any given observer being due to the acoustic energy radiated in the direction of that observer during flight along the infinite segment. The acoustic energy due to the extremities of the infinite flightpath, that do not belong to the real finite segment, is subtracted from the exposure levels. This is known as the finite segment correction, discussed in Section 5.9. Each of the large finite flightpath segments contributes to the total noise exposure contour, in the area on the ground beneath it.

The origin is placed coincident with way-point 1 of the flight path, which depending on the type of total operation, departure or approach, is the point just before the initialisation of the takeoff operation or the stagnation point after a landing operation, respectively (both excluding any taxiing operations).

A key difference to the standard Doc29 methodology is that the noise surface methodology includes observers surrounding the flight path and not only directly below, as in the case of the NPD data.

The following sections detail the process of analytically setting up the flyover and calculating the noise exposure surfaces for a single segment. This process is then effectively repeated for all segment of a flight path. The flyover process is demonstrated for three distinct cases. The simplest case of an omnidirectional noise source, a source with a polar directivity but axi-symmetric in the azimuthal direction, and finally a fully three-dimensional source. The first case, is the one implemented by the original RANE publication [13], however, the derivation and proof of the resulting cylindrical noise surface does not fully exist in literature. In addition, it acts as baseline for building the fully three-dimensional case on top of, and as a comparison.

5.4.1 Flyover procedure overview

The analytical procedure for generating a noise surface corresponds to that of calculating the noise exposure at a static observer due to an infinitely long flyover event.

The aircraft flies along the u axis of the previously defined segment (u, v, w) frame. A moving reference frame is defined. This frame corresponds to the aircraft frame. Correlation of the aircraft frame to the fixed segment frame describes the movement of the aircraft. The locations of all possible observers in three-dimensional space is given in this aircraft frame in terms of a spherical coordinate system (θ, φ, r). The definition of emission angles θ and φ may be seen in Figures 5.8 and 5.9.

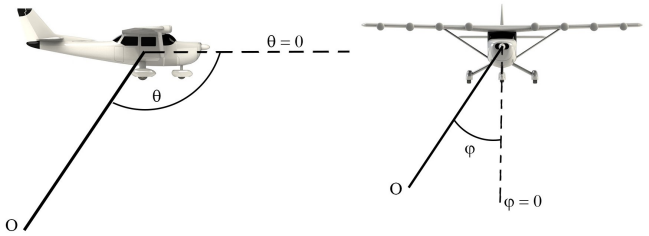

FIGURE 5.8: Polar and azimuthal angles defining observer location. Adapted from [52]

The origin of the aircraft frame is assumed to be at the aircraft CG, defining the distance r between the observer and the aircraft itself. As is obvious, the relative location of the observers changes as the aircraft moves through space, and therefore also will their coordinates in the aircraft reference frame.

Using Figure 5.9 as a reference, let us assume that a test aircraft flies at a fixed engine power setting j, generating sound power $\mathbb{P}_{rad}(j)$ or Sound-Power-Level (PWL) $L_W(j)$. The aircraft reference frame (θ, φ, r) allows the description of every observer, denoted O, location in space surrounding the infinitely long linear flight path. The shortest distance of the observer to the flight path is the slant distance d_p.

In the case that the observer lies directly below the flight path, within the $u - w$ plane, as the aircraft flies along this straight flightpath its position with respect to the observer (or inversely, the observer location with respect to the aircraft) can be defined using the polar directivity angle θ and the slant distance alone. All observers directly below the flight path have an azimuthal angle $\varphi = 0$. Generally, the instantaneous SPL observed at position O due to an lumped acoustic source representative of the aircraft is given by slightly modifying Equation 2.21. It can be seen quite trivially that r is a function of θ and can be written as, $\sin\theta = d_p/r$. Therefore we have,

$$L_p(\theta, \varphi, r) = 10 \log \left[\frac{\mathbb{P}_{rad} D(\theta, \varphi)}{r^2(\theta)} C \right] \tag{5.9}$$

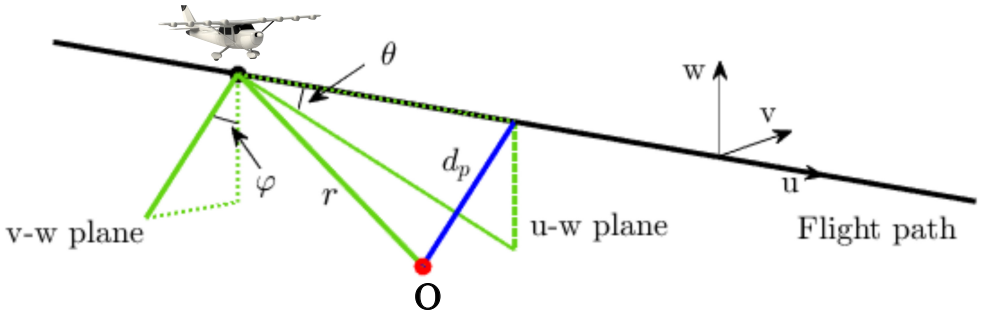

(A) Three-dimensional diagram of flyover in the (u, v, w) frame, with the (θ, φ, r) coordinates also indicated.

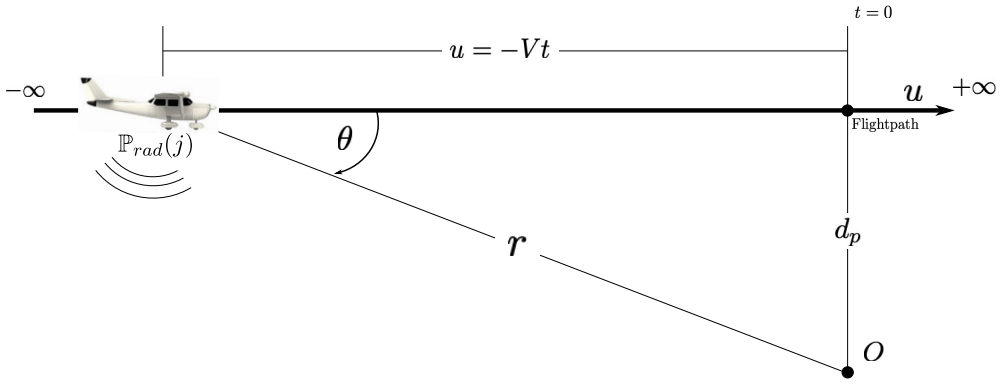

(B) Two-dimensional diagram of the flyover in the $u - w$ plane. This set-up also describes the typical procedure for obtaining NPD data.

FIGURE 5.9: Two views of the flight path/segment system $\mathbf{U} = (u, v, w)$ and the flyover procedure.

In this case, $\mathbb{P}_{rad}$ represents the acoustic energy emitted across all frequencies and by extension L_p is defined as an OASPL. The directivity factor as may be recalled from Chapter 2, is defined as the ratio of the sound intensity in the direction (θ, φ) and the mean intensity, $D(\theta, \varphi) = I(\theta, \varphi)/\bar{I}$. For the case of an omnidirectional source the directivity factor equals 1.

The noise surfaces of interest are essentially contours (or more technically correct, iso-surfaces) of constant sound exposure levels (SEL) in three-dimensional space. Section 2.1.4 defined the SEL as the time integral over acoustic event interval of the SPL, normalise to an event period of 1s. However, adapting the definition in Equation 2.25 to the infinite flyover case we have,

$$\mathrm{SEL} = 10 \log \left(\int_{-\infty}^{+\infty} 10^{\frac{L_p(t)}{10}} \mathrm{d}t \right) \tag{5.10}$$

Substituting Equation 5.9 into 5.10 and performing the following algebraic manipulations we have,

$$\mathrm{SEL} = 10 \log \int_{-\infty}^{+\infty} \frac{\mathbb{P}_{rad}(j) D(\theta, \varphi)}{r^2} C \, \mathrm{d}t \tag{5.11}$$

The SEL at the observer location O (and therefore any observer location in space) may be regarded as a function of three parameters: 1. the sound power emitted by the aircraft, 2. the direction of observer relative to the aircraft and 3. the slant distance between the observer and the flight path. Assuming the aircraft operates at a single power setting and flight condition (indicated by index j), the sound power over the entirety of the flyover may be assumed constant, and therefore not a function of time. The directivity function D, and distance to the observer r however, depend on the aircraft movement and the relative position between the two, and are different at any given instance of time ($D(\theta(t), \varphi)$ and $r(t)$).

The SEL at observer O given in expression 5.10 is in terms of the aircraft reference frame. Assuming that $t = 0$ occurs at $\theta = \pi/2$, giving the observer spherical coordinates of ($\theta = \pi/2$, φ, $r = d_p$), using Figure 5.9 we introduce the substitution:

$$r^2 = d_p^2 + u^2 = d_p^2 + (-Vt)^2 \tag{5.12}$$

We can now perform the change in integration variable from t to θ,

$$\begin{aligned} u &= -Vt = \frac{d_p}{\tan\theta} \\ t &= -\frac{d_p}{V \tan\theta} \end{aligned} \tag{5.13}$$

$$\frac{dt}{d\theta} = \frac{d_p}{V \sin^2\theta} \tag{5.14}$$

Therefore, the sound exposure level at the observer from the flyover in the time interval between $[-\infty, +\infty]$ can be expressed as:

$$\begin{aligned} L_E &= 10 \log \int_{-\infty}^{+\infty} \frac{\mathbb{P}_{rad}(j) D(\theta, \varphi)}{d_p^2 + (-Vt)^2} C \, \mathrm{d}t \\ &= 10 \log \int_0^{\pi} \frac{\mathbb{P}_{rad}(j) D(\theta, \varphi) C}{d_p^2 + (d_p / \tan\theta)^2} \frac{d_p}{V \sin^2\theta} \, \mathrm{d}\theta \\ &= 10 \log \int_0^{\pi} \frac{\mathbb{P}_{rad}(j) C D(\theta, \varphi)}{d_p (1 + 1/\tan^2\theta) V \sin^2\theta} \, \mathrm{d}\theta \\ &= 10 \log \frac{\mathbb{P}_{rad}(j) C}{V d_p} \int_0^{\pi} D(\theta, \varphi) \, \mathrm{d}\theta \end{aligned} \tag{5.15}$$

5.4.2 Case 1: Isotropic/omnidirectional sources

The first and simplest case, is that of an isotropic source, $D = 1$. This is the main assumption of RANE, and it results in noise exposure surfaces of cylindrical cross-section surrounding the flight path. The procedure of actually proving this has not been documented. Therefore, when the source is isotropic Equation 5.11 gives,

$$\begin{aligned} L_{eq,1} &= 10 \log \frac{\mathbb{P}_{rad}(j)C}{V d_p} \int_0^{\pi} D(\theta)\, \mathrm{d}\theta \\ &= 10 \log \frac{\mathbb{P}_{rad}(j)C}{V d_p} \int_0^{\pi} \mathrm{d}\theta \\ &= 10 \log \frac{\pi \mathbb{P}_{rad}(j)C}{V d_p} \end{aligned} \tag{5.16}$$

All observer positions at distance equal to the slant distance d_p away from the flightpath will experience a Sound-Exposure-Level of $L_{eq,1}$. All these observer locations define the surface of a cylinder of radius d_p around the flightpath. This is what we define as the noise surface, and in the case of an omnidirectional source it takes the shape of a cylinder.

To prove this, we begin by using the definition of the flightpath coordinate system (u, v, w) and an equivalent cylindrical coordinate system (d_p, ϕ, u) with the longitudinal axis being the u axis. The correspondence between the two systems is,

$$u = u \tag{5.17}$$

$$v = d_p \cos\phi \tag{5.18}$$

$$w = d_p \sin\phi \tag{5.19}$$

with

$$\begin{aligned} d_p &= \sqrt{v^2 + w^2} \\ &\implies d_p^2 = v^2 + w^2 \end{aligned} \tag{5.20}$$

Using Equation 5.16 and solving for d_p, we have,

$$\begin{aligned} L_{eq,1} &= 10 \log \frac{\pi \mathbb{P}_{rad}(j) C}{V d_p} \\ 10^{\frac{L_{eq,1}}{10}} &= \frac{\pi \mathbb{P}_{rad}(j) C}{V d_p} \\ d_p &= \frac{\pi \mathbb{P}_{rad}(j) C}{V 10^{\frac{L_{eq,1}}{10}}} \end{aligned} \tag{5.21}$$

Using the conversion from cylindrical coordinates to Cartesian,

$$v^2 + w^2 = \left(\frac{\pi \mathbb{P}_{rad}(j) C}{V 10^{\frac{L_{eq,1}}{10}}} \right)^2 \tag{5.22}$$

As the right-hand-side of Equation 5.21 is a constant, the equation is that of a circular cylinder with central axis coincident with the flightpath and radius,

$$R_n = \frac{\pi \mathbb{P}_{rad}(j)}{V 10^{L_{eq,1}/10}} \tag{5.23}$$

Equation 5.23 is the definition of the noise radius R_n for the omnidirectional case. As can be seen, the radius of the cylinder depends on the aircraft power setting and the sound-exposure-level we are looking to create a contour for. As the cylindrical surface is a quadratic form, an elegant way of representing it would be in matrix form,

$$\mathbf{U}^T \mathbf{S} \mathbf{U} = R_n^2 \tag{5.24}$$

where $\mathbf{U} = [u \; v \; w]^T$ is the position vector and the orthogonal matrix,

$$\mathbf{S} = \begin{bmatrix} 0 & 0 & 0 \\ 0 & 1 & 0 \\ 0 & 0 & 1 \end{bmatrix} \tag{5.25}$$

5.4.3 Case 2: Directive Source in Polar angle, θ

For the second case, we assume that the source directivity varies with the polar angle θ, but remains constant in the azimuthal angle. Therefore, the flightpath is essentially a rotational symmetry axis, as the only variation occurs in plane with the flightpath. The SEL at the observer location O, can therefore be calculated by:

$$\begin{aligned} L_{eq,1} &= 10\log\int_0^1 10^{\frac{L_p(t)}{10}}\,\mathrm{d}t \\ &= 10\log\left[\frac{\mathbb{P}_{rad}(j)C}{Vd_p}\int_0^{\pi} D(\theta)\,\mathrm{d}\theta\right] \end{aligned} \tag{5.26}$$

Assuming $\int D(\theta)\,\mathrm{d}\theta = I$,

$$L_{eq,1} = 10\log\left[\frac{\mathbb{P}_{rad}(j)C}{Vd_p}I\right] \tag{5.27}$$

Independently of the form/shape of the directivity function, the value of the definite integral will be constant as there is no azimuthal dependence. Again the SEL is constant and does not depend on the directivity angle θ. All observer locations at distance equal to d_p from the flightpath will experience the same exposure level. Once again this defines a surface of cylindrical shape of radius d_p around the flightpath. This is an interesting conclusion, as the sources polar directivity does not affect the shape of the noise surface, and therefore it does not affect the shape of the contours on the ground. However, it does affect the noise radius, and therefore the distance from the flightpath at which the required noise level occurs.

The implication of the $L_{eq,1}$ not depending on the polar angle, as in Cases 1 and 2, in modelling airport noise using noise exposure surface can be summarised by the finite segment error and the segment interaction error in Sections 5.9 and 7.2.3. Effectively, all points on the generated contour from a noise surface, are exposed to the same $D(\theta)/r$ relationship through the flyover event. Explicitly, this means that the maximum noise immission angle is the same for all observer on the contour, and it occurs at the same distance for all observers.

5.4.4 Case 3: Totally anisotropic sources

Finally, we introduce a variation of the noise emission in the azimuthal direction φ, as well as the polar one. This is the definition of a three-dimensional source. The SEL at any observer in space can be obtained by the expression in Equation 5.15.
Independently of the dependence of D on the polar angle θ, as the single definite integral is evaluated with respect to θ, the azimuthal angle φ may be treated as a constant. Therefore, we essentially get an anti-derivative function $DF(\theta,\phi)$ for which,

$$\frac{\partial DF(\theta,\varphi)}{\partial\theta} = D(\theta,\varphi) \tag{5.28}$$

and the integral can then be evaluated as,

$$\begin{aligned}\int_0^{\pi} D(\theta,\varphi)\,\mathrm{d}\theta &= \Big[DF(\pi,\varphi) - DF(0,\varphi)\Big]_0^{\pi} \\ &= f(\varphi)\end{aligned} \tag{5.29}$$

Substituting this into 5.15, and using the noise radius nomenclature instead of the slant distance,

$$L_E = 10\log\left[\frac{\mathbb{P}_{rad}(j)C}{Vd_p}f(\varphi)\right] \tag{5.30}$$

This indicates that for an directional source, the SEL at any observer location is a function of the azimuthal position of that observer with respect to the flightpath. The polar dependence has been eliminated, through the integration. This expression 5.30 also serves as the definition of the noise surface itself.

Equation 5.30 can be solved for d_p,

$$\begin{aligned}L_E &= 10\log\left[\frac{\mathbb{P}_{rad}(j)C}{Vd_p}f(\varphi)\right] \\ 10^{\frac{L_E}{10}} &= \frac{\mathbb{P}_{rad}(j)C}{Vd_p}f(\varphi) \\ d_p &= \frac{\mathbb{P}_{rad}(j)C}{V10^{\frac{L_E}{10}}}f(\varphi)\end{aligned} \tag{5.31}$$

Using the same cylindrical frame (d_p, ϕ, u) as previously and transforms in Equations 5.17 to 5.19,

$$v^2 + w^2 = \left(\frac{\mathbb{P}_{rad}(j)C}{V10^{\frac{L_E}{10}}}f(\varphi)\right)^2 \tag{5.32}$$

The right-hand-side of Equation 5.32 is a function of azimuthal angle (observer lateral position), the equation is similar to that of a cylinder with central axis coincident with the flightpath with the major difference that the radius is not constant,

$$v^2 + w^2 = R_{iso}^2 D_\Lambda^2(\varphi) \tag{5.33}$$

R_{iso} represents the noise radius of an isotropic source of equal sound power, travelling speed and dB SEL contour requirement. As in RANE the R_{iso} is calculated using NPD databases using the power setting P, aircraft speed V and required SEL contour dB, using Equation 5.3. As will be discussed later in this Chapter, $D_\Lambda(\varphi)$, the function

responsible for the azimuthal radiation of the source can be inputted in both, analytical and numerical forms. Section 5.5 explores the use of Spherical Harmonics as directivity functions. Spherical harmonics prove to be an interesting way of representing a three-dimensional directive source due their analytical properties (expansion capabilities and others) and ease of coefficient interpolation from numerical data or measurements.

Finally, a much more elegant way of representing the noise surface would be in matrix form, as this will make translations and rotations of the surfaces much more straightforward.

$$\mathbf{U}^T\mathbf{S}\mathbf{U} = R_{iso}^2 D_\Lambda^2(\varphi) \tag{5.34}$$

where $\mathbf{U} = (u\ v\ w)^T$ is the position vector and the orthogonal matrix,

$$\mathbf{S} = \begin{bmatrix} 0 & 0 & 0 \\ 0 & 1 & 0 \\ 0 & 0 & 1 \end{bmatrix} \tag{5.35}$$

The term $D_\Lambda(\varphi)$ can also be converted to the orthogonal (u, v, w) system by using Equations 5.17 to 5.19, giving $\mathbf{U}^T\mathbf{S}\mathbf{U} = R^2 D_\Lambda^2(u, v, w)$.

This result can be interpreted in a couple ways:

- All observer positions whose position is defined by the same azimuthal angle will experience the same exposure level.
- The distance from the flightpath at which the same constant exposure level is now not equal to the slant distance R_{SL} for all observers, but it depends on the azimuthal position and therefore the result of the integration, $f(\varphi)$ in Equation 5.30.

These two points help illustrate that the noise surface does not take the shape of a cylinder with a circular cross-section anymore, rather a cross-section of a shape that depends on the azimuthal (or lateral) directivity of the source, Figure 5.10. It is worth remembering that the noise surfaces represent observer locations in space, at which the SEL has the same value (essentially three-dimensional contours).

5.4.5 Constructing the final footprint/contour

The final footprint/contour for any given three-dimensional trajectory consisting of K flight path segments is composed of the contributions of each segment. Equation 5.33 gives the noise surface for each k segment in the coordinate system $\mathbf{U}$. This coordinate

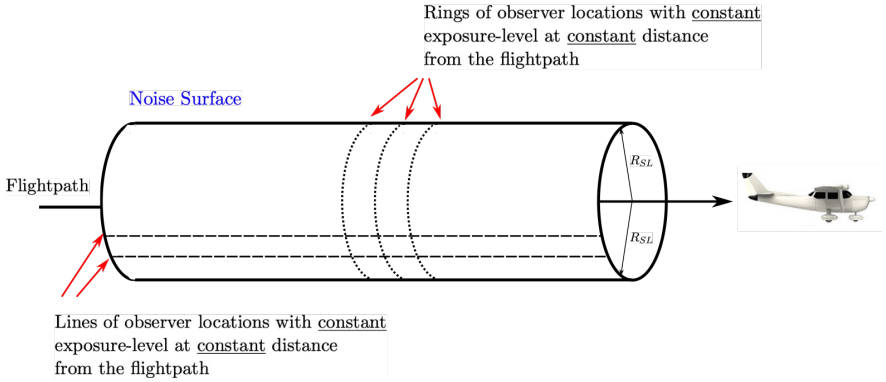

(A) The noise surface of an isotropic or directional in the polar angle noise source. The cross section of the surface is a circle, therefore constant exposure levels always occur at the same minimum distance from the flightpath.

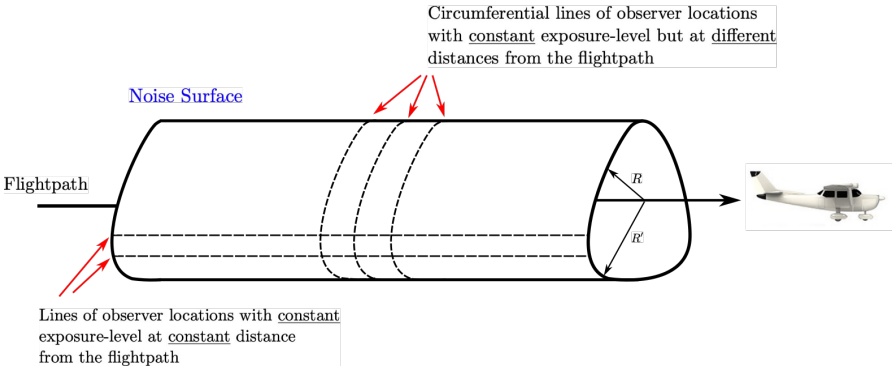

(B) The noise surface of an azimuthaly directional noise source. The cross section of the surface is no longer a circle, therefore constant exposure levels do not always occur at the same minimum distance from the flightpath.

FIGURE 5.10: Diagrams illustrating the difference between noise surfaces resulting from iso-tropic and aniso-tropic noise sources.

system is segment specific and must be related to the global airport coordinate system through a series of transformations (see Figure 5.11).

A *Noise Footprint/Contour* is defined as a 2D line of constant value of sound exposure level (dB) around an airport. The noise footprints/contours will be composed of contribution due to each of the various segments, and the various pieces of the contour must be determined and suitably pieced together to generate the complete contour.

The noise surface in terms of the horizontal projection coordinates, $\mathbf{x} = (x,\ y,\ z)^T$ is given by a rotation about the v (or y) axis, using the following transform:

$$\mathbf{U} = \Lambda_y^T \mathbf{x} = \begin{bmatrix} x\cos\gamma - z\sin\gamma \\ y \\ x\sin\gamma + z\cos\gamma \end{bmatrix} \tag{5.36}$$

Equation 5.33 may therefore be written as,

$$\mathbf{x}^T \Lambda_y \mathbf{S} \Lambda_y^T \mathbf{x} = R^2 D_\Lambda (\Lambda_y^T \mathbf{x}) \tag{5.37}$$

With the use of Equation 5.37 each segment k has now been rotated with respect to the segments' inclination angle within the airport system. The final two transforms are translation of the segments to their correct position in three-dimensional space according to the trajectory geometry and a final rotation about the Z axis to account for trajectory turns. Figure 5.11 depicts all K noise surfaces of a given flight path, after the required transforms. The result is a completely surrounded flight path.

First, the intersection between each noise surface k and the airport plane $Z = 0$ is calculated. This intersection provides the 2-D (line) contribution to the total footprint of segment k. This is achieved by partitioning $\mathbf{x}$ such that $\mathbf{x} = (x\, y\, : 0)^T$. Recalling that each k flightpath segment is characterised by an angle of rotation in the horizontal plane ψ_k, then the final transform to each segment is,

$$\boldsymbol{X} = R_Z(\psi_k)\boldsymbol{x} + \boldsymbol{\Delta x} \tag{5.38}$$

where $\boldsymbol{X} = [X_k,\ Y_k]^T$ the airport coordinate position vector, $\boldsymbol{\Delta x} = [\Delta x,\ \Delta y]^T$ the horizontal projection positions vector and $R_Z(\psi_k)$ the rotation matrix about the Z axis.

The components of the translation vector $\boldsymbol{\Delta x}$ are equal to the X and Y components of the waypoint WP_k, resulting from Equation 5.7. The final contour is stitched together on to the airport coordinate system ground plane (X, Y). An illustration of the processes may be seen in Figure 5.16. The three individual noise surfaces (green, purple and yellow) may be seen in Figure 5.16a, in the airport frame. Figure 5.16b shows the resulting contours of said noise surfaces after the intersection with the airport ground plane (X - Y) has been taken.

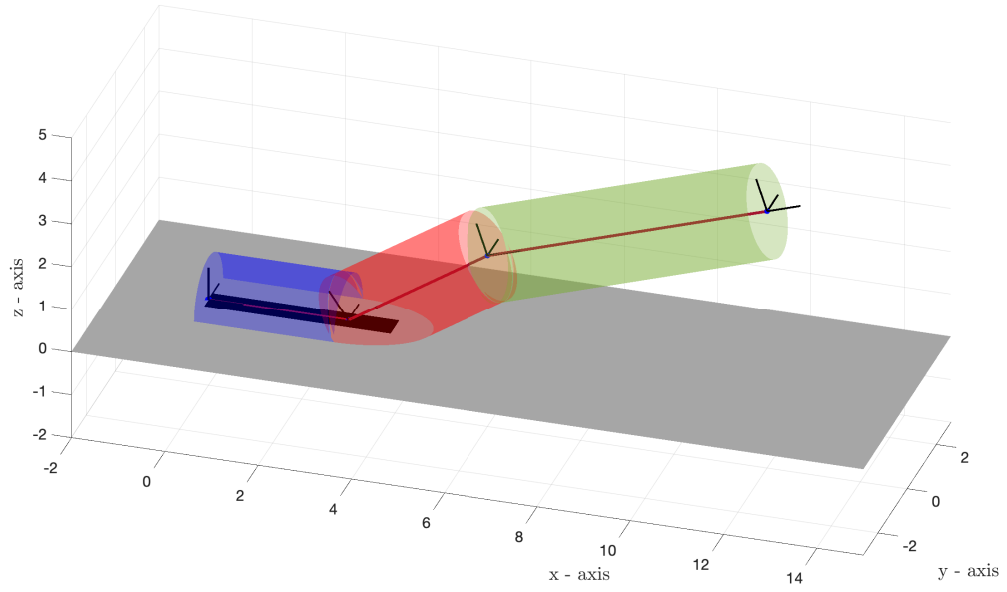

(A) Individual noise surface coordinate systems of a flight path composed of three segments.

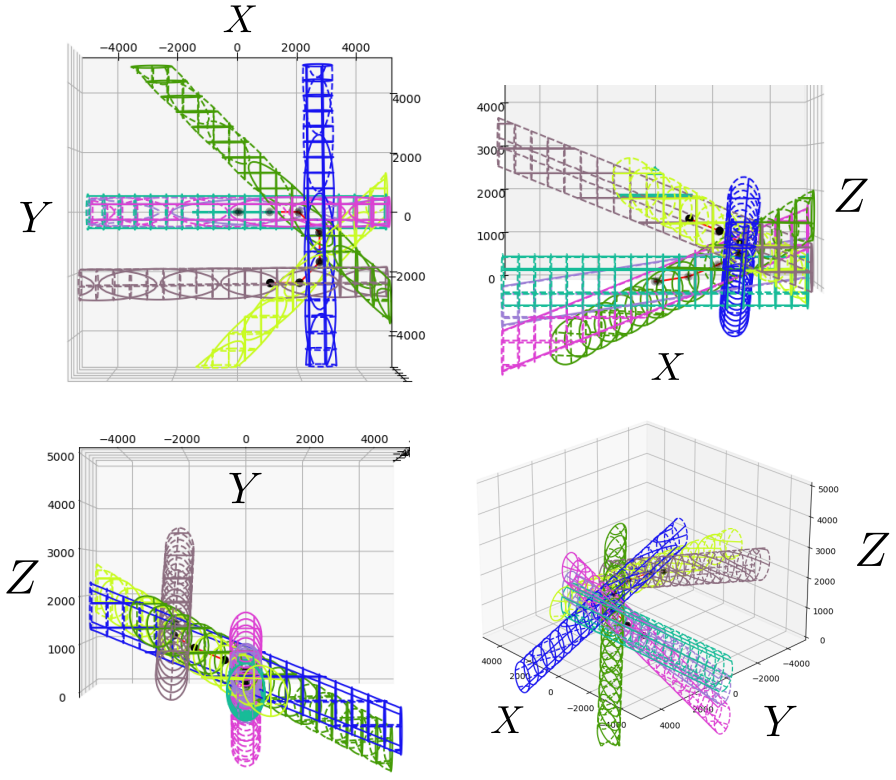

(B) Pre-processed, infinitely long cylindrical noise surfaces surrounding the segments of a discretised flight path.

FIGURE 5.11: Illustrations of noise surfaces surrounding the flight path.

5.5 Modelling Source directivity function using Spherical Harmonics

In order to try and use the previous derivations to generate noise contours on the ground for anisotropic noise sources, we need a directivity function that describes the source behaviour. An interesting way to do this is to use spherical harmonics. Their useful analytical properties and ability to decompose any function defined on a sphere in a sum of spherical harmonics allows for multiple ways of testing and verifying the model. Previous studies [185][186][187],that used spherical harmonics to define a three dimensional source proved effective, although the implementation does differ slightly to the one presented here.

Spherical Harmonics are special functions defined on the surface of a sphere. They form a complete set of orthogonal functions and thus an orthonormal basis. Every function defined on the surface of a sphere can be written as sum of these spherical harmonics. As our directivity function is a two-dimensional surface in three-dimensional space, spherical harmonics are appropriate to describe it.

We define the complex sound emission in the direction defined by the two angles θ and φ using a decomposition into contributions of spherical harmonics:

$$D(\theta,\varphi) = \frac{1}{N}\left|\sum_{\ell=0}^{n}\sum_{m=0}^{\ell} A_\ell^m Y_\ell^m(\theta,\varphi)\right|^2 \tag{5.39}$$

where N is a normalisation factor to ensure unit power.

The directivity function, $D(\theta,\varphi)$ is given in terms of different contributions of Spherical Harmonics Y_ℓ^m and coefficients A_ℓ^m describing the magnitude of contribution of each harmonic. Using the conventional notation, spherical harmonics are defined on a spherical coordinate system, with angles θ, φ representing the colatitude and longitude, respectively. The colatitude θ, is defined from 0 on the flightpath in front of the aircraft to π on the flightpath behind the aircraft ($0 \leq \theta \leq \pi$), whereas the longitude φ or azimuth may assume all values ($0 \leq \varphi \leq 2\pi$) around the flightpath (same convention as used to define observer locations in Figure 5.8).

As we have introduced an orthogonal flightpath coordinate system (u, v, w), the spherical harmonics coordinate system (θ,φ) is related to it by,

$$\varphi = \arctan\left(\frac{v}{u}\right) \tag{5.40}$$

$$\theta = \arccos\left(\frac{w}{\sqrt{u^2+v^2+w^2}}\right) \tag{5.41}$$

or inversely,

$$u = \sin\theta\cos\varphi \tag{5.42}$$

$$v = \sin\theta\sin\varphi \tag{5.43}$$

$$w = \cos\theta \tag{5.44}$$

Now the directivity function has been defined in the two useful coordinate systems we can further refine it to fit our purpose. As mentioned, the directivity function is a ratio of the sound intensity in the direction (θ, φ) and the mean intensity. Therefore, to retain this property we must ensure the $D(\theta, \varphi)$ is normalised in a way, so the overall acoustic power emitted is unaffected. This condition is satisfied if the integration over the entire spherical surface surrounding the source returns the power of the source,

$$\int_S \frac{\mathbb{P}_{rad} D_s}{4\pi}\,\mathrm{d}S = \mathbb{P}_{rad}(j) \tag{5.45}$$

or in terms of the directivity function, $D(\theta, \varphi)$,

$$\int_S D(\theta, \varphi)\,\mathrm{d}S = 1 \tag{5.46}$$

We take the square of the magnitude as we are dealing with intensity ratios rather than pressure ratios. The normalisation factor N ensures that this condition is satisfied.

We have now fully defined our directivity function in terms of spherical harmonics. In order to calculate the noise-surface and therefore noise contours on the ground of such a source, we need to follow the flyover procedure described previously and calculate the exposure levels at different observer locations. This will define the noise surface of the anisotropic source.

$$\begin{aligned} L_E &= 10\log\frac{\mathbb{P}_{rad}(j)C}{VR}\int_0^{\pi} D(\theta,\varphi)d\theta \\ &= 10\log\frac{\mathbb{P}_{rad}(j)C}{NVR}\int_0^{\pi}\left|\sum_{\ell=0}^{n}\sum_{m=0}^{\ell} A_\ell^m Y_\ell^m(\theta,\varphi)\right|^2 d\theta \end{aligned} \tag{5.47}$$

But, as spherical harmonics are complex functions we have,

$$\left|\sum_{\ell=0}^{n}\sum_{m=0}^{\ell} A_\ell^m Y_\ell^m(\theta,\varphi)\right|^2 = \left(\sum_{\ell=0}^{n}\sum_{m=0}^{\ell} A_\ell^m Y_\ell^m(\theta,\varphi)\right)\left(\sum_{\ell=0}^{n}\sum_{m=0}^{\ell} A_\ell^m Y_\ell^m(\theta,\varphi)\right)^* \tag{5.48}$$

In order to demonstrate the analytical calculation of the integral in Equation 5.47, the spherical harmonic expansion has to be truncated, to limit the amount of terms in the product of the complex sum times its conjugate in Equation 5.48. Therefore, we limit the degree ℓ of the spherical harmonic expansion to just 1, this means for this specific demonstration the directivity function will be built of combinations of a monopole the three different dipoles. So,

$$
\begin{aligned}
&\left(\sum_{\ell=0}^{1}\sum_{m=-\ell}^{\ell} A_\ell^m Y_\ell^m(\theta,\varphi)\right)\left(\sum_{\ell=0}^{1}\sum_{m=-\ell}^{\ell} A_\ell^m Y_\ell^m(\theta,\varphi)\right)^* = \\
&= (A_0^0Y_0^0 + A_1^{-1}Y_1^{-1} + A_1^0Y_1^0 + A_1^1Y_1^1)(A_0^0Y_0^0 + A_1^{-1}Y_1^{-1} + A_1^0Y_1^0 + A_1^1Y_1^1)^* \\
&= A_0^0Y_0^0(A_0^0Y_0^0)^* + A_0^0Y_0^0(A_1^{-1}Y_1^{-1})^* + A_0^0Y_0^0(A_1^0Y_1^0)^* + A_0^0Y_0^0(A_1^1Y_1^1)^* \\
&+ A_1^{-1}Y_1^{-1}(A_0^0Y_0^0)^* + A_1^{-1}Y_1^{-1}(A_1^{-1}Y_1^{-1})^* + A_1^{-1}Y_1^{-1}(A_1^0Y_1^0)^* + A_1^{-1}Y_1^{-1}(A_1^1Y_1^1)^* \\
&+ A_1^0Y_1^0(A_0^0Y_0^0)^* + A_1^0Y_1^0(A_1^{-1}Y_1^{-1})^* + A_1^0Y_1^0(A_1^0Y_1^0)^* + A_1^0Y_1^0(A_1^1Y_1^1)^* \\
&+ A_1^1Y_1^1(A_0^0Y_0^0)^* + A_1^1Y_1^1(A_1^{-1}Y_1^{-1})^* + A_1^1Y_1^1(A_1^0Y_1^0)^* + A_1^1Y_1^1(A_1^1Y_1^1)^*
\end{aligned}
\tag{5.49}
$$

Substituting Equation 5.49 in the integral of Equation 5.47, the calculation can be broken down into the sum of much simpler integrals, the first integral for example:

$$
\int_0^\pi A_0^0Y_0^0(A_0^0Y_0^0)^*\,\mathrm{d}\theta \tag{5.50}
$$

All 16 of these integrals are similar and their calculation follows the same procedure. For demonstration, three of these integrals will be analytical calculated here. For the rest, only the final result will be shown.

To begin, we look at the definition of spherical harmonics. Spherical harmonic are the angular solutions to Laplace's equation in spherical coordinates. They are essentially trigonometric functions which can be represented as a complex exponential, and associated Legendre polynomials as follows,

$$
Y_\ell^m = N_\ell^m e^{im\varphi} P_\ell^m(\cos\theta) \tag{5.51}
$$

as mentioned, ℓ represents the degree of the spherical harmonic and m the order. P_ℓ^m are the associated Legendre polynomials, while N_ℓ^m is a normalisation factor.

Legendre polynomials $P_\ell^m(x)$ are the canonical solutions of the general Legendre equation. By re-parameterising in terms of angles, by letting $x = \cos\theta$ we get the more

useful form of the functions that also appears in the Spherical Harmonic definition above. The first few polynomials, parameterised this way can be seen below,

$$\begin{aligned} P_0^0(\cos\theta) &= 1 \\ P_0^1(\cos\theta) &= \cos\theta \\ P_1^1(\cos\theta) &= -\sin\theta \end{aligned} \tag{5.52}$$

Also to include the term for negative values of m, we can use the following expression [180],

$$P_1^{-1}(x) = -\frac{1}{2}P_1^1(x) \tag{5.53}$$

Expressions 5.51 to 5.53 allow for the integrals to be simplified into integrals involving combinations of trigonometric functions that can easily be evaluated using techniques such as integration by parts.

1st Integral: The first integral to evaluate is a diagonal term,

$$\begin{aligned} &\int_0^\pi A_0^0 Y_0^0 (A_0^0 Y_0^0)^* \,\mathrm{d}\theta = \\ &= \int_0^\pi A_0^0 (N_0^0 e^{i.0.\varphi} P_0^0(\cos\theta)) A_0^0 (N_0^0 e^{-i.0.\varphi} P_0^0(\cos\theta)) \,\mathrm{d}\theta \\ &= \int_0^\pi (A_0^0)^2 (N_0^0)^2 e^{i.0.\varphi} e^{-i.0.\varphi} (P_0^0(\cos\theta))^2 \,\mathrm{d}\theta \\ &= (A_0^0)^2 (N_0^0)^2 \int_0^\pi (P_0^0(\cos\theta))^2 \,\mathrm{d}\theta \\ &= (A_0^0)^2 (N_0^0)^2 \int_0^\pi \mathrm{d}\theta \\ &= \pi (A_0^0)^2 (N_0^0)^2 \end{aligned} \tag{5.54}$$

2nd Integral:

$$
\begin{aligned}
&\int_0^{\pi} A_0^0 Y_0^0 (A_1^{-1} Y_1^{-1})^* \, \mathrm{d}\theta = \\
&= \int_0^{\pi} A_0^0 (N_0^0 e^{i.0.\varphi} P_0^0(\cos\theta)) A_1^{-1} (N_1^{-1} e^{-i.(-1).\varphi} P_1^{-1}(\cos\theta)) \, \mathrm{d}\theta \\
&= \int_0^{\pi} A_0^0 A_1^{-1} N_0^0 N_1^{-1} e^{i\varphi} P_1^{-1}(\cos\theta) \, \mathrm{d}\theta \\
&= A_0^0 A_1^{-1} N_0^0 N_1^{-1} e^{i\varphi} \int_0^{\pi} (-\frac{1}{2} P_1^1(\cos\theta)) \, \mathrm{d}\theta \\
&= \frac{1}{2} A_0^0 A_1^{-1} N_0^0 N_1^{-1} e^{i\varphi} \int_0^{\pi} \sin\theta \, \mathrm{d}\theta \\
&= A_0^0 A_1^{-1} N_0^0 N_1^{-1} e^{i\varphi}
\end{aligned}
\tag{5.55}
$$

3rd Integral:

$$
\begin{aligned}
&\int_0^{\pi} A_0^0 Y_0^0 (A_1^{-1} Y_1^{-1})^* \, \mathrm{d}\theta = \\
&= \int_0^{\pi} A_0^0 (N_0^0 e^{i.0.\varphi} P_0^0(\cos\theta)) A_1^{-1} (N_1^{-1} e^{-i.(-1).\varphi} P_1^{-1}(\cos\theta)) \, \mathrm{d}\theta \\
&= \int_0^{\pi} A_0^0 A_1^{-1} N_0^0 N_1^{-1} e^{i\varphi} P_1^{-1}(\cos\theta) \, \mathrm{d}\theta \\
&= A_0^0 A_1^{-1} N_0^0 N_1^{-1} e^{i\varphi} \int_0^{\pi} (-\frac{1}{2} P_1^1(\cos\theta)) \, \mathrm{d}\theta \\
&= \frac{1}{2} A_0^0 A_1^{-1} N_0^0 N_1^{-1} e^{i\varphi} \int_0^{\pi} \sin\theta \, \mathrm{d}\theta \\
&= A_0^0 A_1^{-1} N_0^0 N_1^{-1} e^{i\varphi}
\end{aligned}
\tag{5.56}
$$

Frequency dependence on directivity

A more general problem that the current version of RANE v2 does not address is the dependence of directivity on frequency. The use however, of the spherical harmonic representation of a source allows the methodology to be easily extendable to account for this frequency dependence. Assuming for example a $1/3^{rd}$ octave source spectrum, each individual band could be allocated a three-dimensional directivity function in the form of a spherical harmonic expansion. The lumped source directivity would then be given, by not only the sum over the individual source directivity but also the sum over the directivity of each frequency band. This implementation forms part of the future work. The use of a single lumped source directivity for all spectral bands conforms with the methodology within ECAC Doc29, the ANP database and computational methodology

within SAE-AIR 1845 [89] for the generation of NPD curves, and extends it to lateral location with the inclusion of azimuthal directivity.

Two additional points are interesting relative to this observation:

- the measured NPD spectral data (including the data available in the ANP database) used by RANE and AEDT as common practice (defined in Doc29) ignores this relationship,
- the definition of a fully three-dimensional spectral content would, in many cases, require detailed knowledge and inputs that are not commonly available at the point of application of RANE. The wider capability developed within the authors' research group allows for the use of baseline spectral data (such as data present in the ANP) along with noise prediction methods for the individual sources that make up the total source to modify the spectral content, and a directivity function to account for differences in the source spectral content. This methodology, however, is out of the scope of the present thesis, and still lacks the complete dependency of directionality on frequency in the far-field.

5.6 Power setting variation over time

One of the assumptions made in RANE is that flight parameters (such as inclination angle, segment length, power setting etc.) remain constant on each kth segment. Although this is a reasonable assumption for current aircraft as flight paths can easily be broken down into linear segments whose parameters do not vary much from one to another. When dealing with vehicles capable of vertical takeoff and landing there are regions of their operational procedures (e.g. transition from vertical flight/hover to horizontal) where the flight mechanics and performance changes significantly. In order to be able to study and understand these flight regimes and their effect on the ground contours we need to treat them slightly differently and allow some performance and acoustical parameters to vary within them, rather than assuming they are constant.

In this section we will look at how to treat a flight path segment where the power setting is allowed to vary along the length of it. This corresponds to a typical cut-back procedure that occurs in current fixed-wing aircraft operations, typically at takeoff while performing NADP 1 & 2 (see Section 2.5).

In terms of the analysis preceding this section, the power-setting of an aircraft flying along the kth of its flightpath manifests itself through the radius R_n of the constant sound-level noise surface. The evaluation of this radius R_n comes as a result of a combination linear and logarithmic interpolations between two tabulated power-settings on the NPD database for the particular aircraft, for which the sound-levels are provided

at some set of distances and power-settings. In short, the noise radius R_n is a function of the power setting. This in tern means that if the power-setting is allowed to vary along a segment then the radius will also vary along the length of the segment.

In RANE the flight parameters of the kth segment are defined at the waypoint (WP_k) at the start of it. This means that for a cut-back example where the power drops from 100% to 70% the change will occur instantaneously at the start point of the segments with the power reduction in effect, Figure 5.15a. This procedure can be modelled more realistically without increasing the computational power required by assuming the power is allowed to linearly vary between the two power settings. This can be achieved by modelling the noise surface as a quadratic form cone.

The general equation for horizontal circular cone with apex at origin, Figure 5.12,

$$\frac{y^2}{a^2} + \frac{z^2}{a^2} - \frac{x^2}{b^2} = 0 \tag{5.57}$$

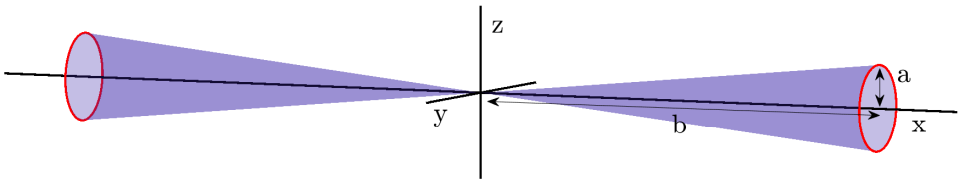

FIGURE 5.12: Generic conical noise surface defined by lengths a and b.

where b is the distance in the x directions at which the cone has a cross-section of radius a. In order for this quadric surface to be useful for this application it needs to be transformed into a form where it can be defined by the noise radius $R_{n,1}$ at the start (located at the origin of the coordinate system) of a segment with length s and the noise radius $R_{n,1}$ at the end of the segment. The two radii $R_{n,1}$ and $R_{n,2}$ corresponding two the two different power settings.

Therefore in terms of Equation 5.57, we require the values a and b that will give us a conical surface which rate of increase in radius matches our requirements ($R_{n,1}$,$R_{n,2}$ and s).

Assuming the radius $R_{n,1} = a$ on the cone with apex at the origin, we only require the value of b in order for $R_{n,2}$ to occur at a distance s from $R_{n,1}$. b can be given by,

$$b = \frac{R_{n,1}}{\tan\theta} \tag{5.58}$$

but $\tan\theta$ can be calculated by

$$\tan\theta = \frac{R_{n,2} - R_{n,1}}{(b+s) - b} = \frac{R_{n,2} - R_{n,1}}{s} \tag{5.59}$$

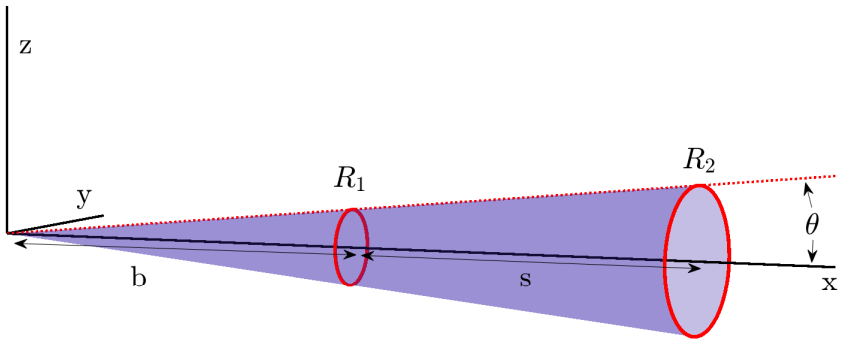

(A) Conical surface define by radii $R_{n,1}$,$R_{n,2}$ and segment length s.

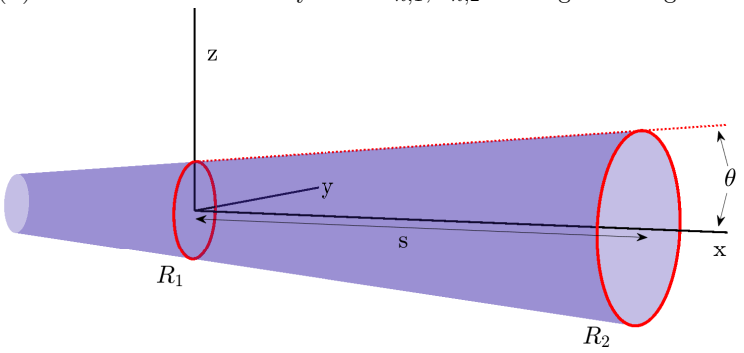

(B) Shifted conical surface, with $R_{n,1}$ radius cross-section appearing in the y-z plane.

FIGURE 5.13: Conical noise surface coordinate shift.

Therefore substituting everything into Equation 5.57 and performing a translation in order for radius $R_{n,1}$ to be at the origin and the cross-section with radius $R_{n,2}$ will be positioned at $x = s$ we have,

$$\frac{y^2}{R_{n,1}^2} + \frac{z^2}{R_{n,1}^2} - \frac{(x-b)^2}{b^2} = 0 \tag{5.60}$$

where

$$b = \frac{R_{n,1}}{R_{n,2} - R_{n,1}} s \tag{5.61}$$

To demonstrate the capabilities of the power variation along a segment, a takeoff operation with cutback is presented. The example is taken from the original work of Stewart and Carson [182], the input data is presented in tabular form in Table 5.1 as well as a visualisation of the takeoff flight path, Figure 5.14.

Using both the original RANE model and the conical surface modification the contour of this operation is calculated on the ground. As evident from the data in Table 5.1, the noise radius changes from segment 2 to 3. This has the effect of causing a discontinuity in the contour lines calculated by RANE, Figure 5.15a. Using the conical surface instead of a circular cylinder, segment 2 can be adjusted to vary over time, using segment 2

TABLE 5.1: Flightpath segment parameters.

Segments			
	1	2	3
s, m	1828.8	6096	6096
γ, deg	0	7.5	3
θ, deg	0	0	0
T, %	100	100	70
R_n, m	3242.77	3242.77	1645.92

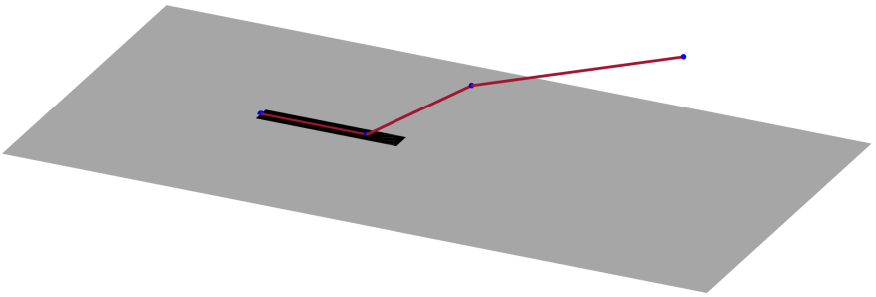

FIGURE 5.14: Flight path generated with three segments.

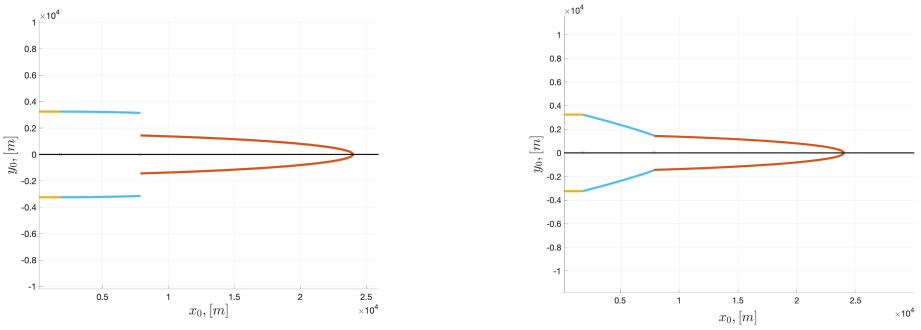

(A) Original RANE prediction

(B) Conical noise surface implementation

FIGURE 5.15: Noise exposure contour for takeoff operation including thrust cut-back. Comparison between original RANE and version 2.

noise radius as the starting noise radius and segment 3 noise radius as the end; thus the transition between power settings can be modelled more realistically. The contours can be seen side by side in Figure 5.15, where the difference can be observed in segment 2 (blue colour). Verification of the use of conical surfaces for linear power variation may be achieved using the methods presented in Chapter 7. Benchmarking against the AEDT model, demonstrates a more realistic application of the conical surface, where shorter segments are used with gradual power variation.

The modifications presented in the previous section can be applied at the same time on a segment allowing a directive source to vary its power setting with time. This gives rise to the question, “how does the directivity of the source vary with time and how can it

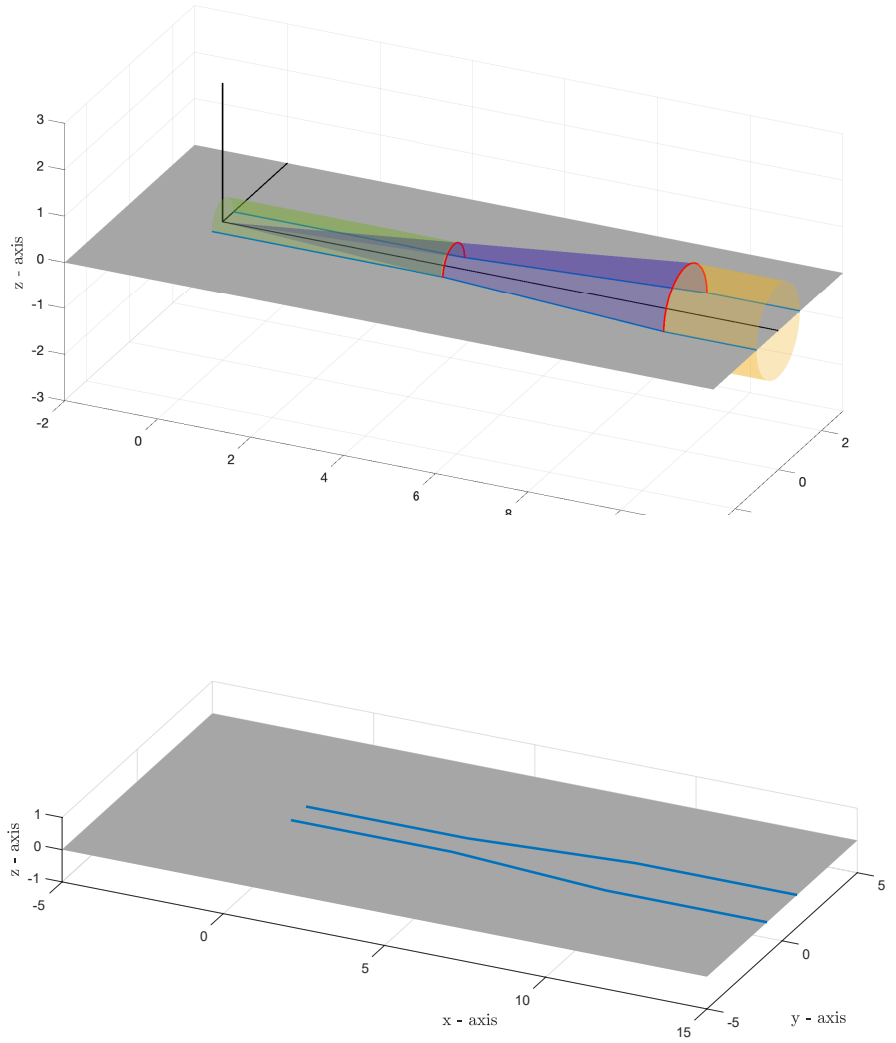

(B) Noise footprint on the ground plane as a result of the intersection of the noise surfaces with it.

FIGURE 5.16: Demonstration of power transition segment and its effect on the ground contour.

be modelled?". As an aircraft's power setting is changed, the parameters that influence the individual noise sources are also modified. Sources that were previously dominant may lose intensity and others may prevail. This has the effect of changing the overall directivity of the aircraft in favour of the dominant's source directivity. Finally, example aircraft such as tilt-rotors, where after the transition from hover to horizontal flight, the propellers rotate from a position of providing 100% lift (hover) to a position where they are only required to produce enough thrust for the fixed wing to generate the lift. In this situation, a power setting alteration is performed as well as the main noise source is rotated about some axis, causing the acoustic energy to be emitted in different directions that previously. The effects are talked about in the next Chapter.

5.7 Contour area

The total noise contour area due to the total of K segments is given by,

$$A_T = \sum_{n=1}^{N} A_k \tag{5.62}$$

where A_k is area corresponding to the contribution of the k^{th} segment. An analytical solution for the estimation of the area of each segment k may be achieved by the use of Equations 8.4b, 8.4b and solving for y. Then the area of the k^{th} could be estimated by,

$$A_k = 2 \int_{\text{ini}\ _k}^{\text{end}\ _k} y(x)dx \tag{5.63}$$

as presented in [13] and [182]. However, $y(x)$ is a function of the azimuthal directivity function $D_\Lambda(\varphi)$ resulting from the integration over the polar angle. When using spherical harmonics as an initial directivity function, the resulting azimuthal directivity will contain contributions from all the diagonal and off-diagonal terms as seen in section 5.5. The long integration may be avoided by using numerical integration techniques, in this case the trapezoidal rule, and the result of section 5.5 are analytical techniques expressions for the contour positions. The only parameter required for the integral in Equation 5.63 to be estimated numerically are the limits of integration. These may be estimated by the use of the method proposed in [13] and [182] or by using the coordinates of the waypoints calculated earlier in this Chapter.

5.8 Contour Extremities

The regions of the contour where the contributions from two different segments meet are of special interest. In many cases (e.g. turns, power setting changes) discontinuity of the contour arises and the transition from one segment to another is not smooth. The lack of predictive ability of the model in these regions is due to the segment interaction error discussed in Chapter 7. The noise at the observer locations in these regions is heavily influenced by both the preceding flightpath segment and the following one.

In order to model these connection regions a simple spline was used, defined by points on the contours of both the segments adjacent to the region. These points, also called control points of the spline, are chosen as points on their respective segments where negligible contribution to noise exposure has occurred from other segments (or sound exposure at these points is predominantly due to the aircraft flying along the segment they belong to). The simple splines used are called Bezier curves. They are parametric curves defined by a set of control points. The first, P_0 and last P_n control points are

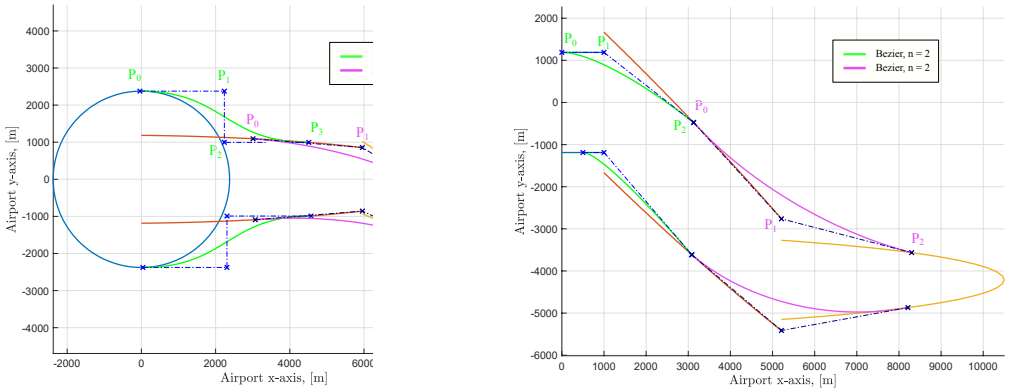

(A) Vertical takeoff with turn, 75 dB SEL contour.

(B) Conventional takeoff with two turns, 75 dB SEL contour.

FIGURE 5.17: Modelling of connecting regions through the use of Bezier curves.

always the end points of the curve; however, the intermediate control points (if any) generally do not lie on the curve. The number of control points also defines the order of the curve (n = 1 for linear, 2 for quadratic, etc.). Figure 5.17 shows two example calculations where Bezier curves were used to model the segment connection regions.

For the contour application, the first and last control points are chosen on the contours of the two connecting segments respectively. The order of the curve and therefore the total number of control points is determined by the type of transition between the two segments. It can be seen that in Figure 5.17 on the left, two types of Bezier curves have been used. The green ones using 4 control points (cubic curve) are modelling the transition from one Noise radius to another. While for a turn transition of the same radius, where the contours mostly match up but a slight miss-alignment occurs, the transition can be modelled using a quadratic (or just three control points) curve, as in the right-hand-side of Figure 5.17. When a noise radius change occurs, a huge discontinuity in the contour is present (a step type discontinuity). This type of transition requires an extra control point for a smooth contour to be modelled.

The exact definition of the locations of the Bezier curve control points is still under investigation. The current implementation uses the following main constraints in the positioning of P_0 and P_n:

- P_0 and P_n must be located on the contour lines generated by the two segments of interest. One on each.
- For P_0 and P_n defining a single Bezier curve, the azimuthal locations relative to the corresponding flightpath segments should lie in the same interval, $(-90° < \varphi < 0)$ for the port side or $(0 < \varphi < 90°)$ for the starboard side.
- the resulting curve is tangent to the predicted contour at the points P_0 and P_1, while not intersecting any of predicted contours.

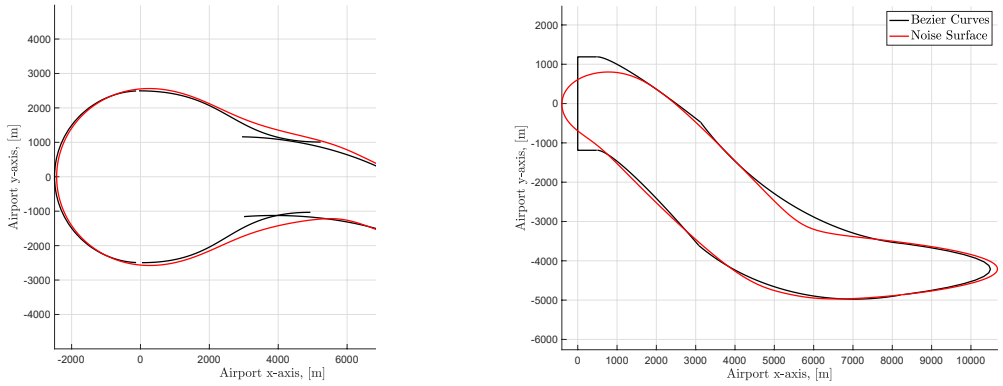

(A) Vertical takeoff with turn, 75 dB SEL contour.

(B) Conventional takeoff with two turns, 75 dB SEL contour.

FIGURE 5.18: Two different cases of using Bezier curves to approximate segment connections compared to the grid-method (See following Section).

- finally, the location of P_0 and P_1 along the length of each segment is determined based on the location of the corresponding contour's centroid, adjusted by the ratio of two contour areas.

At the moment the only weighting factors used in the definitions of the Bezier curves to manipulate the curvature and slope are to ensure the tangent condition at P_0 and P_1.

It is understood that the implantation of the Bezier curves generally increases area of the predicted contour, as would be expected when correcting for the segment interaction error. In the vast majority of cases, especially the cases used for the bench-marking of RANE v2, the Bezier curve corrections deal with the large discontinuity corrections at the expense of introducing errors, as a result of the control point choice. Smaller errors may occur in the case of complicated directivity (especially static start-of-roll directivity) where possibly introduces smoothing effects. For a real flight path however predictions, using relatively high number of discretisation points (and therefore segments) the discontinuities addressed by the Bezier curves are smaller and less pronounced, counteracting the smoothing effect.

To demonstrate the effectiveness of Bezier curves for the modelling of the connecting regions between segments two different examples are presented in Figure 5.18, both implementing different combinations of transitions. The contours are compared against an in house grid-point method, introduced in the validation Chapter 7.

5.9 Finite Segment Correction

The finite segment correction Δ_F is present in all integrated airport noise models. In the case of the standard methodology described within Doc29 [34], the correction factor

adjusts the NPD level to what it would be if the aircraft traversed the finite segment only. Another way of interpreting the correction, is to assume that the aircraft is totally silent for the remainder of the infinite flight path. This trivially gives the finite segment correction a negative sign as it acts to reduces the level corresponding to the infinite flyover to that of the finite fraction.

The notion that the finite segment is a fraction of the infinite flight path, lends its self to the definition of the *energy fraction*, F. The energy fraction is used in the definition of the finite segment correction and corresponds to the ratio of acoustic energy emitted within the limits of the finite segment over the energy emitted during the total infinite flight path. The finite segment correction (FSC) factor is then simply given (in dB) by,

$$\Delta_F = 10 \log_{10} F \tag{5.64}$$

In Doc29, a very general assumption is made about the aircraft directivity in order to analytically calculate the FSC. A fourth-power 90-degree dipole model of sound radiation is used for every aircraft and application. This results in an expression for the FSC,

$$\Delta_F = 10 \log_{10} \left[\frac{1}{\pi} \left(\frac{\alpha_2}{1+\alpha_2^2} + \arctan \alpha_2 - \frac{\alpha_1}{1+\alpha_1^2} - \arctan \alpha_1 \right) \right] \tag{5.65}$$

with

$$\begin{aligned} \alpha_1 &= -\frac{q}{d_\lambda} \\ \alpha_2 &= -\frac{q-\lambda}{d_\lambda} \\ d_\lambda &= d_0 \cdot 10^{[L_{E\infty}(P,d_p) - L_{max}(P,d_p)]/10} \\ d_0 &= \frac{2}{\pi} V_{ref} t_0 \end{aligned} \tag{5.66}$$

where q is distance along the horizontal axis of the aircraft frame (same as in Figure 5.9), d_{lambda} is the scaled distance and will be further defined in the following section. $L_{E\infty}(P, d_p)$ and $L_{max}(P, d_p)$ correspond to the NPD levels of exposure and maximum levels of interest. Finally, d_0 is the reference distance given by the reference speed V_{ref} of 82.31 m/s.

The dipole assumption, in the authors viewpoint, is an attempt to include directivity effects in the calculation of the FSC factor in an efficient and computationally cost-effective way. However, not all air vehicles directivity radiation patterns are described by 90-degree dipoles. Real aircraft have complex three-dimensional radiation patterns. This effectively changes the fraction of energy that is observed at any given observer location as aircraft traverses the finite segment of the flight path.

The following section derives a generalisation of the FSC factor to include three-dimensional directivity patterns. As in Section 5.5, the directivity is expressed in terms of a spherical harmonics expansion.

5.9.1 Derivation of finite segment correction for three-dimensional directivity patterns

As already defined, the FSC factor is a function of the energy fraction, F. The noise exposure at any observer location on the ground as a result of an infinite flyover is denoted E_∞. Whilst the noise exposure corresponding from a finite flight path segment (Figure 5.19) may be denoted E. The definition of the energy fraction as a ratio therefore suggests that,

$$E = F \cdot E_\infty \tag{5.67}$$

The exposures of both the infinite and finite flight paths may be expressed as the time integrals of the instantaneous SPLs,

$$F = \frac{\int_{t_1}^{t_2} 10^{[L_p(t)/10]}\, dt}{\int_{-\infty}^{\infty} 10^{[L_p(t)/10]}\, dt} \tag{5.68}$$

Note, integrands for both numerator and denominator are the same, as the source characteristics are the same. The difference occurs in the integration limits. On the numerator the interval $[t_1,\ t_2]$ denotes the period over which the aircraft traverses the finite segment of interest. Using the instantaneous SPL definition from Equation 2.21, the energy fraction may be re-written as,

$$F = \frac{\int_{t_1}^{t_2} \frac{\mathbb{P}_{rad} D(\theta(t),\varphi)}{r(t)^2} C\, dt}{\int_{-\infty}^{\infty} \frac{\mathbb{P}_{rad} D(\theta(t),\varphi)}{r(t)^2} C\, dt} \tag{5.69}$$

The acoustic power radiated is a constant and may therefore be moved out of the integrals in both numerator and denominator. Assuming the directivity function takes the form of an spherical harmonic expansion, such as the one in Equation 5.39 the individual integrals take the forms,

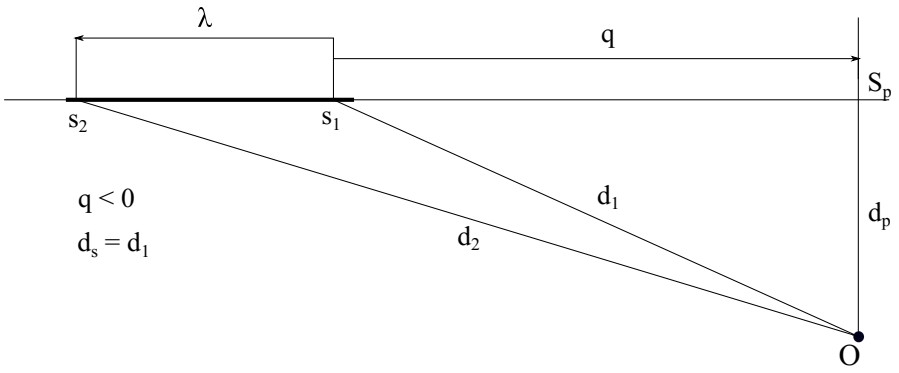

(A) Flightpath geometry for observer behind segment.

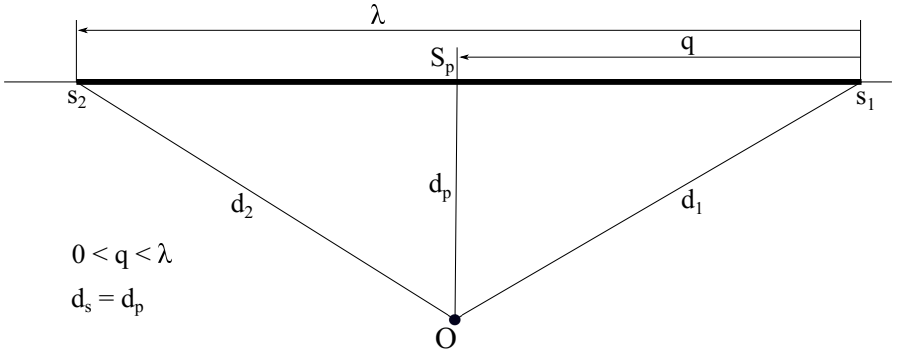

(B) Flightpath geometry for observer alongside segment.

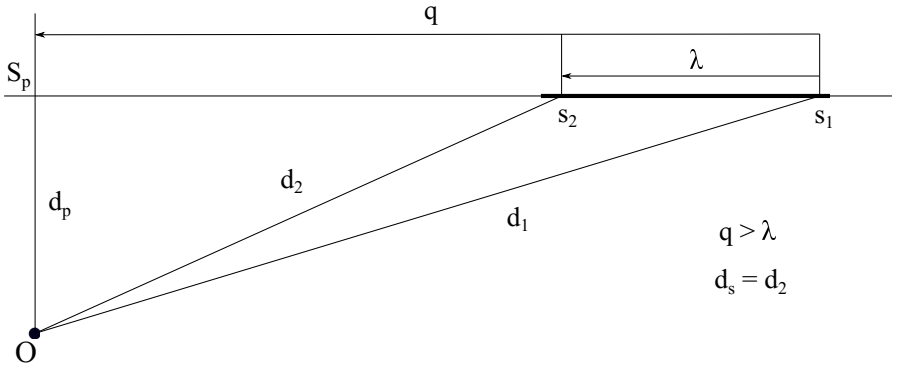

(C) Flightpath geometry for observer ahead of segment.

FIGURE 5.19: Finite segment correction geometry diagram.

$$\int_{t_1}^{t_2} \frac{D(\theta(t),\varphi)}{r(t)^2}\,dt = \int_{t_1}^{t_2} \frac{\left|\sum_{\ell=0}^{n}\sum_{m=0}^{\ell} A_\ell^m Y_\ell^m(\theta(t),\varphi)\right|^2}{r(t)^2}\,dt \tag{5.70}$$

$$\int_{-\infty}^{\infty} \frac{D(\theta(t),\varphi)}{r(t)^2}\,dt = \int_{-\infty}^{\infty} \frac{\left|\sum_{\ell=0}^{n}\sum_{m=0}^{\ell} A_\ell^m Y_\ell^m(\theta(t),\varphi)\right|^2}{r(t)^2}\,dt \tag{5.71}$$

Both integrals in Equations 5.70 and 5.71 are identical to the integral evaluated when generating the noise surfaces in Section 5.4, despite the different limits of the finite

segment one. Again, the infinite series of harmonics must be truncated appropriately. For calculation demonstration purposes the degree $\ell = 1$, limiting the total amount of terms to 16.

The procedure of calculating integrals over the interval $[-\infty, +\infty]$ such as the ones in Equation 5.71 is out lined in Section 5.4 where the integration variable is changed to θ and the interval $[0, \pi]$. A list of the 16 integrals can be seen in Appendix E.

For the estimation of the integrals in Equation 5.70 a similar technique to the approach in Doc29 is used (Noting: the same integrals in θ could be used with the appropriate limits instead of the following approach. However the following method gives a better insight on the geometry of the problem). The integration variable is changed to α, an non-dimensional distance representative of the "finiteness" (measure of how finite) of the segment of interest.

To begin, the integral of Equation 5.70 may be written as the truncated sum of individual spherical harmonic integrals,

$$\begin{aligned}
&\int_{t_1}^{t_2} \frac{\left| \sum_{\ell=0}^{n} \sum_{m=0}^{\ell} A_\ell^m Y_\ell^m(\theta(t), \varphi) \right|^2}{r(t)^2} \, dt = \\
&= \int_{t_1}^{t_2} \frac{(A_0^0 Y_0^0(\theta(t), \varphi))^2}{r(t)^2} \, dt + ... + \int_{t_1}^{t_2} \frac{(A_\ell^m Y_\ell^m(\theta(t), \varphi))^2}{r(t)^2} \, dt \\
&= I_1 + ... + I_\Lambda
\end{aligned} \tag{5.72}$$

where $\Lambda = [(2\ell + 1) + (2(\ell - 1) + 1) + ...]^2$ denotes the total amount of terms (integrals). The sum includes all off-diagonal terms, as well as the diagonal ones. With the identical treatment of the spherical harmonics Y_ℓ^m, each integral may be simplified to,

$$I_1 = \int_{t_1}^{t_2} \frac{(A_0^0 Y_0^0(\theta(t), \varphi))^2}{r(t)^2} \, dt = (A_0^0)^2 (N_y^{0,0})^2 \int_{t_1}^{t_2} \frac{1}{r(t)^2} \, dt \tag{5.73}$$

similarly,

$$I_2 = \frac{1}{2} A_0^0 A_1^{-1} N_y^{0,0} N_y^{1,-1} e^{i\varphi} \int_{t_1}^{t_2} \frac{\sin\theta}{r(t)^2} \, dt \tag{5.74}$$

$$I_3 = A_0^0 A_1^0 N_y^{0,0} N_y^{1,0} \int_{t_1}^{t_2} \frac{\cos\theta}{r(t)^2} \, dt \tag{5.75}$$

The evaluation of the time integral in this case will be performed using the following substitutions,

$$r^2 = d_p^2 + (-Vt)^2 \tag{5.76}$$

$$\alpha = \frac{Vt}{d_p} \tag{5.77}$$

The integrals take the following forms (constants/coefficients omitted),

$$\begin{aligned} I_1 =& \frac{1}{Vd_p} \int_{\alpha_1}^{\alpha_2} \frac{1}{1+\alpha^2}\, d\alpha \\ =& \frac{1}{Vd_p} \Bigg(\arctan \alpha_2 - \arctan \alpha_1 \Bigg) \end{aligned} \tag{5.78}$$

$$\begin{aligned} I_2 =& e^{i\varphi} \frac{1}{V} \int_{\alpha_1}^{\alpha_2} \frac{1}{(1+\alpha^2)^{(3/2)}}\, d\alpha \\ =& \frac{1}{V} \left(\frac{\alpha_2}{\sqrt{1+\alpha_2^2}} - \frac{\alpha_1}{\sqrt{1+\alpha_1^2}} \right) \end{aligned} \tag{5.79}$$

$$\begin{aligned} I_3 =& \frac{1}{V} \int_{\alpha_1}^{\alpha_2} \frac{-\alpha}{(1+\alpha^2)^{(3/2)}}\, d\alpha \\ =& \frac{1}{V} \left(\frac{1}{\sqrt{1+\alpha_2^2}} - \frac{1}{\sqrt{1+\alpha_1^2}} \right) \end{aligned} \tag{5.80}$$

The rest of the integrals are not shown, as the integration procedure is identical. However, integral I_4 presents an interesting solution. The I_4 is an off-diagonal term of the spherical harmonic expansion, capturing the interaction of the monopole spherical harmonic Y_0^0 and the 90-degree dipole $Y_1 1$. The analytical result is expressed below (constants/coefficients also omitted),

$$I_4 = e^{-i\varphi} \frac{1}{2Vd_p} \left(\frac{\alpha_2}{1+\alpha_2^2} + \arctan \alpha_2 - \frac{\alpha_1}{1+\alpha_1^2} - \arctan \alpha_1 \right) \tag{5.81}$$

The solution of the integral for I_4, closely resembles that within the expression for the FSC factor given in Doc29. This is due to the dipole assumption. However it is easy to see how even when considering a directivity defined by a combination of monopoles and

dipoles, the solution provided by Doc29 neglects the remaining 15 terms of the expansion.

Once all integrals from expression 5.70 have been evaluated, the exposure E over the finite segment is known. E_∞, as mentioned is evaluated in a similar manner, over the infinite interval using integrals from Appendix E as demonstrated in Section 5.4. Hence the finite segment correction for a three-dimensional directive source may be estimated.

5.9.2 Comparison between finite and infinite segments

Figures 5.20 to 5.23 present comparisons between values of the integrals in Equations 5.70 and 5.71 calculated for finite and infinite flightpath segments. It is evident that as the ratio of segment length to slant distance s/d_p increases and $\to \infty$ the results converge to the same values. However, the importance of the finite segment correction is evident when the ratio takes small values. A small ratio could be the result of two reasons, first a short segment, or second a large slant distance. The second case is typically of interest when low level contours are being generated.

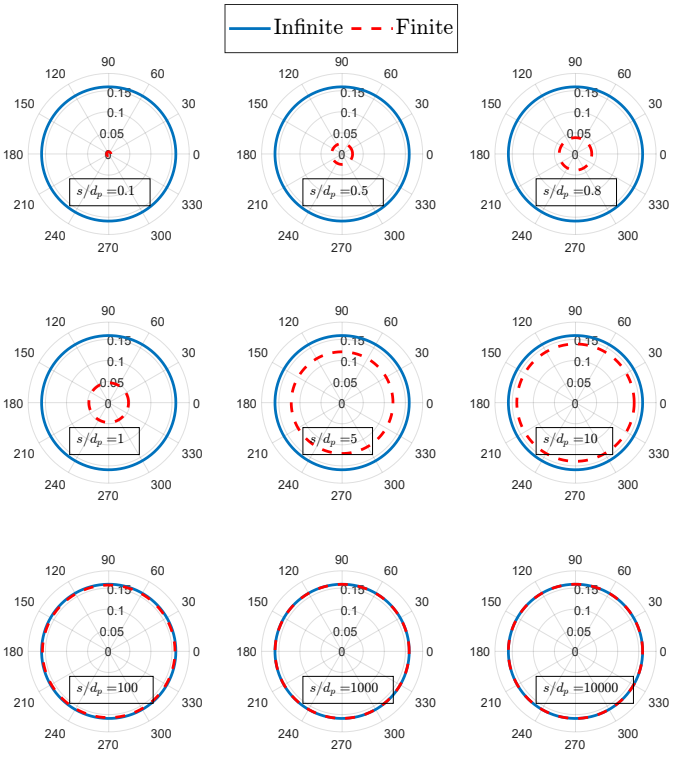

FIGURE 5.20: Comparison of finite and infinite segment length on the noise radius. A spherical harmonic expansion with coefficients $A_\ell^m = [1\ 0\ 0\ 0]$ is used. Subplots indicate a range different values of the segment length to noise radius ratio.

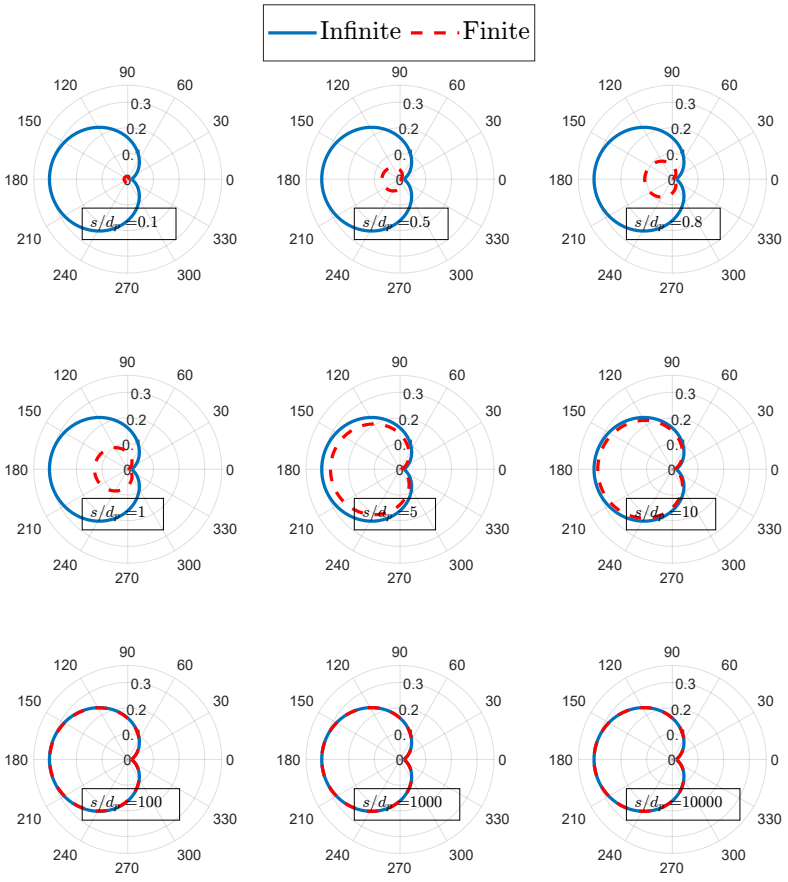

FIGURE 5.21: Comparison of finite and infinite segment length on the noise radius. A spherical harmonic expansion with coefficients $A_\ell^m = [1\ 0\ 0\ 1]$ is used. Subplots indicate a range different values of the segment length to noise radius ratio.

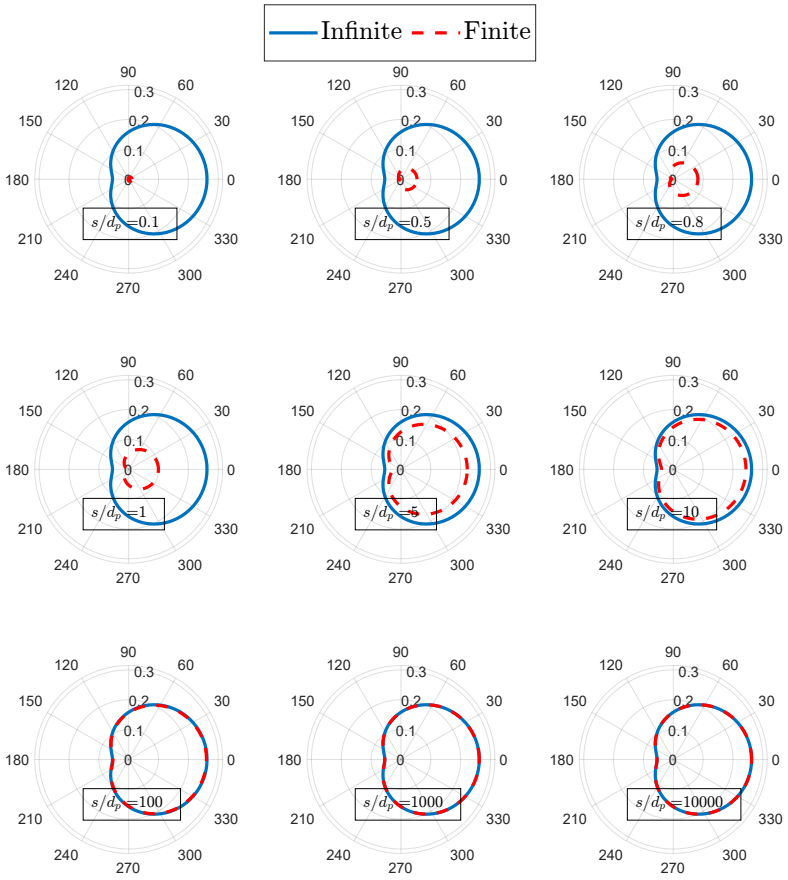

FIGURE 5.22: Comparison of finite and infinite segment length on the noise radius. A spherical harmonic expansion with coefficients $A_\ell^m = [1\ 0.5\ 0\ 0]$ is used. Subplots indicate a range different values of the segment length to noise radius ratio.

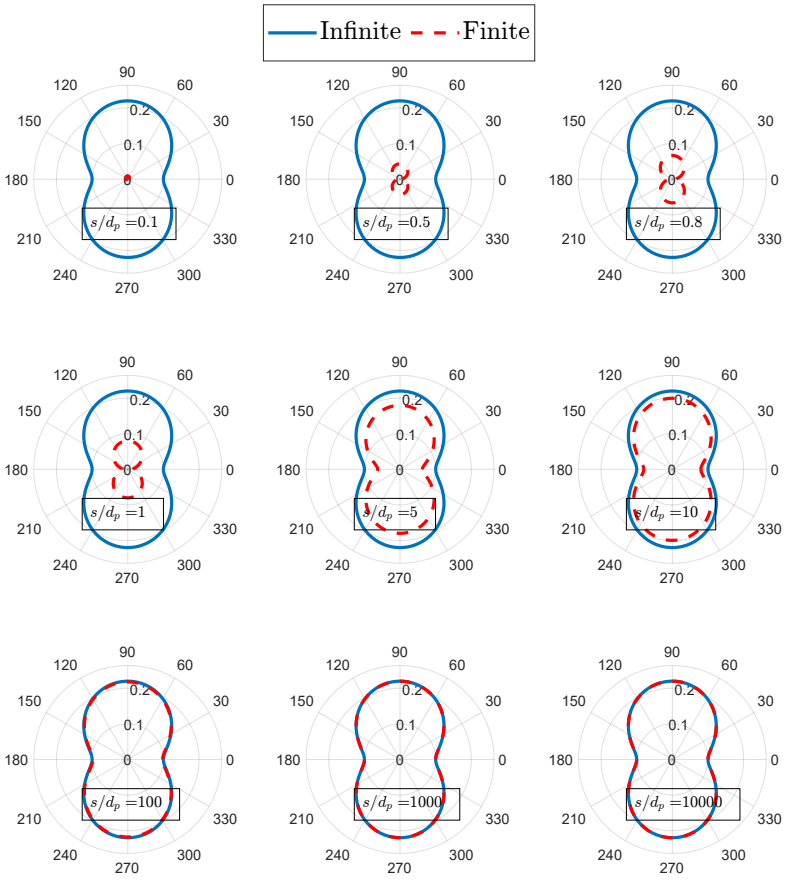

FIGURE 5.23: Comparison of finite and infinite segment length on the noise radius. A spherical harmonic expansion with coefficients $A_\ell^m = [1\ 1\ 1\ 1]$ is used. Subplots indicate a range different values of the segment length to noise radius ratio.

5.10 Airport scenarios and aircraft fleet modelling

When it comes to modelling fleet scenarios, RANE v2 adopts the same averaging techniques as the original RANE model. Aircraft fleets are described by an average set of NPD data curves and a average flight path. These assumptions, and modelling procedures are discussed in detail in the original RANE publications [13, 188]. The main equations will be briefly discussed here, for consistency, and to provide context for the main consideration required for taking into account the additional capability of three-dimensional acoustic lumped sources.

Flight path averaging

For a fleet of aircraft comprised of A total number of aircraft types, and each aircraft performs M number of total operations, an "equivalent" flight path fore the whole path maybe constructed. For a segment n, the inclination angle can be obtained by,

$$\gamma_n = \sum_{a=1}^{A} \gamma_{na} \mathcal{W}_{na} \tag{5.82}$$

where a and m are indexes through the total number of types of aircraft and number of operations, respectively. The weighting coefficients $\mathcal{W}_{na}$ may be calculated,

$$\mathcal{W}_{na} = \frac{\sum_{m=1}^{M} 10^{\left(L_{am}(P_{n,d_i})/10\right)}}{\sum_{a=1}^{A}\sum_{m=1}^{M} 10^{\left(L_{am}(P_{n,d_i})/10\right)}} \tag{5.83}$$

A similar weighting procedure is carried out for the calculation of the average segment length s_n and rotation angle ψ_n.

NPD averaging

The average noise radius R_n is calculated through the process of NPD curve averaging. For the same fleet, for a given slant distance d_i, the noise exposure level $L_{eq,T}(d_i)$ is given by,

$$L_{eq,T}(d_i) = 10 \log_{10} \left[\sum_{a=1}^{A} \sum_{m=1}^{M} 10^{\left(L_{am}(P_{n,d_i})/10\right)} \right] \tag{5.84}$$

The average curves are constructed taking into account the whole fleet in a specific segment n. This process is performed for all segments of the average flight path. Then depending on the noise level required for the construction of the footprint/contour, the noise radius is calculated using Equation 5.3, this time interpolating the average tabulated data. This results in an average noise radius for each segment.

Directivity averaging

Finally, the main difference in the fleet procedure relative to the original RANE method, the averaging of the aircraft directivity patterns. A similar approach is taken, to all other parameters, whereby the an acoustic sound power weighting over the entire fleet is used to determined the average three-dimensional directivity of the fleet. Specifically, the average fleet directivity D_n is given by,

$$D_n(\theta, \varphi) = \sum_{a=1}^{A} D_{na}(\theta, \varphi) \mathcal{W}_{na} \tag{5.85}$$

where $\mathcal{W}_{na}$ is given by Equation 5.83.

5.11 Summary

The MONTANA airport noise tool has now been introduced, with the major concepts of noise radii and exposure surfaces having been defined and analytically derived using NPD curves as a source of noise data input, as well as a directivity function in the form of a spherical harmonic expansion. This allows the creation of noise exposure footprints and contours around airport and heliports.

The next chapter expands on the definition of the noise exposure surfaces, to cases where the source emission axis in not constant during a total operation.

Chapter 6

Methodology III: Rotating Source

6.1 Rotating source

The aim of this Chapter is to extend the capability of the noise surface methodology included within RANE v2 and the broader MONTANA to account for independent source rotation as a function of time. Specifically, the integrated / noise surfaces modelling technique in investigated for the case of directional, rotating sources. We begin the study of independent source rotation by considering the notion of rotational motion of a source of sound. Initially, we assume that this rotational motion, caused by the physical, rigid rotation of aircraft components does not alter the noise generating mechanisms to the point where a change in acoustic sound power output is observed. The directional characteristics of the source, however, are affected by this rotational motion, causing sound to be radiated in different directions compared to a static, non-rotating source.

The directivity of the source is determined by a directivity function, as in the case of a typical RANE flyover. The output therefore, of this function, is relative to the position of the observer with respect to source. The directivity function is independent of distance between the source and observer (this is captured by spherical spreading) and only related to the relative position between the two. As a result, the surface of a unit sphere is the perfect surface to describe a function like this. Every point on the unit sphere can be described by the two angles θ and φ, the polar and azimuthal angles respectively. Figure 6.1a indicates the convention for spherical coordinates used in this Chapter.

The present study is not based on the solution for a particular source type, but rather a general source is considered, with the restriction that the source strength (intensity) and spectral shape be unaffected by the transient external flow, and operation of the concept air vehicle. Whereas installed sources identified in [189] are in some way affected by the

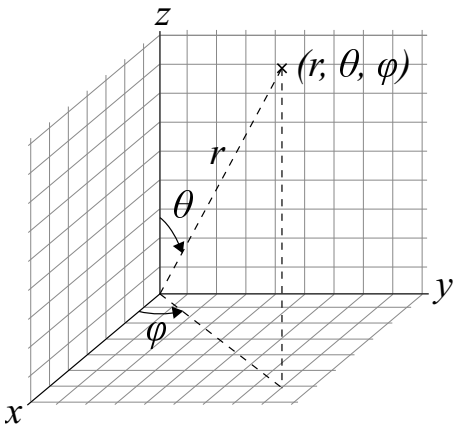

(A) Spherical coordinate system; applies to both source (θ, φ, r) and aircraft (Θ, Φ, R) frame, each with respect to their own principal Cartesian axes.

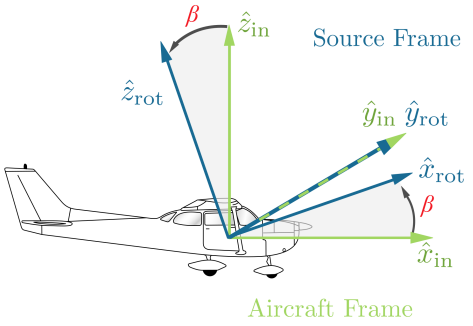

(B) Representation of a rotation of the source frame with respect to aircraft frame by some angle β, about the common $\hat{y}$ axis.

FIGURE 6.1: Source and aircraft coordinate systems.

transition manoeuvre, a basic assumption of the present analysis is that the source intensity and spectral shape is not affected by the flow, however the radiation pattern may independently rotate relative to the emission angle. Such an assumption allows for the study of impact of three-dimensional source directivity, as well as unconventional three-dimensional operational VTOL manoeuvres, on noise exposure on the ground.

Before progressing we must take a step back and define the relative frames in the problem. As the problem will evolve into an aircraft performing a level flyover and a VTOL operation, while the on-board acoustic sources are independently rotating it is important to distinguish between the source, the aircraft and stationary/observer frame of reference. Figure 6.1b illustrates the source and aircraft reference frames, with the source principal axis, rotating about the shared y-axis, through some angle β.

From this point forward, a more general approach to the description of reference frames is taken. First, a simple case of a body frame (representing the source frame), able to rotate freely relative to the fixed inertial frame (representing the airport frame), is given. The orientation of the source can be described by giving the relative orientation between a coordinate frame attached to the body and the fixed coordinate frame. Let A be the fixed frame, B the body frame, and $\boldsymbol{x}_{ab}, \boldsymbol{y}_{ab}, \boldsymbol{z}_{ab}$ the coordinates of the principal axes of B relative to A (noting that all coordinate systems are right-handed). Using these relative coordinate vectors we can define a 3×3 matrix to form what is known as a rotation matrix.

$$\boldsymbol{R}_{ab} = \begin{bmatrix} \boldsymbol{x}_{ab} & \boldsymbol{y}_{ab} & \boldsymbol{z}_{ab} \end{bmatrix} \tag{6.1}$$

Every rotation of the source relative to the ground corresponds to a matrix of this form. A rotation matrix R can also serve as a transformation, taking a source from one frame to another, or in our case from the body frame B to the inertial frame A and vice versa. Let us consider the point q on the unit sphere of the source. Let $q_b = (x_b, y_b, z_b)$ be the coordinates of q relative to frame B. The coordinates of q relative to frame A can be calculated using the previously defined rotation matrix R. The coordinates of q_b are essentially the projection of the point q onto the axes of B, as are the coordinates $\boldsymbol{x}_{ab}, \boldsymbol{y}_{ab}, \boldsymbol{z}_{ab}$ with respect to A, therefore the coordinates of q relative to the frame A are given by,

$$q_a = \begin{bmatrix} \boldsymbol{x}_{ab} & \boldsymbol{y}_{ab} & \boldsymbol{z}_{ab} \end{bmatrix} \begin{bmatrix} x_b \\ y_b \\ z_b \end{bmatrix} = R_{ab} q_b. \tag{6.2}$$

This application of the rotation matrix on a point can also be used to define the action of the same matrix on a vector, as a result of matrix multiplication being linear.

Matrix multiplication can also be used to combine matrices to form new rotation matrices. Assume we introduce a third frame C representing the aircraft. If frame B has orientation R_{cb} relative to frame C, and C has orientation R_{ac} relative to frame A, then the orientation of B relative to A is given by,

$$R_{ab} = R_{ac} R_{cb}. \tag{6.3}$$

When a rotation matrix is used as a map from $\mathbb{R}^3$ to $\mathbb{R}^3$, to rotate the coordinates of a point/vector from a frame B to a frame A it can be said to represent a rigid body transformation, as is to say that distance and orientation are preserved.

The motion we are trying to describe is that of the rotation of the source about a given axis by some amount. Initially we will assume that the aircraft is stationary with respect to the observer, while the on-board source is rotating. Therefore, we wish to describe the rotation of the source about a fixed axis. Let ω be a unit vector which specifies the direction of the rotation and let θ be the angle of rotation in radians. We previously mentioned how every rotation corresponds to some rotation matrix R, we desire to write R as some function of ω and θ.

It is important to note here that multiple representations of the rotation group exist. In this text we will explore the use the exponential coordinates namely the canonical coordinates. Returning to the point q on our unit sphere, we consider its velocity as it rotates about the axis ω by angle θ. Assuming a constant unit velocity about the axis, the velocity of the point, $\dot{q}$ may be written as,

$$\dot{q} = \omega \times q(t) = \hat{\omega} q(t). \tag{6.4}$$

The matrix $\hat{\omega}$ is skew-symmetric matrix, given by

$$\hat{\omega} = \begin{bmatrix} 0 & -\omega_3 & \omega_2 \\ \omega_3 & 0 & -\omega_1 \\ -\omega_2 & \omega_1 & 0 \end{bmatrix}, \tag{6.5}$$

which enables

$$\omega \times q(t) = \hat{\omega} q(t). \tag{6.6}$$

Equation 6.4 is a time-invariant differential equation which may be integrated to give

$$q(t) = \exp^{\hat{\omega} t} q(0), \tag{6.7}$$

where $q(0)$ is the initial ($t = 0$) position of the point q and $\exp^{\hat{\omega} t}$ is the exponential rotation matrix. This can be evaluated using the Maclaurin series for the exponential function as

$$\exp^{\hat{\omega} t} = I + \hat{\omega} t + \frac{(\hat{\omega} t)^2}{2!} + \frac{(\hat{\omega} t)^3}{3!} + ... \tag{6.8}$$

As a result of unit velocity, rotation about ω for θ units of time, the total rotation is given by

$$R(\omega, \theta) = \exp^{\hat{\omega} \theta}. \tag{6.9}$$

As Equation 6.8 is an infinite series, it is of little use from a computational standpoint. The Rodrigues formula is a closed-form expression for $\exp^{\hat{\omega} \theta}$, which gives an efficient method for calculating the matrix exponential and therefore the total rotation matrix $R(\omega, \theta)$, and is presented bellow.

$$\exp^{\hat{\omega} \theta} = I + \hat{\omega} \sin \theta + \hat{\omega}^2 (1 - \cos \theta). \tag{6.10}$$

6.1.1 Stationary (Hovering) aircraft

We start the analysis of the source rotation problem using the simplest case possible. This is to assume a stationary aircraft in terms of translation, allowing for the on-board noise sources to rotate independently of the orientation of the vehicle its self. The single observer is located directly beneath the aircraft at some distance, equal to the altitude h.

To initiate the analysis we need to specify the relative locations of all objects of interest within the study domain, which we will call the airport domain. As briefly mentioned,

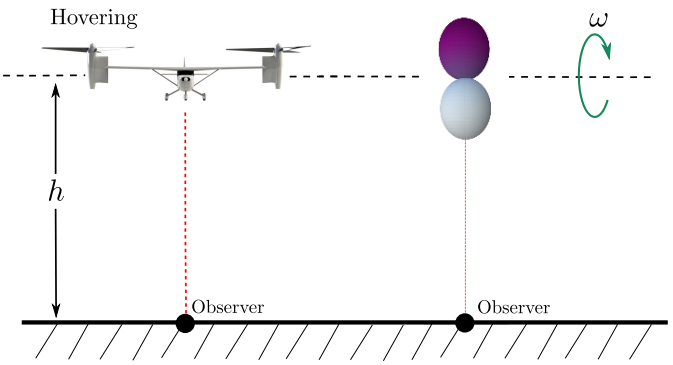

FIGURE 6.2: Rotorcraft hovering at altitude h over an observer location (left) and a lumped acoustic source representation of the rotorcraft performing the same operation (right). Note, the acoustic source is rotating about its horizontal axis, representing the initiation of a transition to horizontal flight by the rotation of the rotor plane from parallel to perpendicular to the ground.

the objects of interest are three, the aircraft itself, the independent acoustic noise source and finally the single observer. (Making a quick note on the acoustic noise source, we are assuming a lumped noise source; meaning that the total aircraft is radiating acoustic energy $\mathbb{P}_{rad}$, which is the sum of the individual aeroacoustic noise sources present on an aircraft, e.g. propeller, fan, jet, airframe etc. The directivity function related to this aircraft is also a combination of the individual noise source directivity. The acquisition of such a function is not a topic for this study).

We can fully define the problem using two coordinate frames, similar to the ones discussed in the introductory section. Following the airport noise modelling convention we will define the aircraft coordinate frame A with position vector $\boldsymbol{\mathcal{X}} = [x_a, y_a, z_a]^T$. The origin of this frame is located at the CG of the aircraft, while the $X-Y$ plane is a horizontal plane. The airport plane, in this case would therefore be defined by the altitude of the aircraft, and by the $z_a = -h$ plane. The equivalent spherical coordinate frame is defined by the position vector $\boldsymbol{\mathcal{R}} = (\Theta, \Phi, R)$. The conversion between the Cartesian and spherical coordinates of frame A is

$$\Theta = \arctan \frac{\sqrt{y_a^2 + z_a^2}}{x_a} \tag{6.11}$$

$$\Phi = \arctan \frac{y_a}{z_a} \tag{6.12}$$

$$R = \sqrt{x_a^2 + y_a^2 + z_a^2} \tag{6.13}$$

This means the single observer location positioned directly underneath the aircraft flying at altitude h is positioned at $\boldsymbol{\mathcal{X}_O} = [0, 0, -h]^T$ or in the spherical coordinates $\boldsymbol{\mathcal{R}_O} = (\pi/2, 0, h)$.

As we are interested in the directivity of the noise, i.e. the direction (Θ, Φ) in which the noise is radiated; while at the moment, the distance between the observer and the source is irrelevant. Therefore, the coordinate R of the spherical system may also be ignored, and the unit sphere may be used to describe the direction in which the observer is located relative to the aircraft using the orientational unit vector $\boldsymbol{\mathcal{R}} = (\Theta, \Phi)$. This results in the observer lying in the $\boldsymbol{\mathcal{R}} = (\pi/2, 0)$ direction.

Next we need to define the source frame S. The source frame position vector is defined as $\boldsymbol{\mathcal{S}} = [x_s, y_s, z_s]^T$ with equivalent spherical coordinate vector $\boldsymbol{r} = (\theta, \varphi, r)$. The origin of the source frame S coincides with the origin of the aircraft frame A. Again, as we are interested in the rotation of the directive properties of the source we may simplify the spherical coordinates of the source frame to the unit sphere and unit vector $\boldsymbol{r} = (\theta, \varphi)$.

Taking a step back we must look at defining the problem we are looking to solve. The aim is to calculate the noise exposure at the observer location. The single event metric used to define the noise exposure is the equivalent continuous sound level, $L_{eq,T}$. The mathematical definition is as follows,

$$L_{eq,T} = 10 \log \frac{1}{T} \left(\int_0^T 10^{\frac{L_p(t)}{10}} \mathrm{d}t \right) \tag{6.14}$$

The calculation of the exposure metric involve the integration of time of the time history (or instantaneous sound pressure level) emitted by the source. This definition involves defining a time period over which the aircraft operation is performed. The length of this period varies from application to application, but common practice is to use the 10 dB below L_{max} time. This however does not hold for noise surfaces, as will be explained later in the text. For the time being the period of integration is arbitrarily defined as some value T, which defines the interval $[0, T]$ in which the source performs some rotation. Assuming a source of sound power $\mathbb{P}_{rad}$ and directivity $D(\theta, \varphi)$ (angles as defined in the source frame), the equivalent continuous sound level may be given by,

$$L_{eq,T} = 10 \log \frac{1}{T} \int_0^T \frac{\mathbb{P}_{rad} D(\theta, \varphi)}{R^2} C \, \mathrm{d}t \tag{6.15}$$

where $C = \rho c / (4\pi p_{ref}^2)$ is a constant, and R is distance between the source and the observer in the aircraft frame.

Returning to the definition of the source rotation, we consider a rotation about the axis $\omega = [\omega_1, \, \omega_2, \, \omega_3]$ at a constant rate $\dot{\theta}$. The angle of rotation at any given time t is therefore given by,

$$\theta(t) = \dot{\theta} t \tag{6.16}$$

assuming $t = 0$, the initiation of the rotation, we have $0 \leq t \leq T$. For ease, we can define the rotation rate using the total angle over which the source rotates in time T,

$$\dot{\theta} = \frac{\theta_{tot}}{T} \tag{6.17}$$

We may define the rotation operation using any of the methods mentioned in the introduction. For this calculation we will use the matrix exponential to relate the aircraft frame A to the source frame S. We assume that at time $t = 0$ the principle axes of the two frames are aligned. The total rotation of the source frame may be given as a function the rotation axis ω and rotation angle $\theta(t)$ by,

$$R_{AS}(\omega, \theta) = \exp^{\hat{\omega}\theta(t)} \tag{6.18}$$

where the under-script "AS" denotes a transform from frame A to frame S, and $\hat{\omega}$ is the skew-symmetric matrix also previously defined. Or using the Rodrigues formula we may write,

$$R_{AS}(\omega, \theta(t)) = I + \hat{\omega}\sin\theta(t) + \hat{\omega}^2(1 - \cos\theta(t)) \tag{6.19}$$

Using this expression we may relate the observer position vector from frame A to frame S. Therefore, at time t,

$$\boldsymbol{\mathcal{S}} = R_{AS}(\omega, \theta(t))\boldsymbol{\mathcal{X}} \tag{6.20}$$

6.1.2 Flyover operation

Moving on to a more complex variant of the source rotation problem, the aircraft flyover. The steady level flyover is an operation used heavily in noise modelling especially in the context of airport noise. It is the preferred method of experimentally generating what are known as Noise-Power-Distance curves that are used as inputs to the most notable airport noise models used in academia and industry.

In this study, we will look at an aircraft flyover operation as the on-board acoustic noise source (using the same definition of a source as previously) rotates independently of the movement of the aircraft. The point of interest will again be observer location on the ground, starting with an observer located directly under the flightpath of the aircraft, then looking at other interesting locations such as lateral locations and locations on a cylinder surrounding the flightpath (the reason for doing so is to be explained in following sections).

The flyover is assumed to take place along an infinitely long path. This will be addressed when the evaluation of the integral is discussed and assumption will be made in order to evaluate the noise exposure integral numerically. The aircraft is assumed to fly at constant speed V and altitude h, while again emitting a constant sound power $\mathbb{P}_{rad}$.

The two coordinate frames A and S remain unchanged from the hovering example, representing the aircraft and source frame respectively. The aircraft is assumed to fly in the direction of the X-axis of the aircraft frame between the time interval $-\infty \leq t \leq +\infty$, resulting in infinite flight time. However, according to Equation 6.15 if the flyover period T is infinitely long, the value within the logarithm goes to zero, resulting in an unusable metric definition. For this calculation we may substitute the equivalent continuous sound level ($L_{eq,T}$) with the Sound Exposure Metric (SEL). The SEL is similar to the $L_{eq,T}$ but assumes $T = 1$ s. Thus is the one-second long steady level containing equivalent total acoustic energy as the actual fluctuating noise. The definition of the SEL therefore may be written as,

$$\mathrm{SEL} = 10 \log \int_{-\infty}^{+\infty} \frac{\mathbb{P}_{rad} D(\theta, \varphi)}{R^2} C \, \mathrm{d}t \tag{6.21}$$

The SEL however still needs to be evaluated at the stationary observer location. As in the hovering scenario the observer position vector is defined in the aircraft frame A, but contrary to the hover it is no longer constant. The aircraft is in motion as is the aircraft frame A, with respect to observer, therefore for every time t the position of the observer in frame A will be different. Specifically, using the orientational unit vector $\boldsymbol{\mathcal{R}_O} = (\Theta, \Phi)$ of the frame A the direction of the observer with respect to the aircraft is defined by angles Θ and Φ. The definitions of the angles are with respect to the frame A principal axes remain the same as in the hovering case. We may write the polar angle Θ component of the vector as a function of the aircraft movement and therefore time as,

$$\Theta(t) = \arctan \frac{h}{Vt} \tag{6.22}$$

also function of the aircraft's speed and altitude. This means at time $t = -\infty$ the observer unit position vector is $\boldsymbol{\mathcal{R}_O} = (0, \Phi)$, at $t = +\infty$ is $\boldsymbol{\mathcal{R}_O} = (\pi, \Phi)$ and at $t = 0$ when the aircraft is directly above the observer the position vector is $\boldsymbol{\mathcal{R}_O} = (\pi/2, \Phi)$ as in the hovering case. The azimuthal component Φ of the position vector denotes the lateral position of the observer with respect to the flightpath. Therefore, for the case where the observer lies directly bellow the flightpath, $\Phi = 0$.

As in the hovering aircraft case, the source is free to rotate in any direction independent of the aircraft movement. The rotation is defined by a rotation axis ω and rotation rate $\dot{\theta}$. The rate of rotation is again by the total angle θ_{tot} that the source rotates during the integration period T.

As evident, there are two time dependant operations happening simultaneously during the integration interval (the source rotation and the aircraft flyover). The value of the directivity function at any instance t is given by the observer unit position vector in the source frame S. As discussed the observer position vector in frame A is a function of time (Equation 6.22), and must be transformed in to the source frame. Therefore, we have

$$\boldsymbol{\mathcal{S}}(t) = R_{AS}(\omega, \theta(t))\boldsymbol{\mathcal{X}}(t) \tag{6.23}$$

where $\boldsymbol{\mathcal{S}}$ and $\boldsymbol{\mathcal{X}}$ are the Cartesian form of the observer position vector in frame S and A respectively, and may be simply converted to the unit sphere coordinates using equivalent expressions to Equations 6.11 to 6.13 (noting, the conservation of the unit sphere between Cartesian and spherical). The only difference between the hovering case and the flyover case is the dependence of the observer location on time. Again the analytical integration of these transforms is out of the scope of this study, therefore the trapezoidal rule is used to numericaly evaluate the integrals.

6.1.3 Vertical takeoff/landing operation

A simplified approach is taken in order to perform a preliminary assessment of a vertical takeoff of a rotating source. The manoeuvre is defined by two linear finite segments, as illustrated in Figure 6.3. The mathematical setup is identical to the flyover case, whereby three frames of reference are used: a source frame, an aircraft frame and finally an airport frame. The distinction occurs in the geometry of the flightpath, and the relatively placed observer locations. The vertical segment of the flightpath is aligned with the Z-axis of the airport coordinate frame. The horizontal segment is parallel to the X-axis, at some altitude $Z = h$, while remaining in the X-Z plane. Figure 6.3 indicates this geometry for three points in time: $t = 0$ source is on the ground before takeoff, $t = t_{alt}$ the source is at the peak of the vertical segments and has reached cruise altitude and $t = t_{crs}$ source is flying horizontally along the flightpath. The geometry between the source and stationary observers on the ground is also indicated. Details about the locations of the observers are in Section 6.1.5.

The vertical takeoff operation introduces a significant change relative to the hover and flyover. The complex nature of the manoeuvre, even in its simplest form, consists of two segments. The contribution of each segment to the cumulative noise levels must be accounted for and captured in the generated noise surfaces. These segments are perpendicular to each other disrupting the symmetry across the Y-Z plane, as the aircraft flies along only the positive X-axis.

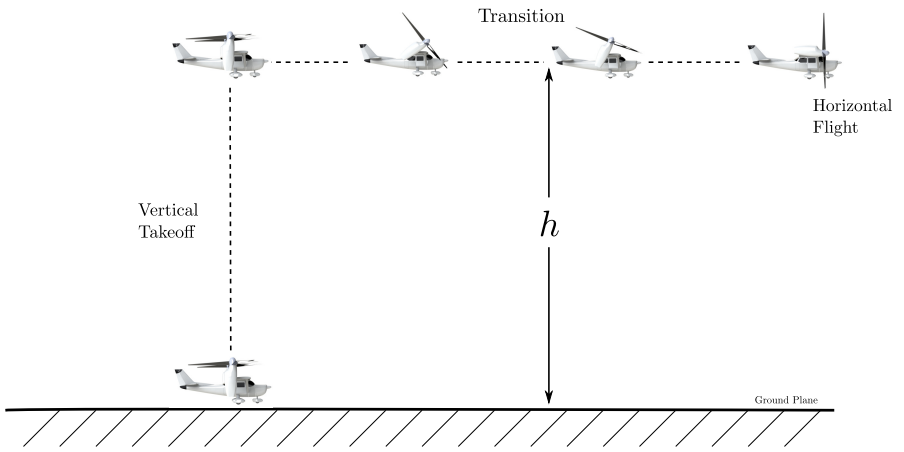

FIGURE 6.3: Diagram of simplified vertical takeoff operation.

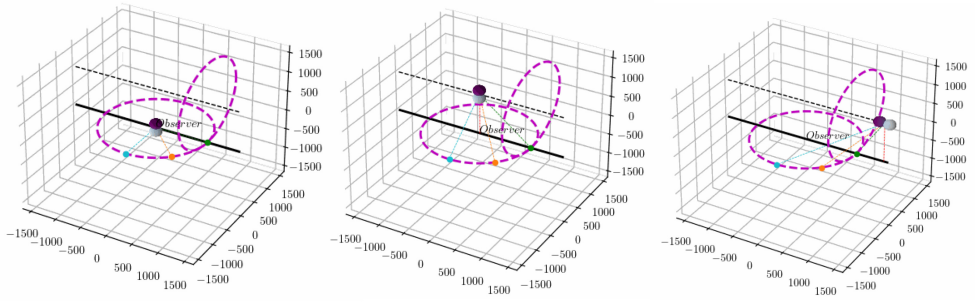

FIGURE 6.4: Simple dipole source performing a two segment vertical takeoff operation. Purple rings indicate observer positions at equal distances from the two segments. Three observer locations are positioned on the ground, one directly under the horizontal flight path (green), one at $\varphi = 45^o$ w.r.t the vertical segment, and one at $\varphi = 90^o$.

6.1.4 Aircraft as a lumped noise source & directivity

In the implementation calculations in Section 6.1.6 we will be essentially looking at the variation of the directivity function as function of time, while the source is performing a rotation of total angle $\theta_{tot} = 2\pi$ over a time period T. We will also discuss the evaluation of the integral in Equation 6.15 in order to calculate the exposure metric.

In order to study the variation of the directivity function as function of time we must first define a directivity function. In this study we will define the directional characteristics of the source with the help of spherical harmonics, as they are functions defined on the surface of a sphere. Therefore, we may define our directivity function as,

$$D(\theta, \varphi) = Y_\ell^m(\boldsymbol{\theta}) = Y_\ell^m(\theta, \varphi) \tag{6.24}$$

where Y_ℓ^m is the spherical harmonic of degree ℓ and order m. For this simple example we will use single spherical harmonics and not a spherical harmonics expansion.

Moving on to the evaluation of the exposure metric, we may simplify the integral in Equation 6.15 to simply,

$$\int_0^T D(\theta, \varphi)\, \mathrm{d}t \tag{6.25}$$

As we assume constant acoustic sound power emission, as the aircraft is hovering in a single power setting, and also the distance R between the source and observer is also constant and equal to altitude of hovering. Therefore, the evaluation of the integral depends only on the directivity function and in our case the spherical harmonic Y_ℓ^m.

In order to understand the integration by time of the directivity we speculate what the integral would look like for a non-rotating source. As the principle axes of the source frame S and aircraft frame A would be aligned, and the position vector of the observer in frame A is also constant, meaning angles $\theta = \Theta$ and $\varphi = \Phi$ are constant, and the whole directivity function also outputs a constant. Leaving a trivial integral in time, for evaluation.

However, while the source is rotating the principle axes of the source frame S rotate away from the axes of frame A. This simply implies that $\theta \neq \Theta$ and $\varphi \neq \Phi$ and the value of the directivity function in the direction of the observer vector is no longer constant.

Therefore, at any given time t, we need to evaluate the observer position vector in the source frame S as that will give us the values of θ and φ to plug in to the directivity function.

This total methodology (chain of operations) may be done simply by following the steps described in the previous section, to rotate the observer position vector $\boldsymbol{\mathcal{R}_O} = (\Theta, \Phi)$ into the source frame S and get the observer vector $\boldsymbol{r_O} = (\theta, \varphi)$ at every time t and perform the integration. The analytical integration of these transforms is out of the scope of this project, therefore simple numerical evaluation techniques are used to estimate the value of the integral.

To verify that the transforms are simulating the correct rotation, the results of the numerical integration are compared again to the numerical calculation (could be analytical, as this calculation has been performed) of the directivity function with respect to the observer angle Θ. As integration over different observer locations Θ with a non-rotating source, is analogous to a stationary observer with a rotating source.

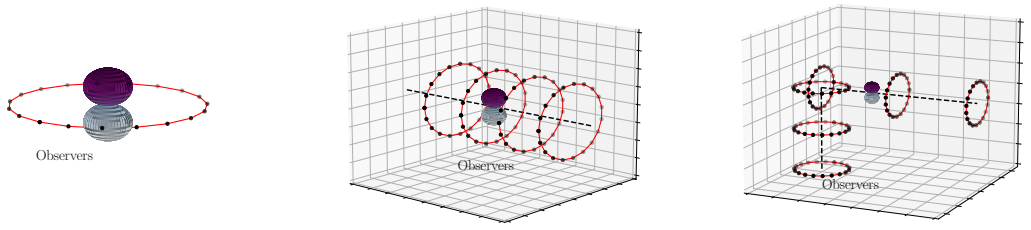

(A) Hover (B) Flyover (C) Vertical takeoff

FIGURE 6.5: Observer rings.

6.1.5 Numerical Simulation

6.1.5.1 Discretisation

The numerical simulation involves calculating the integral in Equation 6.28. This involves a discretisation in time, as the rotational motion of the source frame, and the translational motion of the aircraft frame are both functions of time. The total number of time points are denoted N_t.

For each of the three cases the observer locations at which the integral is evaluated on rings of observers. For the hover case the rings belong to a unit sphere with the source at its centre, while for the flyover and vertical takeoff case, the rings surround the flight path at unit distance. This may be seen in Figure 6.5. Each ring consists of a series of observer locations totalling N_o per ring, while the number of rings themselves is denoted N_r. For the vertical takeoff, the vertical and horizontal segments are discretised independently, to allow for adjustments in fidelity in the transition and vertical regions. This results in $N_{r,v}$ and $N_{r,h}$ for the number of rings in the vertical and horizontal rings respectively.

The time interval dt is defined according to the segment lengths and velocities,

$$dt = \frac{dx}{V} \tag{6.26}$$

where,

$$dx = \frac{s}{N_t} \tag{6.27}$$

At each time increment the position of the source along the flightpath segments is evaluated. Each observer is the allocated a position vector in the aircraft frame (unit vector from the aircraft frame origin pointing in the direction of each observer). This position vector is then rotated to account for source rotation using Equations 6.19 and 6.20. The value of the directivity function is then evaluated at this new vector position

using a simple transform to unit spherical coordinates. The final value of the integral at every observer location may be given by,

$$\mathrm{SEL} = 10 \log \sum_{i=1}^{N_t} \left[\frac{\mathbb{P}_{rad} Y_\ell^m(\boldsymbol{\mathcal{S}_i})}{R_i^2} C \right] \Delta t \tag{6.28}$$

6.1.5.2 Noise surfaces from discretised observer locations

As has been discussed in [13], the general solution for a noise surface surrounding a flightpath may be given by the equation of the cylinder,

$$y^2 + z^2 = R_n^2 \tag{6.29}$$

where y and z belong to the airport orthogonal reference frame and R_n denotes the noise radius of that segment. This holds for omnidirectional sources and was proven earlier in the chapter. In addition, a modified version of Equation 6.29 was proposed, introducing an azimuthal variation in the noise surface. This version may be given by,

$$y^2 + z^2 = R_n^2 D_\Lambda^2(\varphi) \tag{6.30}$$

and was derived analytically for the case of a directivity defined by spherical harmonics. This is the expression used to generate the noise surfaces due to rotating sources within this section. The process of calculating D_Λ is described below.

In addition to the noise surfaces corresponding to flyover operations, we require the definition of a noise surface for static hover like operations. This may be analytically derived as in the case for the dynamic version, however the derivation is skipped for brevity. The solution is rather intuitive however, and may be written as,

$$x^2 + y^2 + z^2 = R_n^2 D_\Lambda^2(X, Y, Z) \tag{6.31}$$

Equations 6.30 and 6.31 describe noise surfaces for aircraft flying along the x-axis and that are stationary at the origin, respectively.

For an infinitely long segment, as is assumed in the derivation of Equation 6.30, D_Λ is independent of the location along the X-axis. However, in the case of finite segments, as are of interest, the azimuthal directivity function is itself a function of the x location, and therefore becomes $D_\Lambda(X, Y, Z)$. It is important to note that R_n as presented in Equation 6.31 represents the noise radius of an omnidirectional source of identical PWL

and D_Λ may be seen as the correction to each individual location to account for 1. the directional properties of the source D and 2. the source rotation.

By evaluating the value of the integral in the observer rings using the simulation method, we have effectively calculated D_Λ at discrete points in space. In order of a noise surface to be generated that can evaluate the location of any noise level in space a 2D curve fitting procedure must be applied to the discrete data. The periodic nature of the source itself and the source movement allow for a harmonic analysis of the azimuthal variation around each ring of observers. The Fourier coefficients may therefore be evaluated for each ring giving an essentially a curve fit expression for each.

For locations between individual rings a simple linear interpolation is used. In order to evaluate the value of D_Λ at one of these locations, the two rings positioned either side of the observer in the x-axis are used. D_Λ is evaluated for the two rings at angle ϕ equivalent to the observer azimuthal location and a simple linear interpolation gives D_Λ for the arbitrary observer.

6.1.6 Implementation

6.1.6.1 Hover

The hover operation as discussed represents the simplest case out of the three. Figure 6.6 shows effect of the observer location relative to the source. Observer locations are varied from row to row. In addition, the second column shows how the time history of the directivity function varies when the rotation axis is changed as well as the function itself. The illustration of the spherical harmonic is at the initial condition when $t = 0$. Over the integration period the source goes through an angle equal to 2π. The various coloured lines, indicate the observer locations of the same colour on the left-hand plots. For every observer location, the integral is evaluated numerically, and the result is plotted in Figure 6.7. The value of the integral is plot against the observer azimuthal location relative to the source. For each D_Λ in columns 1 and 3 of Figure 6.7, columns 2 and 4 show the noise exposure surface generated by the implementation of Equation 6.31. Plots in columns 1 and 3 show the discrete simulated data and the fitted Fourier series.

Finally, Figure 6.8 shows the noise exposure footprints on the ground. They are calculated using the intersection of the noise surfaces and the ground plane. Effects of spherical spreading and atmospheric attenuation are not accounted for in these plots.

6.1.6.2 Flyover

The flyover operation is a common reference operation in airport noise exposure modelling. Typically, a flyover operation is assumed to be steady (constant velocity,

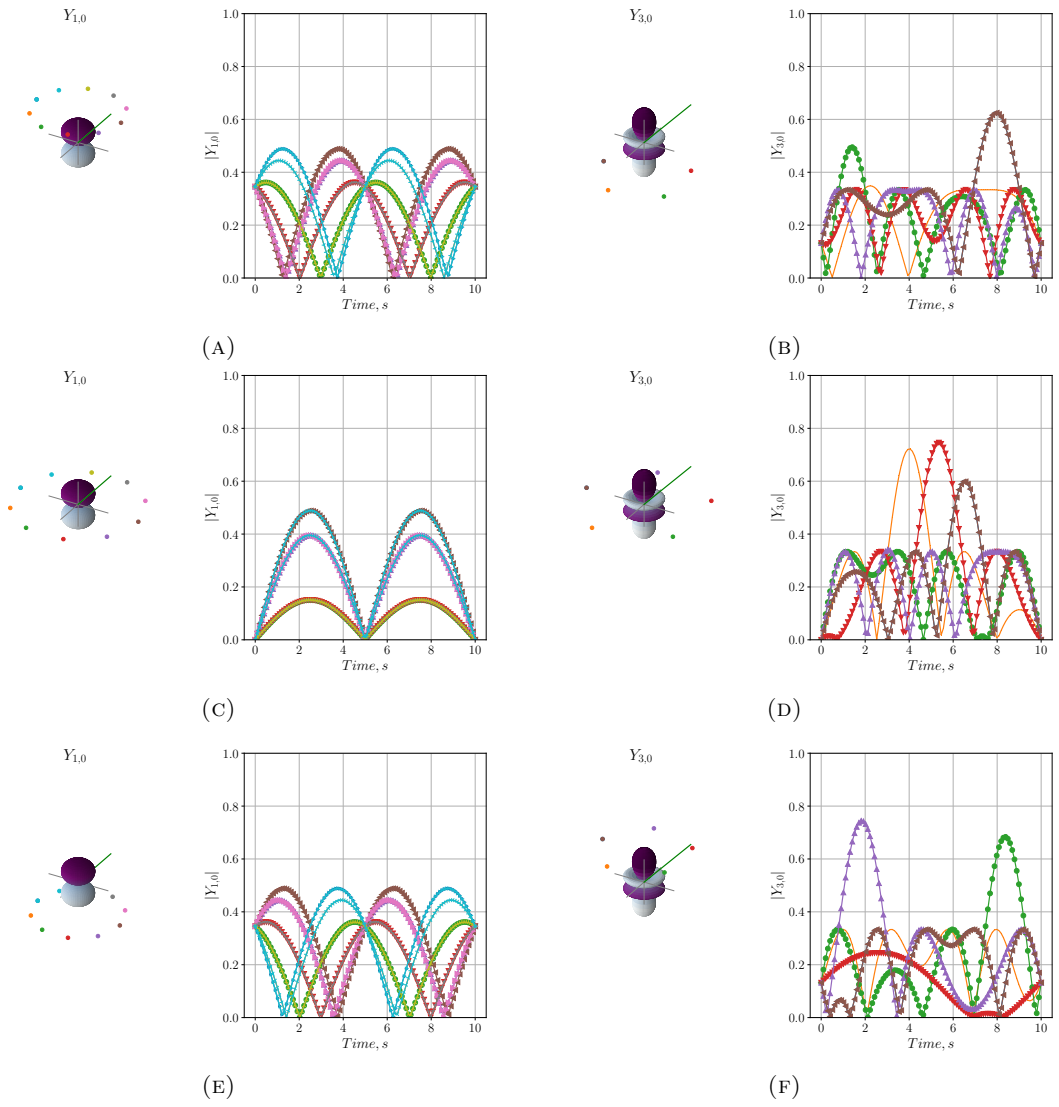

FIGURE 6.6: Observer locations relative to source position (left). Time histories of directivity function values as source rotates. (right). First column shows Y_1^0 rotating about y-axis, while second column Y_3^0 rotating about $\hat{\omega} = [0.57, 0.57, 0.57]$ axis.

power setting and airframe configuration e.g. flaps settings), level (constant altitude) and of infinite length. This allows databases of the acoustic properties of aircraft to built, while flying various types of flyover operations. These flyover operations are then used to model more realistic, complex operation using the pre-integrated segmentation methods, as for example described in [34]. Understanding the effects, therefore, of a rotating source on simple flyovers can provide a stepping-stone for modelling operations of higher complexity.

For this case study, we assume the aircraft performs a flight along a finite segment of the flightpath. The length of the segment s, along with the aircraft speed V determine the noise exposure integration period, which coincides with the numerical simulation length. Table 6.1 provides a summary of the input parameters that define the results presented

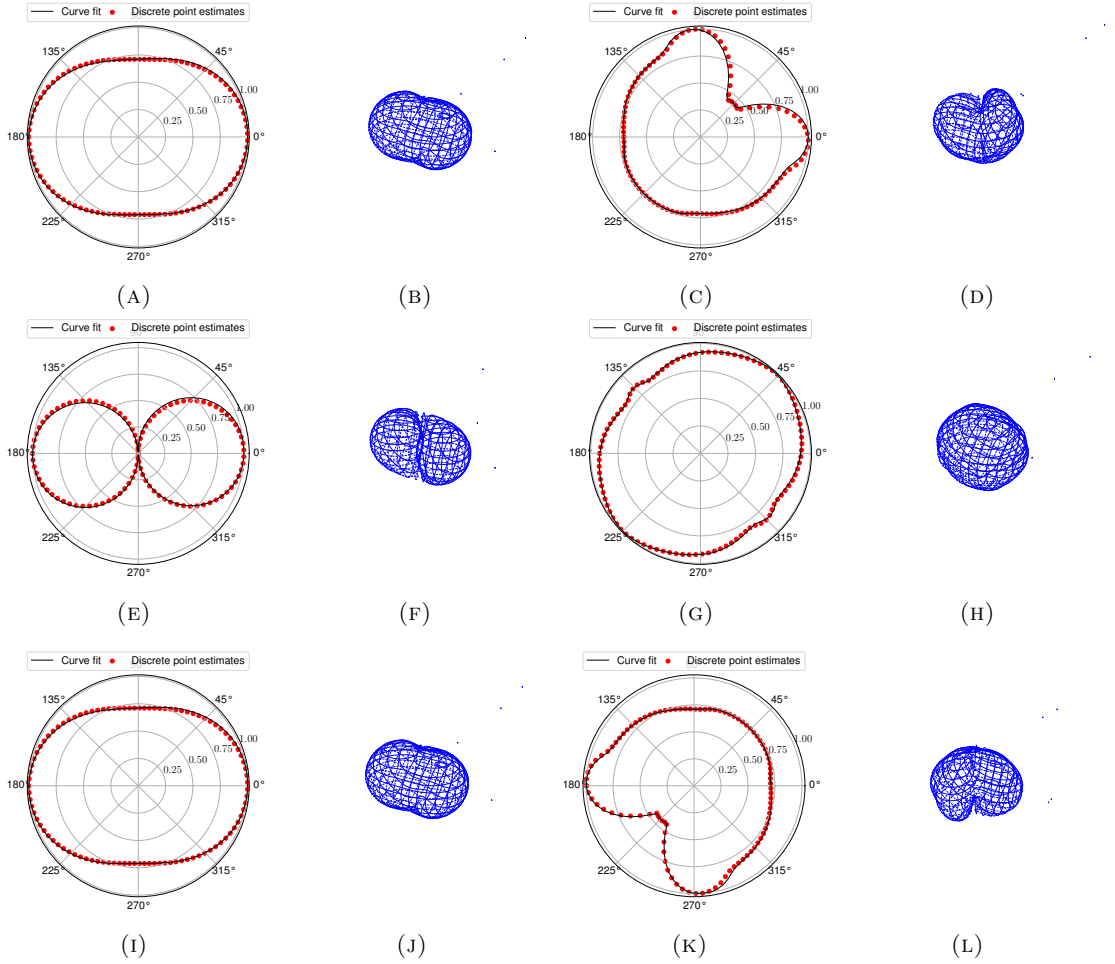

FIGURE 6.7: Cumulative value of spherical harmonic at the observer locations for 6 different scenarios. The resulting noise surface is also shown for each case.

in the remainder of the sections. The period T is defined as the time taken to traverse the finite segment at a constant speed. The trapezoidal rule is used for integration.

The discretisation of the flightpath is guided by the error of the trapezoidal rule, taking into acount that the integrand f is a rotating spherical harmonic,

$$f(\theta(t)) = Y_\ell^m(\theta(t), \varphi) \tag{6.32}$$

and

$$\theta(t) = at + c \tag{6.33}$$

where a and c are some arbitrary constant that define the constant speed roation of the source.

The derivative of f can be defined as,

$$f'(\theta(t)) = \theta'(t)\frac{\partial}{\partial t}(Y_\ell^m(\theta(t), \varphi)) \tag{6.34}$$

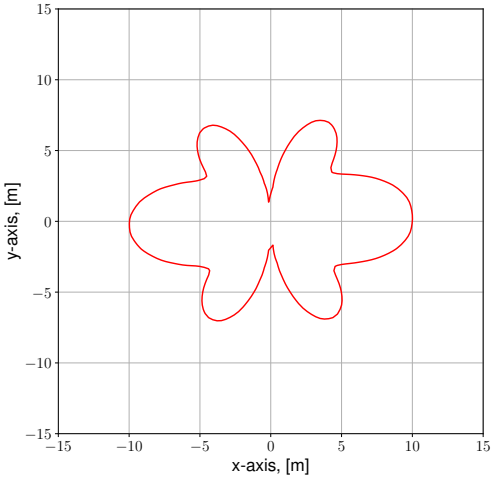

(A) Y_3^0, rotation about the y-axis

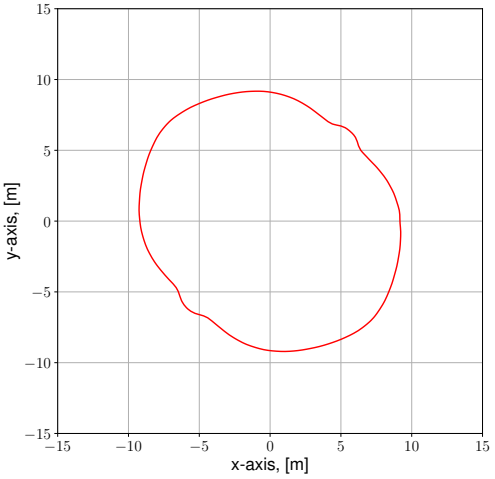

(B) Y_3^0, rotation about $\hat{\omega} = [0.57, 0.57, 0.57]$ axis

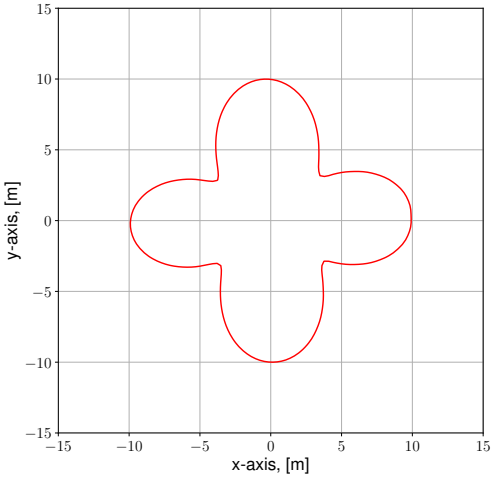

(C) Y_2^0, rotation about the x-axis

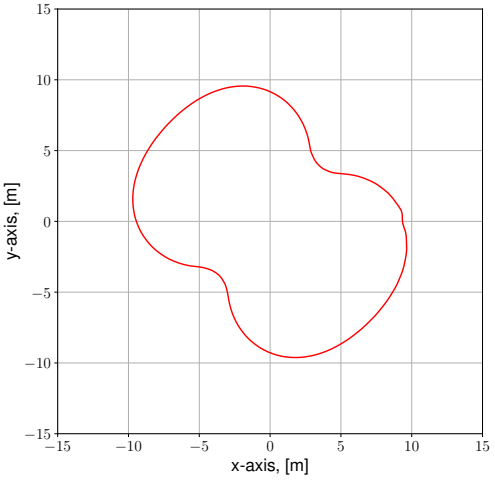

(D) Y_2^0, rotation about $\hat{\omega} = [0.57, 0.57, 0.57]$ axis

FIGURE 6.8: Noise exposure footprints for various source conditions.

where

$$\theta'(t) = a \tag{6.35}$$

and

$$\frac{\partial Y_\ell^m}{\partial \theta} = m * \cot(\theta)\, Y_\ell^m(\theta, \varphi) + \sqrt{(n-m)(n+m+1)}\, e^{-i\varphi} Y_\ell^{m+1}(\theta, \varphi) \tag{6.36}$$

Using an asymptotic approximation for the error E of the trapezoidal rule [190],

$$E = -\frac{(b-a)^2}{12N^2}\left(f'(b) - f'(a)\right) \tag{6.37}$$

where $[a, b]$ the integration interval.

Requiring the error to remain smaller that 1%, as well as allowing the calculation of

higher roation speeds, as well as higher order sherical harminics, the total number of descritization point is chosen as 50, for all cases. For optimal running time, the number of points can be adjusted using Equations 6.32 and 6.37 as guidance.

TABLE 6.1: Parameters defining flyover operation.

Flyover	
Parameters	Value
Aircraft speed, [m/s]	20
Segment length, [m]	400
Flightpath points	50
Integration period, [s]	20

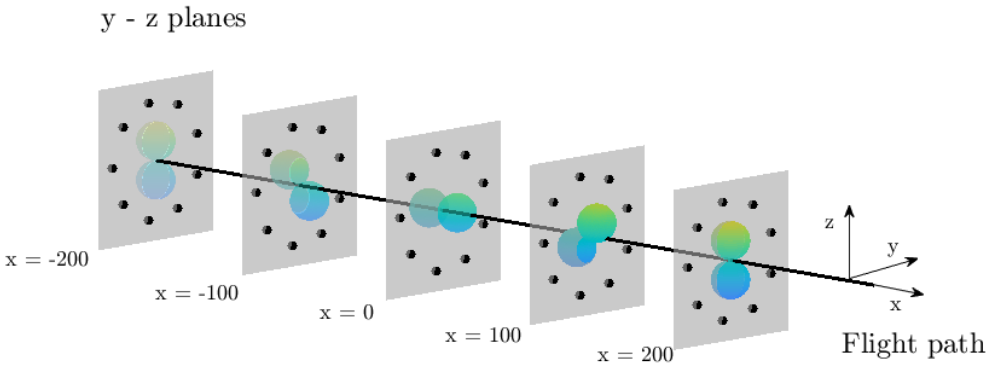

FIGURE 6.9: Illustation of the flyover operation as performed by an ideal rotation dipole, indicated are the vertical planes on which rings of observer points are located.

Time $t = 0$ is assumed to be when the aircraft passes through the midpoint of the segment. The angle of rotation $\theta = 2\pi$ for all cases presented. Figure 6.10 shows the time history of the absolute value of the directivity function as well as the cumulative (or integrated) value at various observer location surrounding the flightpath. Two distinct case are shown: (i) Column 1 assumes a dipole source, Y_1^0, rotating about the y-axis of the aircraft frame. Plots 6.10a, 6.10c and 6.10e show the results for various locations along the segment. (ii) Column 2 also assumes a dipole source, Y_1^0, however rotating about the x-axis of the aircraft frame. Plots 6.10b, 6.10d and 6.10f again show three different locations of observer along the flightpath segment. Each point on the polar plots represents the cumulative value (value of Equation 6.25 for the corresponding coloured line on the Cartesian time history) observed by the observer defined by the angle φ and position x. The number of observers on each ring is limited to 10 for visualisation purposes.

Figure 6.11 shows the estimated noise surface cross-sections for a range of different source directivity types and rotation axes. Each plot shows five distinct lines representing five locations along the flightpath segment. Each line represents the cumulative value of the directivity function as the flyover is performed at observer rings surrounding the flightpath. The presented cross-sections essentially represent slices of

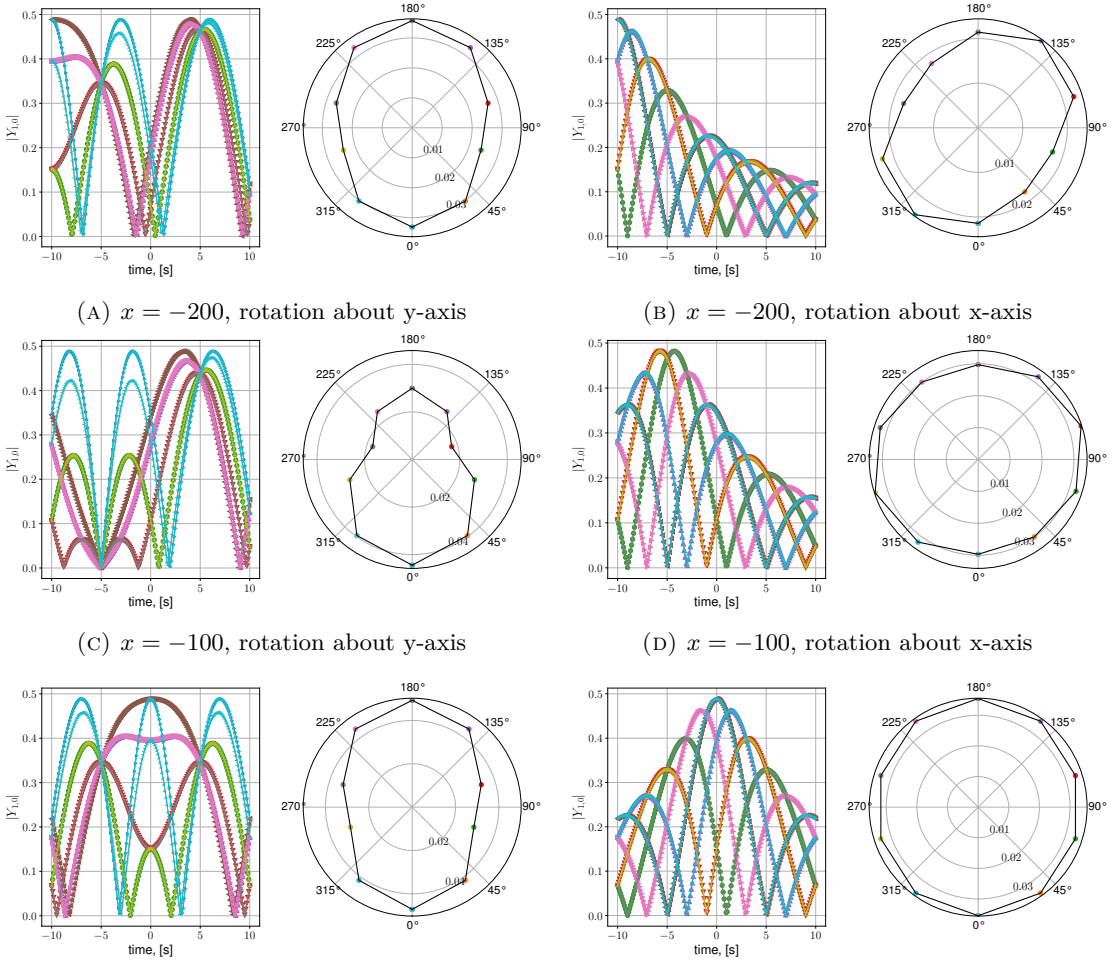

(A) $x = -200$, rotation about y-axis

(B) $x = -200$, rotation about x-axis

(C) $x = -100$, rotation about y-axis

(D) $x = -100$, rotation about x-axis

(E) $x = 0$, rotation about y-axis

(F) $x = 0$, rotation about x-axis

FIGURE 6.10: Cartesian plots: Time history of spherical harmonic value directed at each observer. Polar plots: Cumulative value of the spherical harmonic as a result of a level flyover at each observer. Plots (a) to (f) show the variation in the cross-section along the length of the segment during a single flyover operation.

the full three-dimensional noise surface. All data is normalised to the maximum value across each noise event.

Increasing the number of observer rings along the length of the observer, and applying a simple linear interpolation, the full three-dimensional noise surfaces may be generated surrounding the flightpath. Example surfaces using the previously presented cross-sections are shown in Figure 6.12. As the surfaces presented are the resulting quadric forms generated by the implicit relation in Equation 6.31, an arbitrary noise radius R_n has been chosen for demonstration purposes. In Figure 6.12, $R_n = 100$ m for all cases. This would equate to the noise surface representing a 3D contour in the range 80 dB $<$ SEL $<$ 90 dB for medium size utility helicopter.

Finally, taking the intersection of the three-dimensional noise surface and the X-Y plane, a 2D noise exposure contour is retrieved. Figure 6.13 shows the ground contours of the

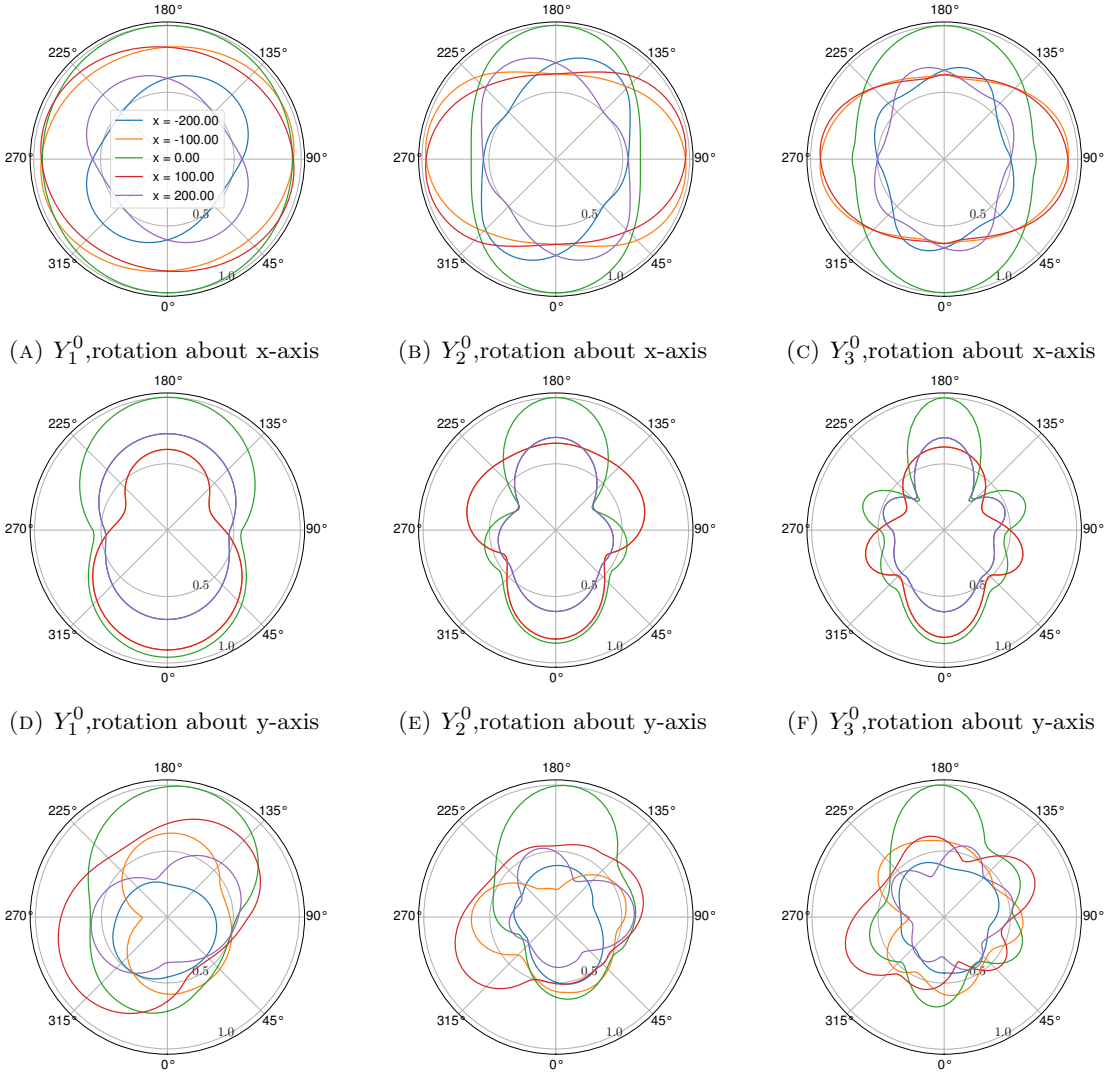

(A) Y_1^0,rotation about x-axis (B) Y_2^0,rotation about x-axis (C) Y_3^0,rotation about x-axis

(D) Y_1^0,rotation about y-axis (E) Y_2^0,rotation about y-axis (F) Y_3^0,rotation about y-axis

(G) Y_1^0,rotation about $\hat{\omega} = [0.57, 0.57, 0.57]$ axis (H) Y_2^0,rotation about $\hat{\omega} = [0.57, 0.57, 0.57]$ axis (I) Y_3^0,rotation about $\hat{\omega} = [0.57, 0.57, 0.57]$ axis

FIGURE 6.11: Estimated noise surface cross-sections. Each plot represents a single flyover operation. The different coloured lines indicate different locations along the x-axis.

equivalent surfaces from Figure 6.12.

6.1.6.3 Vertical takeoff

Assuming the operation is defined as in Section 6.1.3 the aircraft will travel along the two segment flightpath, one vertical and one horizontal. The parameters defining this motion are the vertical speed V_v and the horizontal speed V_h along with the segment lengths s_v and s_h respectively. The source is assumed to rotate through an angle $\theta = \pi/2$ during both of the segments, for a total rotation of π. A summary of the chosen values for the following results may be seen in Table 6.2.

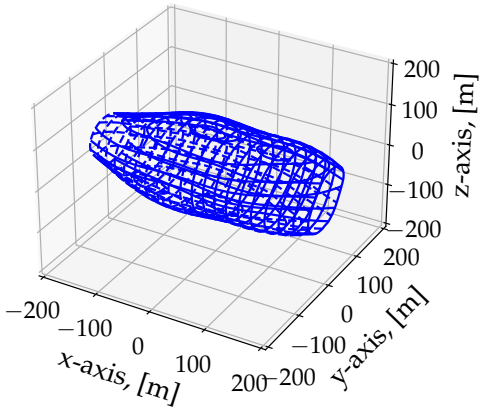

(A) Y_1^0,rotation about x-axis

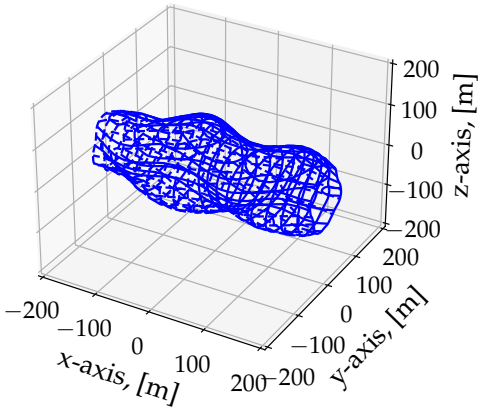

(B) Y_3^0,rotation about x-axis

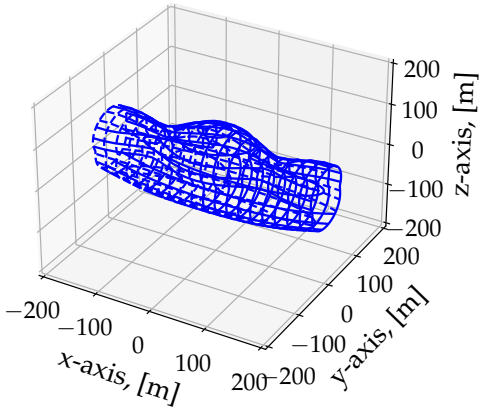

(C) Y_1^0,rotation about y-axis

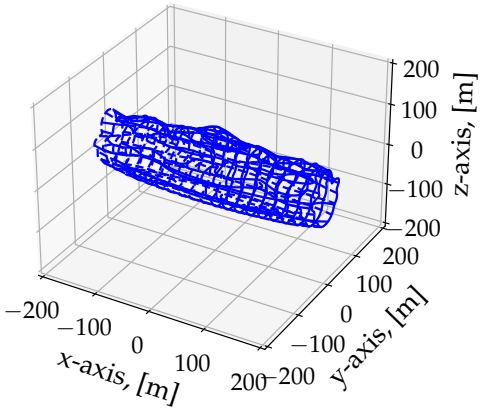

(D) Y_3^0,rotation about y-axis

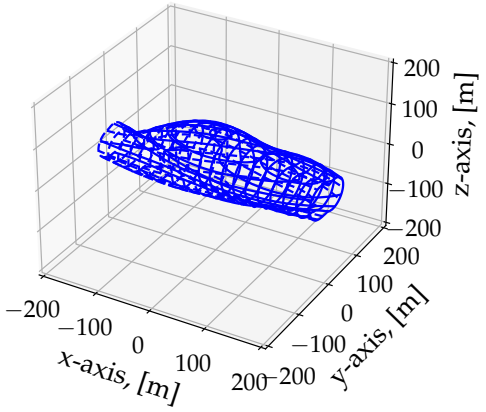

(E) Y_1^0,rotation about $\hat{\omega} = [0.57, 0.57, 0.57]$ axis

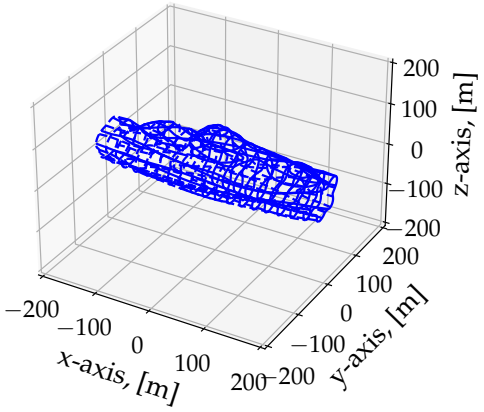

(F) Y_3^0,rotation about $\hat{\omega} = [0.57, 0.57, 0.57]$ axis

FIGURE 6.12: Flyover noise surfaces. Cross-sections such as the one presented in Figure 6.11 are used to generate the three-dimensional surfaces.

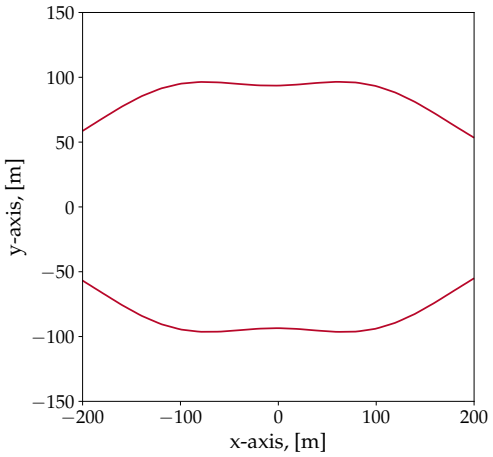

(A) Y_1^0,rotation about x-axis

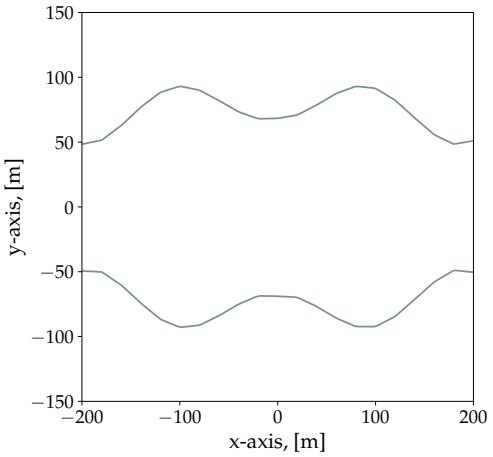

(B) Y_3^0,rotation about x-axis

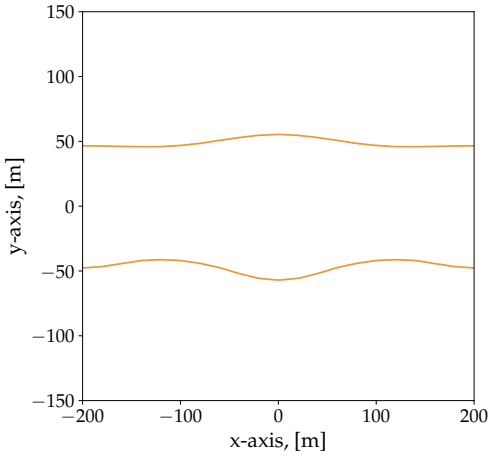

(C) Y_1^0,rotation about y-axis

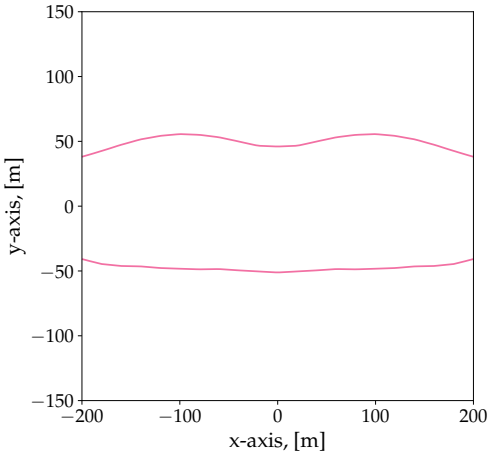

(D) Y_3^0,rotation about y-axis

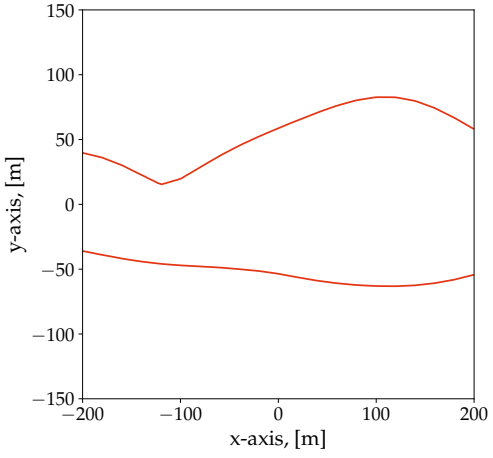

(E) Y_1^0,rotation about $\hat{\omega} = [0.57, 0.57, 0.57]$ axis

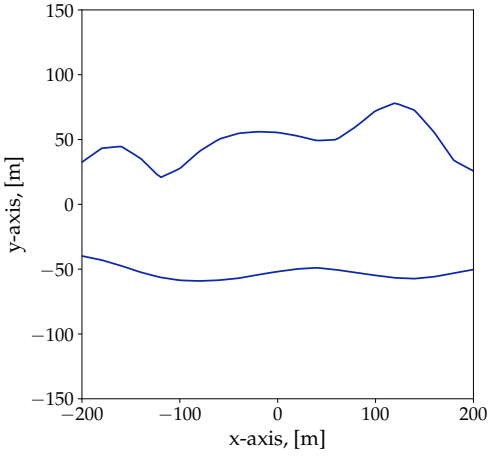

(F) Y_3^0,rotation about $\hat{\omega} = [0.57, 0.57, 0.57]$ axis

FIGURE 6.13: Ground noise exposure footprints. The result of the intersection of the noise exposure surfaces in Figure 6.12 and the airport ground plane.

TABLE 6.2: Parameters defining takeoff operation.

takeoff	
Parameters	Value
Vertical speed, [m/s]	2
Horizontal speed, [m/s]	5
Vertical segment length, [m]	10
Horizontal segment length, [m]	25
Total flightpath points	500
Integration period, [s]	10

This results in the position of the aircraft/source varying linearly as function of time. The components of the source position vector $\boldsymbol{\mathcal{X}} = [x_a, y_a, z_a]^T$ relative to the airport frame are shown in Figure 6.14.

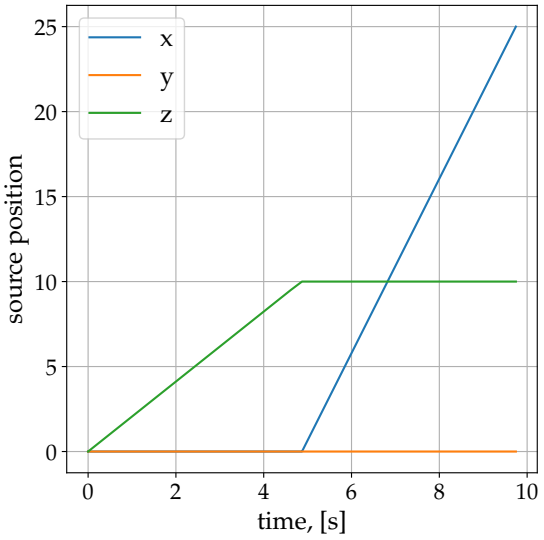

FIGURE 6.14: Source coordinate time history.

As before, observers are defined on rings surrounding the vertical and horizontal segments. The direction of the observers relative to the source is given by position vector $q_b = (q_1,\ q_2,\ q_3)$. Figures 6.17 and 6.18 illustrates how the direction unit vector components vary as the manoeuvre progresses through time for all the different observer rings. The plots are colour coded according the location of the ring within the flightpath. The colour coding is visible in the corner of Figure 6.17a. Lines of the same colour indicate observers on the same ring with different azimuthal location relative to the flight path.

Once the position of the source in known for each observer, rotation must be accounted for, using Equation 6.19. The value of the directivity function may then be estimated. This value indicates the relative level of PWL radiated in the direction of each observer as a function of time. Diagrams in Figures 6.15 and 6.16 illustrate the position vector q.

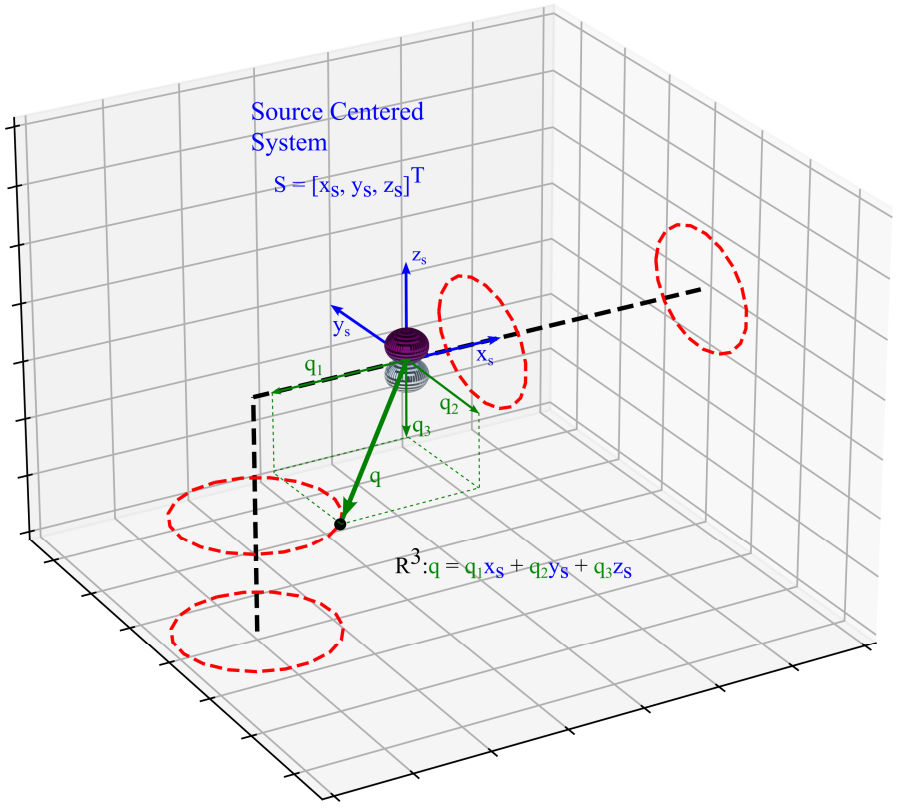

FIGURE 6.15: Perspective of the source reference frame in three-dimensional space. The vector q and its orthogonal components are also illustrated.

Assuming a dipole, the absolute value, $|Y_1^0|$ is plotted as a function of time in Figures 6.19 and 6.20. The same is done for Y_3^0 in Figures 6.21 and 6.22. The various line types indicate different positions within a single observer ring.

As the directivity values have been evaluated as a function of time, sound power and distance between the source and each observer may be accounted for, through Equation 6.28. As the radiated sound power remains constant, we may normalise to get SEL per unit of sound power, given in dB / W. The sum is evaluated at each observer location for the vertical and horizontal segments. The results may be seen in Figure 6.23 and 6.24. The plots are normalised to the maximum value occurring throughout an entire segments. For Figures 6.23a and 6.23c representing the vertical segment, the Z-axis would be coming out of the page with the 0° being in the positive X-axis direction, while for Figures 6.23b and 6.23d the horizontal segments, the X-axis would be coming out of the page with the 0° being directly below the flightpath. Figure 6.23 presents a case where the source only rotates during the horizontal segment about the aircraft frame y-axis. The effects of introducing source rotation to the vertical segments may then be seen in Figure 6.24.

Using the calculated cross-sections, three-dimensional noise surfaces are defined. The use of Equation 6.31 requires the introduction of a linear interpolation to connect the regions between the estimated cross-sections. Assuming an arbitrary noise radius

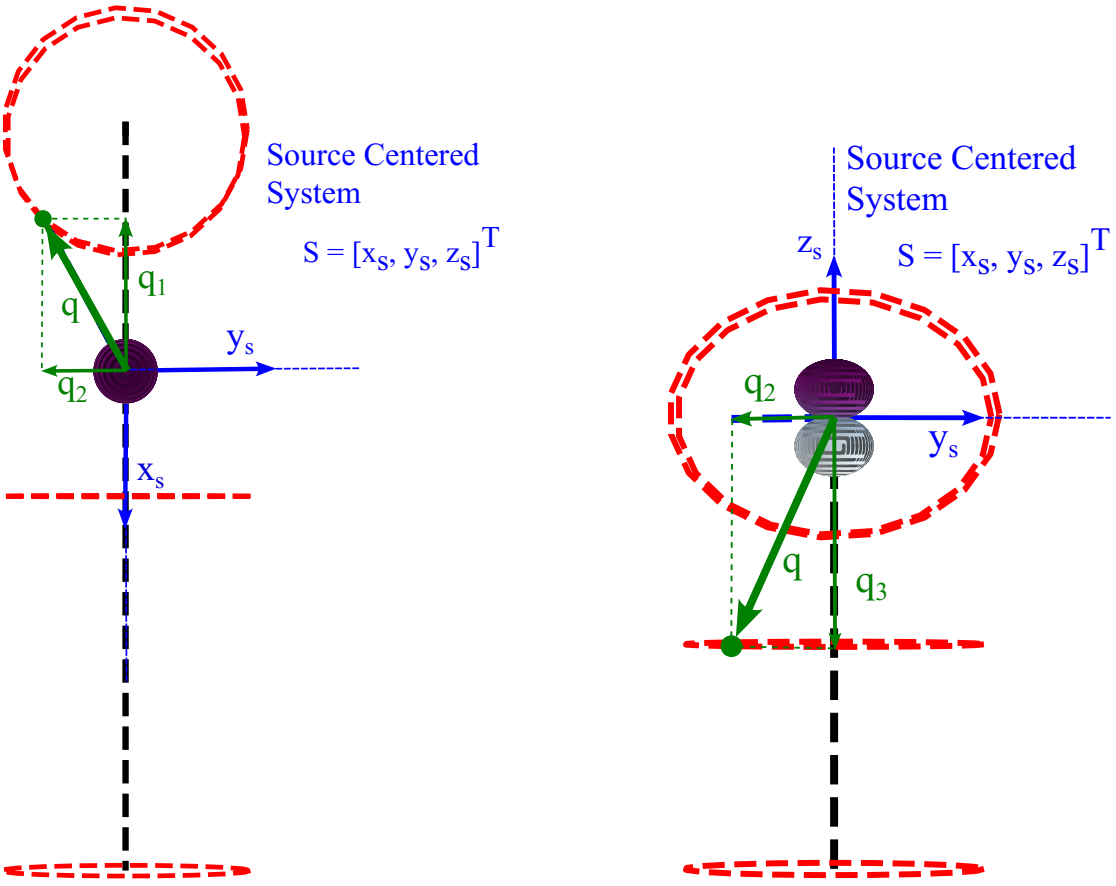

(A) $x_s - y_s$ plane (B) $y_s - z_s$ plane

$$R^3: q = q_1 x_S + q_2 y_S + q_3 z_S$$

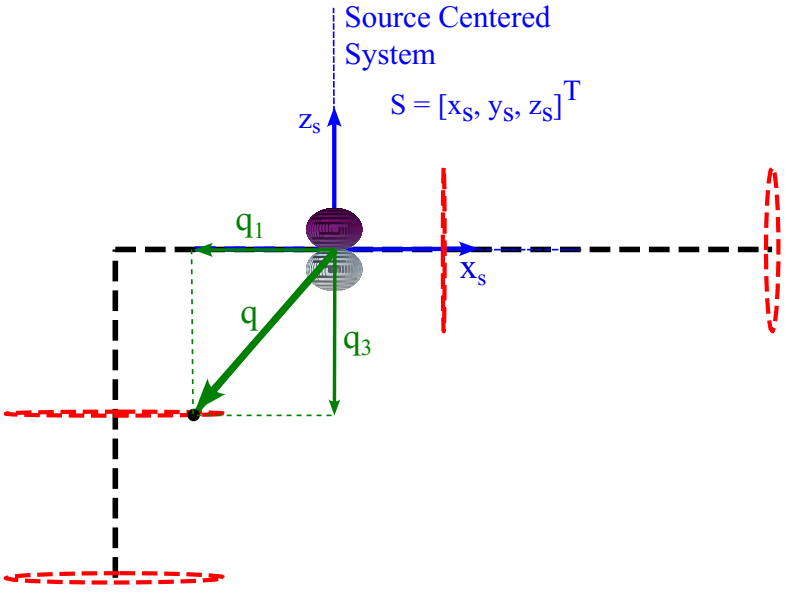

(C) $x_s - z_s$ plane

FIGURE 6.16: Illustration of the source reference frame translating along the flightpath. The vector q indicates the position of an observer, on one of the rings, in the perspective of the source frame. The orthogonal components of vector q, q_1, q_2, q_3 are also illustrated.

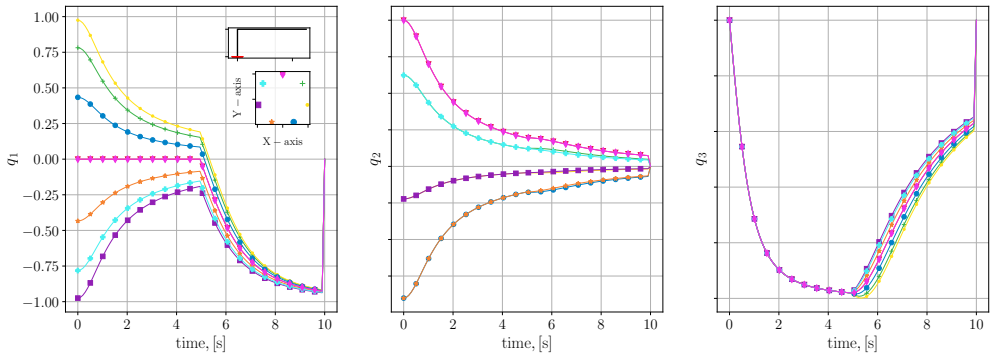

(A) First observer ring.

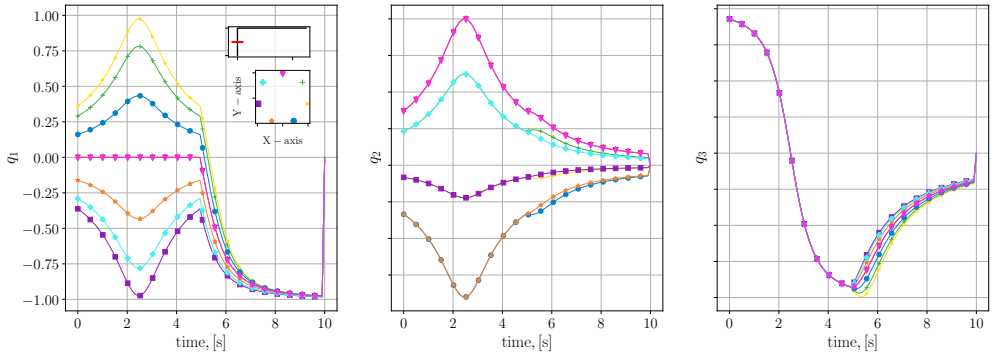

(B) Second observer ring.

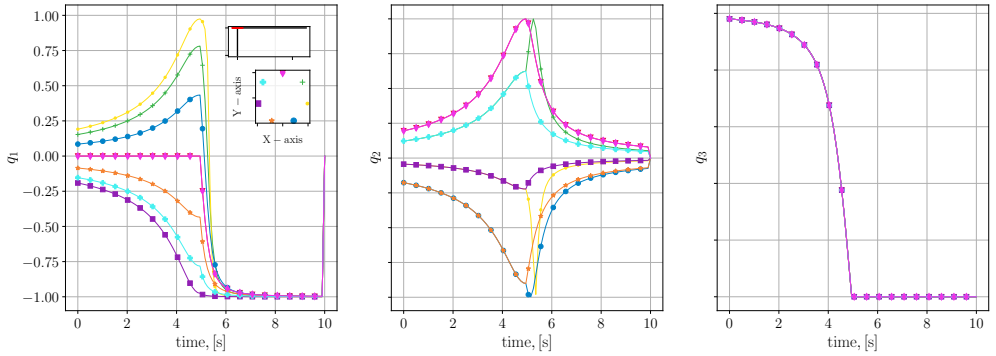

(C) Third observer ring.

FIGURE 6.17: Components of position vector $q = (q_1, q_2, q_3)$ indicating direction to the vertical rings of observers relative to the source. A side view of the flightpath (black) is embeded in the first sub-plot indicating the position of the observer ring (red). The lines representing q_1, q_2, q_3 are coloured depending on the specific observer on the ring, also embeded in the first sub-plot with each observer having its own colour and marker shape.

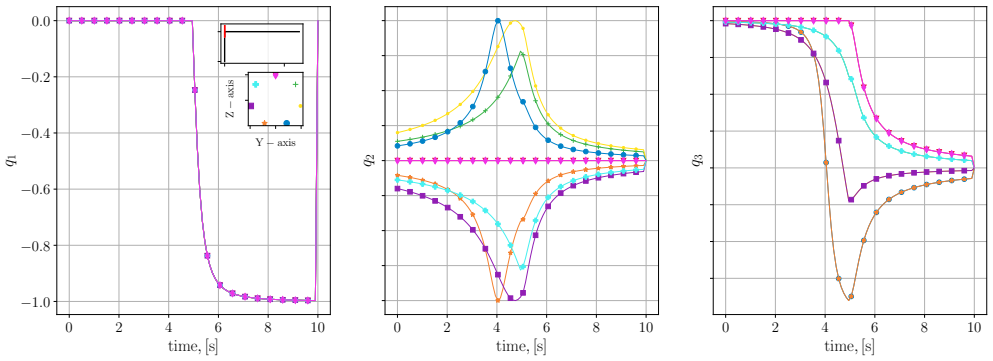

(A) First observer ring.

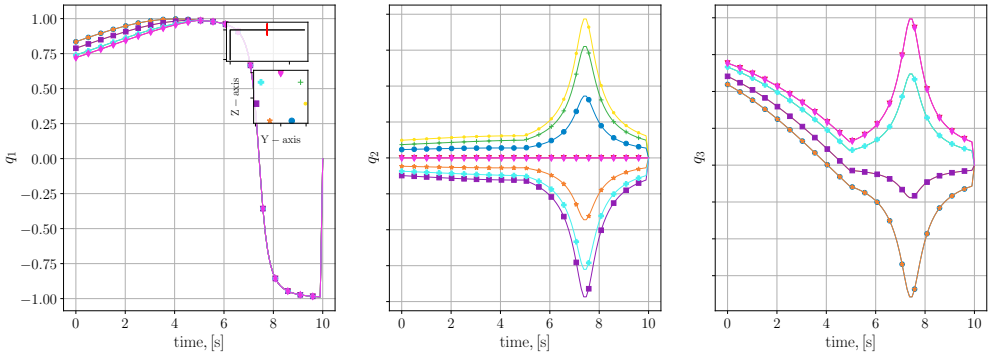

(B) Second observer ring.

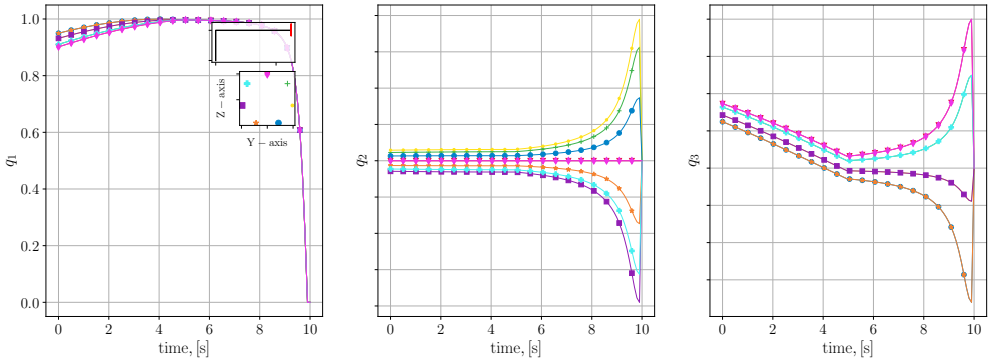

(C) Third observer ring.

FIGURE 6.18: Components of position vector $q = (q_1, q_2, q_3)$ indicating direction to the horizontal rings of observers relative to the source. A side view of the flightpath (black) is embeded in the first sub-plot indicating the position of the observer ring (red). The lines representing q_1, q_2, q_3 are coloured depending on the specific observer on the ring, also embeded in the first sub-plot with each observer having its own colour and marker shape.

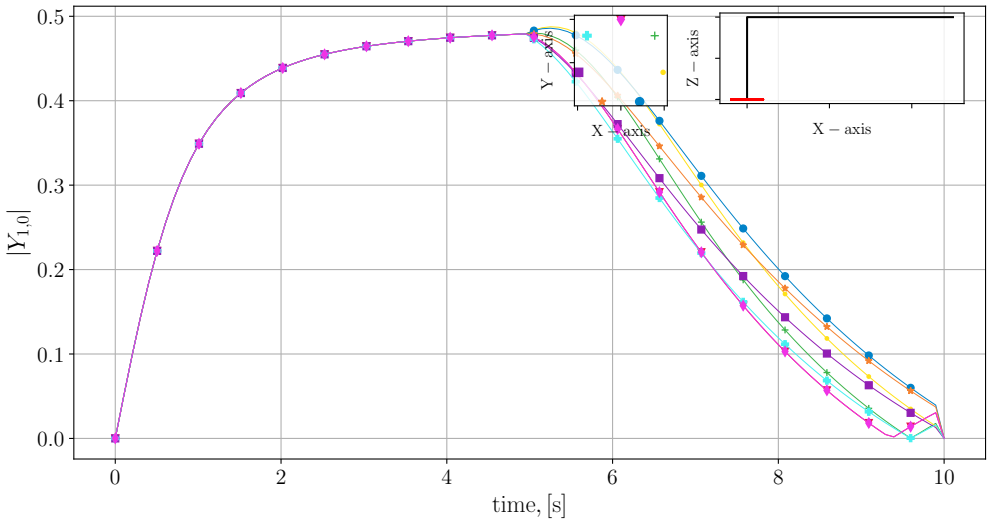

(A) First observer ring.

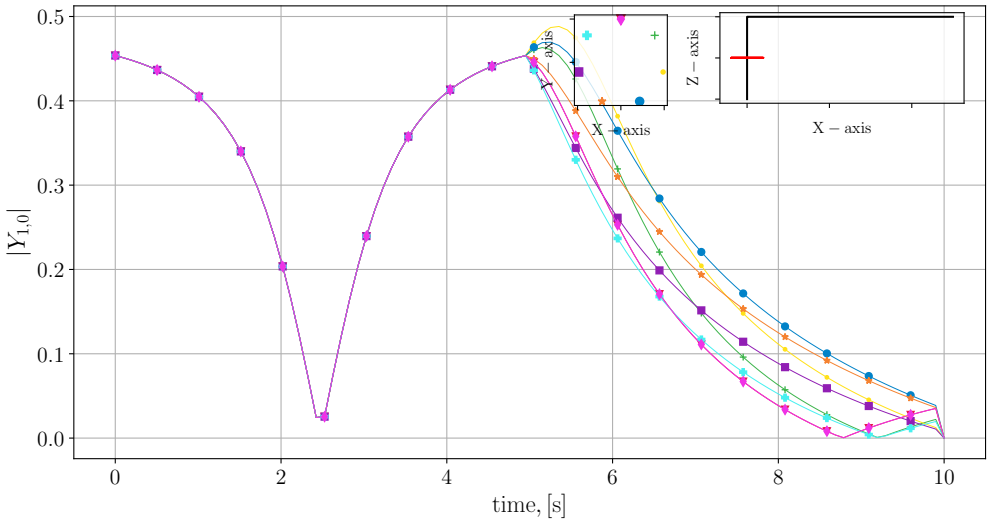

(B) Second observer ring.

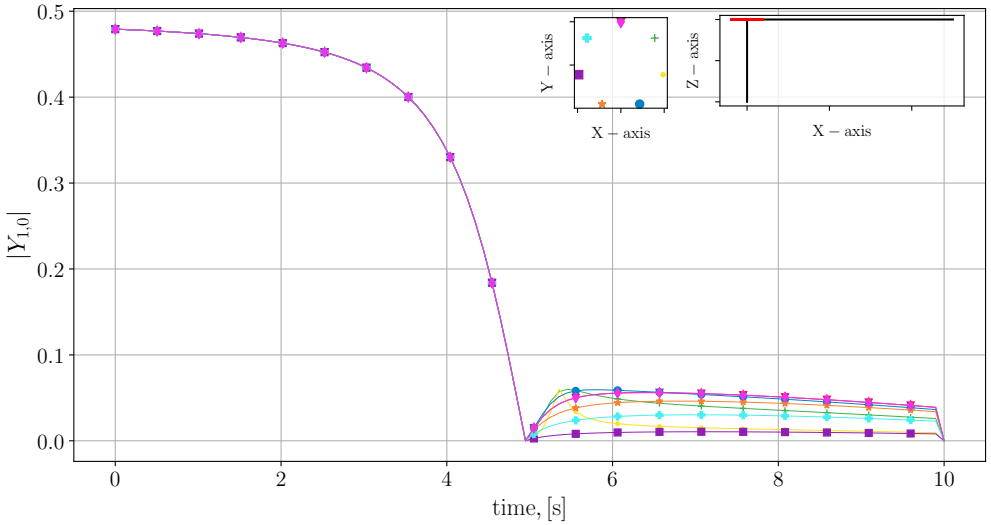

(C) Third observer ring.

FIGURE 6.19: Time history of spherical harmonic,$|Y_1^0|$, value pointing in the direction of each observer location on the rings. A side view of the flightpath (black) is embeded in the first sub-plot indicating the position of the observer ring (red). The lines representing q_1, q_2, q_3 are coloured depending on the specific observer on the ring, also embeded in the first sub-plot with each observer having its own colour and marker shape.

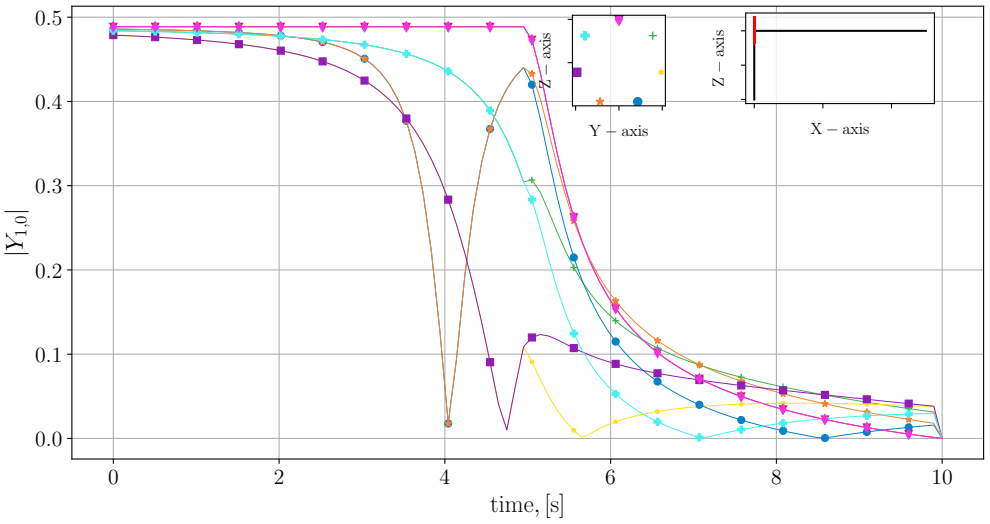

(A) First observer ring.

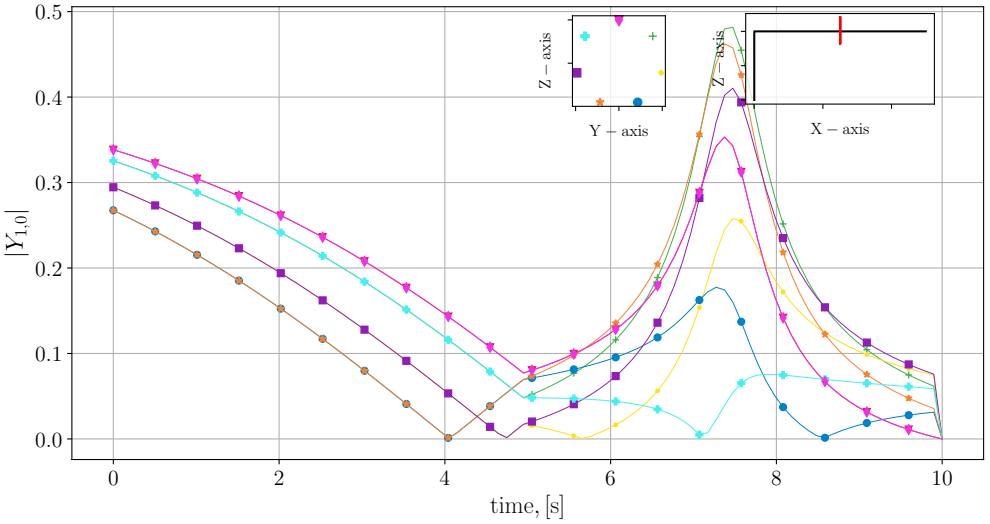

(B) Second observer ring.

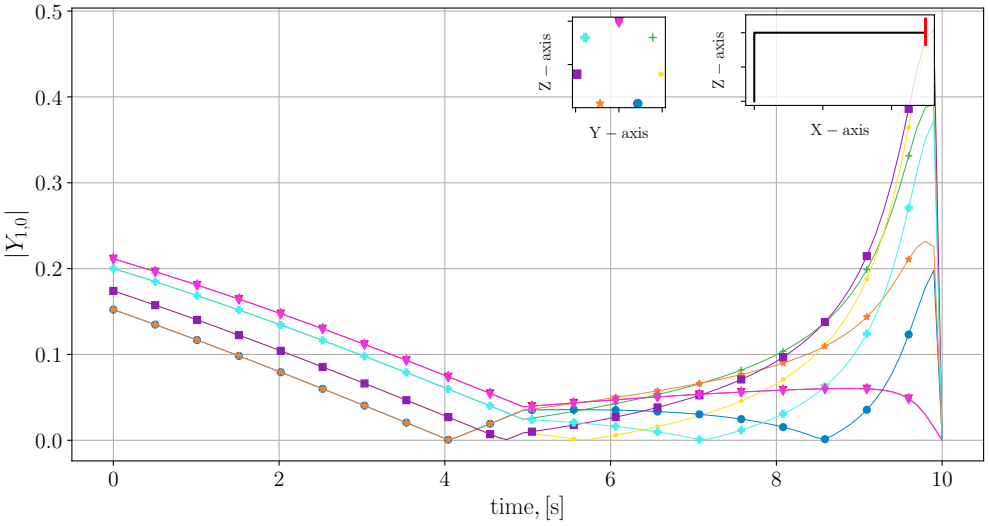

(C) Third observer ring.

FIGURE 6.20: Time history of spherical harmonic,$|Y_1^0|$, value pointing in the direction of each observer location on the rings. A side view of the flightpath (black) is embeded in the first sub-plot indicating the position of the observer ring (red). The lines representing q_1, q_2, q_3 are coloured depending on the specific observer on the ring, also embeded in the first sub-plot with each observer having its own colour and marker shape.

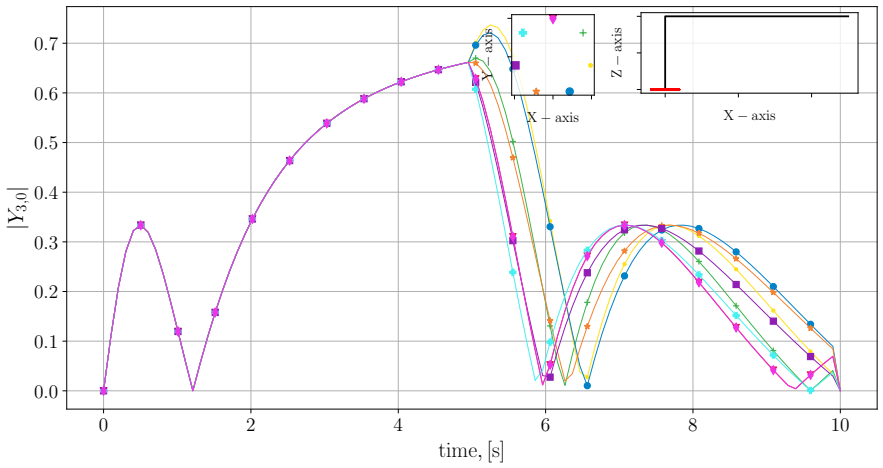

(A) First observer ring.

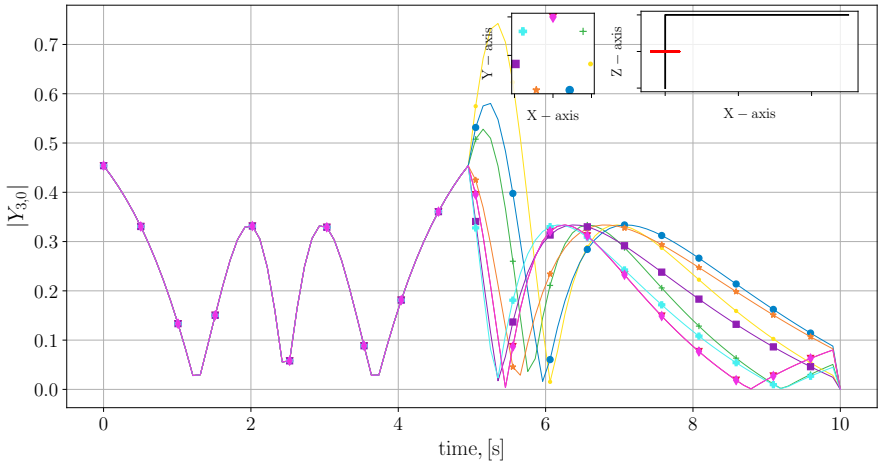

(B) Second observer ring.

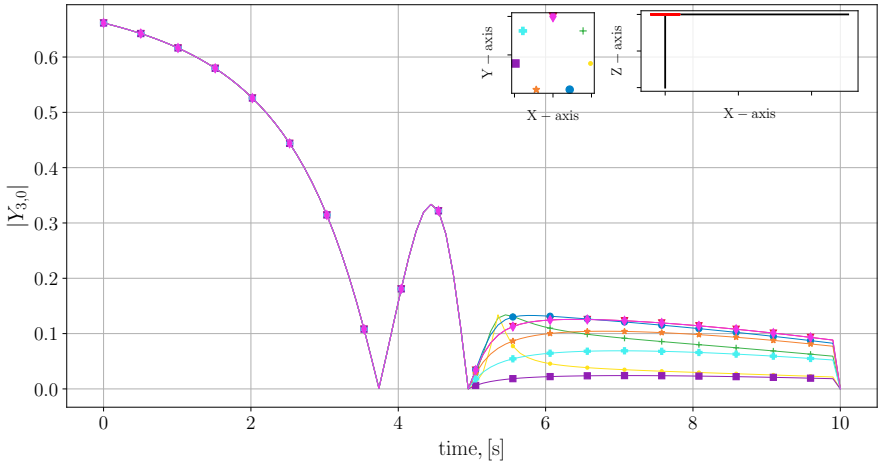

(C) Third observer ring.

FIGURE 6.21: Time history of spherical harmonic,$|Y_3^0|$, value pointing in the direction of each observer location on the rings. A side view of the flightpath (black) is embeded in the first sub-plot indicating the position of the observer ring (red). The lines representing q_1, q_2, q_3 are coloured depending on the specific observer on the ring, also embeded in the first sub-plot with each observer having its own colour and marker shape.

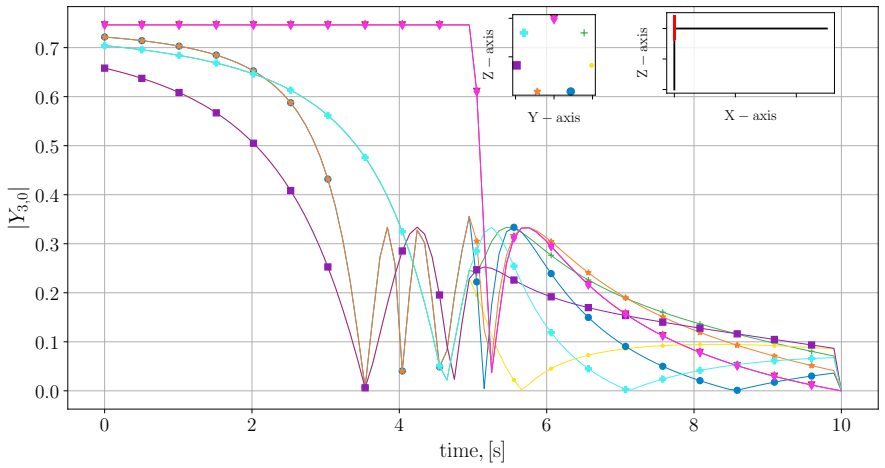

(A) First observer ring.

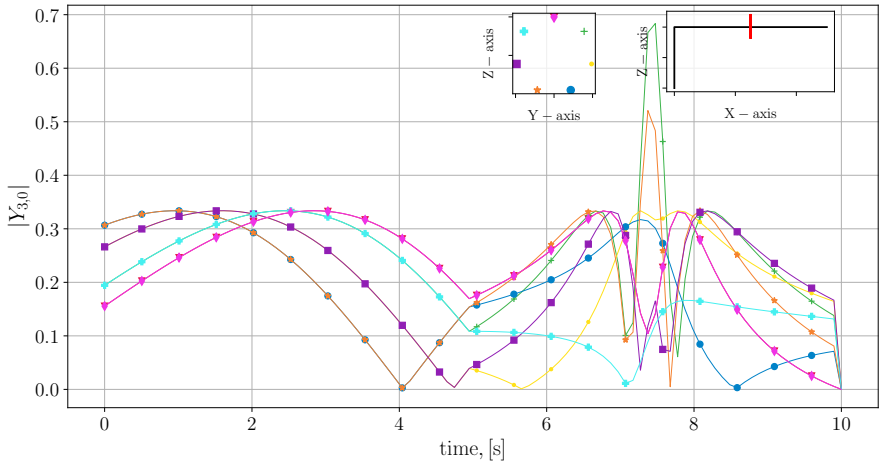

(B) Second observer ring.

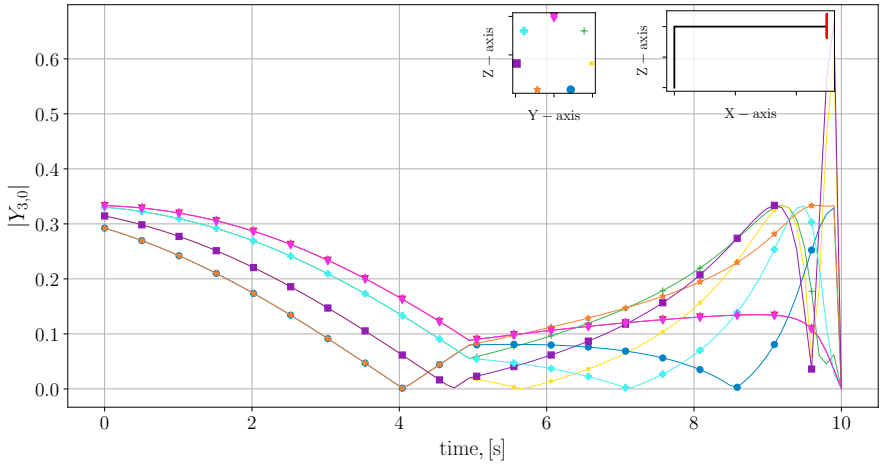

(C) Third observer ring.

FIGURE 6.22: Time history of spherical harmonic,$|Y_3^0|$, value pointing in the direction of each observer location on the rings. A side view of the flightpath (black) is embeded in the first sub-plot indicating the position of the observer ring (red). The lines representing q_1, q_2, q_3 are coloured depending on the specific observer on the ring, also embeded in the first sub-plot with each observer having its own colour and marker shape.

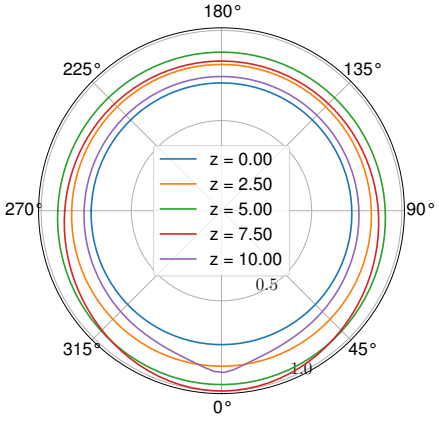

(A) Y_1^0 rotation about y-axis during the vertical segment.

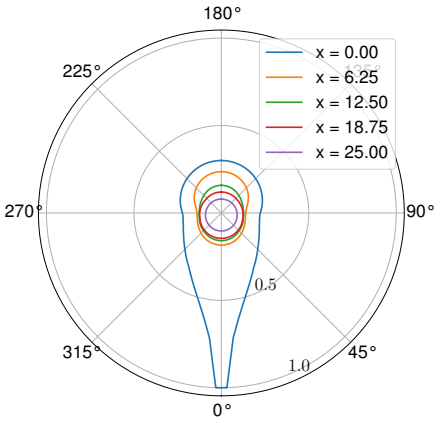

(B) Y_1^0 during the horizontal segment.

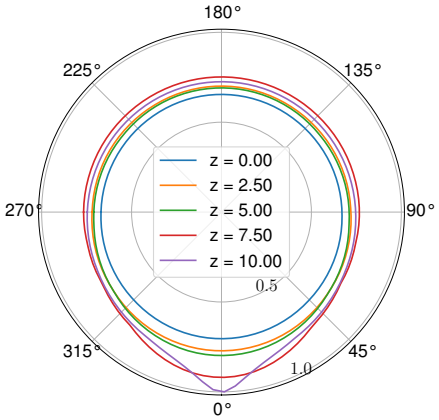

(C) Y_3^0 rotation about y-axis during the vertical segment.

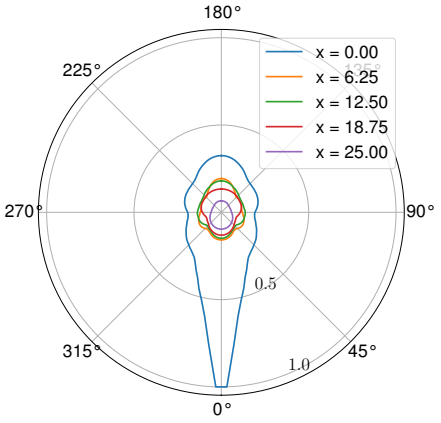

(D) Y_3^0 during the horizontal segment.

FIGURE 6.23: Noise surface cross-sections for vertical takeoff operation. Rotation of angle $\theta = \pi/2$ occurs during horizontal segment.

$R_n = 10m$, the noise surface corresponding to each of the segments may be evaluated implicitly. Figure 6.25 shows the resulting noise surface for the horizontal segments assuming two different directivity functions, Y_1^0 and Y_3^0. It is evident that the surfaces are derived from cross-section in Figures 6.23b and 6.23d respectively.

Figure 6.26 shows the noise surfaces generated by the entire two segment flightpath. The red colour is assigned to the noise surface surrounding the vertical segment, while the blue colour to the horizontal segment. The individual plots are derived using the identical source motion and cross-sections presented in Figure 6.24.

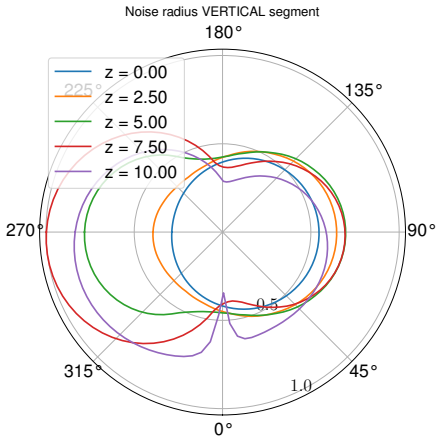

(A) Y_1^0 rotation about x-axis during both vertical and horizontal segments.

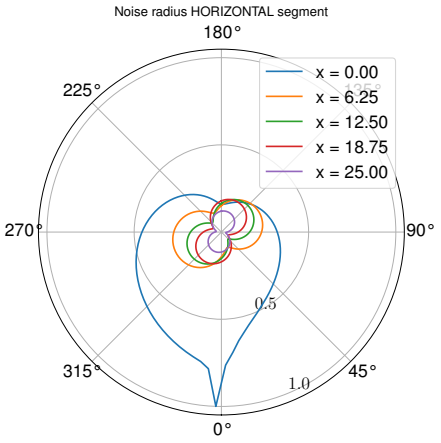

(B) Y_1^0 rotation about x-axis during both vertical and horizontal segments.

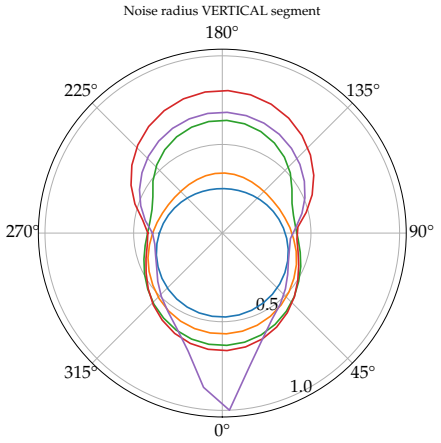

(C) Y_1^0 rotation about y-axis during both vertical and horizontal segments.

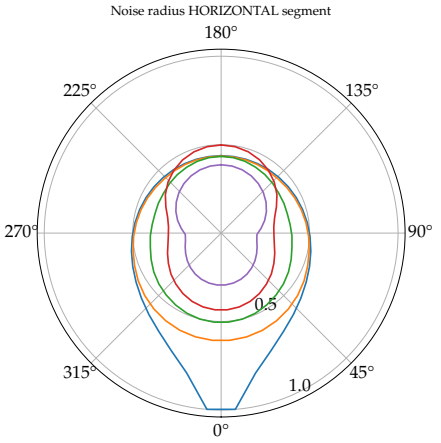

(D) Y_1^0 rotation about y-axis during both vertical and horizontal segments.

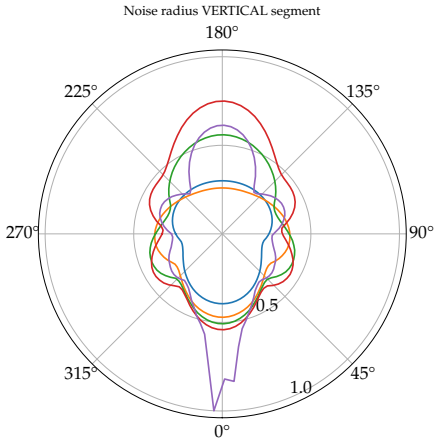

(E) Y_3^0 rotation about y-axis during both vertical and horizontal segments.

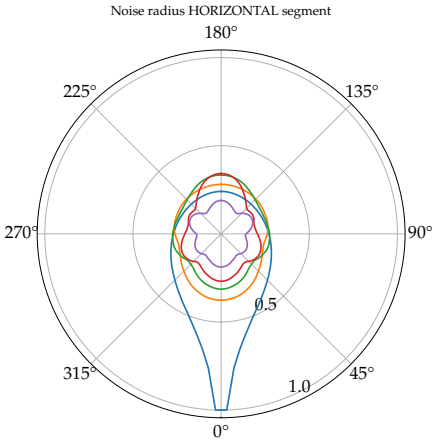

(F) Y_3^0 rotation about y-axis during both vertical and horizontal segments.

FIGURE 6.24: Cross-section of vertical (first column) and horizontal segments (second column).

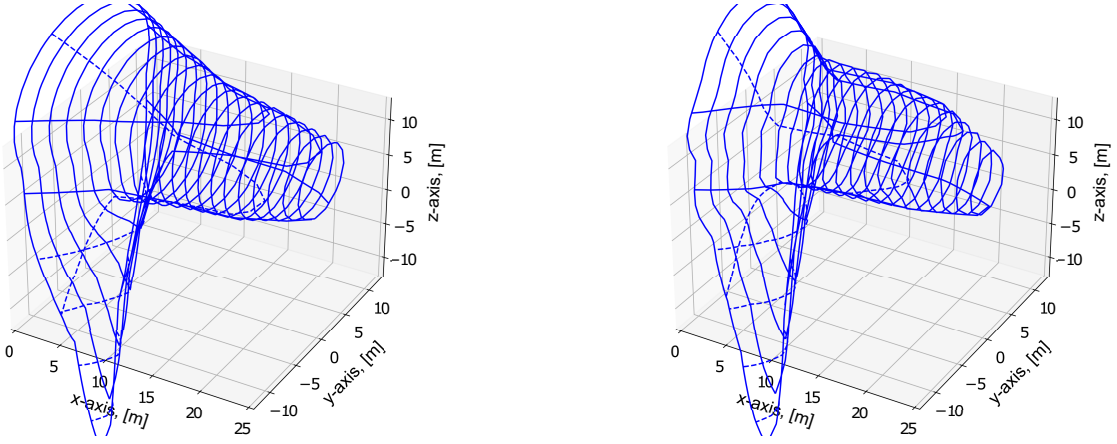

(A) Y_1^0 rotation about y-axis.

(B) Y_3^0 rotation about y-axis.

FIGURE 6.25: Noise exposure surfaces generated for horizontal segment of takeoff operation. Vertical segment is accounted for in the calculation of the cumulative noise level on the observer rings surrounding the flightpath.

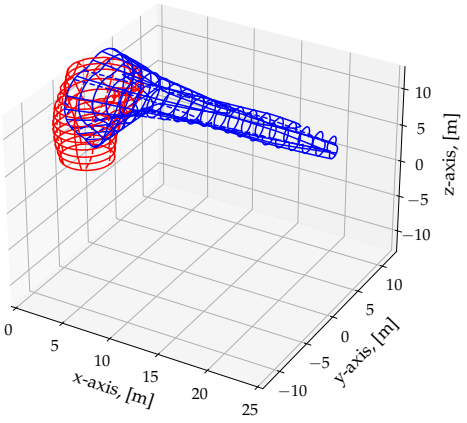

(A) Y_1^0 rotation about x-axis during both segments.

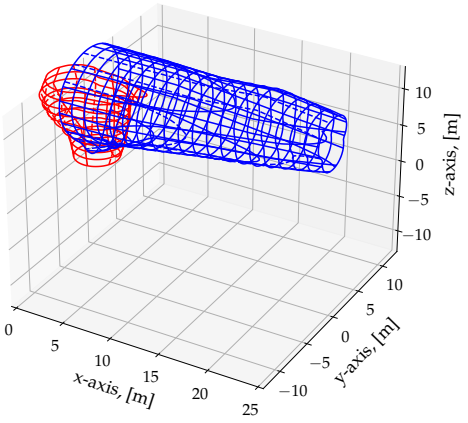

(B) Y_1^0 rotation about y-axis during both segments.

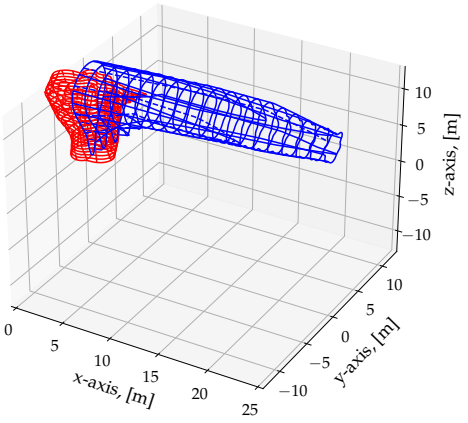

(C) Y_3^0 rotation about y-axis during both segments.

FIGURE 6.26: Noise exposure surfaces generated for vertical takeoff operation. The red surface represents the observer locations surrounding the vertical segment, while the blue surface the horizontal ones respectively.

6.2 Summary

This Section presented preliminary work, within RANE v2, to capture the effects of a rotating noise source on noise exposure footprints and contours. The inteded application of the added capability is in the complex manoeuvre of transition of UAM vehicles perform during VTOL operations. The ability to study its effect on the noise on the ground can prove to be crucial to the development of such vehicles as VTOL operations are high power, low altitude operations. The transition of flight is modeled as a rotation of the inherent total three-dimensional directivity of the vehicle. This is described as a spherical harmonic expansion.

The problem of generating noise exposure footprints and contours is approached in the same ways as presented in RANE [13]. Noise surfaces of constant noise levels are calculated surrounding the flightpath. However, the highly asymmetric nature of vertical takeoff operations leads to the development of a numerical procedure to generate the required "integrated" directivity for inputs to RANE.

The study was approached in three stages that ultimately built up to the vertical takeoff operation. The three stages comprised of 1. hover: a simple acoustic source stationary in space (no translation) able to rotate freely about any axis. 2. flyover: a simple acoustic source performing a straight and level flyover operation able again to rotate freely about any body axis. Finally, 3. vertical takeoff: a simple acoustic source performing a vertical takeoff operation. The operation comprised of two segments, one vertical and one horizontal.

Immediate future work lies in the estimation and quantification of the finite segment error. The magnitude of the error may be estimated numerically as a function of the noise radius to segment length ratio, while also providing the possibility for a hybrid numerical-analytical solution to reduce computational effort. Expansion on the application of RANE and the accompanying numerical methodology include the following possible features:

- Investigate the effect of variable power setting. As flight shifts from powered to fixed wing flight, the power output of the propulsion system varies significantly. Possible studies include the effect of this transient behaviour on the ground noise, in addition to current effects of rotation and directivity.
- Effect of dominant noise source shifting. This effect could cause variations in the acoustic power output as well as in the total directivity during the operation interval.
- Realistic trajectory modelling. Although singular vertical and horizontal segments allow for a first approximation of VTOL operation, in practice these prove to be inefficient. Hover power requirement is too high for any substantial altitude gain

through vertical flight and horizontal accelerated flight delays the ascent to the optimised cruise altitude.

Finally, future work includes a series of bench-marking tests for validation purposes. Once the assumptions and results have been verified, the model will be applied to real application in the form of a tilt-rotor UAV and / a full scale UAM vehicle. Footprint and contour comparisons between estimated and measured noise would provide the conclusive effectiveness of the proposed models. However, due to the lack of publicly available NPD data this process may be delayed.

This Chapter concluded the noise surface methodology with amendments to RANE v2 to account for independent rotation of the source and aircraft reference frames relative to the global airport coordinate system. This allows for preliminary insights to the effect of changes to the source and vehicle axis orientation duting an operation on the noise exposure footprints/contours on the ground.

The methodologies presented in Chapters 4 to 6 comprise the MONTANA prediction framework, with the main outputs being NPD curves, and noise exposure footprints/contours. The following chapter focuses on the verification of the proposed methodologies, as well as an error analysis on the outputs of interest.

Chapter 7

Verification

This Chapter examines the validity of the proposed MONTANA model and the individual components within. The chapter is divided into three parts. The first corresponds to the benchmarking of the model derived in Chapter 4. The extent of the validity of the asymptotic expansion is compared against a full implementation of the Hanson frequency domain model. Next, estimated NPD curves using the MONTANA model are compared against publicly available ones for current existing fixed wing and rotorcraft vehicles. The third part analyses the capability of the simplified airport noise model within MONTANA. Two methods of benchmarking are explored; the first an in-house simplified simulation model is developed following the guidelines within Doc 29 [34] for grid-method approaches. The second is a direct comparison to predictions by the industry standard AEDT model. Contour directivity capabilities within MONTANA are compared against contours produced by AEDT that follows the conventional lateral three-curve methodology applied to helicopters and start of roll directivity effects. The final section discusses potential sources of errors and analyses the applicability range of the models.

7.1 Source Model verification

The source model verification refers to a quantification study on the effect of the asymptotic approximation and resulting scaling laws accuracy compared to a full implementation of a harmonic noise prediction method. The effectiveness of the proposed scaling laws is tested on two levels. A low level, where the capability of the proposed models in predicting the absolute noise harmonics due to propeller thickness and loading sources. The comparison will be done against i. an analytic model for loading noise by Gutin [191] (but as later interpreted by Blake [192]) and two propeller noise tool by ESDU, 76020 [193] and ii. a full implementation of the Hanson model as described in Appendix A.

The high level verification will use the capabilities of the model to estimate changes in noise compared to a baseline to predict current air-vehicle NPD curves. NPD curves for fixed wing and rotorcraft (helicopters) vehicles for a variety of operating procedures are compared to published ones generated by a combination of experimental measurements and computational extrapolation. The vehicles are chosen to cover a wide range of sizes and configurations regarding the propulsion system. The main feature requirement of the propulsion systems of choice is the use of propeller as the main mean of thrust production.

7.1.1 Absolute levels and harmonic shape

The noise source models within MONTANA are hereafter referred to as either the method or model, with all benchmarking tools referred to explicitly by their name. The two main components of the model that need characterising and benchmarking are the ability to predict absolute levels of the propeller tonal sources, as well as the shape of the spectral content of the signal, specifically the harmonics.

Despite the main idea behind MONTANA being the gradients and therefore changes in noise produced of any particular noise prediction tool, and applying them to baseline absolute level; as an initial test, the comparison of absolute levels forms a sanity check of the major underlying assumption regarding the asymptotic approximation, the source functions, the blade description and the thickness and loading distributions of the propeller.

The tools used for the verification study in this section are: the Gutin solution for propeller steady loading harmonic noise as given by Blake [14]. The expression is reproduced directly from the reference, for the ease of the reader,

$$\begin{aligned}\frac{p_{Lm}(x)}{q_T} = \frac{-i}{\pi^3} k_T \frac{mBM_t}{1+(J/\pi)^2}\left(\frac{D}{r}\right) \\ \left\{\cos\beta + 2\left[\frac{\Omega(0.35D)}{c_0}\right]^{-1}\frac{k_Q}{k_T}\right\} \\ \times J_{mB}\left(\frac{mB\Omega(0.35D)}{c_0}\sin\beta\right) \\ \times \exp\left\{i\left[\frac{mB\Omega r}{c_0} + mB\left(\theta - \frac{\pi}{2}\right)\right]\right\}, \quad -\infty < m < \infty\end{aligned} \tag{7.1}$$

where k_T, k_Q and J are propeller performance coefficients [14]. $q_T = 0.5\rho_0\left(\Omega^2 r_t^2 + V_a^2\right)$ is the dynamic pressure. This solution is referred to as "Gutin from Blake".

Next, is a spectral density function of the above solution, referred to as "Spectral density from Blake". Again an expression for the estimation of propeller steady loading harmonic noise using a small argument asymptotic relation. The spectral density function is,

$$\begin{aligned}\frac{\Phi_{p,rad}(\mathbf{x},\omega)}{q_T^2} = &\frac{1}{4\pi^6}\frac{mBk_T^2M_t^2}{\left[1+(J/\pi)^2\right]^2}\left(\frac{D}{r}\right)^2 \\ &\times\left[\frac{1}{2}(0.7)eM_t\sin\beta\right]^{2mB} \\ &\times\left[\cos\beta+\frac{2}{(0.7)M_t}\frac{k_Q}{k_T}\right]^2 \\ &\times\left[\frac{e}{\sqrt{2\pi}}\left(\frac{mB}{mB+1}\right)^{mB+1/2}\right]^2\left[\delta(\omega\pm mB\Omega)\right], \quad m>0\end{aligned} \tag{7.2}$$

where $e = 2.71828$. Whereas the asymptotic formula used is,

$$\lim_{\xi\to 0} J_n(\xi) = \frac{(\xi/2)}{\Gamma(n+1)} \tag{7.3}$$

which may be reduced to Equation 4.27 implemented within MONTANA.

Finally, the ESDU 76020 tool implements a method again based on the original Gutin model, to estimate the first harmonic sound pressure level, together with corrections that enable estimates of higher harmonic levels to be derived. The method is applicable to rotors up to 20 m/s (accurate to approximately 0.2 dB up to a flight Mach number of 0.46 and a propeller tip rotational Mach number of 0.677). Details of the specific models, corrections and graphical tools may be found through the ESDU distribution.

MONTANTA predictions

Two types of MONTANA predictions are looked at. All results in this section concern the loading noise source, therefore SPL refers to $p_{mL} + p_{mD}$. OASPL refers to the sum over all harmonics. First, the outcome of expression 4.84, which is referred to as "MONTANA". All harmonics are computed independently and compared to the benchmark tools. The second type of prediction, uses the fundamental tone and normalised spectral shape function method developed for the used within MONTANA. This is referred to as "fundamental and shape function", and is the outcome of Equation 4.86, when using the Hanson approximation to estimate the change in fundamental tone (Equation 4.88) and shape function 4.91.

Test Case

A representative aircraft for the application of MONTANA is the Cessna 172 Skyhawk. A typical operating profile for the Cessna propeller (and any single engine general

aviation aircraft) would encounter a maximum tip Mach number of ≈ 0.85. General characteristics in terms of performance and operation may be seen in Table 7.1.

Typical certification conditions for GA vehicles, as per Chapter 6 and 10 of the Annex 16, require flyover noise to remain below a limit. Relatively low advance flight Mach numbers (0.2-0.3), ensure that the helical (or relative) tip Mach number also remains subsonic. Although the propeller tip remains subsonic, such rotational speeds increase the energy in the higher harmonics, meaning the harmonic range of concern at the flyover condition is between $m = 1$ and $m = 10$. All following results are presented at an observer located at a distance of 100 m and at a polar angle of $\beta = 105$deg. The emission angle is assumed to be the angle of maximum emission, and is the same angle used in the ESDU tool.

Loading for the flyover operating condition was calculated using a combination of XFOIL and XROTOR. A generic NACA 2412 aerofoil was decided upon, rather than more advanced GA aerofoil designs [194, 195] such as the GA(W)-2 and ARA-D family of aerofoils. As defined in the noise source method, average quantities are assumed over the entire blade.

TABLE 7.1: Design and operation characteristics of the Cessna 172

Cessna 172 Skyhawk		
Parameter	Value	Units
Power	134.23	kW
Rotation speed (@ Max Take-off)	2700	rpm
Number of blades	2	-
Diameter	2	m
Average blade thickness	0.012	m

Figure 7.1 compares the SPL (not A-weighted) predictions of the first ten harmonics of the BPF for three different rotational speeds. The average chord length of the propeller blade is $c = 0.15$, and constant loading of the blade is assumed. Good agreement of the fundamental tone is seen across all tools, with variation being < 0.4 dB, for all rotational speeds. An RPM of 2,500 corresponds to a tip Mach number of $M_t = 0.77$. The MONTANA prediction, is almost identical to that of the spectral density function by Blake, which makes sense as the underlying assumption of the small argument approximation is the same. Slight differences are due to blade definition and operation in the evaluation of the integral over the chordwise and radial directions.

MONTANA agrees with the ESDU tool prediction well for the first four harmonics, with a slight over-estimation occurring on behalf of MONTANA between $m = 5$ and $m = 8$, and an under-estimation for $m > 8$. It is expected that the shape of the harmonics in the ESDU predictions deviates from those of the generic Gutin implementations, as empirical corrections have been applied within 76020 [193] to account for higher modal content.

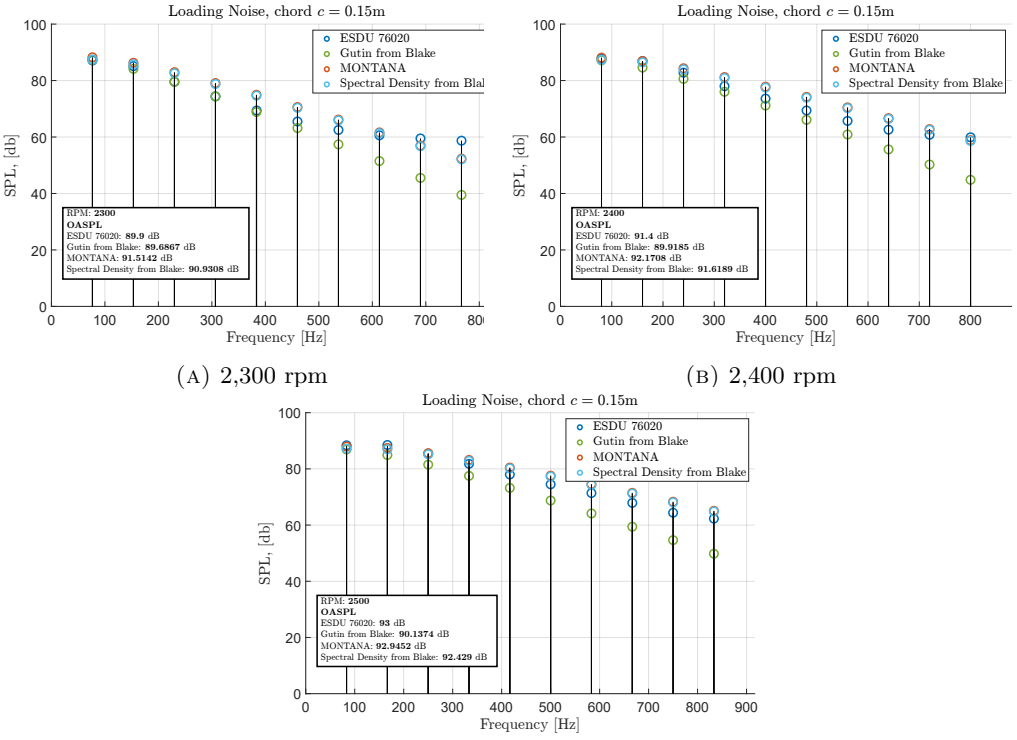

(A) 2,300 rpm

(B) 2,400 rpm

(C) 2,500 rpm

FIGURE 7.1: Comparison of first 10 harmonics as predicted by four different methods for an average chord length of $c = 0.15$m. OASPL values are indicated in the box on the bottom left of each figure.

Finally, the "Gutin from Blake" result shows a higher rate of decay relative to the all other tools. This is an indication that the difference between the Bessel function and its small argument approximation increases for higher orders.

In the case of Figure 7.1 the first four harmonics dominate the OASPL, with a difference of 1.37 dB between the MONTANA and the "Gutin from Blake" predictions for 2,300 RPM and 2.7 dB for the high RPM setting of 2,500.

Figure 7.2 shows the equivalent A-weighted harmonic spectrum of the SPL results in Figure 7.1. The application of the A-weighting shifts the dominance from the fundamental tone to the harmonic of $m = 3$. It is more evident that the higher harmonics have a larger contribution with increasing rotational speed, as the harmonic shape flattens out. The variation of the OASPL increases as a result.

The difference in the estimation of higher harmonics between MONTANA and ESDU is illustrated in Figures 7.3 and 7.4. The ESDU results have an sigmoid-like shape, while the "fundamental and shape function" ones decay almost linearly after the fundamental and second harmonic.

Referring to Figure 4.6 of Chapter 4, it is evident that in the case of the high rotational speeds as indicated in Figures 7.3 and 7.4 the higher order modes are increasingly

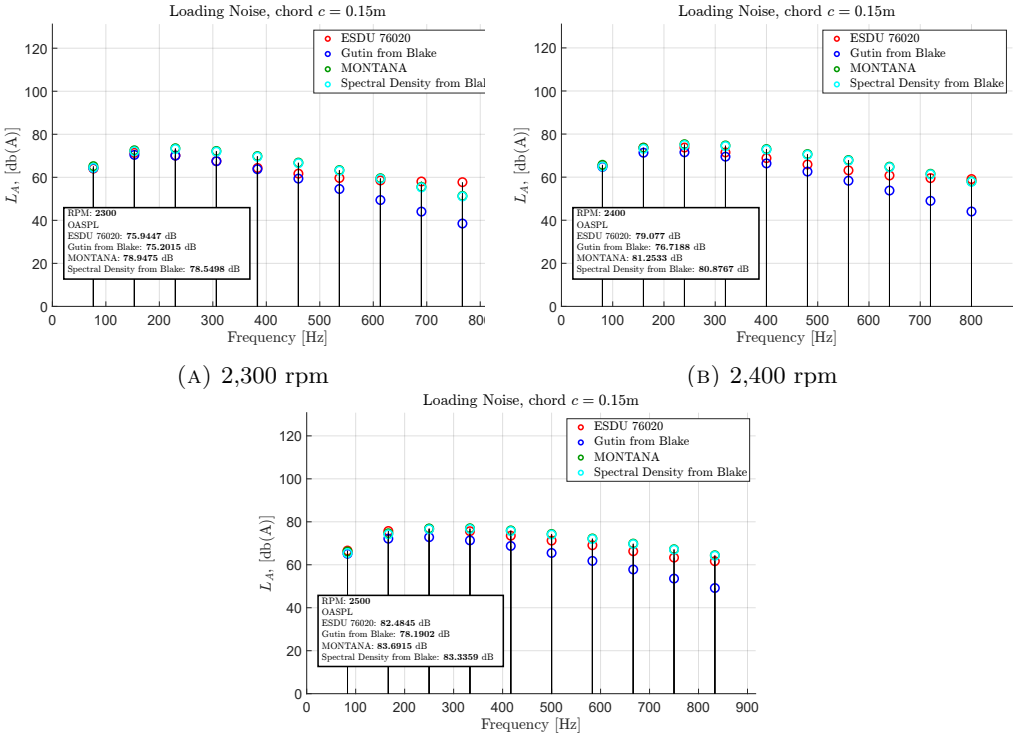

(A) 2,300 rpm

(B) 2,400 rpm

(C) 2,500 rpm

FIGURE 7.2: Comparison of first 10 harmonics as predicted by four different methods for an average chord length of $c = 0.15$m. A-weighting has been applied to the noise levels. OASPL values are indicated in the box on the bottom left of each figure.

becoming more efficient contributing to the OASPL. The over-estimation observed in the higher harmonics is once again attributed to the deviation from the asymptotic behaviour of the Bessel function as $\arg J_{mB} \to 0$.

The "fundamental and shape function" solution does not deffer to the MONTANA solution in principle, however Equation 4.86, allows for any spectral shape normalised to the fundamental tone to be used in the place of ΔF_1. This is the key feature of MONTANA, introduced within this thesis, allowing the use of any shape function that the user has access to. This function, may be in the form of an analytical method or empirical data (as is the case with ESDU). This allows MONTANA to be modular and flexible in regard to its use, and the amount of data available. The shape function investigated with this section (which is a result of the Hanson model approximation), any form a starting point of an analysis, with MONTANA being fed data of increased fidelity as the design progress and test or rig data is available.

An additional scenario was calculated and compared, for average blade chord length of $c = 0.2$ m. Unweighted results can be seen in Figure 7.5, while the equivalent weighted ones in Figure 7.6 Over all the trends remain the same, with good agreement observed in the first few harmonics of the spectrum and under-prediction relative to the ESDU corrected higher harmonics.

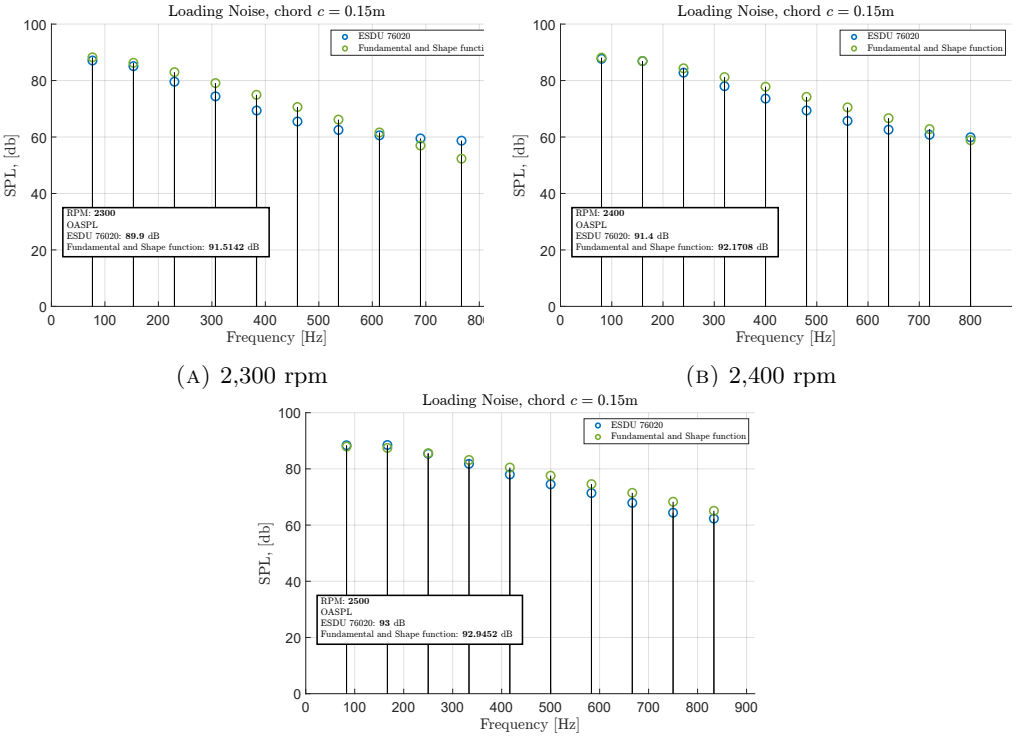

(A) 2,300 rpm

(B) 2,400 rpm

(C) 2,500 rpm

FIGURE 7.3: Comparison of first 10 harmonics as predicted by ESDU 76020 model and the proposed fundamental and shape function method based on Hanson, for an average chord length of $c = 0.15$m. OASPL values are indicated in the box on the bottom left of each figure.

An observation is made in Figure 7.5 in the case of the higher rotational speeds 2,400 and 2,500 RPM. The harmonic shape predicted by the asymptotic approximation tends to match the exact Gutin solution offered by the ESDU model, indicating that fewer corrections are applied at higher operational tip speed and the approximation more accurately captures the trend.

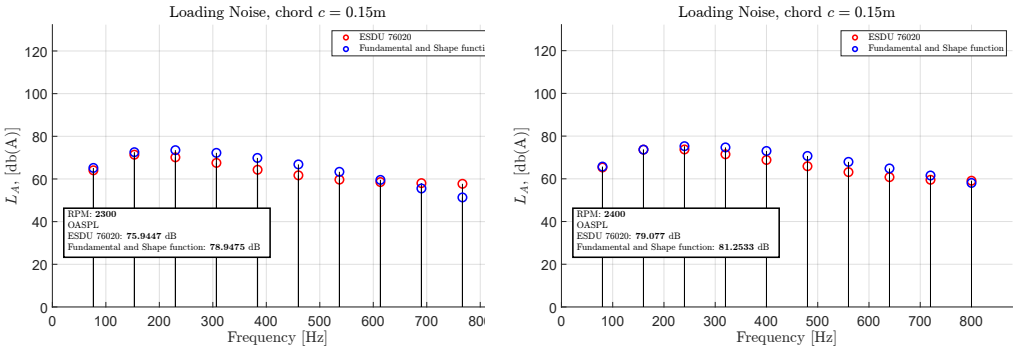

(A) 2,300 rpm

(B) 2,400 rpm

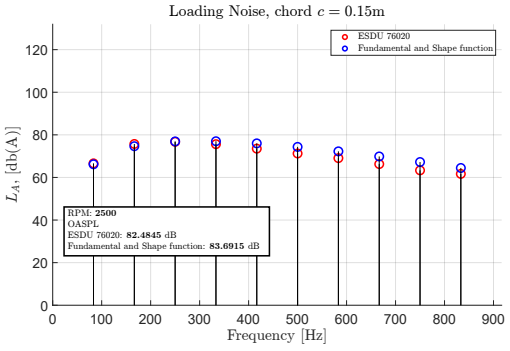

(C) 2,500 rpm

FIGURE 7.4: Comparison of first 10 harmonics as predicted by ESDU 76020 model and the proposed fundamental and shape function method based on Hanson, for an average chord length of $c = 0.15$m. A-weighting has been applied to the noise levels. OASPL values are indicated in the box on the bottom left of each figure.

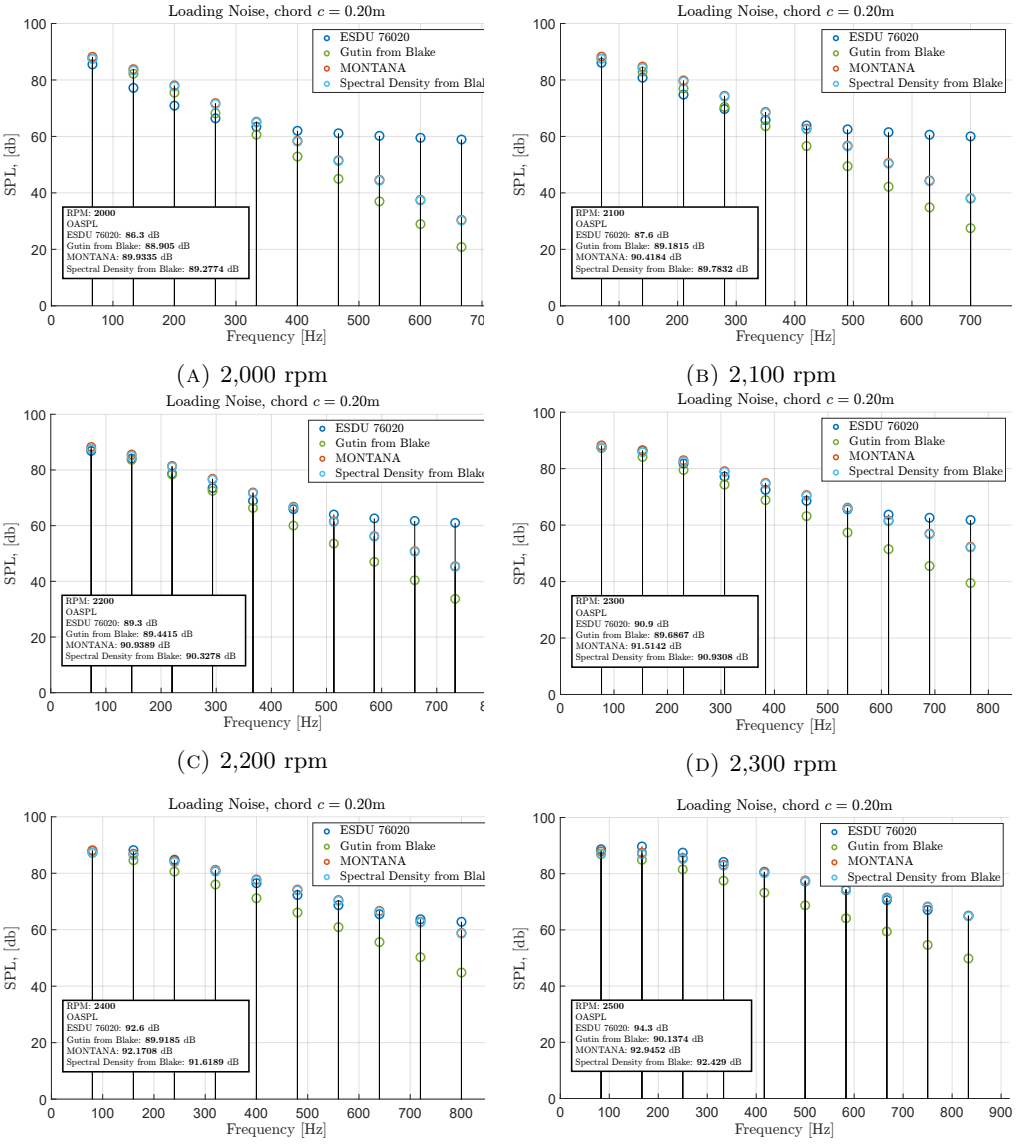

(A) 2,000 rpm

(B) 2,100 rpm

(C) 2,200 rpm

(D) 2,300 rpm

(E) 2,400 rpm

(F) 2,500 rpm

FIGURE 7.5: Comparison of first 10 harmonics as predicted by four different methods for an average chord length of $c = 0.20$ m. OASPL values are indicated in the box on the bottom left of each figure.

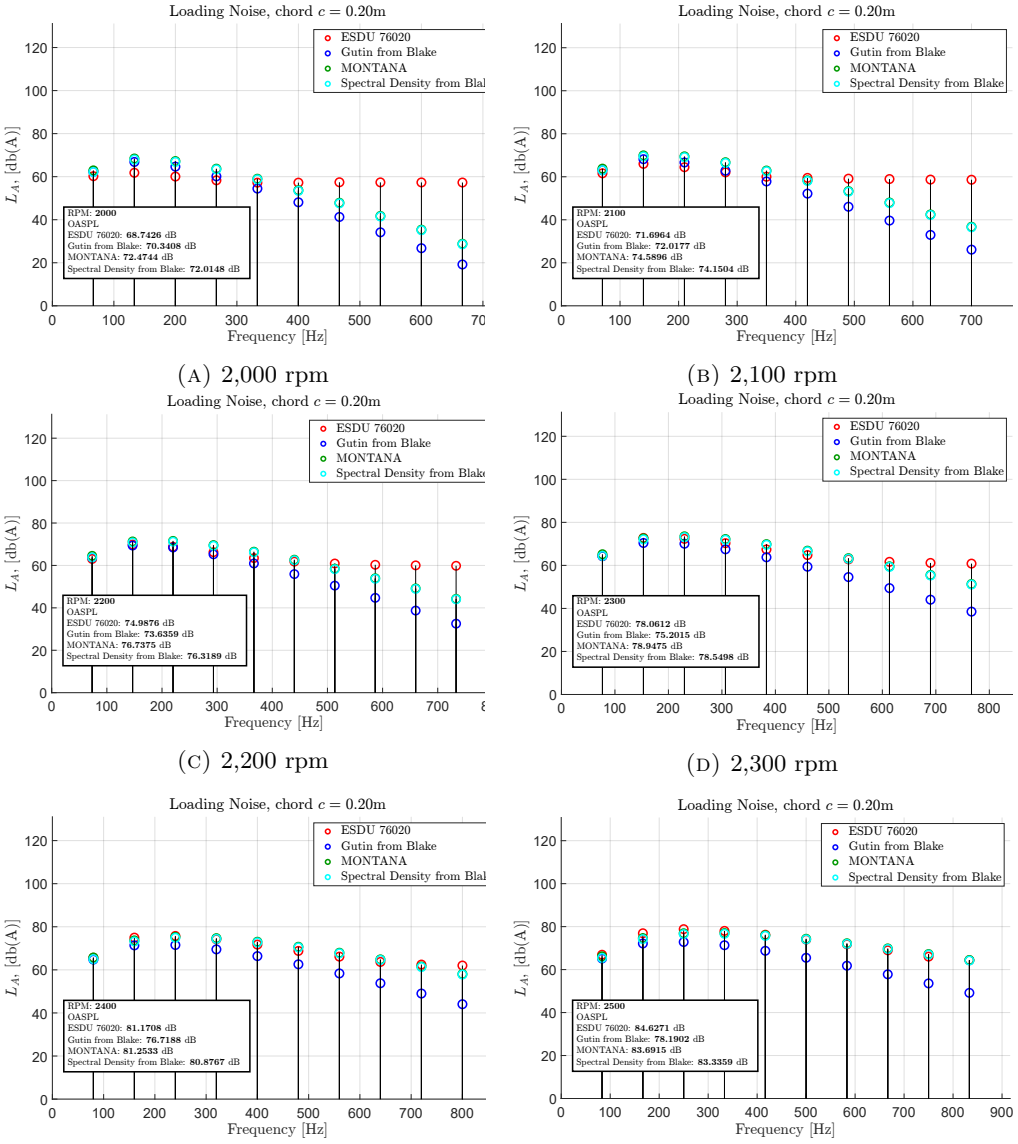

(A) 2,000 rpm

(B) 2,100 rpm

(C) 2,200 rpm

(D) 2,300 rpm

(E) 2,400 rpm

(F) 2,500 rpm

FIGURE 7.6: Comparison of first 10 harmonics as predicted by four different methods for an average chord length of $c = 0.20$m. A-weighting has been applied to the noise levels. OASPL values are indicated in the box on the bottom left of each figure.

7.1.2 Comparison to Hanson frequency domain model

The predictive capability of the results obtained in Chapter 4 are compared to that of the original Hanson model. The implementations of the Hanson model used within this Chapter, is described and validated in detail within Appendix A. It utilises a combination of the open source XFOIL [196] and XROTOR [197] for the calculation of propeller aerodynamic performance used as inputs. The actual far field frequency domain noise model is based on original papers by Hanson et al. [60, 198, 199] and also the propeller and propfan noise chapter in [36] by Magliozzi, Hanson and Amiet.

Two sets of calculations are presented. First, calculations of the loading noise source of two-bladed and four-bladed, GA propellers have been made in order to evaluate the magnitude of error of the asymptotic approximation. In this case, three different flight Mach numbers are compared, 0 (static), 0.2 and 0.4 (on the high end of GA operational conditions) and a tip rotational Mach number of 0.3 and 0.6. These results are presented in Figures 7.7 and 7.8.

Figure 7.7 shows the results for the two-bladed 2 m propeller. As expected, for low tip Mach number and the fundamental and second harmonic dominate the spectrum, and the difference in estimation between the approximation and the full model are almost negligible. Over-prediction in the harmonic levels is evident as axial flow is introduced. The shape of the spectrum is conserved, with the error increasing (however at a slower rate) as the harmonic number increases.

In the case of the four-bladed 1.4 m diameter propeller, the trends remain the same. The nature of the now harmonic series with fundamental tone at, $mB = 4$, defined by the Bessel function has shifted the "cut-off" (as described by Roger et al. [200]) point reducing the efficiency of the loading source. However, the argument remains relatively large (larger in fact than in the case of the two-bladed propeller) when compared to the order, meaning that the error in the estimation of the levels has slightly increased. These results can be seen in Figure 7.8.

Overall, two interesting observations can be made regarding the case of the four-bladed propeller; i. the reduction in over all noise and ii. the reduced influence of flight Mach number of the levels and harmonic shape. MONTANA demonstrates the ability to capture this effect almost identically to the Hanson model.

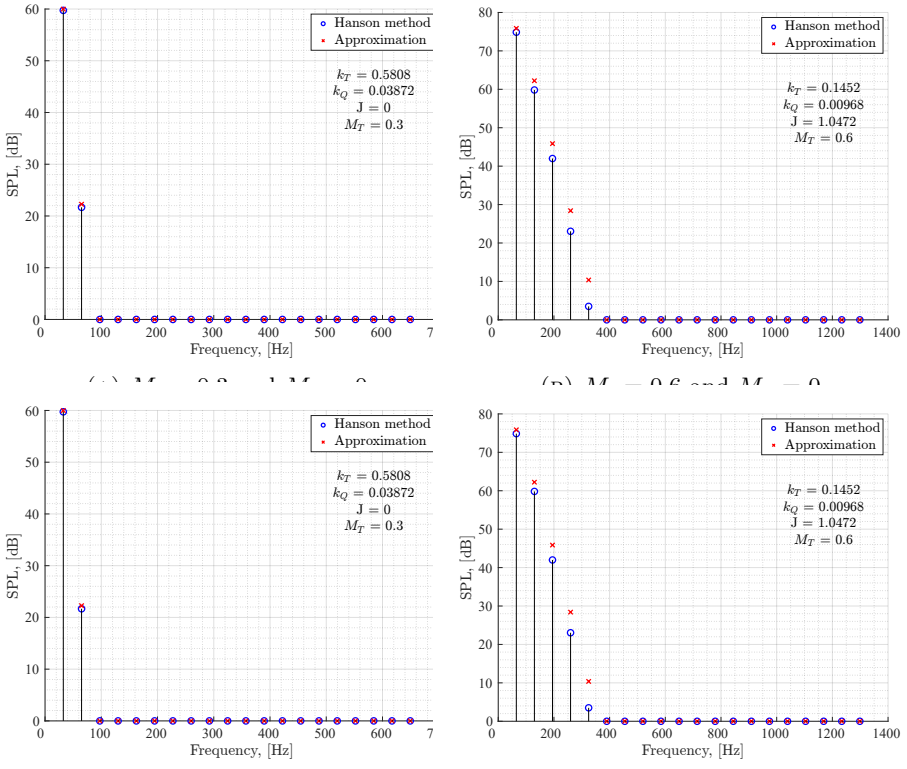

(c) $M_t = 0.3$ and $M_x = 0.2$ (d) $M_t = 0.6$ and $M_x = 0.2$

FIGURE 7.7: Loading noise of a two-bladed, 2 m diameter propeller.

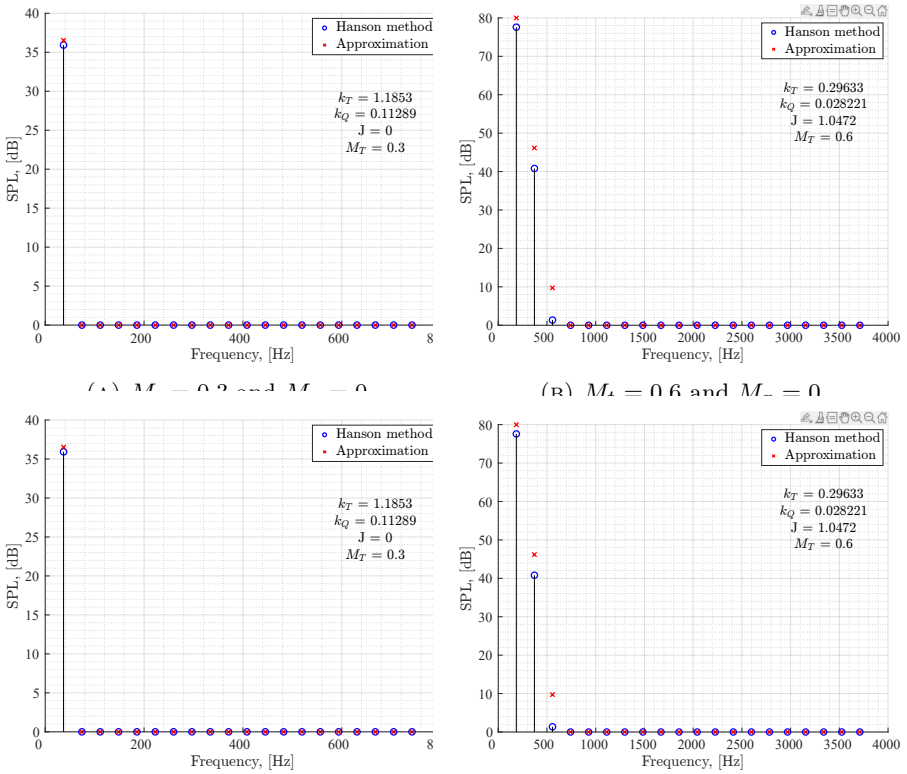

(c) $M_t = 0.3$ and $M_x = 0.2$ (d) $M_t = 0.6$ and $M_x = 0.2$

FIGURE 7.8: Loading noise of a four-bladed, 1.4 m diameter propeller.

In the second set of results, a parametric sweep of operating conditions is looked at in Figures 7.9 to 7.14. The comparisons in all figures illustrate the difference in predictive capability between MONTANA and the Hanson implementation, when estimating changes in noise levels between two cases. Absolute noise level comparisons have been shown previously.

Results are presented in terms of deltas (Δ) relative to a baseline case of a static four-bladed, 1.4 m diameter GA propeller running at 2,237 rpm (equivalent to a 0.48 tip Mach number) and producing 785 N of thrust. The parameter sweep is performed over the thrust and rotational speed of the propeller, with thrust T in Newtons ranging from between $0 \leq T \leq 2,000$ and rotational speed between $0 \leq \text{RPM} \leq 4,100$ or $0.3 \leq M_t \leq 0.88$. Results are presented at an observer location 10 m away from the propeller hub centre, at a polar angle of $\beta = 105$ deg.

The surfaces in Figure 7.9 show the predicted change in sound level of the fundamental tone or $\Delta SPL_{f,1}$ as functions of the rotational speed and average lift coefficient of the propeller blades, referenced to the baseline scenario level (i.e. the baseline point would be represented by a single point on the surface).

Specifically, the deltas in each subplot of Figure 7.9 represent i.(top left),

$$\Delta L_{\text{Hanson}} = L_{\text{Hanson}} - L_{Hanson,baseline} \tag{7.4}$$

ii. (top right),

$$\Delta L_{\text{MONTANA}} = \Delta L_{f_1} \tag{7.5}$$

with Δ_{f_1} defined in Equation 4.88 corrected in the previous section. And iii. (bottom),

$$\text{Error} = \Delta L_{\text{Hanson}} - \Delta L_{\text{MONTANA}} \tag{7.6}$$

The results of Equations 7.4, 7.5 and 7.6 are referred to as “Hanson”, “Montana” and “Error” respectively in the rest of this Section.

Throughout the entire parametric sweep, the Error ϵ introduced by the asymptotic approximation is between $-9\text{dB} < \epsilon < +2\text{dB}$. A range of 10 dB is substantial, however these occur at the extremes of propeller loading and rotational speed. These extremes represent great deviation from the original baseline scenario, meaning that the linear approximation of the lumped source model potentially breaks down. An investigation into the limitation of this deviation is presented in Section 7.3.

However, considering the variation within what could be considered as an operational envelope of a single design, the Error remains limited significantly to $-2\text{dB} < \epsilon < +1.5\text{dB}$.

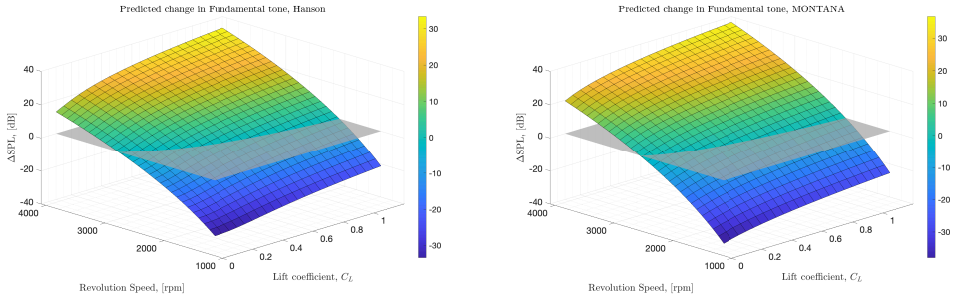

(A) Hanson

(B) MONTANA

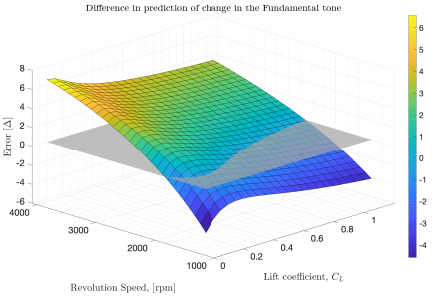

(C) Difference between the two estimation models.

FIGURE 7.9: Estimated change in the fundamental tone as a function of axial loading and propeller rotation speed (rpm). The $z = 0$ plane is indicated with grey colour.

Following comparisons are made using the Overall Sound Pressure Level (OASPL), as measure of noise intensity (quantifying PWL and directivity changes as functions of geometry and operation), and not subjective human response. Constant loudness metrics are reconsidered in the generation of the NPD curves and calculation of certification point limits in the appropriate metrics, when quantifying noise on the ground.

For a constant rotational speed, Figure 7.10 shows how MONTANA captures the dependence on axial loading. On the other hand, 7.11 gives the OASPL as function of rotational speed for a given thrust. Both these figures may be interpreted as 2D slices of the surfaces in Figure 7.9 if all contributions from the harmonics where added to give the OASPL. The Error is measured on the right-hand y-axis, as it is of different scale relative to the predicted deltas.

In Figure 7.10 the rotational speed is kept at the nominal value of 2,040 RPM (or $M_t = 0.44$, i.e. below that of the baseline case). Both models predict the reduction in noise level due to the reduced RPM, with an interesting pattern emerging for the error. The error (or better interpreted in this case as the difference) becomes zero around an average $C_L = 0.5$, shifted from the baseline value of $C_L = 0.75$. As the 2,040 RPM plane , the error ranges between $-1.5\text{dB} < \epsilon < 1.2\text{dB}$ for any value of C_L, for almost feathered propeller to an almost stalled average condition of the blade.

In Figure 7.11 the point at which the two predictions cross the $x = 0$ axis, indicates the baseline configuration and therefore a 0 dB change in noise level as expected is returned.

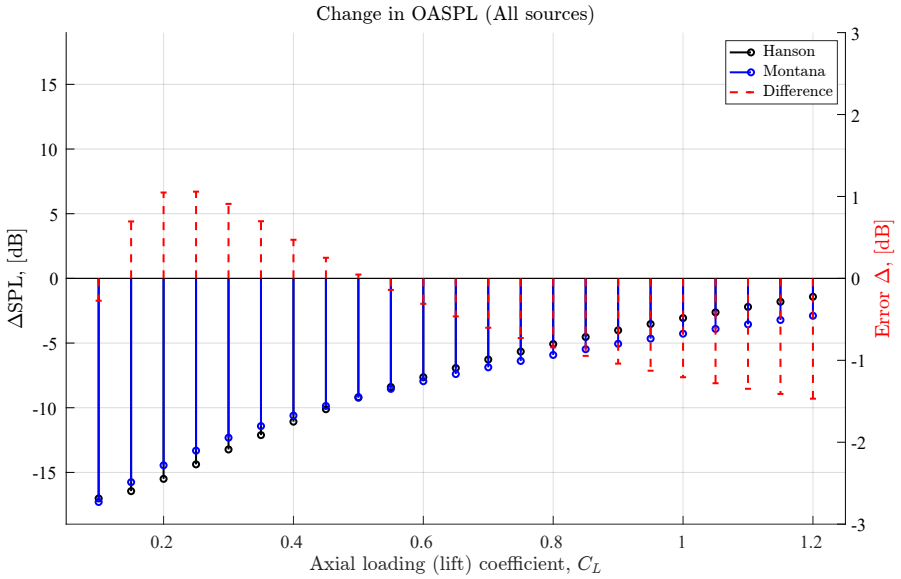

FIGURE 7.10: Estimated change in OASPL between a baseline case and a modified (novel) scenario for various loading conditions. Comparison is made between original Hanson model and MONTANA in estimating changes, and error (difference) between the two models is given on the right-hand axis.

The dependence of OASPL on rotational speed is almost identical between the two, with MONTANA once again over estimating the changes. The logarithmic nature of the noise level is evident in the trend, and as will be discussed in the following section the exact scaling of the OASPL with Ω is not global. In the regions of low rotational speed, the trend follows the fundamental tone. However, as the propeller tip approaches supersonic speeds and the higher harmonics contribute more to the total acoustic field, the trend follows the scaling of the dominant harmonics, although not perfectly, as energy in the adjacent modes is significantly contributing.

Figures 7.12 to 7.14 show how the harmonics of the fundamental also change as functions of the two parameters, with respect to the baseline. Harmonics up until harmonic mode number $m = 5$ are shown. The variation in the scaling of the harmonics is evident, and MONTANA once again captures this relation, as can be seen in the Error plots. The error, as expected grows for larger harmonic numbers and for large deviation from the baseline scenario.

With the analysis presented, the asymptotic approximation to the Hanson model in combination with the main MONTANA framework is regarded as capable in capturing changes in noise levels of steady harmonics as function of operation and design changes and providing predictions of the noise source behaviour when detailed propeller design and operation is not available.

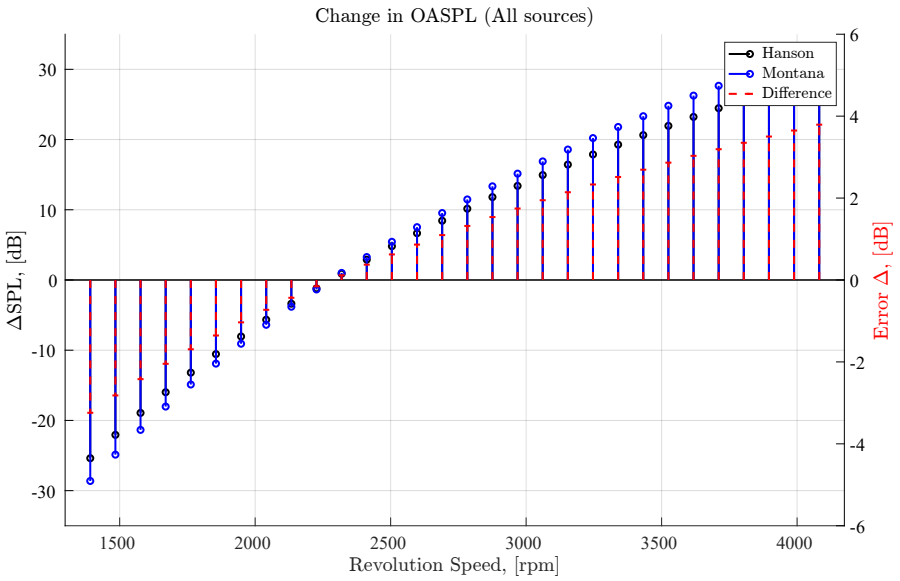

FIGURE 7.11: Estimated change in OASPL between a baseline case and a modified (novel) scenario for various propeller rotation speeds. Comparison is made between original Hanson model and MONTANA in estimating changes, and error (difference) between the two models is given on the right-hand axis.

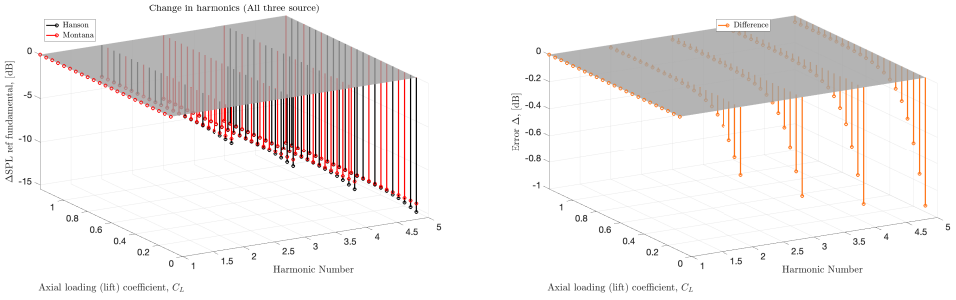

(A) Hanson compared to MONTANA. (B) Difference between the two models.

FIGURE 7.12: Estimated change in the harmonics relative to the fundamental tone as a function of axial loading. The $z = 0$ plane is indicated with grey colour.

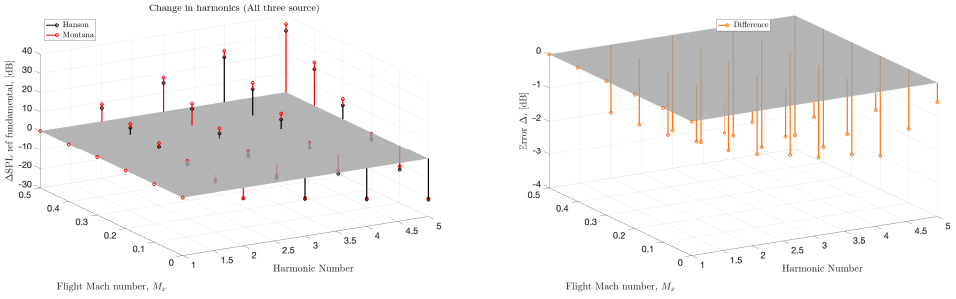

(A) Hanson compared to MONTANA. (B) Difference between the two models.

FIGURE 7.13: Estimated change in the harmonics relative to the fundamental tone as a function of flight Mach number. The $z = 0$ plane is indicated with grey colour.

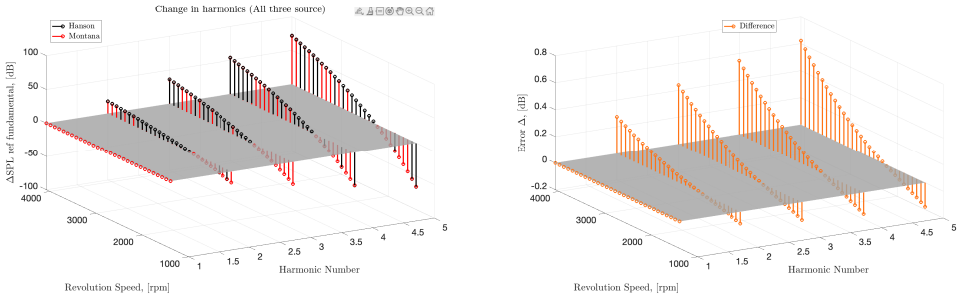

(A) Hanson compared to MONTANA. (B) Difference between the two models.

FIGURE 7.14: Estimated change in the harmonics relative to the fundamental tone as a function of propeller rotation speed (rpm). The $z = 0$ plane is indicated with grey colour.

7.1.3 Propeller noise scaling parameters

Figure 7.15 shows the results of different noise components for a two-bladed rotor with the rotation speed ranges from 60 to 120 RPS, when calculated using the full Hanson implementation. The observer radius is $R = 15$ m (i.e. in the far field). The secondary axis in each of the Figures shows a collapsed version of the results, when they are normalised by parameters identified in the analysis and integral evaluation of Section 4.4.

In the case of the thickness noise p_{Vm} determined by Equation 4.54, in a hovering case ($M_x = 0$), the dependence on the tip Mach number is of the order M_t^{mB+2} or by setting $M_t = \Omega r_t / c_0$, the results collapse when normalising with Ω^{mB+2}. The drag loading (azimuthal) noise p_{Dm}, follows the same trend when normalising Equation 4.66 by the same factor.

The results for the lift (axial) loading noise p_{Lm} in Equation 4.64 are proportional to M_t^{mB+3} in a hovering case. Converting to a rotational speed, it scales with Ω^{mB+3}, as may be seen in Figure 7.15b. The total noise radiated by the propeller also scaled well by Ω^{mB+2} as may be seen in Figure 7.16 for the fundamental tone.

An obvious difference in the sound directivity patterns is observed between the thickness and drag noise components and that of the lift noise. For p_{Vm} and p_{Dm} the radiation pattern is symmetric about $\theta = \pi/2$, while for the axial loading noise p_{Lm} the peaks occur around $\theta = \cos^{-1}(\pm\sqrt{3})$ (about 54.7° and 125.3°). Due to the influence of the lift loading noise, the total sound pressure is asymmetric about $\theta = \pi/2$.

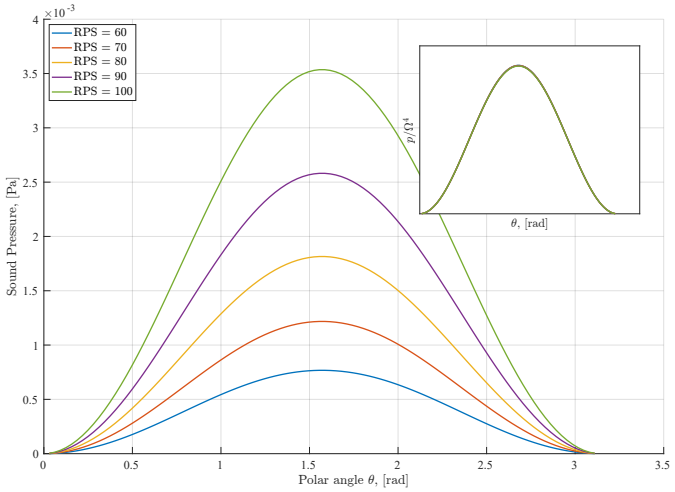

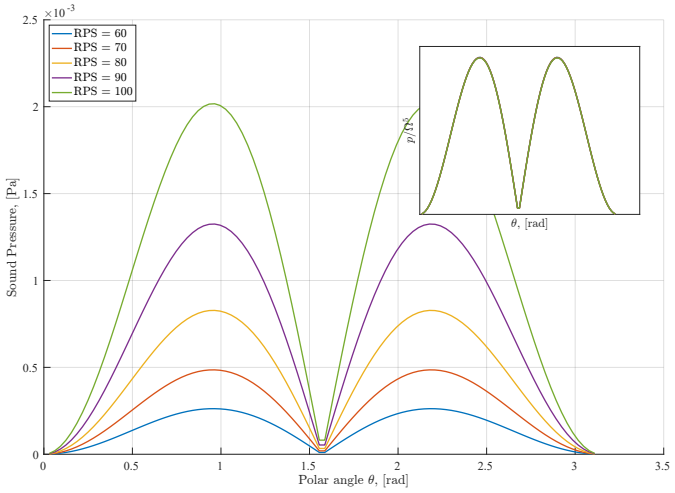

(B) Axial loading noise (lift) source.

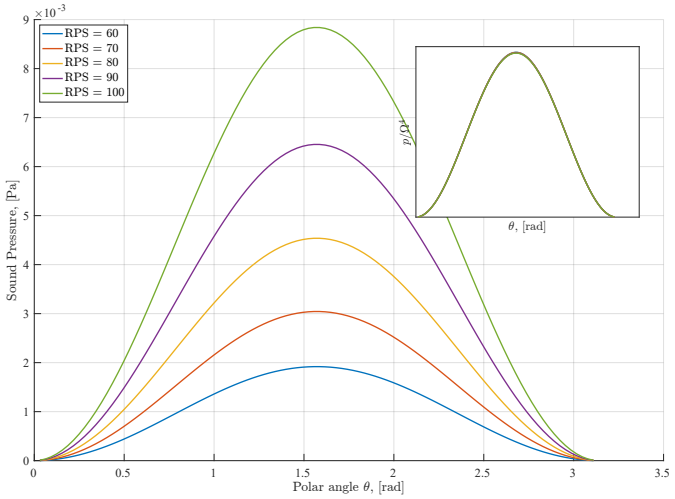

(C) Volume (thickness) noise source.

FIGURE 7.15: Individual propeller noise sources as function of observer polar location. Sound pressure of fundamental tone (m = 1) indicated for a range of rotation speeds. Scaling laws indicated in top right axis, showing the collapsed results.

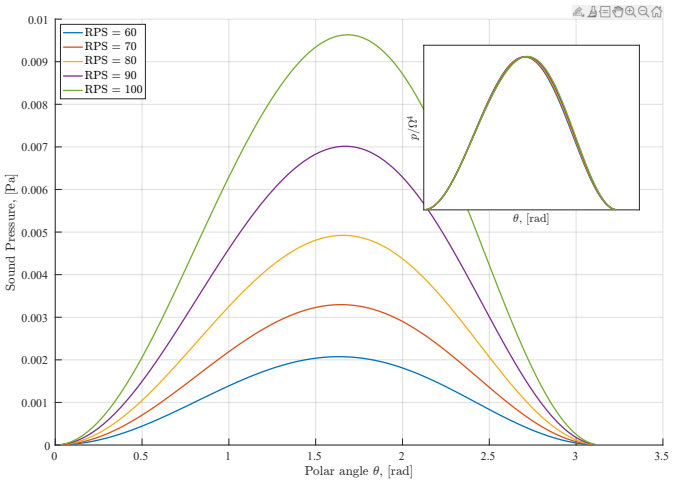

FIGURE 7.16: Total propeller harmonic noise as function of observer polar location. Sound pressure of fundamental tone (m = 1) indicated for a range of rotation speeds. Scaling laws indicated in top right axis, showing the collapsed results.

7.1.4 Comparison between estimated and published NPD curves

The benchmarking study consists of comparing predicted NPD curves with published ones. The prediction capability is demonstrated through the prediction of multiple power settings, for a variety of operational configurations, using single point baseline reference. The single point baseline reference refers to the fact a single operating condition of the baseline (denoted by a red cross in result figures) aircraft is used to predict the NPD curves over a range of possible power settings. Two categories of aircraft are investigated, fixed wing and rotorcraft.

Fixed-wing propeller aircraft

The fixed wing aircraft for which predictions are made are: the Cessna 172 Skyhawk, the Britten-Norman BN-2 Islander, the de Havilland Canada DHC-6 Twin Otter, the ATR 42-300, the ATR 72-212A (or ATR 72-500) and the De Havilland Canada Dash 8 Q400. An extra aircraft is studied, the Airbus A400M Atlas, due its significantly different application (military transport aircraft) but primarily due to the combination of its unique propulsion system configuration and size. These aircraft were chosen as they cover a great variety in size and design configurations, aiming at proving that the model is applicable to subsonic propeller powered vehicles. Performance and design characteristics for each of the aircraft may be seen in Tables 7.2 and 7.3. The results for the fixed wing NPD benchmark prediction are seen in Figures 7.17 to 7.23.

Rotorcraft

Rotorcraft trajectories in AEDT are defined in terms of a sequence of flight path segment described by operational modes. A simple departure operation may be constructed from the following sequence of operational mode procedural steps: ground

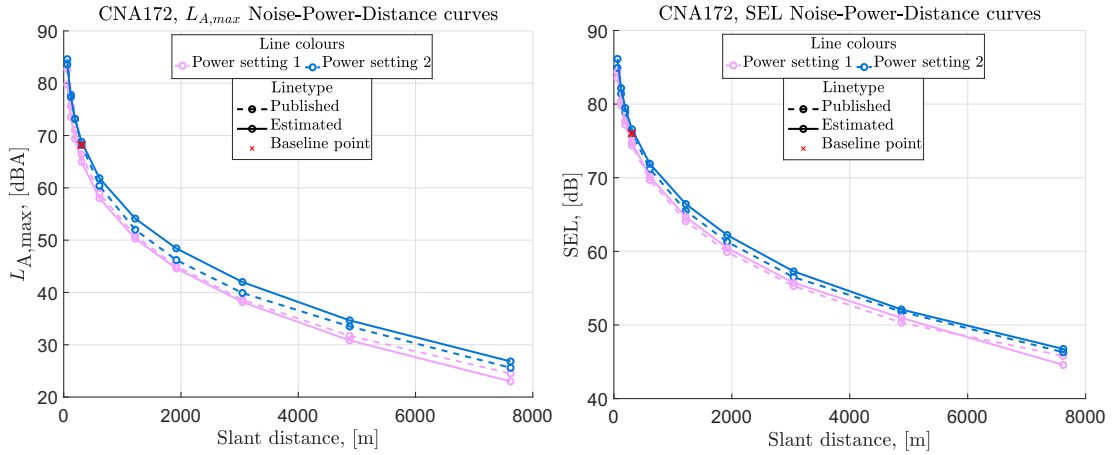

(A) $L_{\mathrm{A,max}}$ (B) SEL

FIGURE 7.17: Comparison between the predicted (by MONTANA) and published (measured [98]) departure NPD curves for the Cessna 172.

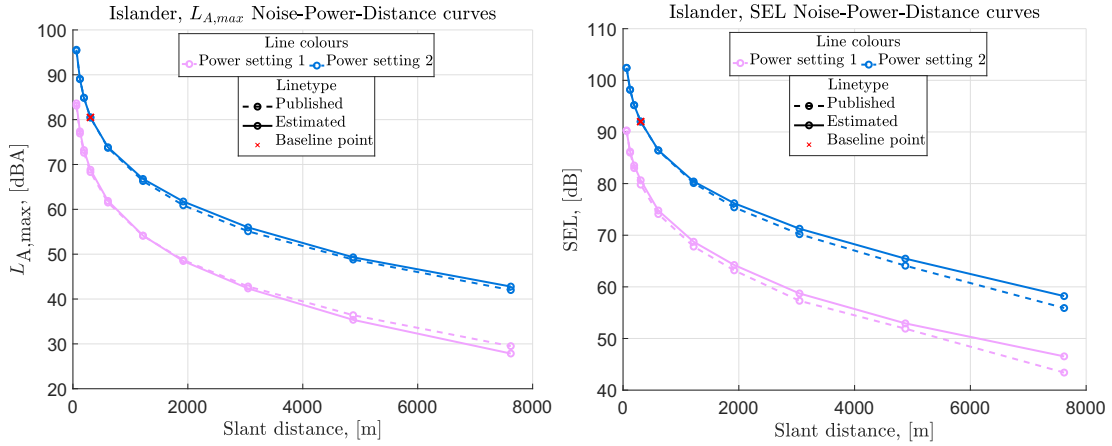

(A) $L_{\mathrm{A,max}}$ (B) SEL

FIGURE 7.18: Comparison between the predicted (by MONTANA) and published (measured [98]) departure NPD curves for the BN-2 Islander.

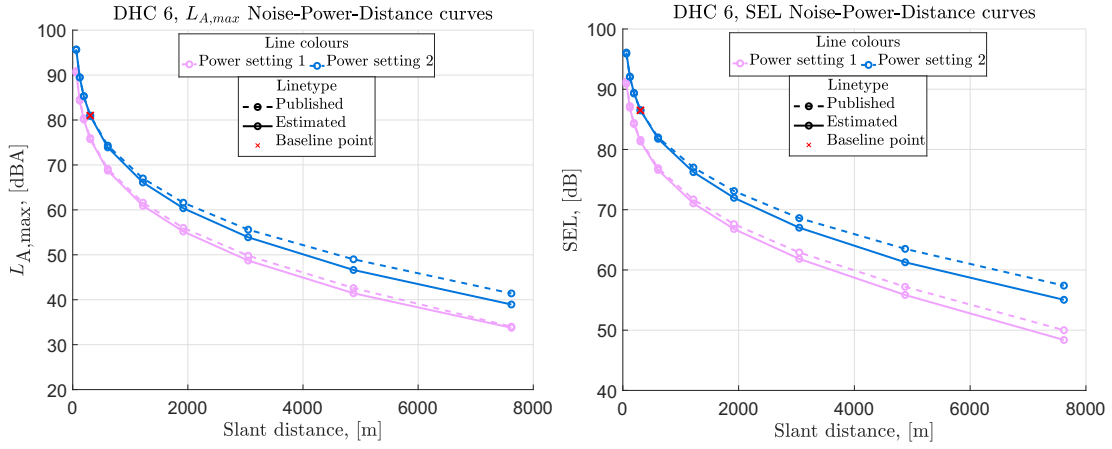

(A) $L_{\mathrm{A,max}}$ (B) SEL

FIGURE 7.19: Comparison between the predicted (by MONTANA) and published (measured [98]) departure NPD curves for the DHC-6 Twin Otter.

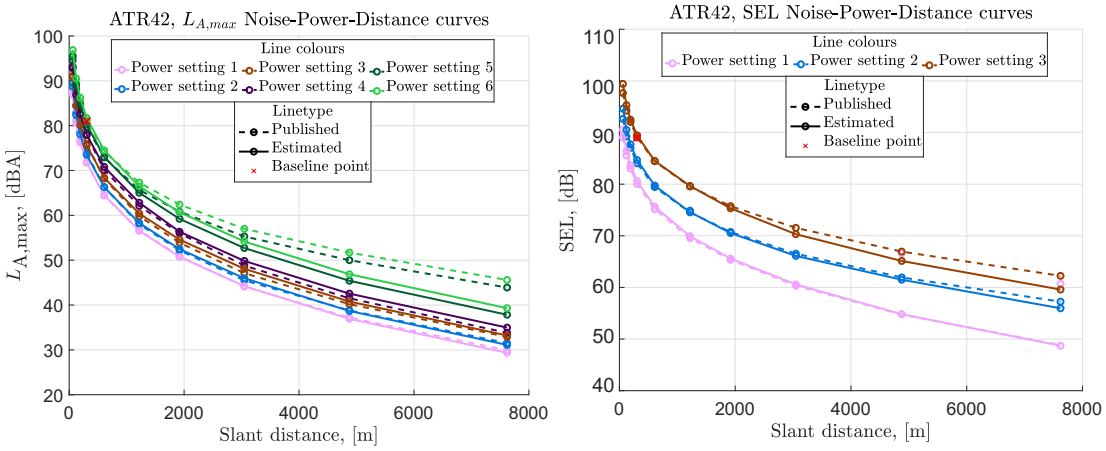

(A) $L_{A,max}$ (B) SEL

FIGURE 7.20: Comparison between the predicted (by MONTANA) and published (measured [98]) departure NPD curves for the ATR42-600.

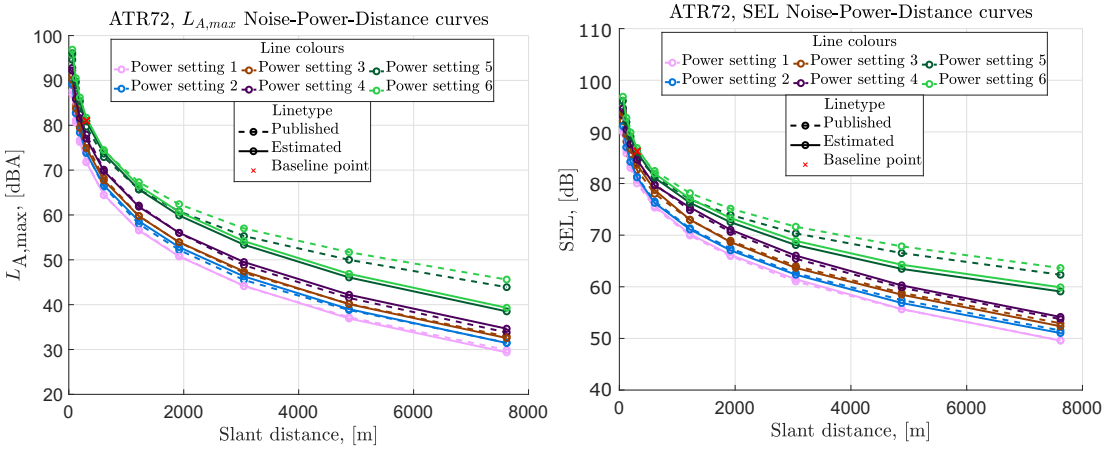

(A) $L_{A,max}$ (B) SEL

FIGURE 7.21: Comparison between the predicted (by MONTANA) and published (measured [98]) departure NPD curves for the ATR72-212A.

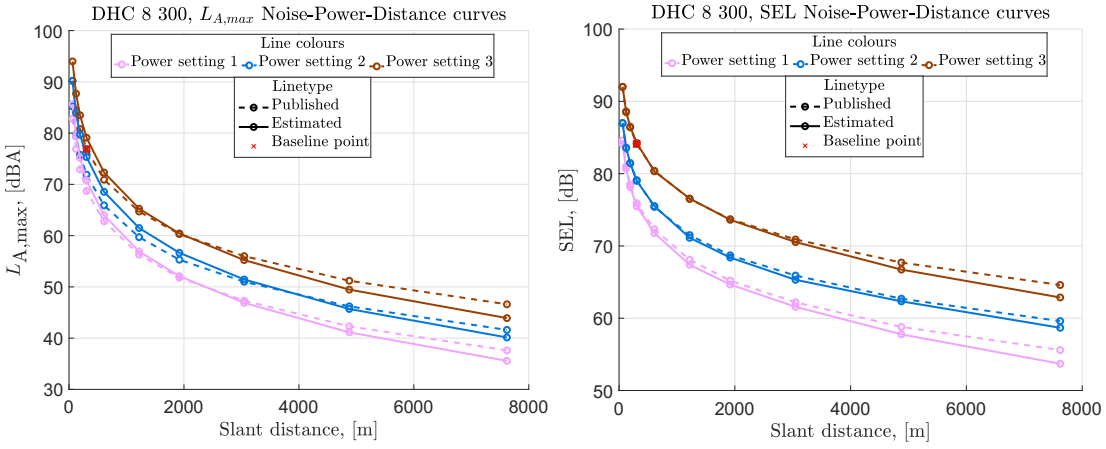

(A) $L_{A,max}$ (B) SEL

FIGURE 7.22: Comparison between the predicted (by MONTANA) and published (measured [98]) departure NPD curves for the DHC-8 (Dash 8) Q400.

TABLE 7.2: Propeller powered aircraft performance inputs used for verification study.

Aircraft				
	Cessna 172	BN-2 Islander	DHC-6 Twin Otter	ATR 42-300
No. of Engines	1	2	2	2
Prop Diameter, m	1.98	1.98	2.6	3.93
No. of Blades	2	2	3	6
RPM	2,700	2,700	2,110	1,200
MTOW, kg	1,156	2,994	5,670	18,600

TABLE 7.3: Continuation of Table 7.2.

Aircraft			
	ATR 72-212A	Dash 8 Q400	Airbus A400M Atlas
No. of Engines	2	2	4
Prop Diameter, m	3.93	4.11	5.3
No. of Blades	6	6	8
RPM	1,200	1,020	860
MTOW, kg	23,000	27,987	141,000

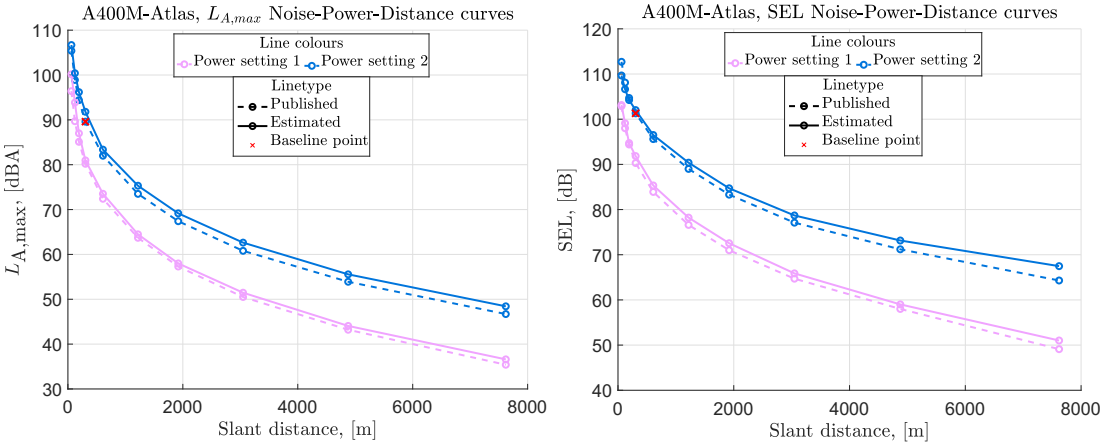

(A) $L_{A,max}$ (B) SEL

FIGURE 7.23: Comparison between the predicted (by MONTANA) and published (measured [98]) departure NPD curves for the Airbus A400M.

idle → flight idle → vertical ascent → departure with climbing acceleration → level flyover with constant speed. The noise data are specified as a function of operational mode (instead of power) and distance, though are still referred to as NPD data. Procedures for the AEDT rotary-wing operational mode might be either dynamic or static. A list of all operational modes considered within AEDT, as well as the different classifications may be seen in the technical manual [201]. In the case of MONTANA, and this benchmarking case, NPD curves for four types of operations are generated and compared. Those are departure, idle, hover and level flyover noise curves. In the level flyover case, directivity effects are investigated by comparing the two lateral NPD curves

used along with the under flightpath (conventional) curve. The benchmark predicted NPD curves are shown in Figures 7.24 to 7.26.

As discussed by Rizzi et al. [112] a grey region exists between what is considered a vertical ascent and a constant speed departure. In the context of AEDT, this region could be populated with multiple sets of different operational modes, depending on the nature of the operation itself and the configuration of the vehicle. For this section static operational modes assume flow into the rotor due to vehicle translation, this applies to the idle and hover operations. Departure and flyover include an inflow velocity component to the rotors.

The rotorcraft studied are, the Schweiser 300C, the Eurocopter AS365 Dauphin and the Boeing CH-47 Chinook. These choices also cover a range of size and configurations. Rotorcraft NPD curves, are different to conventional fixed-wing NPD curves due to different types of operations they are capable of performing (see Chapter 2). In addition, the flyover operation comes with an additional complexity, that is directivity effects.

Table 7.4: Helicopter performance inputs used for verification study.

Helicopter			
	Schweiser 300C	Eurocopter AS365 Dauphin	Boeing CH-47 Chinook
No. Main Rotors	1	1	2
No. Blades	3	4	3
Rotor Diameter, m	8.18	11.94	18
RPM	471	350	225
MTOW, kg	930	4,300	22,680

It should be noted that there is no standard for producing rotary-wing NPD data, in contrast to the techniques used to produce fixed-wing NPD data, which largely follow AIR 1845A23. The procedures employed in this thesis, to the greatest degree practicable, are in line with those for helicopter certification specified in 14 CFR Part 36 Appendix H, implemented in a computational way as in the case for the fixed-wing. Details of the directivity assumptions are given in Section 7.2.2 where a contour comparison is presented.

Effect of baseline aircraft choice

This section demonstrates the ability of MONTANA to provide estimates for novel aircraft irrespective of the baseline aircraft. This is important as available data may limit the options available for choosing appropriate reference aircraft. However, as discussed, an aircraft qualifies for consideration as a baseline for the prediction model when the dominant noise sources are assumed to match those of the concept being examined. This makes aircraft of the same line and variants the ideal first options. Typically, aircraft are designed based on replacing current technology, therefore predecessors are typically

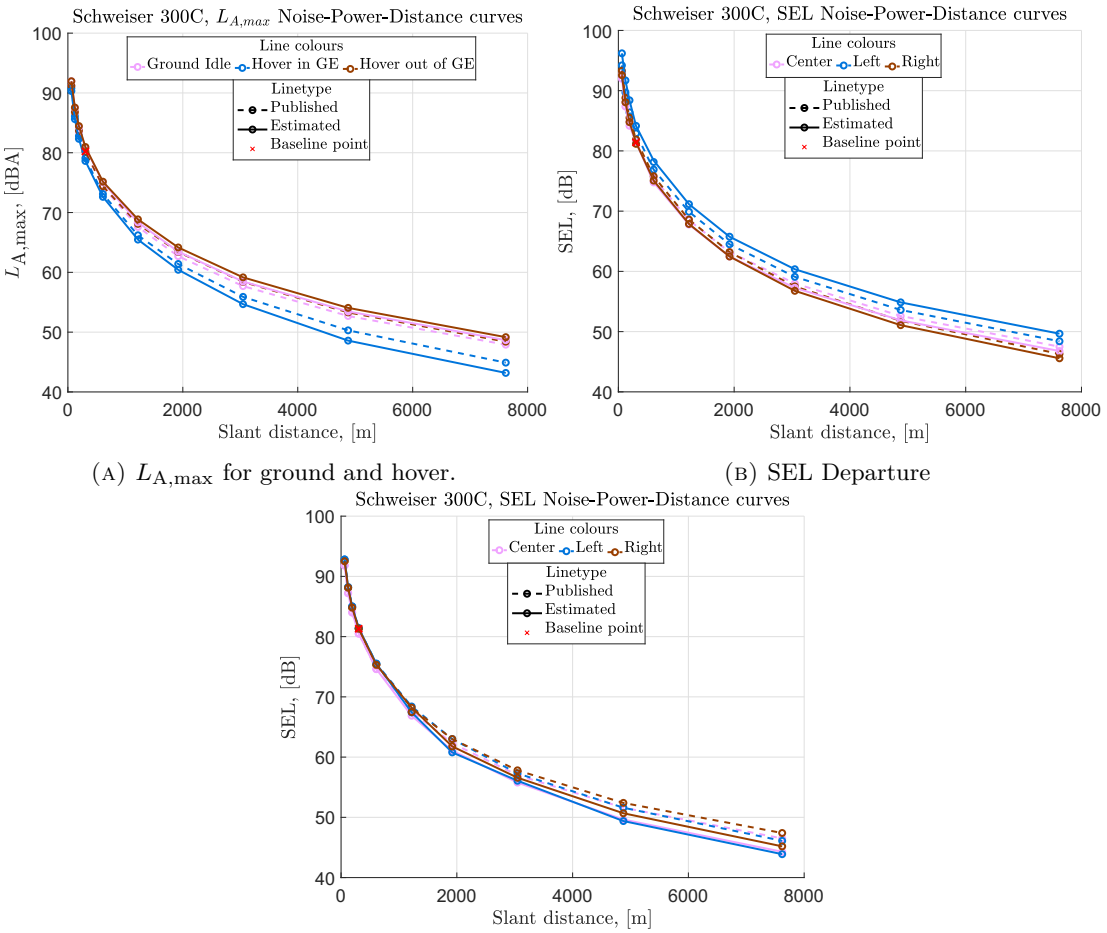

(A) $L_{A,max}$ for ground and hover.

(B) SEL Departure

(C) SEL Flyover

FIGURE 7.24: Comparison between the predicted (by MONTANA) and published (measured [98]) departure NPD curves for the Schweiser 300C helicopter.

the closest design and performance-wise to the concept being developed. In the absence of reliable performance and noise data for the direct predecessors (manufacturers often do not publicly share such data for current operating aircraft), predictions should be made by previous generation data or in the worst case by a representative aircraft in the operating class of the concept (classification is a complex matter, however as discussed in Chapter 2, noise classification is typically done according to MTOW).

To demonstrate this capability, predictions for the De Havilland Canada Dash 8 Q400 are made using four different baseline aircraft: predecessors (Dash 8-100, Dash 8-300); same class by other manufacturer (ATR 72-212A); and finally an aircraft with a different propulsion system architecture (De Havilland Canada Dash 7). Table 7.5 lists the basic performance parameters of the baseline aircraft along with those of the Dash 8 Q400. The resulting NPD curves are shown in Figure 7.27.

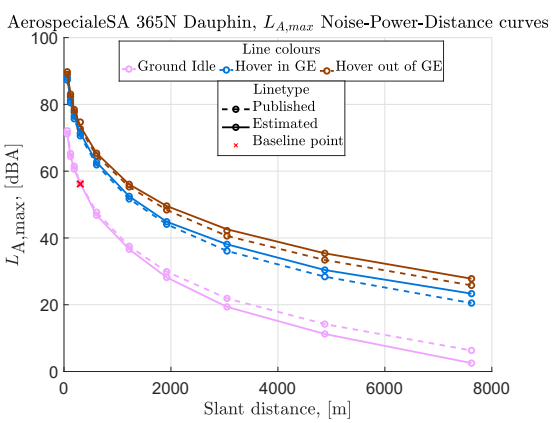

(A) $L_{A,max}$ for ground idle and hover.

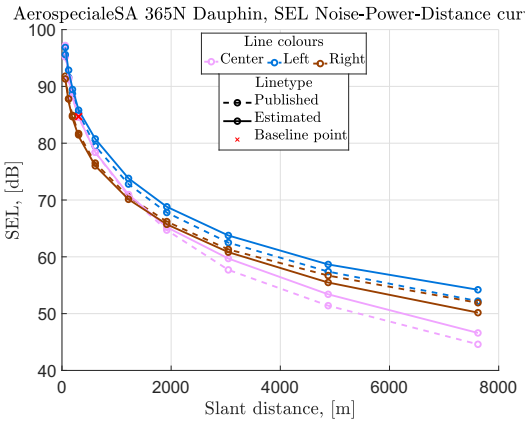

(B) SEL Departure

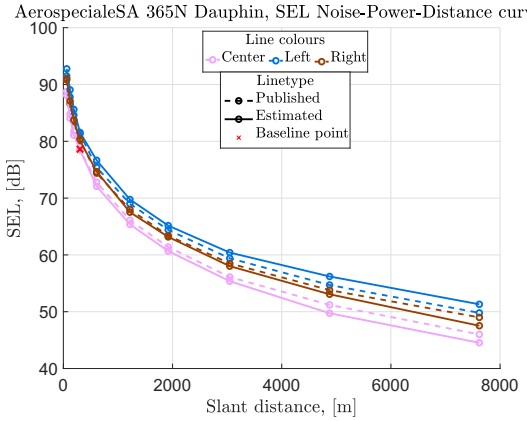

(C) SEL Flyover

FIGURE 7.25: Comparison between the predicted (by MONTANA) and published (measured [98]) departure NPD curves for the Aerospeciale SA 365N Dauphin helicopter.

TABLE 7.5: List of basic performance and design parameters of the Dash 8 Q400 and the baseline aircraft of choice.

Aircraft					
	No. of Engines	Prop Diameter [m]	No. of Blades	RPM	MTOW [kg]
Dash 7	4	3.4	4	1,210	20,000
ATR 42-500	2	3.93	6	1,200	18,600
ATR 72-212A	2	3.93	6	1,200	23,000
Dash 8-100	2	3.98	6	1,200	16,465

7.1.5 Discussion: Sources of errors in outdoor aircraft noise prediction

Overall, the NPD calculation procedure is high-level procedure with many intermediate steps between the generation of noise at the individual source level and the reception of the total aircraft noise level, after propagation, at any observer location. Replication of experimental results depends on the methods and model employed at each step of that

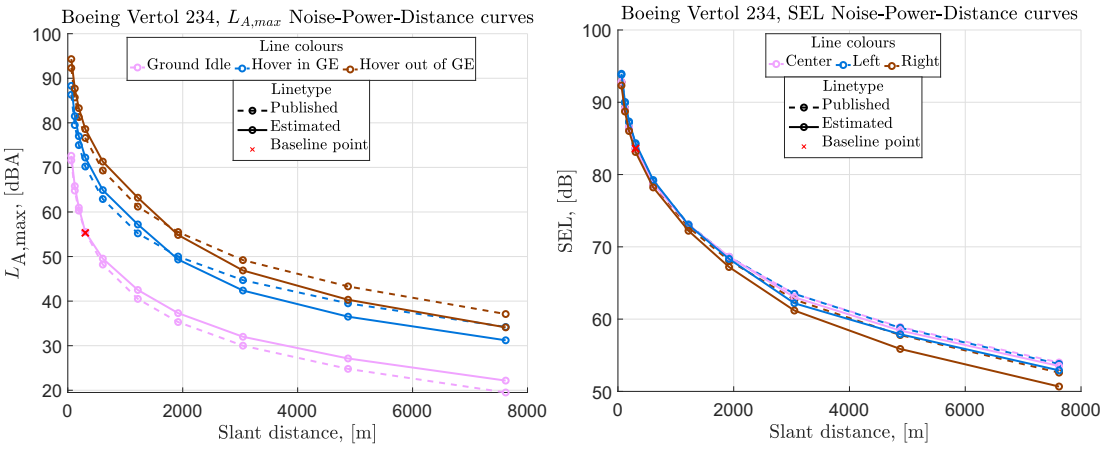

(A) $L_{A,max}$ for ground and hover. (B) SEL Departure

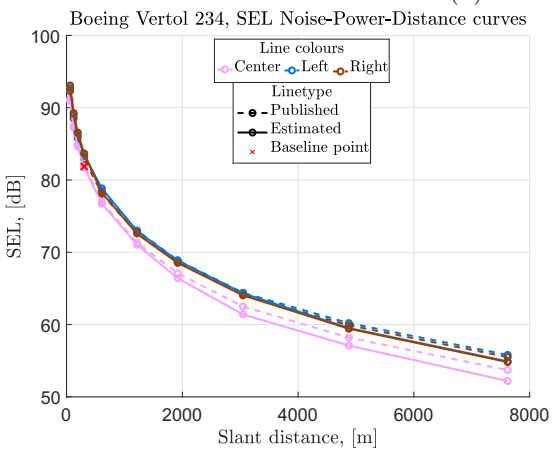

(C) SEL Flyover

FIGURE 7.26: Comparison between the predicted (by MONTANA) and published (measured [98]) departure NPD curves for the Boeing Vertol 234 helicopter.

procedure, but also knowledge of the experimental set-up/strategy, conditions and processing techniques that results in comparison data.

The main sources of error are due to two main components of the computational method for generating NPD curves: i. noise source definition and ii. propagation. Representing an air vehicle/ aircraft as a lumped acoustic source requires empirical assumptions about the contribution of each individual source mechanism to the overall sum, and the balance between them as a function of aircraft and engine operation. The subsequent propagation of the acoustic signature is heavily influenced by atmospheric effects such as temperature, humidity and wind direction and magnitude on an average but also local basis. Gradients and fluctuations of these parameters can alter the propagation paths and levels of the initial signal, through refraction and scattering effects.

More specifically, three main factors contribute to an erroneous lumped source definition, which then has a knock on effect in the NPD process. These are, i. unaccounted for individual noise source mechanisms, ii. the far-field radiation directivity of individual noise sources and their effect on the overall air vehicle directivity, and the spectral

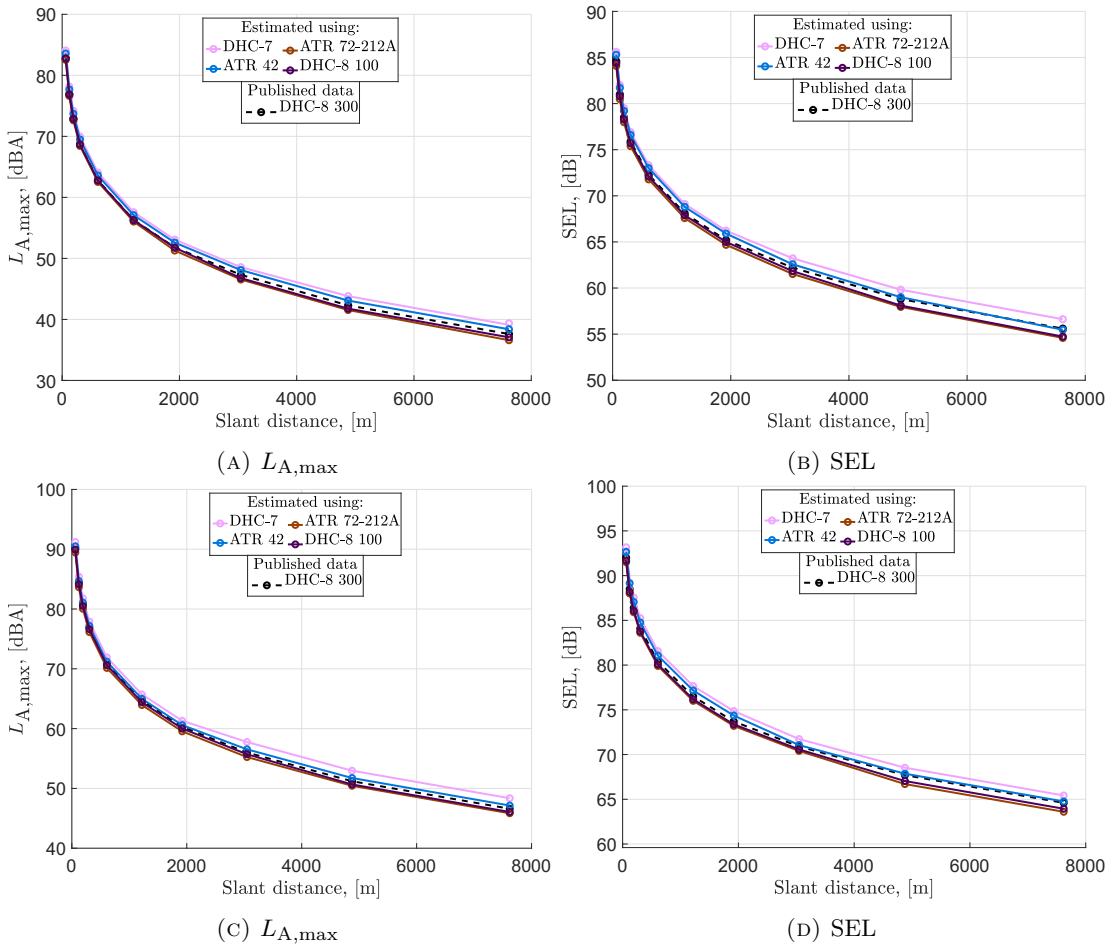

(A) $L_{A,max}$ (B) SEL

(C) $L_{A,max}$ (D) SEL

FIGURE 7.27: NPD departure predictions (continuous lines) for the De Havilland Canada Dash 8-300 using four different baseline aircraft. The predicted NPD curves are compared to published NPD data.

content of individual noise sources and their effect on the overall sound frequency spectrum.

In the context of the NPD curve creation, each of these factors can alter the final results causing under or over estimation of noise levels at observer locations.

Although propeller noise is dominated by low-frequency tones that are accurately captured by modelling the steady loading and thickness noise source contributions, it is worth considering the impact of two additional sources, unsteady loading harmonic noise, and broadband noise due to turbulence ingestion.

For propeller noise, static to flight projection is driven by this effect of turbulence ingestion [202]. Significant noise is produced during static conditions as a result of input turbulence ingestion. This noise source vanishes during flying. Intense higher harmonics dominate the noise spectrum when things are static. The intensities of these upper harmonics are significantly lowered during flight. It is clear from this that static propeller noise data projections to flight frequently produce large over-predictions.

Therefore, static propeller noise statistics are of limited use. Even static noise trends should be taken with a grain of salt. This is significantly important in the context of UAM hover or low forward speed operations. Under-predictions are expected on behalf of MONTANA, unless broadband noise is explicitly accounted for. A fist improvement could be the use of the Pegg model [62], or the Brooks, Pope and Marcolini model [86] as presented in section 2.3.

Unsteady loading is expected to cause the largest contribution to the error evident in the MONTANA lumped source model for propeller powered aircraft, especially the difference observed in forward flight. Nonuniform flow onto the propeller is known to cause significant increase in the noise signature [82, 203, 204, 16]. Not accounting for changes in unsteady loading noise would result in over-predictions in the case of reductions of the noise source in the study aircraft, and under-predictions in the case where the noise is expected to increase.

Zhong et al. [179] take a similar approach to the asymptotic approximation in this thesis for unsteady propeller loading harmonic noise. With minimal modifications, MONTANA could adapt to include such this as an additional source. The nature of the frequency domain model, and careful consideration loading harmonics could be leveraged to perform parametric studies. However, blade unstable loading is rarely accurately determined, especially at the preliminary design stage.

The number of acoustic sources that are sufficient for the particular type of aircraft under consideration depends on the type of the engine in its power plant and on aircraft flight mode. In the case of propeller/rotor powered aircraft, the noise sources related to the propeller itself tend to dominate across power settings and radiation angles. However, additional noise source mechanisms can contribute to the final OASPL and finally exposure levels. As with the additional propeller sources, depending on the case, over or under estimations of noise levels could be observed. Examples of such additional noise sources are discussed in chapter 8 specifically for hydrogen powered aircraft.

Interactions can be a source of additional error and complexity in the definition of a lumped source acoustic model. Interactions may be classified into two categories, aerodynamic and acoustic. Aerodynamic interactions are typically causes for additional acoustic energy generation, and therefore additional aeroacoustic mechanisms. These may be accounted for by modifying individual noise source models or adding additional ones in the definition of the lumped source. Acoustic interactions are defined by the effects of constructive and destructive interference of the sound fields. Typically, understanding such effects involves high fidelity calculations or computations when detailed geometry and operation is available. In an acoustic power radiation basis, the far-field surface integral surrounding the source is unaffected by the presence of acoustic interference effects.

Unaccounted for sources, have an impact on the overall directivity and spectral content of the lumped source, not just the PWL. As discussed next, these parameters impact the NPD process in their own way.

Directivity has an impact on the estimation of $L_{\mathrm{A,max}}$. The interplay of the directivity and the distance to the observer impact the location (temporal or spacial dependent on reference), level and spectral content of the $L_{\mathrm{A,max}}$ for any single event.

The SAE AIR 1845 [89] procedure uses a "simplified adjustment procedure" to calculate the sound exposure levels, L_{AE} at distances other than the one the baseline level was calculated/measured at. The adjustment is empirical and is known to cause discrepancy in the levels when the difference in slant distance between the estimation point the baseline point are large, as the assumption that $D_{\mathrm{AE,d}} \propto d^{0.751}$ breaks down. The application of this simplified procedure can be avoided by manually calculating the L_{AE} performing simulated flyover at each slant distance. This is the solution used by Rizzi et al. [112].

In addition, the procedure assumes a constant emission angle for $L_{\mathrm{A,max}}$ for distances greater than 800 m. The calculations suggested SAE AIR 1845 are done with the presumption that the sound emission angle at the moment of the maximum sound level for the test distance does not change with increased distance. Assuming a constant sound emission angle, the minimum (closest approach) distance, denoted by either d_{Tm} or d_{rm}, can be used to define the sound propagation distance,

$$d_{Tpi} = d_{Tm} \csc \beta_{ei} \quad \text{and} \quad d_{rpi} = d_{rm} \csc \beta_{ei} \tag{7.7}$$

which results in the noise level being estimated as,

$$L_{pr}(j) = L_{pT}(j) - 20 \log \left[d_{rm} / d_{Tm} \right] - a_r(j) \left[d_{rm} - d_{Tm} \right] \csc \beta_{ei} \tag{7.8}$$

Because atmospheric-absorption processes greatly lower the high-frequency sound pressure levels at large distances, the assumption of a constant sound emission angle during the time of occurrence of the highest sound level is not necessarily true. As a result, as the distance grows, the relative time at which the maximum sound level occurs may shift.

The implications of an erroneous directivity are beyond the two points made above, in the case of sound exposure calculation. As an example, take the extreme case of an axially (parallel to the flight axis) oriented dipole ($D_{\max}$ occurs at $\beta = 0$ and $\beta = pi$)

[1] Experimental results suggest that the empirical relation $D_{AEr} - D_{AET} = 7.5 \log_{10} (d_{rm}/d_{Tm})$ accurelty descirbes the effective duration difference between the NPD point of interest and the reference data point, where D_{AEr} and D_{AET} are the flight durations of the point of interest and the reference point, while d_{rm} and d_{Tm} are the equivalent slant distances [89].

and one perpendicular to that ($D_{\max}$ occurs at $\beta = \pi/2$). In the first case maximum radiation occurs early and late in the event time history, relative to the observer, where the distances are large (and $\to \infty$ for a flight path of infinite length), whereas minimum radiation occurs at the point of closest approach. The integrated exposure level for a flyover of the dipole would be significantly lower than that of other case, where maximum radiation occurs at the point of closest approach. This trivial example, indicates the effect that is believed to contribute to the error observed in the NPD curves calculated in this chapter.

Reflection and refraction effects caused by the interaction of the noise waves with elements of the airframe are not included in the definition of the lumped source model. It has been shown [205, 206] that these effects can effectively re-distribute and/or reduce the overall acoustic energy radiated in the direction of observers directly below and laterally offset from the aircraft flight path. Shielding and jet blockage effects can also contribute to the error observed.

As with directivity, spectral content if affected by the variation of distance throughout a flyover. In the case of MONTANA, the field shape is the same across all frequencies. This results in high frequency dominated spectra to be attenuated to a greater extent than those with dominant low frequency content. In the case of propeller harmonic noise, the majority of the energy is located in the low frequency BPF and its harmonics. For low slant distances and low tip relative Mach numbers it is expected that atmospheric absorption will have little impact on the received signal. However, in MONTANA, as seen in Section 7.1, there is a tendency to over-predict high frequency content. This means for a given OASPL energy is shifted to the high frequencies which are more vulnerable to be attenuated by the atmosphere.

Finally, the dependence of frequency on directivity is worth repeating, as this is a gross assumption within MONTANA that alters levels received at the observer locations.

Doppler effects also modify the initial source levels and spectrum. The Doppler frequency shift, in the case of a uniform stationary atmosphere, is a well understood phenomenon, and may be corrected for. Additional Doppler effects, such as amplitude modulation and refraction [207] also may cause over-prediction of noise levels if not accounted for. Standard methods for accounting for Doppler effects are implemented in most aircraft/airport tools [208].

Propagation effects also influence the characterisation of source. The standard SAE-AIR 866 applied in this thesis, adequately captures the effects of atmospheric absorption through empirical attenuation constants for conditions that do not deviate largely from a homogeneous atmosphere assumptions and the reference parameters. Atmospheric turbulence can be a reason for that deviation. Daytime influence of atmospheric turbulence is generally underappreciated [24] and may impact propagation through random variation in temperature, wind velocity, pressure, and density. An in-depth

review and analysis of the effect the homogeneous atmosphere assumption is presented in [209]. Additional standards for the measurement of outdoor sound exist, most notably the ANSI S1.13-2020 Procedures [210].

Propagation characteristics vary significantly in the presence (proximity) of the ground. For airport noise this is significant at low elevation angles of the aircraft. Typically, in the case of NPD curves and overhead flyovers, the only impacted portions of the event SPL time histories are the extremities (where the observer is at very large or very small polar angles relative to the observer). These portions do not significantly contribute to a integrated exposure metric with 10 dB-down definition. However, empirical corrections are standard practice, and predictions can be improved with the application of methods such as ESDU [211] and SAE AIR-1751 [212].

Large scale outdoor acoustics campaigns, for certification and NPD curve creation purposes are difficult to replicate for two fundamental reasons. The first pertains to the noise source definition, however knowledge of the state and conditions of the aircraft and propulsion systems (and therefore the parameters that feed into the individual noise source models) at any given time throughout a measurement event.

Additionally, the discrepancy between flight parameters in real operation and their values defined from reverse engineering or calculating them based on power setting parameters such as RPM (in the case of propellers), presents another source of error relative to outdoor measurements. Global control parameters may be tracked, as they form inputs for pilots (e.g. $N1$ speed, EPR and OPR for turbofans), however their correlation to flow characterising parameters is often also done through modelling techniques.

Performance transient conditions (aircraft and propulsion system) are avoided in the process of NPD curve creation, as steady state conditions are the targets. The impact of transient conditions on the aeroacoustics is twofold: i. time dependent driving parameters (due to acceleration or deceleration of rotating machinery for example) and ii. the influence in noise source breakdown. Obviously, both of these conditions impact the assumption of MONTANA.

Finally, all predictions and experimental data should be returned to reference atmospheric conditions. This is standard procedure for the development of NPD curves, in order to provide a basis of comparison. Although, conditions are typically monitored at standard intervals during the measurement campaign, at the observer location and at the aircraft flyover altitude, variation in atmospheric conditions may still introduce errors in the observed acoustic signal.

The ICAO Annex16 certification process uses a *confidence limit process* for the generation of the aircraft noise level from measured (and in some cased hybrid of measured and predicted level) data, that are to be assessed against the noise certification criteria. For the purpose of certification 90% confidence limits are used,

corresponding to an acceptable ±1.5 EPNdB range statistically for each of the three average noise certification levels. NPD data is also part of the certification process, implying that the ±1.5 EPNdB tolerance is also applicable to the baseline data used for benchmarking MONTANA.

NPD prediction however, relies on noise models to calculate noise exposures by simplified mathematical representations of the real, complex processes of aircraft noise generation and propagation. Compounding errors through this process inevitebly results in larger uncertainty levels that measurements. However, for the application of MOTANTA in the conceptual design space, absolute accuracy is be less important than realistic sensitivity to key input variables. As suggested in Doc29, accuracy in many cases is defined in terms of: fidelity, sensitivity and relative accuracy.

Certification levels calculated using NPD data are subject to the same accuracy (error tolerance) as the NPD curves themselves. Extrapolation of NPD data to certification points does not introduce any additional error, assuming NPD data exists for the required certification metric. An exception might be the flyover (cutback) conditions, as the transient phase of power reduction (spool-down) is not captured in NPD data. The impact of NPD accuracy in contour estimation is significatly larger. As elequently described by Smith [21], contours are extremely sensitive to small input data changes. Accuracy of ±1 dB of instantaneous input noise can result in 40% variation of the contour area. Despite this sensitivity of contour area prediction to accuracy of input, with the use of average airport noise monitoring data, airport noise tools and methedologies have been “validated” within ±2 dB [21, 89]. Recommended interpretation of contour results, as with NPD data, is relative changes between scenarios, quantifying the variation (changes) in noise exposure around a given airport resulting from changes in design and the operational of aircraft, through driving parameters. Absolute contour area and contour location, becomes raliable at small distances to the flightpath (i.e small slant distances), as is the case with NPD curve data previously discussed.

The benefit of modifying NPD data sets to account for changes in individual sources alone, means that many of the effects previously described, that are contained with the experimental data, are also present in the noise predictions. Predicting absolute source levels requires the application of many corrections before is may be compared to outdoor certification measurements.

Modifying existing NPD data implicitly accounts for propagation, ground reflection and signal processing adjustments, typically applied to absolute prediction of individual noise source levels. Specifically, in the case of propagation, the computational algorithm involved (standard Doc29 and SAE AIR 1845 methods) used to reverse the NPD data into source levels (as explained by Synodinos [12, 52]), is the same used to propagate back to the observer location after the application of source deltas. This implies that the

propagation uncertainty between predicted and measured NPD data is only due to the deltas applied to the individual sources, which comprises only of a part of the new total level.

Despite the errors discussed, the value in MONTANA in obtained when comparing two MONTANA predictions, one for the baseline aircraft and one for the study (modified) aircraft. As discussed, MONTANA contains various errors that are consistent across all predictions. By looking at the relative difference NPD curves predictions, it is possible to gain a perspective on how changes in individual noise source levels manifest themselves in the context of a whole aircraft and on the ground.

The question of whether this uncertainty (or systematic deviation) allows for a reliable estimation of differences between aircraft concepts and their baseline counterparts, comes down to two different parts of MONTANA:

1. The fundamental linear approximation of MONTANA when applying deltas to baseline levels of a particular source. A systematic error is observed when the limits of the linear approximation are exceeded, and substantial deviation from the full non-linear solution/method has occurred. This statement also holds for the particular propeller noise source model implemented within this thesis. An expected deviation from the original model is observed when for example the small argument approximation breaks down.

2. Second, and possibly harder to quantify, is the error between the individual noise prediction methods and reality. Understanding the limitations as well as strengths of the baseline methods and the intended application of the models used to generate the deltas is crucial to restricting the scale of the introduced errors. This is the reason for the extensive error study and limitations analysis, as well as the extensive benchmarking against actual measured NPD data.

7.2 Airport noise model verification

Validation of the MONTANA airport noise module is performed under guidance from the ECAC CEAC Doc29 [123] quality *Control and Validation* process, specifically the sequence of task defined under Section 9.6 “Practical Recommendations”. This process fundamentally aims at increasing confidence in the results and provide insgihts to the limitations of the tool.

The validation of the updated airport noise model within MONTANA implies comparing noise footprints for single operations. Two methods of benchmarking are used, an in-house simulation method and an industry standard for generating noise contour around airports, the FAA’s AEDT. The in-house simulation model was developed as a

simple alternative to the fully featured AEDT. It allows for simple setup, minimal input requirement, while the straightforward nature of a simulation / grid-point model minimises the possible points of discrepancy when comparing to MONTANA predictions. AEDT is a fully developed airport noise model capable of accounting for aircraft / fleet type, detailed flight trajectories and aircraft performance amongst others. Acoustic effects such as atmospheric attenuation, lateral directivity and attenuation, ground effects are dealt with by default through the input requirements (NPD's) or by amending noise at the observer location through a series of corrections.

Both tools are used to generate a series of noise contours and compared to MONTANA predictions. Simple iso-tropic sources and three-dimensional ones are explored, while the power variation noise surfaces are compared to equivalent cut-back footprints generated by AEDT. Finally, a range of exposure level contours are explored, as lower level footprints are notoriously hard to predict due to the small elevation angle, introducing lateral attenuation effects and dominating ground effects.

7.2.1 Grid-point method

In the grid-point model, the ground surface or airport coordinate system is defined by a Cartesian coordinate system (X, Y, Z) with the runway laying in the $X - Y$ plane. The origin of the coordinate system is positioned at the start of the ground roll with the runway extending out in the positive X direction. In the case of a vertical take-off the origin is again placed at the point where vertical flight is initiated. The set-up for a conventional fixed-wing take-off is seen in Figure 7.28.

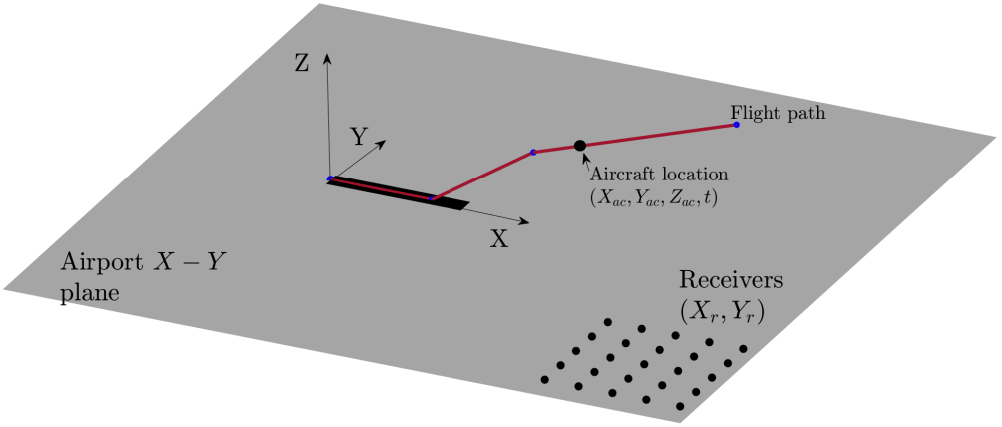

FIGURE 7.28: Set-up of grid-point method flight path and receivers.

The grid-method provides a trivial, simulation solution to check three items in particular:

- the preservation of acoustic energy output after the application of the spherical harmonics and,

- that the noise surface transformation (rotations and translations) have been implemented correctly, and
- the Bezier curve corrections.

The grid method consists of a point source radiating a noise level of a specified constant PWL. The only effect that takes place during the propagation between the source and the observer locations is spherical spreading.

The aircraft location is given by the vector $[X_{ac},\ Y_{ac},\ Z_{ac}]$, and is a function of time. Each individual aircraft movement is described by its three-dimensional flightpath, engine power setting and speed along it. The flightpath is discretised into simple linear segments defined by a waypoint at the start of each segment. The waypoints carry information that describes the operation and movement of the aircraft along the following segment. The flight parameters, as they're called are assumed to remain constant along the length of the segment and are the following: (1) an inclination angle, (2) an angle of rotation, (3) the length of the segment, (4) the engine power setting (or in this case, the source PWL) and (5) the speed of the aircraft along the segment. These parameters are almost identical to the ones describing the flightpath of RANE v2, as the flightpath is the same. Each segment is further discretised in to a number of points N_s modelling the movement of the aircraft along this segment.

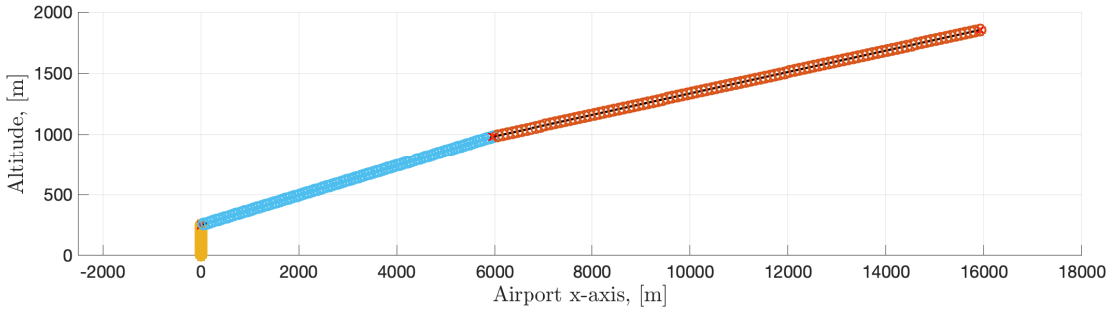

FIGURE 7.29: Discretisation example of flightpath segments for grid-point method.

Using the coordinates of the final point on the last segment of the flightpath an appropriately sized rectangular grid is defined on the ground ($X-Y$ plane). Each individual receiver location is given by $[X_r,\ Y_r,\ Z_r]$. Each point on the grid represents an observer location at which the sound exposure levels of the aircraft movement will be calculated. As the aircraft continues to fly even after the end of the final segment, an extension to the final segment is added. The segment is extended linearly until the acoustic contribution (SPL) to all points on the grid beneath the 10 dB down mark relative to $L_{A,\max}$.

The sound level at each grid point due to the aircraft at any point in time is given by:

$$Lt_{k,i} = L_{p,\text{source}} - 20\log_{10}(r) \tag{7.9}$$

where r is the distance between the specific grid point (observer) and the aircraft at that point in time, and k,i are counters indicating the position of the aircraft along the discretised flightpath. Therefore, as the aircraft performs a take-off/approach operation (assuming $t = 0$ occurs when the aircraft is positioned at the origin for at take-off procedure) the SEL at each individual grid point may be calculated as,

$$\mathrm{SEL} = 10 \log \left(\sum_{k=1}^{K} \sum_{i=1}^{N_s} 10^{\frac{Lt_{k,i}}{10}} \Delta t \right) \tag{7.10}$$

where K denotes the number of segments including the extension to the last segment. Δt is defined as per the ICAO Annex 16 analysis system requirements equals to 0.5 seconds. Unlike Annex 16 the discrete signals received by the grid-points are not averages, rather instantaneous values. Using Δt and the constant aircraft velocity along finite length segments, the position of the aircraft can be estimated at each time t. That results in each segment being discretised into a number of points N_s. Once the SEL of

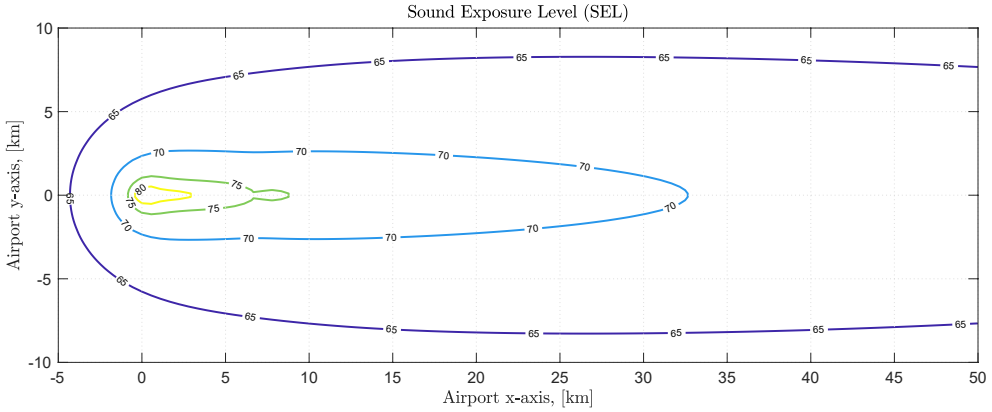

FIGURE 7.30: An example contour map calculated using the grid method.

The contour map is composed of multiple contour lines, ranging (in this example) from 65 to 80 dB SEL. The calculation time is highly dependent on the size of the grid and the number of discretisation points in each dimension. The flightpath discretisation also contributes to significantly to the computation times. This example computation with 1,000,000 grid points took a total time of 238.258 s. this scale of computation times for simple single runway, 3-5 segment flightpaths examples is manageable for running verification test cases. The equivalent Noise Surface example was calculated in 36.194 s, almost 6.6 times faster. (NOTE: these calculations were performed on personal laptop computers). Grid-method generation and optimisation techniques are out of the scope of this project. Larger more complex test examples will be tested against FAA's AEDT.

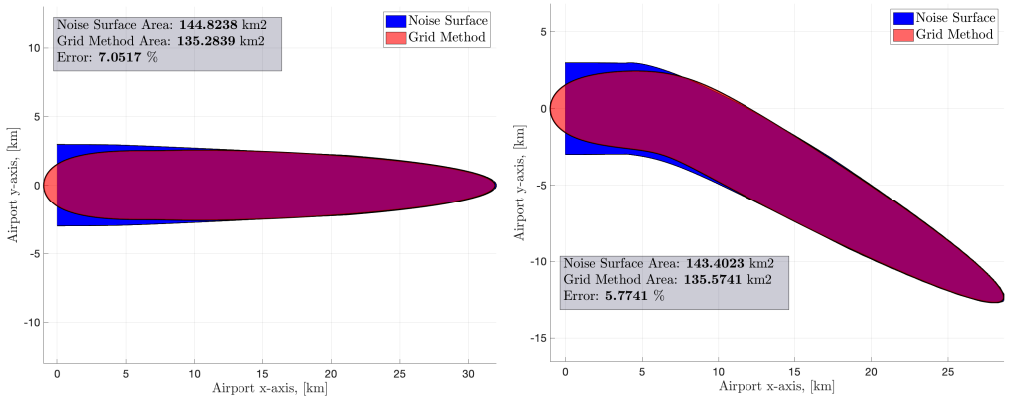

(A) Conventional take-off. (B) Conventional take-off.

FIGURE 7.31: The 70 dB SEL contour of an isotropic source. Contour area comparison between RANE v2 and the grid-point method.

In order to make to comparison to RANE v2, the inputs need to be chosen appropriately. For a given source strength and required sound-level contour, the noise radius input, R_n for the noise surface method is calculated using the discrete definition of the SEL metric, Equation 2.26 by performing an artificial flyover.

All examples assume an omnidirectional source by setting all Spherical Harmonics coefficient to zero other than the monopole term. The decision to first test an isotropic source was made due to the fact that, designing a grid-point method with directivity features in also out of the scope of this project. Thus, for initial verification, isotropic sources were used.

The inputs parameters for the case of a simple three segments take-off (Figure 7.31) are presented in Table 7.6. Slight alterations to the inputs are made for the cutback and turn examples.

TABLE 7.6: Example input parameter table for conventional procedures of an omnidirectional noise source.

Conventional			
Segment	One	Two	Three
Inclination angle, γ (deg)	0.5	7.5	5
Rotation angle, ψ (deg)	0	0	0
Segment length, s (m)	1000	6,000	60,000
Speed, v (m/s)	100	100	100
Source SPL, L_p (dB)	120	120	120
Noise radius, R (m)	1,110	1,110	1,110

The following Figures from 7.31 to 7.33 showcase example calculations using RANE v2 and comparing to the grid-point method, with Figure 7.33 illustrating an interesting case of a vertical take-off procedure.

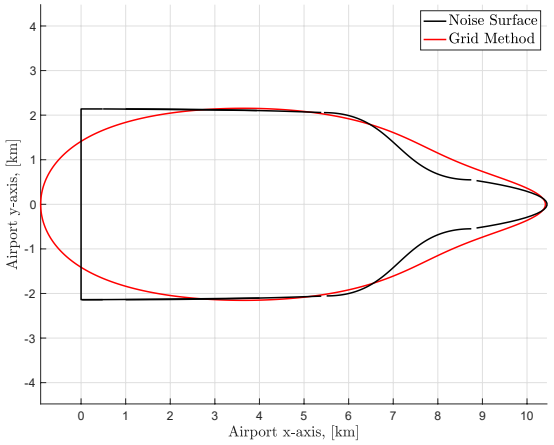

FIGURE 7.32: The 75 dB SEL contour of an isotropic source, conventional Take-off with cutback. Contour area comparison between RANE v2 and the grid-point method.

Table 7.7 also shows the different inputs required for a vertical take-off compared to a conventional fixed wing flightpath. Interesting parameters have been highlighted in red and green. It is interesting to point out the short vertical segment and the speed along it. These features were modeled after typical flight profiles and operational procedures of helicopters, operating at helipads according to the FAA [99].

TABLE 7.7: Example input parameter table for vertical take-off procedures of an omnidirectional noise source.

Vertical			
Segment	One	Two	Three
Inclination angle, γ (deg)	90	7.5	5
Rotation angle, ψ (deg)	0	0	0
Segment length, s (m)	100	6,000	60,000
Speed, v (m/s)	1	100	100
Source SPL, L_p (dB)	120	120	120
Noise radius, R (m)	2,000	1,050	1,050

The results in Figures 7.31 to 7.33 validate the implementation of the spherical harmonics as a directivity factor. Although omni-directional, the distribution of energy generates the noise radii of appropriate length relative to the simple point source simulated flyover. Mismatches occur at the start-of-roll in the case of conventional fixed-wing aircraft, but this is expected due to the simplified modelling of the flightpath and the nature of the infinitely long noise surfaces. In addition, for the omnidirectional case, the Bezier curve correction performed adequately for simple turns and in the case of the veritical take-off. In the case of the take-off with cutback, although it managed to improve on the previous capability of RANE and the noise surface method (see cutback calculation in [182]); additional considerations need to be made to appropriately model these transient regions.

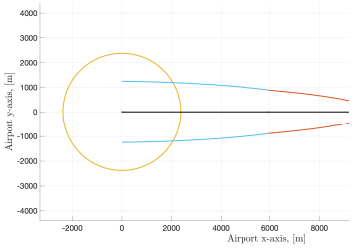

(A) RANE v2 set-up and conto flightpath indicated in l

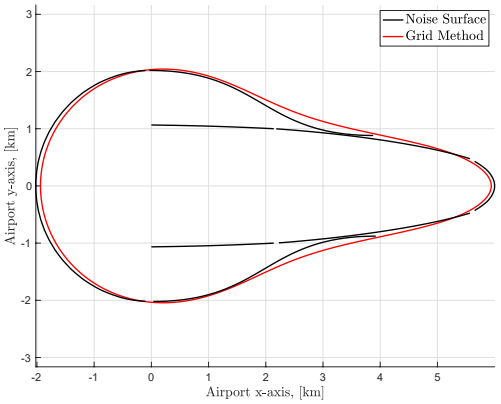

(B) Comparison between RANE v2 and the grid-point method of the 75 dB SEL contour.

FIGURE 7.33: Isotropic source during vertical take-off.

7.2.2 Comparison with AEDT

As previously mentioned, AEDT is a comprehensive, grid-point model that operates similarly to the in house grid-point method previously described. It assesses the noise impact of conventional aircraft fleets around airports, in various metrics, typically noise exposure contours around airports. In addition to conventional fixed wing aircraft, AEDT carries capability of assessing helicopter operations around airport and helipads/heliports. The Heliport Noise Model (HNM) module was incorporated into INM (Integrated Noise Model) with a helicopter noise database collected through both FAA and manufacturer certification measurements and later into the current version of AEDT.

For the RANE v2 benchmarking campaign, both fixed wing and rotorcraft (helicopter) scenarios were chosen. The noise data inputs to RANE are the same NPD curves used by AEDT and are acquired from the ANP database [98]. In order to compare the same flight operations and trajectories, simple linear flight tracks were set-up in AEDT along with the "STANDARD" or "DEFAULT" profiles for each air-vehicle of interest.

As AEDT uses aircraft/helicopter flight performance models to simulate the actual trajectories based on the target tracks and profiles, the AEDT outputs represent the actual flight trajectory and performance. These were used as the inputs to RANE v2, accompanied by the NPD data for each air vehicle.

Fixed-wing aircraft

The fixed wing aircraft of choice range from GA piston powered propeller aircraft, to regional turboprop aircraft and finally different configurations of turbofan aircraft. A summary is available in Table 7.8. Example of the flight profiles for the fixed-wing conventional aircraft may be seen in Figure 7.34. For each aircraft, the recommendations

of the ANP database, Doc29 and the AEDT technical manual were followed in applying the appropriate corrections to the noise levels (e.g. impedance adjustment, duration correction engine installation and lateral attenuation) before calculating the appropriate noise radius for each segment of the flightpath.

The finite segment correction was also applied, but instead as calculated in section 4 of this thesis. An important consideration is that of the start-of-roll directivity, as this has a strong contribution to the shape of the final contour. To provide a representative comparison, the same directivity functions as the Doc29 recommendation were used. The directivity function Δ_{SOR} is given as a delta relative to the overall takeoff ground roll noise level at the point distance d_{SOR} at $\psi = 90°$, $L_{\mathrm{TGR}(d_{\mathrm{SOR}},90°)}$. Two empirical expressions are provided, one for turbofan-powered jet aircraft and another for turboprop-powered aircraft. Both are applied in the rear arc relative to the aircraft, $90° \leq \psi 180°$, where in this case ψ is measured from the aircraft forward axis in the counterclockwise direction. For the application in RANE v2, the directivity index Δ_{SOR} was converted from a directivity index to a normalised directivity factor, and expanded in terms of spherical harmonics.

Lateral attenuation and ground effects are treated differently relative to Doc29, due to the details of the noise surface method. As RANE solves for observer locations that experience a certain value of noise level, the conventional grid method empirical corrections applied to the levels at each observer location are not applicable. Therefore, these corrections are inverted to the source coordinate frame and therefore definition of the three-dimensional directivity function and included in the implicit solution of the noise surface equation, through a correction to the noise radius. This results in the corrections being a function of the already calculated noise radius, the segment inclination angle, γ, which directly correlates to elevation angle β, (in which these corrections are typically defined [34]), and are manifested in the aircraft frame through the polar and azimuthal angles (θ, φ). This assumes that all observer locations that result from one segment's noise surface experience the same corrections. For realistic cases the granularity of the flightpath discretisation is already high to account for performance and trajectory geometry accuracy. In the case of long segments at high inclinations angles, additional discretisation points are introduced for these corrections alone. This bypasses the need for applying the individual corrections to each observer location independently, as the corrections are included in the initial calculation of each noise surface of interest, further cutting down calculation times.

The Doc29 engine installation correction is also included in the source directivity definition. The empirical corrections $\Delta_I(\varphi)$ for wing-mounted and fuselage-mounted engines are expanded into the series of simple harmonics before performing the flyovers. Finally, the appropriate noise surfaces are generated for each segment of the flightpath.

TABLE 7.8: Fixed wing aircraft used for benchmarking RANE v2.

ANP aircraft								
	Cessna 172	DHC-7	DHC-8	ATR72-212A	Boeing 717	A320neo	A400M-Atlas	MD-11
Type	Piston	Turboprop	Turboprop	Turboprop	Jet	Jet	Turboprop	Jet
No. Engines	1	4	2	2	2	2	4	3
MGTW [lb]	2,450	41,000	34,500	50,710	121,000	142,198	310,852	682,400
MGLW [lb]	2,450	39,000	33,900	49,270	110,000	142,198	271,000	433,300
MSLST[a]/MSLT[b] [lb]	436	2,850	4,750	7,587	18,000	25,000	-	61,500
Noise Chapter	6	14	14	14	3	4	4	3
Config.	FNM[c]	WM[d]	WM	WM	FM[e]	WM	WM	WFM[f]

[a]Max Sea Level Static Thrust only valid for propeller powered aircraft.
[b]Max Sea Level Thrust only valid for turbofan powered aircraft.
[c]Fuselage noise mounted
[d]Wing mounted
[e]Rear fuselage mounted
[f]Wing and fuselage mounted

The contours, or more appropriately, single event footprints, in Figures 7.35 to 7.38 represent the benchmarking comparisons of RANE v2 against AEDT for fixed-wing aircraft. Each figure depicts the AEDT prediction in red, while the RANE prediction in black. Three noise levels are chosen for each aircraft, each presenting a high, medium and low level of SEL. In the case of the "quieter" aircraft, this range these values are 50, 60 and 70 dB SEL. For the larger and noisier aircraft the levels are 55, 65 and 75 dB SEL. The range on the x-axis is different depending on the aircraft depicted, for example the footprint for the A400M extend all the way to approximately 90 km beyond brake-release (start-of-roll) while the Cessna 172 a mere 40 km.

The prediction trends are similar across all aircraft. RANE v2 footprints almost directly overlap those of AEDT at high noise exposure levels. Details in the shape of the footprints are lost (or smoothed out) in the region of 0 - 5 km across all levels for all aircraft. This is caused for two reasons, the way lateral attenuation and ground effects are applied and the effect of the Bezier curve corrections. Overall however, the predicted area of exposure is not affected, giving good agreement.

RANE does exceptionally well in the regions of long straight segments. These are parts of the flightpath that more closely conform with the RANE infinite flightpath and constant performance (power setting) assumptions, as also seen in the comparison with the grid-point model, and require the least amount of corrective adjustments. Finally, as may be seen in all figures, the RANE footprint abruptly cut-off, whereas the AEDT ones do not. The discrepancy is due to the finite flightpath in AEDT, a real aircraft would continue to fly beyond what is modeled in this case in AEDT.In the case of RANE, the last segment of the flightpath, although finite, defines an infinitely long noise surface, arguably a more correct approach. However, the depictions in the figures have limited the extent of the footprints to the length of the equivalent levels of the AEDT predictions for comparison reasons.

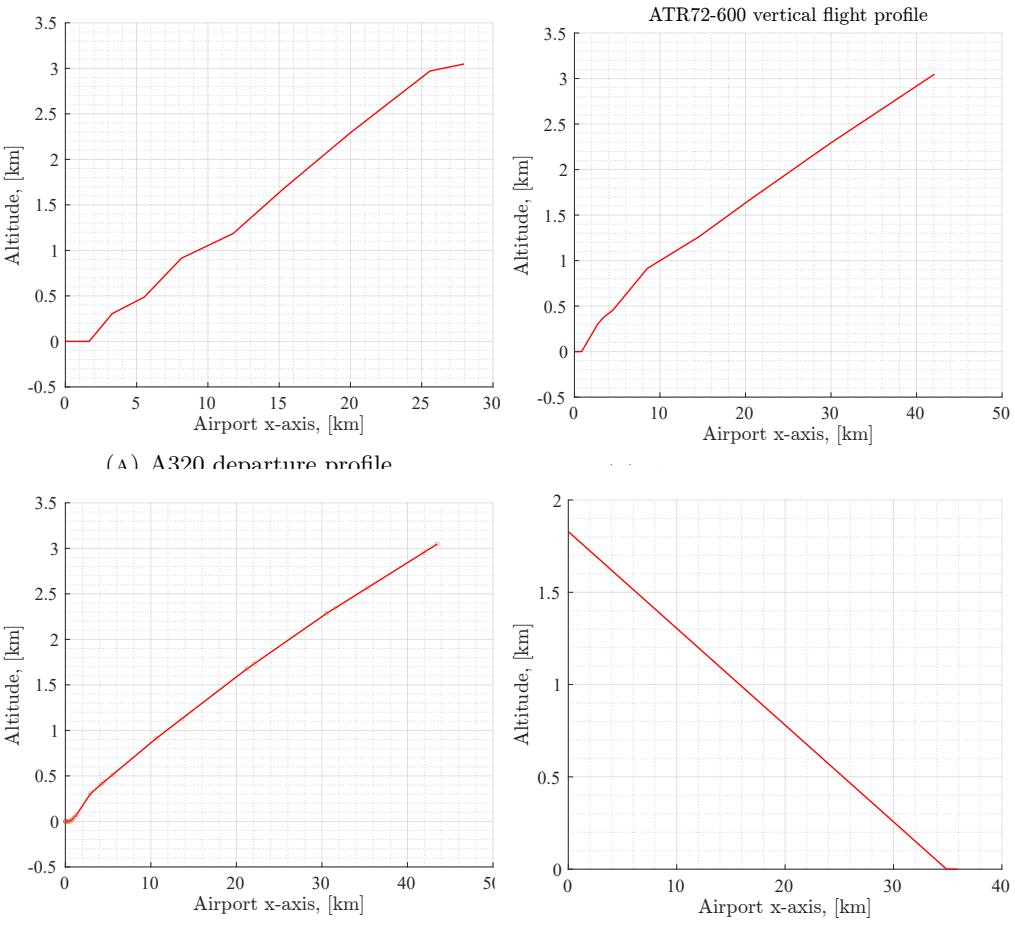

(A) A320 departure profile.

(C) Cessna 172 departure profile.

(D) Common approach profile.

FIGURE 7.34: Vertical flight profile for various fixed wing aircraft.

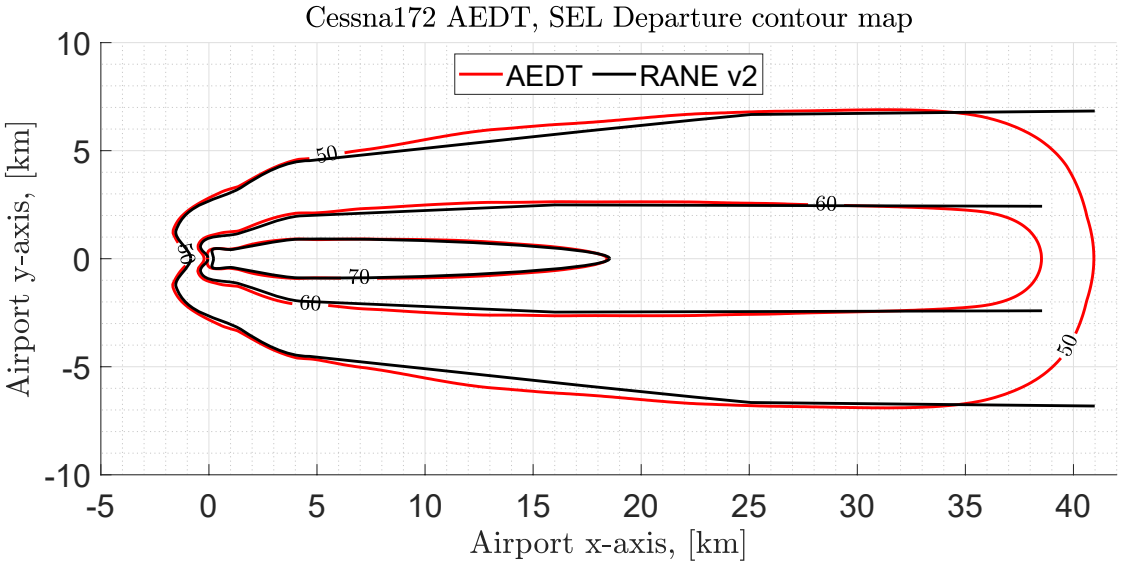

(A) Cessna 172

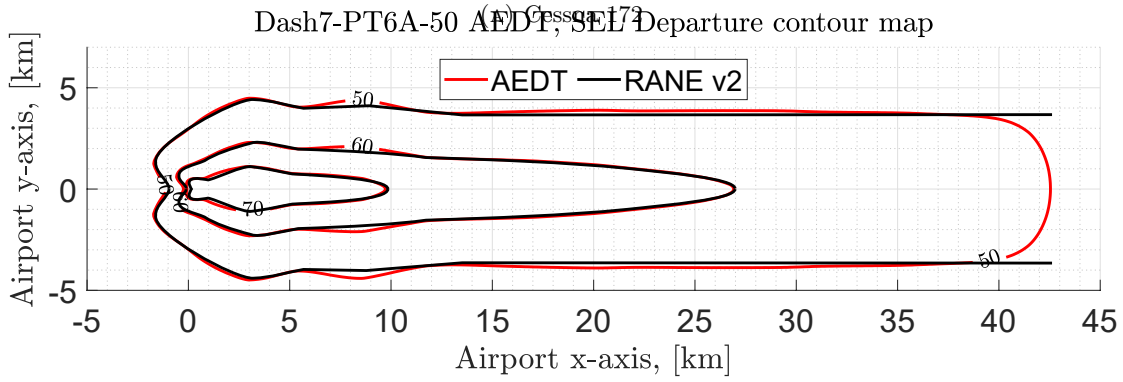

(B) De Havilland Canada DHC-7 (Dash 7)

FIGURE 7.35: Comparison between the RANE v2 and AEDT 3c prediction for fixed wing aircraft.

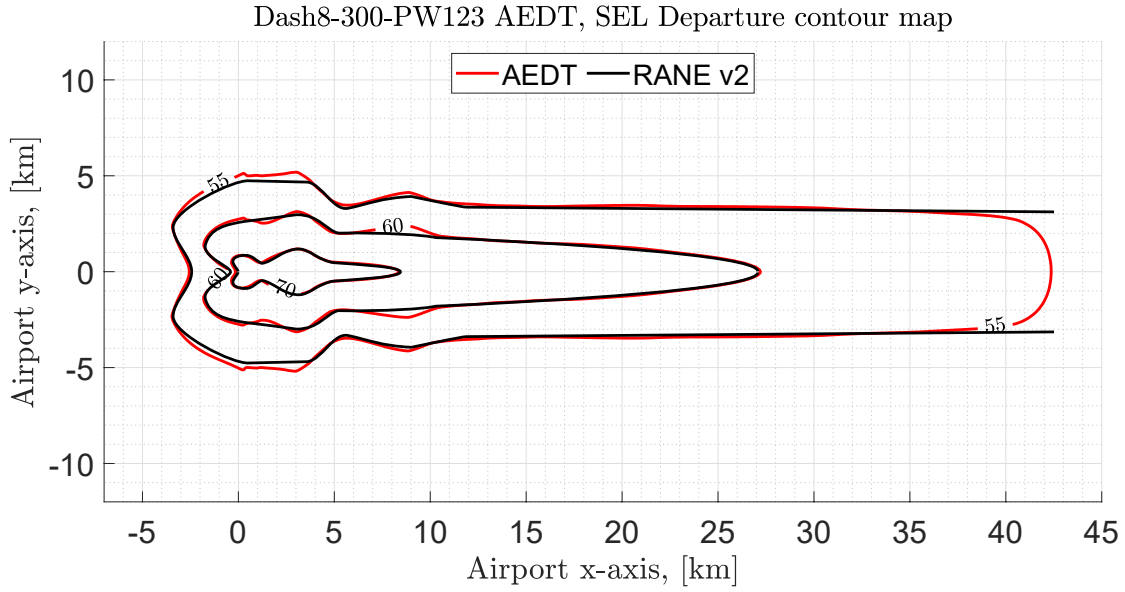

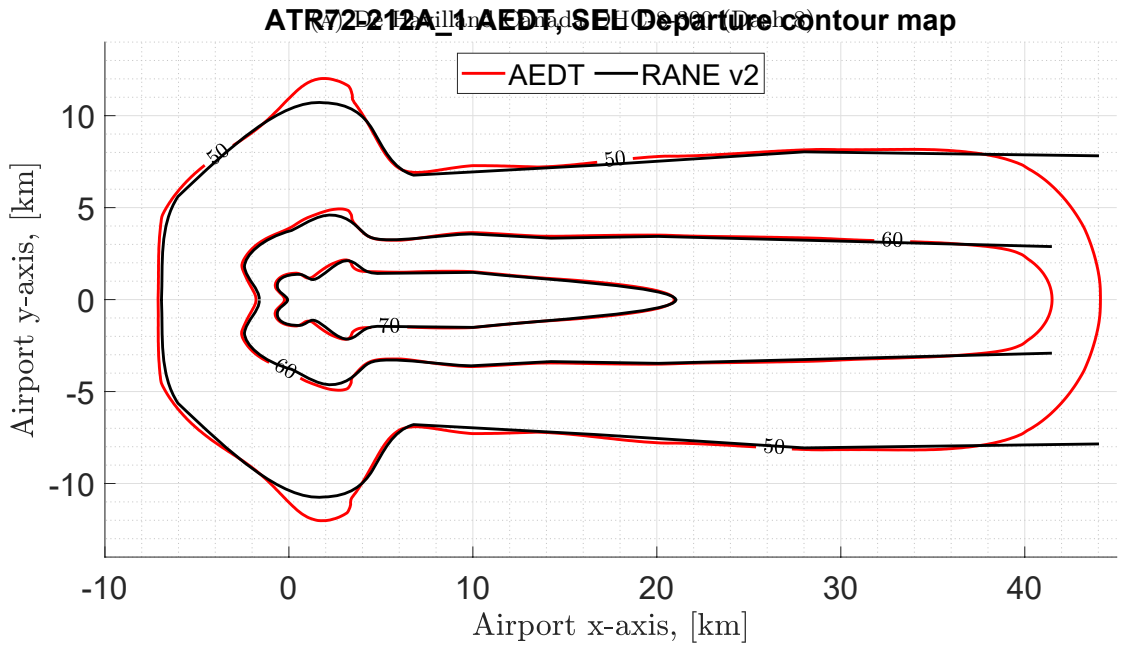

(B) ATR72-212A

FIGURE 7.36: Comparison between the RANE v2 and AEDT 3c prediction for fixed wing aircraft.

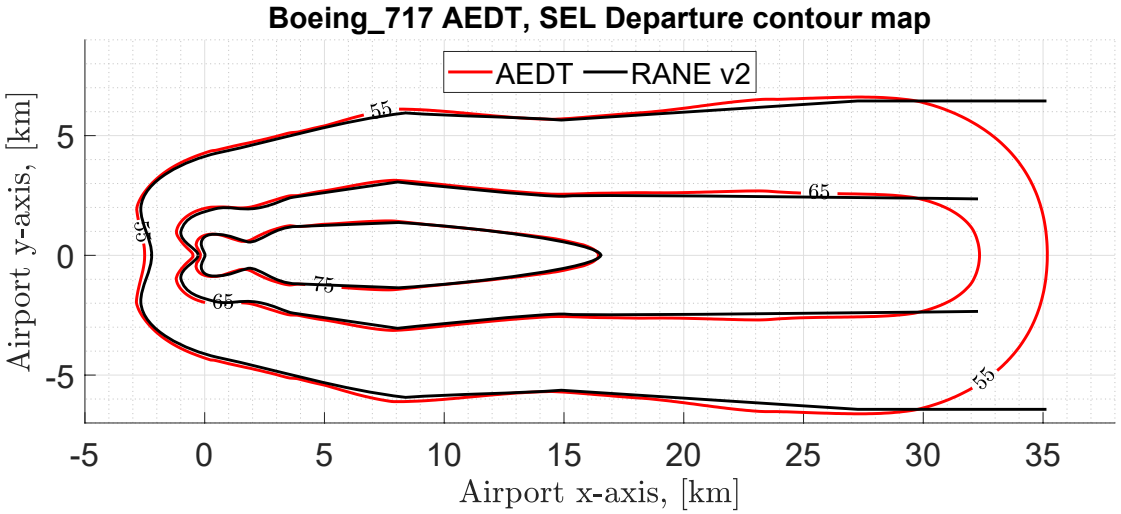

(A) Boeing 717

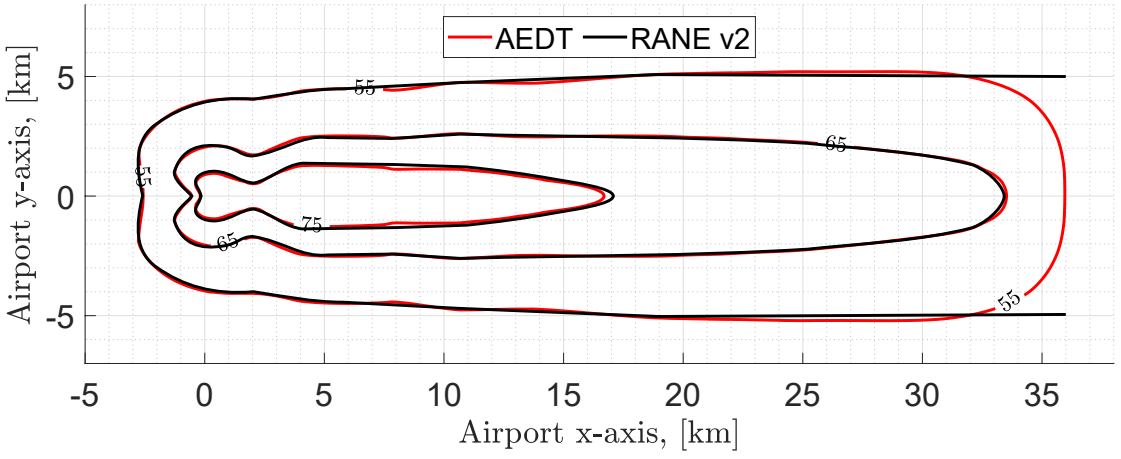

(B) A320neo

FIGURE 7.37: Comparison between the RANE v2 and AEDT 3c prediction for fixed wing aircraft.

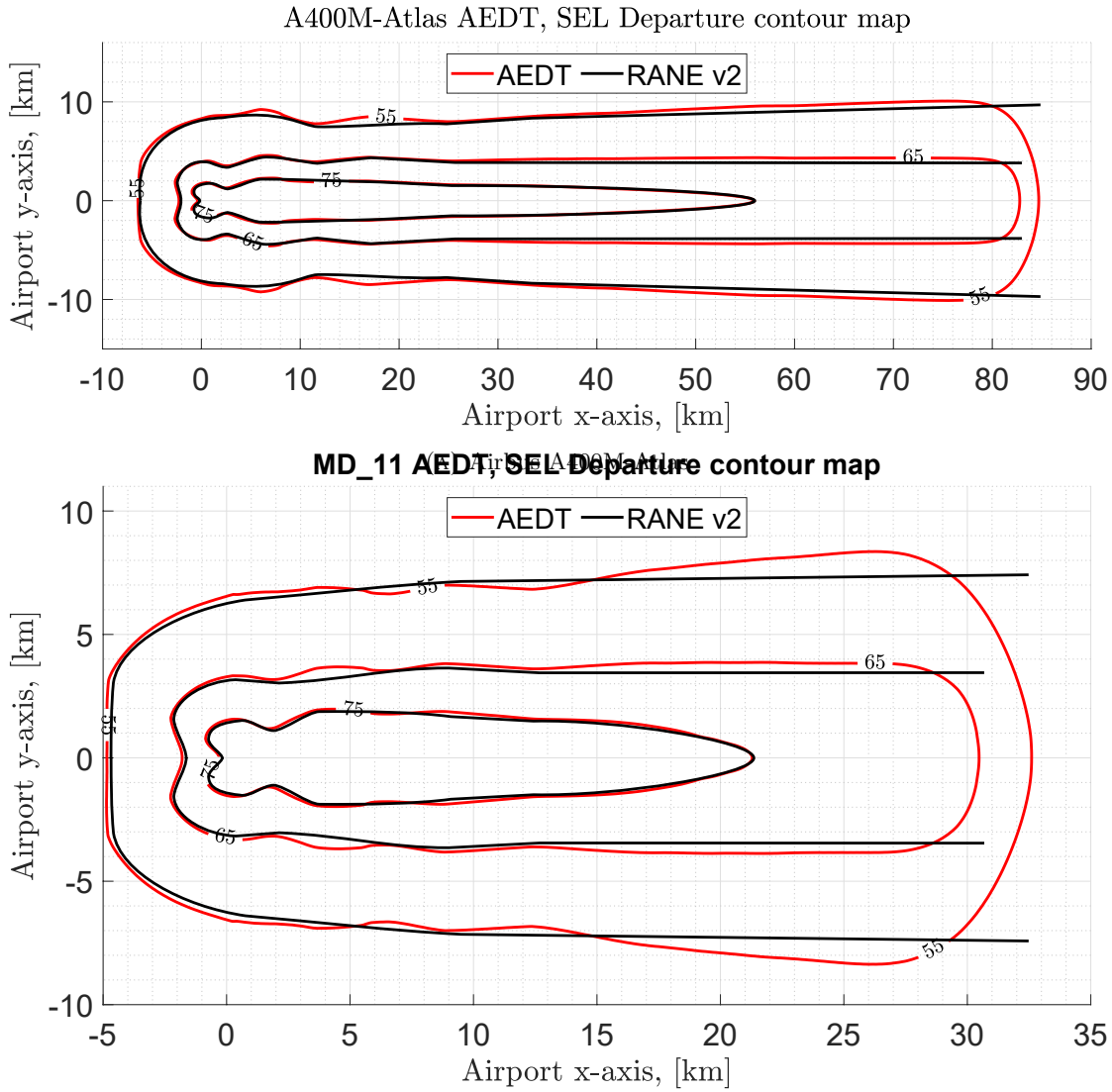

(B) McDonnell Douglas MD-11

FIGURE 7.38: Comparison between the RANE v2 and AEDT 3c prediction for fixed wing aircraft.

Rotorcraft

The reason helicopters were used as a part of the verification and benchmarking of RANE v2 is three-fold:

1. as the main feature introduced in RANE v2 is the ability to treat three-dimensional directive sources, the studied aircraft should also be characterised by inherent directional properties, a feature well documented in rotorcraft vehicles and specifically helicopters.
2. Allows the comparison to an industry proven tool, namely AEDT, with the starting input NPD and static directivity data being exactly the same, allows for a fair comparison of the capability of RANE v2.
3. The main assumption about novel aircraft is the presence of a rotor / propeller base propulsion system. The capabilities (and shortcomings) of RANE have already been proven for conventional turbofan aircraft, however rotor / propeller (and their associated aeroacoustic characteristics) have not.

Finally, a fourth reason, not relevant to the context of this thesis but the development of the greater capability within our research group, a method for the generation of NPD curves for rotorcraft vehicles is also under development. This coupled RANE v2 allows the assessment of rotor / propeller powered aircraft from the definition of individual sources all the way to noise exposure on the ground.

In order to compare results to AEDT predictions two types of directivities must be specified. First, the start-of-roll directivity function. For helicopters, this directivity correction in AEDT accounts for static radiation patterns that occur while the vehicle is on or slowly ascending vertically from the helipad. To account for this, static directivity data was fitted by a sinusoidal curve fitting model and then decomposed into spherical harmonics. The spherical harmonics expansion was then used as an input for the directivity function on the initial segment of the flightpath. This whole procedure is outline in Figure 7.40.

Secondly, lateral directivity corrections in AEDT for helicopters are accounted for using 3 NPD curves for every operation, a centre one (directly under the flightpath), a left one ($\varphi = -45°$ with respect to the flightpath) and a right one ($\varphi = 45°$). Examples of the constant speed departure NPD's of the Boeing Vertol may be seen in Figure 7.41 (left). All levels at azimuthal angles between the left and centre curves are interpolated logarithmically (the same applies for all values of φ between the right and centre). For values of $\varphi > 45°$ and $\varphi < -45°$ the level at the right ($\varphi = 45°$) is taken and for the left-hand side NPD respectively.

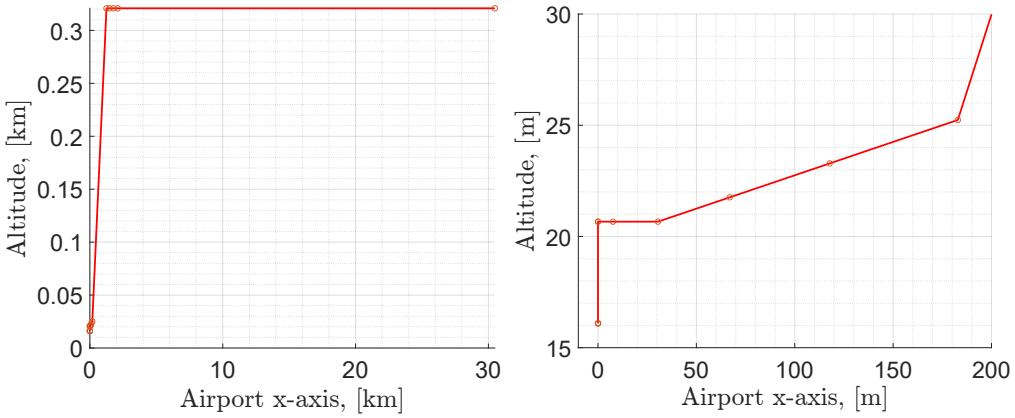

(A) Whole flight profile (B) Initial ascent

FIGURE 7.39: Vertical flight profile for the Eurocopter AS365 Dauphin for departure.

Three helicopter models were used in this comparison, to cover three different weight (size) groups. The Schweiser 300C, a light utility helicopter, the Eurocopter AS365 Dauphin, a medium sized also utility helicopter; and the Boeing CH-47 Chinook, a large transport helicopter. The default helicopter flight profile from AEDT 3c was used along with a default linear flight track. An example departure flight profile for the Eurocopter AS365 Dauphin can be seen in Figure 7.39. The total flightpath is broken down into four major segments: a. A vertical take-off, b. a horizontal acceleration, c. a climb to altitude and d. a horizontal steady level flight. These are also the segments used to model the take-off operation in RANE v2. The resulting contour comparison for all three helicopters may be seen in Figure 7.42.

In order to generate a directivity function suitable for RANE v2, the three distances at the sound exposure (in the case of the example Figure 7.41, 55 dB SEL is chosen) of interest were used to generate a polynomial curve fitting for all values of φ between $-90°$ and $90°$, Figure 7.41. The black crosses on the right-hand-side of Figure 7.41 represent the distance obtained by the green crosses on the NPD's (left), referenced to the distance of the centre NPD. The correction $\Delta R(\varphi)$, is then used along with the nominal centre NPD to generate the required noise surface and contour.

It is worth noting that the polynomial fit in Figure 7.41 is an aid that allows the fitting of a spherical harmonic expansion to a function that otherwise has a discontinuous first derivative. It is not an exercise in attempting to replicate or extending the lateral corrections used by AEDT. The discontinuous nature of the correction, as it is implemented by AEDT, would result in multiple high order modes being required in the spherical harmonic expansion to capture those discontinuities. The AEDT methodology for lateral correction is in itself a simplifying assumption as well as a compromise, that balances the need of applying a lateral correction, and the cost and time expense of generating lateral NPD curves for all applicable helicopter and air vehicles. The largest

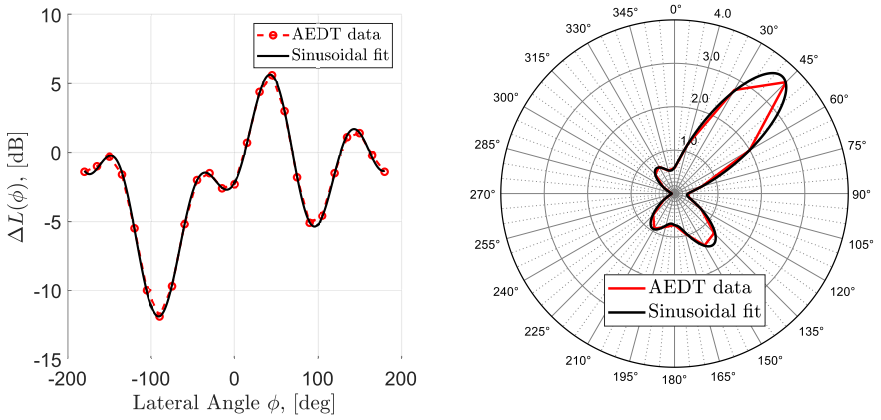

(A) Static directivity index, DI [dB] pattern of the Boeing CH-47 Chinook. (Left) Cartesian plot showing the raw AEDT data [213, 214, 98] and a polynomial fit. (Right) Polar plot of the same data and fit in the form of a directivity factor, D [-].

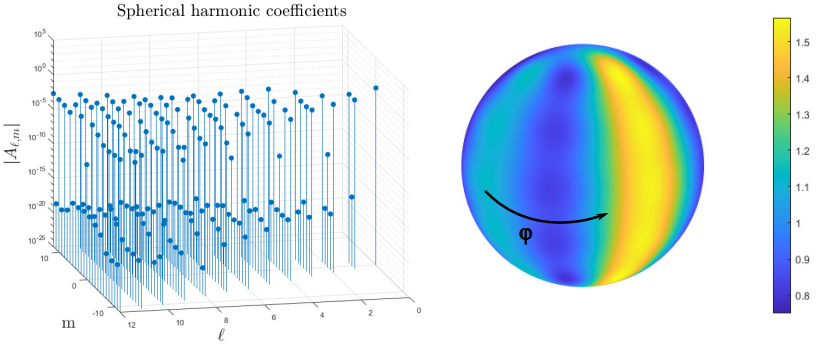

(B) (Left) magnitude of the spherical harmonic expansion coefficients for the static directivity data fit of Figure 7.40a. (Right) Spherical harmonic representation of the static directivity on a spherical colour-map plot. Output of Equation 5.39.

FIGURE 7.40: Procedure of treating numerical data as inputs to RANE v2. The output spherical harmonic expansion of Figure 7.40b is then used to generate the required noise surfaces.

errors introduced are at the extremities and beyond of the domain of interest ($\varphi \approx \pm\pi/2$), at which point the noise is not radiated to the ground.

Finally, Figure 7.43 shows a contour map comparison for the Boeing CH-47 Chinook. The map includes sound level of 75 db, 65 dB and 55dB. RANE again matches the AEDT prediction very well, however it is evident that error increases as we look at lower SEL levels.

7.2.3 Discussion

Ground effect/reflection

One of the shortcomings of the RANE / pre-integrated noise surface methodology are ground effect/reflection corrections. Typically, Doc29 and Doc9911 methodology suggests application of such corrections at the obsever location, resulting in different

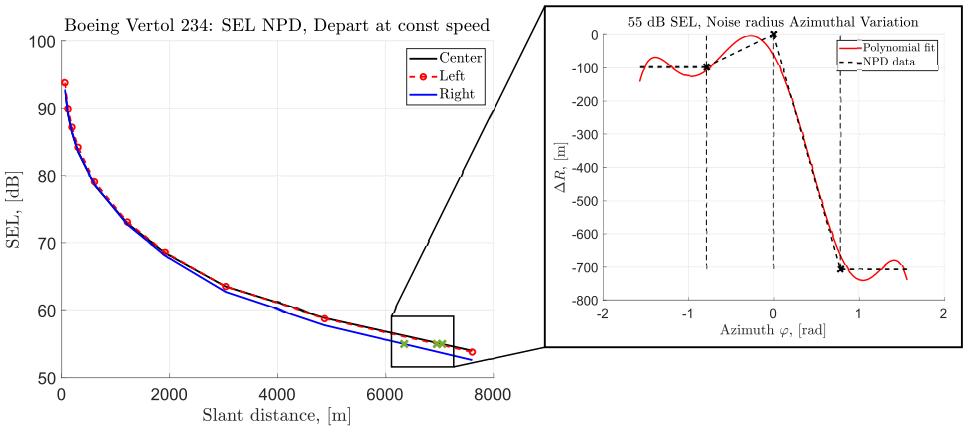

FIGURE 7.41: (Left) SEL Noise-Power-Distance curves for the Boeing Vertol 234 for a constant speed departure. The three curves indicate three lateral locations of observers. The green crosses indicate the intersection of the 55 dB SEL line with the curves. These points are used to generate a polynomial function that describes the variation in the azimuthal direction (Right).

corrections being applied for every observer location. As RANE calculates the location at which a certain noise level occurs on the ground, and not the noise levels at a specific (fixed) location, it is not possible to treat ground effects (and any observer location dependent corrections) in the traditional way of applying a ΔdB noise level correction to the already calculated levels. This would interfere with the generation of a single level contour through the constant level iso-surface (noise surface).

The workaround implemented is applying a correction ΔR to the noise radius calculated for the that particular segment. The correction ΔR is a function of γ the segment inclination angle, φ the azimuthal angle, and R the noise radius itself. As this correction is implemented from the source perspective for an entire segment, the resulting correction factor is applied to all observer locations calculated from that noise surface. The effect of this result may be mitigated by further discretising segments into shorter segments with different ΔR, allowing a single noise surface to determine the locations of fewer observers. In a realistic scenario, the degree of discretisation to correctly capture performance variation, allows for the gross result of ground effects to also be captured adequately.

Number of Spherical Harmonics considered

The point of truncation of the infinite sum in the spherical harmonic expansion is an important parameter to consider when describing the directivity factor using spherical harmonics. The higher the variability in the directivity, the larger the number of higher order terms required to accurately capture the variability. However, the example Figure 7.40, allows for an easy assessment of the relative scale and dominance of certain terms over others, proving that even for a realistic directivity as the one presented in for the Boeing CH-47 Chinook, a reasonable approximation could be obtained when using only $\ell = 4$, increasing computational efficiency even further.

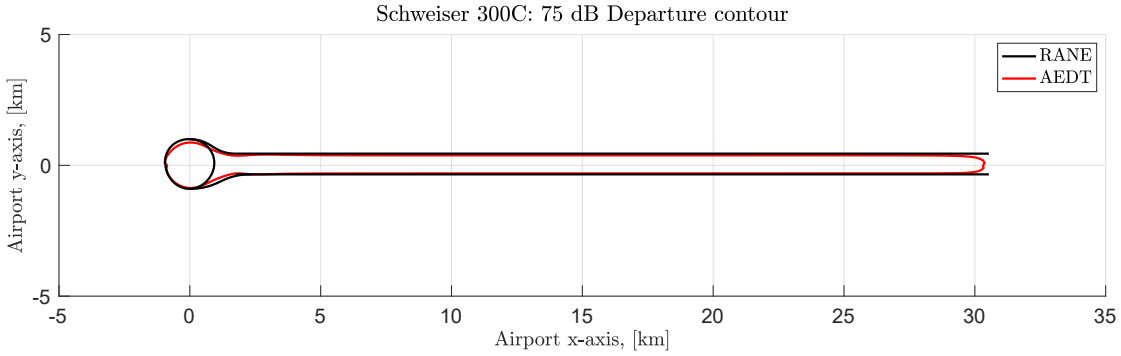

(A) Schweiser 300C

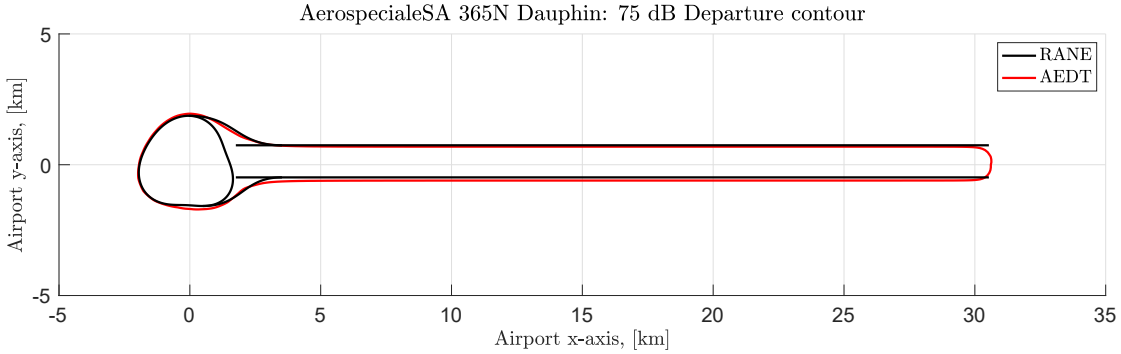

(B) Eurocopter AS365 Dauphin

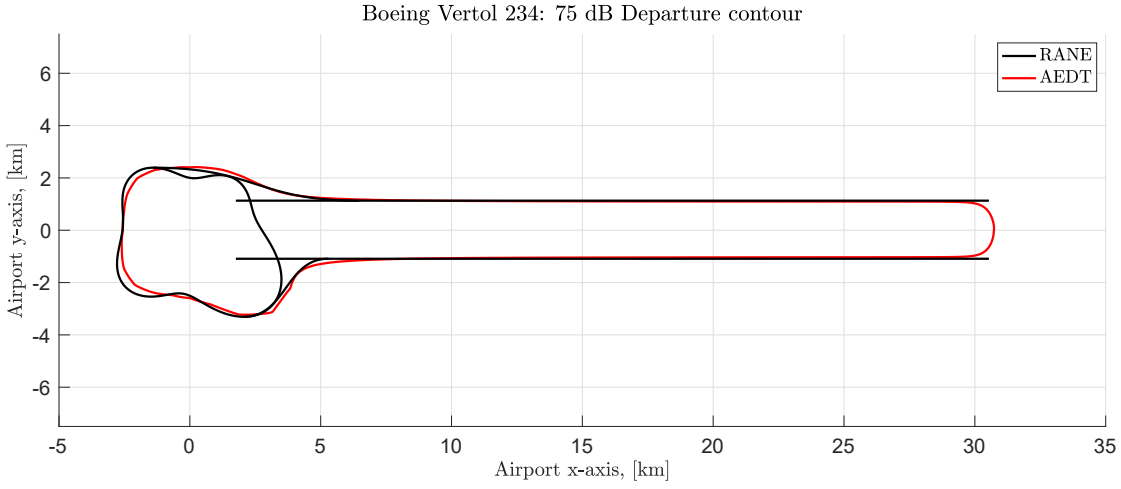

(C) Boeing CH-47 Chinook

FIGURE 7.42: Comparison between the RANE v2 and AEDT 3c prediction for three different helicopters.

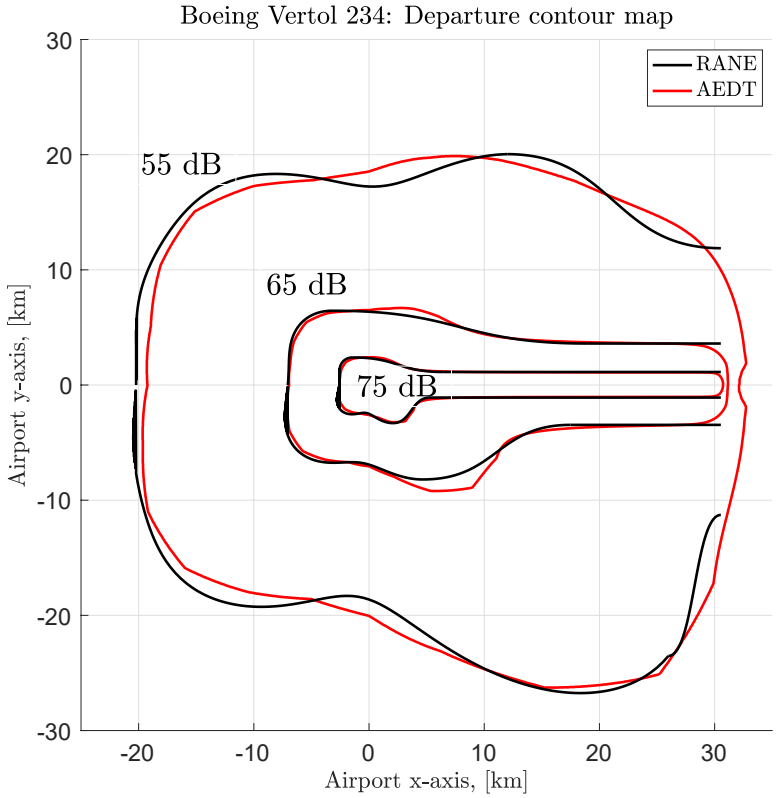

FIGURE 7.43: Departure SEL noise exposure contour map for Boeing CH-47 Chinook. Comparison between AEDT and RANE predictions.

Segment interaction error

The noise radius for each individual segment is calculated using NPD curves for a specific power setting, speed and sound exposure level. NPD curves assume a steady level fly-over a single observer from effectively $-\infty$ to $+\infty$ for the calculation of the exposure levels. Therefore, for any given point on the contour, the noise is due to one segment alone. The contribution of all other segments to that specific contour is neglected; this causes the noise segment method to underestimate the noise radius, as contributions from other segments would increase noise exposure at these observer locations causing the contour to move further away from the flightpath.

To demonstrate this, two tests were performed. One was using the grid method alone, where a vertical take-off operation was modelled in two different ways. (a) All segments of the flightpath contributed to the calculation of the exposure contour maps and (b) the vertical segment of the flightpath was calculated separately than the two horizontal ones. The results can be seen in SM Figure 4. The segment interaction error is similar to the finite segment error in the way that, as segments tend to an infinite length, the error reduces, and therefore the correction required is also reduced. When the noise at a particular observer is predominantly induced by the flight along a single (long) segment, the contribution of other segments is negligible. The interaction error becomes significant at observers in the vicinity of the waypoints, where the noise from the

proceeding and following segments are important. The Bezier curve implementation tries to correct this behaviour. Future work on expanding the capabilities of RANE beyond single runway airports and will introduce a correction factor ΔR to the calculation of the noise radii of all segments to account for the presence of other contributing segments. However, this is out of the scope of this work.

Overall RANE v2 does a good job of matching the contours generated by AEDT. Slight errors in the static directivity prediction (occurring in the first segment, around the $(0, 0)$ origin of the airport plane) are due to curve fitting errors and the truncation of the spherical harmonic expansion to only $\ell = 12$. Errors associated with the noise surface method its self are described in the following Section.

Bezier Correction

The Bezier curve implementation has been introduced, and is currently being further developed for two primary reasons:

i. the discontinuity that arises due to differences in the noise radius from one segment to the next and, ii. addressing the segment interaction error, an issue inherent to the main assumption of the noise surface methodology.

While addressing these two issues, the error relative to both the grid-method and AEDT reduces in terms of the total noise exposure area and the actual location (coordinates) of the contour. Trivially, from the cases examined this error is reduced from the range of 10-20% to 5-12% as per the example in the text, for estimation of absolute values of area.

Extensive error analysis and the further development of the Bezier curve correction should be part of future work. However, the material and cases presented form adequate proof of the value added by using it.

Generally, it is observed that the Bezier corrections increase the areas enclosed by the contours. This is partially due to the fact that they address the segment interaction error, which has the effect of underestimating the area enclosed by contours as the locations of the contour is calculated through the contributions from a single segment.

As also correctly observed, on some occasions, the location of the control points are not appropriately chosen, and the resulting correction may not have a logical interpretation. A discussion on the constraints of the Bezier control points has been added in Section V and how edge cases could be explicitly handled, through their definition.

Contour verification summary

However, in airport noise, complete contour (measured/experimentally obtained) data sets are almost non-existent. Airports base their noise reporting on a combination of predictions using as accurate as possible flight, trajectory and performance and calibrations obtained by various monitoring microphones in the vicinity of the airports.

For the intended use of RANE v2, a comparison to AEDT forms a concrete benchmark/ verification study for the capability added within this thesis.

7.3 Error analysis

7.3.1 Comparison between analytic and numerical integration of Directivity Functions

The calculation of the integral in Equation 5.15 has been performed numerically, in order to accommodate discretised directivity data, and analytically (using spherical harmonics) as presented in the previous sections. In order to validate the numerical integration, a few examples are presented below for different directivity functions using combinations of the monopole and the three different dipoles. The figures compare the value of the following integral, for different $D(\theta, \varphi)$. They are presented in polar plots, with the axial variation being in the variable φ.

$$\int_0^{\pi} D(\theta, \varphi)\, \mathrm{d}\theta \tag{7.11}$$

Figure 7.44 presents example calculations using the monopole and dipole to define the directivity functions. The result of the integration along the polar angle θ, is a function in φ, the azimuthal angle. The polar plots show how the function varies with φ. In each case the coefficients of the spherical harmonic expansion are presented in matrix form as, $A_\ell^m = [A_0^0\ A_1^{-1}\ A_1^1\ A_1^0]$ to distinguish between the coefficients of different order and degree.

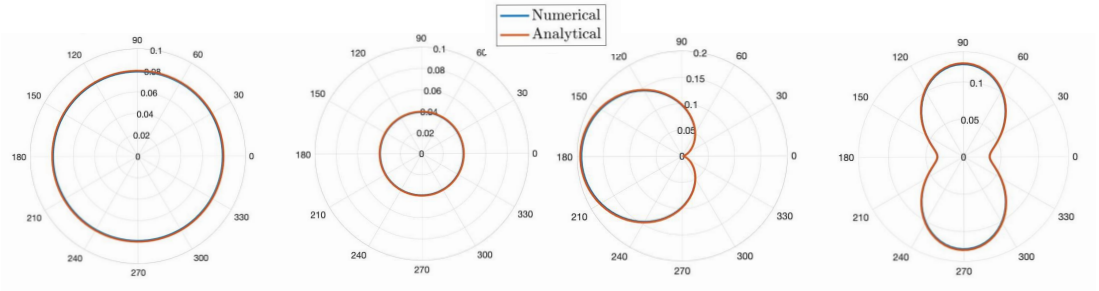

FIGURE 7.44: Comparison of the analytical and numerical calculation of the integral in Equation 5.47 for four different directivity functions of which the coefficients from left to right are: $A_\ell^m = [1\ 0\ 0\ 0]$, $A_\ell^m = [0\ 0\ 0\ 1]$, $A_\ell^m = [1\ 1\ 0\ 0]$, $A_\ell^m = [1\ 1\ 1\ 1]$.

7.3.2 Linear approximation error analysis

Section 4.5 calculates the fundamental tone of the modified scenario, in terms of a baseline level and some Δ correction as,

$$L_{f_1} = L_{f_1,0} + \Delta L_{f_1} \tag{7.12}$$

ΔL_{f_1} is by definition the difference of the level in dB produced by the baseline and the modified scenario of interest. In some cases, this may be called the absolute difference. However, in order to practically evaluate ΔL_{f_1} using the Hanson model as in Sections 4.3 and 4.5, a linear approximation assumption is used. Virtually, this means that the estimated change in noise, neglects the changes in the higher order terms. The crux of this assumption is that the linear approximation is performed on the logarithmic output function of the noise.

Assuming the noise level L_p is a function of parameters η_j, where j is an index through the total number of parameters influencing source i, a baseline condition denoted with subscript 0, may be expressed as,

$$L_p = f(\eta_{0,j}) = f(\eta_{0,1}, \eta_{0,2}, \cdots, \eta_{0,n}) \tag{7.13}$$

After implementing changes in operation and design, the parameters become, $\eta_1, \eta_2, \cdots, \eta_n$ where $\eta_j = \eta_{0,j} + \Delta\eta_j$, the sound levels become,

$$L_p = f(\eta_j) = f(\eta_{0,1} + \Delta\eta_1, \cdots, \eta_{0,n} + \Delta\eta_n) \tag{7.14}$$

The function f will be used to denote the exact value of the noise function while g the linear approximation of f. The SPL of an aircraft of s noise sources may be given by,

$$L_{p,0} = 10 \log \left(\sum_{i=1}^{s} 10^{L_{p,0,i}/10} \right) \tag{7.15}$$

where $L_{p,0,i}$ are the sound pressure levels of the individual incoherent noise sources that make up the total aircraft noise. If changes to parameters η_j are made to the individual sources, the new SPL may be written as,

$$L_p = 10 \log \left(\sum_{i=1}^{s} 10^{[L_{p,0,i} + \Delta L_i(\eta_0 + \Delta\eta)]/10} \right) \tag{7.16}$$

Each individual noise sources i may be expressed as a sum of the baseline value and the changes due to variation to each of the parameters:

$$L_{p,i} = L_{p,0,i} + \sum_{j=1}^{n} \Delta L_{i,j}(\eta_{0,j} \rightarrow \eta_{0,j} + \Delta\eta_j) \tag{7.17}$$

In order to estimate the change terms $\Delta L_{i,j}$ for each source with respect to all the parameters influencing it, we take the multi-variable Taylor series of the function $L_{p,i}$ at the point of the baseline aircraft. Taking into account the logarithmic nature of the function L_p, the fact that for the typical applications the baseline levels are already reasonably high, meaning the argument of the logarithm is $p^2_{rms}/p^2_{ref} >> 1$. Modifications to the parameters are assumed to be small as incremental improvement to design and operation are expected. Taking these assumptions into account, the single term linear approximation is assumed, and higher order terms are neglected. Comparing the single order Taylor series with Equation 7.17 we have,

$$\sum_{j=1}^{n} \Delta L_{i,j}(\eta_{0,j} \rightarrow \eta_{0,j} + \Delta\eta_j) = \sum_{j=1}^{n} \frac{\partial L_{p,i}(\eta_{0,1}, \cdots, \eta_{0,n})}{\partial \eta_j}(\eta_j - \eta_{0,j}) \tag{7.18}$$

or the change to a single individual source is,

$$\Delta L_i = \sum_{j=1}^{n} \frac{\partial L_{p,i}}{\partial \eta_j}\Delta\eta_j \tag{7.19}$$

In the case of the Hanson propeller harmonic noise model, the baseline case may be written as ,

$$L_{p,0} = 10\log\left(\sum_{m=1}^{\infty} 10^{L_{0,m}/10}\right) \tag{7.20}$$

where $L_{0,m}$ are the SPLs of the individual harmonics tones. For added modularity to the proposed model, the levels are referenced to the fundamental tone. This is the method implemented in Equation 4.83 and 4.84.

The new level of the fundamental tone, and the new shape function are therefore given by,

$$L_{f_1} = L_{f_1,0} + \Delta L_{f_1}(\eta_j \rightarrow \eta_j + \Delta\eta_j) \tag{7.21}$$

and

$$F_1(m) = F_{1,0}(m) + \Delta F_1(m, \eta_j \rightarrow \eta_j + \Delta\eta_j) \tag{7.22}$$

In order to estimate ΔL_{f_1} and ΔF_1, the linear approximation in Equation 7.19 is employed. As in MONTANA this approximation means that in the region of interest (baseline point) the output noise levels repsond linearly to changes in the independent parameters. In most cases this is true for small changes in parameters. Non-linear relationships would have to be modelled with additional temrs in the expansion in order to avoid gross under or over-prediction(an example of a non-linear parameter-source relation is that of buzzsaw noise or multiple pure tone noise as a function of fan blade

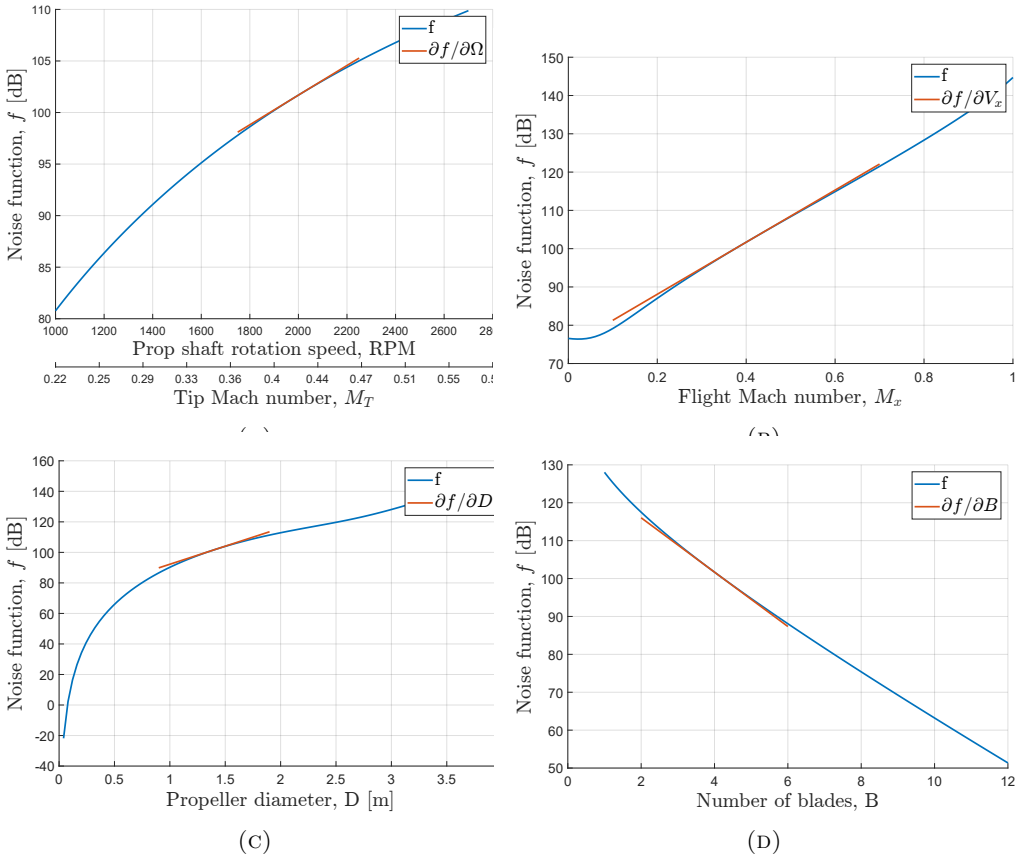

(C) (D)

FIGURE 7.45: First order Taylor series (linear) approximation of the Hanson model. The tangent line slopes are calculated using the partial derivative w.r.t each parameter $\Delta\eta_j$. Baseline parameters shown, $D = 1.4m$, $B = 4$, $M_x = 0.4$, RPM $= 2000$.

tip relative Mach number in the region of transition to supersonic tip speeds [36]). The changes are expressed as,

$$\Delta L_{f_1} = \sum_{j=1}^{n} \frac{\partial L_{f_1}(\eta_{0,1}, \cdots, \eta_{0,n})}{\partial \eta_j}(\eta_j - \eta_{0,j}) \tag{7.23}$$

and

$$\Delta F_1(m) = \Delta F_1\left(\frac{f}{f_1}\right) = \sum_{j=1}^{n} \frac{\partial F_1(m, \eta_{0,1}, \cdots, \eta_{0,n})}{\partial \eta_j}(\eta_j - \eta_{0,j}) \tag{7.24}$$

Equation 7.23 and 7.24 form the generalised versions of the previously derived Equation 4.88 and 4.90.

In order to calculate the error caused due to the linear approximation, the partial derivatives are calculated using a numerical central differencing scheme using 6 points. Illustrations of the function and the tangents calculated by the numerical derivative for four different parameters may be seen in Fig. 7.45. The tangent of the function is calculated at the baseline point.

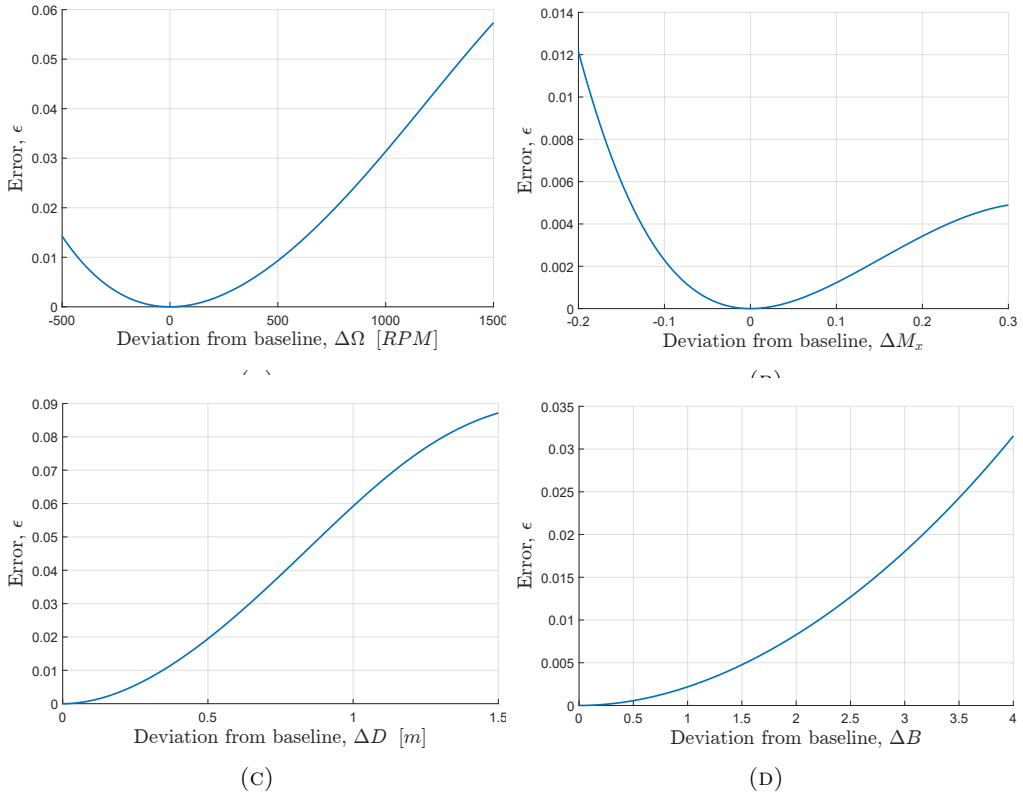

(C) (D)

FIGURE 7.46: Approximation error as a function of change in parameters $\Delta\eta_j$.

This section compares the linear approximation with the exact variation in the noise function on a dB basis. The calculations are performed for a single propeller whose design and operation parameters are varied. The error ϵ, is defined as a relative error,

$$\epsilon = \left\| \frac{f - g}{f} \right\| \tag{7.25}$$

where f represents the exact value of the functions, while g the linear approximation. Fig. 7.46 shows the error between the actual function values and the linear approximation for four different parameters. The chosen baseline point has parameters of, diameter $D = 1.4$ m, number of blades $B = 4$, flight Mach number $M_x = 0.4$ and rotational speed of, RPM = 2000. The x-axes portray $\Delta\eta_j$ as the prediction start to deviate from the baseline, where j indexes through parameters η.

A more physical way of interpreting the error would be to look at the absolute change in noise level in decibels. By any means however, the error remains small ($\epsilon < 0.1$) even for relatively large changes.

7.4 Summary

Chapter 8

Case Studies I: Next generation regional aircraft

8.1 Overview

Zero/low emission goals are driving the development of the next generation of regional airliners and the accompanying aviation system. In order to generate the required knowledge and develop a plan of action, the UK through various government or otherwise funded projects has brought together various consortiums of leading industry and academic partners. Projects such as the UK Research and Innovation (UKRI) funded project NAPKIN (New Aviation, Propulsion, Knowledge and Innovation Network) [215] and the Aerospace Technology Institute (ATI) project FlyZero aim to deliver insight into the design of zero/low emission aircraft concepts as well as the infrastructure and market required to support such a transition. The similar EU funded project Clean Sky 2 Joint Undertaking, has similar goal of improving competitiveness and mobility in Europe.

All projects however, have additional noise abatement goals. This Chapter investigates the noise immissions of a variety of regional sized aircraft concepts, applicable to the scenarios considered by project NAPKIN. MONTANA is applied to calculate NPD curves, and the predicted noise certifications levels of the proposed hybrid/electric regional aircraft. Changes to noise exposure area around airports with respect to the reference aircraft are also estimated.

8.2 Baseline regional aircraft

The quantification of improvements in noise immissions and specifically noise abatement technology and operations requires the precise definition of the reference conditions,

(A) Britten Norman BN-2

(B) De Havilland Canada DHC-6 Twin Otter

(C) BAe Jetstream 31

FIGURE 8.1: Small regional aircraft.

relative to which improvements are sought after. This assumption is also the basis of MONTANA in terms of developing the representative lumped source models and performing the whole aircraft noise comparison.

The concept aircraft discussed in this Chapter fall in two categories: i. modified (retro-fitted) designs and ii. clean sheet designs. The modified concepts fundamentally base their design on current existing aircraft, their airframe as well as mission and performance objectives. New technology is then introduced to replace current systems and subsystems (e.g. retro-fitted novel hydrogen propulsion systems), requiring adaptation of the reference aircraft to give a viable design. In the case of the clean sheet designs, the reference aircraft mission and performance objectives drive the design of a new aircraft, from the ground up. In both cases, however, reference aircraft have been defined from a design perspective.

The reference, or baseline, aircraft chosen for MONTANA and the subsequent noise comparisons, are the ones chosen as the design baseline aircraft. These aircraft are the B-N Islander, the de Havilland Canada DHC-6 Twin Otter 400, the British Aerospace Jetstream 31, the ATR 42-600, the ATR 72-600 and the Airbus A220-100 (Figures 8.1 and 8.2). Design and performance data for the baseline aircraft may be found in the supplementary material of this thesis. The baseline aircraft were chosen to cover a range of sizes in the regional category of aircraft and for being a representative sample of the type of aircraft operating in each class; as well as being well documented in the public domain.

Noise metric comparison is not as straight forward when dealing with realistic fleet environment. The number of operations and fleet composition heavily influence the output noise metrics and are functions of parameters such as aircraft maximum range capability, maximum passenger capacity specific fuel consumption etc. In order to access the effects, on and airport level, of introducing novel technological changes to aircraft appropriate comparisons need to be defined, taking into account the variation of the previously mentioned parameters.

For this chapter, the focus remains on direct 1-1 comparison, from noise certification perspective, as well as single event noise footprints, of the concept aircraft and its

(A) ATR 42 - 600

(B) ATR 72 - 600

(C) A220 - 100

FIGURE 8.2: Large regional aircraft.

respective reference aircraft. As per current certification standards, in this case the MTOW is the appropriate parameter to base the comparisons on. This may be easily established when considering a simple single event comparison between two identically sized aircraft. The noise in dB (for no metric in particular) per kg of aircraft mass to be lifted into the air will be function of the operating technology and design decisions used on-board the two aircraft, this is related to design efficiency (with respect to noise) and noise abatement at the source. Variations in performance and operation of the two aircraft will impact the noise generation and pinpoint beneficial characteristics. This paradigm essentially captures the intent of the ICAO and other organisations, when comparing previous, current and next generations of a single aircraft model, and looking for continuous improvement.

8.3 Concepts

The concept aircraft, as suggested, are alternative hydrogen-powered aircraft at similar sizes to those they already use. The propulsion systems as well as energy storage and delivery system architecture variation from concept to concept is the main differentiating factor between concepts other than size. The concepts are slit into five categories with respect to the seating capacities of the representative reference aircraft. The categories are:

- ***A***: 9 passenger aircraft based on the B-N Islander.
- ***B***: 19 passenger aircraft based on the DHC-6 Twin Otter.
- ***G***: 19 passenger aircraft based on the Jetstream 3100 series.
- ***D***: 40 passenger aircraft based on the ATR 42-600.
- ***Z***: 90 passenger aircraft based on the Airbus A220-100.

Each category contains one or more concept aircraft based on the performance and/or airframe geometry of the category reference aircraft. The differences between the

concepts of a single category relate to the implementation of novel energy storage and propulsion systems. The thesis supplementary material contains the performance and design parameters relevant to all presented concepts. A summary is provided in Table 8.1.

TABLE 8.1: Design and performance parameter overview for concepts developed by project NAPKIN.

Concept Parameters							
Concepts	A1	B4	G1	B7	B8	D1	Z1
Noise Chapter	14	14	14	14	14	14	14
MTOW (kg)	2,994	6,311	8,470	10,000	10,000	19,055	48,222
Range (km)	236	1,151	1,102	550	550	1,148	2,654
PAX	7	19	19	19	19	40	90
Max Static Thrust (kN)	4.77	5.08	11.67	14.90	14.90	-	-
Net takeoff Thrust (kN)	3.90	3.20	11.49	9.697	9.697	-	-

The main technology leveraged and investigated by the concepts revolves around hydrogen as the main energy source for future aviation. Four key factors will determine the viability of such architectures, on an aircraft design level, but also on a market basis: hydrogen storage, hydrogen handling safety, certification and regulation and hydrogen production. In the context of the aircraft concepts, these factors manifest into specific design choices that can be summarised as follows:

- Liquid versus gaseous hydrogen.
- Onboard liquid/gaseous hydrogen storage.
- Fuel cell systems.
- Hydrogen combustion.
- Thermal management.
- Power distribution system and its efficiency
- Electric motor specific power.

These specific technology considerations have been interpreted in different ways and implemented into the different concepts.

In addition to the introduction of hydrogen and its knock-on effects on design, the clean-sheet concepts explore novel wing geometry set-ups and propulsion system configurations aimed to explore greater variation and flexibility allowed versus current technology. Such concepts may help identify possible performance efficiency gains as well as noise abatement technology and/or noise preferable design geometry architectures.

All the concepts are in conceptual stages of development, with many important component masses, sizes, and attributes lacking detailed design. However, it is anticipated that the current fidelity will allow for suggestive research on noise and operating costs. The results presented are from Concepts A1, B4, B7, B8, G1, D1 and Z. Departure and approach NPD curves have been calculated for $L_{\mathrm{A,max}}$ and SEL metrics, representing one instantaneous and one exposure metric.

A short summary of each of the concepts follow, to provide the discriminating context between the method chosen to implement hydrogen propulsion systems.

Concept A1 is based on a 9-seater Britten-Norman (B-N) Islander BN2B-26 aircraft. The retro-fitted design, removed the conventional 260 hp Lycoming 0-540-E4C5 engines, supplied with aviation gasoline fuel (91/96 octane Avgas 100L or 100LL), and replaced them with electric motors to drive the same 2-bladed Hartzell HC-C2YK-2B constant speed propellers of 1.98 m diameter, propellers. The motors are supplied with power from fuel cells that are fed with hydrogen which is stored in a high pressure gaseous form. The general arrangement of the proposed A1 concept may be seen in Figure 8.3.

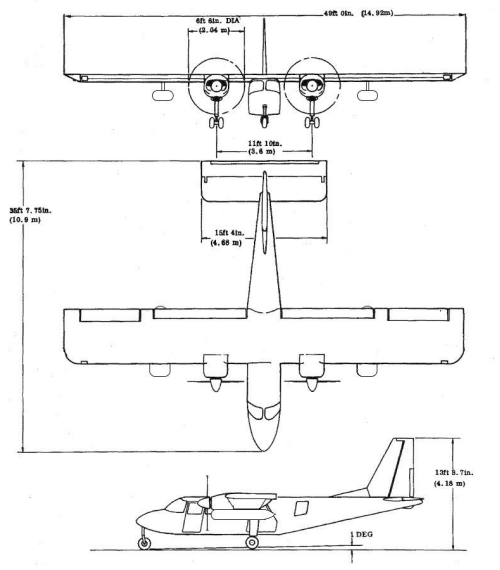

FIGURE 8.3: General arrangement of Concept A1, with gaseous hydrogen supplied fuel cell electric propulsion [215].

Concept B4 is a clean-sheet design derived from the specifications and performance parameters of the de Havilland Canada DHC-6 Twin Otter Series 400 aircraft. The number of passengers matches that of the DHC-6, while range has increase by approximately 400 km, at the cost of increasing the MTOW. The design implements LH2 fed to fuel cells that power electric motors, instead of conventional turboprop kerosene-powered engines. This liquid state hydrogen is stored in cryogenic tanks located at the rear of the fuselage, behind the passenger cabin and baggage bay. These tanks are then connected to the fuel system to directly supply wing-mounted fuel cell units to power four wing-mounted electric motors. The quad-prop design introduces significant change in the architecture of the previously twin DHC-6. The fitted props are identical to those on the reference aircraft (3-bladed Hartzell HC-B3TN3DY reversible pitch and fully feathering propeller), however operating at reduced the rotation speed of 2016 rpm (max takeoff) versus the 2110 rpm of the DHC-6. As expected, loading on each of the propellers is also reduced.

Concepts B7 and B8 are clean sheet designs, with mission and performance requirements also driven by those of the baseline Twin Otter. Both concepts are based on a hydrogen

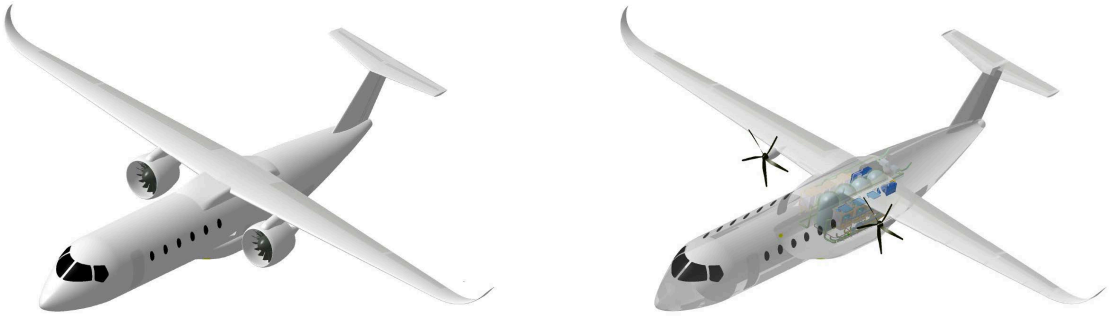

(A) B7 (B) B8

FIGURE 8.4: Renderings of Concepts B7 and B8.

fuel cell propulsion system, capable of carrying 19 passengers. At an identical MTOW of 10,000 kg the concepts mange a maximum range of 550 km. Renderings of the two concepts may be seen in Figure 8.4.

The main difference in configurations are the propulsor units themselves, with concept B7 using twin electric motor powered ducted fans, while concept B8 uses a more traditional twin propeller set-up, also powered by electric motors.

The concepts feature a high wing configuration with wing mounted propulsor units. The concept B8 architecture resembles that of a traditional turboprop. Both concepts store energy in the form of liquid hydrogen (LH2) and convert it to useful electrical power through the use of fuel cells. The aircraft and the propulsion systems have been designed to comply with CS-25.

The ducted fan configuration of concept B7 has a fan diameter 1.65 m, and operates at 1,760 rpm at MTOW power. The duct overall pressure ratio is 1.1. The configuration of concept B8 features a 5 blade open propeller of 2.2 m, operating at 2,200 rpm at MTOW power. Additional details of the fan and propeller design and operation, as well as detailed specification of the nacelle, duct and stator vanes (if applicable) for the ducted fans were not available at the conceptual stage of the designs. This results in a series of assumptions made on behalf of the author, guided by the designers, in order for acoustic predictions to be made using MONTANA. This is discussed in section 8.5.

Concept G1 is a clean-sheet design derived from the specifications of the BAe Jetstream 31 (Series 3100) aircraft. For acoustic analysis, the G concepts will also be referenced to the Twin Otter as a similarly sized turboprop aircraft. This is due to limitations in the openly available noise data (NPD curves) in the ANP database.

Design-wise concept G1 has been produced by taking the specification of the Jetstream 31 aircraft, including its cabin dimensions and attempting to match its performance with an aircraft powered by electric-motor-driven propellers. The electric power is provided by fuel cells which are supplied with hydrogen that is stored in cryogenic liquid form. The two propulsor/propeller configuration remains the same. Generally, the

performance of the Jetstream in terms of thrust-to-weight is very similar to that of the Twin-Otter at takeoff, with a ratio of ≈ 0.27 compared to ≈ 0.28 of the Twin-Otter. However, the chosen propeller configurations largely differ, due to different cruise and climb characteristics.

Once again the concept uses the same 4-bladed constant-speed propellers (Dowty Rotol Type (c)R.333/4-82-F/12) as the reference Jetstream 31. Operation remains at 1,591 rpm at max takeoff power meaning a more aggressive pitch is required to produce the additional 2 kN of thrust.

The increase in thrust requirement in due, in part, to the increase in mass of the electric propulsion system relative to that of the gas turbines as well as increases fuselage length aft of the passenger cabin to accommodate the hydrogen storage tanks. Therefore, although the mass of hydrogen is less than the mass of kerosene carried by the conventional aircraft, the overall mass is increased. Regardless, concept G1 remains within the Part 23 airworthiness requirements (8,618 kg or 19,000 lb), as well as the Annex 16 Chapter 10 noise certification requirements.

Concept D1 is a 40 passenger high wing, wing-mounted ducted fan configuration aircraft. The 40 seat aircraft was based on data generated as a result of the 19 seat concept B7 and B8 studies. The propulsion system is a liquid hydrogen fuel cell propulsion system, driving electric motor ducted fans. The wing has been resized to meet principle operational constraints consistent with the approach used for the 19 seat aircraft. Once again details of the propulsor units are not available.

Concept Z1 is a liquid hydrogen burning turbofan, based on the Airbus A220-100. The concept has been produced by matching the existing baseline aircraft mission profile in cruise only. The lift-to-drag ratio is kept constant, as well as the structural mass and airframe dimensions. The concept uses a liquid hydrogen turbofan propulsion system. In order to accommodate the hydrogen tank volume a reduction of passenger capacity from 125 pax at 30in pitch to 90 pax at 30in pitch is implemented. This gives a hydrogen storage volume of 34.3 m^3, with reserve requirements being matched to the baseline A220-100. All electrical components are assumed to have constant efficiency values. Details of the modifications required to directly combust hydrogen fuel within the turbofan engines are not available. The following noise predictions assume identical architecture to current technology high-bypass ratio, geared fan engines used be the .

The concept was designed with MTOW target of that of the baseline aircraft. This target was set from two perspectives, first propulsion system sizing and second noise certification classification. For the former, a major redesign of the installed propulsion system was being avoided, the assumption being that minor modifications to the existing baseline gas turbines would allow the direct combustion of hydrogen. Assuming the modified engines could match the A220-100 (Pratt & Whitney PW1000G) engine

rating requirements, size and mass, allowing for the installation on the airframe to be very similar, in not identical.

From the noise perspective, targeting the same MTOW as the baseline implies that the concept will be certified under the same Chapter of the ICAO Annex16 and will be positioned in a similar region as the baseline with respect to the maximum acceptable noise limits, as these are functions of MTOW. Additionally, considering similar propulsion system rating and MTOW, both noise certification and operational performance will closely resemble that of the baseline. Undeniably, this assumption of constant MTOW between concept and baseline, impacts the final design in other critical areas, such as useful payload (and therefore number of passengers in the case of a civil aviation aircraft) and maximum range, in order to accommodate the hydrogen fuel storage and distribution systems. Such an assumption may result in some practical flaws both from an engineering design point of view, as well as the business argument and viability of an aircraft concept with reduced payload and range capability relative to its predecessor. Detailed design can reveal major changes required to both airframe and propulsion system in order to accommodate the hydrogen systems. Examples of such incurred penalties relative to conventional kerosine aircraft are, tank structure, pressurisation/cryogenic components, fuel delivery components etc. On an airframe level, major design changes could be necessary to accommodate changes in centre of gravity positioning due to the tanks size and positioning.

These implications on the choice for MTOW, demonstrate the closely coupled field of aircraft design and noise prediction, and allow for trade studies to be performed on the conceptual design stage, as chosen by the author and NAPKIN consortium [215].

8.4 Concept Performance

Performance data at the conceptual design stage is limited. Operational performance data at different aircraft configurations and weights can not be estimated due to lack in design definition. The noise predictions, as a result have to assume constant performance at max takeoff power, which is a direct consequence of being at MTOW. This is not a problem for the estimation of sideline certification point levels, as this is a full-power at MTOW event. However, the other two certification points (flyover, approach), as well as operational noise for the estimation of noise exposure contours, are impacted.

The flyover certification point is a complex point to estimate. This is due to engine cutback taking place, as well as a change in the flight climb profile. The location and time, relative to the certification microphone, at which cutback occurs may significantly change the levels at the flyover certification point. In addition to the complexity of timing and flightpath geometry, the aircraft power setting is reduced. This would require additional thrust and operational parameters in order to calculate a cut-back

power NPD. For this reason, an empirical method of estimating the flyover certification point is used. The difference between the reference aircraft lateral and flyover certification points is used a correction factor. Using the estimated lateral certification levels for the concepts and adding this correction factor, the flyover level for the concepts are estimated. This approach is taken in the estimation of the flyover certification points for the larger Chapter 14 certified aircraft.

The approach operation and certification point requires additional considerations. Limited data is available for all concepts for the approach operation. As MLW thrust requirements and high-lift devices have not been provided, it was decided to model the approach performance using % of maximum takeoff thrust. Using performance data of the reference aircraft at MLW approach conditions, ratios of MLW to MTOW thrust were calculated. In addition to MLW performance settings, the same ratios were calculated for the minimum landing power setting (minimum landing weight) available in the ANP database for the reference aircraft. These ratios were then used on the concept MTOW to estimate the approximate maximum and minimum lading power settings. The resulting ratios are presented using a % in Table 8.2.

Although these values may not be the realistic operational values of thrust, this method allows for direct comparison to the reference aircraft, while also providing a possible range within which the aircraft might be expected to lie. Assuming identical % of max takeoff thrust assumes the concepts have the same landing performance (lift and drag characteristics etc.) as the reference aircraft. This might be the case for retro-fit design, whilst clean sheet designs might look to improve on the reference design. Where given, landing airspeeds have been taken into account.

TABLE 8.2: Power setting range assumptions for the approach operation, and NPD calculation.

Power settings					
	Islander	Twin Otter	ATR42-600	ATR72-600	A2202-100
Min (%)	26.6	30	16.7	16.7	12
Max (%)	58.2	100	30	30	26

8.5 Noise source considerations

In order to put together an appropriate lumped source model for each of the concept aircraft within MONTANA, the dominant source of noise need to be considered. As evident from previous sections, in many concepts minimal changes occur in the thrust generating portion of the propulsion system. This means the dominant noise source mechanisms will be the same between reference aircraft and concept; with exceptions discussed in sections 8.5.2.

The principal aircraft noise sources considered for the estimation of the NAPKIN concept NPD data are, propulsion system noise sources and airframe noise sources. Propulsion system noise sources considered, depending on the concept, are the fan and jet components of engine noise for ducted fan configuration and turbofan configurations; steady loading and thickness noise for propeller configurations.

First, the airframe noise source ΔPWL contribution is calculated, as in previous section of this thesis, using the Fink model [64]. In most cases, takeoff and landing configurations between the concepts and reference aircraft are non-existent. In the cases that differences do exist, the adapted Fink model [12] takes into account high-lift (specifically flap) devices deflection angles and landing gear size and shape. The main parameter changing the airframe noise is the airspeed.

Fan noise is modelled using the Heidmann model [53] while jet noise variation is modelled using the Stone model [69, 216] for coaxial nozzle jets, again as modified by Synodinos [12] for the use within the lumped source model. Both of these sources are used in the case of the ducted fan implementations (concepts B7 and D1) as well as the direct hydrogen combustion turbofan implementation (concept Z1). Fan variation is captures as function of net thrust F_N, bypass ratio BPR, fan diameter d_f, aircraft speed V_0, primary (core) jet speed V_j, secondary (bypass) jet speed V_{BP} and finally LP shaft speed (or fan speed) N1. Jet noise variation is calculated using net thrust F_N, geometric jet exit area A_j, aircraft speed V_0 and a mixed jet velocity V_m which is a function of the core and bypass jet velocities.

In the case of propeller aircraft, the propeller itself is the dominating source of noise. For the concept lumped source models, the modifications to Hanson's steady discrete noise from chapter 4 are used. A summary of the individual noise sources, the baseline noise predictions model and the specific parameters that determine the noise emission that were applied in MONTANA, are listed below:

- Ducted fan / turbofan engine
  - Fan (F_N, BPR, d_f, V_0, V_j, V_{BP}, N1), Heidmann model [53]
  - Jet (F_N, A_j, V_0, V_m), Stone model [69]
- Propeller (Hanson frequency domain model [60, 198])
  - Steady loading noise (F_N, D, RPM, V_0, V_m, blade geometry)
  - Thickness noise (D, RPM, V_0, V_m, blade geometry)
- Airframe (Fink model [64])
  - High-lift devices (δ_f, V_0)
  - Fuselage + wing (F_N, V_0, D)

– Landing gear (F_N, V_0, D)

The selection of these particular individual sources and respective models has been made following the results of total aircraft noise breakdowns for conventional turboprop aircraft [217]. References [218, 219] provide source breakdowns for conventional turbofan engines and identify the dominant sources. The methodology used within MONTANA that performs the source balance is presented by Synodinos in [12, 52].

Particular attention is given to concepts B7 and D1 using the ducted fan architecture. The fan configuration was modelled with the following assumptions:

- The Heidmann model was used, although strictly its is applicable to turbofan (and turbojet) aircraft. The main assumption of a single stage fan justified the use for concepts B7 and D1.
- The directivity pattern was assumed to be similar to that of a turbofan [20]. Specifically, two dominant lobes, one in the forward arc and one in the rear arc, represent the emission of the fan source in the forward arc, and the fan and jet combination in the rear respectively. The purpose of the specific directivity pattern is to capture the blockage effects due to the duct.
- Flight effects and additional sources due turbulence (including boundary layer) ingestion were not taken into account, as per the Heidmann model.
- Stator/strut interaction contributions are not taken into account at this stage due to limited design data. Duct characteristics and stator size, number and position were not specified therefore rotor-stator interaction (multiple pure tone noise) noise was not accounted for.
- Typically, ducted fan configurations lend themselves to the implementation of acoustic liners for further noise abatement. However, again due to lack of knowledge of the dimensions of the ducts, benefits due to liner technology are not implemented.
- The number of blades and fan geometry was not specified, therefore the parameters of the 19pax high-wing, wing mounted propeller configuration were used. Essentially assuming that the ducted fan has 5 blades.

Finally, a few notable amendments were made due to the limitations of available noise (NPD) data in the ANP database. These come in the form of substitutions of the baseline aircraft used in the noise prediction within MONTANA. First, concept G1 predictions were made based on the DHC-6 Twin Otter. This aircraft was chosen to maintain consistency amongst the smaller regional concepts. Both the Jetstream 31 and the Twin Otter are certified for noise under Chapter 10 of the ICAO Annex 16. Second,

is the substitution of the ATR42 baseline aircraft of concept D1 with data from the ATR72. This is a minor substitution, as the design and operation of aircraft is very similar.

Probably the largest (and possibly most impactful) substitution was that for concept Z1. The reference aircraft chosen for calculations is the A320neo, a significantly larger single aisle aircraft (MTOW = 79 t compared to 48.2 of the concept). As, no NPD data is available for A220-100, the NPDs of the A320neo are used and an appropriate power setting chosen as the baseline point. Both the A220-100 and A320neo are powered by high-bypass ratio, geared turbofans of the P&W PW1000G family, using common technology levels.

8.5.1 Directivity and Installation effects

Two main categories can be used to categorise installation effects. First, impacts that change the aircraft's directivity and how the determined sound power is dispersed. Usually, shielding and reflection effects are involved. The second category consists of installation effects, which themselves produce noise and add to the total system's sound strength. The source balance of propeller-wing interactions setups has recently been quantified by investigations [220, 221, 222], whereas the installation effects that are evident on traditional tube and wing aircraft are reviewed in reference [176].

Examples of total aircraft measured noise for turbofan aircraft with underwing and fuselage tail mounting are given in the reference [21]. Effects of installed shielding and noise reflection are also described. Due to the ground microphones being protected by the aircraft wing, the forward noise, where fan noise is dominating, is significantly reduced for engines installed on the tail of the fuselage. Because of the wing's sound reflection, underwing placed engines make more noise that travels to the ground. Finally, the azimuthal variation of noise due to jet blockage effects and wing reflections is demonstrated by Moore et al. [206].

Taking the above as considerations a series of corrections are applied to the lumped source models of each concept depending on the configuration of each. These corrections are applied as a delta dB change to the OASPL of the noise sources that are dominant at the angle of interest. A summary of installation effect noise adjustments pertinent to the ideas computed from the cited references is given in Table 8.3.

The directivity of the individual noise sources is modelled using data from the NASA ANOPP tool [20], Appendix F briefly discusses this data, while the use and implementation of the data in the MONTANA model are discussed in Chapters 4 and 5 while also by Synodinos [52] when implementing a lumped source model specifically for turbofan aircraft architectures. Propeller loading and thickness noise directivity is

TABLE 8.3: Summary of installation effect noise corrections for ducted-fan and propeller propulsion systems.

Installation effects corrections			
	Correction (dB)	Direction	Ref
Under-wing mounted ducted-fan, flap noise (forward arc)	-2	$0° < \theta < 45°$	[9]
Under-wing mounted ducted-fan, flap noise (rear arc)	2	$140° < \theta < 180°$	[9]
Underwing mounted ducted-fan, jet, turbomachinery flap noise	2	$0° < \theta < 180°$	[8, 10]
Underwing mounted ducted-fan, fan forward arc reflection	2	$0° < \theta < 90°$	[11,12, 13,14]
Underwing mounted ducted-fan, fan rear arc reflection	2	$90° < \theta < 180°$	[11,12,13,14]
Fuselage tail mounted ducted-fan.	-3	$0° < \theta < 90°$	[15]
Underwing mounted propeller reflection	3	$45° < \theta < 135°$	[15]

modelled using the Hanson model approximation of Chapter 4 surprised by the following directivity indices[1] (DI),

$$(DI)_V = \frac{\sin\theta}{(1 - M_x \cos\theta)^3} J_{mB}\left(\frac{mBzM_T \sin\theta}{1 - M_x \cos\theta}\right) \Psi_V(k_x) \tag{8.1}$$

for propeller steady loading noise, and,

$$(DI)_L = \frac{\sin\theta}{(1 - M_x \cos\theta)^2}(M_r^2 \cos\theta - M_x) J_{mB}\left(\frac{mBzM_T \sin\theta}{1 - M_x \cos\theta}\right) \Psi_L(k_x) \tag{8.2}$$

for propeller steady loading noise.

8.5.2 Noise prediction risks

It is important to identify potential additional sources of noise that are unique to the hydrogen concepts discussed herein, and that could have potential of dominating the sound profile under specific operating conditions if care is not taken. In addition to the risks of additional sources, the noise prediction methodology used does not account for noise abatement design choices implemented or planned for the concept aircraft. Examples of such design choices could be the use of fan intake liners or the use of novel propeller/fan design for quiet operation.

[1] Nomenclature of Equations 8.1 and 8.2 is as presented in Chapters 2 and 4.

Table 8.4 summarises the risks associated with unaccounted for noise sources.

TABLE 8.4: Potential unaccounted for noise sources.

Source Mechanism	Description
Rotor Stator interaction	Interaction of periodic velocity fluctuations with downstream outlet guide vanes (stator) produces discrete frequency noise or pure tones. Increasing the strength of the interaction or increasing the efficiency with which the source radiates acoustic waves. Correct choice of blade/vane count ratio and vane location.
Multiple propulsor interaction	Interaction of individual propulsor potential fields, as well as wake/tip-vortex interaction with or without the interference of the propulsor structure itself.
Propulsor-airframe interaction	Interaction of airframe component potential fields with the propulsor field causing unsteady effects on noise generating mechanisms. Propulsor wakes interacting with the airframe structure and vice-versa.
Fuselage Scoop/Intake noise	Flow over open cavities or cut-outs in the surfaces of aircraft often produces intense pressure oscillations in the cavity which radiates discrete noise.
Hydrogen combustion noise	Flame attachment due to high reactivity of H_2 has a significant effect on how low-swirl injectors respond to self-excited flame oscillations. This leads to significantly higher acoustic driving due to the compact shape of the flame and its flame folding dynamics. Mitigation of flame attachment and/or deferring the formation of the outer shear layer is needed to avoid such noise generation dynamic mechanisms. Approach operations are at risk due to the higher impact of core noise, and possible higher idling power settings to maintain flame.
Electric motor	The dominant source of noise in electric motors comes from the interaction of a rotor and stator that induces vibration of the motor frame. Preliminary research shows that levels are expected to be low compared to other propulsion noise sources like the fan, however, it is possible that a portion of a flyover during approach will include motor noise depending on the motor installation.

8.6 Noise predictions

8.6.1 NPD curves

Taking the above modelling assumptions and practices in regard to performance and noise sources of the concept aircraft, Figures 8.5 to 8.11 present takeoff NPD curves for all concepts. Approach NPD curves are presented in Figures 8.12 to 8.18.

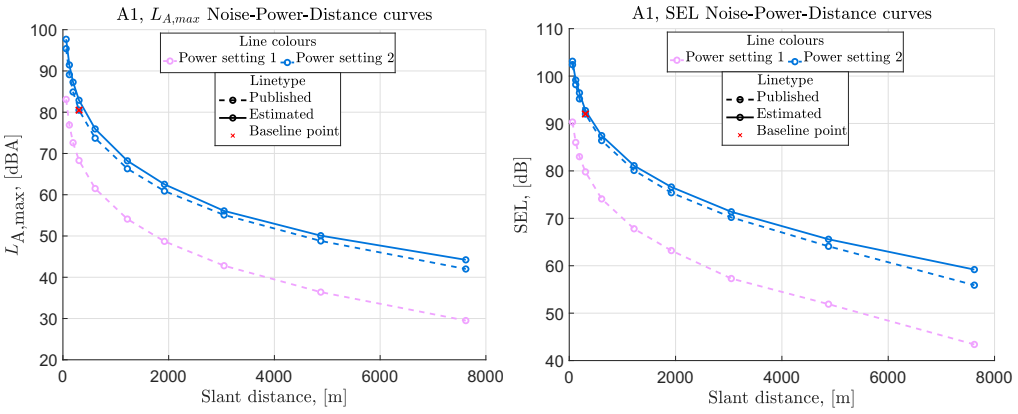

(A) $L_{A,max}$ (B) SEL

FIGURE 8.5: Predicted departure NPD curve for Concept A1 (solid line) compared to the baseline Islander departure NPD curves (dashed lines).

NPD curves are presented in two metric, $L_{A,max}$ and SEL, both represent single event metrics with the first being instantaneous and the second an exposure metric. $L_{A,max}$ is chosen an indication of maximum sound power emission, whereas SEL being an exposure metric, is used to demonstrate the effect of directivity over an event. Additionally, these two metrics are used for the certification of small regional aircraft as discussed in Chapter 2.

Departure

For takeoff NPD curves maximum power setting is assumed at MTOW. This is indicated with the solid line for the concept aircraft. For comparison, the baseline NPD data for the reference aircraft at MTOW, in each case, is shown in dashed lines of the same colour. For the reference aircraft (with the discussed substitutions), additional power settings have been plotted in other colours. A red cross indicated the baseline noise point chosen for the predictions. The noise level at this point is back-propagated to the source (1 m lumped source sphere) to determine the baseline level to which deltas are then applied. The spectra for the baseline aircraft are the normalised one-third octave band spectra provided within the ANP database [98].

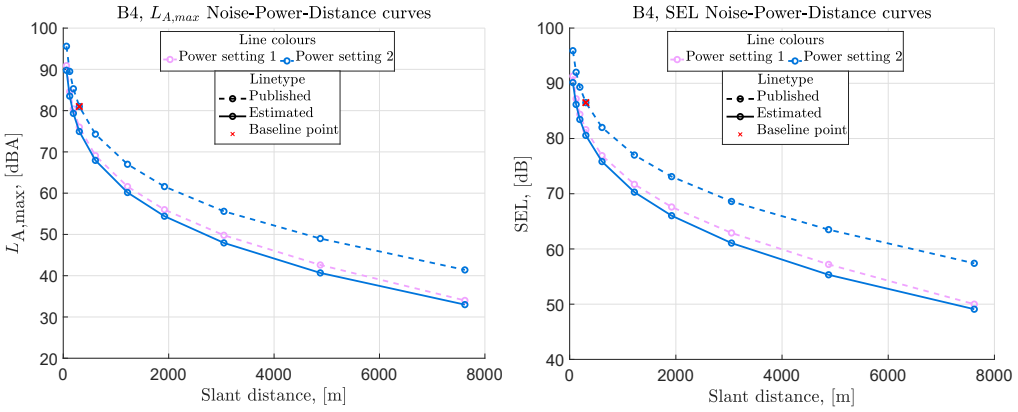

(A) $L_{\mathrm{A,max}}$ (B) SEL

FIGURE 8.6: Predicted departure NPD curve for Concept B4 (solid line) compared to the baseline Twin Otter departure NPD curves (dashed lines).

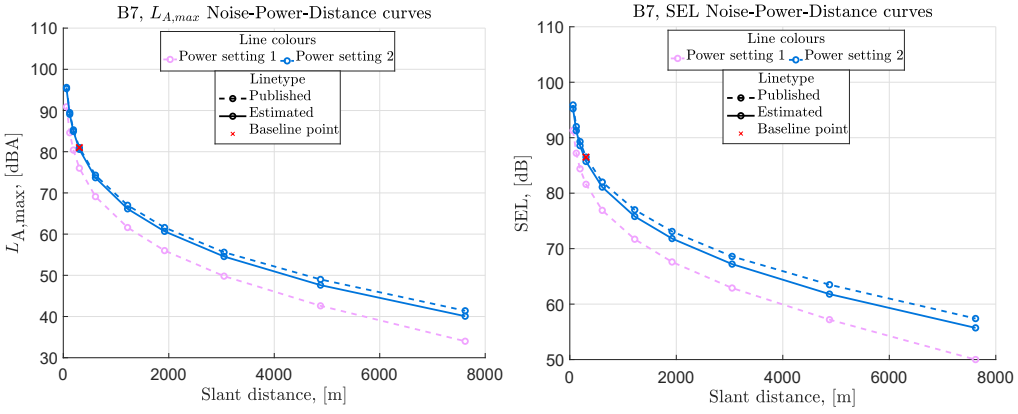

(A) $L_{\mathrm{A,max}}$ (B) SEL

FIGURE 8.7: Predicted departure NPD curve for Concept B7 (solid line) compared to the baseline Twin Otter departure NPD curves (dashed lines).

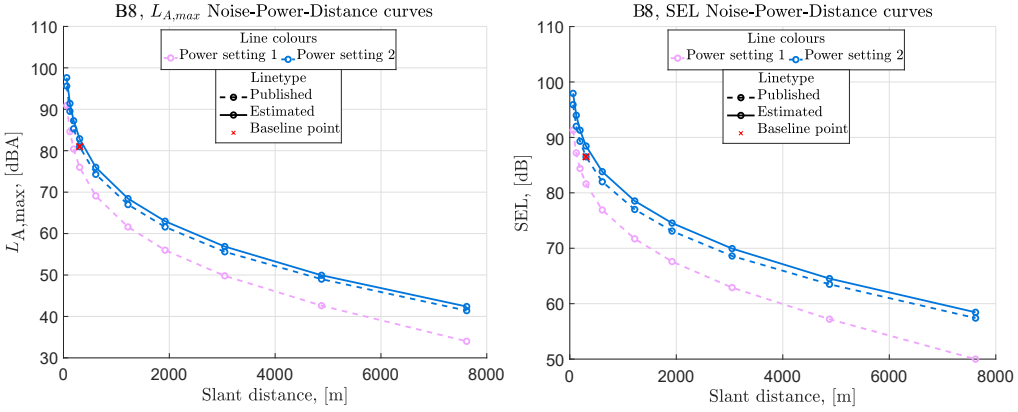

(A) $L_{\mathrm{A,max}}$ (B) SEL

FIGURE 8.8: Predicted departure NPD curve for Concept B8 (solid line) compared to the baseline Twin Otter departure NPD curves (dashed lines).

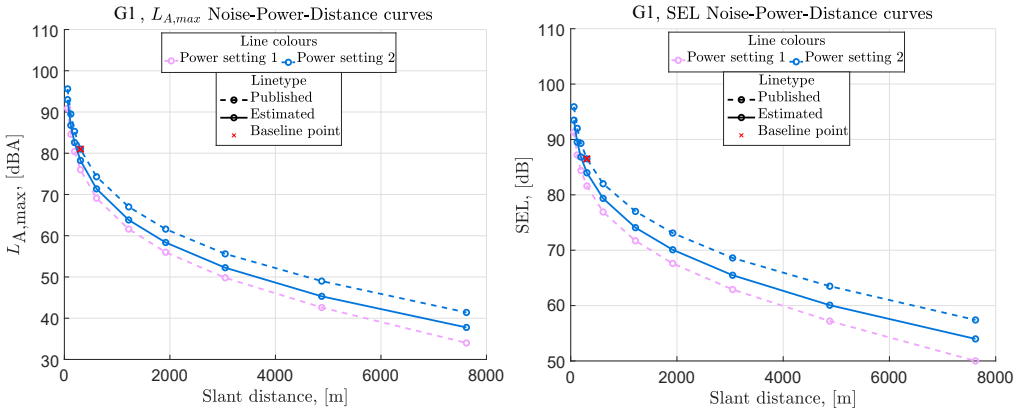

(A) $L_{A,max}$ (B) SEL

FIGURE 8.9: Predicted departure NPD curve for Concept G1 (solid line) compared to the baseline Twin Otter departure NPD curves (dashed lines).

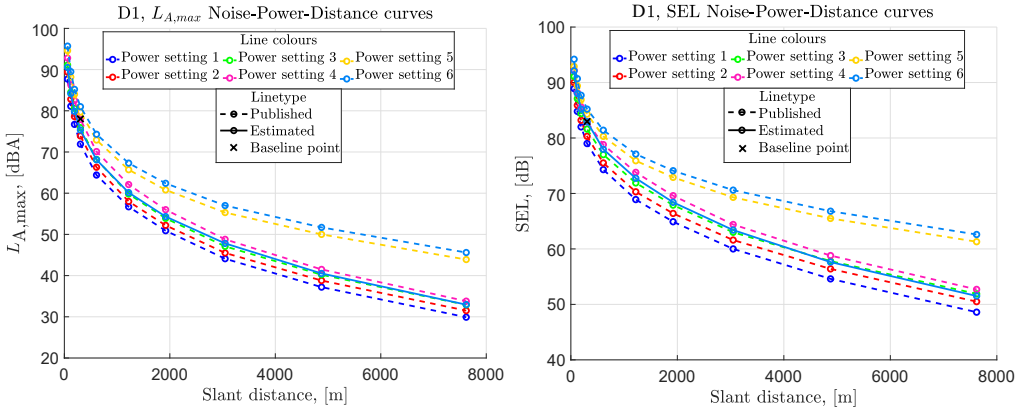

(A) $L_{A,max}$ (B) SEL

FIGURE 8.10: Predicted departure NPD curve for Concept D1 (solid line) compared to the baseline ATR72-600 departure NPD curves (dashed lines).

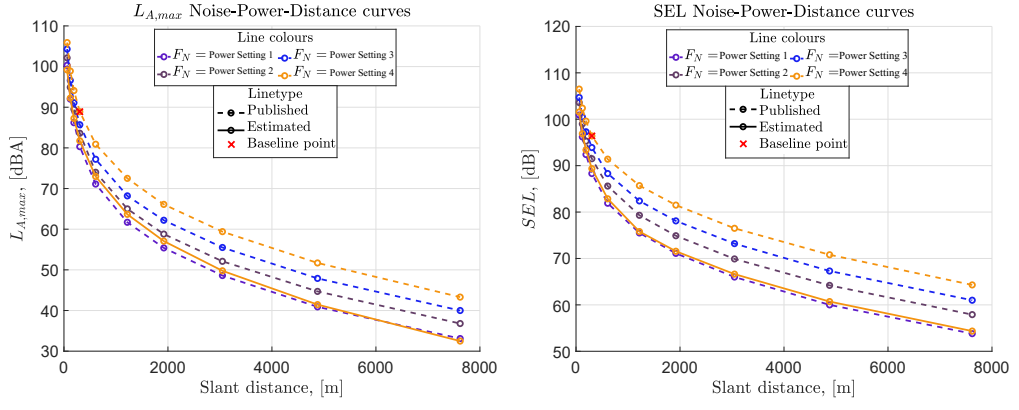

(A) $L_{A,max}$ (B) SEL

FIGURE 8.11: Predicted departure NPD curve for Concept Z1 (solid line) compared to the baseline A320neo departure NPD curves (dashed lines).

Approach

In the approach scenario the upper limit of the range of % of max takeoff thrust (as presented in Table 8.2) was chosen for NPD curve calculation, to represent worst case scenario. This is indicated in Figures 8.12 to 8.18 with the solid lines. For the reference aircraft, that same power condition (in terms of % of max takeoff representing approach at MLW) is indicated with a dashed line of the same colour. An additional power setting is shown for the reference aircraft, representative of the minimum power setting available in the ANP and as shown in Table 8.2. Again, a red cross indicates the baseline level chosen for the MONTANA predictions.

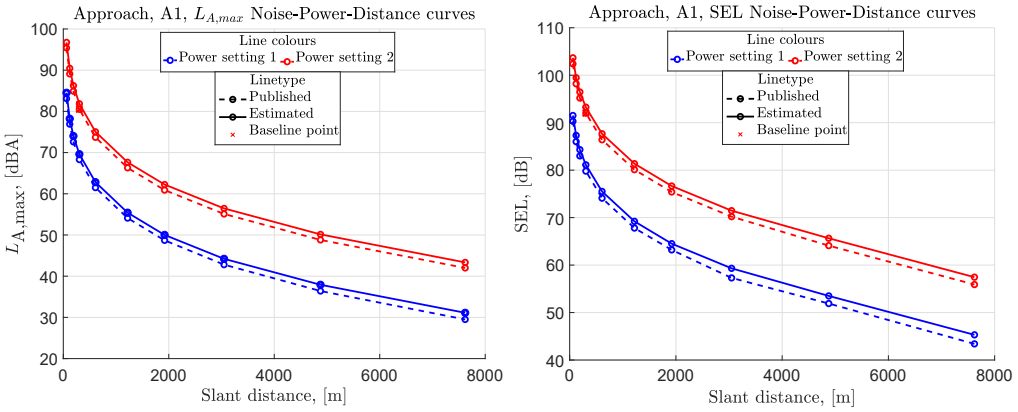

(A) $L_{A,max}$ (B) SEL

FIGURE 8.12: Predicted approach NPD curves for Concept A1 (solid line) compared to the baseline Islander approach NPD curves (dashed lines).

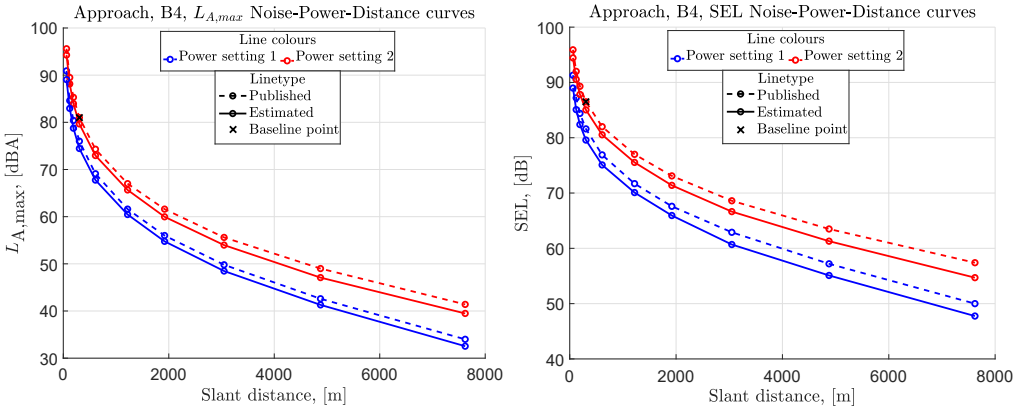

(A) $L_{A,max}$ (B) SEL

FIGURE 8.13: Predicted approach NPD curves for Concept B4 (solid line) compared to the baseline Twin Otter approach NPD curves (dashed lines).

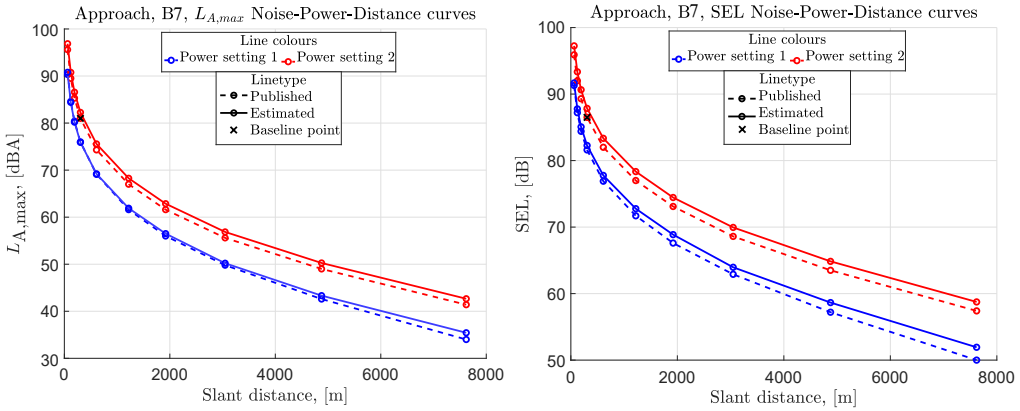

(A) $L_{A,max}$ (B) SEL

FIGURE 8.14: Predicted approach NPD curves for Concept B7 (solid line) compared to the baseline Twin Otter approach NPD curves (dashed lines).

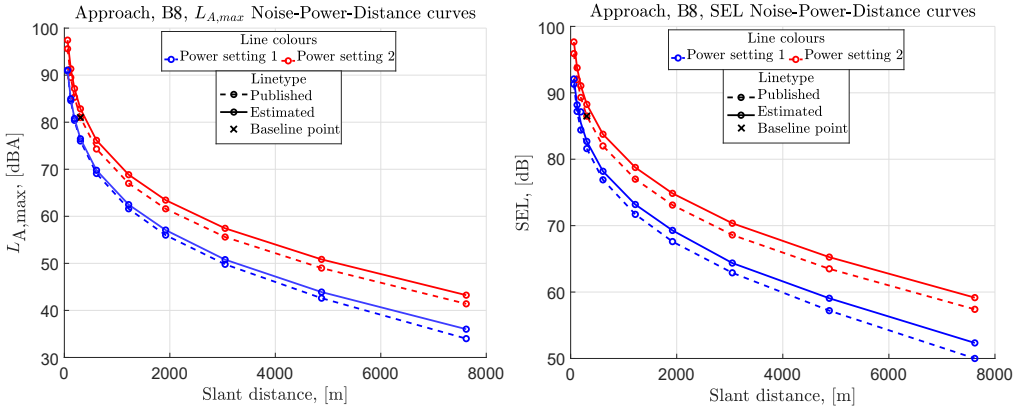

(A) $L_{A,max}$ (B) SEL

FIGURE 8.15: Predicted approach NPD curves for Concept B8 (solid line) compared to the baseline Twin Otter approach NPD curves (dashed lines).

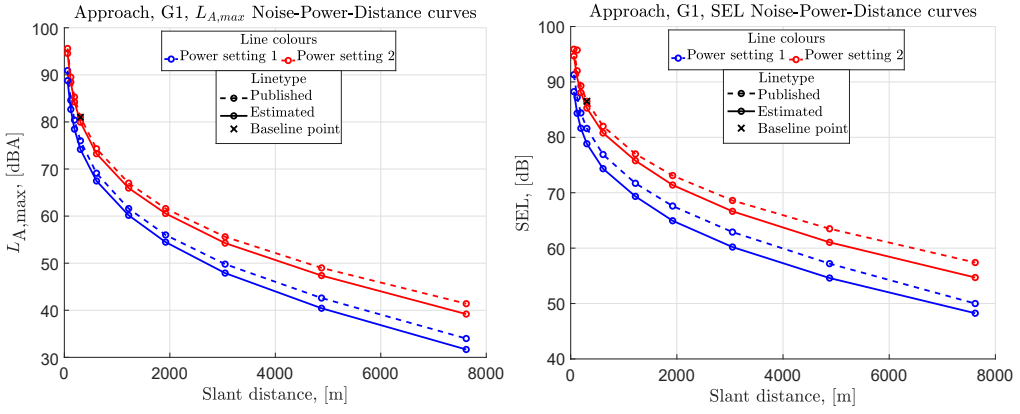

(A) $L_{A,max}$ (B) SEL

FIGURE 8.16: Predicted approach NPD curves for Concept G1 (solid line) compared to the baseline Twin Otter approach NPD curves (dashed lines).

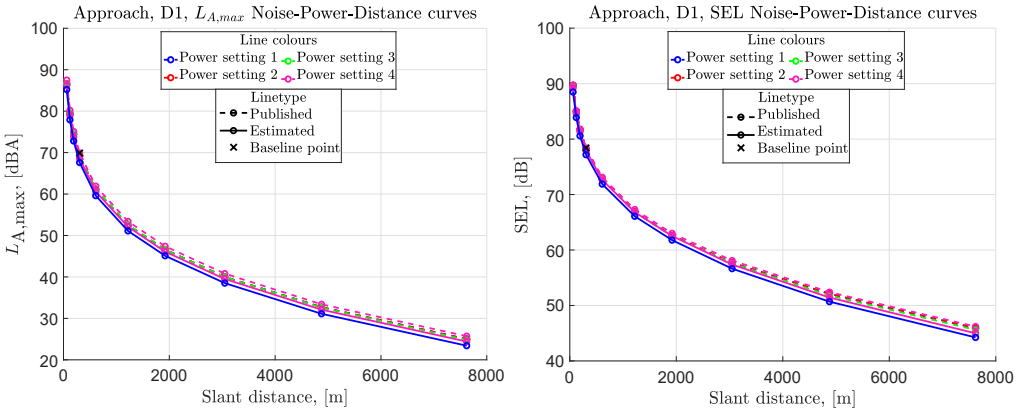

(A) $L_{A,max}$ (B) SEL

FIGURE 8.17: Predicted approach NPD curves for Concept D1 (solid line) compared to the baseline ATR72-600 approach NPD curves (dashed lines).

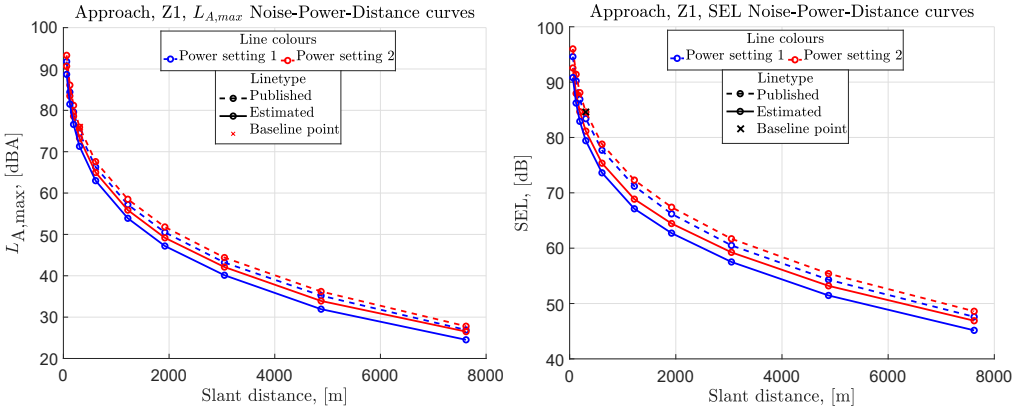

(A) $L_{A,max}$ (B) SEL

FIGURE 8.18: Predicted approach NPD curves for Concept Z1 (solid line) compared to the baseline approach NPD curves (dashed lines).

8.6.2 Discussion

Concept A1

As expected the NPD curves of concept A1 very closely resemble those of the reference aircraft. Instantaneous maximum sound pressure level ($L_{A,max}$) of straight level flyover increases by 1.4dB at all altitudes, relative to baseline. The time averaged sound exposure level (SEL) remains relatively unchanged at low altitudes, with a small increase observed at higher altitudes due to increase in levels of the lower frequency harmonics, which are less affected by atmospheric attenuation. The frequency signature is dominated by propeller discrete tone sources and remains unchanged relative to reference aircraft B-N Islander. Operation requires higher loading of blades and increase in power to accommodate slight increase in thrust requirement during takeoff. The tip Mach number is 0.823, equal to that of reference aircraft. The increase in noise levels observed is primarily due to difference in operating thrust, equivalent to higher power

setting operation. The margin to Chapter 6 is therefore reduced, however still within current limits.

The noise of the 7-seater NAPKIN aircraft is dominated by propeller tone sources. The propeller geometry remains unchanged relative to the reference aircraft, the Britten-Norman Islander, resulting in higher loading of blades and increase in power to accommodate a slight increase in thrust requirement during takeoff. The tip Mach number of 0.823 equals that of the reference aircraft, considered relatively high, so the design could benefit significantly by a reduction in tip speed. During operation, the need for increased thrust leads to an increase in instantaneous maximum SPL of 1.4dBA relative to the baseline aircraft. Despite this, there is still significant margin to ICAO Chapter 10 levels and the time averaged sound exposure level (SEL) remains relatively unchanged at low altitudes, with a small increase observed at higher altitudes due to increase in levels of the lower frequency harmonics, which are less affected by atmospheric attenuation.

Concept B4

As with concepts A1, the main sources of sound due to the propulsion system are relatively unchanged with respect to the reference aircraft. The geometry of the propeller is identical to the reference Twin otter. Despite this, Concepts B4 shows the greatest noise benefits relative to reference aircraft. Reduction of loading of individual propellers due to the increase in number of propulsors to four.

Additional benefits occur due to the reduction in tip speed as takeoff and landing rpm of the propeller is reduced. A reduction in Tip Mach number from 0.8472 to 0.8072 has a significant effect, as operation is already in the transonic regime. Exposure times of Concept B4 are slightly increased (contributing to approximately +0.36 dB SEL), however are almost negligible relative to the noise benefits due to reduction at the source (of the order of 6 dB SEL). Overall noise benefits are observed, regardless of the increase in MTOW.

Concepts B7 & B8

The reference aircraft for B7 & B8 is the DHC-6 Twin Otter, despite the huge difference in MTOW. It is important to note that the Twin Otter is certified under Chapter 10 of the ICAO Annex 16, however both 19-PAX concepts exceed the MTOW limit and would be certified under Chapter 14.

Despite the relative increase in MTOW, comparing the NPD curves, the noise performance relative to the DHC-6 is almost identical. Slight benefits are seen in the case of concept B7 and its ducted fan configuration, versus the propeller powered B8. The increase in number of blades to 5 also account for additional noise reduction.

The significantly reduced tip Mach number of approximately 0.45 of concept B7 and therefore per unit thrust, a much-improved design relative to the reference aircraft provides that benefit. The tip Mach number is also significantly reduced in the case of concept B8 at $M_t = 0.74$. Both designs take advantage of the higher solidity propeller due to the increased number of blades, therefore reducing both the lift and drag contributions of the propeller harmonic noise. Finally, in both cases exposure times are reduced, and distances to the flyover microphones are larger due to increased takeoff and landing performance (ground speed and climb speed).

Concept G1

As with A1 and B4 concepts, propeller geometry and operation is unchanged relative to the design reference aircraft (Jetstream 31), however relative to the Twin Otter, design and operation vary. The change in noise immissions of the Concepts relative to the Twin Otter can be attributed to: the difference in MTOW and therefore thrust requirement per engine. The design and operation of the propeller is significantly better in the case of the Jetstream 31 and therefore the concepts, relative to those of the Twin Otter, in the context of noise output. This can be trivially verified by the significant difference in certification values of the Jetstream 31 and the Twin Otter (77.1 dBA and 85.6 dBA).

First the propeller Tip Mach number at takeoff is approximately 0.66 relative to 0.8472 of the Twin Otter. The almost 25% reduction in rotational speed of the propeller contributes to a reduction in instantaneous SPL in the order of 5-7dB. Additional reductions are observed due to the additional blade of the concept propeller bringing the total number of blade per propeller to 4. The increase in number of blades counterbalances the reduction in rotational speed, to slightly increase the BPF (blade passing frequency). This has an effect of increasing the frequency of all subsequent harmonics, therefore maintaining (or even improving) atmospheric attenuation. The increased performance capabilities of the concepts contributes to additional reductions due to reduced noise exposure times, and larger distance to certification microphones.

Concept D1

The reference aircraft was chosen as the ATR42-600. In terms of Noise-Power-Distance curves the ATR42 is indistinguishable from the ATR72 in the ANP noise database, although EASA certification levels for the two aircraft are different.

The fan configuration of the GKN-40 aircraft was modelled as a propeller with the following modifications: the directivity was changed from the dipole like directivity of a typical open propeller, to a directivity pattern similar to that of a turbofan. Two dominant lobes, one in the forward arc and one in the rear arc, represent the emission of the fan source in the forward arc, and the fan and jet combination in the rear respectively. The purpose of the specific directivity pattern is to capture the blockage effects due to the duct. Corrections to account for reflections of main wing and

horizontal tailplane reflections, and reductions in blockage effects have been added. The high wing, wing-mounted design offers no benefits due to shielding effects.

It is important to note that the only source modelled is the fan rotational self-noise. Effects and sources due to acoustic coupling with the duct, turbulence (including boundary layer) ingestion, stator/strut interaction are not taken into account at this stage as detailed design of the ducted fan geometry would be required. Typically, ducted fan configurations lend themselves to the implementation of acoustic liners for further noise abatement. However, due to lack of knowledge of the dimensions of the ducts, benefits due to liners are not implemented. The number of blades and fan geometry was not specified, therefore the parameters of the 40-seat high-wing, wing mounted propeller configuration were used. Essentially, assuming that the ducted fan has 5 blades. Data on stator number, geometry and position was not available at this stage of the design process.

Operation of such a fan at the rotational values specified would mean a significantly reduced tip Mach number of approximately 0.45 relative to the ATR tip Mach number of 0.72. Additionally, the low pressure ratio, ducted fan geometry, reduces blade loading,and per unit thrust to an improved low noise design relative to the ATR reference aircraft; further contributing to noise reductions. These two design choices, although preliminary, with major assumptions, are the major contributors to the reduced noise footprint, with fundamental tone SPL reductions of the order of $40\log_{10}\left(M_h/M_{h,0}\right) = -6.16\text{dB}$, while the second harmonic is reduced approximately by -3.21 dB, for maximum takeoff power condition.

Overall, the concept leverages the position of the fan, and its preferential directivity to reduce maximum SPL and SEL noise levels relative to the ATR42-600. The cumulative (arithmetic sum of levels at the three certification points) change in noise level relative to the current generation baseline aircraft is -13.06 EPNdB. The largest benefit is achieved at the flyover certification point with a reduction of -5.15 EPNdB (lateral delta - 4.15 EPNdB, and approach delta -3.76 EPNdB).

Concept Z1

The takeoff $L_{\text{A,max}}$ of the 90-seat concept is equivalent to the noise generated by the larger A320neo at an operational weight significantly below MTOW. Specifically, the power setting on the A320neo required to match the noise of the concept would equate to an operational weight of approximately 63t (identical to the MTOW of the A220-100), or 16t below MTOW. This gives a lateral certification value of 81.2 EPNdB relative to 86.1 EPNLdB of the A320neo and a flyover value of 76.5 EPNLdB relative to the 81.3 EPNLdB of the A320neo. Approach levels are reduced by approximately 3 dBA relative to the A320.

Noise recommendations

The above results indicate that noise considerations were not appropriately taken into account in these iterations of the concept aircraft. Design for low noise could be achieved through the leverage of the operational characteristics of electric motors, which replace the constant speed operation of the propeller/turboprop configuration. High torque electric motors could be coupled with modifications to propeller geometry such as diameter, pitch etc. to gain noise benefits due to reduction in Tip Mach number. The design could benefit significantly by reduction in tip speed, and more consideration in propeller choice.

Overall, from an acoustic/noise point of view, preliminary calculations point to the fuselage mounted fan being the best choice for noise reduction on the ground (in-line with literature).

The design however could benefit from more closely replicating the design choices of the Jetstream 31 (and therefore the CAeS Concepts G1, G2 and G3) or in a slightly more extreme case the set-up of the ATR42. In both cases the combination of a larger diameter and decreased rotational speed are used to meet thrust requirements. In both cases this achieves a reduced Tip Mach number. The number of blades of the concept would not require a change, as any acoustic benefit from increasing the count further would diminish when considering the complexity of hub design at this scale.

8.6.3 Certification points compared to baseline

This section outlines the predicted certification levels for each of the concepts. The process for calculating the levels follows that outlines in Section 2.6 of Chapter 2, taking into account the performance and noise consideration discussed previously. A single NPD curve is used for each prediction, assuming constant power at MTOW and MLW for takeoff and landing respectively. The trajectory is assumed to be linear at the takeoff and approach angles as specified by the design capability or certification requirements (e.g. approach glide scope of 3 deg.).

Two types of deltas are presented, the first being the delta relative to the reference aircraft. In the context of the certification levels, the reference aircraft is original design reference aircraft. The second delta is the difference between the predicted noise level at the certification point and limit as indicated by the appropriate Annex 16 chapter; this is also referred to as a “margin”.

Figure 8.19 shows the deltas for concept A1 relative to Chapter 6 and the B-N Islander for the flyover conditions, and for all three conditions for concept D1 relative to chapter 14. As expected from the NPD curves, concept A1 reduces the margin to the limits as it receives a 1.4 dB penalty relative to the Islander. Conversely, concept D1 outperforms the ATR42 at all certification points further increasing the margin to the limit.

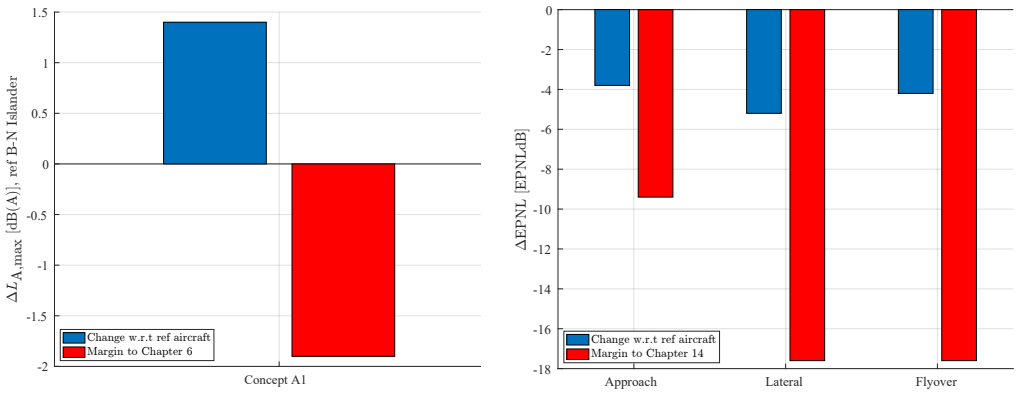

(A) Concept A1 (B) Concept D1

FIGURE 8.19: Difference in concept flyover certification level relative to reference aircraft and margin to corresponding limits.

Concepts B4, G1, B7 and B8 leverage their superior propulsion system configurations and designs relative to the Twin Otter to provide large benefits to the flyover certification point of Chapter 10. The results are seen in Figure 8.20.

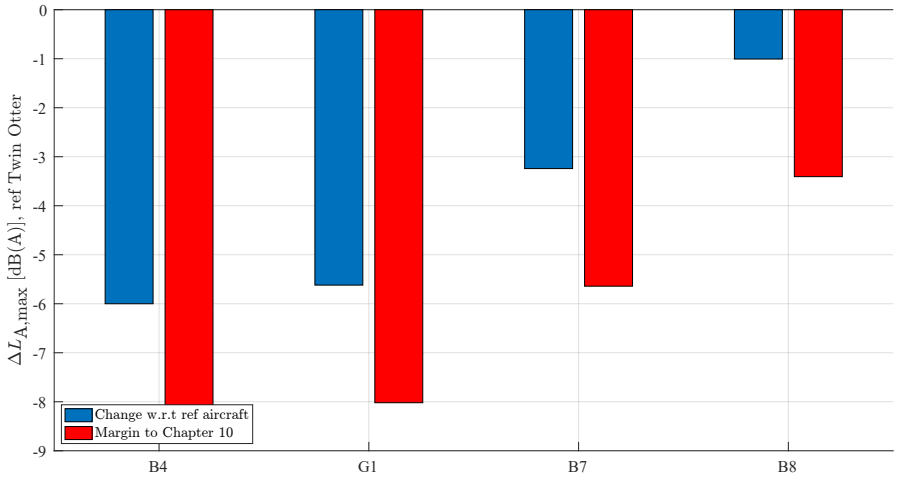

FIGURE 8.20: Difference in concept flyover certification level relative to reference aircraft and margin to Chapter 10 limit.

Finally, the larger D1 and Z1 certification levels for Chapter 14 concepts are plotted on a diagram against the regional market current generation dominant aircraft; these are the ATR42-600, the ATR72-600 (or -212A) in terms of turboprops and the Embraer E190-E2, the Airbus A220-100 and A320neo in terms of jets. The direct hydrogen combustion turbofan concept Z1, outperforms all aircraft in the category due to significant reduction in MTOW. This reduction, comes at a penalty in terms of number of PAX, but allows room for possible noise penalties induced by risks of the hydrogen combustion turbofan and subsystems.

Concept D1 significantly increases the margins across all point to the limits, through the low speed ducted fan configurations. No weight penalties are induced by the addition of

the duct nacelles, that would otherwise manifest through increased thrust requirement. However, the payload carrying capacity is almost half that of the similarly sized ATR72.

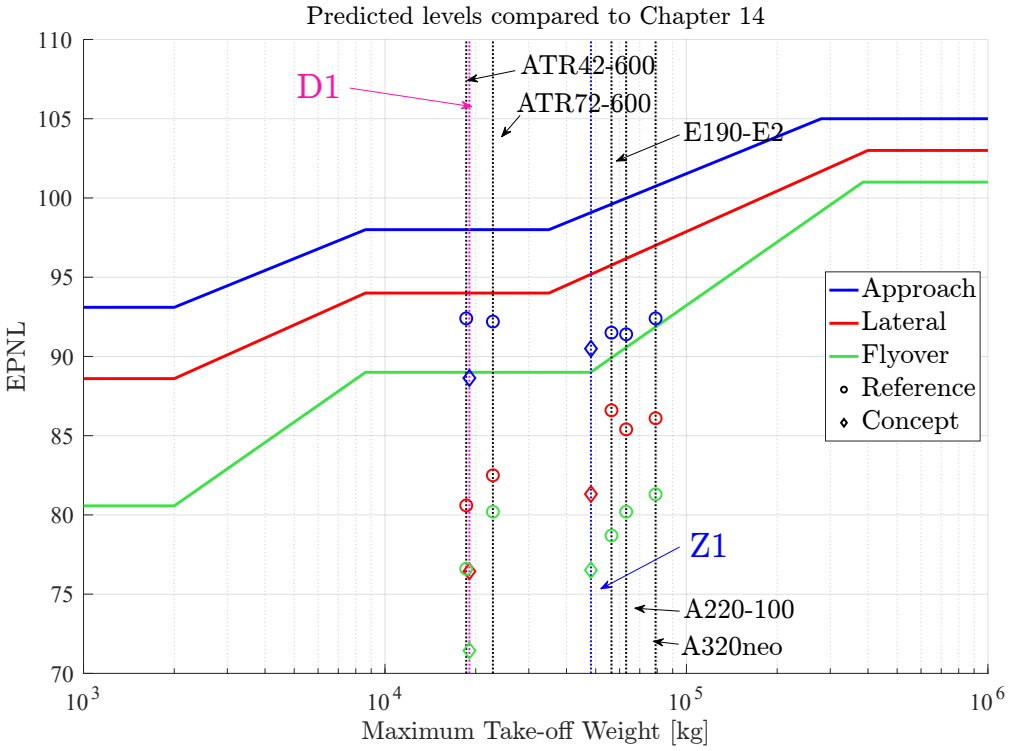

FIGURE 8.21: Summary of certification level for larger regional concepts. Chapter 14 limits for flyover, lateral and approach certification points are indicated for reference as well as the level of the baseline aircraft.

The choice of takeoff and approach flight profiles impact the noise estimated on the ground. Certification point levels calculation also suffer from this subtlety, despite being a rigorously defined procedure. As was previously said, the concept aircraft's certification and operational takeoff and/or approach flight profiles might differ from those of the baseline ones. Therefore, defining these profiles would be necessary for further in-depth noise comparisons, which is a work outside the purview of the current case study.

Differences in the flightpath impact the noise exposure on the ground, through the following main mechanisms: changes in geometrical trajectory, changes in air vehicle configuration, and changes in the propulsion system power (and therefore thrust). Changes in geometrical trajectory impact the distance between the observer (or certification microphone locations) and the source of the noise, as well as the time period the air vehicle spends close to the ground. Steep approach glide-scopes, as a part of a continuous decent approach strategy (CDA), as well as steep departure climbs are often chosen as noise mitigation operational procedures. Depending on the aircraft aerodynamic and propulsion system performance, alterations the air vehicle configuration, such as high-lift devices and landing gear, introducing new sources of noise at sensitive parts of the flightpath. Finally, required power for approach and

takeoff operations, is a function of the above, as well as being driven by the operational mass of the air vehicle and the sizing process to account for requirements, as is the case for safety, in the case of the one engine inoperative condition. Variation in engine power requirement inevitably impact the noise generation at the source.

8.6.4 Single operation footprints

From a noise perspective, it is of interest to understand the impact of the concepts surrounding airports. The differentiating factors between the concepts in terms of noise are therefore two: i. the noise generated at the source i.e. the acoustic performance of each individual concept relative to the baseline/replacement aircraft, ii. the impact of the concept operational differences.

The assessment, therefore, has been performed on a 1-1 basis to the current generation baseline aircraft. For each of the Concepts A1, B8, D1 and Z1 the combined noise contours were calculated as a result of two events, a departure and approach. Three predictions were performed, a benchmark AEDT prediction for the reference aircraft, a baseline RANE v2 prediction for the reference aircraft and finally a prediction for the concept itself. The metric of choice is the single event SEL footprint. Two contours are shown for each case, representative of two levels.

Discrepancies in modelling methodology between RANE and AEDT result in expected variation in the contours predictions, primarily due to the finite nature of the aircraft flight trajectory. AEDT assumes that the aircraft trajectory ends abruptly at some specific altitude. This has no effect when looking at high noise levels and metrics that are averaged over a large period of time. However, in the case of the SEL metric and low dB levels (e.g. < 60 dB SEL) this has the effect of limiting the calculation of the contour to the contribution of the flight trajectory that has been modelled, giving the contour a semicircular like closing shape rather than the expected ellipsoidal shape. RANE's assumption of infinite length segments allows for the last segment of the modelled trajectory to be extended to infinity, therefore providing the correct closure to the contour. An example of such an effect may be seen in Figure 8.22 where between x = 40 km and x = 60 km there is a large discrepancy in the shape and area of the two contours. In the case of RANE this effect has been depicted in two different way: as in Figure 48 the whole contour is depicted, as it is not significantly different to the AEDT prediction, and as is Figure 8.23 where the rest of the contour is not depicted and has been cut to match the length of the AEDT contour to allow for comparison.

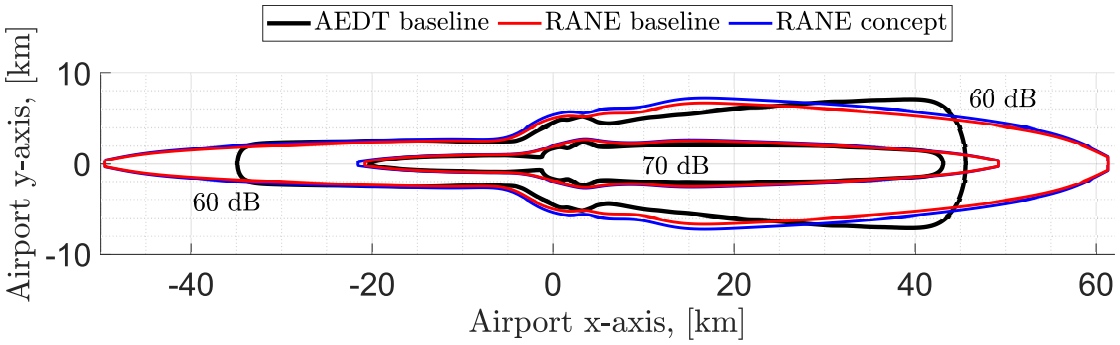

FIGURE 8.22: SEL noise footprint comparison for one approach and one departure operation of the baseline B-N Islander and Concept A1. Calculations for baseline aircraft performed with AEDT and RANE.

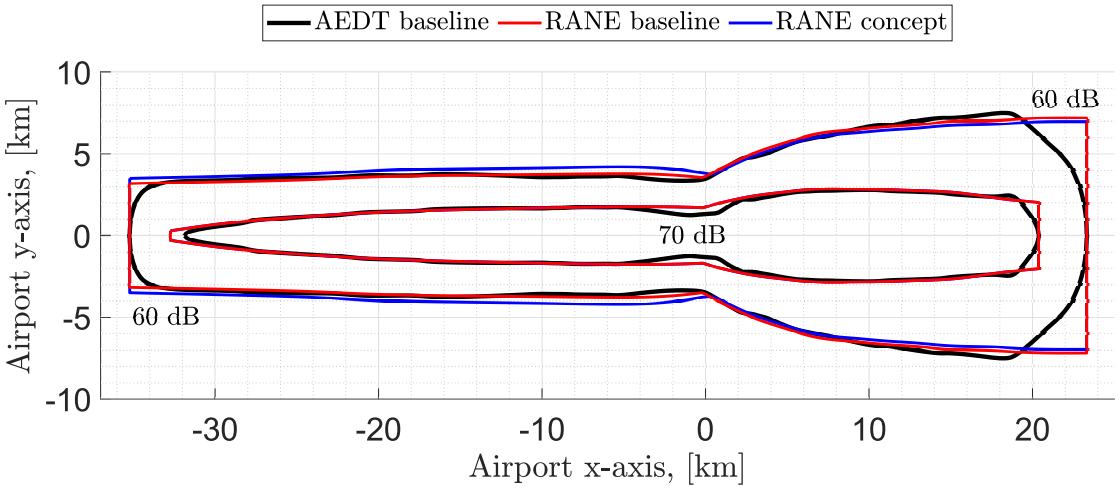

FIGURE 8.23: SEL noise footprint comparison for one approach and one departure operation of the baseline DHC-6 Twin Otter and Concept B8. Calculations for baseline aircraft performed with AEDT and RANE.

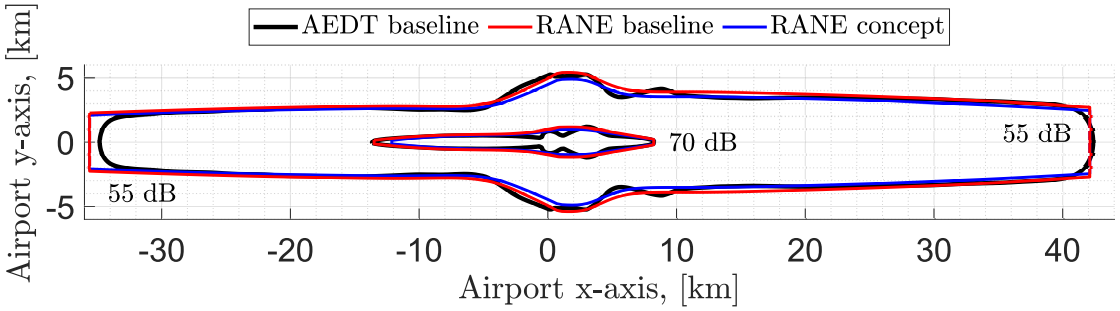

FIGURE 8.24: SEL noise footprint comparison for one approach and one departure operation of the baseline ATR42-600 and Concept D1. Calculations for baseline aircraft performed with AEDT and RANE.

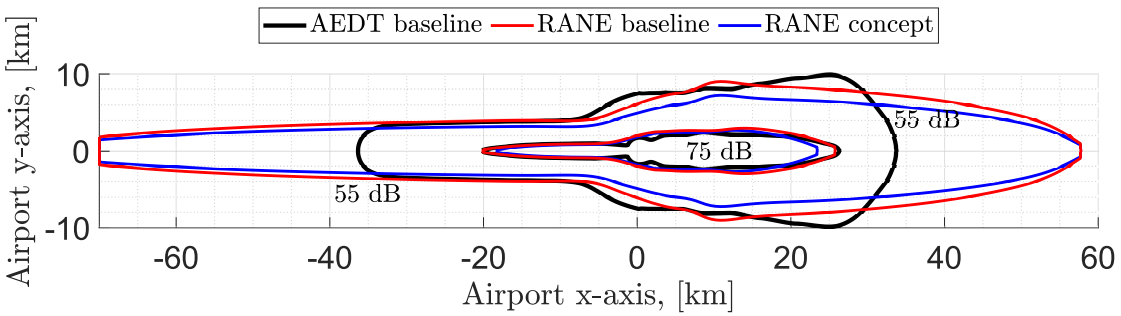

FIGURE 8.25: SEL noise footprint comparison for one approach and one departure operation of the baseline A220-100 and Concept Z1 (Rolls-Royce plc). Calculations for baseline aircraft performed with AEDT and RANE.

8.7 Discussion & Final Remark

Overall, the performance of the NAPKIN aircraft relative to the expected noise reduction goals set by the ICAO (see Table 1.1) is in line with what is expected of the next generation of regional aircraft.

Tables 8.5 and 8.6 summarise the cumulative certification levels relative to the reference aircraft and Chapter 14. These margins however, as a result of the three-point certification procedure, are based on single event operation and classification using the absolute value of MTOW of the aircraft. This disregards the effect of reduced passenger capacity and range capability of some concepts. The notion of applying a correction factor (noise penalty, Δ EPNLdB) to account for these reductions, before calculation of the applicable limits for these aircraft is something to be considered. Another approach to classifying and generating the limits for noise certification levels of future aircraft would be the use of payload (kg/tonnes) or payload fraction. This could help identify the efficiency of an aircraft of a specific MTOW at carrying useful payload and reward or penalise said aircraft appropriately. This discussion forms part of the future work required on noise impact of novel hydrogen aircraft.

Table 8.5: Predicted noise margins expressed as cumulative EPNdB below reference aircraft noise levels for project NAPKIN concepts.

Margin to reference aircraft (Δ dB)				
EIS	Medium Regional Concept D1	Medium Regional Concept E1	Medium Regional Concept E2	Single Aisle Concept Z1
2035	13.2	8.3	16[a]	11.4

[a]Based on empirical evidence and previous work on regional DEP architectures. Actual predictions are part of future work recommendations.

Table 8.6: Predicted noise margins expressed as cumulative EPNdB below Chapter 14 levels for project NAPKIN concepts

Margin to Chapter 14 (Δ dB)				
EIS	Medium Regional Concept D1	Medium Regional Concept E1	Medium Regional Concept E2	Single Aisle Concept Z1
2035	44.5	34.4	42.1	34.9

The impact of the NAPKIN concept fleet will have on noise immissions is best assessed through the method described by the ICAO Balanced Approach to Aircraft Noise Management [5, 6]. Reduction of the noise at the source involves the design and introduction of quitter aircraft relative to current generation aircraft. This involves aircraft manufacturers including noise specific input into the design process. The next three points on the balanced approach involves the operation of the aircraft in the vicinity of airports while attempting to optimise for minimal noise exposure on the ground. The main stakeholders responsible for aircraft operations are airports and

airlines alongside organisations and authorities such as the CAA and EASA who set and oversee the regulations regarding these operations. Finally, and maybe the most important is the impact on the community itself.

Historically technology improvements have had the effect of lowering the noise immission of individual aircraft. Broadly this trend is continued with hydrogen fuelled aircraft when judged against their corresponding kerosene fuelled baseline, but with less (or no) improvement in approach noise compared to takeoff noise.

Limitations of the NAPKIN noise study mean that there is an element of risk in this conclusion in so far as additional sources of noise introduced by the fuel change have been underestimated (or not included at all). For example, direct hydrogen combustion noise is assumed comparable to that of kerosene combustors and any additional noise due to fuel cell cooling systems has been disregarded. To offset this, however, there are opportunities for noise mitigation that have not been considered, such as advanced liners.

Hydrogen aircraft concepts often involve propeller or ducted fans as propulsors, and it should be noted that these aircraft have a more tonal noise signature than turbofan powered aircraft. Thus, there is likely to be a change in the overall nature of noise heard around airports and the impact of this may not be correctly captured by current certification metrics.

To maximise the potential for decreased noise R&D programmes addressing both risk and opportunities will be required. There is also the opportunity to decrease noise via changed operational procedures such as increased approach angle.

Whilst individual aircraft noise may decrease, airport noise is also dependent on the number of operations which, given aviation growth, tends to act to increase noise. How the introduction of hydrogen aircraft affects airport noise depends broadly on the size of the airport and the fleet composition.

For small airports (in terms of aircraft movements) there is little change in noise. Equally, for large airports such as Heathrow, the size of aircraft considered in NAPKIN have such a small contribution to the overall airport noise that, again, little or no difference in noise is discernible.

Between these two extremes it has been found that for medium airports the introduction of hydrogen aircraft may act to decrease or increase noise. This is because the (generally) lower PAX capacity of hydrogen aircraft may entail an increased number of operations to maintain overall passenger numbers (although this depends on assumed load factors).

8.8 Summary

Chapter 9

Case Studies II: Electric VTOL rotorcraft

9.1 Overview

This Chapter aims at demonstrating the full capabilities of MONTANA in terms acoustic prediction, as well as incorporating the initial sizing algorithm presented in Appendix A to explore the noise impact of a simple AAM network operating in the city of London. The chapter may be viewed as three individual sections, starting from the definition and intentions of the mission, each section feed into the next, leading to the final assessment of noise in the London urban area.

In order to assess an AAM network, two main components must be defined. Firstly, the operating network, a series of London locations that would benefit from the existence of a vertiport providing connections to other such locations around the city. Second, the aircraft or rotorcraft in this particular case operating within this supposed network. To tackle the network part of the study, a series of London locations were chosen according to current means of public transport (e.g. London Underground and buses) popularity. Included within these locations are the 5 London airports, Heathrow, Gatwick, London City, Luton and Stansted, in order to provide city-airport connection alternatives.

The aircraft flying these networks are defined according to individual missions (point-to-point). Three aircraft concepts are explored. All concepts are fully electric Vertical takeoff and Landing (VTOL) rotorcraft. The distinction between concepts is the propulsion system of choice. Concepts 1 through 3 as they are referred to as, vary in the number of propulsor units (or simply rotors) starting at 4, 12 and 2 for concept 3 respectively.

After performing preliminary performance analysis and sizing of the aircraft, NPD curves are constructed for three different operating conditions, departure, approach and

level flyover for each concept. The NPD curves are then used to generate noise footprints and contours along the previously defined networks. The noise exposure around vertical takeoff helipads is assessed as functions directivity, allowing for possible population exposure effects to be carried out in the communities bellow the operation of these concepts.

9.2 Mission Planning

The problem of creating an efficient AAM transport network, that integrates efficiently and seamlessly with existing infrastructure and transportation networks is a logistics problem beyond the scope of this thesis. However, simple assumptions and a high level approach allow for the demonstration of the MONTANA model capabilities, that may be used in the future to estimate noise and community noise exposure of actual optimised routes and flightpath trajectories. Example networks have been presented by AAM manufacturers, with a prominent proposal being that of Lilium and the network connecting major cities in the south-west of Germany (Figure 9.1 from reference [223]).

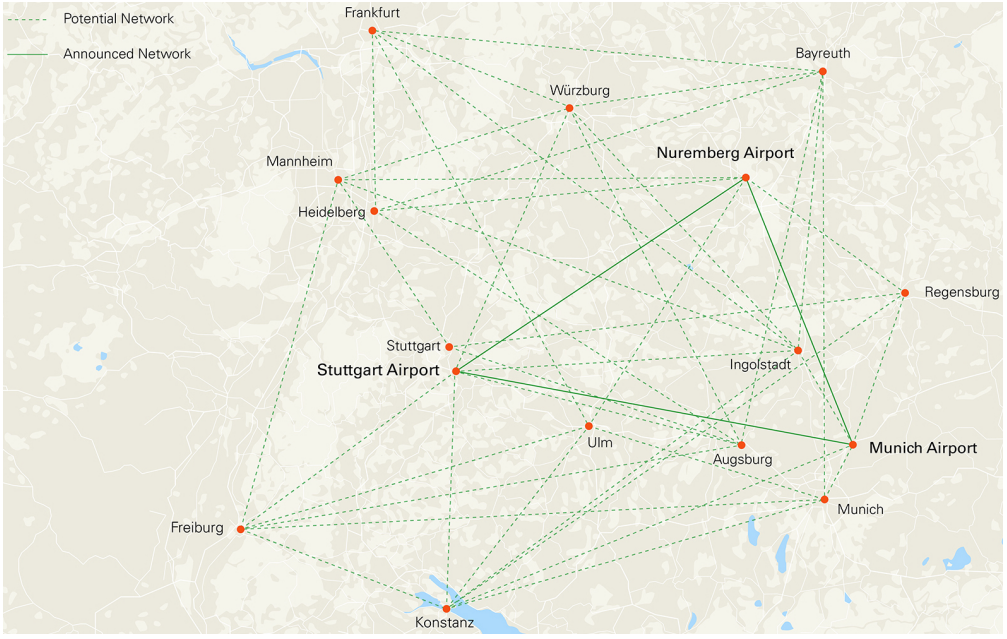

FIGURE 9.1: Conformed and proposed AAM network operating in the south-west of Germany currently being designed and studied by Lilium and partners [223].

9.2.1 London VTOL network

A similar approach is taken in this Chapter, in order to design a simplified AAM network that operates over London. The decision of where to situate potential AAM vertiports in central and suburbs of London is based on data from the London underground. According to Transport for London (TfL) [224, 225] and London train

station usage [226], London's busiest underground stations from 2004 to 2019 have approximately stayed the same. Figure 9.2 shows the number of passengers in the busiest stations in 2019 and 2020, noting the large decrease due to the COVID-19 pandemic. Ignoring the unprecedented effect of the pandemic and assuming traffic will resume as normal in the following years a list of possible vertiport locations is created. The list includes the five major London airports as well. Figure 9.3 shows these locations on the map of London. In addition, four locations in districts of Greater London are added to the networks. These may be seen in Figure 9.4.

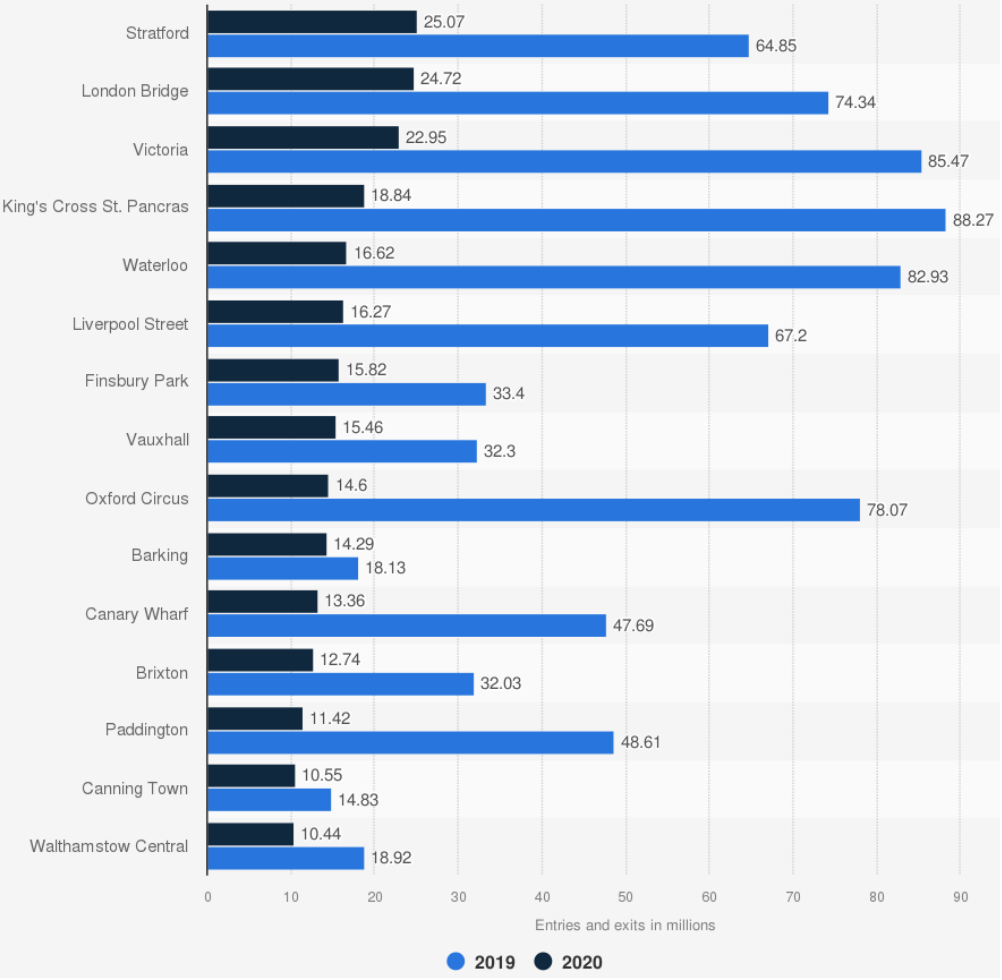

FIGURE 9.2: Busiest London underground stations of passengers in 2019 and 2020 (in million entries and exits to tube stations). Figure and data by [227].

In order to generate a reasonable network of connections between these possible vertiports, a distinction is made between airport connections and what is referred to as inner city connections. For the London airport network, the main hubs are assumed as Heathrow, Gatwick and London City airports. These hubs are used for connecting the airports with the inner city network. Single route length range between 2 and 17 km for the inner city network, whilst for the airport network the connections are between 9 and 86 km long. The maximum distance within the networks will act as range objective for

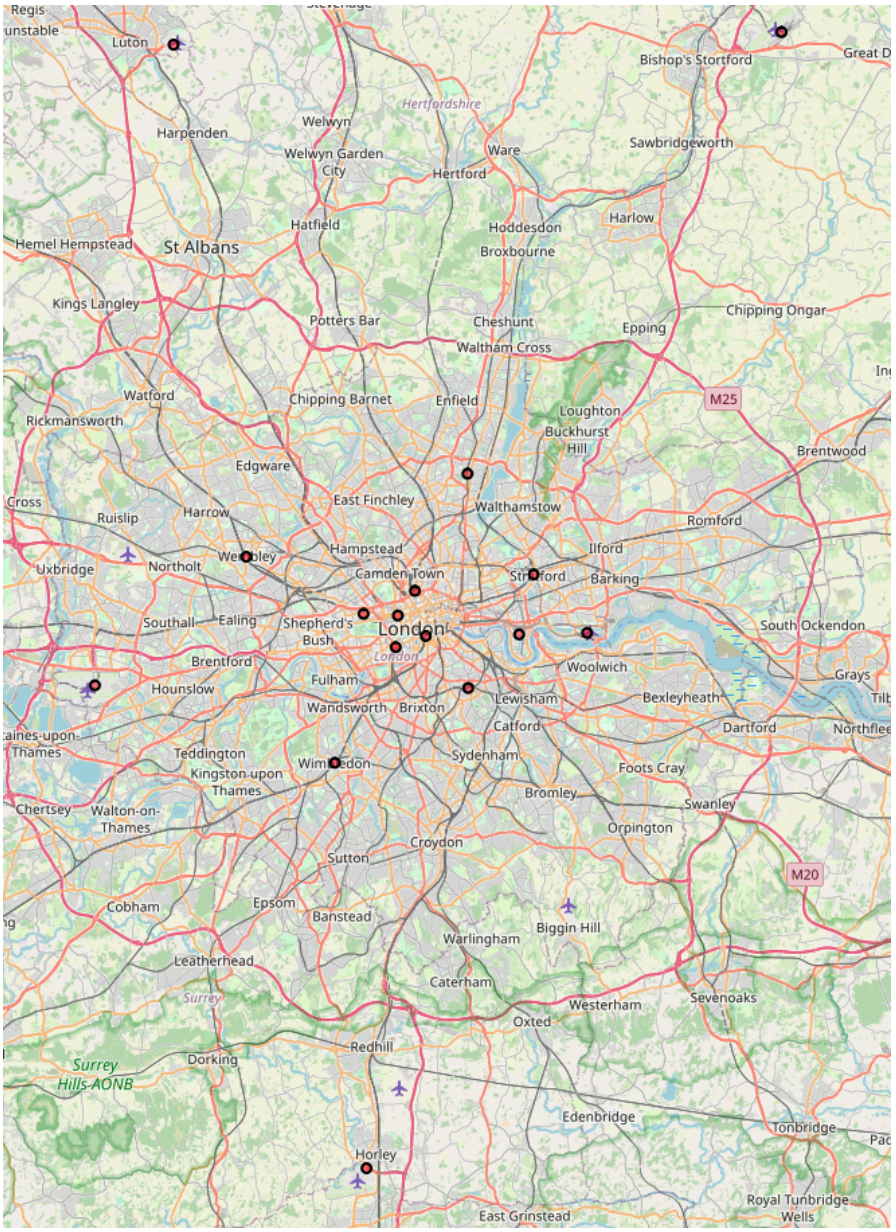

FIGURE 9.3: Map of Greater London, identifying possible locations for vertiports in a future AAM network. All five major London airports are included. Red dots show these possible locations.

the sizing procedure of the rotorcraft concepts to follow. Diagrammatic representations of what is referred to as the "inner city" network can be seen in Figure 9.5.

The routes have been coloured according to the airport hub that it belongs to, with black red and green, being Heathrow, London city and Kings Cross, respectively. The networks and their connections are not optimised for operation or efficiency by any metric. They do however try and cover a wide range of possible scenarios of short hop style flights to mid and longer range urban connections.

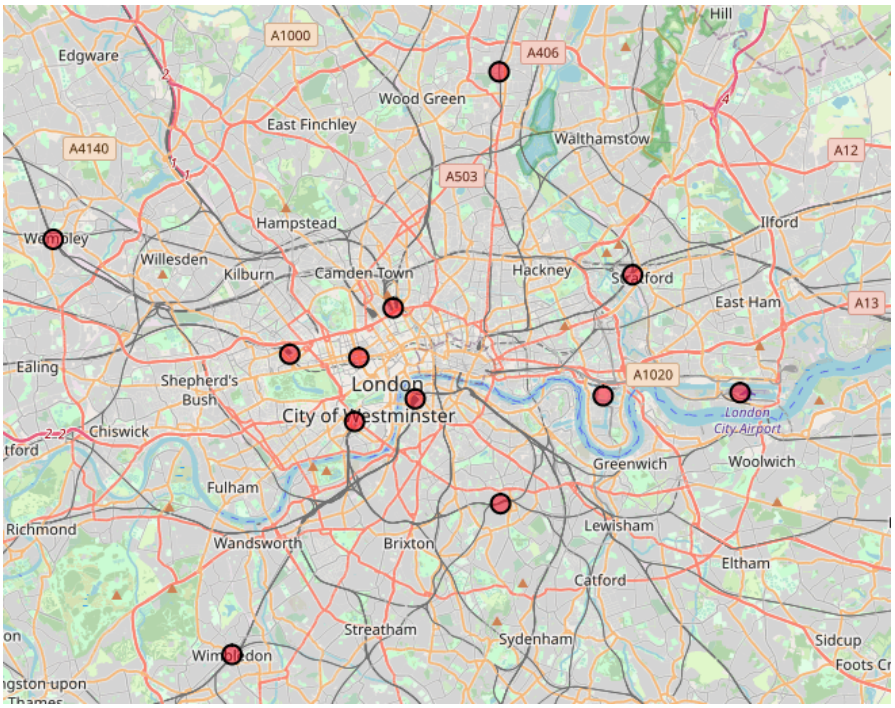

FIGURE 9.4: Map of central London, identifying possible locations for vertiports in a future AAM network. Red dots show these possible locations.

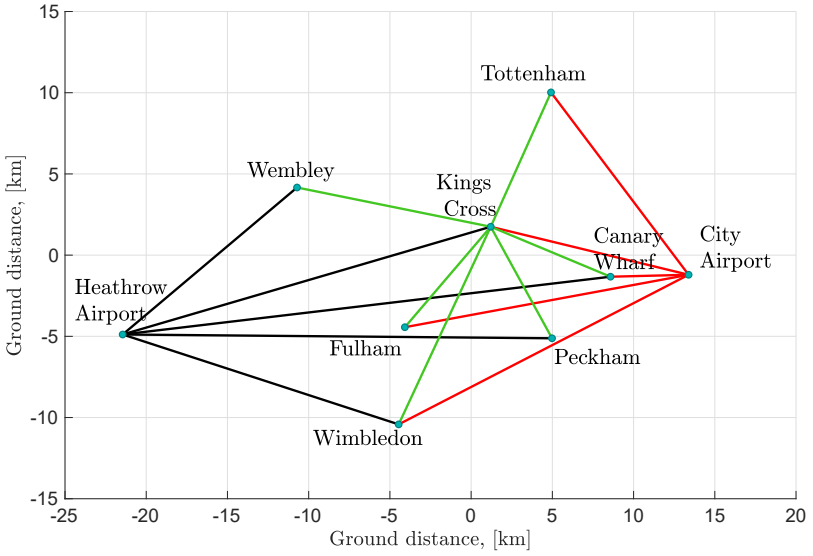

FIGURE 9.5: London inner city AAM network.

9.2.2 Vertical flight profiles

Three vertical flight profiles are assumed to be flown by the aircraft. The distinction is done according to the flight altitude. Three flight altitudes are flown depending on the total distance covered. For connections above 20 km the flown altitude is assumed to be 2,000 m. Between 5 and 20 km the altitude is 1,000 km and for any connection smaller

than 5 km the altitude is that of 500 m. All profiles are comprised of 5 main segments. These are: vertical takeoff, climb, cruise, decent and vertical landing. The vertical takeoff height is assumed to be 20 m, at which horizontal acceleration and climb may begin (as holds for landing operation). The climb and decent angles vary with the altitude/length of the connection. Short, low altitude hops are assumed to have nearly perpendicular (75°) to the ground climb and decent phases, in order to maximise the cruise segment. Whilst climb angles of 45° and 10° are chosen for the remaining altitudes of 1,000 m and 2,000 m. It is worth noting that these climb angle may not represent the minimum power climb constraint (best climb velocity) for each concept, rather represent a variation in operating geometry in and out of vertiports. Concept performance will be discussed in the following section.

Transition from vertical to horizontal flight is mostly relevant for concept implementing lift plus cruise configuration; whereby lift generation transitions from the rotors to the main wing. Such transition phases are not explicitly modelled herein. From a power requirement perspective, and therefore considered in the sizing process, transition power requirement bridges the gap from high power vertical flight phase, to the lower power climb and/or cruise. Other authors choose to model this phase explicitly by estimating the transition power requirement as the average value between the power at the start of transition (hover or vertical climb) to the end of transition (design dependant - in this case fixed wing climb). Additionally, time spent in transition is negligible relative to cruise. In this thesis, the transition power is assumed to be included in the hover or vertical climb phase for a conservative approach, slightly increasing the time spent in this phase. For pure rotorcraft design, transition is neglected all together, as the step jump from vertical climb/ hover to accelerated climb is smaller.

From the noise modelling perspective, the typical NPD process for helicopter operation is followed as discussed in Chapter 2. This involves the generation of NPD curves for hover, flyover, approach and departure operations, all of which are steady state operations. This is enforced by the lack of concrete baseline data for such manoeuvres. Additionally, in terms of noise exposure, the time period in transition is outscaled by that in hover and cruise.

However, future studies could consider noise during the transition phase, leveraging the modelling approach in Chapters 4 and 6, using appropriate noise methods, to capture the complex aeroacoustic interaction noise (a possible risk as the source balance transitioning meaning interaction sources could dominate the signature), and appropriate baseline NPD data.

The simplified diagram of the three flight profiles may be seen in Figure 9.6.

Figure 9.7 shows a three-dimensional view of the network, where the differences in altitudes and vertical flight profiles may be seen.

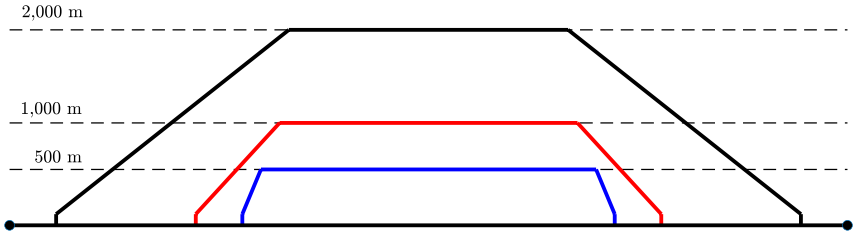

FIGURE 9.6: Vertical flight profiles possibilities. Flight altitude is determined by total distance covered.

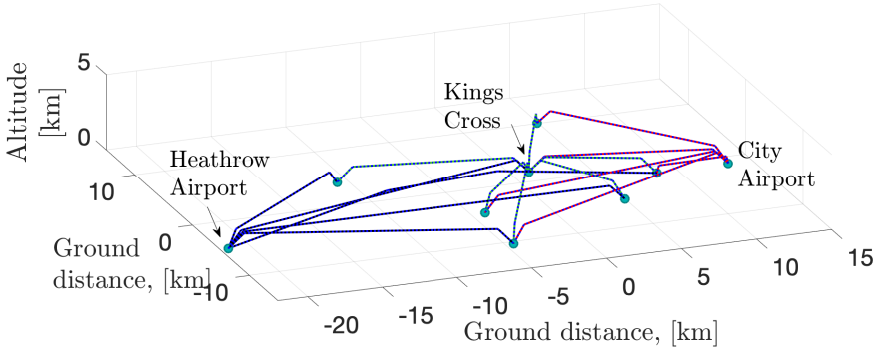

FIGURE 9.7: Three-dimensional illustration of network connections and the trajectories of aircraft operating the inner city connection network.

9.3 Architecture and design space discussion

This section is dedicated to the design, performance assessment, and sizing of three electric vertical takeoff and landing (e-VTOL) rotorcraft concepts. As will be evident the performance is largely limited by the nature of fully electric air vehicles and the battery technology available. The vehicles are conceptualised as rotorcraft meaning that rotors provide lift throughout the entire flight. As discussed in Chapter 3, hover efficiency grossly benefits large rotors with low loading. Helicopters are typical examples of high hover efficiency, as they are commonly designed to have high loiter endurance for surveying applications. The concepts are based on a Bell 429 GlobeRanger, a single rotor vehicle.

The distinguishing factor between concepts is the propulsion architecture system. The main parameters that are different between concepts are: i. number of propulsors, ii. diameter of rotors, iii. number of blades. . These parameters are not allowed to vary, for optimisation or design convergence purposes. In addition, one concept is designed as a tilt-rotor with lift + cruise (VTOL and fixed wing flight) capability.

The other two are assumed to take a multirotor approach. The multirotor architecture nature, lacks in cruise efficiency compared to a fixed-wing aircraft or lift & cruise architecture AAM vehicle. However, the application within this chapter, considers

flights of maximum distance of 86 km with the majority of trips being in the 20 to 40 km range. This allows for a significant sacrifice in terms of maximum capable range of the vehicles in order to accommodate the electric propulsion systems. As range is not the primary objective, the propellers may be sized for 'hover' condition alone and not the intermediate state of a typical lift & cruise where drag penalties of the inoperative hover propellers drive the cruise efficiency significantly. Hover condition sizing allows for rotors of larger blade numbers and chord lengths.

All other parameters are assumed to be the same for the across the concepts, unless otherwise specified in the following sections. These constraints will allow for acoustically examining three majorly different interpretations of what could be the same design, within the context of conceptual design.

The driving mission design parameters are payload and range. These parameters will allow the aircraft to operate within the networks previously defined. In the case of a comprehensive design, other parameters may also be of equal importance such as cost and operational safety. A single design iteration is considered, with no optimisation techniques utilised. Noise analysis, and other subsystem and performance studies, would feedback into the design calculations in order to generate the next iteration of the concepts. The goal of MONTANA is to provide the aircraft and airport noise analysis at each iteration of conceptual design.

9.3.1 Baseline Aircraft

The concepts are referenced to the baseline helicopter, Bell 429 GlobalRanger (Figure 9.8), a multipurpose utility helicopter of a MTOW of 3,175 kg and a passenger capacity of 7 (8 including the pilot).

The Bell 429 GlobalRanger is a twin-engine, light-medium helicopter designed for a variety of roles including corporate transport, air ambulance, law enforcement, and utility operations. It is manufactured by Bell Textron Inc., a major aerospace and defence company based in the United States.

The Bell 429 is powered by two Pratt & Whitney PW207D1 turboshaft engines, each capable of producing up to 738 horsepower. It has a maximum speed of 155 mph and a range of up to 345 miles, depending on the mission and payload. The helicopter can accommodate up to seven passengers in its standard configuration, but can be modified to carry up to 12 passengers or additional cargo. The helicopter is equipped with a four-blade main rotor with composite blades, which provide increased performance and stability in a variety of conditions.

FIGURE 9.8: Baseline aircraft, Bell 429 GlobalRanger.

9.3.2 Design

Although the concepts presented in the rest of this section are far from optimised detailed design points, the constraints chosen for the initial sizing procedure are those reflecting realistic requirements and specifications of this class of air vehicles. As certification specifications (EASA CS) for AAM vehicles are currently not available, the airworthiness standards used to guide the design are those of EASA CS-27 for "Small Rotorcraft". However, at this level of conceptual design, the CS does not constrain the designs significantly, with the exception for the following considerations:

- CS 27.65 a.1: "The steady rate of climb, at V_Y must be determined: (i) With maximum continuous power on each engine;"
- CS 27.65 a.2: "The climb gradient, at the rate of climb determined in accordance with sub-paragraph a.1, must be either: (i) At least 1:10 if the horizontal distance required to take off and climb over a 15 m (50 ft) obstacle is determined for each weight, altitude, and temperature within the range for which certification is requested; or (ii) At least 1:6 under standard sea-level conditions."

As a result, the maximum climb velocity requirement is set to a conservative 5 m/s (or $\approx$ 984 fpm), which also limits the climb power requirement. Horizontal flight velocity is chosen separately for each concept according to rotor performance. The one-engine-inoperative climb requirements of CS 27.67 is also applied.

In order to meet the network requirements set in the previous sections the aircraft range it set between a minimum of 50 km and a maximum of 100 km. The upper limit on the range ensures that the energy storage system is not oversized. The concepts are assumed to be capable of carrying 8 persons in total including one crew member or an equivalent of 1,250 kg of payload. Assuming an initial MTOW identical to the baseline helicopter,

the payload mass fraction is therefore $m_p/m_0 = 0.3937$, where m_p is the payload mass and m_0 is the total air-vehicle mass.

An overall hover efficiency factor of 0.7 is assumed [228, 229]. This includes sub-system individual efficiencies such as the motor, power electronics and battery efficiency. A reserve requirement of 20 min which is a FAA standard for helicopters is also applied.

9.3.2.1 Subsystem considerations

Fuselage

The concepts are assumed to use approximately the same 10 m long by 2 m wide by 1.5 m-ft tall fuselage, adapted from the baseline helicopter to carry the eight-passenger payload. Weight and drag estimations are based on empirical models [230, 228, 229, 231, 232] through NASA NDARC model [233]. The fuselage drag is taken into account by applying a fixed drag coefficient to the calculated fuselage drag area.

Landing gear

For simplicity, all three concepts are assumed to have the same fixed main landing gear. The decision to use fixed landing gear was made because the weight penalty and complexity of retractable gear was not worth the modest improvement in cruising efficiency. A simple frontal area model is also used to estimate the drag.

Rotors

The precision of low fidelity analysis is constrained since the rotor is a complicated system. As momentum theory is used to estimate the rotor performance, the diameter specification suffices. However, for the estimation of operating rotation speed, XROTOR is used with its classic lifting-line representation of propeller/rotor blades. Due to this, existing rotor systems with comparable dimensions and operational characteristics were used to estimate the basic rotor aerodynamic dimensions and performance parameters. These are the same inputs that are carried over into MONTANA for the noise estimation, and NPD curves.

Aerodynamic surfaces

Concepts A and B are assumed to employ helicopter/multirotor control and stability techniques. This results in no additional aerodynamic surfaces. On the contrary, Concept C fundamentally relies on a fixed-wing for the cruise phase of its missions. The first-order conceptual design tool PHOENICS requires information regarding the lift-to-drag ratio (L/D) to perform the sizing. For Concept C the lift-to-drag ratio is estimated for cruise condition only.

L/D estimation is configuration arrangement dependant. A suitable place to start for the baseline model are the Bell XV-15 [234] and Bell Boeing V-22 Osprey [235, 236] wing specifications. Optimizing trust-weight ratio and wing loading is out of the scope of this conceptual sizing approach. The aspect ratio and and configuration arrangement, determines the wetted area ratio(by extrapolating statistical data [237]). Wing wetted area and span are scaled accordingly using MTOW and initial values for those of the Bell Boeing V-22 Osprey. Due to the large prop-rotors and power delivering motors on the wingtips, tiltrotors require rather thick wings, hence the wing thickness is 20%, based on insight from Raymer [237]. The wing's conceptual design does not rely on any particular aerofoils.

A typical tail design is used for conceptual sizing, although considerations for a H-tail or V-tail design in accordance should be made in subsequent design phases to account for the large rotor wakes, and stability characteristics.

Propulsion

The design code will scale the motor's size, but the parameters are based on the 500-hp model. The motor weight will scale with power because the weight of the motor in this model scales to be 34% of the engine's horsepower.

Battery

Battery technology may well be the greatest limiting factor. Lithium-ion batteries are assumed as currently they offer several technical advantages in comparison to other chemistry based batteries, in particular shallow-cycling capabilities, charge acceptance, and low weight. An initial value of $e_b = 350$ Wh/kg is chosen for the battery specific energy, which is on the optimistic side current technological capability [238, 151]; this takes into account a mark-down due to unusable energy and installation weight. Similar level of technology is assumed by Lilium [239] to be deployed in their first built concept. The upcoming, lithium metal or lithium sulphur chemistries promise batteries that could deliver 650 Wh/kg on a battery cell level and 400 Wh/kg of installed power density [240].

Table 9.1 summarises the high level design characteristics that defer between concepts.

9.3.3 Performance

The performance and sizing calculations are executed by tool PHOENICS (**P**reliminary **He**lic**o**pt**e**r & **N**ovel a**i**r vehicle **C**onceptual **S**izing) from Appendix A. The tool combines the previously described design and performance parameters with momentum theory for rotors and propellers, first-principle flight mechanics and an energy sum to evaluate the power requirement and hence energy requirement for the concept air vehicles to perform a specific mission.

TABLE 9.1: Design characteristics of the Concepts.

Design of AAM Concepts			
	Concept 1	Concept 2	Concept 3
MTOW [kg]	3,341	3,515	3,232.8
No. of rotors	4	12	2
No. of blades per rotor	6	4	4
Rotor diameter [m]	4	2	8
Hover RPM	1,200	2,200	500
M_t	0.73	0.67	0.61
Battery mass [kg]	1,022	1,075	990

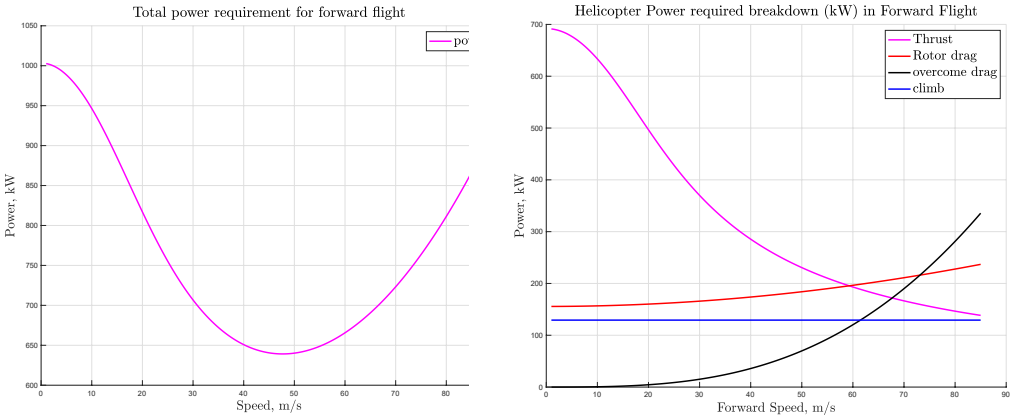

(A) Total power requirement versus forward flight velocity.

(B) Power requirement breakdown versus forward flight velocity.

FIGURE 9.9: Forward flight performance of Concept 1 rotorcraft.

After calculating the power required for the given flight condition, the engine sizing is performed based on a combination of electric machine scaling laws from data of existing electric motors [150, 73]. The performance estimations are completed when the estimated weight of the air-vehicle converges with the power requirement.

The tools findings for the forward speed variation closely mirror the well-known relationship between forward speed and power, with the typical minimum required power occurring at medium forward speeds, as expected from momentum theory. Figures 9.9, 9.10 and 9.11 show the power demand for the three driving flight conditions as a function of forward speed.

A summary of the power requirement for the three main operational modes: hover, forward flight and climb for the three concepts can be seen in Table 9.2.

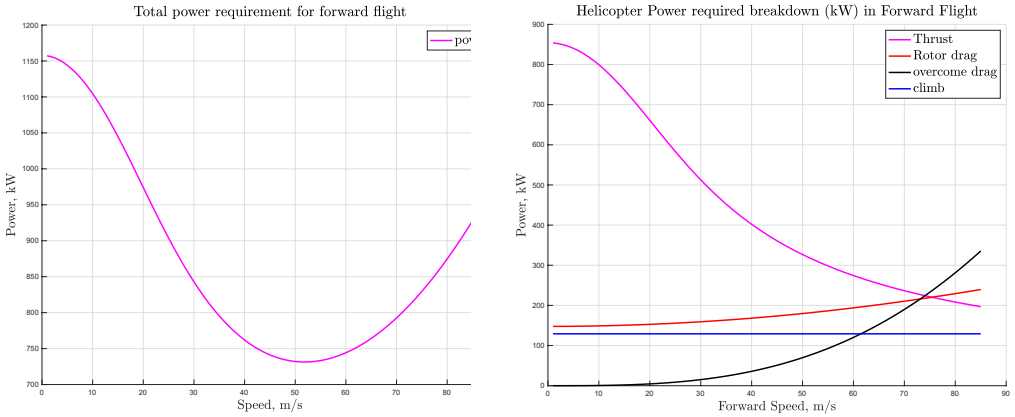

(A) Total power requirement versus forward flight velocity.

(B) Power requirement breakdown versus forward flight velocity.

FIGURE 9.10: Forward flight performance of Concept 2 rotorcraft.

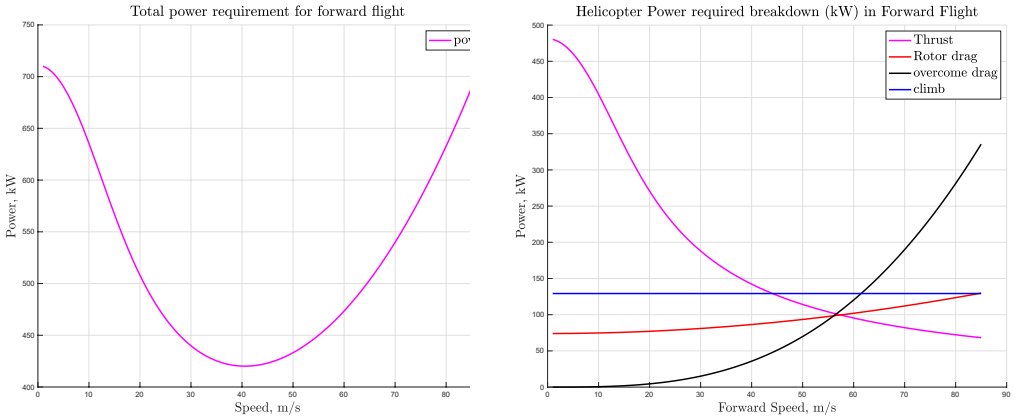

(A) Total power requirement versus forward flight velocity.

(B) Power requirement breakdown versus forward flight velocity.

FIGURE 9.11: Forward flight performance of Concept 3 rotorcraft.

TABLE 9.2: Performance characteristics of the Concepts.

Performance of AAM Concepts			
	Concept 1	Concept 2	Concept 3
Range [km]	56	46	117
Hover power [kW]	1,433	1,653	1,014
Forward flight power [kW]	690	821	377
Climb power [kW]	1,061	1,237	696
Installed power [kW]	1,500	1,700	1,050
Forward flight speed [m/s]	48	52	40
Climb speed [m/s]	5	5	5

9.4 Noise Predictions

A note on noise metrics: SEL versus Lden,Lnight

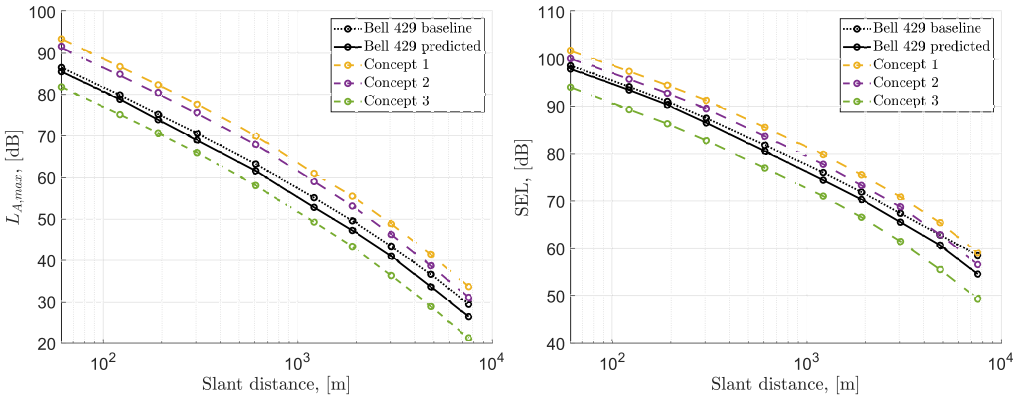

(A) $L_{A,max}$ (B) SEL

FIGURE 9.12: Departure NPD curves generated with MONTANA for all Concept rotorcraft.

Arguably, a more appropriate noise metric for an AAM/UAM scenario would be one that weights against the time of day the operations take place. An example of such is Lden which averages the noise out over an 8-hour day, a 4-hour evening and an 8-hour night, with 5 and 10 decibels added to the evening and night figures respectively to account for generally lower background levels at those times. Lnight averages the noise only during the night period.

9.4.1 NPD curves

NPD curves for the three concepts are constructed for the three main operating conditions defined for a mission. These are hover, departure, approach and flyover. The process for generating the NPD curves follows exactly that of Chapter 7 for the three helicopters. Figures 9.12 to 9.15 show the computationally generated $L_{\mathrm{A,max}}$ and SEL NPD curves. These will form the main inputs for the noise exposure footprint study in Section 9.4.2.

In Figures 9.12 to 9.15 two curves for the baseline rotorcraft are shown, one representing the published data provided by AEDT, while the other is a baseline prediction using MONTANA.

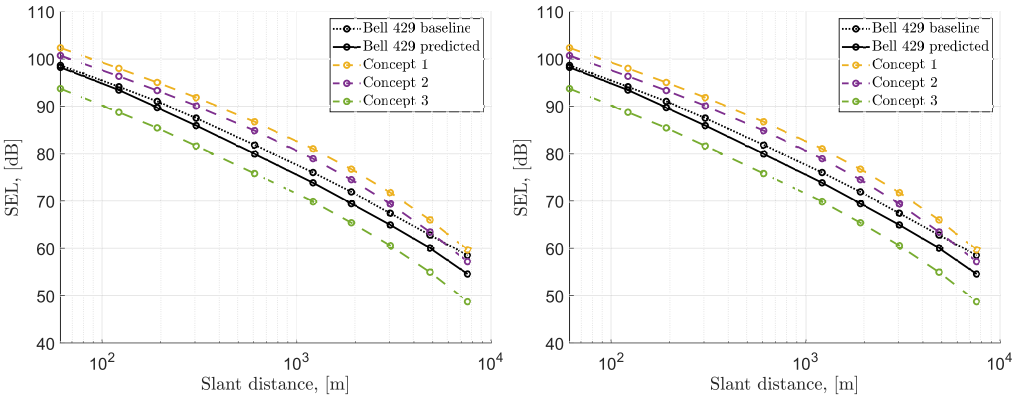

(A) $L_{A,max}$ (B) SEL

FIGURE 9.13: Approach NPD curves generated with MONTANA for all Concept rotorcraft.

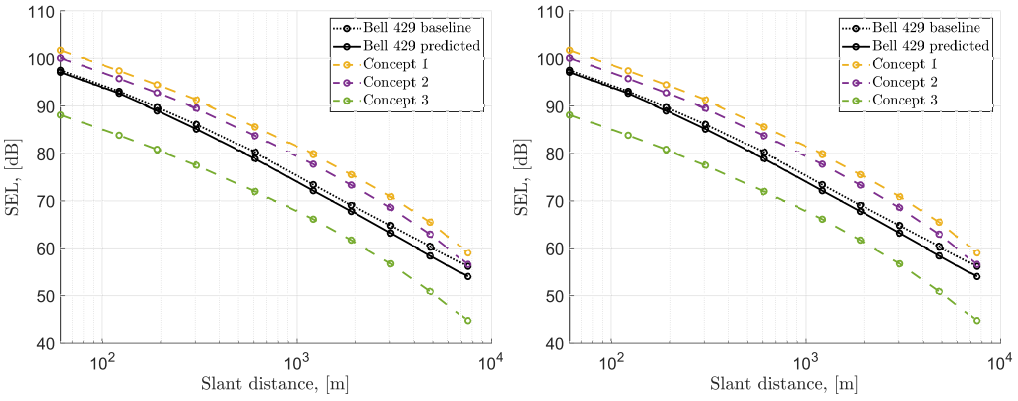

(A) $L_{A,max}$ (B) SEL

FIGURE 9.14: Flyover NPD curves generated with MONTANA for all Concept rotorcraft.

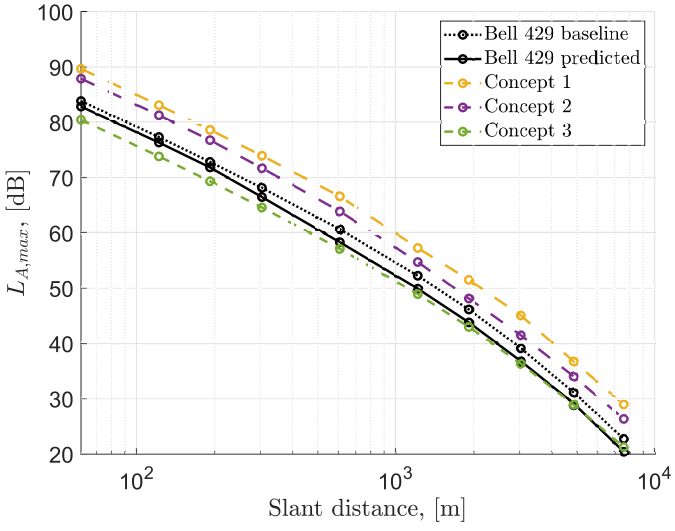

FIGURE 9.15: Hover NPD curves generated with MONTANA for all Concept rotorcraft.

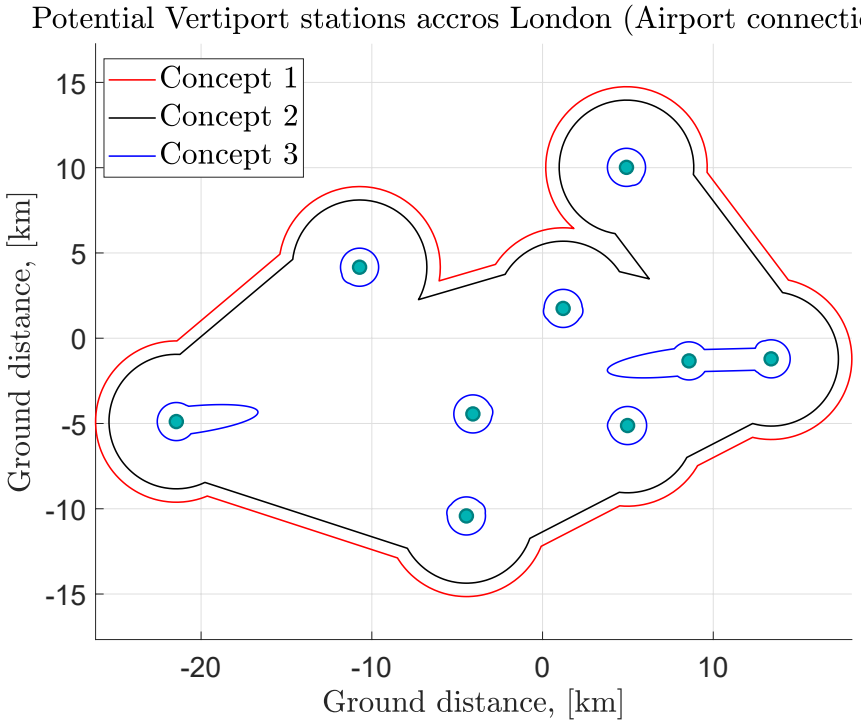

(A) Noise exposure contours.

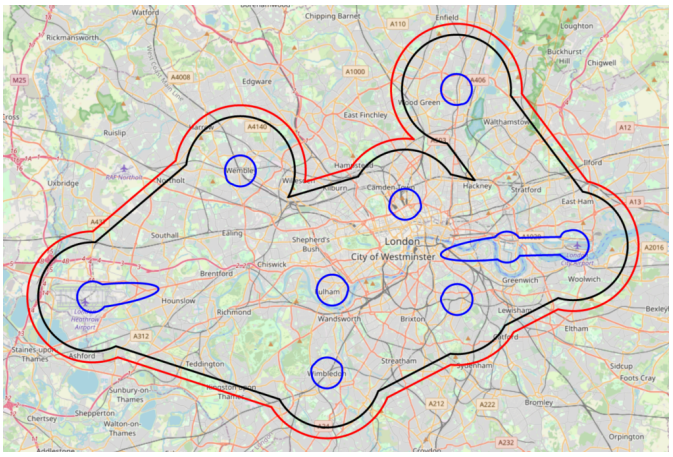

(B) London map.

FIGURE 9.16: 65dB SEL sound exposure contour comparison between the three Concept air vehicles.

9.4.2 Noise exposure contour maps

The following contour maps have been generated assuming single flight events over each of the routes between the 9 vertiports chosen within London. Geographic and population data has not been incorporated in the generation of the contours. A flat ground plane across the entire map is assumed. As discussed, the missions between the concepts are identical, but vary slightly depending on distance between the origin and destination vertiports.

Figure 9.16 show the 65 dB SEL noise exposure map the three different concepts.

Noise benefits of Concept 3

It is evident that Concept 3 demonstrates the least noise exposure over the entire map. As operational differences can be neglected (identical missions flown - note: transition noise has not been explicitly accounted for in any of the concepts.), the benefits in noise immissions are related to performance and operation differences, which are direct results of the starting (and differentiating) design assumptions/decisions. These may be summarised as:

- Larger rotor diameter - hover efficiency and therefore hover power requirements are directly influenced by the diameter of the rotor. The larger diameter rotors of the tilt-wing have a positive impact on performance in two ways: lower power draw overall resulting in reduced battery size for a given distance flown and reduced power requirement impacts the size and weight of the propulsion system. Thrust requirements reduce relative to the other concepts resulting in beneficial loading characteristics of the rotor.
- Fixed wing cruise capability - the rotor power requirement for cruise is significantly reduced as it no longer need to support the weight of the aircraft. This increases cruise efficiency, resulting in lighter batteries for a given distance flown.
- Reduced tip Mach number - as a result of the previous design decisions, the resulting required rotational speed in hover reduces the loading and thickness noise contribution of the rotor.

However, it is worth noting that the weight of Concept 3 could be underestimated at this initial design stage, with subsystems and components contributing to the til-rotor mechanisms and additional weight of the larger fairings and fixed-wing not being accurately captured. Further iterations of the vehicle, with increased detail in weight estimation would be required to confirm. These are beyond the scope of this Chapter.

Figures 9.17, 9.18 and 9.19 show the 65dB and 75dB SEL contour areas for the three concepts, except in the case of concept 3 were the 55dB contour is added as its area scale is almost identical to the 65 dB contour of the other two concepts. In addition, reduction of the 65 dB and 75 dB contours for concept 3 is attributed to the absence of cruise noise to the contours separating the contours into two individual contours surrounding the vertiports. This is not the case for concepts 1 and 2, when flying at the identical altitudes and routes.

The effect of simple route optimisation may be interpreted by analysing the contours in all three Figures. Creating flight “corridors”, by overlapping individual segments of the network, alleviating noise exposure from areas that could be otherwise not affected.

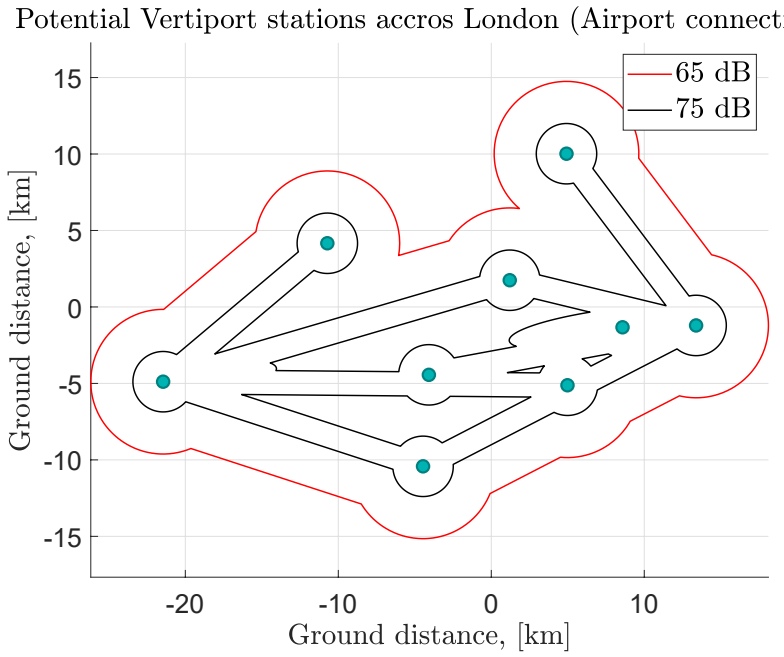

(A) Noise exposure contours.

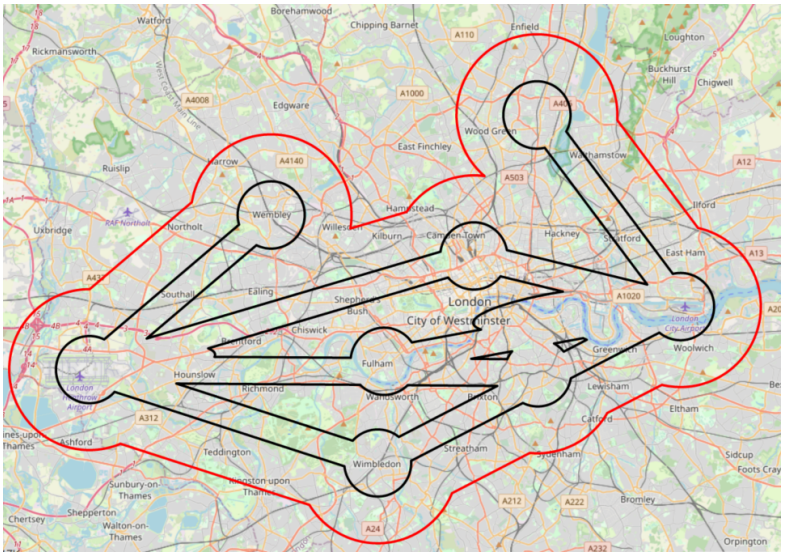

(B) London map.

FIGURE 9.17: SEL sound exposure contour map for Concept 1. Inner city network.

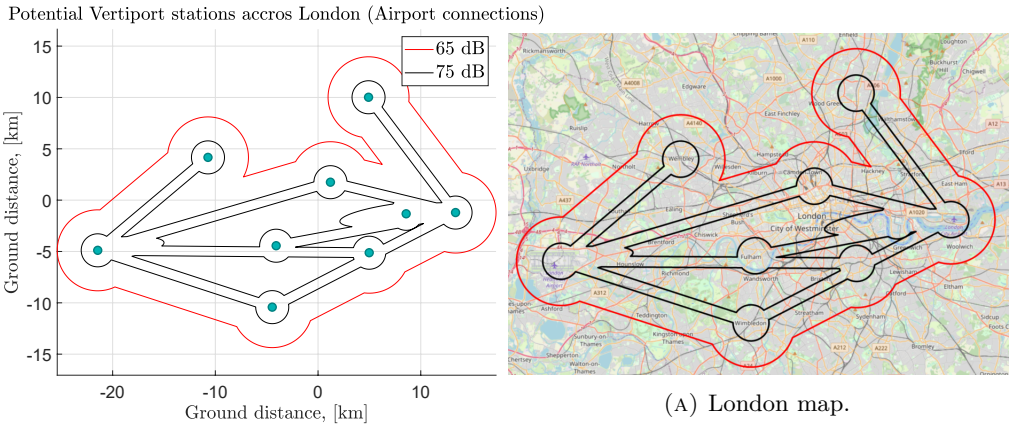

(A) London map.

FIGURE 9.18: SEL sound exposure contour map for Concept 2. Inner city network.

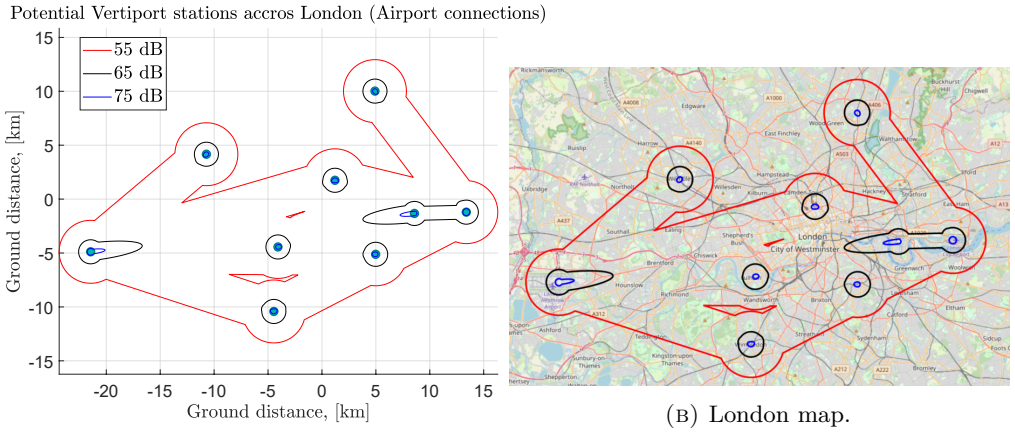

(A) Noise exposure contours.

(B) London map.

FIGURE 9.19: SEL sound exposure contour map for Concept 3. Inner city network.

9.4.3 Effect of noise source Directivity

An assessment of the effect of the overall directivity of the AAM vehicles on community noise exposure is carried out. Three different patterns are used to demonstrate the flexibility of the directivity functionality added to MONTANA in Chapter 5.

First, a case where the assumption is that no available directivity data is available. In this case a simple three-dimensional analytical function may be used, in particular, a spherical harmonic, to define the radiation pattern. This allows a quick definition of a radiation pattern, based on empirical knowledge of the designers and the design choices they have made. The impact of changing the directivity of the vehicle may be quickly assessed by swapping out simple spherical harmonics, or even spherical harmonic expansions. Once more data is available, it may be used to generate more detailed representations of the overall directivity as will be illustrated in the following two cases.

In this first case, a single spherical harmonic of degree $\ell = 2$ and order $m = 2$, leading the directivity function to $D(\theta, \varphi) = Y_2^2(\theta, \varphi)$. This choice is made arbitrarily, and does not physically represent the AAM concepts in this Chapter. The highly directive pattern of Y_2^2 was chosen to precisely illustrate the effect, a simple dominant directive source for example, may have in redistributing the energy to different areas on the ground. A simple illustration of the Y_2^2 spherical harmonic can be seen in Figure 9.20. Figure 9.21 shows the resulting noise exposure contours for concept 3.

The change in the shape of the contour is obvious, with regions of the map the previously unaffected by levels of a specific value now falling in the contour, and possibly experiencing noise levels much higher that the level indicated by the contours.

A more general observation is made in regard to power normalisation and acoustic energy conversation. Although the directivity function ensures that the same amount of energy is generated and radiated from the source relative to the omnidirectional case, the energy radiated in the direction of the ground may be different in each scenario

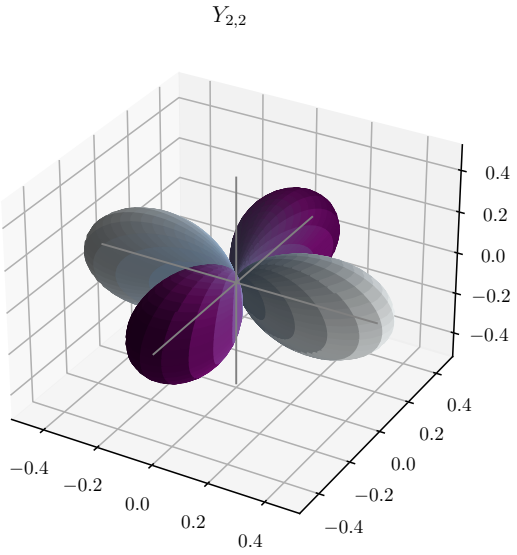

FIGURE 9.20: Visual illustration of the Y_2^2 spherical harmonic. The distance of any point on the surface from the origin equals the value of the spherical harmonic at that location defined by (θ, φ).

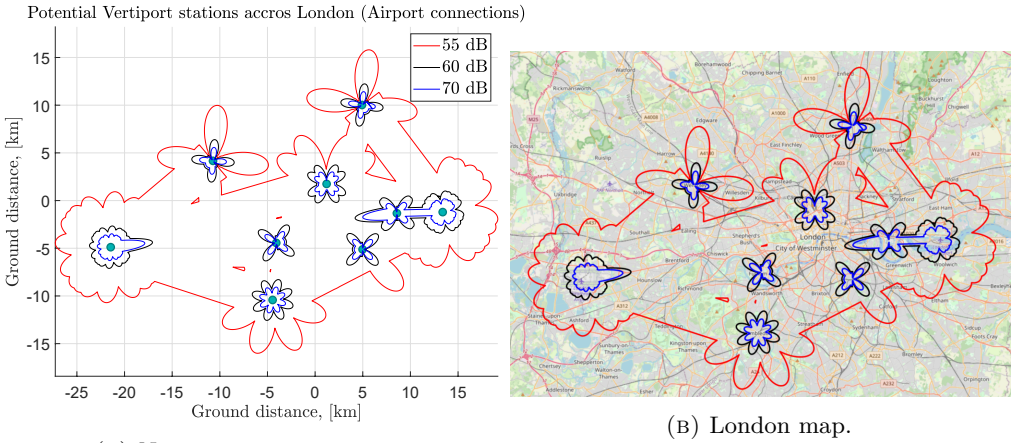

(A) Noise exposure contours.

(B) London map.

FIGURE 9.21: SEL sound exposure contour maps for Concept 3, using with the directivity function defined as $D(\theta, \varphi) = Y_2^2(\theta, \varphi)$. Inner city network.

depending on the directivity function of choice. This results in contour areas not necessarily having the same areas is addition to the differences observed in the position of the contour lines (or otherwise shape of the contours).

Examples of such highly directional noise source, that could be modelled using single spherical harmonics (or a combination of few) propeller/rotor self noise, tones generated by cavity resonance, bleed valve noise, noise exiting ducts. In the case such sources of noise become dominant, the whole aircraft noise signature also takes a highly directive nature, the effect of which was demonstrated.

For the second case, the directivity function is constructed from the spherical harmonic expansion coefficients (Table 9.3 gives the vales of the coefficients for the 500 Hz band, while Figure 9.22 provides a visual illustration of the noise radiation pattern) calculated by Krebs et al. [185] after flyover directivity measurements were made for fixed wing aircraft. Once again, this directivity function does not represent that of the concept, however it illustrates the versatility of using experimental measurements to generate the required coefficients for the expansion. The noise exposure contour results are presented in Figure 9.23.

TABLE 9.3: Spherical harmonic directivity coefficients A_ℓ^m of the 500 Hz one-third Octave band for a fixed-wing turbofan aircraft. Data from [185].

$\mathbf{A_\ell^m}$ **coefficients**								
	m							
ℓ	0	1	2	3	4	5	6	7
0	76.1	3.31	-7.38	3.16	-0.976	-0.428	-1.314	-0.146
1		-1.48	0.06	-0.14	0.052	-0.214	-0.029	-0.196
2			0.19	0.06	-0.021	-0.037	-0.019	-0.009
3				0.02	0.004	0.006	8.0E-04	-1.3E-03
4					-0.003	0.004	5.6E-04	2.1E-04
5						0.001	1.2E-04	4.6E-05
6							1.9E-05	-3.4E-07
7								8.7E-06

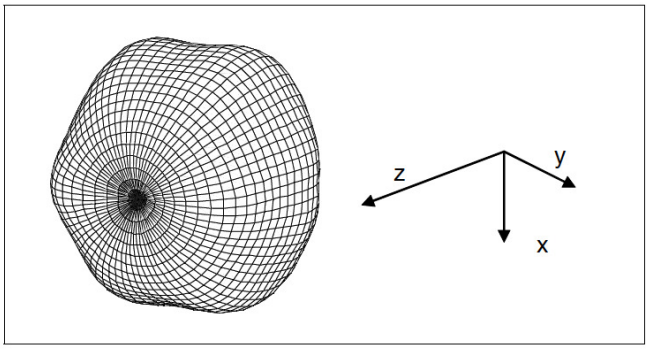

FIGURE 9.22: Visual illustration of the spherical harmonic expansion given by coefficients of Table 9.3. The distance of any point on the surface from the origin equals the value of the spherical harmonic expansion at that location defined by (θ, φ). Data from [185].

Finally, the Boeing Vertol directivity used in Chapter 7 is once again implemented. Figure 9.24 shows the effect of it on the London AAM network. The large lobe of the static directivity impacts the overall shape of the contour, connecting regions that in the previous cases were not.

The preliminary results presented within this Chapter can already trigger questions regarding the noise immissions of any concept AAM vehicles in the conceptual design stage. These questions can feed into more detailed parametric or trade-off studies, on

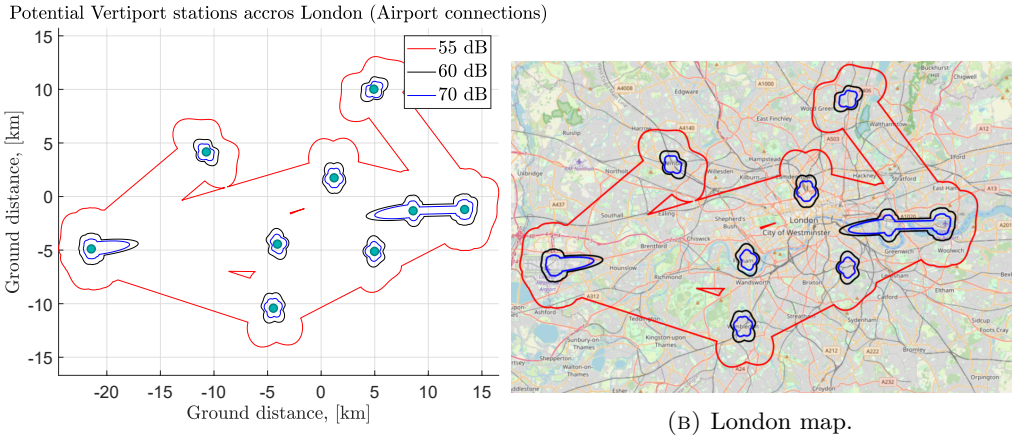

(A) Noise exposure contours.

(B) London map.

FIGURE 9.23: SEL sound exposure contour maps for Concept 3, using with the directivity function defined as a spherical harmonic expansion using coefficients measured by Krebbs et al. [185]. Inner city network.

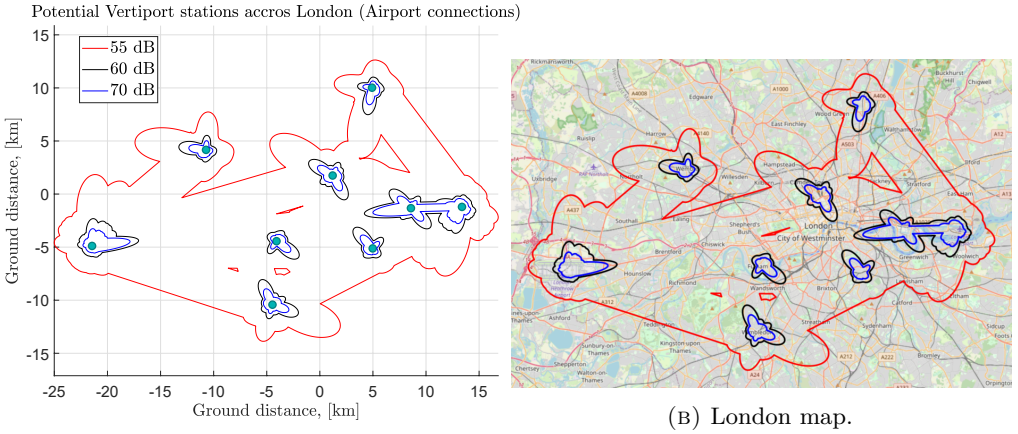

(A) Noise exposure contours.

(B) London map.

FIGURE 9.24: SEL sound exposure contour maps for Concept 3, using with the directivity function defined as a spherical harmonic expansion using static directivity data for a Boeing Vertol, [214]. Inner city network.

behalf of performance, weight and also noise. Such studies can impact the design space exploration and steer the design in a direction completely different to what may have been originally intended. Some questions are discussed bellow:

- Hover and vertical climb decent are high power operation that dominate the contour from a PWL perspective. This is especially true for cases where cruise levels are not audible on the ground. As expected, communities around vertiports become the sensitive areas. Route optimisation and careful location selection for the vertiports could reduce the number of them required, while achieving a level of noise mitigation.

- The number of vertiports poses an interesting problem. Assuming the operation of the same fleet of AAM vehicles (number of operation, and composition - types of aircraft) at all vertiports, the overall exposure area over a city like London is

directly proportional to the number of vertiports. Typically, for conventional aircraft, this is not a problem as the origin and destination airports of flights are hundreds if not thousands of kilometers apart. In the case of the AAM, in the worst case scenario, a single observer location may be impacted by multiple vertiports, and their flight paths.

- Directivity during high power operational modes significantly drives the overall shape of the contour. This is not the case for the climb/decent and cruise part of the mission. Although the area within the contour is affected by directivity during these phases of flight, the overall shape of the contour is driven by the flight track. In the static cases however, a single observer is exposed to the same source directivity angles throughout the event, therefore influencing the shape of the contour. Leveraging VTOL capability as well as individual air vehicle directivity it is possible to direct noise to unpopulated areas. Additional noise exposure alleviation may be achieved by taking advantage of takeoff orientation in the same way as flightpath dispersion to spread noise over a larger area, rather that concentrating it in one direction. Finally, this effect can help optimise trajectories and flight paths according weather, wind in particular, conditions. The ability to control the direction of the noise, through knowledge of the directivity and the flexibility of VTOL operations, could in fact make highly directional air vehicles more desirable over omnidirectional ones.

- At the altitudes considered within this Chapter, low to medium noise exposure levels will affect the majority of urban population in London. This is especially true when cruise noise is audible on the ground, and flight levels are not chosen carefully with noise in mind. As in the case of the number of vertiports, if cruise noise for a particular noise level is audible on the ground, the total area of the corresponding contour is proportional to the length of the mission and to the number of distinct routes within the network. Consideration of other urban noise sources (e.g. rail, roads) in trade-off studies, could allow masking of the subordinate sources, to reduce overall exposure area.

- Finally, a trade-off exists between exposure area during vertical takeoff/landing and accelerated climb - equivalent to cutback procedure in conventional turbofan aircraft. Tilt rotor transition altitude provides an interesting case study from the noise perspective for future research.

9.5 Summary

Chapter 10

Conclusions and Future studies

The aim of this research was to extend the capability of the whole aircraft and airport noise tools SyNoPoD and RANE, to account for novel propeller powered aircraft, including the effects of three-dimensional noise source directivity. Of particular interest is the problem of estimating the noise that future novel aircraft types are likely to make. This includes electric and hybrid electric aircraft both as replacements for conventional gas turbine powered aircraft and for completely new types of aircraft such as air taxis.

The objectives set-out were: (i) to develop scaling laws for the noise due to novel sources that novel aircraft will possess, (ii) adapting the scaling laws for known sources to apply to the novel aircraft types (iii) integrating such scaling laws into a whole aircraft noise model that includes the effects of three-dimensional directivity, (iv) implement said model into an airport/community noise tool to research the likely operational characteristics of novel aircraft while evaluating the effect of a number of potential design scenarios, and how they affect communities around airports.

The results of this research is presented in the form of the MONTANA (Modular Novel Transport Aircraft Assessor), a whole aircraft noise prediction framework. The existing ISVR methodologies and tools were brought together and developed upon to meet the new aims and objectives.

The principal behind the MONTANA framework is that of a lumped noise source definition. The individual noise source mechanisms that contribute to the overall noise emissions are described by a single point source, some PWL, a directivity and a spectral shape, equivalent to the sum of the contributing components. The characteristic PWL, directivity and spectral shape are estimated by calibrating existing NPD data for conventional aircraft with noise level deltas of the individual noise source components to account for changes in design and operation. The calibration deltas are calculated through simple scaling relations resulting from modifications to existing empirical, semi-empirical or analytical models.

Specific attention was given to the development and implementation of a scaling relation for propeller steady harmonic noise, as propellers were identified as a common propulsion system archetype, and therefore dominant noise source, across novel fixed-wing and rotary air vehicles.

The framework was designed to include the following functionality:

- Generalisation of the framework introduced by Synodinos et. al. A mathematical insight to the dependency of changes in noise levels, relative to a baseline scenario, on the Jacobian matrix of the function giving the noise for any particular noise source.
- Three-dimensional lumped source definition. The acoustic radiation pattern is no longer restricted to the polar angle, with use of spherical harmonic expansion.
- Derived scaling relations for propeller harmonic noise based the model proposed by Hanson [60]. These scaling relations were used to derive variation in PWL, spectral (tonal) content and directivity between baseline scenarios and novel aircraft designs.
- Modification of the simplified airport noise tool RANE, to include three-dimensional characterisation of noise sources
- Modification to the flightpath definition of RANE, to allow for the flexibility required to capture the unconventional operation of helicopter and UAM air vehicles.
- Use of Bezier curves to correct errors and discontinuities in the contour generating process of RANE.
- Modification to the definition of noise surfaces to include the possibility of defining conical surfaces in order to model linear power variation along a single segment.
- Methods for accounting for aircraft power setting variation and noise source rotation were also introduced.
- Preliminary design and implementation of a framework for the generation of noise exposure contours due to lumped source rotation and translation, and application to a VTOL scenario.

Generally, prediction accuracy drops for large deviations of the concepts from the baseline aircraft, as the underlying linearisation of the individual noise prediction breaks down. In general use cases, appropriate baseline vehicles may be chosen, for both fixed-wing and rotorcraft air vehicles, resulting reasonable and reliable results.

MONTANA provides the means to assess the noise exposure of concept aircraft at a wide range of design stages; from “paper” aircraft and propulsion systems to detailed

designs. It allows for the assessment of fixed-wing aircraft and rotorcraft against all four elements of the ICAO balanced approach to aircraft noise management, looking at how advances in technology and design influence noise generation at the source and how changes in operation have a meaningful impact on communities in their vicinity.

The assessment of design/technology variation on noise output was complemented by an additional module developed within the scope of this thesis.PHOENICS (Preliminary Helicopter & Novel air vehicle Conceptual Sizing) is the first version a preliminary sizing tool for propeller powered fixed wing aircraft and rotorcraft, aimed at integrating the noise as an additional objective in conceptual aircraft design.

Lumped noise source and propeller noise scaling relations

A scaling relation for propeller steady tonal noise was presented. A linear approximation assumption was used as a method to estimate changes in noise levels between a known baseline scenario and an unknown modified case. The changes in noise levels are coupled with the well established SAE AIR 1845 methodology for generating NPD curves. An error analysis of the linear approximation assumption showed that under reasonable deviation of the design and operating parameters from the baseline condition, the method produces highly accurate predictions. Depending on the parameters, for ±50% variation in parameters the error remains below 3%, while for variation of ±100% the error remains below 10%.

The scaling of the fundamental tone and first few harmonics (up to $m = 4$) was demonstrated by the collapse of the results when normalising to Ω^4 for the axial (lift) component of the loading noise, and Ω^3 for the tangential (drag) component and thickness noise source.

The capability of predicting changes in noise levels was compared against ESDU 76020 and an detailed implementation of the full Hanson model, using XFoil and CRotor to estimate the aerodynamic inputs of rotors. Changes in the fundamental tone levels, were in most scenarios predicted within ± 1.5 dB, depending on the variation of the input parameters described above. Harmonic shape was captured accurately for $M_T < 0.6$, with large errors being introduced for Mach numbers above that. Large errors were also evident for non-static cases as the argument of Bessel function no longer obeyed the small argument approximation.

The framework produced estimates with an average error of ± 1.5 dB for the $L_{\mathrm{A,max}}$ NPD curves and ± 2 dB for the SEL NPD curves, both of which are within the ECAC Doc 29 [34] tolerance, despite the sources of error described. Due to the framework being computational by design, it eliminates the inaccuracies associated with experimental measurements of flyover techniques. The effect of the choice of the baseline aircraft was investigated using the DeHavillad Canada Dash 8-300 (DHC-8 300). Four

different aircraft were chosen as baseline aircraft with the aim of replicating the DHC-8 300 measured NPD curves. The spread of the results was approximately 2.5 dBA SEL for large slant distance, while only 1.2 dB dBA SEL for slant distance smaller than 1,500 m, with difference from the baseline being on average only 0.55 dBA SEL.

The applicability of the model to helicopters and more generically rotorcraft was tested with prediction of three-types of steady state NPDs, characteristic of helicopter operation: idle/hover, departure and flyover. Errors followed the same trends as the conventional fixed wing aircraft.

The NPD curve prediction capability was bench-marked using published NPD for propeller piston engine aircraft, as well as larger turboprops. Using a single initial point a number of different power settings at all standard slant distances were calculated. The error was deemed acceptable by the standards of the ECAC Doc 29. This reinforced the assumption that the dominant noise sources in take-off for the particular aircraft are the loading and thickness contributions of the steady tonal propeller noise.

The proposed framework therefore provides NPD calculations in a time and computationally efficient manner, that captures all the high level design variations expected to occur at the preliminary design stage of a propeller powered aircraft. Noise calculations of the entire vehicle may be performed in parallel to the design iteration process and leveraged to provide constructive feedback. As the design matures the details in design will improve the predictions, and coupled with higher fidelity aeroacoustic and airport noise models can provide a comprehensive assessment of the noise for certification purposes as well as impact of the novel concepts around communities.

RANE v2

The introduction of a directivity function to describe the three-dimensional emission patterns of real aircraft was validated in two specific ways. The first comparisons against the in-house grid point method, confirmed that acoustic energy is preserved over the flyover procedure. Contour predictions for simple turns, cut-back procedures and vertical take-off provided proof that the Bezier curve treatment to extremities and connecting regions provides a simple, yet highly effective method for interpolating between contour segments and eliminating discontinuities. Decrease in the error of contour area prediction were also observed. Secondly, RANE v2 was bench-marked using realistic fixed wing and helicopter case studies. The air vehicles of choice were propeller powered fixed-wing aircraft of varying size, design and operation and three helicopters, due to the inherent high directivity. Two different examples of input data were used in order to generate the required directivity function as input to RANE v2. The presented case studies provide reassuring evidence that the framework can provide predictions and

may be integrated within design systems of UAM and AAM (Advanced Air Mobility) air vehicles to help minimise the impact of such vehicles on community noise.

On an aircraft level, assessment of individual noise source directivity effects on noise contours, allows the exploration of engine installation, reflection and blockage effects to maximise the potential benefits on noise exposure. The incorporation of directivity effects may then be coupled with models for generating NPD curves for novel aircraft [12, 241] and therefore predicting the PWL outputs, to provide global assessment of the noise impact of new technology and/or implementation of noise abatement operational procedures Improved assessment of single runway, single event or fleet movements is possible.

The capabilities of MONTANA to predict changes in noise emissions were demonstrated through two case studies, appropriate to the two major applications areas of the tool. First, a case study on the noise performance of next generation regional hydrogen powered aircraft, and second a case study of a simplistic UAM network operating in London. The study demonstrated the impact of high level design decisions and noise source directivity on the final noise exposure contours. The studies included several air vehicle concepts, raging from regional fixed-wing aircraft to UAM rotorcraft:

- Current generation reciprocating engine and turboprops.
- Novel hydrogen powered aircraft:
  - fuel cell electric propulsion (propeller and ducted-fan driven)
  - gaseous/liquid hydrogen gas turbines (propeller driven)
- Current generation single or dual (main) rotor helicopters
- Novel UAM rotorcraft, with novel operation characteristics

10.1 Recommendations for future research

A series of improvements have been identified throughout this research, that could provide opportunities for further development of whole aircraft and airport noise prediction and specifically the MONTANA tool.

The definition of a lumped aircraft noise source for propeller powered aircraft in this thesis lacks contributions from three other propeller noise sources, that literature indicates, could be dominant in certain operating conditions and emission angles. These are propeller broadband noise due to turbulence ingestion and trailing edge self noise and, unsteady loading noise. Inclusion of the sources could provide a better insight to the propeller source balance and explain the consistent NPD under-prediction observed in this thesis.

The three-dimensional directivity function implemented in MONTANA through the spherical harmonic expansion assumes common directional features across all frequencies. This is fundamentally inaccurate, especially for spectra with high tonal content. However, the use spherical harmonics would allow a simple solution, as the directivity of each frequency band (one-third octave or otherwise) could be described by its own spherical harmonic expansion. This would allow for the total aircraft directivity to be described as the sum over the individual directivities of each band for each contributing noise source. Such an implementation would resolve the subsequent limitation of propagation across all polar and azimuthal emission angles.

Current NPD development practices correlate power setting parameters (e.g. thrust, rpm) and aircraft configuration modes to sets of noise levels. Complex operations are then modelled by describing phases of the flightpath by these constant NPD curves. Complex operations in UAM (i.e. hover, transition, etc.) may not lend themselves to adopting such techniques. Transient non-linear modelling approaches for flight paths (continuous curved), power setting and velocity variation (accelerated, decelerated flight) throughout segments of flight could provide more accurate description of realistic operations. Such improvements would require the balancing of the trade-off between computational cost, complexity and predictive capability.

Finally, the preliminary sizing tool (PHOENICS) although adequate for the requirements of this thesis, is based on first principle flight mechanics and open source empirical data for initial weight and size estimation. Limitations exist in the capability to assess general fixed wing and rotorcraft configurations beyond an initial power and energy requirements. Two key elements identified as critical to future updates to the model are: propeller performance evaluation (beyond the capability of momentum theory) as the outputs are direct inputs to the noise estimation modules of MONTANA; aircraft/airframe aerodynamic performance evaluation. Currently, the air-vehicles lift and drag configurations are not included in the sizing-loop, grossly limiting the design space and capability of the tool.

Appendix A

PHOENICS: Preliminary sizing tool

This Appendix describes the PHOENICS (**P**reliminary **He**lic**o**pt**e**r & **N**ovel a**i**r vehicle **C**onceptual **S**izing) tool. PHOENICS is a conceptual air-vehicle design tool, aimed to complement MONTANA and its components discussed in part I and II of the methodology chapters. It is a model that provides performance (power requirement) assessment and initial sizing for both fixed-wing propeller powered aircraft along with rotorcraft vehicles flying particular missions. The approach uses momentum theory (actuator disk theory) to estimate the ideal performance of the installed propeller/rotors, first-principle flight mechanics for both rotorcraft (based on helicopter theory) and fixed-wings, while also a typical, energy based, aircraft sizing procedure is implemented to size the energy storage requirements of fully electric air vehicles.

A.1 Outline

The design of any air vehicle starts at the requirements set by the stakeholders or potential customers of the given aircraft. These requirements may range from nominal operating speed, number of passengers, mission range and ability to perform VTOL operations etc. Other requirements that are not performance indicators may also be required, such as low noise and air pollutant emissions, specifically CO_2 and NO_x. All these requirements have an effect on the design choices implemented at any stage of the design process and may cause the designers to back-track or re-iterate a version of the concepts in order to meet all of them. An example of the design process typical of civil aircraft may be seen in Figure A.1.

The requirements enable the creation of a simplified flight mission. A flight mission is considered as the entirety of a single operation performed by a vehicle from

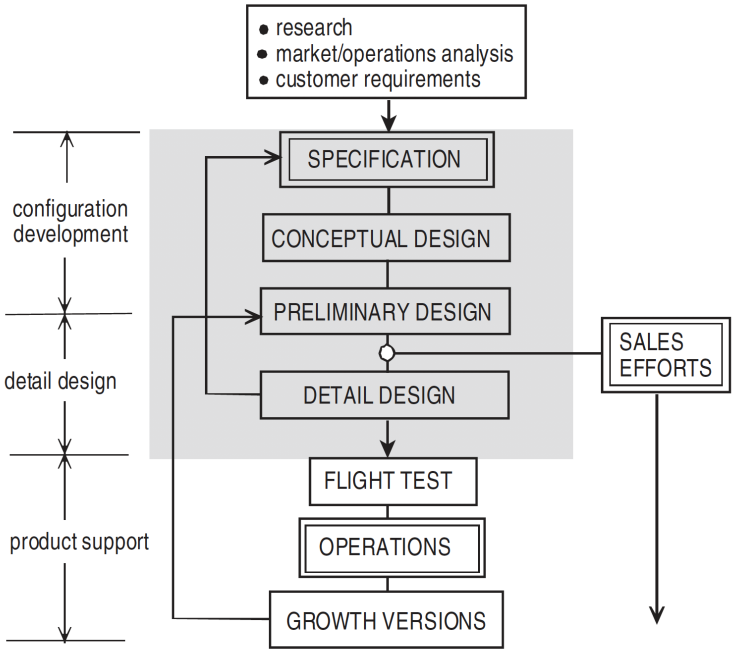

FIGURE A.1: Schedule of the civil aeroplane development process [242]. Adapted from J.H. McMasters

start-of-engine at takeoff to engine shut-off at landing (usually taxing is not included at this not included at this stage). The study of the mission allows for the power requirements of the vehicles at the various phases of flight to be estimated. The peak power requirement over the entirety of the mission will be used along with safety buffer considerations to size (choose) the propulsion system. The power requirement of each individual phase is used to appropriately size the energy storage and delivery system. PHOENICS performs exactly this analysis for two very different types of vehicles, however using a very similar thrust generating apparatus, the propeller/rotor. The two types of vehicles are the typical fixed-wing aircraft and the VTOL rotorcraft.

A.2 Background: Aircraft performance

Aircraft performance falls under the general discipline of flight mechanics (or flight dynamics). It dictates how an aircraft will "interact" with the air surrounding through the management and response to the four forces of flight: lift, drag, thrust, and weight A.2. These forces will dictate the aircraft's performance and to what degree the mission objectives are satisfied. These may be, a maximum cruise velocity, climb capability, maximum range or for civil aviation applications fuel economy, emission and noise.

An aircraft's performance in closely tied to the eventual size and weight. Efficient cruise aircraft for example require high aspect ratio wings, leading large wing spans increasing

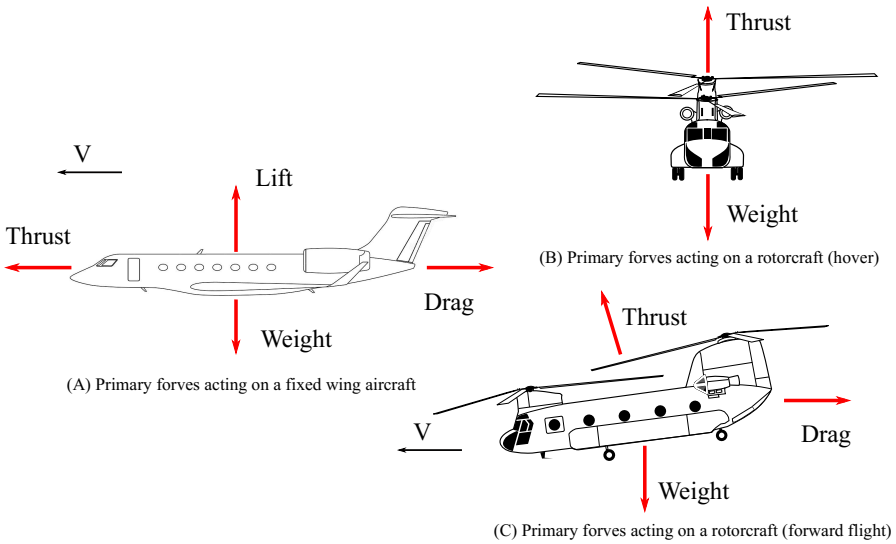

FIGURE A.2: Primary forces acting on fixed wing aircraft (A) and rotorcraft during hover (B) and forward flight (C).

the demand and size of structural components within it, such as the spars and ribs. The propulsion system, in charge of thrust generation, has to do so in manner that allows the aircraft meet the mission and certification requirements, while at the same time not incurring a weight penalty to the entire aircraft. The ability to generate thrust and lift while minimising drag (and losses in general) also dictates the type of operations and manoeuvres an aircraft if capable of performing.

Understanding the operation of an aircraft is important when studying an aircraft as a noise source for two particular reasons: 1. The acoustic sources on the aircraft are heavily dependent on the operational/performance parameters during any specific phase of the flight. This is important for what is known as noise mitigation at the source, which discussed is focused in reducing the total amount of energy radiated as noise. 2. Understanding the capabilities of an aircraft and the trade-offs that exist within aircraft design allow for aircraft operations to be optimised for noise, through noise abatement operational procedures.

Constraint analysis

The performance analysis of an aircraft may be initialised by the construction of constraint analysis diagram. It is used to assess the relative importance of the various phases of flight performance required to be met in the final design. A couple of example diagrams may be seen in Figures A.3 and A.4. The diagrams are constructed using the equations of motion for each individual operation and are commonly presented in the form of thrust-to-weight ratio (T/W) versus wing loading (W/S). The involvement of wing loading implies the use of constraint analysis is typical applied to fixed-wing aircraft (see Anderson [232] for more details).

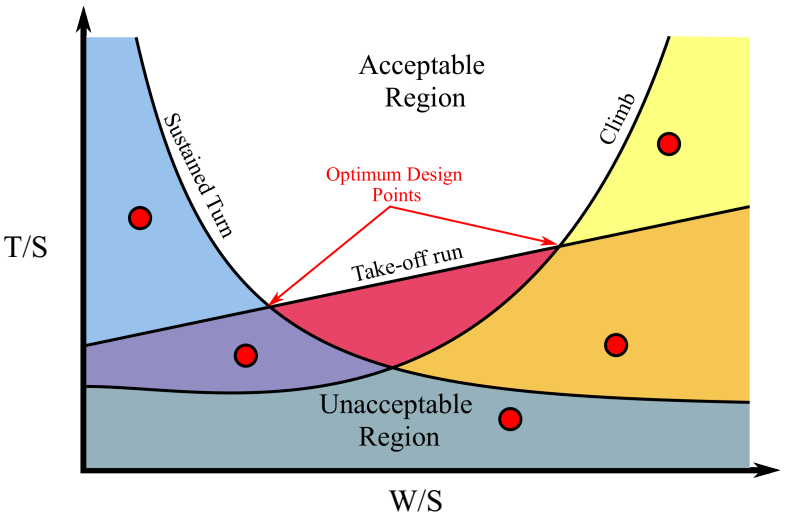

FIGURE A.3: Typical constraint analysis diagram indicating the possible design space for a fixed wing aircraft. Combination of T/W and W/S that lie in the white region constitute viable design. Adapted from [243].

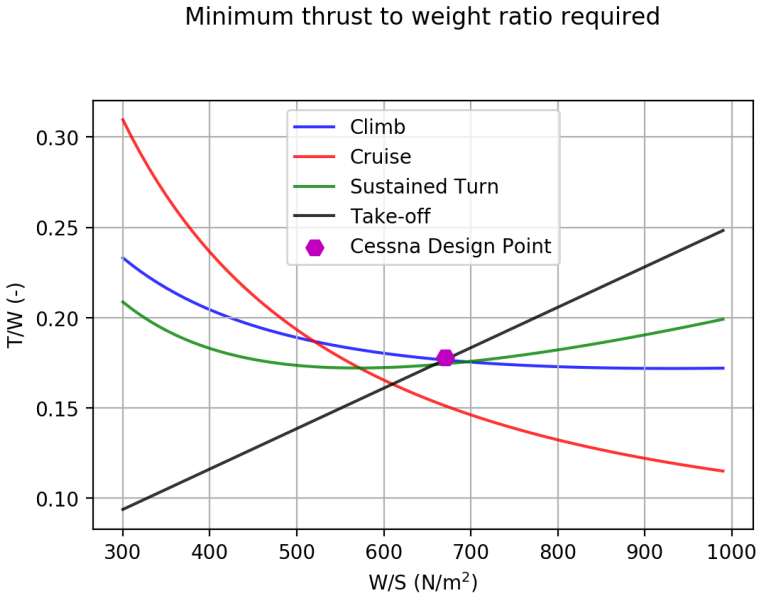

FIGURE A.4: Calculated wing-loading versus thrust-to-weight-ratio diagram. The indicated design point is that of a Cessna 172 Skyhawk.

Helicopter performance on the other hand is analysed using power requirement diagrams, an example of which may be seen in Figure A.5. The power requirement for every operation (hover, forward flight, vertical ascending and descending etc.) through the calculation of the induced, profile, parasite and climb powers. An important parameter is the power loading, P/T (or power-to-thrust ratio).

For every operation an optimum disk loading exists that minimises the power loading. For a given gross weight, this optimal disk loading will determine the optimum radius of the rotor.

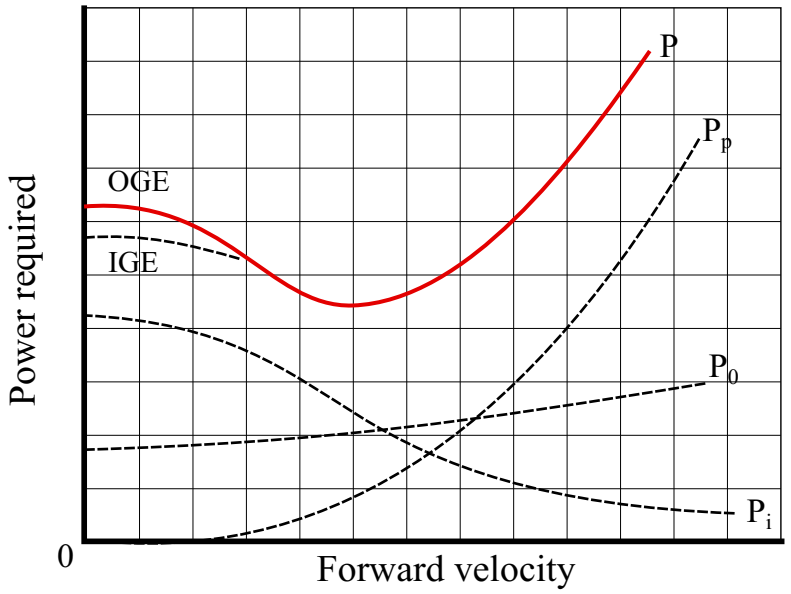

FIGURE A.5: Helicopter power required for level flight at a given gross weight and altitude. Figure replicated from expressions in reference [244].

A.3 Propulsive efficiency in electric aircraft design

The use of rotating wings, in all the different applications begs the questions of why so many variants of rotating wings exist, what parameters drive the decision-making and of particular interest to this thesis, which of these parameters drive the quest for performance and which that of low noise emission. Rotating wings are propulsive devices used by certain air vehicles to generate thrust (propulsion), such examples are propellers and fans on convectional fixed wing aircraft. Others utilise them to provide lift, propulsion and control. The traditional example is that of a helicopter using one or maybe two rotors to generate the required aerodynamic forces.

The reason of existence of the various propulsion systems may be understood by the simplified analysis of any generic propulsive device illustrated in Figure A.6. The device is set in a medium (fluid) of uniform flow velocity V_∞. The function of the device is to generate a propulsive force or else thrust T, acting towards the left direction. This force is generated as a reaction (Newton's third law) to the force imparted on the fluid by the propulsive device itself. The thrust may be given by Newtons second law, stating that the net force imparted on an object is equal to its time rate of change of momentum.

Therefore, for a generic propulsive device the *thrust equation* may be written,

$$T = \dot{m}(V_j - V_\infty) \tag{A.1}$$

where V_j is the jet velocity down stream of the propulsive device, and $\dot{m}$ is mass flow rate through the propulsive device. It is interesting to note at this point that the thrust

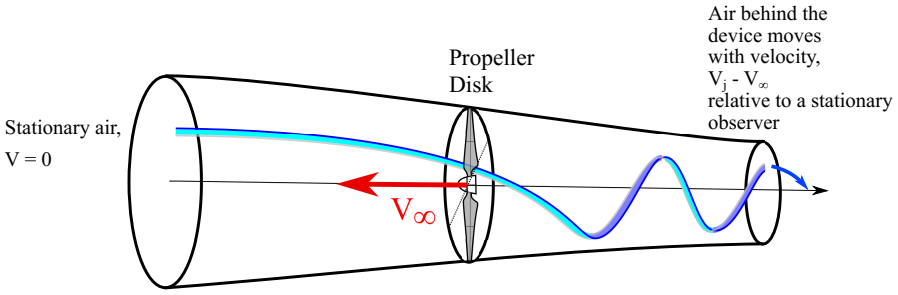

FIGURE A.6: Illustration of a propulsive device moving through stationary air with velocity V_∞

generated by any propulsive device of this nature, is directly proportional to the change in velocity it imparts on the fluid.

The propulsive efficiency of such a device may be quantified by the ratio of the useful available power, P_A (the power required to generate thrust T to propel an aircraft forward at velocity V_∞) to the total power generated by the device. The total power generated is equal to the useful power plus the additional wasted power (flow recirculation, vertices etc., phenomena that do not contribute to the generation of thrust but carry part of the energy imparted on to the fluid by the propulsive device). After some algebraic simplification, the propulsive efficiency may be given by,

$$\eta_p = \frac{2}{1 + V_j / V_\infty} \tag{A.2}$$

At this point it is evident that a contradiction exists between the generation of thrust, and the efficient generation of thrust. High jet velocities with respect to the freestream velocity result in high thrust, but in low efficiency. This means that in order to generate a give amount of thrust, the propulsion device must be supplied by enough power to account for the wasted power.

However, thrust may also increase with mass flow rate, Equation A.1. The larger the amount (mass-wise) of air accelerated by the device the larger the change in momentum, resulting in a larger thrust. Efficient propulsive devices therefore, accelerate vast quantities of air to velocities not much higher than the freestream velocity. This trade-off between jet-velocity and mass flow rate is what contributes to the various propulsion devices including propellers, rotors and fans.

To gain a slightly more detailed insight to the flow generated by a propeller, and the effect of the previously mentioned parameters a useful analysis is that of momentum-theory. The momentum-theory model is based on placing a propeller within a uniform flow, as in Figure A.6. The propeller its-self is modelled as a uniform actuator disk providing a static-pressure jump across is surface. It is a result of applying the principle of conservation of mass, momentum and energy assuming an inviscid,

incompressible, irrotational, radially uniform, and azimuthally uniform flow. Momentum-theory thus relates the thrust and the induced velocity at the propeller/rotor by the use of the result $w = 2v_i$, which states that the induced velocity in the far wake (w) is twice that at the rotor/propeller disk. An induced power loss may then be calculated. Equations A.3 and A.4 show the induced power loss results that momentum theory gives for a static or hover ($V_\infty = 0$) operation and for cruise or vertical climb ($V_\infty > 0$) operation respectively.

$$P = Tv = T\sqrt{\frac{T}{2\rho A}} \quad \text{(Static / Hover)} \tag{A.3}$$

$$P = T(v + V_\infty) = T\left(\frac{V_\infty}{2} + \sqrt{\left(\frac{V_\infty}{2}\right)^2 + \frac{T}{2\rho A}}\right) \quad \text{(Cruise / Vertical Climb)} \tag{A.4}$$

These expressions may be used in an equivalent fashion to Equation A.2 to estimate the ideal efficiency of a rotor/propeller.

$$\eta_i = \frac{Tv}{P_{tot}} = \frac{T\sqrt{T/(2\rho A)}}{P_{tot}} \quad (\text{ Hover}, V_\infty = 0) \tag{A.5}$$

$$\eta_i = \frac{TV_\infty}{T(V_\infty + v)} = \frac{2}{1 + \sqrt{1 + \frac{T}{qA}}} \quad (V_\infty \neq 0) \tag{A.6}$$

where q is the free stream dynamic pressure. The efficiency η_i is similar to the propulsive efficiency of a rotor/propeller, although the latter is not appropriate for a hovering rotor as the useful power is that required to generate the thrust. Generalising the propulsive efficiency to $\eta_p = T(V_\infty + v)/P_{tot}$ and may be used to cover the entire range of axial flow.

As evident by Equations A.5 and A.6, the efficiency of a propeller/rotor at hover and moving through the air at $V_\infty$is a function of thrust and the area over which its produced. This yields the singular parameter called the *disk loading* which has a direct correlation to the achievable level of efficiency in the production of the required thrust. Figure A.7 depicts the hover efficiency of various implementations of propulsive systems for VTOL with their associated disk loading's.

The helicopter (large single rotor) and all low disk loading lifting systems are capable of delivering significantly more thrust per kW than higher disc loading devices. This makes them favourable for missions involving extended-duration hover or loitering manoeuvres. Powered flight however, is unfavourable for cruise missions as the rotor power requirement extends beyond the typical requirement of the propulsion system, that

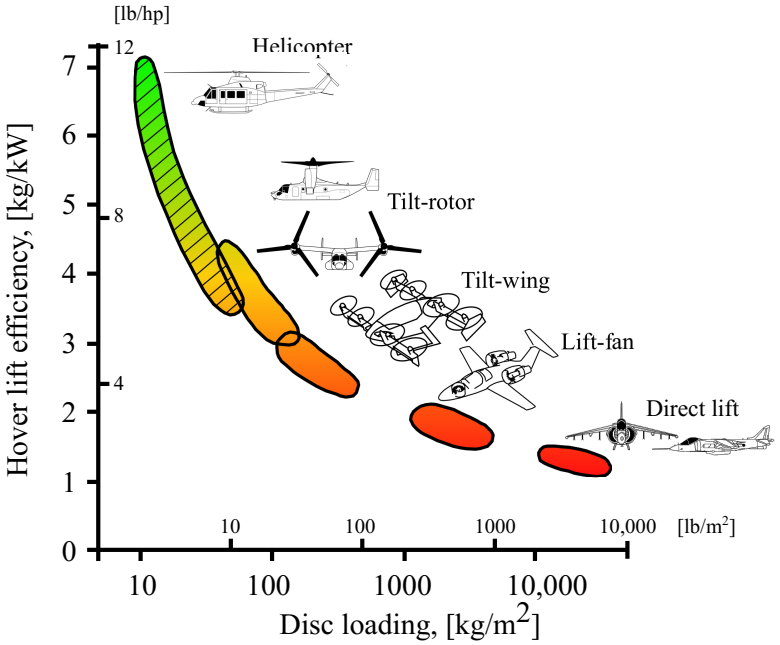

FIGURE A.7: Comparison of the hover efficiency of various aircraft designs. Figure adapted from [245].

being the generation of a forward propelling force. The rotors must also supply the lift, due to the absence of the fixed wing. The efforts of optimising both hover and cruise performance lead designers to highly unconventional designs, including those of the tilt-rotor / tilt-wing aircraft as well as the more recent electric AAM lift + cruise concepts.

Conventional eVTOL aircraft designs follow the steps of traditional helicopters, attempting to minimise this disk loading via larger diameter rotors but at the expense of other attributes, such as noise, cruise efficiency and ground footprint. This leads to aircraft architectures that are either (i) low-disc load, low range, multicopter concepts or (ii) more complex open-rotor, higher range concepts.

DEP concepts attempt to maximise both hover and cruise performance, by utilising technology and architectures discussed in Section 3.3 and 3.1.1. The distribution of many propulsor units across the airframe generally leads to a decrease of the individual propulsor area and therefore the overall effective propulsion area. This was simply demonstrated by A. M. Stoll and colleagues [246], where using the momentum theory approach they showed the relation between the installed power and total thrust generated as a function of number of distributed propulsion units to be,

$$\frac{8N_p\eta_i P_{tot}}{q_\infty V_\infty \pi b_{blown}^2} = T_c(1+\sqrt{1+T_c}) \tag{A.7}$$

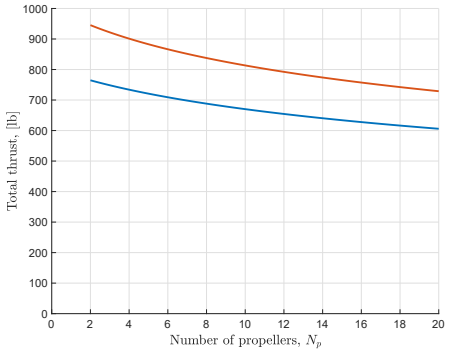

(A) Effect of propeller count on thrust coefficient.

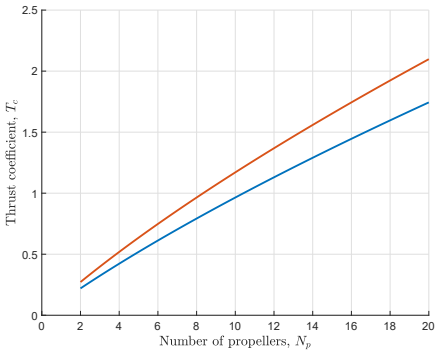

(B) Effect of propeller count on total thrust.

FIGURE A.8: Figure generated using Equation A.7 from method within [246].

where $T_c = T/(q_\infty A)$ is the ratio of disk loading to free-stream dynamic pressure or ideal thrust coefficient, N_p is the number of propeller distributed across a fixed wing aircraft of wing span b_{blown}.

In Figure A.8, the total thrust generated decreases as the number of propulsors increases, for a given installed total power. This is effectively due to the fact that increasing the number of propulsors over a constant "blown" wing span, causes the diameter of the individual propulsor units to decrease. For a given propulsor unit the thrust generated would be $T_p = T_{tot}/N_p$, however its area over which the thrust is produced is given by $A_P = \pi(b_{blown}/2N_p)^2$. It is evident that area decreases at a faster rate than the thrust, causing the disk loading of each individual propulsor to increase as N_p grow larger. This again proves that single rotor helicopters are the most efficient implementation of the rotating wing (especially for hover), although novel DEP architectures allow for a middle solution to the trade-off problem. An exchange of hover efficiency for cruise efficiency, allows aircraft to maintain the capability to perform sufficiently efficient VTOL manoeuvres while at the same time providing a much more optimal cruise operation than traditional helicopters.

A.4 Momentum Theory

Three distinct cases for momentum theory are used for the estimation of ideal power requirement of propeller/rotor for both fixed wing aircraft and rotorcraft. These cases are as follows,

- Hover; the rotor is assumed to be stationary relative the air surrounding it. The pressure differential across the rotor creates an induced velocity at the rotor plane which propagates into a wake down stream. This application of momentum theory is used only the case of rotorcraft hover operations.

- Forward flight in the direction of the on coming flow; The rotor plane is perpendicular to the on coming freesteam air. The total velocity at the rotor plane is equal to the freestream velocity plus the induced velocity. The down stream wake is now a combination of the induced velocity and the freestream velocity. This application of momentum theory is used in the case of cruise (assuming the rotor axis is aligned to the direction of flight), climb and takeoff condition of fixed wing aircraft.
- Forward flight at an angle to the on coming flow;The rotor plane is at an angle to the on coming freesteam air. The total velocity at the rotor plane is equal to a component of the freestream velocity perpendicular to the propeller plane plus the induced velocity. The down stream wake is now a combination of the induced velocity and that component of the freestream velocity. This application of momentum theory is used in the case of forward flight of rotor craft (similar to helicopters).

As typical for momentum theory, for each of the three cases, conservation of mass, momentum and energy is applied to generate three equations used to calculate the induced velocity at the propeller/rotor plane. The induced velocity is then used to calculate the ideal induced power requirement.

For brevity and to avoid duplication of derivation, the final expressions for the induced velocities and power are given. For exact details on the derivations, the reader is encouraged to see references [244, 228].

A.5 PHOENICS: Conceptual design tool

The conceptual design methodology in this thesis may essentially be seen in Figure A.9. It is comprised of three different main components that each require their own inputs and outputs. These three components are the contents of the larger light blue and red boxes in Figure A.9, and they are: Initial weight estimate, performance requirements and analysis, and finally better weight estimate whose output is appropriately sized aircraft capable of performing the mission requirements and ready to move to the preliminary design stage. The outputs however of this stage are useful to the contents of this thesis as the high-level acoustic model components are designed in such a way as to intervene at this stage of the design and provide important insight on the acoustic performance of the aircraft. This information may then be used in a feedback loop to adjust design parameters, and after an additional iterative procedure the output is now a conceptual design that has accounted for noise immissions.

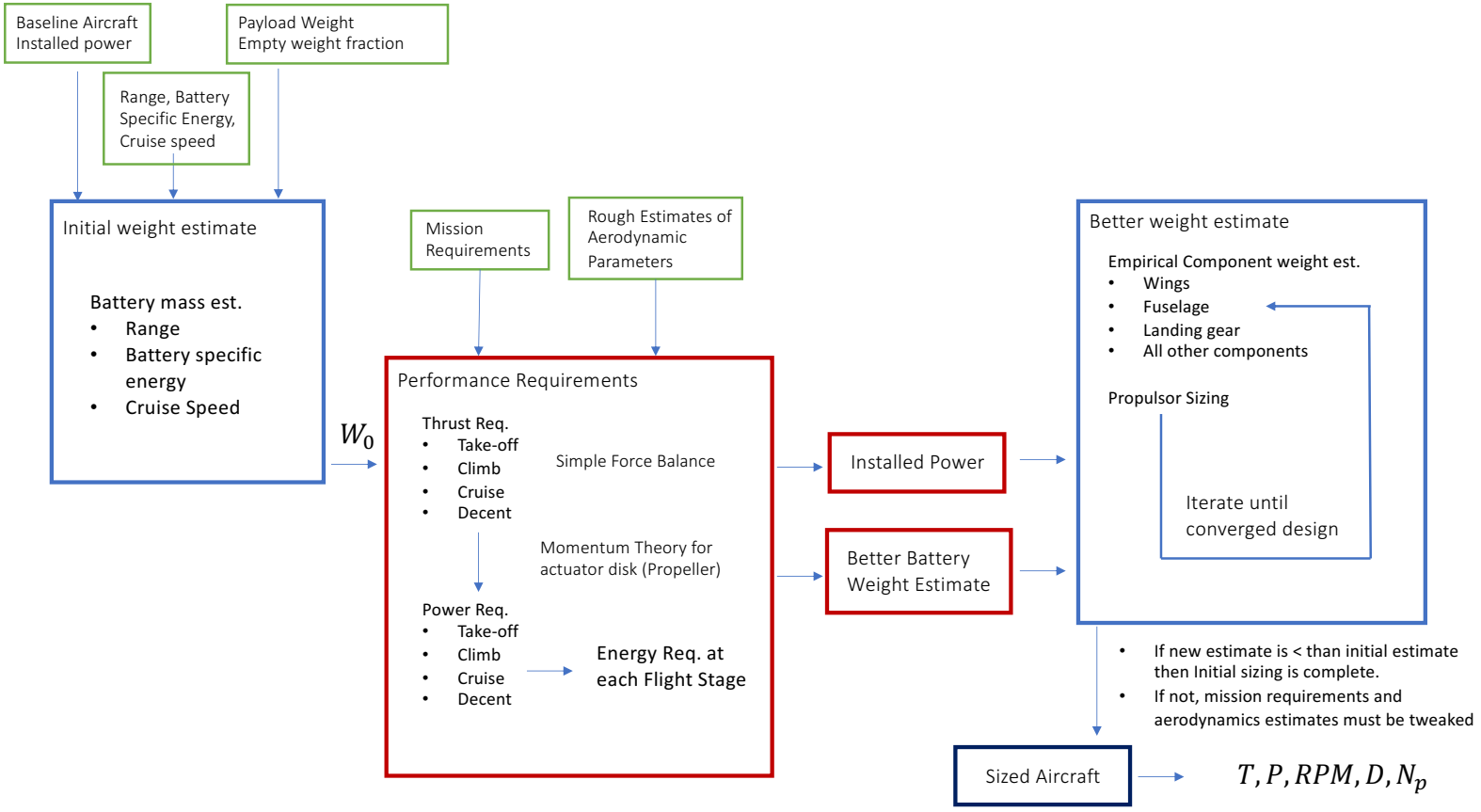

FIGURE A.9: Diagram of conceptual design flowchart as performed in this thesis. The methodology is applied to both fixed-wing and rotorcraft vehicles.

The initial weight estimate block relies on traditional aeronautical design practices. The requirements are best fit to a current aircraft with similar capabilities and size. This is regarded as the baseline aircraft. All initial parameters (can be thought of as initial conditions) are based off of the baseline line, along with reasonable assumptions that would differentiate the concept aircraft from the baseline and allow it to meet all requirements. The performance analysis block uses simple Newtonian force analysis and balance equations to estimate the thrust, or specifically for fixed-wing aircraft the thrust-to-weight ratio (T/W) as a function of the wing loading (W/S). This is done with the use of a constraint analysis diagram. The required thrust is then used to estimate the required power if propellers/rotors are used. The efficiency of conversion of shaft power to propulsive power is estimated using momentum theory for each of the flight phases. The required shaft power may therefore be used in the final block, along with simple empirical models for estimating aircraft component weight to get a better estimate of the aircraft total weight.

The performance block brings together different models from traditional aircraft and helicopter design texts such as the ones in the following references
[232, 237, 228, 244, 243].

A.6 PHOENICS: Performance estimation

Fixed-wing performance

A typical mission for a fixed wing aircraft is made up five simplified successive operations: takeoff, climb, cruise, decent and landing. The analysis is performed using the equations of motion for steady flight (for manoeuvres/phases of the flight that are non accelerating i.e. cruise, steady climb) and for accelerated flight (i.e. takeoff, landing, turning). As a simplification only translational is of interest therefore the aircraft is assumed as a point mass at the centre of gravity, with all forces acting through this point. Anderson [232] gives the three equations of motion of the aeroplane of mass m as (diagrams of the forces acting in each of the three directions/planes may be seen in Figure A.10),

$$m\frac{dV_\infty}{dt} = T\cos\epsilon - D - W\sin\theta \tag{A.8}$$

$$m\frac{V_\infty^2}{r_1} = L\cos\phi T\sin\epsilon\cos\phi - D - W\sin\theta \tag{A.9}$$

$$m\frac{(V_\infty\cos\theta)^2}{r_2} = L\sin\phi T\sin\epsilon\sin\phi \tag{A.10}$$

where L, D, W and T represent the four main forces, lift, drag, weight and thrust, respectively. V_∞ the instantaneous aircraft speed along a given flightpath. The angles ϕ, θ and ϵ represent the roll angle (angle of the aircraft plane of symmetry w.r.t the vertical), the local climb angle (instantaneous angle of the flight path with respect to the horizontal) and the angle of thrust vector w.r.t the flight path direction. r_1 and r_2 are the local radius of curvature of the flight path in the vertical and horizontal directions respectively.

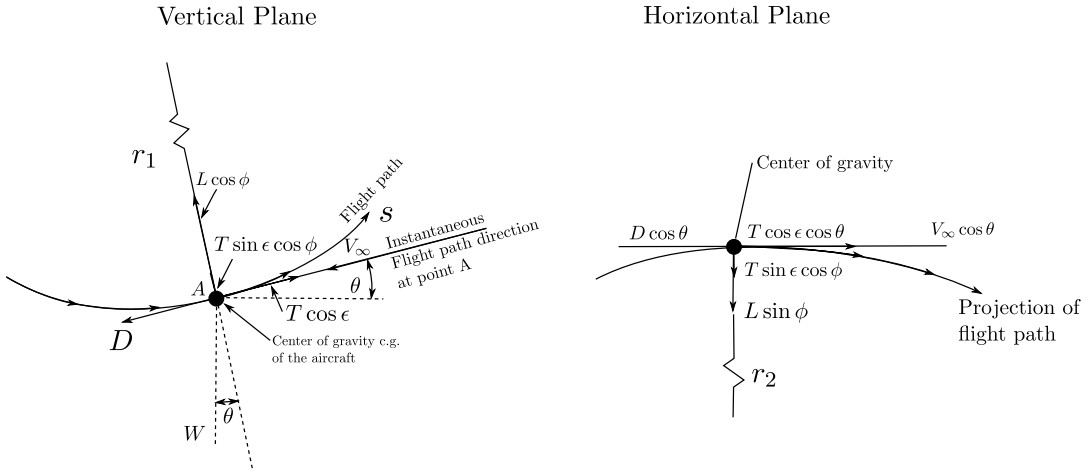

FIGURE A.10: Force balance diagram for aircraft following arbitrary tree-dimensional flightpath. The vertical (left) and horizontal (right) planes are shown.

These equations of motion may be applied to the various flight conditions to address performance characteristics of the desired aircraft.

For all phases of flight of a propeller/rotor, we may assume that the total power required by a propeller/rotor may be given by,

$$P = P_i + P_0 + P_P + P_c \tag{A.11}$$

where the individual components are induced, profile, parasite and climb power terms. In non-dimensional terms

$$C_P = C_{P_i} + C_{P_0} + C_{P_P} + C_{P_c} \tag{A.12}$$

where

$$C_P = \frac{D_P V_\infty}{\rho A \Omega^3 R^3} + \frac{D_0 V_\infty}{\rho A \Omega^3 R^3} + C_T \lambda_i \tag{A.13}$$

where the non-dimensional parameters are the coefficient of thrust and power given by,

$$C_P = \frac{P}{\rho A V_{\text{tip}}^3} = \frac{P}{\rho A \Omega^3 R^3} \tag{A.14}$$

$$C_T = \frac{T}{\rho A V_{\text{tip}}^2} = \frac{T}{\rho A \Omega^2 R^2} \tag{A.15}$$

The most commonly used profile power model given by [228] and [229] is used, providing an estimate for the coefficient as,

$$C_{P_0} = \frac{\sigma C_{d_0}}{8}(1 + 4.6\mu^2) \tag{A.16}$$

where μ is the advance ratio of the rotor. Frequently used approximation for rotor profile drag, it is accurate to about 1% for $\mu = 0$ to 0.3 and to about 5% for μ up to 0.5. The parasitic drag is calculated using an estimated drag area S_{ref}, giving

$$C_{P_P} = \frac{D_P V_\infty}{\rho A \Omega^3 R^3} = \frac{0.5 \rho V_\infty^2 S_{ref} C_{D_f} V_\infty}{\rho A \Omega^3 R^3} \tag{A.17}$$

or

$$C_{P_P} = \frac{1}{2}\left(\frac{S_{ref} C_{D_f}}{A}\right)\mu^3 = \frac{1}{2}\left(\frac{f}{A}\right)\mu^3 \tag{A.18}$$

Obviously, the power required for climb, P_c, is zero for all flight phases where vertical speed is zero, this includes takeoff and cruise for the fixed-wing case; and hover for rotorcraft. The rest of the section concerns the estimation of thrust and the induced velocity at the rotor/propeller disk.

takeoff and Landing

The performance analysis of any aircraft starts with the takeoff. The takeoff manoeuvre is important from both performance and noise perspectives. It is important to understand the implications design parameters have on the take of performance and recognise the capabilities along with the limitations and sensitivity of various designs. The lift-off speed (speed at which the aircraft lifts-off the runway) is assumed to be 1.1 times the stalling speed [247],[248],[243], therefore it may be calculated using the maximum lift coefficient, the reference area and air density. And therefore, the following expression may be used to determine the T/W required to achieve a given ground roll distance during takeoff, [243]:

$$\frac{T}{W} = \frac{V_{LOF}^2}{2 g S_G} + \frac{q C_{D,TO}}{(W/S)} + \mu\left(1 - \frac{q C_{L,TO}}{(W/S)}\right) \tag{A.19}$$

Landing performance, in many cases does not contribute directly to the propulsion system sizing (unless particular requirement have been set e.g. short landing distance, STOL). However the ability to generate lift at low speeds and range of different aircraft mass significantly impacts the aerodynamic considerations for aircraft sizing.

Additionally, the landing gear must also be considered and sized appropriately to withstand landing at all operational configurations.

Given the takeoff thrust requirement may be estimated using equation A.19, the ideal power requirement may now be estimated using momentum theory. Figure A.11 illustrates an aircraft in a takeoff manoeuvre, with the associated slipsteam created by the propeller. Momentum theory may be applied assuming a forward speed of the aircraft, and therefore airflow through the rotor, V_∞. The mass flow through the propeller is simply,

$$\dot{m} = \rho A U, \quad \text{with} \quad U = (v_i + V_\infty) \tag{A.20}$$

where v_i is the induced velocity in the rotor disk plane and A is the propeller disk area. Applying Conservation of Momentum in the direction normal to the disk:

$$T = \dot{m}\,(w + V_\infty) - \dot{m} V_\infty = \dot{m} w \tag{A.21}$$

where w is the flow velocity in a plane located in the far wake.

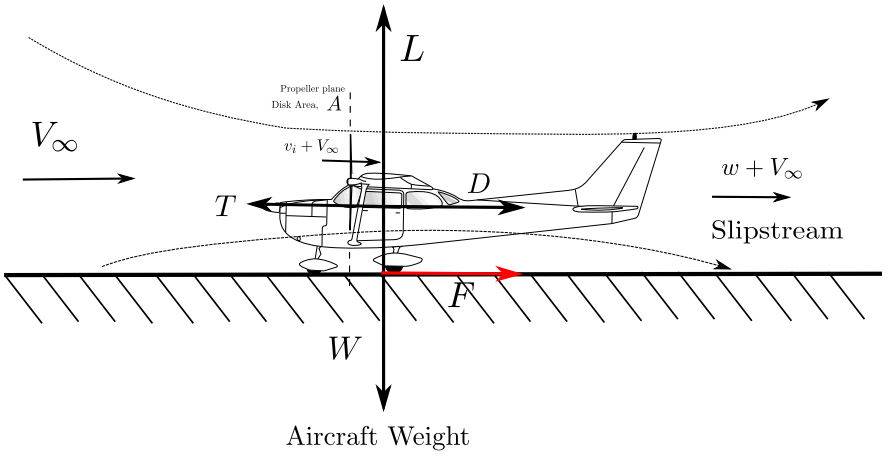

FIGURE A.11: Force diagram of fixed-wing aircraft in the takeoff operation. Momentum theory considerations are also shown.

Finally, conservation of energy of the closed system gives,

$$P_{\text{to}} = T\,(v_i + V_\infty) = \frac{1}{2}\dot{m}\,(w + V_\infty)^2 - \frac{1}{2}\dot{m}{V_\infty}^2 = \frac{1}{2}\dot{m}\left(w^2 + 2wV_\infty\right) \tag{A.22}$$

Therefore, it is clear that:

$$w = 2v_i \tag{A.23}$$

Substituting into Equation A.21 and rearranging:

$$v_i = \frac{T}{2\rho A\left(v_i + V_\infty\right)} \quad \Leftrightarrow \quad v_i^2 + V_\infty v_i = \frac{T}{2\rho A} \tag{A.24}$$

We get a quadratic equation for v_i , with solution:

$$v_i = \frac{-V_\infty \pm \sqrt{V_\infty^2 + 4\frac{T}{2\rho A}}}{2} \tag{A.25}$$

Simplifying and recognising the negative sign in front of the radical represents a non-physical condition we get,

$$v_i = \frac{1}{2}\left[-V_\infty + \sqrt{{V_\infty}^2 + \frac{2T}{\rho A}}\right] \tag{A.26}$$

Therefore the inflow ratio can be written as,

$$\begin{gathered}\lambda_i = \frac{v_i}{\Omega R} = \frac{1}{2}\left[-\frac{V_\infty}{\Omega R} + \sqrt{\left(\frac{V_\infty}{\Omega R}\right)^2 + \frac{2T}{\rho A \Omega^2 R^2}}\right] \\ \text{or} \quad \lambda_i = \frac{1}{2}\left[-\mu + \sqrt{\mu^2 + 2C_T}\right]\end{gathered} \tag{A.27}$$

Cruise

The cruise manoeuvre is typically what an aircraft is designed to perform, that should highlight its importance. While fundamentally a simple manoeuvre the goal is to achieve this as efficiently as possible; meaning reducing fuel consumption for a given cruising airspeed. The analysis of the cruise condition requires a drag model in order for calculations to be carried out. For the purpose of this preliminary study, a simplified drag model is assumed, whereby the drag consists of a zero angle of attack drag (profile drag) and lift induced drag. Therefore, the thrust requirement for a given aircraft weight in order to achieve a specified cruising speed at a desired altitude is given by [243]:

$$\frac{T}{W} = qC_{D,min}\left(\frac{1}{(W/S)}\right) + K\left(\frac{1}{q}\right)\left(\frac{W}{S}\right) \tag{A.28}$$

Considering the set-up in Figure A.12 for cruise, using a similar approach as in the takeoff condition, the propeller power requirement may be given by,

$$P_{\text{cr}} = T\left(V_\infty + v_i\right) = TV_\infty + Tv_i \tag{A.29}$$

the first term TV_∞ represent the power required to propel the rotor (and entire vehicle) forward and is called the useful power. On the other hand the second term Tv_i is the induced power and represents the rotor inefficiencies in generating thrust.

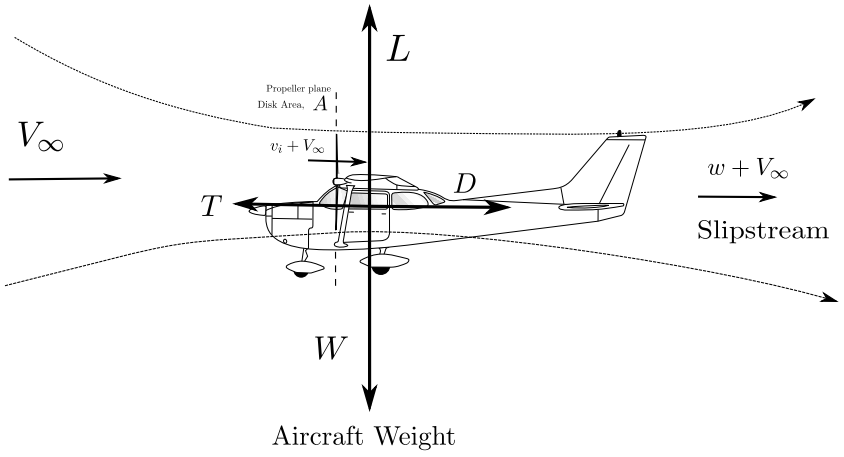

FIGURE A.12: Force diagram of fixed-wing aircraft in the steady, level cruise operation. Momentum theory considerations are also shown.

Climb and decent

The takeoff manoeuvre is followed by the climb manoeuvre. It is vital to study and understand the climb rates and slopes, as great climb performance not only determines the time and rate at which an aircraft can reach an altitude but also its noise footprint. The climb analysis primarily involves the definition of one of two parameters, the rate at which the aircraft gains altitude, rate-of-climb (ROC) or the angle its flight path makes to the ground, the angle-of-climb (AOC).

The power requirement during climb is again given as the sum of the useful power and the induced power. However the useful power must account for the power required to overcome drag and the power required to gain altitude. Simple force balances on the diagram in Figure A.13 result in the following expressions,

$$\sin\alpha = \frac{T-D}{W} \quad \text{or} \quad V_\infty \sin\alpha = \frac{V_\infty T - V_\infty D}{W} \tag{A.30}$$

$V_\infty \sin\alpha$ is defined as the vertical component of the flight velocity (or Rate-of-climb) and denoted V_v .

After algebraic rearaging and using a simple drag polar for the aircraft drag, The required T/W in order to achieve a specific rate-of-climb can be calculated by [243]:

$$\frac{T_{cl}}{W} = \frac{V_V^2}{V} + \frac{qC_{D,min}}{(W/S)} + \frac{K}{q}\left(\frac{W}{S}\right) \tag{A.31}$$

Decent on the other hand, may be seen as a negative climb. Descent is usually flown at cruise velocity and idle power, unless this cause extreme descent rates/angles.
Rearranging Equation A.31 for the vertical velocity gives,

$$V_V = V\left(\frac{T}{W}\right) - \frac{\rho V^3 C_{D,0}}{2(W/S)} - \frac{2K}{\rho V}\left(\frac{W}{S}\right) \tag{A.32}$$

Its trivial to notice that for $T = 0$, the vertical velocity becomes negative and denoting a descent. By setting the thrust to $T \neq 0$ the descent phase may be extended, by essential reducing the ROC and AOC at the cost having an addition power requirement to generate said thrust.

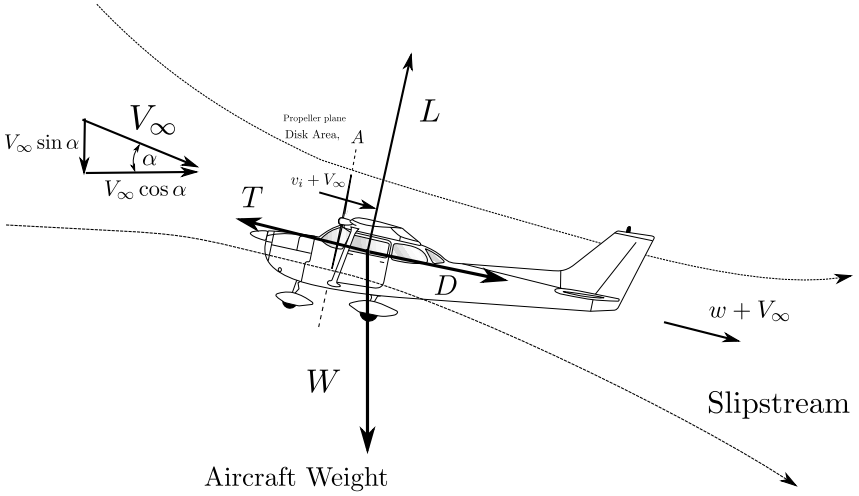

FIGURE A.13: Force diagram of fixed-wing aircraft in the climb operation. Momentum theory considerations are also shown.

Substituting in to the main power equation we now have:

$$P = T\left(V_\infty + v_i\right) = DV_\infty + WV_V + Tv_i \tag{A.33}$$

Decent is essentially a negative climb, thus the thrust is less than the drag.

- For a loiter decent (i.e. thrust = 0) the power requirement is obviously also zero.
- For a prolonged decent, the thrust requirement to maintain a specific decent rate (which is less than for T = 0), can be calculated by the decent rate its self:

$$T = \frac{V_V}{V_\infty} W + \frac{1}{2}\rho S V_\infty^2 C_{D,0} + \frac{2K}{\rho S}\left(\frac{W}{V_\infty}\right)^2 \tag{A.34}$$

The same drag model is used as in cruise and climb and in this case L = W is assumed. Decent is usually flown at cruise velocity and idle power setting, unless this produces an extreme descent angle:

$$\sin^{-1}\left(\frac{V_V}{V_\infty}\right) \tag{A.35}$$

VTOL performance

The aim of this section is to provide an insight to the performance considerations when sizing an VTOL aircraft, particularly an fully-electric variant. The particular methodology is applied to tilt-rotor or tilt-wing type aircraft, where the lift in the vertical takeoff and landing is provided by the rotors/propeller whilst in the cruise configuration a fixed wing is used. This implies a transition region (or phase) in the flight envelope that allows the vehicle to accelerate to the point where enough lift is generated by the fixed-wing thereby allowing the propulsion system to reduce the power delivery in order to maintain the appropriate thrust requirement.

The analysis begins from the definition of an average flight mission. As with the fixed wing case, the mission may be broken down into smaller individual phases. These phases are,

- Hover: During this phase the aircraft is landing or taking-off vertically. The ascending and descending speeds are very small and may almost constitute a constant altitude hover. The power requirement from the power supply (battery in this case) may be denoted P_h, and is constant.
- Transition and re-transition: This is flight phase where the aircraft transitions from vertical/hovering flight to horizontal forward flight, and reversely respectively. As mentioned the source of lift transitions from the propulsion system to the wings, meaning that the power requirement is not constant. Specifically, a simple approximation of a quadratic relation of the power reduction with time is used [239]. The power during this phase is denoted P_{tr}.
- Climb and Decent: During this phase of flight the aircraft accelerates to cruise velocity and altitude. This phase is almost identical to fixed wing aircraft as the flight forces are identical. The power requirement is denoted P_{cl} and is assumed constant for a given climb rate.
- Cruise: This phase is assume to be a steady level flight, meaning the aircraft is kept at a constant altitude and cruise velocity. The power requirement is denoted P_{cr} and is assumed constant.

The aim of performing such an analysis this the understanding of the power requirement to perform a whole mission. This information is used to appropriately size the power supply system, and to gain physical understanding of the key trades that are involved. As discussed already in this Chapter, designing electric aircraft to meet range requirements is almost impossible due to the limitations imposed by current battery technology. The approach many take is to try and maximise the range of a given installed power supply by minimising the power and energy requirement of the hover and climb phase as efficient and short at possible to enable the vehicle to spent the majority of the flight time in the cruise phase (the most efficient in terms of aerodynamics and propulsion phase). Nevertheless, cruise optimisation is also a crucial factor.

Hover Power

In the case of hover (Figure A.14), the mass flow through the rotor is given by,

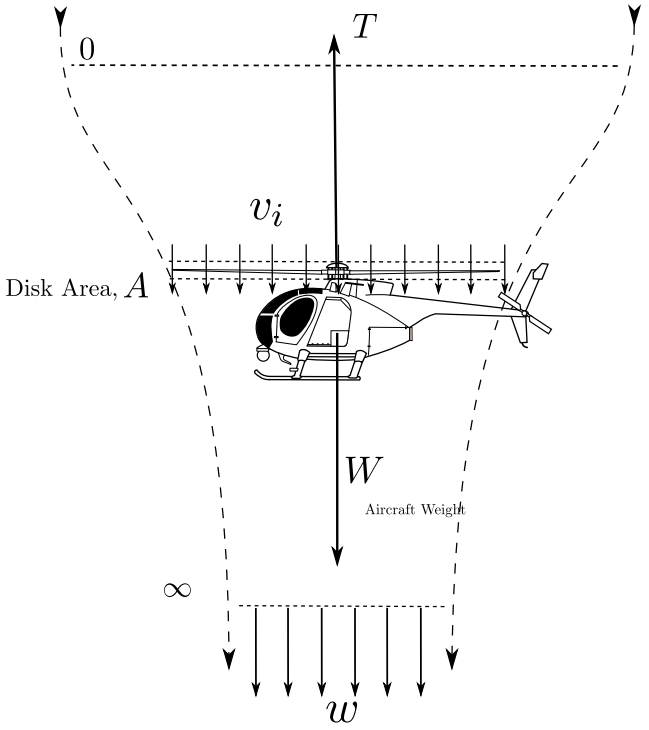

FIGURE A.14: Force diagram of rotorcraft vehicle in a hover operation. Momentum theory considerations are also shown.

$$\dot{m} = \rho A U, \quad \text{with} \quad U = (v_i) \tag{A.36}$$

while the conservation of energy and momentum again give $w = 2v_i$.

Thrust may therefore be given as

$$T = \rho A v_i w = 2\rho A v_i^2 \tag{A.37}$$

Rearranging and defining the induced velocity for Hover:

$$v_h \equiv v_i = \sqrt{\frac{T}{2\rho A}} = \sqrt{\left(\frac{T}{A}\right)\frac{1}{2\rho}} \tag{A.38}$$

And the Power required to Hover is therefore:

$$P = T v_i \equiv T v_h = T\sqrt{\frac{T}{2\rho A}} = \frac{T^{3/2}}{\sqrt{2\rho A}} \tag{A.39}$$

Inflow ratio:

$$\lambda_h \equiv \lambda_i = \frac{v_i}{V_{tip}} = \frac{v_i}{\Omega R} = \frac{1}{\Omega R}\sqrt{\frac{T}{2\rho A}} = \sqrt{\frac{C_T}{2}} \tag{A.40}$$

In the case of hover, a simple force balance in the vertical direction requires $T = W$.

Forward Flight Power

In forward flight, the mass flow rate through the rotor:

$$\dot{m} = \rho A U \quad \text{where} \quad U = \sqrt{(V_\infty \cos\alpha)^2 + (V_\infty \sin\alpha + v_i)^2} \tag{A.41}$$

Again using the simple result from momentum theory that $w = 2v_i$ and $T = \dot{m}w$, the thrust in forward flight may be written as,

$$T = 2\rho A U v_i = 2\rho A v_i \sqrt{(V_\infty \cos\alpha)^2 + (V_\infty \sin\alpha + v_i)^2} \tag{A.42}$$

Rearranging for the induced velocity,

$$v_i = \frac{T}{2\rho A\sqrt{(V_\infty \cos\alpha)^2 + (V_\infty \sin\alpha + v_i)^2}} \tag{A.43}$$

From Momentum Theory for hovering flight we have $v_h^2 = T/(2\rho A)$ therefore:

$$v_i = \frac{{v_h}^2}{\sqrt{(V_\infty \cos\alpha)^2 + (V_\infty \sin\alpha + v_i)^2}} \tag{A.44}$$

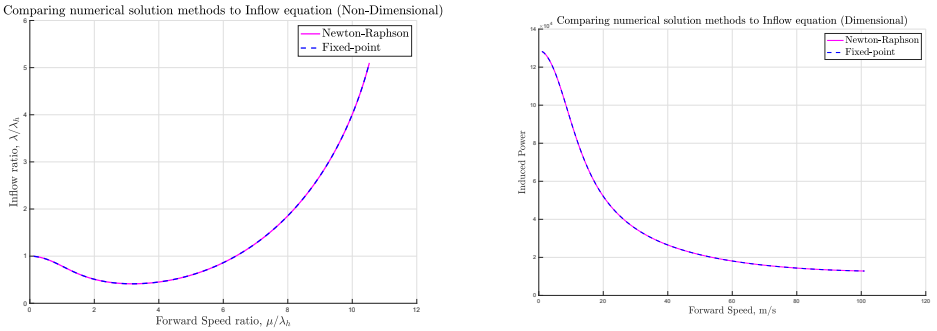

(A) Inflow ratio

(B) Induced power

FIGURE A.15: Solution to the inflow equations A.49 and A.50 for a series of forward speeds, using two different numerical solutions.

Deviding by the advance ratio $\mu = V_\infty \cos\alpha/(\Omega R)$ of the rotor,

$$\lambda_i = \frac{\lambda_h^2}{\sqrt{\mu^2 + \lambda^2}} \tag{A.45}$$

Therefore the inflow ratio (non-dimensional normal velocity) :

$$\lambda = \frac{V_\infty \cos\alpha}{\Omega R} + \frac{v_i}{\Omega R} = \mu \tan\alpha + \lambda_i \tag{A.46}$$

Again the power required for forward flight may be written as the sum of the induced and useful power,

$$P = \underbrace{TV_\infty}_{\text{Useful power}} + \underbrace{Tv_i}_{\text{Induced power}} \tag{A.47}$$

We can reference the rotor power in forward flight to the hover results:

$$\frac{P}{P_h} = \frac{P}{Tv_h} = \frac{T\left(V_\infty \sin\alpha + v_i\right)}{Tv_h} = \frac{V_\infty \sin\alpha + v_i}{v_h} = \frac{\lambda_i}{\lambda_h} \tag{A.48}$$

It is also obvious that the result depends on the disk angle of attack, which must always be tilted forward slightly for propulsion. From Equation A.46,

$$\lambda = \mu \tan\alpha + \lambda_i = \mu \tan\alpha + \frac{\lambda_h^2}{\sqrt{\mu^2 + \lambda^2}} \tag{A.49}$$

or

$$\frac{P}{P_h} = \frac{\lambda}{\lambda_h} = \frac{\mu}{\lambda_h} \tan\alpha + \frac{\lambda_h}{\sqrt{\mu^2 + \lambda^2}} \tag{A.50}$$

Using the vertical and horizontal force balance with reference to Figure A.16, we get the ratio of power in forward flight to power in hover to be,

$$\frac{P}{P_h} = \frac{\mu}{\lambda_h}\left(\frac{D}{T}\right) + \frac{\lambda_h}{\sqrt{\mu^2 + \lambda^2}} \tag{A.51}$$

where drag it assumed to be the total drag (rotor and airframe parasitic drag). Assuming again the simple polar drag model, the power required,

$$P = TV_\infty \sin\alpha + Tv_i = \frac{W}{\cos\alpha} V_\infty \sin\alpha + Tv_i \tag{A.52}$$

relying on the assumption that $\tan\alpha \approx D/W$ the power is,

$$\begin{aligned} P &= WV_\infty \frac{D}{W} + Tv_i = \mathrm{D}V_\infty + Tv_i \quad \text{or} \\ P &= (D_P + D_0)\, V_\infty + Tv_i \end{aligned} \tag{A.53}$$

where D_P and D_0 represent the parasite and profile drag of the vehicle.

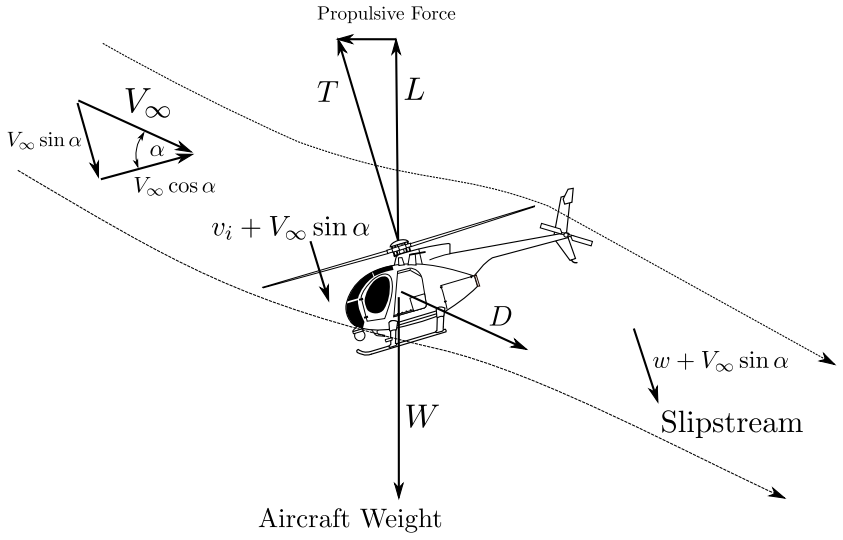

FIGURE A.16: Force diagram of rotorcraft vehicle in a forward flight operation. Forward flight accounts for climb and decent operations. Momentum theory considerations are also shown.

A comprehensive expression for the power requirement during forward flight is given bellow,

$$P_{req} = \rho A \Omega^3 R^3 \left(\frac{C_T^2}{2\sqrt{\mu^2 + \lambda^2}} + \frac{\sigma C_{d_0}}{8}(1 + 4.6\mu^2) + \frac{1}{2}\left(\frac{f}{A}\right)\mu^3 \right) \tag{A.54}$$

A.7 PHOENICS: Range estimation

For conventional aircraft, the fuel mass is commonly determined using the Breguet range equation. Many analytical variations of the Breguet range equation have been proposed

for fully-electric vehicles [232], [139] and [249]. Simple analysis of the cruise condition for a fixed wing aircraft ($T = D$ and $L = W$) allow for the distance covered to calcuated by,

$$R = E^* \frac{m_{\text{batt}}}{m_{\text{tot}}} \frac{1}{g} \frac{L}{D} \eta_{tot} \tag{A.55}$$

where R the range of the aircraft and E^* the battery specific energy. This formulation captures the biggest difference in the range calculation with respect to fuel burning aircraft, constant mass (weight) throughout the length of the flight, opposed to the gradual decrease in aircraft mass due to fuel being burned that traditionally takes place. This effect drastically changes the power requirement of electric aircraft during the cruise phase, leading to decreased range for a specific amount energy stored.

A slightly more in depth analysis by Traub [139] investigated the impact of battery behaviour and whilst also implementing a polar drag model for the aerodynamic force calculation.

In the case of PHOENICS, cruise is not the only part the flight envelope of interest. The mission range is estimated as the sum of the individual components that make up the entire flight. This requires the consideration of the power requirements in those various flight conditions as discuseed previously. It is worth noting that, the two main parameters of interest are range and battery mass. For a given battery mass, the aircraft has a predetermied range, and vice versa.

Battery mass estimation

First assuming a target range is set, we estimate the mass of the required bettery to perform a mission. The vailable energy stored on board in the form of batteries:

$$E_a = E^* m_{\text{batt}}\, \eta \tag{A.56}$$

The required energy to perform a segment i of flight at overall power requirement of P_{req} is,

$$E_{req,i} = \int_0^{t_R} P_{req,i} \mathrm{d}t \tag{A.57}$$

Assuming constant power requirement, mass and speed and additional conditions that assure that the power estimation techniques of this Appendix are valid for each phase of flight independantly

$$E_{req,i} = P_{req,i} t_i \tag{A.58}$$

The total required energy therefore is:

$$E_{req,i} = \sum_i^s P_{req,i} t_i \tag{A.59}$$

where R is the range covered during that particular segment of flight. Therefore if the available energy onboard is equal to the energy required to perform a flight of range R, we have,

$$E^* m_{\text{batt}}\, \eta = \sum_{i}^{s} P_{req,i} t_i \tag{A.60}$$

Expression A.60 gives the mass of the battery m_{bat} given its specific density, E^*. The specific density of the battery depend on battery technology available. However, the size of the installed battery depends on the mission requirement for the particular concept.

Finally, the total range for a given mission may be estimated as the sum of the ranges covered in the individual segments,

$$R = \sum_{i}^{s} R_i = V_i t_i \tag{A.61}$$

where s is the total number of flight segments and V_i is the constant horizontal speed along that segment.

Cruise Range

In the case a battery specification and mass are provided, the total range of the aircraft may estimated in reverse. The energy required by the battery for the entire mission may be given by the integral of the power requirement with respect to time. The time interval $[t_{ini},\ t_{end}]$ represents the time between lift off and touch down. As with fossil fuel aircraft, assuming certification will require aircraft to carry additional energy for cases of emergency or possible diversion from the flight plans due to weather. Whilst for battery systems a minimum state-of-charge (SOC_{min}) is assumed therefore giving the final accessible energy, E_{acc} for mission to be,

$$E_{acc} = \varepsilon_{safe} E_s (1 - \text{SOC}_{min}) \tag{A.62}$$

where E_s is total energy stored in the battery and ε_{safe} is the additional energy fraction required for safety. The accessible energy for the mission is therefore given by,

$$E_{acc} = \int_{t_{ini}}^{t_{end}} P_{req}(t)\, dt \tag{A.63}$$

The integral may evaluated for each individual segment of the flight separately, and since the power requirements for each of the flight phases is assumed constant, Equation A.63 may be written,

$$E_{acc} = t_h P_h + 2t_{tr} P_{tr} + t_{cl}(P_{cl} + P_{des}) + t_{cr} P_{cr} \tag{A.64}$$

Finally, the cruise range of the aircraft may calculated as the distance that the air vehicle can cover while requireing P_{cr} power at cruise, at speed v_{cr} using up the remaining energy stored in the battery,

$$R = \frac{v_{cr}}{P_{cr}} \Big[\varepsilon_{safe} P_s (1 - \text{SOC}_{min}) - t_h P_h - 2t_{tr} P_{tr} - t_{cl}(P_{cl} + P_{des}) \Big] + 2t_{cl} v_{cl} \tag{A.65}$$

This range equation may be applied to the preliminary sizing of any electric vehicle. The approach of calculating the required power for each of the individual phases of the flight will deffer depending on the operations and the type of vehicle being assessed.

Before the powers for the various phases of flight are integrated over the mission, a few additional considerations are made.

Hover

The power requirement during hover P_h may be evaluated using the overall efficiency of the propulsion system during the hover phase. This may be done with the use of the ideal efficiency of a open rotor/propeller from Equation A.5, accounting for additional losses due to the motor, power electronics, batteries and propeller itself through the use of efficiency terms,

$$P_h = \frac{\text{Ideal hover power}}{\eta_{h,tot}} = \frac{T_h \sqrt{\frac{T_h}{2\rho N_p A_p}}}{\eta_{h,b}\eta_{h,p}\eta_{h,m}\eta_{h,pe}} \tag{A.66}$$

where $\eta_{h,b}$, $\eta_{h,p}$, $\eta_{h,m}$, $\eta_{h,pe}$ denote the battery, propeller, motor and power electronics efficiencies respectively. T_h denotes the thrust which is equal to the MTOW for the hover operation.

Cruise

The power required during the cruise phase is equal to the power required to overcome the total drag on the aircraft, D_{cr}. Therefore using the same energy train of losses as the hover phase, the cruise power may be calculated as,

$$P_{cr} = \frac{\text{Ideal crise power}}{\eta_{cr,tot}} = \frac{\sum_i D_{cr,i} v_{vr}}{\eta_{cr,b}\eta_{cr,p}\eta_{cr,m}\eta_{cr,pe}\eta_{cr,ideal}} \tag{A.67}$$

where the index i indicates the sum over all the individual components of drag, and v_{cr} the cruise velocity of the aircraft. In addition, the ideal propulsive efficiency, $\eta_{cr,i}$ is

added to the chain as a conversion factor between the power from the jet to the the power to the aircraft.

Transition and re-transition In the case of a tilt-rotor, an additional power requirement term is added to the sum, this transition and retransition. A simple linear variation of power is assumed. The transition phase relates the power requirement from hover to that of the beginning of climb. As mentioned the power requirement drops quadratically with time, from the power at the start of transition which is equal to the hover power, P_h to the power $P_{tr,end} = P_h/\kappa$, at the start of the climb phase. κ represents the factor by which the power at hover relates to the power at the end of the transition phase. It depends on the climb gradient and acceleration chosen during climb. For initial estimates it is common to size the transition phase using the average power, meaning,

$$P_{tr,av} = \frac{P_h + P_{tr,end}}{2} \tag{A.68}$$

This approach is conservative as assuming an average power requirement overestimates the required energy for the entire transition phase. The same power requirement may be assumed for the re-transition phase of the flight.

Climb and descent

The climb and decent phases are again similar those of the fixed wing aircraft. Additionally the only difference between the climb phase and cruise is the extra power required to overcome the weight component in the direction of flight. This may be written as,

$$P_{cl} = \frac{\text{Ideal climb power}}{\eta_{tot,cl}} = \frac{\left(\sum_i D_{cl,i} + W \sin\gamma\right) v_{cl}}{\eta_{cl,b}\eta_{cl,p}\eta_{cl,m}\eta_{cl,pe}\eta_{cl,i}} \tag{A.69}$$

where γ the constant climb angle and W the MTOW, as discussed in previous sections. In practice, the velocity of the aircraft does not remain constant throughout this phase, as it is still accelerating to cruise velocity. Again for initial sizing approximation, the velocity is assumed to be constant at a mean climb velocity $v_{cl,mean}$, whilst the power is calculated at a constant altitude.

The descent power in many cases may be assumed to be negligible as the weight components during this phase is in the direction of flight, allowing for the propulsion system to be set to idle. However, for conservative approaches, and allowing for the possibility of extending the decent phase, the power requirement may be assumed to be 20% that of cruise, or $P_{des} = 0.2P_{cr}$.

Appendix B

Technical details and assumptions of the SAE AIR 1845 procedure for developing NPD curves

This Appendix is essentially identical to Appendix C of reference [52] replicated for the ease of the reader.

The main steps of the SAE AIR 1845 [89] experimental procedure for developing NPD curves are:

- Atmospheric conditions for each sound recording are established experimentally.
- The terrain around the microphones is at and unobstructed.
- The test flight path is parallel to the ground (SAE AIR 1845 describes it as 'nominally level') at a nominal height ranging from 100 m to 800 m.
- Noise measurements are made directly under the flight path so are unaffected by lateral attenuation.
- The aircraft configuration remains constant throughout each flyover duration.
- Flyover effective duration is normally determined by the 10 dB down-time (i.e. the period during which the noise level is within 10 dB of the maximum level).
- The noise is recorded at 0.5 seconds intervals. SPLs are obtained for the 24 1/3-octave-bands with centre frequencies from 50 to 10000 Hz.
- Measured SPLs are corrected for instrument calibration and adjusted to account for differences between actual and reference atmospheric conditions.
- A flyover at the nominal height is repeated for each engine power setting.

The noise at the remaining NPD standard distances is then evaluated using extrapolation, accounting for effects of spherical wave spreading, atmospheric absorption as well as for differences on the effective duration. This procedure is detailed in Appendix C.

Appendix C

Step by step methodology of applying the SAE AIR 1845 computational step

This Appendix presents the methodology of computationally generating NPD curves using the knowledge of how propeller noise changes as a function of changes in the design and operational parameters. The same approach to the derivation of computational NPD curves can be seen in [12], where NPD curves for fan, jet and airframe noise sources were calculated. The work in this section is novel in regard to the propeller noise sources, and aims at extending the methodology presented in said publications.

The steps in producing NPD curves for propeller powered aircraft from a baseline measured NPD point and aircraft noise variation due to design or operational changes are almost identical to that of conventional aircraft, although differences do occur in the treatment of the spectral content of the sound levels, as changes to the discrete tonal content are also accounted for by the propeller scaling model. For brevity reasons a detailed explanation is omitted but is intended for future publications. For detailed explanation the reader is encouraged to follow the procedure described in [12] and [34] along with the SAE AIR1845 [89] computational step.

The procedure is outlined in a number of bullet points where differences between propeller aircraft and conventional turbofan aircraft are specified.

- A baseline scenario is chosen with experimentally measured $L_{A,max}$ NPD level at distance d and polar angle θ
- The change in SPL ($\Delta L_p(d, j)$) is calculated using the changes in individual noise sources noise level. The changes in individual sources are calculated using publicly available noise prediction methods. In the case of propeller harmonic noise source,

the change in noise is calculated with the procedure describe in the previous section.

- $\Delta L_p(d, j)$ is added to the baseline NPD level to yield the aircraft L_p corresponding to the new scenario at the same power setting, and slant distance.
- Changes ΔL_p reflecting changes in power settings of the modified scenario are calculated using the same procedure only using the L_p corresponding to the new scenario as a baseline.
- The levels at the remaining engine power settings at the same distance d are obtained by adding the noise level variation ΔL_p resulting from changing the engine power to the first level $L_p(d, j)$ of the modified scenario.
- The SAE AIR1845 computational step is then used to propagate the levels at distance d, the remaining NPD distances.

At this point $L_{A,max}$ NPD curves have been derived. The next few steps summarise the procedure for the development of SEL or L_{AE} NPD curves,

- Using the estimates of the total sound power emitted (at power setting j) of the modified scenario and the directivity characteristics of the aircraft, computational flyover is performed at an altitude equal to distance d, and the SEL / L_{AE} is calculated at an observer point directly under the flightpath.
- Using the SEL / L_{AE} and the previously derived $L_{A,max}$ NPD curve (at power setting j) the SEL / L_{AE} is calculated at the remaining NPD slant distances.
- This procedure is carried out for every power setting of interest.

Appendix D

Implementation of full Hanson frequency domain model for discrete propeller noise

The implementation of the Hanson propeller tonal noise model in the frequency domain has followed the methodology presented by Hanson [60, 198], while also using the numerical workflow for generating the required inputs (geometry and aerodynamic loading).

An overview of the implementation used in this thesis is given. The whole procedure from generating aerodynamic inputs to performing the aeroacoustic prediction is visualised through the help of a flow diagram.

The propeller loading and geometry are important as they determine the performance of the propeller and are the main inputs for the Hanson harmonic noise model. A well documented process for propeller preliminary design is used in calculation of the propeller performance. This calculation is performed with two well-established tools, XFoil [196] and XRotor [197]. A more detailed flow diagram of the calculations performed by the propeller performance tools and how these interface with Matlab is also provided. Details on the Hanson model are not replicated here, as an in-depth discussion is already in place in the main text, and can be found in original article by Hanson [60]. The "Helicoidal Surface Theory" are a set of far-field radiation equations that predict the axial (lift), tangential (drag) components of steady loading noise as well as thickness noise. The combination of XFoil, XRotor and the Helicoidal Surface Theory is used a validation and bench-mark in the thesis for comparisons to the developed asymptotic scaling relations.

D.1 Methodology Overview

In order to integrate the three individual codes (XFoil, XRotor and Hanson model) a main script was developed within Matlab to interface with the aero component of the calculation.

The computational methods from the different disciplines involved in the calculation of propeller noise are all implemented in Matlab. Figure D.1 gives a general overview of the process. The first step is the definition of the propeller geometry and operational conditions. The variables (inputs) are processed and used to generate the input

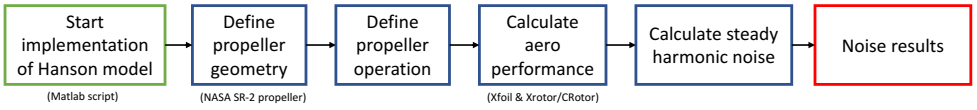

FIGURE D.1: Flowchart showing the general overview of the main processes involved in the implementation of the Hanson method.

D.2 Propeller Performance

The decision to use XFoil and XRotor (more specifically CRotor) for propeller aerodynamic estimation was trivial, as they provide a well-documented, robust frameworks that support preliminary design process of a wide range of fluid dynamics applications. The general XFoil methodology is described in [196]. Various additions were later implemented to account to for viscus boundary layer, blunt trailing edges and others [250, 251, 252]. XRotor [197] is a program for the design and analysis of ducted and free-tip propellers and windmills. It allows for rotor/propeller design and analysis using three main formulations for the calculation of the induced velocities: 1. Graded Momentum Formulation [253, 254, 255], 2. Potential Formulation [256] and 3. Vortex Formulation [257]. Due to being easier to establish an easier interface with matlab, CRotor (an modified version of XRotor for enabling the option of counter-rotating propellers) was used. In addition to the simplicity and robustness of these tools, it is important that the run time is kept low while still being flexible in changing design parameters of a propeller.

A propeller lifting line theory is applied by XRotor. The circulation, induced velocities, local angles of attack, lift, and drag coefficients are all iteratively calculated using this

lifting line theory until convergence is reached. The propeller performance coefficients and the loading of the propeller blades are output once a solution has converged.

Details of the three approaches of calculating the induced velocities are summarised bellow:

- The Betz-Prandtl tip loss fudge factor is used in the graded momentum formulation, which is a classical theory. Up to $pi/2$ advance ratios can use this loss factor. As a result, higher advance ratios should not be calculated using this approach. The computational efficiency provided by the graded momentum formulation is a benefit. The range of advance ratios for which the propeller performance parameters can be estimated is constrained, which is a drawback.
- The prospective formulation is a more complex strategy. The helically-symmetric potential flow around a stiff helicoidal wake is solved using this technique. It is applicable to all blade counts and has a wide range of radial load distribution capabilities. Although this approach is more computationally intensive than the graded momentum formulation, it is nonetheless promising. However, the possible formulation enables the inclusion of rotor hubs and nacelle assembly. The Betz-Prandtl fudge factor, for which a low advance ratio is assumed, prevents the graded momentum formulation from handling this issue correctly.
- Finally, XRotor incorporates the vortex formulation, which determines the induced velocity by using a discrete vortex wake. The distinct vortices are found on the rigid helicoidal wake surface and extend downstream from the lifting line. This method enables the analysis of propellers with swept blades and raked tips as well. Compared to the other two approaches, the computational runtime is longer, but a wider range of propeller geometries can be considered.

In this particular implementation, the induced velocities are calculated using the potential formulation. This method is chosen as the propellers analyses throughout this thesis utilise straight blades and thus do not have sweep. The slight increase in fidelity provided by the vortex formulation, is not required as this will increase the computational run time.

A summary of the required inputs (and particular nomenclature) required by XRotor can be seen below:

- $\alpha_{0,L}$, the zero-lift angle of attack
- $\frac{dC_l}{d\alpha}$, the lift slope
- $\left(\frac{dC_l}{d\alpha}\right)_{\text{stall}}$, the lift slope at stall
- $C_{l,\max}$, the maximum lift coefficient

- $C_{l,\min}$, the minimum lift coefficient
- ΔC_l, increment to stall
- $C_{d,0}$, the minimum drag coefficient
- $C_{l,0}$, C_l at minimum C_d
- $\frac{dC_d}{dC_l^2}$, quadratic coefficient
- $\mathrm{Re}_{\mathrm{ref}}$, reference Reynolds number
- f, Reynold number scaling exponent
- C_m, the pitching, moment coefficient
- M_{crit}, the critical Mach number
- Geometry of the propeller

XFOIL & XROTOR operation details

All the required inputs for XRotor are generated by a combination of XFoil outputs and additional parameters specified in the main Matlab script. XFoil is responsible for carrying out the 2D analysis of the pre-specified aerofoil sections. The aerodynamic performance (in terms of non-dimensional aerodynamic coefficients) are determined for every location that is distributed radially from the propeller hub to the tip.

The parameters used to define the XFoil calculations, are the geometry of the propeller, the Reynolds number scaling exponent f, [250, 196] and the critical Mach number.

A relatively detailed description of the geometry of the propeller is required and is defined through the chord-to-radius ratio $\frac{c_{\mathrm{local}}}{R}$, the local blade pitch angle β for every blade section that is used in the calculation. The location of each blade section is referred to as $z = \frac{r}{R}$, as in the rest of the thesis. Finally, the radius and the total number of blades complete the definition of the propeller/rotor. XRotor uses the Reynolds number scaling exponent f is used to calculate the

The drag is scaled by a Reynold's number scaling based on a reference Reynold's number and a scaling exponent. In the unstalled region, C_D has a quadratic dependence on CL and a power-law dependence on Reynolds number as follows,

$$C_d = \left(C_{d,0} + \frac{dC_d}{dC_l^2} \left(C_{l,0} - C_l \right)^2 \right) \left(\frac{\mathrm{Re}}{\mathrm{Re}_{ref}} \right)^f \tag{D.1}$$

where Re is the local blade section Reynolds number and Re_{ref} is the reference Reynold number, i.e. the Reynolds number at which XFoil is run for a blade section. This scaling

parameter is not required in this case as all sections' aerodynamic performance are being calculated independently by XFoil.

The critical Mach number is the Mach number of the flow in front of the blade section for which the flow over the blade section reaches a Mach number of 1 locally. The critical Mach number can be estimated using the relation between the pressure coefficient and Mach number. This relation is known as the Prandtl-Glauert relation [231]

$$C_{pr} = \left[\left(\frac{1 + [(\gamma - 1)/2] M_\infty^2}{1 + \frac{\gamma}{\gamma - 1}} \right)^{\frac{\gamma}{\gamma - 1}} - 1 \right] \tag{D.2}$$

where C_{pr} is the pressure coefficient, γ is the specific heat ratio and M_∞ is the free-stream Mach number. Equation 3.3 is used to generate the so-called aerofoil independent curve which can be seen in Figure 3.2. In order to determine the critical Mach number an additional relation is used.

The pressure coefficient is computed with the following $C_{pr} = C_{pr,0}/\sqrt{1 - M_\infty^2}$, where $C_{pr,0}$ is the minimum incompressible pressure coefficient at the suction side and C_{pr} is the compressible pressure coefficient. The pressure distribution of a blade section depends on the local angle of attack. The critical Mach number therefore depends on several parameters like the local angle of attack, Reynolds number and aerofoil thickness and camber. Estimation of a critical Mach number is performed for each aerofoil section using independent calls to XFoil.

M_{cr} is used to a Prandtl-Glauert compressibility correction $\Delta C_d = K(M_{\text{local}} - M_{cr})^n$ where n is an exponent which is set to 3 by default in XRotor and K is a scaling constant. The viscosity option is turned on and the Reynolds numbers are given as input. The Mach number is set to zero in XFoil. If a Mach number is given, XFoil performs the same compressibility correction using the Prandtl-Glauert Δ from above, therefore to avoid this correction being applied twice, the Mach number given in XFoil is set to zero but the correct Reynolds number is given as input in XFoil. The angles of attack for which every section is run for is from -30 to 30 degrees with increments of 0.25 degrees.

Finally, an the e^n method [196] that models the boundary layer, attempts to simulate the effect of disturbances on the transition point.

The default value for n used within XFoil is 9 for the e^n method, which represents the situation of an average wind tunnel. Based on a sensitivity analysis by [258] a value of $n = 0.01$ is chosen as most appropriate for propeller application.

After XFoil is run and a 2D aerodynamic data set is created, a fitting is performed. The input for this fitting are the lift, drag and moment coefficients together with the corresponding angles of attack. The output of this fitting are the other input parameters for XRotor that are given in the previous section which are not assumed. All the input

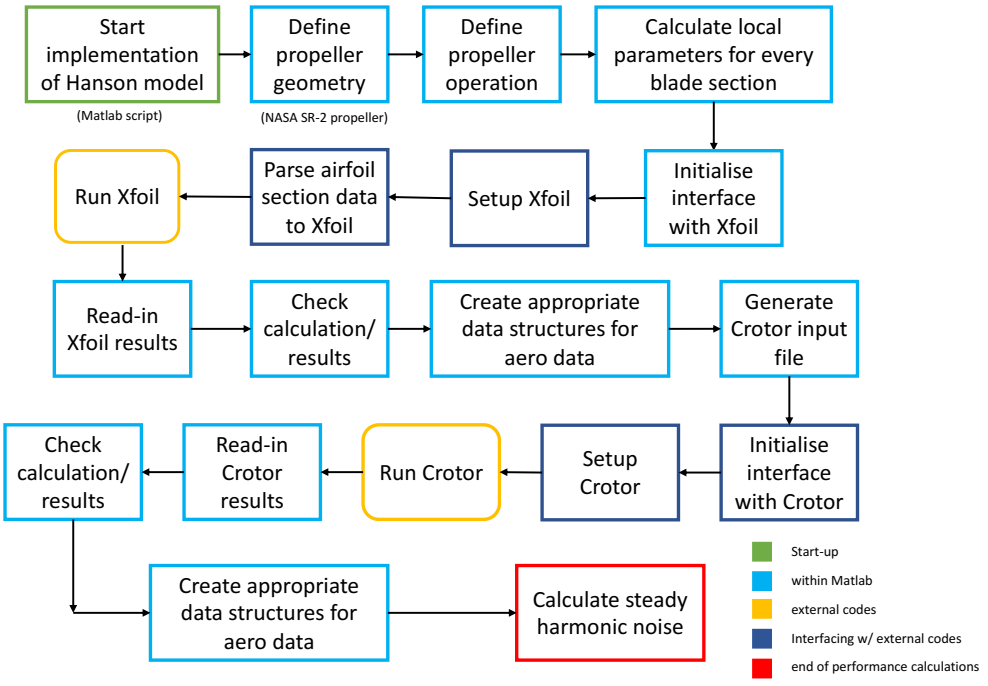

FIGURE D.2: Flowchart of the performance calculation process in order to generate the appropriate inputs for the Hanson method.

variables are written in an input file for XRotor with a specified format. In XRotor the settings can be changed as well. As is addressed before the potential formulation is used for the calculation of the induced velocities of propeller blade sections. Furthermore, the number of iterations is set to 150 which is found to be sufficient. Often a convergence is achieved before this amount of iterations is reached. When XRotor is run, all the outputs are written in a specified file. This is then checked for convergence and the performance coefficients and induced velocity components are obtained.

D.3 Hanson method for propeller harmonic noise

Section 2.3 and in particular Equation 2.29 is implemented in order to generate the complex Fourier coefficients and therefore the time domain noise signal. At this stage all required input parameters have either been explicitly defined or calculated using the combination of XFoil and XRotor.

An important notable difference exist in the definition of lift and drag coefficients between XRotor and the advance frame in which they are defined in the Hanson implementation. Notes on this may be seen in [60, 36]. The procedure for changing the frame of reference is briefly discussed bellow.

The lift and drag coefficients used in Equation 2.29 need to be defined in the advance direction. The coefficients obtained from the propeller performance tool XRotor however

are slightly rotated due to the induced effects of the propeller as can be seen in Figure D.3.

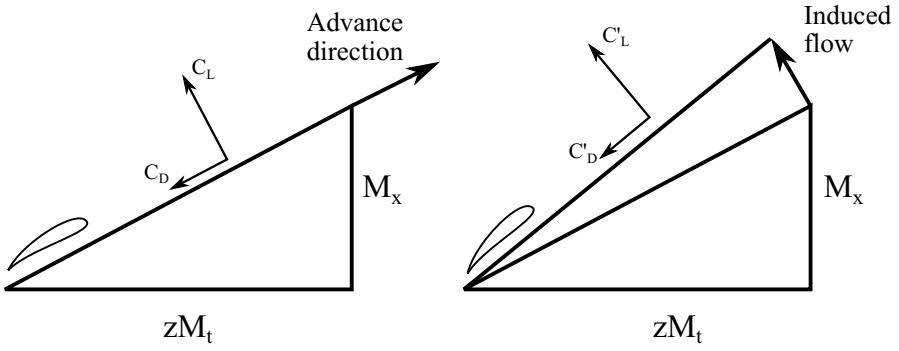

FIGURE D.3: Lift and drag axes in advance direction and including induced flow [60]. Note that the term z is also referred to as r/R

Using Figure D.4 as a reference, the following expressions may be used to calculate the rotated lift and drag coefficients,

$$C_l = \frac{V_e^2}{\left(V_\infty + \Omega \frac{r}{R} R\right)^2} \left(C_l' \cos \phi_{\text{induced}} - C_d' \sin \phi_{\text{induced}}\right) \tag{D.3}$$

$$C_d = \frac{V_e^2}{\left(V_\infty + \Omega \frac{r}{R} R\right)^2} \left(C_l' \sin \phi_{\text{induced}} + C_d' \cos \phi_{\text{induced}}\right) \tag{D.4}$$

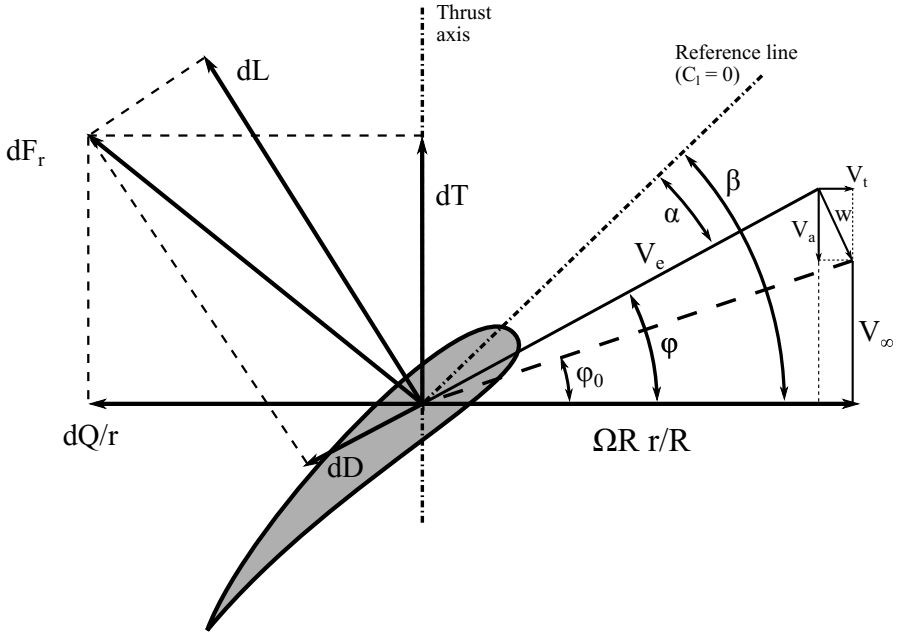

FIGURE D.4: Velocity diagram including the induced velocity.

All required inputs may be calculated using the data generated by XRotor and the geometry of the propeller; including the local angle of attack a_i and local pitch angle β_i. The relationship $\phi_i = \beta_i - \alpha_i$ can be used to compute the inflow angle including the

induced effects, which is referenced as ϕ_i (the subscript i indexes through all the various aerofoil sections). The local inflow angle $\phi_{i,0}$ can be calculated using the formula $\phi_{i,0} = \tan^{-1}\left(V_\infty / \left(\Omega \frac{r}{R} R\right)\right)$, where R is the propeller radius and $\frac{r}{R}$ is the location of the radial blades with respect to the radius. The angle of the induced velocity vector may be calculated using the formula $\phi_{\text{induced}=\phi_i} - \phi_{i,0}$. The equation for the effective velocity experienced by a propeller blade section, which takes into account the effects of induced velocity, is $V_e = \sqrt{\left(V_a + V_\infty\right)^2 + \left(\Omega \frac{r}{R} R - V_t\right)^2}$, where V_a denotes the induced velocity component parallel to the axis of rotation and V_t.

D.4 Validation

Validation of the Hanson model implementation was performed using input and predicted noise level data from references [259, 260, 261]. The propeller used, was the SR-2 propeller in various full scale and model configurations. The full scale propeller is an eight-bladed propeller with a diameter of 0.622 meters and adjustable pitch developed at NASA. Results presented in this section are for two variations of the SR-2, one 4-bladed configuration with a diameter of 0.429 meters operating at 7,200 rpm and 10,080 rpm. The second, is a eight-bladed configuration at 0.622 meters operating at 6,420 rpm and 7,059 rpm, representative of helical tip Mach number of $M_h = 0.664$ and $M_h = 0.741$, respectively. The two configurations were part of separate experimental campaigns, detailed in [259] for the 4-blade configurations and [261] for the 8-bladed configuration.

The NACA-65 series aerofoil makes up the blade sections of the SR2-propeller from the root to about 37% of the radius, while the NACA-16 series aerofoil makes up the blade sections from about 45% of the radius till the tip. Other design parameters (twist, thickness etc.) of the blade may be seen in Figure D.5.

As discussed, the combination of XFoil and XRotor where used to generate the loading characteristics of the propeller blades. Examples of a range of predicted thrust and power coefficients as a function of propeller advance ratio are shown in Figure D.6. The literature data used as a comparison is published by Stefko et al. [260] for the SR-2. A much larger test matrix and experimental campaign was performed than what is shown herein. Figure D.7 shows the spanwise lift distribution for a single condition, for an advance ratio of $J = 1.4$ and flight Mach number of $M_x = 0.1$.

Figure D.8 shows comparison between the experimental data in [259] and predictions made the implementation of the Hanson model, for the four-bladed SR-2 propeller. At a tip Mach number of $M_t = 0.67$ and low flight Mach number of $M_x = 0.09$ the fundamental tone matches the data reasonably well for polar angles between 20 deg and 160 deg. Under predictions are observed at angles approaching the propeller axis, while the maximum radiation is observed at an angle of approximately 100 deg, similar to the

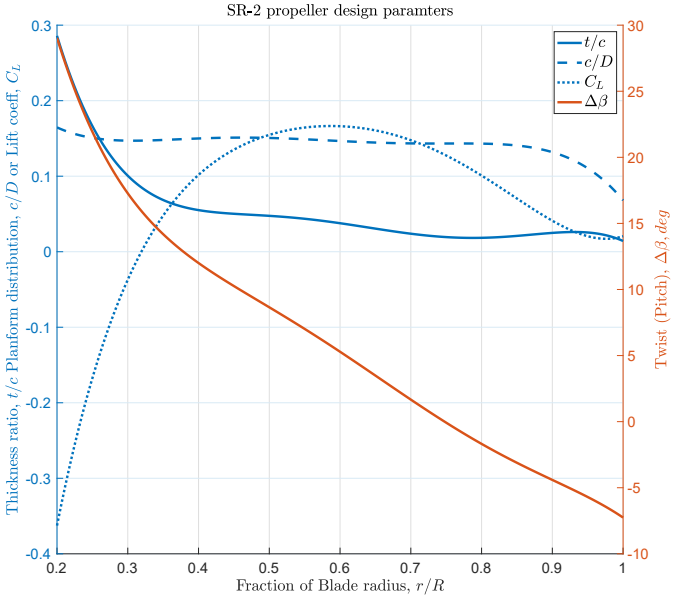

FIGURE D.5: SR-2 propeller design characteristics.

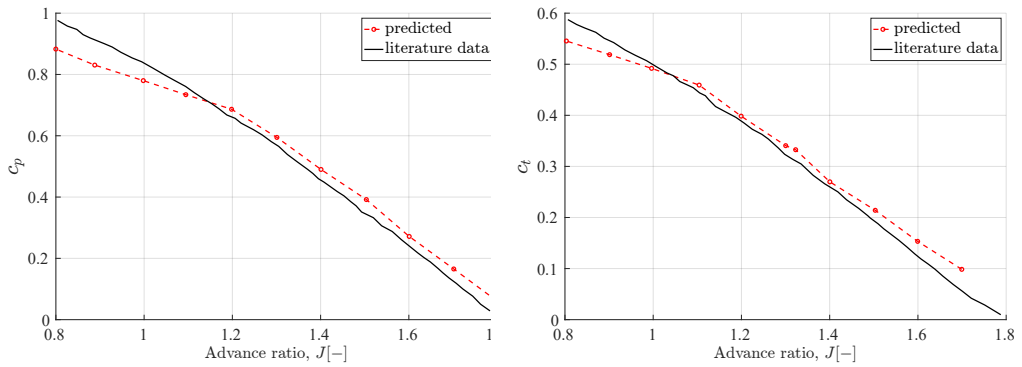

(A) Pressure coefficient, c_p (B) Thrust coefficient, c_t

FIGURE D.6: Validation of performance parameters of the propeller at various operational conditions. Flight Mach number is set to $M_x = 0.1$ and 75% pitch set to 38 deg. Literature data from [260].

results of ESDU 76020[193]. The OASPL matches data the field shape in the forward arc, while an over-prediction is observed in the rear arc, with differences greater than 5 dB at an angle of 120 deg.

Larger errors are observed in the prediction of the eight-bladed propeller, shown in Figure D.8, in both levels and field shape. The flatter field shape indicates the possible presence of broadband noise sources, not captured by the Hanson model. Figure D.9b presents an example of a comparison to data at a distance of 0.8D (0.8 times the diameter) measured from the tip. A distance $< D$ from the tip of the propeller is typically considered in the near field [261]. Nevertheless, sufficient agreement is found in the prediction of the field shape. It is noted that for predictions of the eight propeller validation performance data was not available.

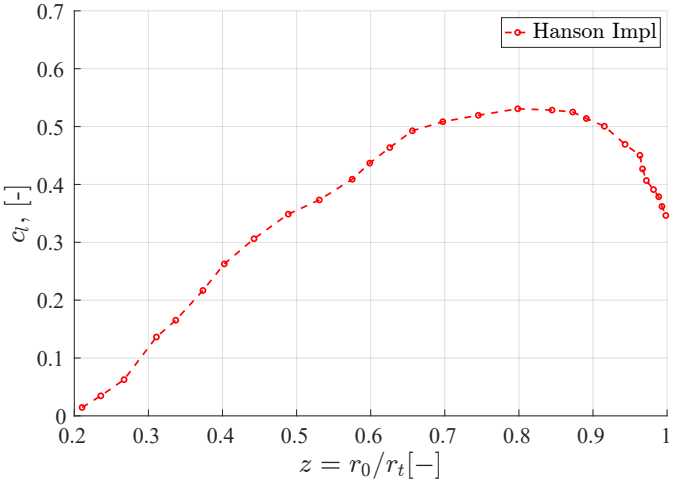

FIGURE D.7: Radial lift distribution for the same conditions as Figure D.6 and an advance ratio of $J = 1.4$, representing tip relative Mach number of $M_t \approx 0.24$

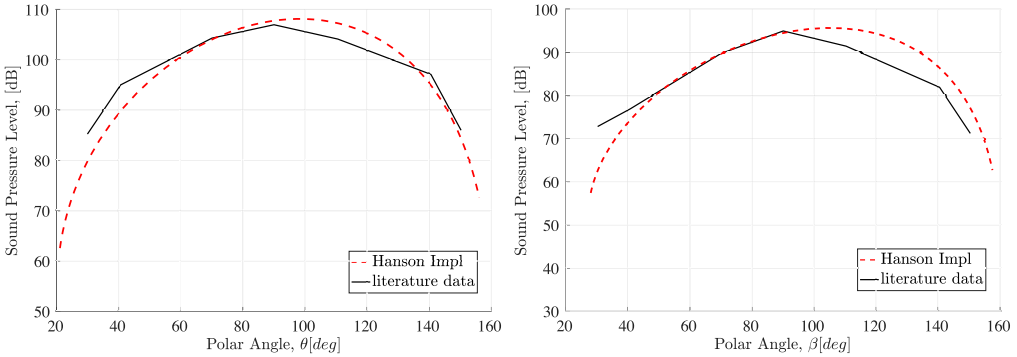

(A) Fundamental tone, $m = 1$ (B) OASPL

FIGURE D.8: Comparison of the fundamental tone and OASPL polar directivity prediction versus literature data [259]. Conditions replicated, $J = 0.423$, $M_t = 0.67$ and $M_x = 0.09$

Predictions for additional test cases at relative tip Mach number above $M_h = 0.85$ were performed with accuracy and reliability of the results greatly diminishing.

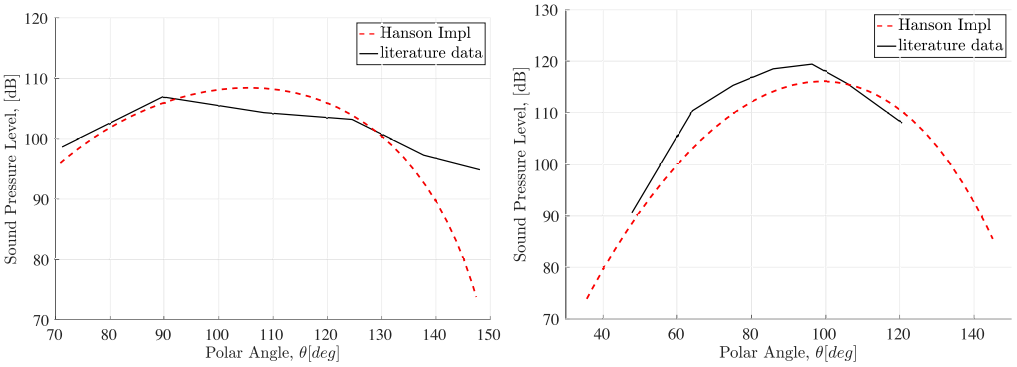

(A) Conditions, $J = 1.05$ and $M_x = 0.203$ and 75% pitch 32.8 deg

(B) Conditions, $J = 1.50$, $M_x = 0.32$ and 75% pitch 40.3 deg.

FIGURE D.9: Comparison of far-field OSPL polar directivity prediction versus literature data [261].

Appendix E

Finite segment correction integrals.

$$(A_0^0)^2(N_y^{0,0})^2 \int \; d\theta \tag{E.1}$$

$$\frac{1}{2}A_0^0 A_1^{-1} N_y^{0,0} N_y^{1,-1} e^{i\varphi} \int \sin\theta d\theta \tag{E.2}$$

$$A_0^0 A_1^0 N_y^{0,0} N_y^{1,0} \int \cos\theta d\theta \tag{E.3}$$

$$-A_0^0 A_1^1 N_y^{0,0} N_y^{1,1} e^{-i\varphi} \int \sin\theta d\theta \tag{E.4}$$

$$\frac{1}{2}A_1^{-1} A_0^0 N_y^{1,-1} N_y^{0,0} e^{-i\varphi} \int \sin\theta d\theta \tag{E.5}$$

$$\frac{1}{4}(A_{-1}^1)^2(N_y^{-1,1})^2 \int \sin^2\theta d\theta \tag{E.6}$$

$$\frac{1}{2}A_1^{-1} A_1^0 N_y^{1,-1} N_y^{1,0} e^{-i\varphi} \int \sin\theta\cos\theta d\theta \tag{E.7}$$

$$-\frac{1}{2}A_1^{-1} A_1^1 N_y^{1,-1} N_y^{1,1} e^{2i\varphi} \int \sin^2\theta d\theta \tag{E.8}$$

$$A_1^0 A_0^0 N_y^{1,0} N_y^{0,0} \int \cos\theta d\theta \tag{E.9}$$

$$\frac{1}{2}A_1^0 A_1^{-1} N_y^{1,0} N_y^{1,-1} e^{i\varphi} \int \sin\theta\cos\theta d\theta \tag{E.10}$$

$$(A_1^0)^2 (N_y^{1,0})^2 \int \cos^2\theta d\theta \tag{E.11}$$

$$-A_1^0 A_1^1 N_y^{1,0} N_y^{1,1} e^{-i\varphi} \int \sin\theta\cos\theta d\theta \tag{E.12}$$

$$-A_1^1 A_0^0 N_y^{1,1} N_y^{0,0} e^{i\varphi} \int \sin\theta d\theta \tag{E.13}$$

$$-\frac{1}{2}A_1^1 A_1^{-1} N_y^{1,1} N_y^{1,-1} e^{2i\varphi} \int \sin^2\theta d\theta \tag{E.14}$$

$$\frac{1}{2}A_1^1 A_1^0 N_y^{1,1} N_y^{1,0} e^{i\varphi} \int \sin\theta\cos\theta d\theta \tag{E.15}$$

$$(A_1^1)^2 (N_y^{1,1})^2 \int \sin^2\theta d\theta \tag{E.16}$$

Appendix F

Individual noise source directivity data.

This Appendix purely reproduces the directivity adjustments used throughout this thesis for the modelling the jet (single and dual stream) and fan (inlet and discharge) individual noise sources. The data herein is from the original ANOPP theoretical manual part 2 [20], and does not by any means reproduce the entirety of the data sets included in the methods, it is merely a reference.

The figures depict the directivity index (DI) versus the polar angle θ for various operating conditions in the case of the jet, and a distinction between the broadband and tonal source of the fan inlet and discharge.

For more information about the data itself, acquisition, and the jet and fan noise models they were used with, the reader is strongly advised to refer to the ANOPP manual, and the individual publications for the prediction methods [53, 262, 263, 264, 265].

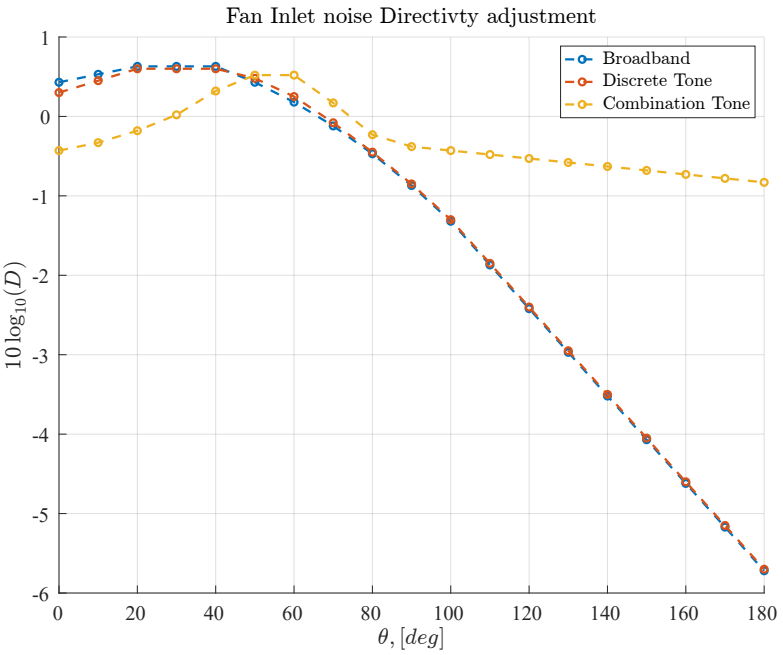

FIGURE F.1: Fan inlet noise directivity index [53, 20].

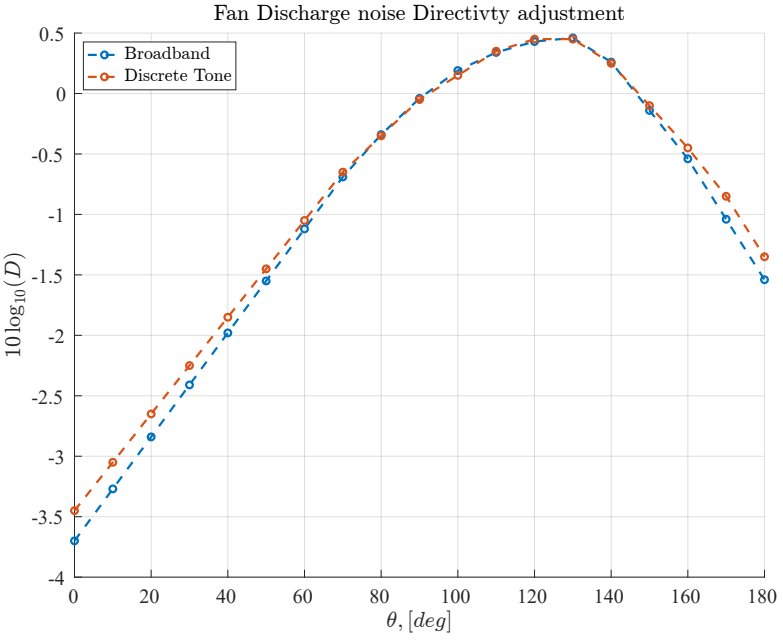

FIGURE F.2: Fan discharge noise directivity index [53, 20].

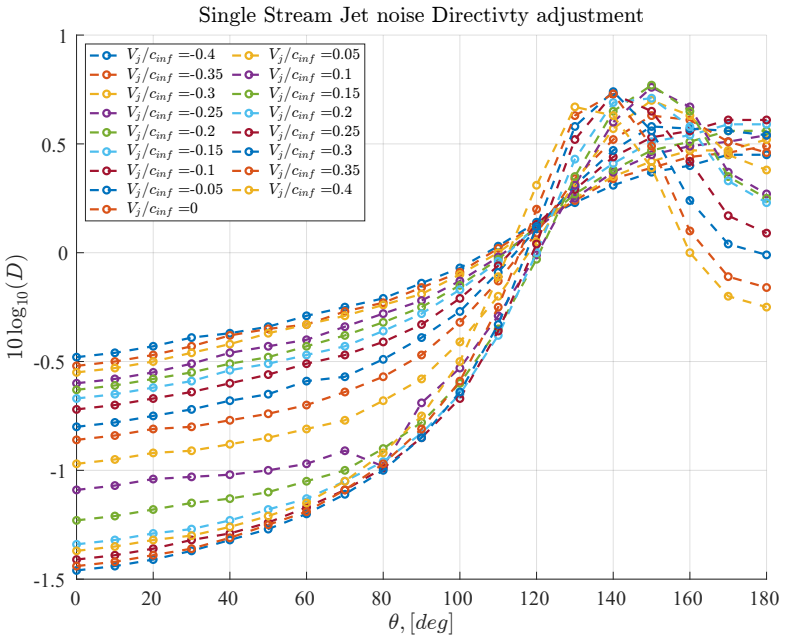

FIGURE F.3: Single stream jet noise direcitivity adjustment [262, 263, 20].

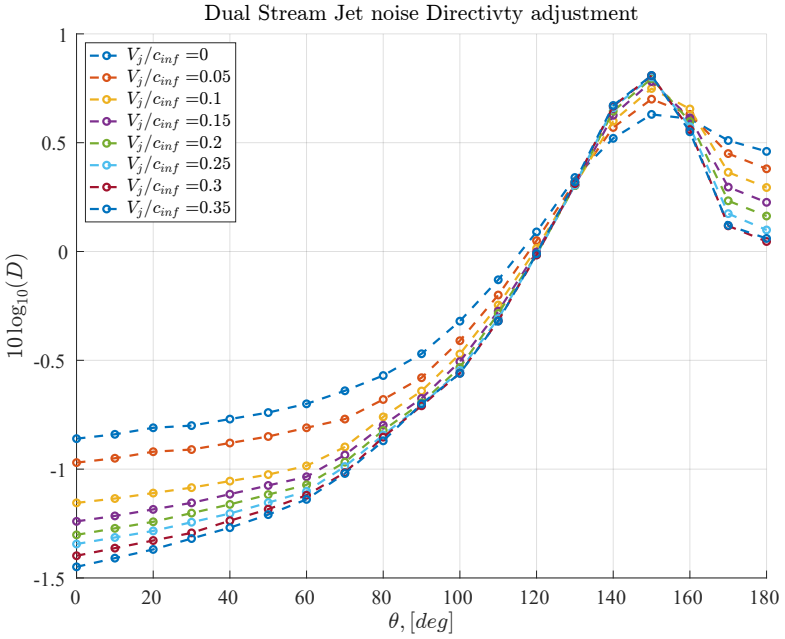

FIGURE F.4: Dual stream jet noise directivity adjustment [264, 265, 20].

Bibliography

[1] R. M. Arnaldo Valdes, S. Burmaoglu, V. Tucci, L. M. Braga da Costa Campos, L. Mattera, and V. F. Gomez Comendador. Flight path 2050 and ACARE goals for maintaining and extending industrial leadership in aviation: a map of the aviation technology space. *Sustainability, Multidisciplinary Digital Publishing Institute*, 11(7):2065, 2019.

[2] NASA. Strategic implementation plan: 2019 update. [Online]. Available: https://www.nasa.gov/wp-content/uploads/2015/11/sip-2019-v7-web.pdf, 2019.

[3] Nasa strategic plan 2022. [Online]. Available: https://www.nasa.gov/wp-content/uploads/2018/01/2022_nasa_strategic_plan_0.pdf, 2022.

[4] EASA, EEA, and Eurocontrol. European aviation environmental report 2019. [Online]. Available: https://ec.europa.eu/transport/sites/transport/files/european-aviation-environmental-report-2016-72dpi.pdf/, 2016.

[5] Environmental report 2019 chapter 1: Aviation and the environment outlook. [Online] Available: https://www.icao.int/environmental-protection/pages/envrep2019.aspx/, 2019.

[6] Environmental report 2019 chapter 2: Aircraft noise. [Online] Available: https://www.icao.int/environmental-protection/pages/envrep2019.aspx/, 2019.

[7] Department for Transport. Uk aviation forecasts. [Online]. Available: https://assets.publishing.service.gov.uk/media/5e8dec2786650c18c9666633/uk-aviation-forecasts-2017.pdf, October 2017.

[8] Airbus. Global market forecast: Cities, airports and aircraft 2019-2028, 2019.

[9] Aerospace Technology Institute. Flyzero reports archive. [Online]. Available: https://www.ati.org.uk/flyzero-reports/.

[10] UK Department for Transport. Jet zero strategy: delivering net zero aviation by 2050. [Online]. Available:

https://assets.publishing.service.gov.uk/government/uploads/system/uploads/attachment_data/file/1095952/jet-zero-strategy.pdf/.

[11] M. Alder, E. Moerland, J. Jepsen, and B. Nagel. Recent advances in establishing a common language for aircraft design with CPACS. 2020.

[12] A. P. Synodinos, R. H. Self, and A. J. Torija. Framework for predicting noise–power–distance curves for novel aircraft designs. *Journal of Aircraft*, 55(2):781–791, 2018.

[13] A. J. Torija, R. H. Self, and I. H. Flindell. A model for the rapid assessment of the impact of aviation noise near airports. *The Journal of the Acoustical Society of America*, (2):981–995, 2017.

[14] William K. Blake. Chapter 1 - introductory concepts. In W. K. Blake, editor, *Mechanics of Flow-Induced Sound and Vibration, Volume 1 (Second Edition)*, pages 1–45. Academic Press, second edition edition, 2017.

[15] W. K. Blake. Chapter 2 - theory of sound and its generation by flow. In W. K. Blake, editor, *Mechanics of Flow-Induced Sound and Vibration, Volume 1 (Second Edition)*, pages 47–135. Academic Press, second edition edition, 2017.

[16] P. M. Morse and K. U. Ingard. *Theoretical acoustics*. Princeton university press, 1986.

[17] A. D. Pierce. *Acoustics: an Introduction to its Physical Principles and Applications*. American Institute of Physics, 1989.

[18] F. J. Fahy. *Foundations of engineering acoustics*. Elsevier, 2000.

[19] L. E. Kinsler, A. R. Frey, A. B. Coppens, , and J. V. Sanders. *Fundamentals of acoustics*. John Wiley and Sons, 4th edition, 2000.

[20] W. E. Zorumski. Aircraft noise prediction program theoretical manual. Technical Report Tech. Rep. TM-83199, Parts 1 and 2, NASA Langley Research Center, Hampton, VA, United States, 1982.

[21] M. J. T. Smith. *Aircraft Noise*. Cambridge University Press, 1989.

[22] A. Ishimaru et al. *Wave propagation and scattering in random media*, volume 2. Academic press New York, 1978.

[23] P. Chow, C. Liu, and L. Maestrello. Scattering of coherent sound waves by atmospheric turbulence. In *2nd Aeroacoustics Conference*, page 545, 1975.

[24] H. H. Hubbard. Aeroacoustics of flight vehicles: Theory and practice. volume 2. noise control. Technical report, National Aeronautics and Space Admin, Langley Research Center Hampton VA, 1991.

[25] International Civil Aviation Organization. *Guidance on the balanced approach to aircraft noise management*, volume 9829. International Civil Aviation Organization, 2008.

[26] H. Feng, Y. Zhou, W. Zeng, and C. Ding. Review on metrics and prediction methods of civil aviation noise. *International Journal of Aeronautical and Space Sciences*, 24(5):1199–1213, 2023.

[27] ICAO. Annex 16 to the convention on international civil aviation: Environmental protection, volume i aircraft noise. Technical report, International Civil Aviation Organization, July 2017.

[28] H. Fletcher and W. A. Munson. Loudness, Its Definition, Measurement and Calculation. *The Journal of the Acoustical Society of America*, 5(2):82–108, 06 2005.

[29] Metrics for aircraft noise. Ercd report 0904, CAA, January 2009.

[30] K. D. Kryter. The meaning and measurement of perceived noise level. *Noise Control*, 6(5):12–27, 1960.

[31] Federal Aviation Regulation FAR. Part 36: Noise standards: Aircraft type and airworthiness certification. *Washington, DC: US Federal Aviation Administration*, 2002.

[32] J. Lee, G. Cebrian, L. Edmonds, J. Patel, and E. Weston. Ercd report 1401. noise exposure contours for heathrow airport 2013. Technical report, Technical Report October, CAA, London, 2014.

[33] International Electrotechnical Commission et al. Iec 61260-1: 2014 electroacoustics—octave-band and fractional-octave-band filters—part 1: Specifications. *IEC: London, UK*, page 88, 2014.

[34] Report on standard method of computing noise contours around civil airports, vol. 2: Technical guide. Tech. rep. ecac.ceac doc. 29, 4th ed, European Civil Aviation Conference (ECAC), December 2005.

[35] L. Bertsch, D. G. Simons, and M. Snellen. Aircraft noise: The major sources, modelling capabilities, and reduction possibilities. 2015.

[36] H. H. Hubbard. Aeroacoustics of flight vehicles: Theory and practice:volume 1: Noise sources. Technical report, NASA Langley Research Center, Hampton, Virginia, 1991.

[37] W. R. Sears. Aerodynamics, noise, and the sonic boom. *AIAA Journal*, 7(4):577–586, 1969.

[38] K. J. Plotkin. State of the art of sonic boom modeling. *The Journal of the Acoustical Society of America*, 111(1):530–536, 2002.

[39] R. R. Davis and O. Clavier. Impulsive noise: A brief review. *Hearing research*, 349:34–36, 2017.

[40] F. H. Schmitz and Y. H. Yu. Helicopter impulsive noise: theoretical and experimental status. In *Recent advances in aeroacoustics*, pages 149–243. Springer, 1986.

[41] K. S. Brentner, A. S. Lyrintzis, and E. K. Koutsavdis. Comparison of computational aeroacoustic prediction methods for transonic rotor noise. *Journal of Aircraft*, 34(4):531–538, 1997.

[42] V. Blumenthal, J. Streckenbach, and R. Tate. *Aircraft environmental problems*.

[43] M. R. Fink. *Airframe noise prediction method*. Department of Transportation, Federal Aviation Administration, Systems, 1977.

[44] M. R. Fink. Noise component method for airframe noise. *Journal of Aircraft*, 16(10):659–665, 1979.

[45] Y. Guo. Prediction of flap side edge noise. In *5th AIAA/CEAS Aeroacoustics Conference and Exhibit*, page 1804, 1999.

[46] Y. Guo. Aircraft slat noise modeling and prediction. In *16th AIAA/CEAS aeroacoustics conference*, page 3837, 2010.

[47] M. J. Lighthill. On sound generated aerodynamically. i. general theory. *Proceedings of the Royal Society of London. Series A, Mathematical and Physical Sciences*, 211(1107):564–587, 1952.

[48] A. P. Dowling and Y. Mahmoudi. Combustion noise. *Proceedings of the Combustion Institute*, 35(1):65–100, 2015.

[49] J. E. F. Williams and D. L. Hawkings. Sound Generation by Turbulence and Surfaces in Arbitrary Motion. *Philosophical Transactions of the Royal Society of London Series A*, 264(1151):321–342, May 1969.

[50] F. Farassat and G. Succi. The prediction of helicopter rotor discrete frequency noise. 1982.

[51] K. S. Brentner and United States. *Prediction of helicopter rotor discrete frequency noise: a computer program incorporating realistic blade motions and advanced acoustic formulation*. National Aeronautics and Space Administration, Scientific and Technical Information Branch, 1986.

[52] A. P. Synodinos. *A new framework for estimating noise impact of novel aircraft*. PhD thesis, 2017.

[53] M. Heidmann. Interim prediction method for fan and compressor source noise. Technical report, NASA-TM-X-71763, National Aeronautics and Space Administration, Lewis Research Center Cleveland, OH, United States., 1975.

[54] M. J Benzakein and W. R. Morgan. *Analytical prediction of fan/compressor noise*, volume 80050. American Society of Mechanical Engineers, 1969.

[55] E. A. Krejsa and M. F. Valerino. Interim prediction method for turbine noise. Technical report, NASA-TM-X-73566, National Aeronautics and Space Administration, Lewis Research Center Cleveland, OH, United States., 1976.

[56] SAE ARP. 876c: Gas turbine jet exhaust noise prediction. *Society of Automotive Engineers*, 1985.

[57] B. Henderson and J. Bridges. An mdoe investigation of chevrons for supersonic jet noise reduction. In *16th AIAA/CEAS Aeroacoustics Conference*, page 3926, 2010.

[58] A. Khavaran, J. D. Wolter, and L. D. Koch. Prediction of turbulence-generated noise in unheated jets: Part 2: Jeno users' manual (version 1.0). Technical report, NASA-TM-2009-213827/PART2, National Aeronautics and Space Administration, 2009.

[59] A-21 Aircraft Noise Measurement Aviation Emission Modeling. *Prediction Procedure for Near-Field and Far-Field Propeller Noise*, aug 2012.

[60] D. B. Hanson and B. Donald. Helicoidal surface theory for harmonic noise of propellers in the far field. *AIAA J.*, 18(10):1213–1219, October 1980.

[61] F. Farassat. Derivation of formulations 1 and 1a of farassat. Technical report, 2007.

[62] R. J. Pegg. A summary and evaluation of semi-empirical methods for the prediction of helicopter rotor noise. Technical report, 1979.

[63] B. A. Goldman. Modifications to psu-wopwop for enhanced noise prediction capabilities. Master's thesis, Pennsylvania State University, 2012.

[64] M. R. Fink. Noise component method for airframe noise. *AIAA paper*, October 1977.

[65] R. H. Thomas. Subsonic fixed wing project n+ 2 noise goal summary. *Presentation at the NASA Acoustics Technical Working Group*, 2007.

[66] Y. P. Guo. On trailing edge noise modeling and prediction for aircraft high lift wings. *NASA Contract Report NASA Contract NNL07AA03A*, 2010.

[67] W Bryce. The prediction of static-to-flight changes in jet noise. In *9th Aeroacoustics Conference*, page 2358, 1981.

[68] B. J. Cocking. A prediction method for the effects of flight on subsonic jet noise. *Journal of Sound and Vibration*, 53(3):435–453, 1977.

[69] J. R. Stone, D. E. Groesbeck, and C. L. Zola. Conventional profile coaxial jet noise prediction. *AIAA Journal*, 21(3):336–342, 1983.

[70] M. D. Dahl. Overview of aircraft noise prediction tools assessment. 2007.

[71] L. Bertsch, M. Snellen, L. Enghardt, and C. Hillenherms. Aircraft noise generation and assessment: executive summary, 2019.

[72] A. Filippone. Aircraft noise prediction. *Progress in Aerospace Sciences*, 68:27–63, 2014.

[73] B. S. Henderson and D. L. Huff. Electric motor noise status. Technical report, NASA Glenn Research Center, April 2017.

[74] D. L. Huff, B. S. Henderson, and E. Envia. A first look at electric motor noise for future propulsion systems. *Acoustics Technical Working Group Meeting (NASA)*, 2016.

[75] B. S. Henderson and D. Huff. *Electric Motor Noise for Small Quadcopters: Part II - Source Characteristics and Predictions.*

[76] J.E. Marte and D. W. Kurtz. A review of aerodynamic noise from propellers, rotors, and lift fans. Technical Report TR-32-7462, Jet Propulsion Laboratory California Institute of Technology, Pasadena, California, January 1970.

[77] F. Farassatt and G.P. Succi. A review of propeller discrete frequency noise prediction technology with emphasis on two current methods for time domain calculations. Technical report, Department of Aeronautics and Astronautics MIT, Cambridge, Massachusetts 02139, U.S.A., February 1980.

[78] B. Magliozzi. *Noise characteristics of model counter-rotating Prop-Fans.*

[79] D. Hanson and B. Magliozzi. *Propagation of propeller tone noise through a fuselage boundary layer.*

[80] M. E. Goldstein. Aeroacoustics. Technical report, Special Publication (SP),NASA-SP-346, National Aeronautics and Space Administration, Lewis Research Center Cleveland, OH, United States., 1974.

[81] M. V. Lowson. Thoughts on broad band noise radiation by a helicopter. *Wyle Laboratories Inc., Report WR*, pages 68–20, 1968.

[82] M. V. Lowson and J. B. Ollerhead. A theoretical study of helicopter rotor noise. *Journal of Sound and Vibration*, 9(2):197–222, 1969.

[83] D. Hawkings and M. Lowson. *Noise of high speed rotors.*

[84] H. H. Hubbard. Propeller-noise charts for transport airplanes. Technical report, NACA-TN-2968,National Aeronautics and Space Admin, Langley Research Center Hampton VA, 1953.

[85] R. J. King and R. G. Schlegel. Prediction methods and trends for helicopter rotor noise. In *Proceedings Third Cornell Aeronautical Laboratories/AVLABS Symposium on Aerodynamics of Rotary Wing and V/STOL Aircraft. Volume IRotor/Propeller Aerodynamics and Rotor Noise, Buffalo, New York, 18–20 June 1969*, 1969.

[86] T. F. Brooks, D. S. Pope, and M. A. Marcolini. Airfoil self-noise and prediction. Technical report, NASA-RP-1218, National Aeronautics and Space Admin, Langley Research Center Hampton VA, 1989.

[87] C. M. Harris. Absorption of sound in air versus humidity and temperature. *The Journal of the Acoustical Society of America*, 40(1):148–159, 1966.

[88] A-21 Aircraft Noise Measurement Aviation Emission Modeling. *Standard Values of Atmospheric Absorption as a Function of Temperature and Humidity*, dec 2012.

[89] A-21 Aircraft Noise Measurement Aviation Emission Modeling. *Procedure for the Calculation of Aircraft Noise in the Vicinity of Airports*, sep 1995.

[90] A-21 Aircraft Noise Measurement Aviation Emission Modeling. *Application of Pure-Tone Atmospheric Absorption Losses to One-Third Octave-Band Data*, jan 2021.

[91] E. J. Rickley, G. G. Fleming, and C. J. Roof. Simplified procedure for computing the absorption of sound by the atmosphere. *Noise control engineering journal*, 55(6):482–494, 2007.

[92] L. C. Sutherland, J. E. Piercy, H. E. Bass, and L. B. Evans. Method for calculating the absorption of sound by the atmosphere. *The Journal of the Acoustical Society of America*, 56(S1):S1–S1, 1974.

[93] C. F. Chien and W. W. Soroka. Sound propagation along an impedance plane. *Journal of Sound and Vibration*, 43(1):9–20, 1975.

[94] ESDU. Esdu aircraft noise series. [Online]. Available: https://www.esdu.com/cgi-bin/ps.pl?sess=unlicensed_1220912074644vjd&t=ser&p=ser_nois.

[95] ICAO. Doc 8168–Procedures for Air Navigation Services–Aircraft Operations (PANS-OPS), 2006.

[96] ICAO Doc. 9931 Continuous descent operations (CDO) manual. *Montréal, Canada: International Civil Aviation Organization*, 2010.

[97] N. A. Peart. 17. Flyover-Noise. *Aeroacoustics of flight vehicles: Theory and practice*, 1258(1):357, 1991.

[98] Eurocontrol Experimental Centre. Aircraft noise and performance (anp) database v2.1, 2016.

[99] Helicopter noise exposure curves for use in environmental impact assessment. Tech. rep. report no. faa-ee-82-16, Federal Aviation Administration(FAA), November 1982.

[100] A-21 Aircraft Noise Measurement Aviation Emission Modeling. *Method for Predicting Lateral Attenuation of Airplane Noise*, oct 2019.

[101] L. Lopes and C. Burley. *Design of the Next Generation Aircraft Noise Prediction Program: ANOPP2*. 06 2011.

[102] D. Schwamborn, T. Gerhold, and R. Heinrich. The dlr tau-code: recent applications in research and industry. 2006.

[103] A. Bassetti, S. Guérin, and O. Kornow. *Introducing lined-wall boundary conditions in the DLR time-domain CAA solver PIANO*. 2010.

[104] L. Bertsch and U. Isermann. Noise prediction toolbox used by the dlr aircraft noise working group. In *INTER-NOISE and NOISE-CON Congress and Conference Proceedings*, volume 247, pages 805–813. Institute of Noise Control Engineering, 2013.

[105] K. S. Brentner. Numerical algorithms for acoustic integrals with examples for rotor noise prediction. *AIAA Journal*, 35(4):625–630, 1997.

[106] F Farassat. Theory of noise generation from moving bodies with an application to helicopter rotors. Technical report, 1975.

[107] F. Farassat and G. P. Succi. A review of propeller discrete frequency noise prediction technology with emphasis on two current methods for time domain calculations. *Journal of Sound and Vibration*, 71(3):399–419, 1980.

[108] Doc 9911, recomended method for computing noise contours around airports. Technical report, ICAO, 2018.

[109] J. Li, Y. Zheng, M. Rafaelof, H. K. Ng, and S. A. Rizzi. Airnoiseuam: An urban air mobility noise-exposure prediction tool. In *INTER-NOISE and NOISE-CON Congress and Conference Proceedings*, volume 263, pages 474–485. Institute of Noise Control Engineering, 2021.

[110] W.R. Johnson. Rotorcraft aerodynamic models for a comprehensive analysis. 1998.

[111] S. A. Rizzi, D. L. Palumbo, J. R. Hardwick, and A. Christian. Recent advances in aircraft source noise synthesis. *The Journal of the Acoustical Society of America*, 136(4):2285–2286, 2014.

[112] S. A. Rizzi, S. J. Letica, D. D. Boyd, and L. V. Lopes. Prediction-based approaches for generation of noise-power-distance data with application to urban air mobility vehicles. In *28th AIAA/CEAS Aeroacoustics 2022 Conference*, page 2839, 2022.

[113] S. A. Rizzi and M. Rafaelof. Community noise assessment of urban air mobility vehicle operations using the faa aviation environmental design tool. In *INTER-NOISE and NOISE-CON Congress and Conference Proceedings*, volume 263, pages 450–461. Institute of Noise Control Engineering, 2021.

[114] S. A. Rizzi and M. Rafaelof. Second generation uam community noise assessment using the faa aviation environmental design tool. In *AIAA SCITECH 2022 Forum*, page 2167, 2022.

[115] S. Krishnamurthy, B. C. Tuttle, and S. A. Rizzi. A synthesis plug-in for steady and unsteady loading and thickness noise auralization. In *AIAA AVIATION 2020 FORUM*, page 2597, 2020.

[116] A. Nuic, D. Poles, and V. Mouillet. Bada: An advanced aircraft performance model for present and future atm systems. *International journal of adaptive control and signal processing*, 2010.

[117] V. Mouillet, A. Nuić, E. Casado, and L. J. López. Evaluation of the applicability of a modern aircraft performance model to trajectory optimization. In *2018 IEEE/AIAA 37th Digital Avionics Systems Conference (DASC)*, pages 1–9. IEEE, 2018.

[118] I. M. Cid, X. P. Menéndez, J. L. Leonés, E. Casado, M. Vilaplana, V. Mouillet, A. Nuic, and L. Cavadini. Modelling flexible thrust performance for trajectory prediction applications in atm. 2016.

[119] V. Mouillet and D. Phu. Bada family h-a simple helicopter performance model for atm applications. In *2018 IEEE/AIAA 37th Digital Avionics Systems Conference (DASC)*, pages 1–8. IEEE, 2018.

[120] N. van Oosten. Sondeo: A new tool for airport noise assessment. In *INTER-NOISE and NOISE-CON Congress and Conference Proceedings*, volume 2004, pages 499–504. Institute of Noise Control Engineering, 2004.

[121] ICAO. Environmental Technical Manual, Volume I: Procedures for the Noise Certification of Aircraft(Doc 9501-1), Third Edition, 2018.

[122] Federal Aviation Regulations. Noise standards: Aircraft type and airworthiness certification. Technical report, Technical Report, Technical Report 14 CFR Part 36, 2009.

[123] Report on standard method of computing noise contours around civil airports, vol. 1: Applications guide. Tech. rep. ecac.ceac doc. 29, 4th ed, European Civil Aviation Conference (ECAC), December 2005.

[124] Climate Change Committee. The uk's transition to electric vehicles@ONLINE. https://www.theccc.org.uk/publication/the-uks-transition-to-electric-vehicles/, Dec 2020.

[125] B. Sarlioglu and C. T. Morris. More electric aircraft: Review, challenges, and opportunities for commercial transport aircraft. *IEEE transactions on Transportation Electrification*, 1(1):54–64, 2015.

[126] A. Barzkar and M. Ghassemi. Electric power systems in more and all electric aircraft: A review. *IEEE Access*, 8:169314–169332, 2020.

[127] P. Wheeler, T. S. Sirimanna, S. Bozhko, and K. S. Haran. Electric/hybrid-electric aircraft propulsion systems. *Proceedings of the IEEE*, 109(6):1115–1127, 2021.

[128] D. F. Finger, R. de Vries, R. Vos, C. Braun, and C. Bil. A comparison of hybrid-electric aircraft sizing methods. In *AIAA Scitech 2020 Forum*, page 1006, 2020.

[129] Z. Ji, M. M. Rokni, J. Qin, S. Zhang, and P. Dong. Energy and configuration management strategy for battery/fuel cell/jet engine hybrid propulsion and power systems on aircraft. *Energy Conversion and Management*, 225:113393, 2020.

[130] Pipistrel Aircraft. Wattsup, the new 2-seat electric trainer. https://www.pipistrel-aircraft.com/wattsup-the-new-2-seat-electric-trainer-archive/.

[131] Pipistrel Aircraft. Velis electro. https://www.pipistrel-aircraft.com/aircraft/electric-flight/velis-electro-easa-tc/#next.

[132] B. J. Brelje and J. R. R. A. Martins. Electric, hybrid, and turboelectric fixed-wing aircraft: A review of concepts, models, and design approaches. *Progress in Aerospace Sciences*, 104:1–19, 2019.

[133] M. A. Rendón, C. D. Sánchez R., J. Gallo M., A. H. Anzai, et al. Aircraft hybrid-electric propulsion: Development trends, challenges and opportunities. *Journal of Control, Automation and Electrical Systems*, 32(5):1244–1268, 2021.

[134] A. S. Gohardani, G. Doulgeris, and R. Singh. Challenges of future aircraft propulsion: A review of distributed propulsion technology and its potential

application for the all electric commercial aircraft. *Progress in Aerospace Sciences*, 47(5):369–391, 2011.

[135] A. S. Gohardani. A synergistic glance at the prospects of distributed propulsion technology and the electric aircraft concept for future unmanned air vehicles and commercial/military aviation. *Progress in Aerospace Sciences*, 57:25–70, 2013.

[136] International Air Transport Association et al. Aircraft technology roadmap to 2050. *IATA: Geneva, Switzerland*, 2019.

[137] M. J. Armstrong, C. A. H. Ross, M. J. Blackwelder, and K. Rajashekara. Trade studies for nasa n3-x turboelectric distributed propulsion system electrical power system architecture. *SAE International Journal of Aerospace*, 5(2):325, 2012.

[138] J. L. Felder, G. V. Brown, H. DaeKim, and J. Chu. Turboelectric distributed propulsion in a hybrid wing body aircraft. Technical report, 2011.

[139] L. W. Traub. Range and endurance estimates for battery-powered aircraft. *Journal of Aircraft*, 48(2):703–707, March-April 2011.

[140] H. D. Kim, A. T. Perry, and P. J. Ansell. A review of distributed electric propulsion concepts for air vehicle technology. In *AIAA/IEEE Electric Aircraft Technologies Symposium*, Edwards, California 93523, July 2018.

[141] Hydrogen-powered aviation: A fact-based study of hydrogen technology, economics, and climate impact by 2050. Technical report, Clean Sky 2 and Fuel Cells and Hydrogen 2 Joint Undertakings (Horizon 2020), 2020.

[142] A. Baroutaji, T. Wilberforce, M. Ramadan, and A. G. Olabi. Comprehensive investigation on hydrogen and fuel cell technology in the aviation and aerospace sectors. *Renewable and sustainable energy reviews*, 106:31–40, 2019.

[143] M. J. Sefain. *Hydrogen aircraft concepts and ground support*. PhD thesis, 2005.

[144] Aviation 2050: The future of uk aviation, a consultation. Technical report, HM Government, December 2018.

[145] Study on the societal acceptance of urban air mobility in europe. Technical report, European Union Aviation Safety Agnecy, EASA, May 2021.

[146] Uam vision concept of operations (conops) uam maturity level (uml) 4. Version 1, Deloitte Consulting LLP on behalf of NASA, 2020.

[147] W. Cai, X. Wu, M. Zhou, Y. Liang, and Y. Wang. Review and development of electric motor systems and electric powertrains for new energy vehicles. *Automotive Innovation*, 4(1):3–22, 2021.

[148] J. D. Sinsay, B. Traceya, J. J. Alonso, D. A. Kontinos, J. E. Melton, and S. Grabble. Air vehicle design and technology considerations for an electric vtol metro-regional public transportation system. *AIAA J.*

[149] R. Jansen, C. Bowman, A. Jankovsky, R. Dyson, and J. Felder. Overview of nasa electrified aircraft propulsion (eap) research for large subsonic transports. In *53rd AIAA/SAE/ASEE joint propulsion conference*, page 4701, 2017.

[150] C. Snyder, J. Berton, G. Brown, J. Dolce, N. Dravid, D. Eichenberg, J. Freeh, C. Gallo, S. Jones, K. Kundu, C. Marek, M. Millis, P. Murthy, T. Roach, T. Smith, G. Stefko, R. Sullivan, R. Tornabene, K. Geiselhart, and A. Kascak. Propulsion investigation for zero and near-zero emissions aircraft. 01 2009.

[151] V. Viswanathan, A. H. Epstein, Y. Chiang, E. Takeuchi, M. Bradley, J. Langford, and M. Winter. Author correction: The challenges and opportunities of battery-powered flight. *Nature*, 603(7903):E30–E30, 2022.

[152] L. H. Smith. Wake ingestion propulsion benefit. *Journal of Propulsion and Power*, 9(1):74–82, 1993.

[153] A. Ko, J. A. Schetz, and W. H. Mason. Assessment of the potential advantages of distributed-propulsion for aircraft. In *XVI International Symposium on Air Breathing Engines (ISABE)*, pages 2003–1094, 2003.

[154] J. D. Kummer and T. Q. Dang. High-lift propulsive airfoil with integrated crossflow fan. *Journal of Aircraft*, 43(4):1059–1068, 2006.

[155] J. A. Schetz, S. Hosder, V. Dippold, and J. Walker. Propulsion and aerodynamic performance evaluation of jet-wing distributed propulsion. *Aerospace Science and Technology*, 14(1):1–10, 2010.

[156] L. L. M. Veldhuis. *Propeller Wing Aerodynamic Interference*. PhD thesis, Delft University of Technology, 2005.

[157] M. D. Patterson, N. K. Borer, and B. German. *A Simple Method for High-Lift Propeller Conceptual Design*. American Institute of Aeronautics and Astronautics, 2021/07/27 2016.

[158] M. D. Patterson, J. M. Derlaga, and N. K. Borer. High-lift propeller system configuration selection for nasa's sceptor distributed electric propulsion flight demonstrator. In *16th AIAA aviation technology, integration, and operations conference*, page 3922, 2016.

[159] L. Newton. X-57 technical papers, Sep 2021.

[160] N. Borer, M. Patterson, J. Viken, M. Moore, J. Bevirt, A. Stoll, and A. Gibson. Design and performance of the nasa sceptor distributed electric propulsion flight demonstrator. 06 2016.

[161] D. M. Nark, P. G. Buning, W. T. Jones, and J. M. Derlaga. High-lift propeller noise prediction for distributed electric propulsion flight demonstrator. *AIAA*, 2017.

[162] S. A. Rizzi, D. L. Palumbo, J. Rathsam, A. W. Christian, and M. Rafaelof. *Annoyance to Noise Produced by a Distributed Electric Propulsion High-Lift System*.

[163] C. M. Ekoule. *Advanced open rotor far-field tone noise*. PhD thesis, University of Southampton, 2017.

[164] K. Pascioni and S. A. Rizzi. *Tonal Noise Prediction of a Distributed Propulsion Unmanned Aerial Vehicle*.

[165] P. V. Diaz, W. Johnson, J. Ahmad, and S. Yoon. *The Side-by-Side Urban Air Taxi Concept*.

[166] P. V. Diaz and S. Yoon. *Computational Study of NASA's Quadrotor Urban Air Taxi Concept*.

[167] T. C. A. Stokkermans, D. Usai, T. Sinnige, and L. L. M. Veldhuis. Aerodynamic interaction effects between propellers in typical evtol vehicle configurations. *Journal of Aircraft*, 58(4):815–833, 2021.

[168] T. C. A. Stokkermans and L. L. M. Veldhuis. Propeller performance at large angle of attack applicable to compound helicopters. *AIAA Journal*, 59(6):2183–2199, 2021.

[169] G. Bernardini, F. Centracchio, M. Gennaretti, U. Iemma, C. Pasquali, C. Poggi, M. Rossetti, and J. Serafini. Numerical characterisation of the aeroacoustic signature of propeller arrays for distributed electric propulsion. *Applied Sciences*, 10(8), 2020.

[170] R. Cabell, Robert G. McSwain, and F. Grosveld. Measured noise from small unmanned aerial vehicles. 2016.

[171] F. Christiansen, L. Rojano-Doñate, P. T. Madsen, and L. Bejder. Noise levels of multi-rotor unmanned aerial vehicles with implications for potential underwater impacts on marine mammals. *Frontiers in Marine Science*, 3:277, 2016.

[172] Study on the societal acceptance of urban air mobility in europe. Technical report, EASA, 2021.

[173] A. J. Torija, Z. Li, and R. H. Self. Effects of a hovering unmanned aerial vehicle on urban soundscapes perception. *Transportation Research Part D: Transport and Environment*, 78:102195, 2020.

[174] J. Wothge, C. Belke, U. Möhler, R. Guski, and D. Schreckenberg. The combined effects of aircraft and road traffic noise and aircraft and railway noise on noise annoyance—an analysis in the context of the joint research initiative norah. *International Journal of Environmental Research and Public Health*, 14(8), 2017.

[175] A. W. Christian and R. Cabell. *Initial Investigation into the Psychoacoustic Properties of Small Unmanned Aerial System Noise.*

[176] O. Zaporozhets, V. Tokarev, and K. Attenborouogh. *Aircraft Noise: Assessment, Prediction and Control.* Taylor and Francis, Boca Raton, FL, 2012.

[177] J. C. Burkill. *A first course in mathematical analysis.* Cambridge University Press, 1988.

[178] J. C. Burkill and H. Burkill. *A second course in mathematical analysis.* Cambridge University Press, 2002.

[179] S. Zhong, P. Zhou, R. Fattah, and X. Zhang. A revisit of the tonal noise of small rotors. *Proceedings of the Royal Society A: Mathematical, Physical and Engineering Sciences*, 476(2244):20200491, 2020.

[180] M. Abramowitz and I. A. Stegun. *Handbook of mathematical functions with formulas, graphs, and mathematical tables*, volume 55. US Government printing office, 1964.

[181] A. Gray, E. Gray, G. B. Mathews, and E. Meissel. *A treatise on Bessel functions and their applications to physics.* Macmillan and Company, 1895.

[182] E. C. Stewart and T. M. Carson. Simple method for prediction of aircraft noise contours. *J. Aircraft*, pages 828–830, 1980.

[183] O. I. Zaporozhets and V. I. Tokarev. Aircraft noise modelling for environmental assessment around airports. *Applied Acoustics*, 55(2):99–127, 1998.

[184] J. C. Cuillière. A direct method for the automatic discretization of 3d parametric curves. *Computer-Aided Design*, 29(9):639–647, 1997.

[185] W. Krebs, R. Butikofer, S. Pluss, and G. Thomann. Spectral three-dimensional sound directivity models for fixed wing aircraft. *Acta Acustica united with Acustica*, pages 269–277, 2006.

[186] W. Krebsand, R. Bütikofer, S. Plüss, and G. Thomann. Modeling of three-dimensional sound directivity patterns of helicopters. 89(273 – 279), 2003.

[187] F. S. Mobley. *Further development of 3-D rotary-wing acoustic directivity using spherical harmonic representation.* PhD thesis, 2012.

[188] A. J. Torija, R. H. Self, and I. H. Flindell. Airport noise modelling for strategic environmental impact assessment of aviation. *Applied Acoustics*, 132:49–57, 2018.

[189] S. A. Rizzi, D. L. Huff, D. D. Boyd, P. Bent, B. S. Henderson, K. A. Pascioni, D. C. Sargent, D. L. Josephson, M. Marsan, H. He, et al. Urban air mobility noise: Current practice, gaps. Technical report, and Recommendations, 2020.

[190] E. Süli and D. F. Mayers. *An Introduction to Numerical Analysis*. Cambridge University Press, 2003.

[191] L. Gutin. On the sound field of a rotating propeller. Technical Report TM 1195, NACA, 1948.

[192] W. K. Blake. Chapter 6 - noise from rotating machinery. In William K. Blake, editor, *Mechanics of Flow-Induced Sound and Vibration, Volume 2 (Second Edition)*, pages 505–658. Academic Press, second edition edition, 2017.

[193] Aircraft Noise Committee et al. Estimation of the maximum discrete frequency noise from isolated rotors and propellers. Technical report, Tech Rep Aerounautical Series 76020, ESDU, 2011.

[194] R. J. Jeracki and G. A. Mitchell. Low and high speed propellers for general aviation—performance potential and recent wind tunnel test results. *SAE Transactions*, pages 3549–3561, 1981.

[195] F. Taverna. Advanced airfoil design for general aviation propellers. *Journal of Aircraft*, 21(9):649–657, 1984.

[196] M. Drela. Xfoil: An analysis and design system for low reynolds number airfoils. In *Low Reynolds number aerodynamics*, pages 1–12. Springer, 1989.

[197] M. Drela and H. Youngren. Xrotor: an interactive program for the design and analysis of ducted and free-tip propellers and windmills, 2011.[software] available at: http://web. mit. edu/drela. *Public/web/xrotor/[Accessed 15 November 2012]*, 2015.

[198] D. B. Hanson. Influence of propeller design parameters on far-field harmonic noise in forward flight. *AIAA Journal*, 18(11):1313–1319, 1980.

[199] D. B. Hanson. Near-field frequency-domain theory for propeller noise. *AIAA Journal*, 23(4):499–504, 1985.

[200] M. Roger, D. Acevedo-Giraldo, and M. C. Jacob. Acoustic versus aerodynamic installation effects on a generic propeller-driven flying architecture. *International Journal of Aeroacoustics*, 21(5-7):585–609, 2022.

[201] C. Lee, T. Thrasher, S. Hwang, M. A. Shumway, A. Zubrow, A. J. Hansen, J. Koopmann, Gina B. S., et al. Aedt version 3c [user manual]. Technical report, United States. Department of Transportation. Federal Aviation Administration, 2020.

[202] B. Magliozzi. The influence of forward flight on propeller noise. Technical report, NASA-CR-145105 - NASA, Hamilton Standard Windsor Locks, CT, United States, 1977.

[203] M. V. Lowson. Theoretical studies of compressor noise. Technical report, NASA, 1969.

[204] S. E. Wright. Discrete radiation from rotating periodic sources. *Journal of Sound and Vibration*, 17(4):437–498, 1971.

[205] A. Moore and C. Mead. Reflection of noise from aero engines installed under an aircraft wing. In *9th AIAA/CEAS Aeroacoustics Conference and Exhibit*, page 3151, 2003.

[206] A. Moore. A 3d prediction of the wing reflection of aero engine noise. In *10th AIAA/CEAS Aeroacoustics Conference*, page 2865, 2004.

[207] D. Roy. Doppler frequency shift in a refractive atmosphere. *Journal of Aircraft*, 24(9):577–586, 1987.

[208] Y. Wang and K. M. Li. Doppler's shift on aircraft noise propagation in modern aircraft noise prediction tools. *The Journal of the Acoustical Society of America*, 146(4):2824–2824, 2019.

[209] O. Zaporozhets and L. Levchenko. Accuracy of noise-power-distance definition on results of single aircraft noise event calculation. *Aerospace*, 8(5):121, 2021.

[210] Measurement of sound pressure levels in air. Technical Report ANSI/ASA S1.13-2020, ANSI, 2020.

[211] Aircraft Noise Committee et al. The correction of measured noise spectra for the effects of ground reflection. Technical report, Tech Rep Aerounautical Series 94035, ESDU, 2011.

[212] Prediction method for lateral attenuation of airplane noise during takeoff and landing. Technical Report SAE AIR-1751, Society of Automotive Engineers, 1981.

[213] J. Koopmann, A. Hansen, S. Hwang, M. Ahearn, and G. Solman. The caa aircraft noise contour model: Ancon version 1. Tech. rep. dot-vntsc-faa-16-17, Federal Aviation Administration (FAA), July 2016.

[214] J. Koopmann, A. Hansen, S. Hwang, M. Ahearn, and G. Solman. Aviation environmental design tool (aedt) version 2c technical manual. Technical Report Tech. Rep. DOT-VNTSC-FAA-16-17, Federal Aviation Administration (FAA), July 2016.

[215] Project napkin new aviation, propulsion, knowledge and innovation network: Making zero-carbon emission flight a reality in the uk final report. Technical report, UK Research and Innovation (UKRI), 2022.

[216] J. Stone, D. Groesbeck, and C. Zola. An improved prediction method for noise generated by conventional profile coaxial jets. In *7th Aeroacoustics Conference*, page 1991, 1981.

[217] A. Filippone. Turboprop aircraft noise: Advancements and comparison with flyover data. *The Aeronautical Journal*, 119(1215):565–589, 2015.

[218] L. Leylekian, A. Covrig, and A. Maximova. Aviation noise impact management: Technologies, regulations, and societal well-being in europe, 2022.

[219] N. Cumpsty, D. Mavris, J. Alonso, F. Catalano, C. Eyers, M. Goutines, T. Gronstedt, J. Hileman, A. Joselzon, I. Khaletskii, et al. Independent expert integrated technology goals assessment and review for aircraft and engines. *ICAO Doc*, 10127, 2019.

[220] D. C. Akiwate, A. Parry, P. Joseph, and C. C. Paruchuri. Analytical investigation of propeller-wing interaction noise. In *28th AIAA/CEAS Aeroacoustics 2022 Conference*, page 2877, 2022.

[221] B. Mukherjee. A preliminary investigation of propeller-wing interaction noise for evtol aircraft. 2021.

[222] A. Synodinos, R. Self, and A. J. Torija. Preliminary noise assessment of aircraft with distributed electric propulsion. In *2018 AIAA/CEAS Aeroacoustics Conference*, page 2817, 2018.

[223] M. Bell and R. Ohler. Stuttgart to become regional hub for lilium's planned german network, Oct 2021.

[224] Transport for London — Every Journey Matters. Underground services performance. https://tfl.gov.uk/corporate/publications-and-reports/underground-services-performance.

[225] Transport for London — Every Journey Matters. Our open data. https://tfl.gov.uk/info-for/open-data-users/our-open-data.

[226] TfL. Train station usage. https://data.london.gov.uk/dataset/train-station-usage.

[227] Erick Burgueño Salas. Uk: London underground busiest stations 2020, Sep 2021.

[228] W. Johnson. *Helicopter theory*. Courier Corporation, 2012.

[229] G. J. Leishman. *Principles of helicopter aerodynamics with CD extra*. Cambridge university press, 2006.

[230] O. Rand and V. Khromov. Helicopter sizing by statistics. *Journal of the American Helicopter Society*, 49(3):300–317, 2004.

[231] J. Anderson. *Fundamentals of Aerodynamics (SI units)*. McGraw Hill, 2011.

[232] J. D. Anderson. *Introduction to flight*. McGraw Hill Education, 8th edition, 2016.

[233] W. Johnson. Ndarc nasa design and analysis of rotorcraft. Technical report, 2017.

[234] M. D. Maisel. *The history of the XV-15 tilt rotor research aircraft: from concept to flight*. Number 17. National Aeronautics and Space Administration, Office of Policy and Plans, 2000.

[235] B. Norton. *Bell Boeing V-22 Osprey: tiltrotor tactical transport*. Aerofax, 2004.

[236] S. Markman and B. Holder. Bell/boeing v-22 osprey tilt-engine vtol transport (usa). *Straight up: a history of vertical flight*, 2000.

[237] D. Raymer. *Aircraft design: a conceptual approach*. American Institute of Aeronautics and Astronautics, Inc., 2012.

[238] M. Hepperle. Electric flight – potential and limitations. Technical report, German Aerospace Center.

[239] P. Nathen, A. Strohmayer, R. Miller, S. D. Grimshaw, and J. Taylor. Architectural performance assessment of an electric vertical take-off and landing (e-vtol) aircraft based on a ducted vectored thrust concept, 2021.

[240] Y. Mikhaylik, I. Kovalev, C. Scordilis-Kelly, L. Liao, M. Laramie, U. Schoop, and T. Kelly. 650 wh/kg, 1400 wh/kg rechargeable batteries for new era of electrified mobility. In *Sion Power, Nasa Aerospace Battery Workshop*, 2018.

[241] D. Amargianitakis, R. H. Self, A. R. Proença, A. R. Synodinos, and A. J. Torija. Towards predicting noise-power-distance curves for propeller and rotor powered aircraft. In *INTER-NOISE and NOISE-CON Congress and Conference Proceedings*, volume 263, pages 3909–3920. Institute of Noise Control Engineering, 2021.

[242] J. H. McMasters and R. M. Cummings. Rethinking the airplane design process: An early 21st century perspective. (2004-0693), 2004.

[243] S. Gudmundsson. *General Aviation Aircraft Design: Applied Methodsband Procedures*. Elsevier, September 2013.

[244] J. G. Leishman. *Principles of helicopter aerodynamics*. Cambridge University Press, 2017.

[245] M. D Maisel. *The history of the XV-15 tilt rotor research aircraft: from concept to flight*. Number 17. National Aeronautics and Space Administration, Office of Policy and Plans, 2000.

[246] A. M. Stoll, J. Bevirt, M. D. Moore, W. J. Fredericks, and N. K. Borer. *Drag Reduction Through Distributed Electric Propulsion*.

[247] Airworthiness standards: Transport category airplanes, federal aviation administration regulations, title 14, part 25 (far 25). Technical report, January 2017.

[248] EASA. Airworthiness standards: Normal category airplanes, federal aviation administration regulations, title 14, chapter i, part 23 (far 23). Technical report, European Aviation Safety Agency, 2019.

[249] August 2015.

[250] M. Drela and M. B. Giles. Viscous-inviscid analysis of transonic and low reynolds number airfoils. *AIAA journal*, 25(10):1347–1355, 1987.

[251] M. Drela. Integral boundary layer formulation for blunt trailing edges. In *7th Applied Aerodynamics Conference*, page 2166, 1989.

[252] M. Drela. Low-reynolds-number airfoil design for the mit daedalus prototype-a case study. *Journal of Aircraft*, 25(8):724–732, 1988.

[253] E. E. Larrabee. Practical design of minimum induced loss propellers. *SAE Transactions*, pages 2053–2062, 1979.

[254] E. E. Larrabee and S. E. French. Minimum induced loss windmills and propellers. *Journal of Wind Engineering and Industrial Aerodynamics*, 15(1-3):317–327, 1983.

[255] E. E. Larrabee. Five years experience with minimum induced loss propellers-part i: Theory. *SAE Transactions*, pages 1130–1137, 1984.

[256] S. Goldstein. On the vortex theory of screw propellers. *Proceedings of the Royal Society of London. Series A, Containing Papers of a Mathematical and Physical Character*, 123(792):440–465, 1929.

[257] J. Katz. A discrete vortex method for the non-steady separated flow over an airfoil. *Journal of Fluid Mechanics*, 102:315–328, 1981.

[258] P. Klein. Parametric modeling and optimization of advanced propellers for next-generation aircraft. 2017.

[259] P. J. W Block. *Experimental study of the effects of installation on single-and counter-rotation propeller noise*, volume 2541. National Aeronautics and Space Administration, Scientific and Technical, 1986.

[260] G. L. Stefko and R. J. Jeracki. Wind-tunnel results of advanced high-speed propellers at takeoff, climb, and landing mach numbers. Technical report, 1985.

[261] B. M. Brooks and F. B. Metzger. Acoustic test and analyses of three advanced turboprop models. Technical report, 1980.

[262] A-21 Aircraft Noise Measurement Aviation Emission Modeling. *Gas Turbine Jet Exhaust Noise Prediction*, jan 2021.

[263] R. G. Hoch, J. P. Duponchel, B. J. Cocking, and W. D. Bryce. Studies of the influence of density on jet noise. *Journal of Sound Vibration*, 28(4):649–668, 1973.

[264] S. P. Pao. A correlation of mixing noise from coannular jets with inverted flow profiles. Technical report, 1979.

[265] J. W. Russell. A method for predicting the noise levels of coannular jets with inverted velocity profiles. Technical report, NASA, 1979.